Tracking the short life of highly reactive carbocations:
From the ultrafast bimodal photogeneration
to bimolecular reactions without diffusion

Christian Frank Sailer

Dissertation
an der Fakultät für Physik
der Ludwig-Maximilians-Universität
München

vorgelegt von
Christian Frank Sailer
aus Ulm

München, im November 2012

Erstgutachter: Prof. Dr. E. Riedle
Zweitgutachter: Prof. Dr. H. Mayr

Tag der mündlichen Prüfung: 14.12.2012

Kurzfassung

Carbokationen gehören zu den wichtigsten reaktiven Intermediaten in der organischen Chemie. Von zentralem Interesse ist hierbei ihre Bildung sowie der Ablauf der von ihnen eingegangenen chemischen Reaktionen. Das Wissen, das in den letzten Jahrzehnten über die Reaktionen von Carbokationen gewonnen wurde, stützt sich dabei auf die Auswertung von empirischen Untersuchungen. Eine direkte Beobachtung der Bildungs- bzw. Reaktionsmechanismen selbst ist mit diesen Methoden aber nicht möglich. Im Rahmen dieser Arbeit gelang es mit Hilfe der ultraschnellen transienten Absorptionsspektroskopie einen tiefen Einblick in diese Prozesse zu erlangen. Des Weiteren konnte die Wichtigkeit der bei der Photolyse häufig erzeugten Radikalpaare für die Erzeugung von Carbokationen aufgezeigt werden.

Mit Hilfe eines Aufbaus mit höchster zeitlicher Auflösung von unter 50 fs gelang die direkte Beobachtung des Bindungsbruches nach UV-Anregung von Benzhydrylchlorid. Es konnte dabei gezeigt werden, dass die photolytisch erzeugten Radikalpaare um ca. 80 fs und die Ionenpaare um 125 fs verzögert nach der Anregung erscheinen. Die Verzögerung entsteht durch die träge Bewegung des Wellenpakets im angeregten Zustand in Richtung zweier aufeinander folgender konischer Durchschneidungen, die zu Radikalen bzw. Kationen führen. Die exakte Lage der Durchschneidungen und der Pfad des Wellenpaketes ist demnach ausschlaggebend für die Aufteilung in die beiden Produktkanäle.

Nach dem ultraschnellen Bindungsbruch sind die beiden Fragmente noch in der ursprünglichen Geometrie. Die darauf folgende Relaxation in den nächsten hunderten Femtosekunden geht einher mit starken Veränderungen der elektronischen Zustände. Dies führt zusammen mit der Solvatation zum beobachteten Anstieg des optischen Signals von etwa 300 fs sowohl beim Kation als auch beim Radikal.

Weitere Carbokationen entstehen durch einen Elektronentransfer innerhalb des Radikalpaars, der erst durch diffusive Trennung des Radikalpaars unterbunden wird. Die beobachtete Ausbeute und Dynamik dieser Konversion können mit Hilfe von Simulationen von abstandsabhängigen Radikal- und Ionenpopulationen verstanden werden, die Diffusion und abstandsabhängige Reaktionen explizit einbeziehen. Das bekannte Fehlen von Carbokationen in Lösungsmitteln wie Dichlormethan auf der Nanosekundenzeitskala kann der extrem effizienten geminaten Rekombination des Ionenpaars zugeschrieben werden.

Dieser Nachteil kann umgangen werden, wenn anstatt des geladenen Chloridions das neutrale Triphenylphosphan als Abgangsgruppe verwendet wird. Damit konnten auch in wenig polaren Lösungsmitteln erhebliche Carbokationenausbeuten realisiert werden. Das zur Stabilisierung vorhandene Gegenion kann dabei jedoch, abhängig von den Bedingungen, weitere Reaktionskanäle ermöglichen, die die Kationenausbeute verringern.

Das Beobachten ultraschneller, bimolekularer Reaktionen erfordert, dass die Reaktionspartner in unmittelbarer Nachbarschaft vorliegen. Dies wurde zum einen durch die photolytischen Erzeugung zweier Fragmente innerhalb einer inversen Mizelle realisiert. Die geminate Rekombination zwischen den beiden ist hierbei nicht beeinflusst von Diffusion. Die gemessene Rate entspricht daher dem intrinsischen Reaktionsprozess.

Eine sehr allgemeine Möglichkeit, die im Rahmen dieser Arbeit erarbeitet wurde, ist die ultraschnelle, bimolekulare Reaktion eines photolytisch erzeugten Carbokations mit dem Lösungsmittel. Abhängig von der Wahl des erzeugten Kations und des Lösungsmittels wurden Reaktionen mit Raten zwischen $(388\ ps)^{-1}$ bis zu $(2.6\ ps)^{-1}$ gefunden. Neben der Reaktivität des Kations hängt die Rate dabei vor allem von der Größe der Lösungsmittelmoleküle ab. Vergleiche mit Reaktionen auf langsameren Zeitskalen legen dabei nahe, dass die Reaktionsgeschwindigkeiten auf der Pikosekunden-Skala von molekularen Bewegungen – etwa Rotationen – limitiert werden.

Summary

Carbocations belong to the most important reactive intermediates in organic chemistry. Understanding their generation and the course of chemical reactions where carbocations are involved is hereby of central interest. The knowledge about the reactions of carbocations gained during the last decades is based on the evaluation of empiric investigations. They do not allow, however, for a direct observation of the formation and the reaction mechanism. In the framework of this thesis, a deep insight into these processes was gained with the aid of ultrafast transient absorption spectroscopy. The measurements furthermore revealed the importance of the concomitantly formed radical pairs for the generation of carbocations.

The direct observation of the bond cleavage after UV excitation of benzhydryl chloride was possible with the aid of a setup with highest temporal resolution below 50 fs. The photolytically generated radical and ion pairs are delayed by about 80 fs and 125 fs with respect to the excitation. The delay is caused by the inertial motion of the excited wavepacket towards two successive conical intersections leading to radicals and cations. The exact position of the conical intersections and the path of the wavepacket therefore determines the partitioning into the two product channels.

After the ultrafast bond cleavage, the two fragments are still in a geometry close to that of the precursor. The subsequent relaxation in the next hundreds of femtoseconds is hereby associated with strong changes of the electronic states. This leads to the observed rise of the optical absorption signal for the cation as well as for the radical band.

Further carbocations can be formed by an electron transfer within the radical pair which is eventually terminated by diffusional separation of the radical pairs. The observed yields and dynamics of the interconversion can be understood with the aid of simulations involving distance dependent radical and ion pair populations which are subject to diffusion and distance-dependent reactions. The simulations furthermore reveal that the absence of carbocations on the nanosecond time scale in solvents such as dichloromethane is caused by an extremely efficient geminate recombination of the ion pairs.

This disadvantage can be circumvented by using the neutral triphenylphosphine instead of the charged chloride ion as leaving group. It allows for the generation of carbocations with a reasonable yield even in solvents of moderate polarity. Attention has to be paid, however, to the choice of the counterion. Depending on the experimental conditions, the counterion can open up further reaction channels which deteriorate the cation yield.

The observation of ultrafast, bimolecular reactions requires the immediate vicinity of reaction partners. This was implemented on the one hand by the photolytical generation of two fragments in a reverse micelle. Here, the geminate recombination between both fragments is not influenced by diffusion. The measured rate therefore corresponds to the intrinsic reaction process.

A general possibility, which was established within this work, is the ultrafast, bimolecular reaction of a photolytically generated carbocation with the solvent. Depending on the choice of the generated cation and the solvent, rate constants from $(388 \text{ ps})^{-1}$ up to $(2.6 \text{ ps})^{-1}$ were found. Besides the reactivity of the cation, the size of the solvent molecule is the factor which influences the rate the most. Comparisons with reactions on slower time scales suggest that the reaction rates on the picosecond scale are limited by molecular motions such as rotations.

Publications

This thesis is based on the following publications reprinted in the appendices D1-D6:

1   **Sub-50 fs broadband absorption spectroscopy with tunable excitation: putting the analysis of ultrafast molecular dynamics on solid ground**
U. Megerle, I. Pugliesi, C. Schriever, C. F. Sailer, E. Riedle
Applied Physics B: Lasers and Optics 96, 215-231 (2009).

2   **Encapsulation of Diphenylmethyl Phosphonium Salts in Reverse Micelles: Enhanced Bimolecular Reaction of the Photofragments**
C. F. Sailer, R. B. Singh, J. Ammer, E. Riedle, I. Pugliesi
Chemical Physics Letters 512, 60-65 (2011).

3   **Build-up and Decay of the Optical Absorption in the Ultrafast Photo-Generation and Reaction of Benzhydryl Cations in Solution**
B. P. Fingerhut, C. F. Sailer, J. Ammer, E. Riedle, R. de Vivie-Riedle
Journal of Physical Chemistry A, DOI: 10.1021/jp300986t (2012).

4   **Photolytic Generation of Benzhydryl Cations and Radicals from Quaternary Phosphonium Salts: How Highly Reactive Carbocations Survive Their First Nanoseconds**
J. Ammer, C. F. Sailer, E. Riedle, H. Mayr
Journal of the American Chemical Society 134, 11481-11494 (2012).

5   **A Comprehensive Microscopic Picture of the Benzhydryl Radical and Cation Photo-Generation and Interconversion through Electron Transfer**
C. F. Sailer, S. Thallmair, B. P. Fingerhut, C. Nolte, J. Ammer, H. Mayr, R. de Vivie-Riedle, I. Pugliesi, E. Riedle
To be submitted to ChemPhysChem.

6   **Ultrafast photochemical reaction with two product channels: wavepacket motion through two distinct conical intersections**
C. F. Sailer, N. Krebs, B. P. Fingerhut, R. de Vivie-Riedle, E. Riedle
To be submitted to Physical Review Letters.

Contents

x

1. Introduction

Organic molecules, i.e. carbon-based molecules, are at the heart of the world as we know it. Their importance can hardly be overestimated as they constitute the building blocks for any known organism. Not only the tissue of the organisms is hereby mainly built of organic molecules, even their vital functions are steered and controlled by an orchestrated interplay of carbon-based molecules.

The last decade has witnessed the advent of electronic devices based on organic molecules. Just as inorganic crystals, organic compounds can act as semiconductors [1]. This opens up a series of important applications comprising organic solar cells as first realized by Michael Grätzel [2] and organic light-emitting diodes (OLEDs) [3] which entered into consumer electronics in the last years. The potential for their low-cost production and their flexibility hereby constitutes their undeniable advantage.

Organic molecules are formed by chemical reactions between precursors and can again be converted into further molecules. The exact course of a reaction between two individual molecules is hereby not predetermined and a distribution of products is frequently observed. An in-depth understanding of the reaction processes in organic chemistry and of the species or intermediates involved in the reactions is therefore crucial.

In the last decades, much research effort has been invested to elucidate the physical mechanisms behind chemical reactions on an atomic scale. Due to their relative simplicity, experimentalists and theoreticians hereby mainly focused upon studying the reaction process between small molecules in the gas phase. Seminal developments and results were achieved by Dudley R. Herschbach and Yuan T. Lee upon reactive collisions between molecules by virtue of the crossed molecular beam technique (Nobel Prize in Chemistry 1986) [4,5]. A real-time observation of the reaction process itself was, however, not possible. It needed the integration of ultrashort laser pulses for a direct observation of the processes involved (Nobel Prize in Chemistry for Ahmed H. Zewail 1999). For this, a van der Waals complex of two molecules is excited by a short light pulse which leads to fragmentation of one of the molecules. The hot fragment can then attack the second molecule resulting in the formation of new molecules which can be detected spectroscopically [6].

The majority of reactions between organic molecules occuring in nature or carried out in chemistry laboratories takes place, however, in solution. The large number of solvent molecules, their thermal motion and their interactions with the reactants complicate the description of the system. In many cases the solvent itself is directly involved in the course of the reaction. Therefore, the underlying reaction mechanisms have so far been determined via indirect approaches such as intermediate trapping or product studies. These rather empiric methods allowed to identifiy several reaction classes.

An important class of reactions in organic chemistry are the nucleophilic substitutions in which the leaving group X^- of a substrate R-X is replaced by the nucleophile Y^- (neutral leaving groups or nucleophiles are also possible). The nucleophile exhibits an electron pair which, after the reaction, is located on the leaving group [7]:

$$R\text{--}X + Y^- \longrightarrow R\text{--}Y + X^-$$
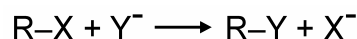
Two important types of nucleophilic substitutions are distinguished:

- In the S_N2 mechanism, the substrate is attacked by the nucleophile on the position opposite to the leaving group. The bond formation between the nucleophile and the substrate and the cleavage of the bond between the substrate and the leaving group are hereby simultaneous.
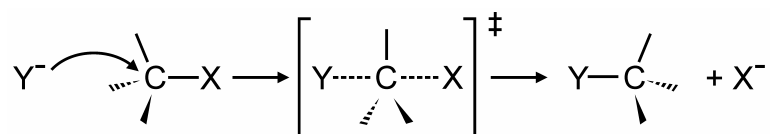

- The S_N1 mechanism proceeds in two steps. In the slow first step, the substrate is ionized (i.e., it dissociates) and a carbocation is formed. In the second step the intermediate carbocation undergoes a fast reaction with the nucleophile:
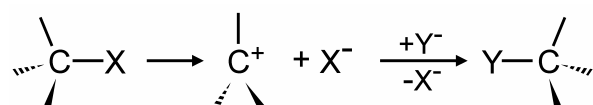
The intermediately formed carbocations constitute one of the most important classes of reactive intermediates [8]. They are organic molecules which exhibit a positively charged carbon atom. As these carbon atoms are electron deficient they are often highly reactive and only highly stabilized carbocations can be observed under ordinary conditions. Pioneering work on these species has been accomplished by George A. Olah which earned him the Nobel Prize in Chemistry in 1994. He found that a large series of carbocations can be generated and stabilized in superacidic solution [8,9]. This discovery allowed Olah and others to investigate the properties of carbocations as well as their chemistry.

The study of chemical reactions of carbocations on the femto- to nanosecond time scale requires a technique for their ultrafast generation under controlled conditions. Such fast reactions cannot be studied by conventional methods, because the reaction times are shorter than the time required for the mixing of the reagents, even when fast methods such as the stopped-flow technique are employed. A possible ultrafast approach is the photochemical production of carbocations R^+ by irradiation of suitable neutral (R-X) or charged (R-X$^+$) precursors according to

$$R\text{--}X \xrightarrow{h\nu} R^+ + X^- \quad \text{or} \quad R\text{--}X^+ \xrightarrow{h\nu} R^+ + X$$
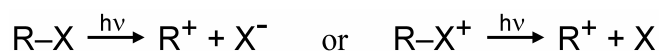
with the (photo-)leaving group X^- or X [10-13]. The photoinduced heterolysis of the precursor can proceed on the sub-picosecond time-scale [14,15] which opens up the observation and investigation of ultrafast processes and reactions of the generated carbocations.

The photolytic generation of carbocations and their detection with femtosecond resolution allow hereby for the direct examination of the first instants of their generation and the subsequent evolution – processes which are not accessible experimentally otherwise. As the leaving group is located in the immediate vicinity of the nascent carbocation, it is conceivable that it plays an important role in the first hundreds of picoseconds in the life of the cations. Only the increase in the mean distance between the two photofragments by diffusion eventually terminates the influence of the leaving group, at least on the sub-nanosecond time scale. Furthermore, the photolysis is frequently accompanied by homolytic bond cleavage which results in a pair of radicals as photofragments. This opens up an alternative pathway for ion pair generation by electron transfer in the radical pairs. The exact mechanism and processes was, however, unclear.

Benzhydryl cations constitute an important class of carbocations which can be generated by photolysis from a series of precursors. Their reactivity can be easily changed over orders of magnitude by suitable substitution on the two phenyl rings. With the aid of benzhydryl cations, a comprehensive electrophilicity and nucleophilicity scale was developed which allows to indicate the reactivity of electrophiles, i.e. electron pair acceptors such as carbocations, and nucleophiles, which can act as electron pair donors [16-19]. The second-order rate constant k (in units of $M^{-1}s^{-1}$) of reactions between an electrophile and a nucleophile can be predicted by the linear free energy relationship:

$$\log k = s\left(N + E\right).$$

The electrophilicity parameter E, the nucleophilicity parameter N and the parameter s are hereby determined empirically by the measurement of the reaction rate for a large number of electrophile-nucleophile combinations on the minutes to nanosecond time-scale. The large set of benzhydryl cations with well-known electrophilicities constitute hereby a prime basis for the investigation of reactions on the ultrafast timescale.

In the framework of this thesis, the quantitative femtosecond transient absorption spectroscopy of carbocations and carbon radicals has been established. Chapter 2 presents the experimental and analytical techniques needed for the observation of theses species and to understand the processes they undergo. For the measurements, a broadband transient absorption spectrometer was developed which allows for the detection of small absorption changes over a large spectral and temporal range. In contrast to typical transient absorption measurements of dye molecules, the precursor solutions studied in this work can degrade rapidly. A short measurement time and an independent examination of the integrity of the sample are therefore essential. Two techniques, namely the interleaving scale and the on-line measure-

ment of the UV/Vis absorption spectra of the sample, were therefore developed. Since the observed processes can be described only in part by classical rate models, new fit functions had to be introduced which account for the modified dynamics. A quantitative evaluation of the transient spectra then allows for an in-depth analysis of the observed processes beyond a mere indication of time or rate constants. The obtained yields and quantum yields provide further insight into the mechanism, and comparisons between different measurements are rendered possible. It was furthermore found, that the transient absorption bands assigned to carbocations and carbon radicals undergo a temporal shift. The shift of the absorption band maxima can be determined by an iterative algorithm with a precision better than 0.1 nm.

With the aid of the introduced experimental and analytical tools, Chapter 3 sheds light on the photo-generation of carbocations and carbon radicals and the processes they undergo subsequent to the bond cleavage. In Section 3.1, the range of precursors studied within this work and the generated carbocations are presented. By introducing substituents on the phenyl rings of the benzhydryl cations, their electrophilicity – and thus their reactivity towards nucleophiles – can be easily changed. The two classes of precursors – neutral benzhydryl chlorides and benzhydryl phosphonium salts – allow to study the influence of the charge on the processes.

The direct observation of the photo-induced bond cleavage for the benzhydryl chlorides leading to radical pairs and ion pairs is presented in Section 3.2. The measurements with highest temporal resolution show that the process cannot be understood in terms of a classical rate model with competing stochastic processes leading to the two observed photoproducts. It must rather be described by the inertial motion of a nuclear wavepacket which is generated by the excitation of the precursor. The passage of two successive conical intersection then leads to the formation of the two photoproducts, benzhydryl cations and radicals.

The subsequent increase of the optical absorption signal within the first picosecond found for a wide range of photo-generated benzhydryl cations and radicals is explained in Section 3.3. It does not originate from the bond cleavage as suggested by earlier studies. The signal increase is rather caused by geometric relaxation and solvation of the nascent photofragments directly after the bond cleavage. These rearrangements are associated with the strength and energetic location of transitions leading to a changing absorption band shortly after the bond cleavage.

The radical pairs generated by photolysis of benzhydryl chloride are in polar solvents thermodynamically less favorable than a pair of ions. The resulting electron transfer leading to the ion pair is only terminated when the mean distance between the radicals becomes too large. As demonstrated in Section 3.4, the electron transfer, the possible recombination and the escape of all species involved in the process can be described by a combined Marcus-Smoluchowski model. It furthermore shows that the insufficient electrostatic shielding of the

ion pair provided by moderately polar solvents, such as dichloromethane, is responsible for the negligible carbocation yield on the nanosecond time scale.

This limitation can be circumvented by the use of phosphonium salts in which the leaving group is uncharged (Section 3.5). They allow for high cation quantum yields even in solvents of rather low polarity. Through the introduction of the counterion, new reaction channels emerge which are operational depending on the precursor concentration, the solvent and the nature of the photolyzed phosphonium salt.

Bimolecular reactions of carbocations with appropriate reactants in solution are usually rather slow as the mean separation between two reactants is large. Since a reaction is only possible when they encounter by diffusion, the reactions take place on the nanosecond time scale or slower. For the investigation of ultrafast bimolecular reactions on the picosecond scale or below new experimental approaches had therefore to be established. In particular, the influence of diffusion on the observed dynamics has to be eliminated which can be accomplished by the encapsulation of two reactants in a reverse micelle as described in Section 3.8. An encapsulated precursor molecule is photolyzed which leads to a benzhydryl cation and the leaving group within the restricted environment. The geminate recombination of the photofragments is therefore not terminated by diffusional separation as observed for the pair generated in bulk solution.

A novel approach to observe ultrafast bimolecular reactions without diffusion is established in Chapter 4. Hereby, the carbocation is generated photolytically in alcohols with which it can react ultrafast. It is furthermore guaranteed that the cation is always encompassed by reactants. The cations were generated from precursors with the rather small and negatively charged chloride as leaving groups, or the electrically neutral and much bulkier triphenylphosphine. The influence of the leaving group on the bimolecular reactions is summarized in Section 4.1.

The ultrafast bimolecular reactions of a large range of benzhydryl cations (Section 4.3) with a series of alcohols (Section 4.2) was investigated. For slower bimolecular reactions of benzhydryl cations with alcohols taking place on the minute to nanosecond time scale, a large set of rates was reported. This data allow for a qualitative and quantitative comparison with the ultrafast reaction rates (Section 4.4). The trend found in the slower measurements, that higher electrophilicity leads to a faster rate, is preserved even for reactions on the single picosecond scale. In contrast to the slower reactions, the length of the alcohols now plays a decisive role for the reaction rate constant. While the fastest rates are observed for the reactions with methanol, reactions with longer alcohols become increasingly slower. The possible origin of this slow-down is discussed in Section 4.5.

2. Ultrafast, quantitative transient absorption spectroscopy

2.1 Femtosecond broadband transient absorption spectroscopy

Many chemical processes such as bond breaking, bond formation, electron or proton transfer, molecular rearrangements and diffusion take place on an ultrafast timescale from a few femtoseconds to pico- and nanoseconds [20]. Pump-probe spectroscopy constitutes a versatile approach to measure ultrafast dynamics and is used in many variations to study the course of a reaction.

The basic idea behind this technique is to induce a well-defined perturbation to the studied system with a first short light pulse (called pump). The second pulse (called probe) then interrogates the change of the sample after a well-defined temporal delay. In femtosecond broadband transient absorption spectroscopy the sample is excited by an ultrashort light pulse typically in the ultraviolet or visible spectral range. The probe pulse detects the change of the optical density (OD) of the sample. Hereby, the utilization of a spectrally broad probe pulse and its wavelength-resolved recording allows for the detection of a variety of processes and/or species within one measurement. Additionally, the interpretation not only relies on the signal measured at one selected wavelength but is supported by the knowledge of the evolution of the absorption spectrum over a large time and wavelength range. This furthermore allows for the recognition of effects such as spectral narrowing or shifts of absorption bands (see Section 2.7).

A schematic of the basic femtosecond broadband transient absorption spectrometer used and developed further within this work is shown in Figure 2.1. It is described in detail in the following publication:

> **"Sub-50 fs broadband absorption spectroscopy with tunable excitation: putting the analysis of ultrafast molecular dynamics on solid ground"**
> *U. Megerle, I. Pugliesi, C. Schriever, C. F. Sailer, E. Riedle*
> Applied Physics B: Lasers and Optics **96**, 215-231 (2009).

The spectrometer is based on a 1-kHz Ti:Sapphire regenerative amplifier, which delivers pulses at a central wavelength of 775 nm and a duration of about 150 fs. The pump is generated by a noncollinear optical parametric amplifier (NOPA) with subsequent second harmonic generation [21-25]. The resulting tunability of the pump wavelength allows for the selective excitation of chosen molecular absorption bands. With the aid of a prism compressor 30 fs-pulses at the position of the sample are readily achievable. The compressor is introduced directly after the NOPA and (pre-)compensates for the chirp introduced by dispersive elements in the optical path of the pump beam. A broadband probe pulse spanning from 285 nm to 720 nm is generated by focusing a small part of the laser fundamental in a cal-

cium fluoride (CaF$_2$) crystal [26-28]. The relative orientation of the pump and probe polarization is set by a half-wave plate in the pump beam after the last mirror (see Section 3.6 for a discussion of the effects linked to the relative pump-probe polarization orientation).
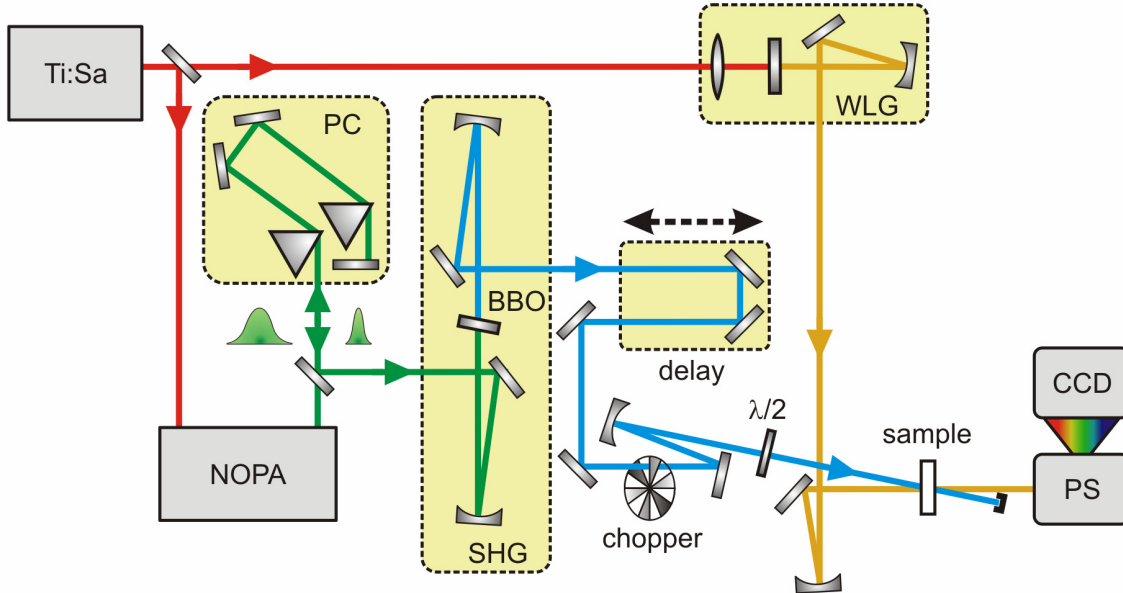
Figure 2.1: Scheme of the femtosecond broadband transient absorption setup. NOPA: noncollinear optical parametric amplifier; PC: prism compressor; SHG: second harmonic generation; BBO: β-barium borate crystal; λ/2: half-wave plate; WLG: white light generation; PS: prism spectrograph.

The pump and probe pulses are focused into the sample and are brought to a maximal spatial overlap. The temporal delay between the pump and the probe pulse is defined by the difference of the optical path length for the two pulses. It can be controlled by a linear translation stage introduced in the pump beam. It allows to adjust the delay up to about 2 ns with a <5 fs precision. While the focal diameter of the probe is typically 30 μm the pump should be significantly larger. This provides the needed robustness of the measured transient signal against small changes in the position of the pump beam, e.g., originating from a non-perfectly aligned translation stage or a slightly diverging pump beam.

After the sample, the probe whitelight is spectrally resolved in a prism spectrograph and detected with a CCD operating at 1 kHz. Since the chopper in the pump branch blocks every second pulse, the CCD records alternately spectra when the pump was blocked (commonly abbreviated with T$_0$) and spectra when the sample was excited by the pump (T). The transmitted spectra T is connected with the concentration c of the absorbing species by the Lambert-Beer Law

$$T = T_0 \cdot 10^{-\mathrm{OD}} = T_0 \cdot 10^{-\varepsilon cd} \tag{2.1}$$

with the optical density of the sample OD, the molar absorption coefficient ε and the sample thickness d (see Section 2.5). The spectrally resolved transmission change of the sample upon excitation is then given by T/T_0. Finally, the transmission change is converted into the change in optical density $\Delta OD = -\log T/T_0$ since ΔOD is the unit closer to the molecular realm: ΔOD is linear in the concentration of the detected species and equals zero if no absorption change is observed.

In Figure 2.2 the observed transient absorption after 270 nm excitation of (tol)$_2$CH-DPPBS in dichloromethane is shown as an exemplary data set (see Table 3.2 for the structure of the molecule). A false color representation of the measured signal is depicted in Figure 2.2b: red colors indicate high transient absorption, blue colors low absorption. The time axis is linear between -1 ps and 1 ps and logarithmic beyond. Transient spectra at selected, characteristic times (see Figure 2.2a) from the temporally and spectrally resolved data allow to identify the optical signatures of the species involved in the photo-induced dynamics. Their kinetics can be followed with the aid of the time-dependent absorption signal at wavelength intervals connected to the species under investigation (shown in Figure 2.2c).
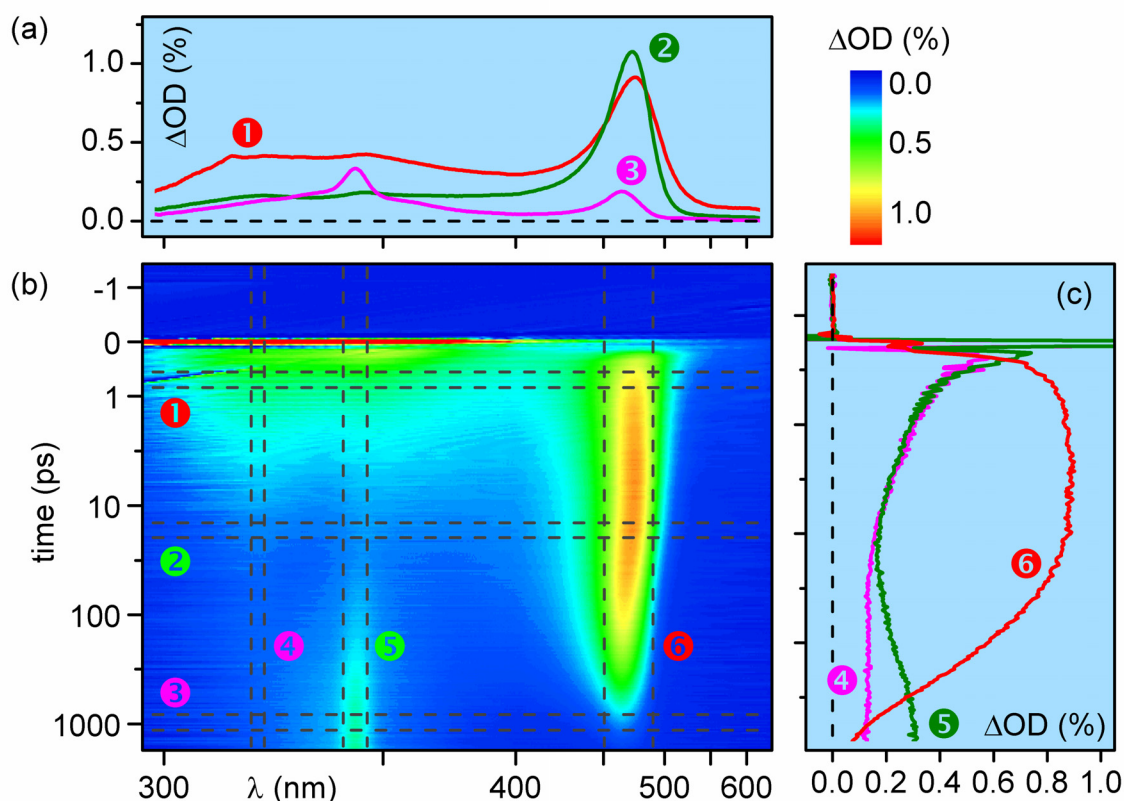
Figure 2.2: Transient absorption measured after UV excitation of (tol)$_2$CH-DPPBS (see Table 3.2 for the structure of the molecule) in dichloromethane. a) Transient Spectra at selected delay times ❶, ❷ and ❸. b) False color representation of the time and wavelength resolved data. c) Time dependence of the absorption signal at selected wavelength intervals ❹, ❺ and ❻. The grey dashed lines indicate the selected regions for the profile representation in a) and c).

Signal Contributions in Transient Absorption Spectra. A series of different transient signals can occur after photoexcitation of molecules in a sample and therefore contribute to the observed transient absorption spectrum:

- **Excited State Absorption,** corresponding to a transition from the excited state to a higher electronic state, e.g., $S_5 \leftarrow S_1$. It leads to an increase in the absorbance of the sample ($\Delta OD > 0$).

- **Ground State Bleach** due to a decreased population of molecules in the electronic ground state and a following increased transmittance ($\Delta OD < 0$).

- **Stimulated Emission**: When a probe photon is in resonance with an transition of an excited molecule to a lower-lying state (e.g., from S_1 to S_0), it can stimulate the emission of a further photon. This photon has the same wavelength and direction as the probe photon and therefore leads to more probe light on the detector at that specific wavelength ($\Delta OD < 0$).

- **Product Absorption**: After photoexcitation the molecule can undergo a chemical reaction such as isomerization, electron transfer or the cleavage of a bond. Frequently, the newly formed products exhibit absorption bands in the UV/Vis spectral range ($\Delta OD > 0$). If the molar absorption coefficient ε_{prod} of the product is known, e.g., from steady state measurements or actinometry, it is possible to determine the product concentration and the quantum yield $\Phi_{product}$ leading to the product (see Section 2.3).

Furthermore, there are coherent signal contributions stemming from non-linear interactions between pump and probe. Especially important for the transient absorption spectroscopy are two-photon absorption, cross phase modulation and stimulated Raman amplification [29]. By these interactions probe photons are depleted as long as the pump-probe delay is within the cross correlation of the pump and probe pulse convoluted with the electronic dephasing time of the sample. Since typical dephasing times are on the order of few tens of femtoseconds [30,31] these signal contributions only occur about 100 fs around time-zero. Although part of the coherent signal originates from non-linear pump-probe interaction with the studied molecule [32] the major part is generated within the solvent and the flow cell windows (see Section 2.5).

Advancing to the nano- and microsecond time scale. The control of the time delay between pump and probe by increasing and decreasing the optical path length of the pump pulse limits the accessible time range to several nanoseconds. Longer delays cannot be realized since all beam parameters – namely the beam position in the sample and the focal diameter – have to be kept constant when introducing additional path length. This turns out to be impossible

for delays larger than several nanoseconds (10 ns delay correspond to 3 m additional path length).
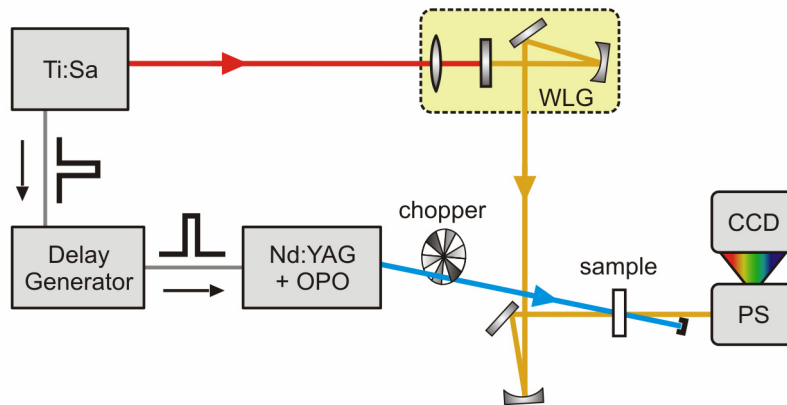
Figure 2.3: Scheme of the modified transient absorption spectrometer (compare to Figure 2.1) for measurements from nanoseconds to microseconds.

In order to measure at delay times longer than about 2 ns a Nd:YAG-pumped OPO was implemented replacing the Ti:Sapphire-pumped NOPA as source of the pump pulses. The OPO generates pump pulses with 2 ns to 3 ns pulse length tunable from 210 nm to the IR. The light pulses can be triggered electronically by the Ti:Sapphire and exhibit a timing jitter smaller than 200 ps with respect to pulses of the Ti:Sapphire. For transient absorption measurements, the time delay between the pump pulses (from the OPO) and the probe pulses (still generated by the Ti:Sapphire) can be controlled by the help of two delay generators [33] (see Figure 2.3 for a scheme of the setup). The small changes on the setup needed and the fast disposition of the pump light generated by the OPO thus allows for two consecutive measurements: a transient absorption measurement with femtosecond resolution for time delays up to 2 ns and a further measurement with nanosecond resolution from 2 ns up to hundreds of microseconds.

2.2 Fitting the dynamics of photo-induced processes

An important step in understanding the measured transient absorption spectra and therefore the photo-induced process, is the numerical fitting of an adapted model to the data. This allows to specify time or rate constants for certain processes and allows for a deeper insight into the sequence of induced processes.

The commonly implemented numerical data analysis fits a sum of exponential functions with different amplitudes and time constants to the transient absorption data. It is multiplied with the Heaviside step function $\Theta(t)$ and convoluted with the instrumental response function which accounts for the finite time resolution of the setup [34]:

$$F(t) = IRF(t) \otimes \left\{ \theta(t) \cdot \left[\sum_i A_i \exp\left(-\frac{t}{\tau_i} \right) + \text{const.} \right] \right\} + \text{coherent artifact} . \quad (2.2)$$

The instrumental response function IRF is a Gaussian-shaped function:

$$IRF(t) = \frac{1}{w\sqrt{\pi}} \exp\left(-4\ln 2 \frac{t^2}{\tau_{FWHM}^2} \right) \quad (2.3)$$

$$\text{with} \quad w = \frac{1}{2\sqrt{\ln 2}} \tau_{FWHM} \quad (2.4)$$

The width of the IRF τ_{FWHM} is given by the cross correlation between pump and probe and might be increased by group velocity mismatch [35]. The convolution with the sum of exponential functions can be solved analytically with the aid of the error function erf(t) and the fit function can be written as:

$$F(t) = \sum_i A_i \cdot \exp\left(\left(\frac{w}{2\tau_i} \right)^2 - \frac{t}{\tau_i} \right) \cdot \frac{1 - \text{erf}\left(\frac{w}{2\tau_i} - \frac{t}{w} \right)}{2} + \text{coherent artifact} \quad (2.5)$$

The coherent signal contributions (commonly called coherent artifact) around time-zero can be fitted by a Gaussian function with the same width as the IRF and its first and second derivatives.

The fit function F(t) is based on several assumptions [36]. It supposes that the complete reaction can be described by invoking well-defined intermediate states with populations N_i and transitions between them. Each state can be assigned a fix, time-invariant spectrum. Therefore, temporal changes of the spectrum – e.g., by solvation or vibrational cooling – can not be modeled. It furthermore assumes that the population change of every intermediate state can be fully described by a system of coupled differential equations:

$$-\frac{dN_i}{dt} = \sum_m \left(-k_{mi} N_m + k_{im} N_i \right) \quad (2.6)$$

where $k_{mi}N_m$ describes the rise of the population N_i due to transfer of population from N_m and $k_{im}N_i$ the transfer process vice versa. Furthermore, it is assumed that the evolution of the populations from the initial conditions starts at t = 0. While these assumptions are fulfilled for a large range of studied system, at least two exceptions exist leading to a deviating dynamics:

- As shown in Section 3.4, the rates for certain processes can be time-dependent which leads to non-exponential dynamics.

- The excitation of a molecule with an ultrafast pump pulse leads to the formation of a wave-packet on the excited state potential energy surface which can propagate on this surface. The encounter of a conical intersection can lead to an ultrafast transition to another potential energy surface. Thus, the transition is temporally delayed with regard to the pump pulse. Furthermore, the assignation of a rate to this process is not meaningful since there is no constant probability of the process to happen. It can be rather described by a jump in the population at a defined delay time.

Therefore, the fit function F(t) has to be adapted to account for the changed preconditions.

Fitting a time-dependent rate with a stretched exponential. As it is shown in Section 3.4 the electron transfer dynamics observed after UV excitation of benzhydryl chlorides is clearly non-exponential since the rate is time-dependent. More general, many processes with a time-dependent rate posses stretched exponential dynamics [37], where the temporal evolution of a signal is given by

$$A(t) = A_{SE} \exp\left[-(t/\tau_{SE})^{\beta} \right] \tag{2.7}$$
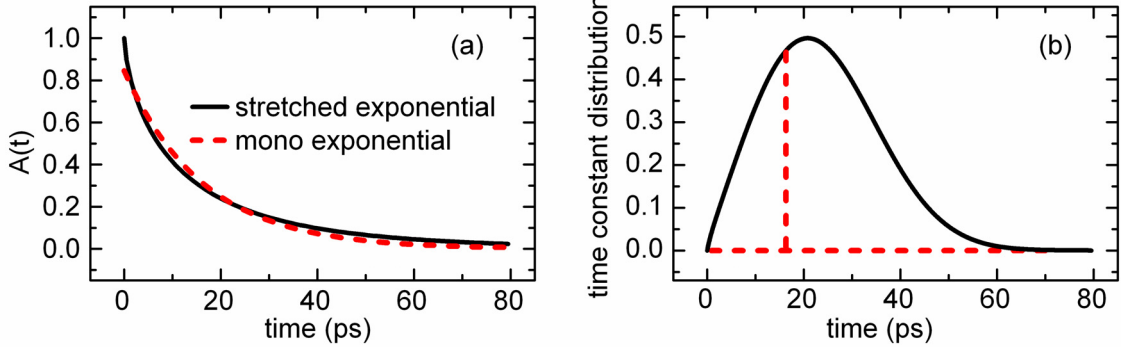
with the stretched exponential time constant τ_{SE} and the stretching parameter β. The average time constant for the stretched exponential is given by [37]

$$\langle \tau \rangle = \int_0^{\infty} \exp\left[-(t/\tau_{SE})^{\beta} \right] \cdot dt = \tau_{SE}\, \Gamma\left(1 + \frac{1}{\beta} \right) \tag{2.8}$$

In many cases it is sufficient to set $\beta = 0.5$ to reproduce the observed dynamics. This prevents the introduction of additional free fit parameters. With $\beta = 0.5$ the average time constant is $\langle \tau \rangle = 2\,\tau_{SE}$.

Compared to an exponential function, the stretched exponential exhibits a faster decay in the very early stage but a significant part of the signal persists for longer times (see Figure 2.4a). The observation of stretched exponential dynamics thus implies the existence of a broad distribution of time constants (or rates accordingly). For instance, the distribution for $\tau_{SE} = 10$ ps and $\beta = 0.5$ exhibits significant contributions between a few picoseconds up to 50 ps (see Figure 2.4b). This is in strong contrast to mono-exponential functions which are

based on a delta distribution. Broad distributions of rates are found, for example, in heterogeneous biological samples [38] or flexibly linked donor-acceptor systems [39] where the system can have a multitude of configurations with differing rates.

Figure 2.4: a) Comparison between a stretched exponential function with $\tau_{SE} = 10$ ps and $\beta = 0.5$ and a mono-exponential fit ($\tau \approx 16$ ps) to it. b) Distribution of time constants leading to the functions shown left. For the mono-exponential function the delta distribution is shown schematically.

In order to acquire the stretched exponential dynamics (as observed for example at the electron transfer dynamics of benzhydryl chlorides), the fitting function (2.1) was extended as follows:

$$F(t) = IRF(t) \otimes \left\{ \Theta(t) \cdot \left[\sum_i A_i \exp(-t/\tau_i) + A_{SE} \exp\left[-(t/\tau_{SE})^\beta \right] + \text{const.} \right] \right\} + \text{artifact}$$

$$(2.9)$$

In contrast to exponential functions, the convolution of the stretched exponential function with the Gaussian-shaped IRF can not be solved analytically. Therefore, a numerical convolution of the stretched exponential function with the IRF is carried out in the fitting routine.

Fitting delayed dynamics. A delayed starting point for a dynamics with respect to the excitation can be implemented by a time delay Δt as free fit parameter. The fit function then consists of two sums of exponential functions – one starting at time-zero, the second starting at time-zero plus the time delay:

$$F(t) = IRF(t) \otimes \left\{ \Theta(t) \cdot \left[\sum_i A_i \exp(-t/\tau_i) + \text{const.} \right] \right\}$$

$$+ \Theta(t - \Delta t) \cdot \left[\sum_i A_i \exp\left(-\frac{t - \Delta t}{\tau_i} \right) + \text{const.} \right]$$

$$(2.10)$$

$$+ \text{ coherent artifact}$$

The undelayed exponential functions have to be implemented as they account for the instantaneous excited-state absorption and any dynamics of it. Since the coherent artifact is a result of the non-linear interaction between the pump and the probe pulse, the coherent artifact is still centered around the time-zero given by the excitation pulse.
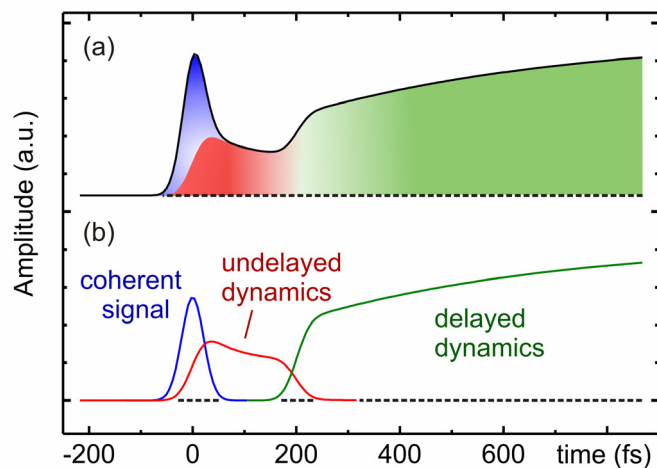
Figure 2.5: a) Simulated transient absorption signal for molecular dynamics delayed to the excitation. b) Signal decomposition with the aid of the fit function (Eq. 2.10) leads to the contributions from the coherent interaction, the undelayed dynamics and the subsequent, delayed dynamics.

Figure 2.5 shows a simulated transient absorption signal for the generic case where a coherent signal, undelayed dynamics as well as delayed dynamics (by 200 fs with respect to the excitation) is observed. A fit with Eq. 2.10 reveals these three contributions and allows to distinguish between them.

2.3 Determination of yields and rates of photoinduced reactions

When evaluating time-resolved transient absorption spectra, fitted time constants are by far not the only information which can be extracted. Especially when the studied molecule undergoes photoinduced chemical transformations the determination of product yields is much more important than the mere knowledge of an exact numerical value for the time constant or rate of the reaction.

The ratio between the number of formed product molecules N_{prod} divided by the number of absorbed photons $N_{ph,abs}$ is called quantum yield Φ_{prod}. Through division by a suitable volume the product quantum yield can be easily expressed in terms of concentrations:

$$\Phi_{prod}\left(t \right) = \frac{N_{prod}\left(t \right)}{N_{ph,abs}} = \frac{c_{prod}\left(t \right)}{c_{excited}} \tag{2.11}$$

where $c_{prod}(t)$ is the concentration of formed product molecules and $c_{excited}$ is the concentration of molecules excited by the pump light. Equation 2.11 is still valid when only considering small volumes irradiated by the pump pulses.

Both quantities − N_{prod} and $N_{ph,abs}$ − can be determined with a number of techniques. N_{prod} can for example be obtained from high performance liquid chromatography (HPLC), gas chromatography or NMR spectroscopy. $N_{ph,abs}$ is often measured by actinometry [40] or by opto-electronic devices such as solar cells [41]. However, the majority of the species observed in femtosecond transient absorption spectroscopy are too short-lived for a quantitative analysis of N_{prod} with the techniques mentioned above. Therefore, a calculus was developed which allows for the determination of c_{prod} directly from the optical signals.

Determination of photoproduct concentrations. For the studied benzhydryl chloride and phosphonium salts the two main photoproducts observed on the femto- to nanosecond scale, benzhydryl radical and cation, exhibit two strong, spectrally separated product bands around $\lambda_{radical} \approx 330$ nm and $\lambda_{cation} \approx 440$ nm (see Section 3). Their molar absorption coefficients $\varepsilon_{radical}$ and ε_{cation} at the maximum of the absorption band are on the order of 50,000 to 100,000 L·mol^{-1}·cm^{-1} and are well-documented in the literature [11] for a variety of derivatives with substituents on the phenyl rings. Therefore, the time-dependent concentration of benzhydryl radicals and cations in the irradiated volume of the sample can be calculated via:

$$c_{radical}\left(t \right) = \frac{OD\left(t; \lambda_{radical} \right)}{\varepsilon_{radical} \cdot d}, \quad c_{cation}\left(t \right) = \frac{OD\left(t; \lambda_{cation} \right)}{\varepsilon_{cation} \cdot d}, \tag{2.12}$$

where d is the sample thickness (see Section 2.5) and OD(t; $\lambda_{radical}$) and OD(t; λ_{cation}) are the measured transient absorbances at the maximum wavelength $\lambda_{radical}$ and λ_{cation} of the prod-

uct bands. Typical concentrations of benzhydryl radicals and cations on the picosecond to nanosecond scale are ~ 10 μM.

Concentration of excited molecules. The concentration of excited molecules is the product of the concentration of the molecules c and the excitation probability P_{exc}. The latter depends on the number of pump photons n_{ph} and the cross section σ of the molecule at the pump wavelength. Assuming that the photons are homogeneously distributed over a surface with diameter D_{pump} the excitation probability is given by [34]:

$$P_{exc} = n_{ph} \cdot \sigma = \frac{E_{pump}}{hc/\lambda} \cdot \frac{4}{\pi D_{pump}^2} \varepsilon \frac{\ln 10}{N_A},$$ (2.13)

where E_{pump} is the pump energy (i.e., without losses by reflection) and ε is the molar absorption coefficient at the pump wavelength λ. However, Eq. 2.13 is a rather crude approximation which does not take into account a realistic pump beam shape and the pump attenuation within the sample.

A more detailed approach accounts for the profile of the Gaussian-shaped pump beam with a FWHM diameter of D_{pump} = 100–150 μm. The excitation probability is then a function of the distance from the center:

$$P_{exc}(r) = \frac{E_{pump}}{hc/\lambda} \cdot \frac{4 \ln 2}{\pi D_{pump}^2} \cdot \exp\left(-\frac{4 \ln 2 \cdot r^2}{D_{pump}^2}\right) \cdot \varepsilon \frac{\ln 10}{N_A}$$ (2.14)

For a probe beam significantly smaller than the pump beam, the excitation probability is then given by the value of $P_{exc}(r)$ at r = 0

$$P_{exc} = \frac{E_{pump}}{hc/\lambda} \cdot \frac{4 \ln 2}{\pi D_{pump}^2} \cdot \varepsilon \frac{\ln 10}{N_A}$$ (2.15)

which means that the use of Eq. 2.13 overestimates the number of excited molecules by about 30%.[1]

For strongly absorbing samples the attenuation of the pump pulse in the absorbing sample has to be taken into account. According to the Lambert-Beer law, the pump energy in an absorbing sample at a penetration depth x is given by

$$E(x) = E_{pump} 10^{-\varepsilon cx}$$ (2.16)

Integration over the sample layer (optical density at the excitation wavelength OD, thickness d) leads to an average pump energy $E_{pump,avg}$ exciting the molecules:

$$E_{pump,avg} = E_{pump} \frac{1-10^{-OD}}{OD \cdot \ln 10}$$ (2.17)

---

[1] The inclusion of a finite probe diameter leads to a further correction by a few percent.

This leads to a further correction of Eq. 2.13 on the order of 10% to 30% for an optical density of the sample between 0.1 to 0.3.

Characterization of the experimental conditions. The evaluation of the concentration of excited molecules $c_{excited}$ needs the precise determination of several experimental quantities. The sample concentration c as well as the molar absorption coefficient ε can be easily obtained from an accurate measurement of the weight of the sample, the volume of the solvent and an UV/Vis spectrum. For the characterization of the pump pulses one has to measure the pump wavelength, the pump energy E_{pump} with which the molecules are excited and the diameter of the pump in the pump-probe overlap region. While the wavelength measurement should be uncritical, attention has to be paid to the last two issues. It is not sufficient to measure the pump energy in absence of the flow cell. The best results and the most information are gained when the energy is additionally measured after the flow cell – once with neat solvent and once with the sample solution to be measured. One hereby obtains important information about the excitation conditions of the sample:

- The pump energy: it corresponds to the geometric mean of the energy value measured before and after the flow cell, filled with neat solvent $E_{pump} = \sqrt{E_{before} \cdot E_{after}}$.

- The optical density of the sample and the energy loss suffered by the introduction of the flow cell, namely due to reflection on the interfaces, due to two-photon absorption in the solution[2] or due to dirt on the flow cell windows.

Since (according to Eq. 2.13) the concentration of excited molecules is proportional to D_{pump}^2, a precise determination of the pump beam diameter in the flow cell is crucial. This can be accomplished by a beam profiler. However, special care has to be taken in the positioning of the camera to ensure that the diameter is measured at the position of the flow cell in the following experiment. Since the pump beam is diverging[3] and astigmatism changes the beam shape the positioning with at least millimeter accuracy should be attained. A possible approach is to overlap pump and probe in a pinhole at the flow cell position. Then both beams have to be attenuated independently since the intensity of the focused pulses is far too high for CCD-based beam profilers. The attenuation should be accomplished in the collimated beams by reflective neutral density filters to prevent the generation of thermal lenses and a resulting falsification of the measured value. Hereby, the back reflection can be used to ensure a perpendicular positioning of the filter to the beam and to avoid a parallel offset. By moving the beam profiler along the propagation direction, the point of overlap between

---

[2] For a compilation of two-photon absorption coefficients of solvents at 264 nm see Ref. [Dra02].
[3] The Rayleigh length of the pump beam before and after the focal point is a few centimeters.

pump and probe can be found which is equivalent to the position of the flow cell in the following experiment.

Determination of efficiencies and intrinsic rates. For a multitude of photo-excited molecules the evolution of the system is not only a sequence of consecutive steps (e.g., A→B→C) but branching to different (final) products occurs. An often encountered and well studied example is the branching between fluorescence, internal conversion and intersystem crossing after excitation of a molecule. Although these processes posses differing intrinsic rates k_f, k_{IC} and k_{ISC}, all three obey the same temporal dynamics with a rate $k_{tot} = k_f + k_{IC} + k_{ISC}$. However, the individual rates determine the overall quantum yield of fluorescence Φ_f, internal conversion Φ_{IC} and intersystem crossing Φ_{ISC} [42]:

$$\Phi_f = \frac{k_f}{k_f + k_{IC} + k_{ISC}} = \frac{k_f}{k_{tot}}, \quad \Phi_{IC} = \frac{k_{IC}}{k_{tot}}, \quad \Phi_{ISC} = \frac{k_{ISC}}{k_{tot}} \qquad (2.18)$$

Therefore, if a quantum yield (e.g., Φ_f) and the total rate k_{tot} is known, one readily obtains the corresponding intrinsic rate (here k_f) according to $k_f = \Phi_f k_{tot}$. This approach can be generalized for any situation where branching occurs and k_{tot} and the yield Φ of a specific process are known.

Competition between geminate recombination and diffusional separation. Immediately after photolysis of a molecule A-B in solution the two generated photofragments are in close vicinity [A···B] and they can recombine to reform the precursor (see Section 3.4 and 3.5 for two examples). This is possible as long as the two fragments are in close distance. As soon as the separation between them is too large, the recombination becomes impossible. Therefore, the geminate recombination competes with the escape of the fragments.
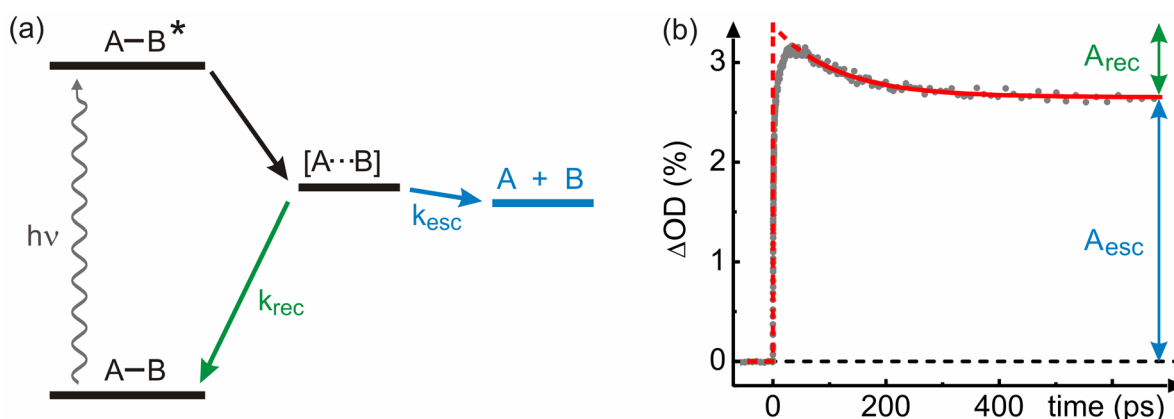
Figure 2.6: (a) Scheme of the processes and rates involved in diffusion terminated geminate recombination. (b) Transient absorption signal after UV excitation of $(tol)_2CH\text{-}PPh_3^+BF_4^-$ in acetonitrile (data: grey dots, fit: red line). The pre-exponential amplitude of the escaped benzhydryl cations A_{esc} and of geminate recombination A_{rec} can be extracted from the fit. The deviation of the fit from the data in the first 50 ps is due to the slow cation generation.

In transient absorption data this manifests as a partial decay of the detected fragment absorption signal with a rate constant k_{tot} and a remaining pedestal which is constant or decays slowly on a much longer time scale. A scheme of the processes is shown in Figure 2.6. The transient absorption signal consists of the contribution of the photofragments in close distance and the one where the photofragments already escaped from each other. Since for benzhydryl cations the absorption band is not influenced significantly by the presence or absence of the leaving group [43] one always detects both species simultaneously.

The observed rate constant k_{tot} is the sum of the rate for geminate recombination k_{rec} and the rate for escape of the two fragments k_{esc}. With the pre-exponential amplitudes linked to the geminate recombination A_{rec} (see Figure 2.6b) and to the escape of the photofragments A_{esc} one readily obtains the yield for geminate recombination $Y_{rec} = A_{rec} / (A_{rec} + A_{esc})$. By solving the rate model associated with Figure 2.6a one can show that the intrinsic rate constants k_{esc} and k_{rec} are given by (see Appendix B for the derivation):

$$k_{rec} = k_{tot} \, Y_{rec} \tag{2.19}$$

$$\text{and } k_{esc} = k_{tot} \left(1 - Y_{rec} \right) \tag{2.20}$$

2. Ultrafast, quantitative transient absorption spectroscopy

2.4 Measuring unstable compound-solvent system within short time

It is often desirable to measure a sample within a short period of time. This minimizes the effects of long term laser power fluctuations, keeps the exposure of the sample to light small and allows for the measurement of a multitude of samples within a short amount of time. However, there are technical limits which impose a minimum of time needed for one measurement. First, a sufficiently high number of delay times is needed spread over the time range for reproducing the dynamics with adequate precision. The spectra at every single delay then have to be averaged in order to gain a low signal-to noise ratio. Typical parameters for a measurement up to 1.8 ns are 350 delay points which are averaged 6000 times resulting in a sensitivity below 10^{-4} OD. With a laser repetition rate of 1 kHz this translates into a measurement time of about one hour. Usually, the recording of one data set is split up into three consecutive scans. This allows to recognize possible systematic deviations between the individual scans and additionally offers redundancy. The duration of one scan is about 15 minutes.

Some of the molecules studied in this work are not stable in certain types of solvents. Benzhydryl chloride (Ph_2CHCl) decays in methanol by solvolysis with a rate of $8.33 \cdot 10^{-4}$ s^{-1} giving rise to the benzhydryl ether [44]. This implies that after 15 minutes the concentration of the precursor Ph_2CHCl is divided into halves and a large amount of the product accumulates. Transient measurements on such systems therefore have to be carried out within minutes. This can be achieved by a modified measurement protocol. The delay times of the individual scans are split up again into four parts. Thereby in the first run the 1st, 5th, 9th,... points are measured, in the second run the 2nd, 6th, 10th,... points and so on. This interleaving scan allows for an overview over the entire measured signals already after the first run. Any changes in the subsequent runs in the experimental conditions, such as pump pulse energy or sample concentration, are than detected in the subsequent runs. A dedicated graph was implemented in the measurement software which overlays all runs and facilitates thereby the recognition of possible differences.

The on-line check of the sample integrity therefore even allows to measure unstable sample solutions which are on a timescale comparable to the measurement duration. The technique enabled us, for example, to record reliable transient data from the photoinduced dynamics of Ph_2CHCl in methanol, a system which was not accessible for ultrafast spectroscopy before.

2.5 Sample exchange techniques

Flow Cells in Transient Absorption Spectroscopy. Transient absorption spectroscopy of molecules in solution requires the continuous replacement of the pumped sample volume, mainly in order to avoid photodegradation and accumulation of photoproducts. Usually a custom-made flow cell was used which is described in detail in Ref. [34]. In brief, the design of the cell is optimized to minimize the optical path length through dispersing material, namely the windows and the solution. The pump and probe pulses have to pass two 200 μm thick fused silica windows and the solution layer of about 120 μm. The small amount of dispersive material provides that the chirp introduced to the pulses is small. The thin solution layer furthermore ensures that the group velocity mismatch (GVM) between pump and probe pulse [35] remains on a small level. Both – the chirp of the pulses and the GVM – should be as small as possible for a high temporal resolution. The short optical path length through dispersive material additionally provides that non-linear interactions between pump and probe pulse in the material such as two-photon absorption, stimulated Raman amplification and cross-phase modulation [29] are kept on a small level.
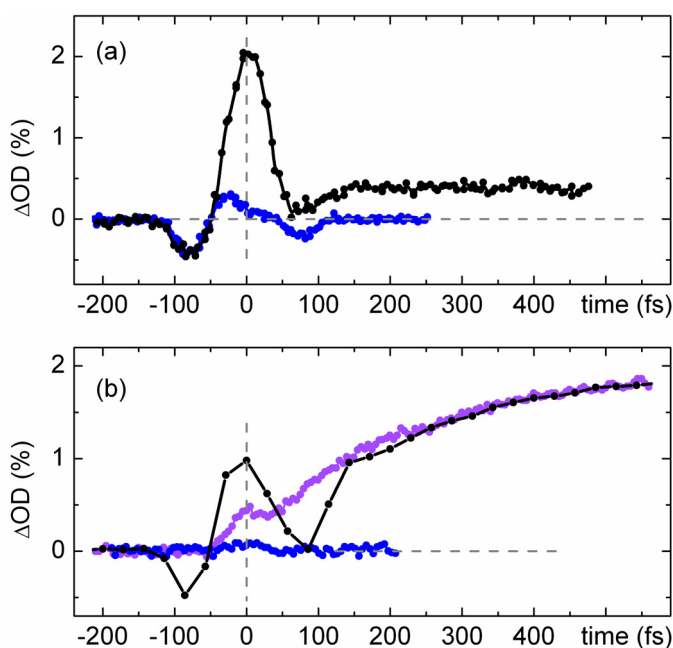

Figure 2.7: a) Influence of the flow cell windows on the measured early signal. Observed signal of $Ph_2CHPPh_3^+BF_4^-$ in CH_2Cl_2 at 329 nm after UV excitation (black) compared to the signal measured in an empty flow cell (blue). b) Comparison of the transient signals at 329 nm after UV excitation of Ph_2CHCl in CH_3CN around time-zero in the flow cell (black) and the liquid jet (purple). The signal of neat CH_3CN in the liquid jet is shown in blue.

These interactions lead to signal contributions within 100 fs to 150 fs around time-zero masking the earliest dynamics of photo-initiated processes (see Figure 2.7). Particularly dis-

turbing are negative absorption changes since they are hardly distinguishable from ultrafast signal rises ($\tau \approx 100$ fs) originating from the molecule. Hereby, the major part of the negative signal contributions seems to stem from the flow cell windows (see Figure 2.7a). However, the achievable time resolution with flow cells of ~70 fs over the entire detection window is suitable to study the major part of the dynamics of the molecules studied in this work.
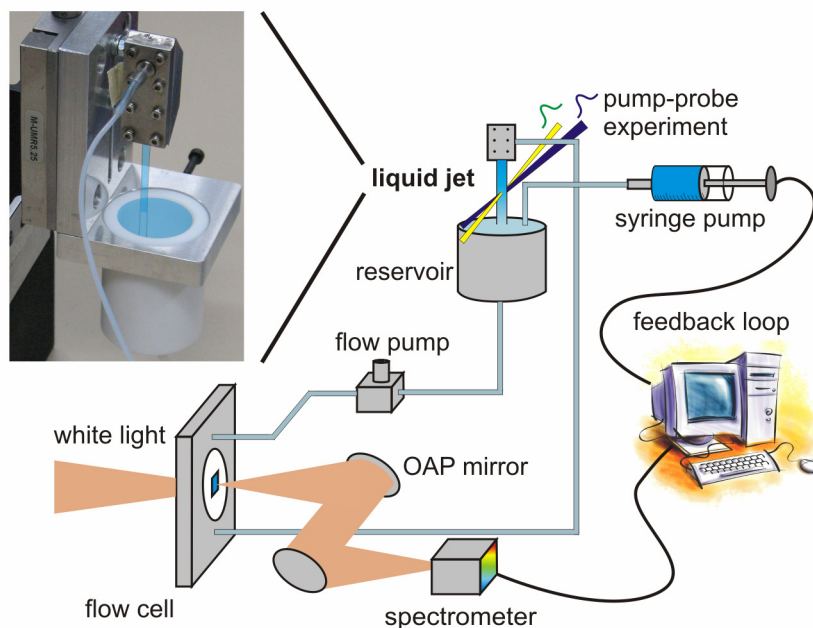

Figure 2.8: Scheme of the liquid jet setup and the concentration control. The pump-probe measurement is carried out with the solution in the liquid jet. The precursor concentration increase by solvent evaporation is quantified by an independent UV/Vis spectrophotometer and is compensated by a feedback loop which controls the addition of neat solvent. Picture: The liquid jet used in the transient experiments. The solution is colored in blue for the sake of visibility.

Liquid Jet Setup. In order to study ultrafast dynamics in the sub-100 fs range, in which the ultrafast photo-induced bond cleavage of benzhydryl chloride is predicted to take place (see Section 3.2) [14], the time resolution of the setup has to be improved and the spurious signal contributions of the flow cell windows have to be removed. Therefore, a wire-guided liquid jet was constructed as a second system which allows for the generation of even thinner solution layers as with the flow cell without any additional dispersive material to be passed by the pulses. It consists of two stainless steel wires (150 µm diameter) in a distance of 2 to 3 mm. Between these wires a thin solution film flows downwards which is sustained by surface tension (see Figure 2.8) [45-48]. The wires lead directly into a reservoir providing minimal back reflections from the end of the layer. The thickness of the sample layer was usually 50 µm to 60 µm but it can be easily varied between 20 µm to 200 µm [49]. The use of a jet in transient absorption measurements leads to a tremendous decrease of the coherent signal contributions compared with a flow cell (see Figure 2.7b). Especially the negative

signals are eliminated to a large extent. A further advantage of the jet compared to the flow cell is that precipitation of the sample on the cell windows can be avoided.

Closed-loop control of the Sample Concentration by Online Broadband Measurements. In contrast to the flow cell the liquid jet is not a closed system – due to the open surface of the jet and the reservoir, the solvent evaporates constantly (e.g., ethanol evaporates in the liquid jet setup with a rate of ~ 2.1 ml/h). Without any compensation this would lead to a strong increase in the precursor concentration making any time-dependent measurement impossible. Therefore, a closed-loop control was developed which keeps the optical density and thereby the concentration of the solution in the jet on a constant level [50]. The optical density is measured in a reference flow cell by a home-made, mobile UV/Vis absorption spectrophotometer consisting of a fiber-coupled light source, a fiber coupled spectrometer and four off-axis parabolic mirrors (see Figure 2.8). The light from the source, ranging spectrally from 210 nm to above 1000 nm, is collimated after the fiber output and focused into the sample down to a diameter of ~ 400 μm allowing for even smallest sample volumes to be measured. After recollimation of the beam and coupling into the second fiber, the light is guided to the small spectrometer where the spectrum is recorded. The use of off-axis parabolic mirrors hereby allows for an efficient imaging of the beam free of astigmatism. For moderate optical densities < 1.5 the UV/Vis absorption spectra measured within single seconds are comparable in quality to spectra recorded within minutes with commercially available spectrophotometers (see Figure 2.9a).
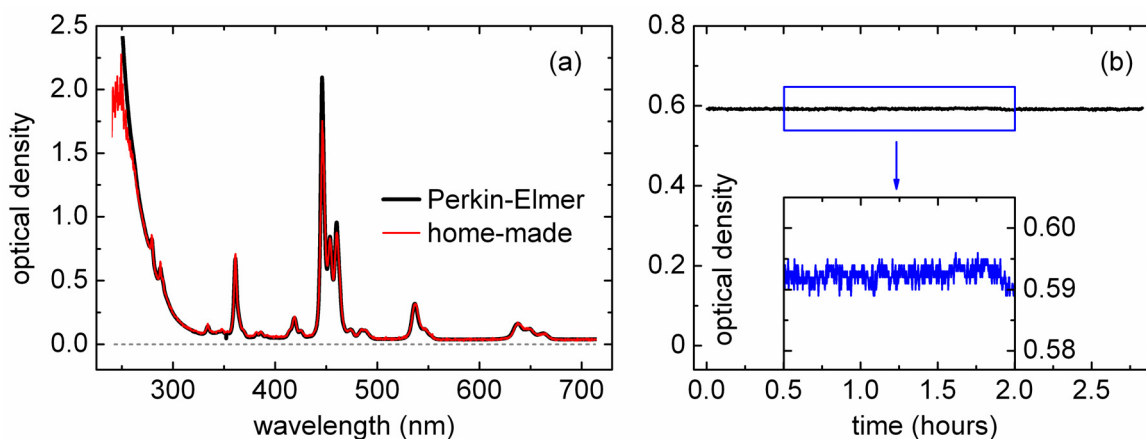
Figure 2.9: a) Absorption spectrum of a holmium oxide glass filter measured with a commercial Perkin-Elmer Lambda 750 (black line) and the home-made absorption spectrophotometer (red line). b) Stabilized optical density of indole in ethanol in the liquid jet setup at 270 nm by compensation of evaporation losses through the control loop.

At the beginning of each measurement, a transmission spectrum of the neat solvent is recorded. A second transmission spectrum of the sample then allows for the determination of the initial optical density. The OD at the excitation wavelength serves as set-point for the

control loop. During a transient absorption measurement in the jet the optical density in the reference flow cell is steadily compared with the value of the set-point. A computer controlled syringe pump then adds neat solvent to the sample with a rate determined by a PID control. This allows to keep the concentration of the sample extremely stable for several hours (see Figure 2.9b). For a measurement of indole in ethanol in the liquid jet setup, the maximum deviation from the initial optical density during three hours was smaller then 0.7% compared to the mean value. The standard deviation was ~ 0.2% of the mean value.

The on-line measurement of absorption spectra during transient absorption measurements additionally allows for the recognition of a possible change or a (photo-)degradation of the sample: the absorption band of the molecule can undergo changes or even new absorption bands of generated (photo-)products can arise. Both effects can be detected by absorption spectroscopy which allows for a reliable identification of changes of the sample.

2.6 Continuous referencing of background signals

Transient absorption spectroscopy is a sensitive method for determining small changes in the optical properties of a sample. Typical sensitivities are on the order of $\Delta OD \sim 10^{-4} - 10^{-5}$. This implicates that small systematic changes within the whole detection system (e.g., the temperature of the CCD detector or a change in the stray light) can also lead to measurable though undesired signal contributions. While unwanted signals which are constant or only slowly varying are greatly suppressed by chopping the pump beam, signals which only appear when the sample is excited cannot be eliminated. There are mainly two sources of such contributions: a) scattering of the pump beam on the surface of the flow cell and b) spontaneous emission (fluorescence) of the excited molecules. While scattering by the flow cell windows is only relevant when the pump wavelength coincides with the probed detection interval, the fluorescence is mainly independent of the excitation wavelength. The impact of the spontaneous emission on the transient data is determined mainly by the fluorescence quantum yield of the molecule.

Since both undesired signals do not depend on the temporal delay between pump and probe pulse, they should in principle be constant. However, the scattered light can increase due to aggregation of photoproducts on the flow cell windows and the fluorescence can increase due to accumulation of (photo-)products with a higher fluorescence quantum yield. Both increases can be expected to occur on a slower time scale compared to the scanning of the time delay points. Therefore, this undesired signals do not have to be measured at every single delay but less points are sufficient. A recording at every 10th delay point turned out to be a good tradeoff between a fast measurement and an efficient suppression of the undesired signals.

The reference measurements necessary for the suppression can be implemented by introducing a shutter into the probe beam path. By closing the shutter, only the pump pulse impinges on the flow cell and the sample, and the CCD camera therefore only detects (besides the ambient light and the dark current) the scattered pump light and the fluorescence of the sample. By virtue of the chopping of the pump pulse one obtains in total four different spectra: 1.) a transmission spectrum of the probe pulse with pump, 2.) a transmission spectrum of the probe pulse without pump, 3.) a spectrum without probe and with pump, 4.) a spectrum without probe and pump. All four are saved separately which allows for an inspection of the development of the undesired signals after the measurement.

2.7 Peak shifts as sensitive probe on a solute's geometry and environment

Spectral Shifts in Time-Resolved Measurements. The electronic transitions of molecules are not static and unalterable but they can be changed by a diversity of effects. A prominent example is the red or blue shift of a molecular absorption band when changing the solvent polarity (solvatochromism). The shift is caused by differential solvation of the ground and first excited state of the molecule [51]. However, solvation shifts are not only visible in steady-state absorption or fluorescence spectroscopy when the solvent is changed. They can also be observed on ultrafast timescales when the solvent adapts to a new charge distribution.

A frequently used technique is the photo-excitation of a chromophore with a pronounced change in the dipole moment upon excitation and a time-resolved measurement of the fluorescence. The evaluation of the fluorescence peak shift then allows for a determination of characteristic solvation times [52-55]. The same information can also be obtained by transient absorption spectroscopy by following the temporal evolution of the spectral position of absorption bands or the stimulated emission [56,57]. However, the interpretation of the observed spectral shift can be complicated due the presence of further contributions, particularly vibrational relaxation [58] and dynamics of the excited state absorption.

The impact of the solvent and dynamic solvation on the transition energies highlights the influence of the dielectric environment on a chromophore. Further changes in this environment – apart from solvent effects – should therefore also have an effect on the peak position. A first insight into the sensitivity of absorption bands of carbocations towards changes in their vicinity was given by Schneider et al. [43] who showed that the absorption band (measured by steady state UV/Vis absorption spectroscopy) of persistent benzhydryl cations in the vicinity of an anion is slightly blue shifted by about 2 nm compared to unpaired cations. A closer inspection of Figure 2.2 reveals that the benzhydryl cation absorption band observed after UV excitation of $(tol)_2CH\text{-}PPh_2Ph\text{-}SO_3^-$ in dichloromethane (see) also exhibits a temporal change of the position. Knowledge on the vicinity of a reactant or the temporal evolution of the distance between two reaction partners – by diffusion or a distance dependent reaction – is an important aspect in the understanding of ultrafast chemical reactions. Therefore, a consistent measure for the position of the absorption band for every measured delay time is needed.

Parabola Fitting Algorithm. The determination of the center of gravity of the benzhydryl cation or radical absorption band is biased by the significant spectral overlap of the two product bands. An iterative algorithm has therefore been developed which fits a parabola to the maximum of an absorption band. This ansatz relies on the Taylor expansion of a function $f(x)$ around an extremum at x_0 which is given by:

2. Ultrafast, quantitative transient absorption spectroscopy

$$f(x) = f(x_0) + \frac{f''(x_0)}{2}(x - x_0)^2 + \frac{f'''(x_0)}{6}(x - x_0)^3 + \dots \qquad (2.21)$$

Hereby, the linear term vanishes since the first derivative is zero at x_0. Therefore, every maximum of an observed absorption band can be – within a sufficiently small interval – well approximated by a parabola. Any other definition of the band position leads hereby at most to a systematic deviation which is constant for all times. The dynamics of spectral shifts is thus not influenced by the choice of the measure for the band position and even the relative shift amplitudes remain unchanged.
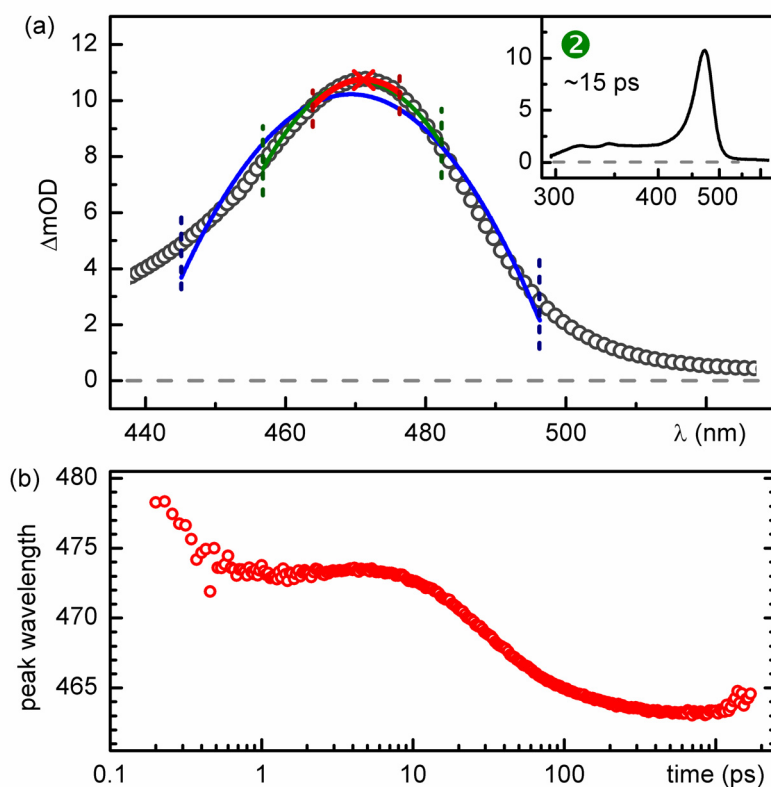

Figure 2.10: Peak position determination for the benzhydryl cation band observed ~15 ps after UV excitation of $(tol)_2CH\text{-}PPh_2Ph\text{-}SO_3^-$ in dichloromethane (see Figure 2.2). (a) Iterative fit of parabolas within a narrowing interval. The first two iterations are shown in blue and green together with the borders of the interval. The last fit and interval is shown in red. The complete transient absorption spectrum is shown in the inset. (b) Temporal evolution of the cation peak position determined by the algorithm.

The algorithm performs an iterative fitting of a parabola to the absorption band maximum within a dynamically adapted data interval around the maximum. In a first step a parabola is fitted to the transient data of an sufficiently large interval comprehending the absorption peak (see Figure 2.10a). Around the maximum of this parabola a new, smaller interval is chosen and a second parabola is fitted to the data. This procedure is repeated with smaller intervals until the identified peak position is independent of the size of the interval. The al-

gorithm allows for the accurate determination of the time-dependent shift of an absorption band maximum with an accuracy of ~ 0.1 nm

The temporal evolution of the band position can be evaluated by applying the algorithm to the entire transient absorption data set, thus allowing to track the peak position for time delays from below 200 fs to nanoseconds or longer (see Figure 2.10b).[4] It allows to track changes in the observed solute (e.g., rearrangements) or its environment (e.g., solvation or diffusional separation) and to indicate the time scale on which these changes occur.
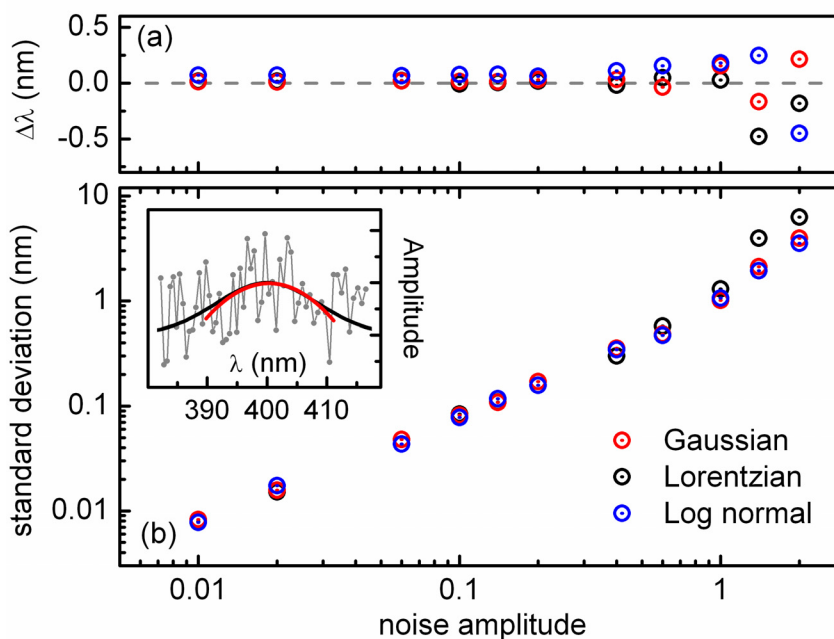
Figure 2.11: Influence of the noise amplitude on a) the deviation $\Delta\lambda$ of the fitted to the nominal peak position and b) the standard deviation for a series of 100 spectra with a Gaussian, a Lorentzian and a log-normal peak shape. A Gaussian-shaped spectrum (grey dots) for a signal-to-noise ratio of 1 is shown in the inset, together with the noise-free Gaussian (black) and the parabola fit (red).

Performance of the algorithm. The influence of noise on the precision of the fitted peak position was simulated with three peak shapes often found in spectroscopy: a Gaussian, a Lorentzian and a log-normal[5] function. All three were set to have their maximum at 400 nm and a FWHM (full width at half maximum) of 20 nm. The spacing of the wavelength axis (~0.6 nm) was taken from the experiment. A series of 100 different spectra for each of these three peak shapes was generated by adding white noise (see inset in Figure 2.11 for a showcase). The ratio between the noise and the peak amplitude was varied between 0.01 and 2.

---

[4] The upper temporal limit is given by the ability to measure absorption spectra at such long delays.

[5] The log-normal function is defined as $f(\lambda) = A \cdot \exp \dfrac{-\left[\ln \lambda \big/ \lambda_{max}\right]}{2w^2}$.

The generated spectra were fitted with the algorithm with a final data interval of 20 nm. As a measure for the accuracy of the peak position determination the deviation $\Delta\lambda = \overline{\lambda} - 400\,\mathrm{nm}$ of the mean peak position $\overline{\lambda}$ from the nominal value of 400 nm and the standard deviation σ_λ were evaluated.

In Figure 2.11a the deviation $\Delta\lambda$ of the fitted mean peak position from the nominal value of 400 nm is shown. It is most notable that no significant systematic deviation is found for all three peak shapes although a rather large fit interval was chosen. This insensitivity allows to fit the parabola to a large part of the spectrum around the peak without biasing the result. The standard deviation of the fitted peak position for the generated 100 spectra is shown in Figure 2.11b. While at small noise levels the standard deviation is negligible small it rises monotonously with the amplitude of the noise. However, even when the noise amplitude is twice as large as the amplitude of the peak and the bare eye has already problems to recognize the presence of a peak (see inset in Figure 2.11), the algorithm is able to find the maximum with a standard deviation of only a few nanometers.

Technical and Spectral Prerequisites. In order to obtain a reliable band position with subnanometer precision several prerequisites (both, technical, i.e., related to the transient absorption setup, and spectral) have to be fulfilled:

- The studied absorption band has to be strong enough. The position determination for bands with absorption changes $\ll 1\,\mathrm{mOD}$ is difficult and special care has to be taken in order to obtain sufficiently low-noise transient spectra.

- The absorption band should not be overlapped by a further evolving band. However, an underlying broad and unstructured absorption background (e.g., many excited state absorption bands) will not change the result significantly.

- The achievable precision of the band position determination is directly linked to the width of the absorption band.[6] The broader a band becomes the less defined is the fit of a parabola on it.

- The absorption band has to be covered by a sufficiently high number of detection channels, thus increasing the stability of the fit against statistical deviations. For the benzhydryl radical and cation absorption bands typically 20 to 40 points are used for the fit.

- Over one transient spectrum the noise from detection channel to detection channel should be as small as possible. On the contrary, the variations between several spectra are only of minor importance. Interestingly, when using CaF_2 white-light the signal fluc-

---

[6] It suffices if a part of the entire absorption band exhibits a sharp feature which can be fitted by a parabola. The vibronic progression of a transition leads to such a behavior.

tuations are highly correlated leading to a systematic increase or decrease over a large part of the spectrum. The origin of this behavior is not yet fully understood. However, it seems to originate from the concerted generation of different parts of the whitelight spectrum.

The high accuracy allows for the observation of even tiny effects on time scales ranging from 100 fs to microseconds. In the sub-picosecond range solvation and intramolecular rearrangements (e.g., planarization) are dominant. Both can lead to a distinct shift of the peak wavelength. After their completion further processes can lead to a shift of the absorption bands. As pointed out above, the presence of an anion in the vicinity of a benzhydryl cation blue shifts the cation absorption band by about 2 nm. Therefore, the change in the mean cation-anion distance can be followed by the dynamic peak shift.

By analyzing the benzhydryl cation and radical peak shift after UV excitation of Ph_2CHCl in CH_3CN we were able to corroborate the microscopic reaction scheme proposed by the theoretical Marcus-Smoluchowski model. While the distance increase in the first tens of picoseconds is mainly due to a efficient reaction of the sub-population in close vicinity, diffusional separation becomes dominant after ~ 100 ps and finally leads to free ions and radicals.

3. Generation and reactions of highly reactive carbocations and carbon radicals

3.1 Photogeneration of carbocations

The generation of carbocations by photolysis of a suitable precursor is a well established technique [12,13]. Hereby, the carbocation R^+ is formed by photoinduced heterolytic bond cleavage from a neutral (R-X) or charged (R-X$^+$) precursor according to

$$R\text{–}X \xrightarrow{h\nu} R^+ + X^- \quad \text{or} \quad R\text{–}X^+ \xrightarrow{h\nu} R^+ + X$$
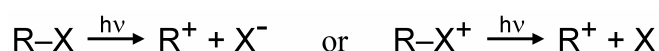
with the photo-leaving group X^- or X. A wide range of precursors has been used for the carbocation generation, amongst others halides (e.g., R-Cl), acetates, aryl ethers and phosphonium salts.[7] Many of the generated carbocations exhibit strong, characteristic absorption bands in the UV or visible range making them suitable candidates for spectroscopic investigations [12,13].

The ultrafast generation and observation of highly reactive carbocations raises hereby specific requirements which should be met for a broad range of applications and a reliable evaluation of the measured data:

- The bond cleavage should be faster than the subsequent ultrafast process to be observed.

- The quantum yield for cation generation should be at least some percent for a sufficiently high transient absorption signal.

- The yield of the geminate recombination between the carbocation and the leaving group should be as small as possible.

- Ideally, the carbocation generation should not be restricted to highly polar solvents (such as acetonitrile or 2,2,2-trifluoroethanol) but should also be viable in solvents of moderate polarity (e.g., dichloromethane).

In this work the photogeneration and subsequent chemical reactions of a series of benzhydryl cations Ar_2CH^+ (Ar: Aryl) is presented. Their appearance is easily detectable due to their strong, characteristic absorption band (typical molar absorption coefficients are in the range of 40,000 to 100,000 L mol^{-1}cm^{-1} [11]) in the visible (see Figure 3.1).

The reactivity of the cations is highly variable which allows for a systematic investigation. By changing the substituents on the phenyl rings of the benzhydryl cations their reactivity can be changed over 18 orders of magnitude [17,59]. The reactivity of benzhydryl cations
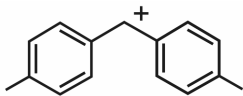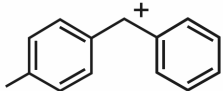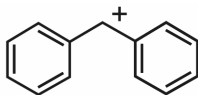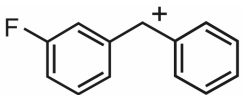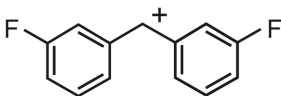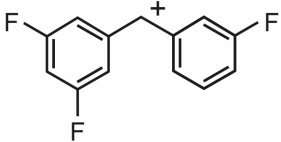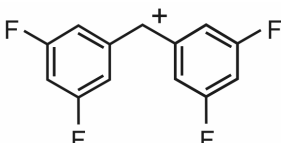
---

[7] A comprehensive list of publications reporting on the photolysis of these and further precursors can be found in J. Ammer et al. *J. Am. Chem. Soc.* **2012**, 134, 11481.
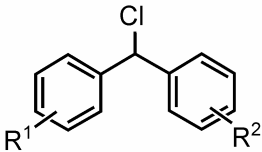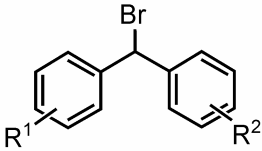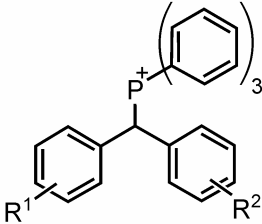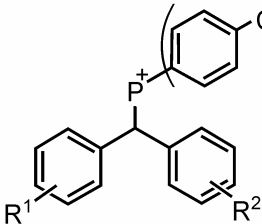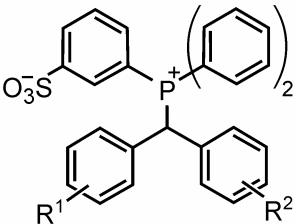
(or - more general - of electrophiles) is quantified by the empirical electrophilicity parameter E (see Appendix A). Since E is a logarithmic measure, an increase of one in E leads to a ten times higher reaction rate constant. In order to observe ultrafast reactions on the low pico- to nanosecond scale, the studied benzhydryl cations are on the upper limit of the reactivity scale covering more than four orders of reactivity. The benzhydryl cations investigated within this work and their electrophilicity parameters are summarized in Table 3.1.

Table 3.1: Investigated benzhydryl cations Ar_2CH^+ (Ar: Aryl) and the empirical electrophilicity parameters E.

compound	abbreviation	E
	$(tol)_2CH^+$	3.63
	$tol(Ph)CH^+$	4.43
	Ph_2CH^+	5.47
	$mfp(Ph)CH^+$	6.23
	$(mfp)_2CH^+$	6.87
	$dfp(mfp)CH^+$	7.52
	dfp_2CH^+	8.02

Table 3.2: Precursors used for the photogeneration of benzhydryl cations Ar_2CH^+ (Ar: Aryl). The four studied counterions (Cl^-, Br^-, BF_4^- and SbF_6^-) of the phosphonium salts are not shown.

compound	abbreviation
	Ar_2CHCl
	Ar_2CHBr
	$Ar_2CH\text{-}PPh_3^+$
	$Ar_2CH\text{-}P(p\text{-}Cl\text{-}C_6H_4)_3^+$
	$Ar_2CH\text{-}DPPBS$

The benzhydryl cations studied within this work were generated from different precursors: benzhydryl halides, benzhydryl triarylphosphonium salts and 3-(benzhydryl-diphenylphosphonio)benzenesulfonate (see Table 3.2 and Figure 3.1). All precursors were excited at their first absorption band in the UV at ~270 nm for the halides and ~280 nm for the phosphonium salts and the sulfonate (see Figure 3.1). This corresponds to a π-π* excitation located on one of the aryl rings.
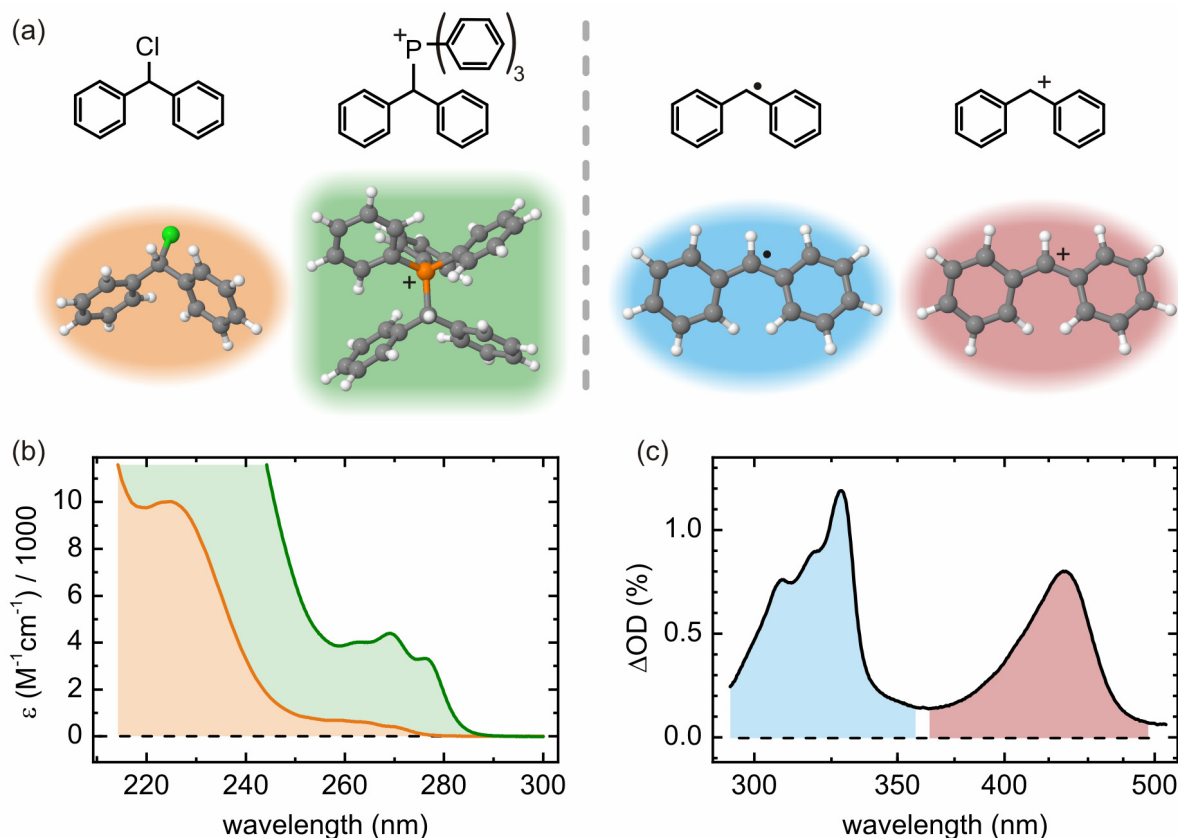
Figure 3.1: (a) Structural formula and optimized geometries of benzhydryl chloride (Ph_2CHCl), the benzhydryl triphenylphosphonium cation (Ph_2CH-PPh_3^+ without the counterion), the benzhydryl radical $Ph_2CH^\bullet$ and cation Ph_2CH^+ (from left to right). (b) Steady state absorption spectrum of Ph_2CHCl (orange) and Ph_2CH-PPh_3^+ (green). Transient absorption spectrum recorded 40 ps after UV excitation of Ph_2CHCl in acetonitrile. Two distinct product bands associated with the benzhydryl radical (blue) and benzhydryl cation (red) can be observed. The exact position of the band maxima depends on the substituents and the solvent.

An often formed byproduct for the photolysis of benzhydryl cation precursors is the benzhydryl radical. It is formed when the bond between the photo-leaving group and the carbon atom is cleaved homolytically instead of the desired heterolytical bond cleavage. After the cleavage, the photo-leaving group therefore possesses one electron less than after heterolysis and a chlorine radical $Cl^\bullet$ or a $PPh_3^{\bullet+}$ radical cation forms. The benzhydryl radical has a characteristic absorption band deeper in the UV (typically with the maximum between 325 nm and 350 nm, see Figure 3.1c) with a molar absorption coefficient comparable to that of the cation [11]. Generally, the formation of benzhydryl radicals greatly depends on

- the photo-leaving group: significantly more radicals are formed after UV excitation of the benzhydryl chloride precursor,

- the substituents: more radicals are formed for cations with higher electrophilicity,

- and the solvent: lower solvent polarity leads to more radicals.

As it is shown in Section 3.4, the benzhydryl radical / Cl radical pair can be interconverted by electron transfer to a pair of benzhydryl cation / Cl anion, which makes them an important source for carbocations.

3.2 Delayed cation and radical formation after inertial wavepacket motion through two conical intersections

Theoretical investigations on the potential energy surface of the excited state of benzhydryl chloride showed that both the homolytic and the heterolytic bond cleavage pathway are accessible from the $S_1 \leftarrow S_0$ Franck-Condon region via conical intersections [14]. Furthermore, only a small barrier of about 200 cm^{-1} exists between the Franck-Condon region and the potential energy surfaces leading to the bond cleavage. This provides the opportunity of an ultrafast, femtosecond bond cleavage and a competing benzhydryl ion and radical generation.

The investigation of the femtosecond bond cleavage process is described in detail in the following manuscript:

"Ultrafast photochemical reaction with two product channels: wavepacket motion through two distinct conical intersections"
*C. F. Sailer, N. Krebs, B. P. Fingerhut, R. de Vivie-Riedle, E. Riedle*
To be submitted to Physical Review Letters.

A novel, dedicated experimental setup was developed in close collaboration with Nils Krebs for measuring the signal evolution of the photofragments with a sub-40 fs time resolution. This was accomplished by using two ultrashort pulses (generated in two NOPAs) as pump and probe [60]. In order to minimize the group velocity mismatch between the two pulses [35] and spurious signals from two-photon absorption in the solvent and in the cell windows, the liquid jet setup was used instead of the flow cell (see Section 2.5). Simultaneously to the transient absorption in the jet, the two-photon absorption signal in a BBO crystal was measured independently in a second pump-probe branch. This allowed for an absolute calibration of the temporal zero-point with an accuracy $\ll$ 5 fs. A precise determination of temporal delays between the optical excitation and the appearance of product absorption signals was therefore rendered possible.

We measured the signal evolution at the maximum wavelength of the benzhydryl cation (~435 nm) and radical (~330 nm) absorption band after UV excitation (270 nm) of benzhydryl chloride. From the observed signals it is evident that the photofragments do not appear directly after the photoexcitation (see Figure 3.2). After the excitation the signal remains on a stable level for several tens of femtoseconds for both benzhydryl radical and cation. Only after a time delay of ~80 fs the benzhydryl radical signal exhibits a pronounced rise. Analogously, a time delay of ~125 fs is found for the benzhydryl cation signal. The subsequent signal rise on the hundreds of femtosecond scale can be explained in view of the planarization of the photofragments after the bond cleavage (for details see Section 3.3). The determination of the yields for homolytic and heterolytic bond cleavage (presented in Section 2.3)

shows that 20 times more benzhydryl radicals than cations are generated when irradiating benzhydryl chloride in acetonitrile.
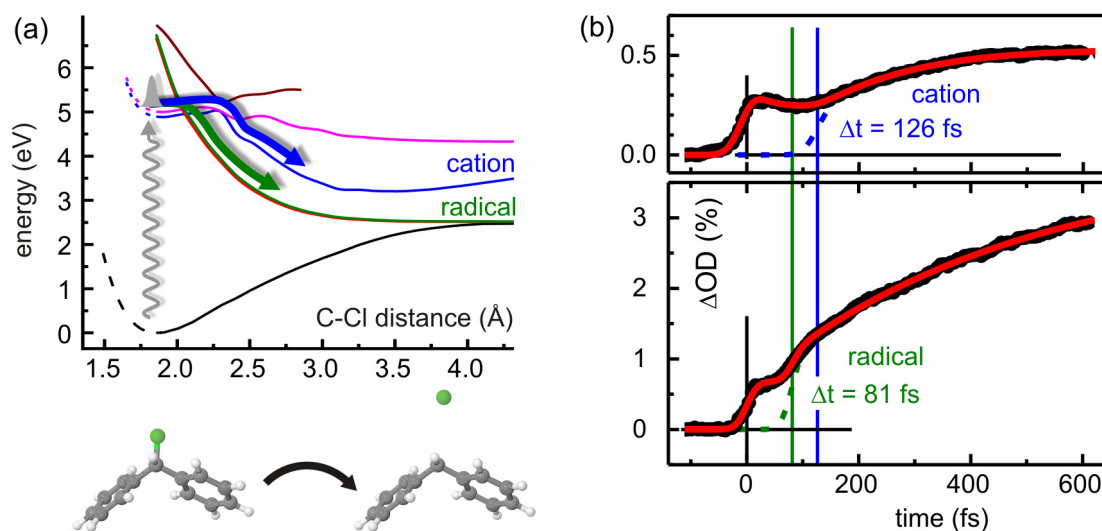
Fig 3.2: (a) Schematics of the wavepacket evolution leading to benzhydryl cations or radicals on the potential energy surfaces. (b) Measured transient absorption signal at the absorption band of cation and radical. A significant delay for the rise of the photoproduct absorption bands with respect to the optical excitation is found.

The experimental observation of the delayed bond cleavage can be explained by the photo-induced wavepacket dynamics on the potential energy surfaces of the precursor [14]. By the ultrafast UV excitation of the $S_1 \leftarrow S_0$ transition at 270 nm, a nuclear wavepacket in the Franck-Condon region is created. The transition from the S_1 to a higher electronic state leads to the observed small absorption in the first tens of femtosecond. Due to a small gradient it evolves towards longer C-Cl distances until it encounters the first conical intersection after ~80 fs. A large part of the excited wavepacket passes through the first conical intersection to the potential energy surface which leads to homolytic bond cleavage (radical pairs). The residual wavepacket moves towards a second conical intersection which is encountered ~120 fs after the optical excitation. After passing this intersection the wavepacket is on the potential energy surface which leads to ion pairs (by heterolytic bond cleavage). Due to the efficient coupling between the potential energy surfaces at the first conical intersection homolysis is largely favored over heterolysis.

In contradiction to earlier expectations, the bond cleavage is not caused by two competing stochastic processes and a consequential rate model. It can rather only be described by the inertial motion of a wavepacket on the excited state potential energy surface and through two distinct, successive conical intersections. The dynamics and the branching ratio between the channels depend on the detailed position of the potential energy surfaces and the motion of the wavepacket on these.

3.3 Formation of the photoproduct absorption band after bond cleavage

For many solvent-precursor combinations an initial signal rise with a time constant of about 300 fs is found for both the benzhydryl radical and cation. Early studies by Peters and co-workers assigned the early signal rise to the bond cleavage [15,61]. The reported time constants of 345 fs for the radical signal rise and 833 fs for the cation correspond, however, well to the group velocity mismatch (GVM) between pump and probe of about 350 fs and 750 fs [35] in the used 2 mm flow cell. A molecular origin of the reported signal rise can therefore be ruled out. Furthermore, as shown in Section 3.2, the bond cleavage process is terminated after ~125 fs and it cannot be the origin of this signal increase. In order to understand the generic 300 fs time constant a combined experimental and theoretical investigation was needed which is described in

"Buildup and Decay of the Optical Absorption in the Ultrafast Photo-Generation and Reaction of Benzhydryl Cations in Solution"
B. P. Fingerhut, C. F. Sailer, J. Ammer, E. Riedle, R. de Vivie-Riedle
 Journal of Physical Chemistry A, 2012, DOI: 10.1021/jp300986t.

A model system was investigated consisting of a benzhydryl cation precursor surrounded by eight or nine methanol molecules. The solvent molecules are arranged around the precursor and form a hydrogen bond network upon geometry optimization of the cluster. The ultrafast bond cleavage of the precursor is modeled by removing the leaving group artificially from the cation and by leaving the other molecules unchanged. Thus, the newly formed cation and the solvent molecules are still in the geometry optimized before the bond cleavage. The evolution of this non-equilibrium configuration is studied by the calculation of on-the-fly molecular dynamics trajectories.

Before the bond cleavage, the four substituents bound to the central carbon atom of benzhydryl chloride (two aryl rings, one chlorine atom and one hydrogen atom) are arranged tetragonally. In contrast, the structure of the benzhydryl cations and radicals is almost planar (see Figure 3.3). The planarization of the nascent benzhydryl cation can be followed by the on the on-the-fly molecular dynamics calculations. Due to the size of the phenyl rings this motion is rather slow. It takes several hundreds of femtoseconds until the benzhydryl cation relaxes to its favorable geometry.
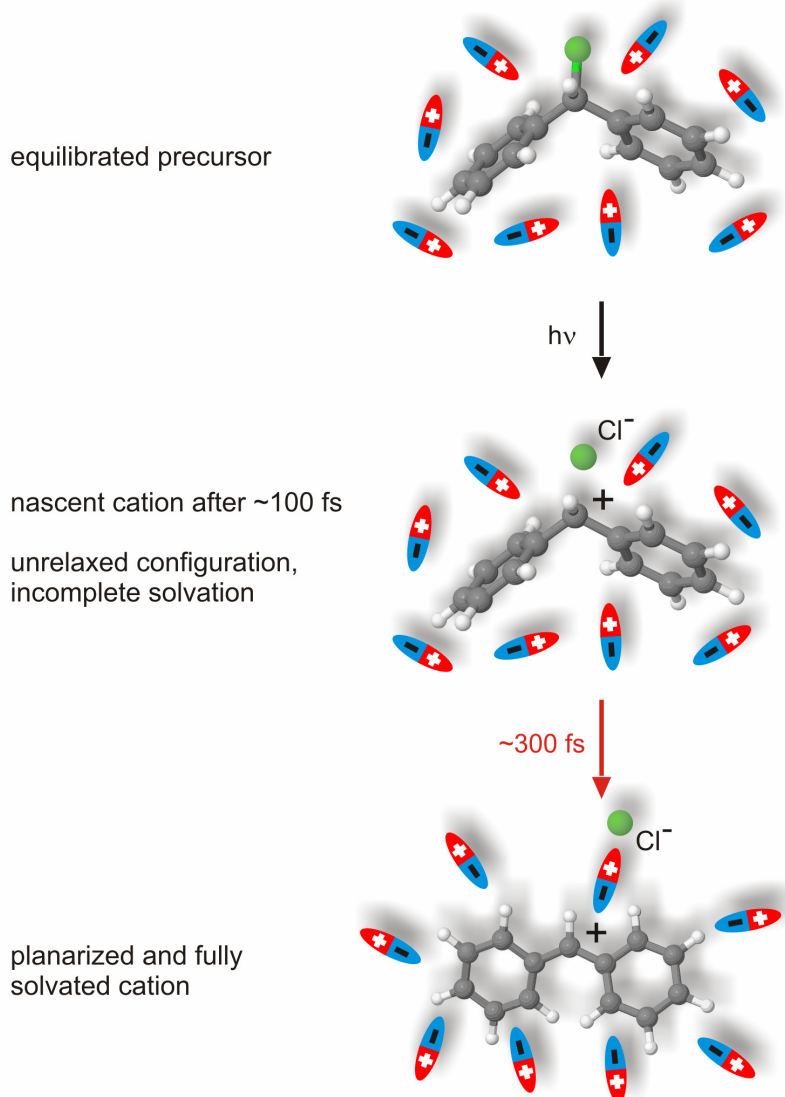
Figure 3.3: Temporal change of the configuration of the solute and the surrounding solvent molecules. Before the excitation, the precursor and the solvent molecules are in a favorable configuration.[8] The photo-induced bond cleavage is extremely fast and does not allow for a simultaneous rearrangement of the generated cation and the solvent shell. Only within the next hundreds of femtosecond the cation planarizes and is fully solvated by the surrounding solvent.

Ab initio calculations show that the shape and height of the benzhydryl cation absorption band depend on the geometry of the cation. For the initial tetragonal geometry, the $S_1 \leftarrow S_0$ transition, which is responsible for the characteristic benzhydryl cation absorption band around 440 nm, is shifted to longer wavelengths and weaker compared to the planar geometry [62]. Instead, transitions to higher electronic states (especially $S_4 \leftarrow S_0$ and $S_5 \leftarrow S_0$) have

---

[8] The geometries of benzhydryl chloride and the benzhydryl cation are calculated by density functional theory (DFT) with the B3LYP functional in the gas phase. The calculations have been performed by Dr. Igor Pugliesi.

important contributions to the absorption signal. Upon planarization of the cation, the $S_1 \leftarrow S_0$ transition shifts to the blue and increases in strength while the transitions to higher states become less important. Only the cation with planar configuration exhibits the full, strong absorption band as reported for example in Ref. [11]. Therefore, the geometric relaxation of the cation after the bond cleavage leads to the generic strong absorption signal increase with time constants of about 300 fs. The decreasing influence of transitions to higher electronic states leads to a simultaneous narrowing of the absorption band. As the initially generated radicals also undergo a planarization from the tetragonal conformation, an analogous behavior of the radical absorption signal can be safely expected.

The bond cleavage process causes furthermore a strong change in the dipole moment: benzhydryl chloride exhibits a rather small dipole moment which increases significantly when the ion pair is formed. The surrounding solvent molecules respond to this change and start solvating the new charge distribution (see Figure 3.3). The solvation leads to a change in the energy difference between the electronic states and thus to a spectral shift of the absorption bands (see also Section 2.7) [51]. Since, for the solvents studied within this thesis (e.g., acetonitrile or dichloromethane), typical solvation times are on the order of several hundreds of femtoseconds [54], a spectral shift of the benzhydryl radical and cation absorption band can be observed on this time scale. It can be determined by the algorithm described in Section 2.7. Figure 3.4 depicts the cation peak position after photolysis of differing benzhydryl chlorides in acetonitrile. A pronounced blue shift can be observed for all different species in the first picosecond. The temporal evolution can be well fitted with an exponential function with a time constant of about 230 to 300 fs. These values are in excellent agreement with the published average solvation times of 260 fs for acetonitrile [54].
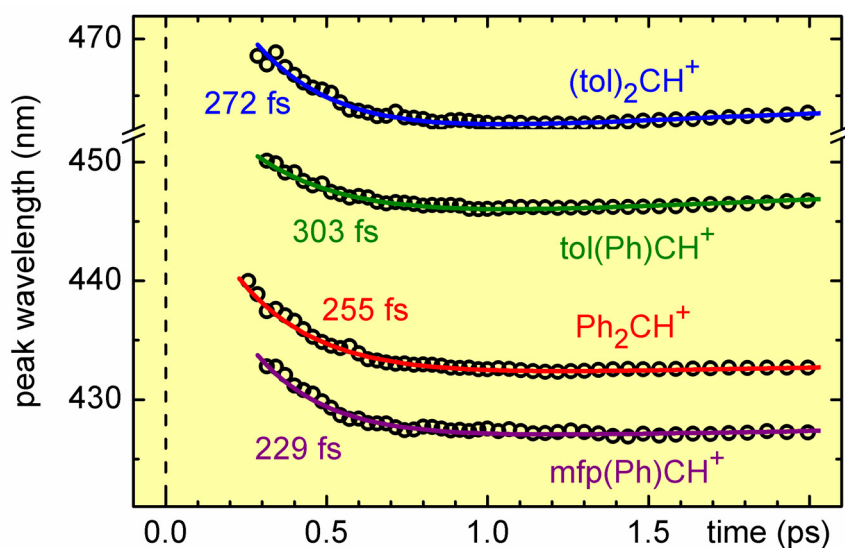
Figure 3.4: Evolution of the absorption band position (black circles) for different benzhydryl cations (see Table 3.1) after photogeneration from the benzhydryl chlorides in acetonitrile. The exponential fits are shown as colored lines.

The absorption signal increases with a time constant of 300 fs and the solvation-induced spectral shift of the band position is observed in both benzhydryl chlorides and phosphonium salts. However, the effects are much more pronounced for the chloride precursors. The generation of benzhydryl cations from phosphonium salts takes about 5 ps to 10 ps depending on the substituents on the phenyl rings. It is therefore significantly slower than the subsequent planarization and solvation. Therefore, these effects can not be fully resolved within these systems anymore. Furthermore, the effect of solvation is less important, since in contrast to the chloride the precursor is already cationic and the change in the charge distribution is relatively small upon the bond cleavage.

3.4 Carbocation formation through electron transfer within the radical pair

The photoexcitation and subsequent bond cleavage of benzhydryl chloride Ph_2CHCl leads predominantly to the formation of radical pairs $Ph_2CH^\bullet$ / $Cl^\bullet$. Heterolytic bond cleavage leading to ion pairs (Ph_2CH^+ and Cl^-) is only a minor channel. In acetonitrile the ratio between radical pair to ion pair formation is 20 to 1. This dominance of homolysis over heterolysis is found for a wide range of solvent polarity: from apolar solvents like cyclohexane or n-heptane up to polar solvents such as acetonitrile (CH_3CN). The ion pair in (moderately) polar solvents is, however, thermodynamically more stable than the radical pair: The Gibbs free reaction energy of the electron transfer ΔG_{ET} is about -1.7 eV for the $Ph_2CH^\bullet$ / $Cl^\bullet$ radical pair in acetonitrile as found from experiment [63] and theoretical calculations. In the less polar solvent dichloromethane, the driving force is still highly exergonic ($\Delta G_{ET} \approx$ -1.3 eV). In other words, the formation of ion pairs Ph_2CH^+ / Cl^- from the radical pair $Ph_2CH^\bullet$ / $Cl^\bullet$ by the transfer of an electron within the radicals is energetically favorable in these solvents. However, only in acetonitrile a significant amount on benzhydryl cations was detected on the nanosecond time scale while in dichloromethane almost no cations were found [11].

The photo-generation and dynamics of the benzhydryl radical and cations and their solvent dependence was therefore studied within a combined experimental and theoretical investigation

"A Comprehensive Microscopic Picture of the Benzhydryl Radical and Cation Photo-Generation and Interconversion through Electron Transfer"
C. F. Sailer, S. Thallmair, B. P. Fingerhut, C. Nolte, J. Ammer, H. Mayr, R. de Vivie-Riedle, I. Pugliesi, E. Riedle
To be submitted to ChemPhysChem.

In Figure 3.5, the observed transient absorption after 270 nm excitation of Ph_2CHCl at the maximum wavelength of the benzhydryl cation and radical band is shown. In the first picosecond a strong rise of the radical signal and a less pronounced rise of the cation signal due to bond cleavage and subsequent planarization is observed (see Section 3.2 and 3.3). The subsequent decay of the radical population and the simultaneous rise of the cation population on the tens of picosecond scale can be assigned to the electron transfer. Since the rate of the electron transfer $k_{ET}(r)$ decreases exponentially with the distance between electron donor and acceptor[9] [64] it is terminated when the distance between the benzhydryl radical and the chlorine radical becomes too large, e.g., by diffusion. Therefore, a fraction of the radical pair population does not undergo electron transfer and remains stable for the next nanoseconds

---

[9] Strictly speaking, the (solvent) reorganisation energy in the Marcus theory is also distance dependent and leads to a correction to the purely exponential behavior.

(see Section 3.7). In contrast, part of the cation population decays within the next hundreds of picosecond which can be attributed to geminate recombination. Again, geminate recombination is only possible as long as the ions are in close vicinity and a sizeable fraction of the carbocations escapes from the Cl⁻ and survives.
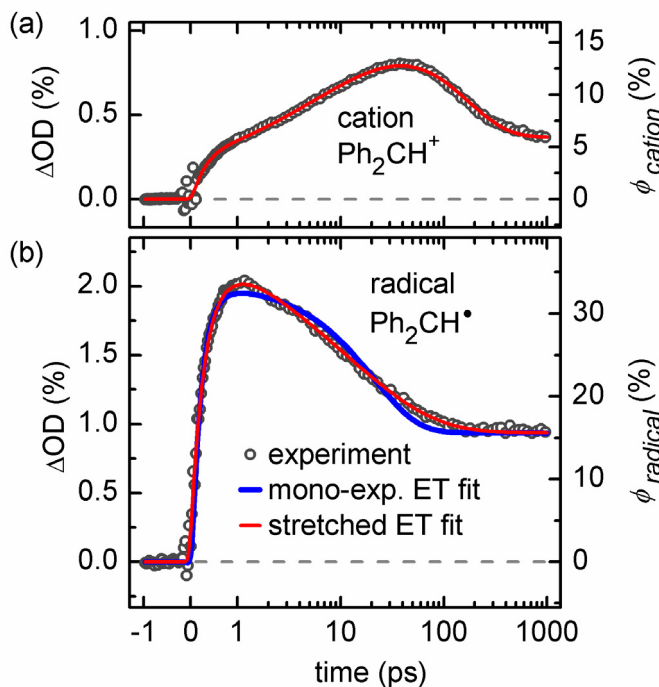
Figure 3.5: Transient absorption (grey dots) observed after 270 nm excitation of Ph$_2$CHCl in acetonitrile at the absorption maximum of the (a) benzhydryl cation and (b) benzhydryl radical band. The mono-exponential fit of the electron transfer dynamics of the radical is shown in blue, the stretched-exponential fit in red. The further dynamics (e.g., planarization and geminate ion pair recombination) are fitted with a sum of exponential functions.

Marcus-Smoluchowski model. The experimentally observed photo-induced dynamics of benzhydryl chlorides in various solvents can be understood by the consideration of time and distance dependent radical and ion pair population distributions $P_{RP}(R,t)$ and $P_{IP}(R,t)$ which are subject to diffusion and distance dependent rates and processes. The benzhydryl radical / cation and the chlorine radical / chloride anion are modeled as spheres with radii $R_{benzhydryl}$ and R_{Cl}. R denotes the distance between the centers of the two spheres and $R_C = R_{benzhydryl} + R_{Cl}$ is the contact distance. The evolution of a given radical and ion pair population distribution and their interconversion cannot be obtained directly by the propagation of $P_{RP}(R,t)$ and $P_{IP}(R,t)$. Two underlying distribution functions $S_{RP}(R,t)$ and $S_{IP}(R,t)$ have to be used instead [65,66]:

$$P_{RP}(R,t) = 4\pi R^2 \, S_{RP}(R,t) \exp\left[-V_{RP}(R)/k_B T\right] \qquad (3.1)$$

$$P_{IP}(R,t) = 4\pi R^2\, S_{IP}(R,t)\exp\left[-V_{IP}(R)/k_BT\right] \tag{3.2}$$

with the intrapair potentials $V_{RP}(R)$ and $V_{IP}(R)$. The potentials account for the influence of the solvent structure and, for the case of the ion pair, the Coulomb attraction (see Appendix C for a discussion of the individual terms). The temporal evolution of $S_{RP}(R,t)$ and $S_{IP}(R,t)$ is given by two coupled partial differential equations [66-68]:

$$\frac{\partial}{\partial t}S_{RP}(R,t) = L^+ S_{RP}(R,t) - k_{ET}(R)S_{RP}(R,t)$$
$$- k_{rec}^{RP}(R)S_{RP}(R,t) - k_{esc}^{RP}(R)S_{RP}(R,t) \tag{3.3}$$

$$\frac{\partial}{\partial t}S_{IP}(R,t) = L^+ S_{IP}(R,t) + k_{ET}(R)S_{RP}(R,t)\exp\left[-\frac{e^2}{4\pi\varepsilon_0\varepsilon_{st}k_BT}\frac{1}{R}\right]$$
$$- k_{rec}^{IP}(R)S_{IP}(R,t) - k_{esc}^{IP}(R)S_{IP}(R,t) \tag{3.4}$$

L^+ is the adjoint Smoluchowski operator in spherical coordinates [68]:

$$L^+ = \frac{1}{R^2}\exp\left[V(R)\right]\frac{\partial}{\partial R}\left(D(R)R^2\exp\left[-V(R)\right]\frac{\partial}{\partial R}\right) \tag{3.5}$$

where $D(R)$ is the mutual diffusion coefficient of the particles.

The equations 3.3 and 3.3 are coupled by the electron transfer term. It is a sink term for the radical pairs and a source term for the ions. The factor $\exp\left[-e^2/\left(4\pi\varepsilon_0\varepsilon_{st}k_BT\cdot R\right)\right]$ in the electron transfer source term in 3.4 is hereby needed for a consistent transfer from the radical to the ion pair distribution. The rates k_{rec}^{RP} and k_{rec}^{IP} account for the geminate recombination of radical or ion pairs and the escape rates k_{esc}^{RP} and k_{esc}^{IP} lead to the formation of free, unreactive photofragments.

The rate for the distance dependent electron transfer $k_{ET}(R)$ is modeled by Marcus theory [64]:

$$k_{ET}(R) = \frac{2\pi}{\hbar}\cdot\frac{V_{eff}^2}{\sqrt{4\pi\lambda(R)k_BT}}\cdot\exp\left(-\frac{\left(\lambda(R)+\Delta G_{ET}\right)^2}{4\lambda(R)k_BT}\right)\cdot\exp\left(-\beta(R-R_c)\right) \tag{3.6}$$

with the effective electronic coupling V_{eff} and the change in Gibbs free energy ΔG_{ET} which can be obtained by quantum chemical calculations. The last term describes the exponential fall-off of the rate with increasing distance ($\beta = 0.7\ \text{Å}^{-1}$). The reorganization energy λ is also distance dependent:

$$\lambda(R) = \lambda_{in} + \frac{e^2}{8\pi\varepsilon_0}\left(\frac{1}{\varepsilon_{op}} - \frac{1}{\varepsilon_{st}}\right)\cdot\left(\frac{1}{r_{benzhydryl}} + \frac{1}{r_{Cl}} - \frac{2}{R}\right) \tag{3.7}$$

with λ_{in} the internal reorganization energy and ε_{op} and ε_{st} the relative optical and static permittivity of the solvent.

The rate for geminate recombination of the photofragments $k_{rec}(R)$ is assumed to fall off exponentially with distance with a somewhat shorter range than the electron transfer [69]. Influences of the solvent structure are modeled by an effective, intrapair potential. This accounts for the fact that it is more favorable for a photofragment pair to be in a distance which corresponds to zero, one or two solvent diameters. The ion pair is additionally subject to the Coulomb potential originating from the two opposite charges, which makes it more difficult for the ions to separate diffusionally.

The mutual diffusion coefficient $D(R)$ is given by:

$$D(R) = D_F \left[1 - \frac{1}{2} \exp \left(-\frac{R - R_c}{d_{solv}} \right) \right] \qquad (3.8)$$

with the solvent diameter d_{solv} (≈ 3.6 Å for acetonitrile [70]). $D(R)$ corresponds to the bulk value of the mutual diffusion coefficient D_F for large distances. At contact distance it is reduced to the half which accounts for the hydrodynamic effect. The particles have to force the solvent out of the path which is more difficult when the particles are close to each other [71].

The solvation of the photofragments in the Marcus-Smoluchowski model is described by a continuum approach. The basic assumption of this approach is that the fragments are surrounded with a complete solvation shell for all fragment distances. A fully stabilizing solvation shell is only formed, however, at distances large enough to accommodate a solvent molecule between the two ions, i.e., about 4 Å for acetonitrile. The formation of a solvation shell leads to a sudden decrease of the energy of the system as the photofragments move apart and prevents them from reencounter. We model this solvation induced barrier by the introduction of the distance dependent escape rates $k_{esc}^{RP}(R)$ and $k_{esc}^{IP}(R)$. By the escape rates, part of the radical and ion pairs are transferred to distributions of unreactive species. These are also propagated by equations similar to Eqs. 3.3 and 3.3 without, however, the possibility to undergo electron transfer or geminate recombination.

Related models, based on the Smoluchowski equation and Marcus theory, have already been used for the description of the electron transfer between statistically distributed electron donors and acceptors in solution [66,68]. The system of equations developed within this work constitutes a consequent evolution of these models. It allows for the theoretical modeling of the evolution of photolytically generated pairs from their generation to the time scale where they are fully separated. In contrast to the previous models, arbitrary initial populations of differing species can be propagated and interconverted without restrictions of source or sink terms. In this way, it was possible to include the electron transfer as well as radical recombination into the calculations which was not feasible with the earlier models.
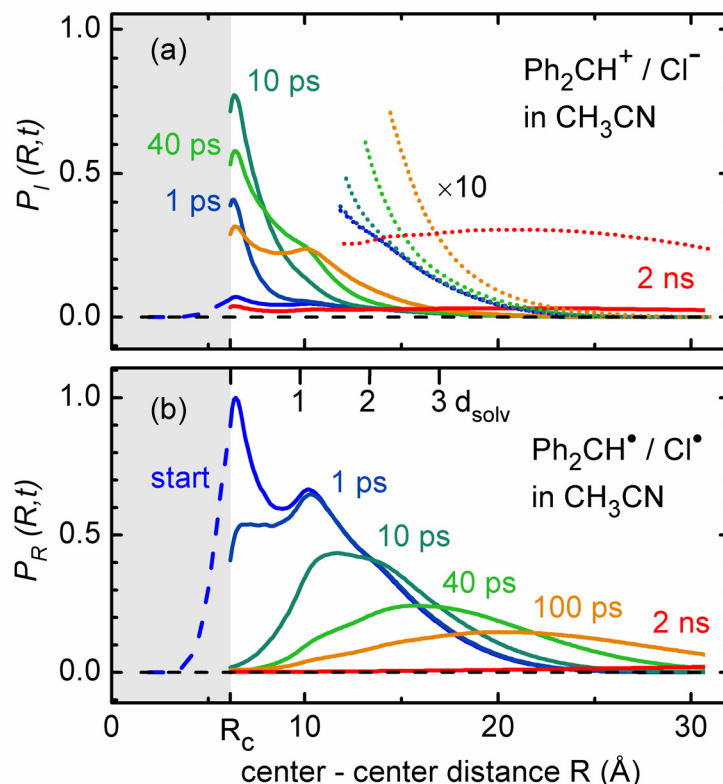
Figure 3.6: Temporal evolution of the population distribution of a) the ion pair Ph$_2$CH$^+$ / Cl$^-$ and b) the radical pair Ph$_2$CH$^\bullet$ / Cl$^\bullet$ in acetonitrile. The shaded areas indicate distances smaller than the contact distance R$_c$.

Population distributions. The initial distance distribution of the radical and ion pair populations is assumed to be Gaussian with the maximum near to contact distance. It comprises species separated by one and two solvent molecules as well as pairs which are in contact (see Figure 3.6). Similar broad distance distributions have been reported for electrons that are photo-ejected from I$^-$ in aqueous solution [72]. Narrower initial conditions were also tested. They led, however, to strong deviations from the observations.

The simulations show that within the first ten picoseconds, radical pairs in close vicinity undergo electron transfer very efficiently, while radical pairs at larger distances survive with a significantly higher probability (see Figures 3.6 and 3.7). This leads to an increase in the mean radical separation. With advancing time, diffusion becomes increasingly important and leads to a further separation of the radicals until – for sufficiently large distances – free radicals are generated. The time-dependent distance distribution of the ion pairs reflect the conditions of their formation. The ion pairs generated within the first ten picoseconds are in close vicinity. Up to 100 ps the mean ion pair separation increases since they are generated from radical pairs with larger separations. Only after 100 ps the diffusion is the main process leading to a further separation of the ions and which leads to the formation of free ions.
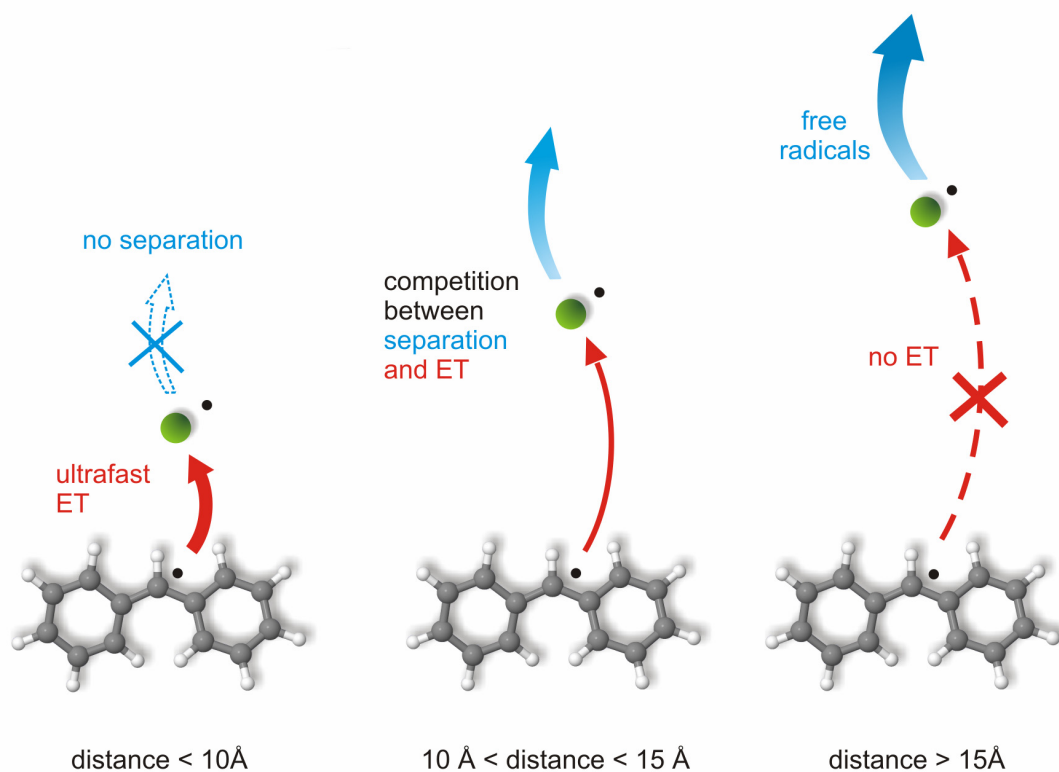
Figure 3.7: The three benzhydryl radical - Cl$^\bullet$ distance regimes which determine the fate of the generated radical pairs. For small separation distances, the radical pairs undergo a very fast electron transfer giving rise to ion pairs. For large distances diffusional separation dominates and free radicals are formed. At intermediate separations, the electron transfer competes with the diffusional separation.

Comparison to the experiment. The integration of the distance dependent population distributions of radical pairs $P_R(R,t)$ and ion pairs $P_I(R,t)$ over the distance R leads to the radical and ion populations $P_R(t)$ and $P_I(t)$ which are proportional to the experimentally observed absorbance of the species (see Figure 3.8). A close agreement between the simulated populations and the optical signals is found for both species from 1 ps up to the end of the measurement. The deviation for times smaller than 1 ps originates from the increase in optical signal strength due to planarization and solvation of the benzhydryl radicals and cations as described in Section 3.3.

The resulting radical and ion populations $P_R(t)$ and $P_I(t)$ without the inclusion of escape rates are shown in Figure 3.8 as green dashed lines. Without the escape, the radicals undergo a slow but lasting electron transfer up to at least 1 ns which leads to a further decrease of the radical population. Only for even longer times a certain leveling of the radical population occurs. Due to the longer lasting electron transfer, the cation population between about 100 ps to 1 ns is slightly higher when compared to the simulated population with escape rates. The geminate recombination, however, becomes more efficient and leads to a pronounced depletion of the cations up to tens of nanoseconds.
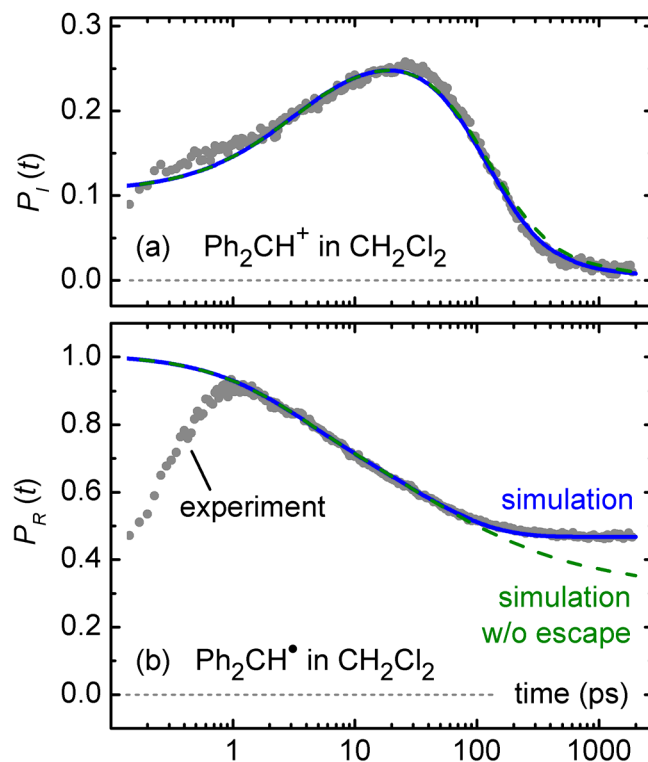
Figure 3.8: Comparison of the simulated population (blue line) with the experiment (grey dots) in dichloromethane. The simulated populations without the inclusion of a radical escape rate is shown as green dashed line.

Microscopic model. In a classical analysis, the experimental data are interpreted by postulating distinct states and intermediates which are converted into each other with respective, well-defined rate constants. The rate constants are then determined by fitting exponential functions to the observed signals (Section 2.2) or by the procedure described in Section 2.3. This approach is however a simplification of the conditions encountered in the real, microscopic system. Small differences of the microscopic configuration of the system can lead to significant changes in the rate. The experiment, however, observes always an ensemble averaged rate.

In the case of the photo-induced processes of benzhydryl chlorides, the broad population distribution P(R) of distances between the photofragments is the main reason for variations of rates. These variations are inherently included in the microscopic simulations developed in this work by the distance dependent rates k(R). From (quantum) chemical considerations, the distance dependence of the electron transfer [64] or the geminate recombination [69] are known precisely. By spatial averaging of the rate over the time-dependent spatial distribution the experimentally observable rate is obtained:

$$k(t) = \frac{\int k(R) P(R,t) \, dR}{\int P(R,t) \, dR} \qquad (3.9)$$

From the population distribution together with the distance dependent rate a new, refined microscopic model arises. It replaces the kinetic model with defined transitions between distinguishable species by a unified description of the population evolution. The probability of a transition, i.e., its rate, is then depending on the microscopic conditions of the system.

Stretched exponential electron transfer dynamics. The electron transfer dynamics is clearly not exponential. Significant deviations from the measured signal results, when the electron transfer dynamics of the radical is fitted mono-exponentially. The fit reproduces, however, the data faithfully when a stretched exponential function is used instead (see Figure 3.5b). The rise of the cation due to the electron transfer can be fitted with the same stretched exponential function (i.e., the same time constant).

The non-exponential dynamics is caused by the broad distance distribution of radical pairs after the bond cleavage and the distance-dependent electron transfer rate. As described above, the radical pairs with small separations undergo electron transfer very fast and efficiently. With increasing separation the electron transfer becomes slower and less efficient. According to Eq. 3.9 this leads to a time-dependent rate and thus to a stretched-exponential electron transfer dynamics [37]. A similar behavior was reported for the photoinduced electron transfer in a flexibly linked donor-acceptor system [39].

Peak Shifts as probe for the distance. The temporal increase of the mean separation within the radical and ion pairs – first due to the electron transfer, then by diffusion – can also be observed in the transient UV/Vis spectra. As was shown by Schneider et al. the position of the benzhydryl cation absorption band maximum can be a sensitive probe for the presence of anions [43]: A blue-shift of about two nanometers was reported for the cation absorption band upon adding anions, attributed to the formation of ion pairs.

An analogous effect can be recognized upon evaluation of the benzhydryl radical and cations peak position from the measured transient spectra (see Section 2.7 for the precise evaluation of band positions). The cation absorption band undergoes an initial blue shift in the first picoseconds (see Figure 3.9a) due to planarization and solvation after the bond cleavage (as described in Section 3.3). Within the next 500 ps the cation absorption band maximum shifts by about 2 nm to the red until it reaches a constant value of about 436.1 nm. The red-shift reflects the increasing separation between the two fragments making up the ion pair. In analogy to the findings of Schneider et al. the absorption band of the ion pair is slightly shifted to the blue compared to the free ions.
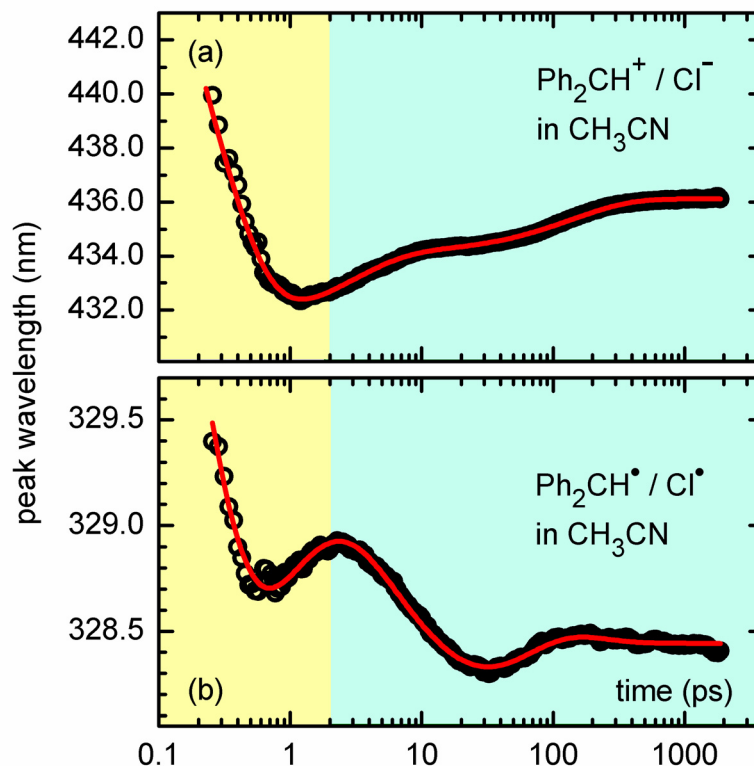
Figure 3.9: Experimentally observed (circles) and fitted (red line) time dependent peak position of the benzhydryl a) cation and b) radical after photogeneration from Ph_2CHCl in acetonitrile. The range where the shift is dominated by changes in the radical and ion pair distance distributions caused by electron transfer, geminate recombination and diffusion is highlighted in light blue. The evolution in the first 2 ps for the cation has already been shown in Figure 3.4.

The temporal evolution of the radical absorption band position is shown in Figure 3.9b. After the initial dynamics in the first picoseconds due to solvation and relaxation, the radical undergoes a significant blue shift within 30 ps. After a subsequent small red shift the peak position reaches the constant value of 328.4 nm. The blue shift originates from the better stabilization of the radical ground state upon exchange of the $Cl^\bullet$ radical by acetonitrile molecules.

Geminate ion pair recombination. The mayor loss channel for the generated benzhydryl cations within the first nanosecond is geminate recombination with the Cl^- in close vicinity. Only when the separation between the two ions becomes large enough by diffusion the cation becomes stable at least for the next hundreds of nanoseconds (see Section 3.7). However, the diffusional separation is strongly hindered by the Coulomb attraction between the two oppositely charged ions. In moderately polar solvents (e.g., dichloromethane) the time for an efficient separation is far too long. Therefore, nearly all of the cations present after bond cleavage and electron transfer undergo geminate recombination within a few hundreds of picoseconds and no cations can be detected on longer time scales (see Figure 3.10b).
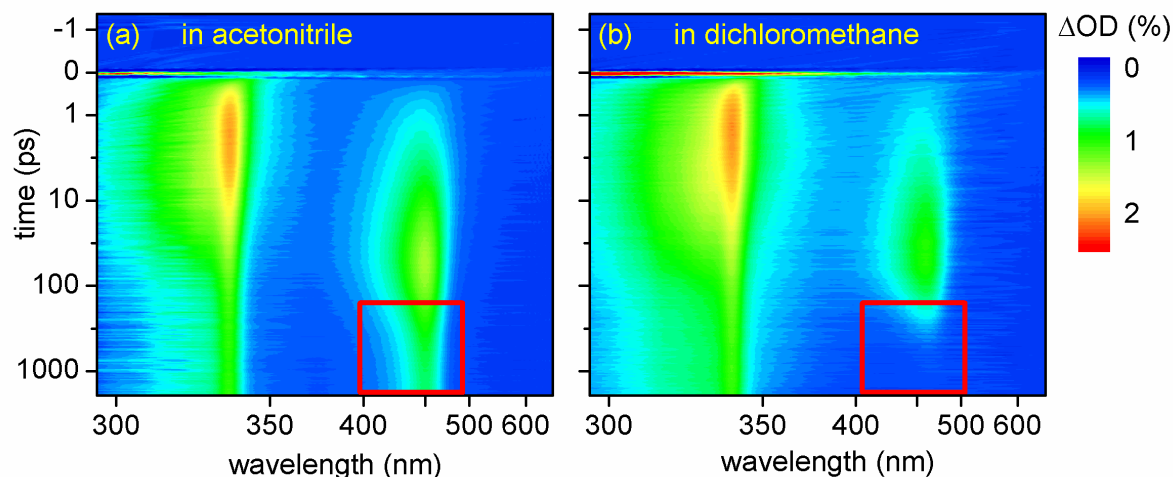
Figure 3.10: Transient absorption after 270 nm excitation of tol(Ph)CHCl in a) acetonitrile and b) dichloromethane. The dynamics is very similar within the first 200 ps. For longer delays, the benzhydryl cation signal in dichloromethane is quenched almost completely by geminate recombination while in acetonitrile a significant fraction survives (highlighted by the red boxes, see text for details).

Only in the highly polar acetonitrile a reasonable yield of benzhydryl cations is observed (see Figure 3.10a). The high permittivity of the medium ($\varepsilon_r = 35.94$) provides a good shielding of the charges and permits for the diffusional separation of the photofragments. Still, a mayor part (70%) recombines since the rate for geminate recombination is higher than the one for the escape ($(198\,\text{ps})^{-1}$ vs. $(456\,\text{ps})^{-1}$).

3.5 Cation generation from phosphonium salts: The role of the counterion

The photolysis of neutral precursors (namely benzhydryl halides) is a suitable method for the generation of series of different substituted benzhydryl cations in polar solvents [11]. However, the use of this class of precursors comes to a certain price:

- On the nanosecond time scale, benzhydryl cations are only observed in highly polar solvents (such as acetonitrile). In less polar solvents the Coulomb attraction between the benzhydryl cation and the anion is not sufficiently well shielded and no free ions are formed (see Section 3.4).

- Highly electrophilic cations (e.g., $(dfp)_2CH^+$) on the nanosecond time scale can only be generated with a quantum yield of ~1%.

- With the benzhydryl radical, a further highly reactive species is generated simultaneously which eventually can influence the reactivity measurement with an added nucleophile.

It was already shown by Modro and coworkers that triphenylphosphonium salts can act as precursors for the carbocation generation [73]. The use of benzhydryl phosphonium salts $Ar_2CH\text{-}PAr_3^+ X^-$ as precursor for the carbocation generation can lead to a significant improvement compared to the situation discussed above [74]. The escape of the benzhydryl cation Ar_2CH^+ from the neutral leaving group (PAr_3) should be more efficient. Furthermore, theoretical investigations suggest that after UV excitation, an efficient pathway exists which leads to benzhydryl cations and PAr_3 on the picosecond scale [75]. However, the choice of the leaving group and the counterion can strongly influence the mechanism of the photolysis and the obtained quantum yield of benzhydryl cations. A detailed, mechanistic investigation is reported in:

"Photolytic Generation of Benzhydryl Cations and Radicals from Quaternary Phosphonium Salts: How Highly Reactive Carbocations Survive Their First Nanoseconds"
J. Ammer, C. F. Sailer, E. Riedle, H. Mayr
Journal of the American Chemical Society **134**, 11481-11494 (2012).

After UV excitation (at 280 nm) of the benzhydryl phosphonium salt $Ph_2CH\text{-}PPh_3^+ BF_4^-$ in acetonitrile two signal contributions are observed within the first tens of picoseconds. The benzhydryl cation band at 435 nm which reaches its maximum within 25 ps and a broad absorption band below 400 nm which simultaneously disappears within 30 ps and which can be assigned to the absorption of the excited state. The formation of cations is thus much slower than for the chlorides (compare Section 3.2). This indicates that a significant potential

energy barrier exists which hampers the evolution of the excited molecule from the Franck-Condon region towards the cleaved photofragments [62].

The observed transient absorption data can not clarify ultimately whether the cations are generated directly from the excited precursor by heterolytic bond cleavage or whether the bond is cleaved homolytically and the generated radicals $Ph_2CH^{\bullet}$ / $PPh_3^{\bullet+}$ undergo an ultrafast electron transfer to give rise to the benzhydryl cation and PPh_3 (see Figure 3.11). For the latter process, the effective electron transfer rate between $Ph_2CH^{\bullet}$ / $PPh_3^{\bullet+}$ would have to be much higher than for the $Ph_2CH^{\bullet}$ / $Cl^{\bullet}$ radical pair (see Section 3.4). This is, however, conceivable as – due to the photofragments size – a larger fraction of $Ph_2CH^{\bullet}$ / $PPh_3^{\bullet+}$ compared to $Ph_2CH^{\bullet}$ / $Cl^{\bullet}$ should be formed in close contact. As the electron transfer rate falls off exponentially with distance (see Eq. 3.6), this would lead to a significantly higher electron transfer rate, given that the rate at contact distance remains the same for both cases. Analogously to the cations generated from the benzhydryl chloride precursor, the cations formed by photolysis of the phosphonium salt can undergo geminate recombination with the leaving group as long as they are not separated diffusionally.
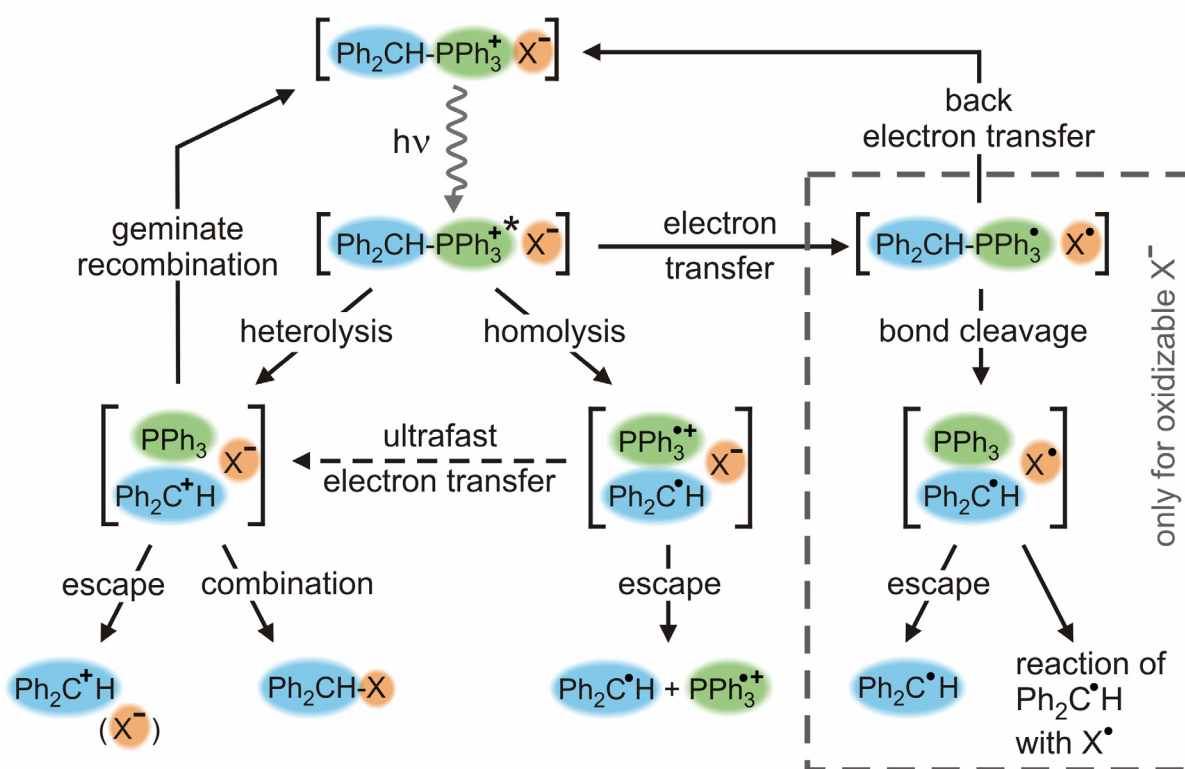
Figure 3.11: Photogeneration of benzhydryl cations and radicals from phosphonium salts (e.g., $Ph_2CH\text{-}PPh_3^+$ Cl^-). The electron transfer mechanism on the right is only possible for ion pairs with oxidizable counterions (e.g., $X^- = Cl^-$ or Br^-).

Influence of the counterion. We studied the influence of the counterion X^- ($X^- = Cl^-$, Br^-, BF_4^- or SbF_6^-) on the photo-induced dynamics. For low precursor concentrations and high solvent polarity, the association equilibrium between paired benzhydryl phosphonium cations and the counterion with the free ions is clearly on the side of the free species:

$$\left[Ar_2CH - PPh_3^+ X^- \right] \quad \underset{\longleftarrow}{\overset{\longrightarrow}{}} \quad Ar_2CH - PPh_3^+ \quad + \quad X^-$$
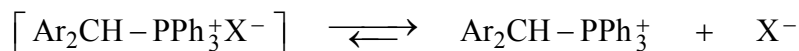
The dynamics after UV excitation is therefore influenced by the counterion at the earliest on the nanosecond time scale when diffusional encounter can take place.

The situation is different in solvents of moderate to low polarity or for high precursor concentrations where the equilibrium is shifted towards the side of the paired ions. For the precursor concentrations used in the transient absorption measurements ($\sim 10^{-3}$ M^{-1}), 10% to 60% exist as ion pairs in dichloromethane.

We found no changes in the photo-induced dynamics on the femto- to low nanosecond scale when we used BF_4^- or SbF_6^-. However, in the presence of oxidizable counterions (Cl^- and Br^-), we observed a competition between the aforementioned heterolytic bond cleavage leading to benzhydryl cations and an electron transfer from the counterion to the excited precursor leading to the $Ph_2CH\text{-}PPh_3^\bullet$ / $X^\bullet$ radical pair (see Figure 3.11). The radical $Ph_2CH\text{-}PPh_3^\bullet$ is not stable and undergoes bond cleavage which gives rise to the benzhydryl radical $Ph_2CH^\bullet$ and PPh_3. The thus formed $Ph_2CH^\bullet$ / PPh_3 / $X^\bullet$ pair resembles the radical pair $Ph_2CH^\bullet$ / $Cl^\bullet$ generated by to the homolysis of benzhydryl chlorides described in Section 3.4. Just as the latter, it can escape leading to free radicals, it can undergo electron transfer giving rise to the ion pair or the radicals can combine.

Comparison to Cl^- as leaving group. The photolysis of benzhydryl phosphonium salts leads to a significantly higher yield of benzhydryl cations on the nanosecond time scale. While for Ph_2CHCl in acetonitrile the cation quantum yield is 6%, the quantum yield for the generation of the same cation is 18% when $Ph_2CH\text{-}PPh_3^+$ BF_4^- was used as precursor (see Figure 3.12). The difference becomes even more striking when dichloromethane is used as solvent: While from Ph_2CHCl the quantum yield for free ions is too small (<1%) to be determined with adequate accuracy, the yield is 9% when the phosphonium salt is photolyzed. The higher cation quantum yields in both solvents are a consequence of the higher initial cation yield[10] as well as the less efficient geminate recombination: while typically ~70% of the benzhydryl cation / Cl^- recombine, only ~25% of the cations undergo geminate recombination with PPh_3. This can be explained by the faster separation of the two photofragments. Although the PPh_3 leaving group is larger than the Cl^-, the escape rate is about four times higher ($\sim(120\,ps)^{-1}$ vs. $\sim(450\,ps)^{-1}$) due to the strongly reduced Coulomb interaction.

---

[10] after the heterolytic bond cleavage for the phosphonium salt or the electron transfer for the chloride
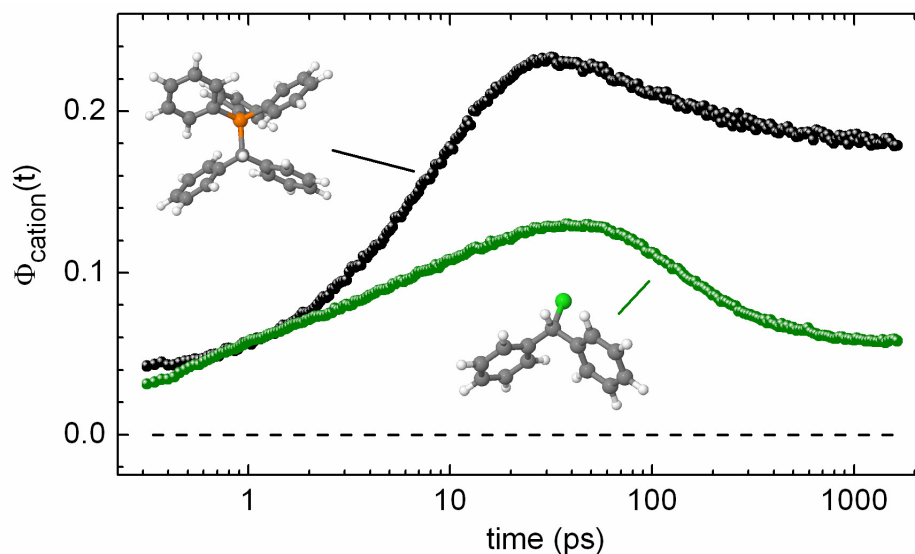
Figure 3.12: Comparison of the time-dependent quantum yield for benzhydryl cation generation from Ph_2CHCl (green) and $Ph_2CH\text{-}PPh_3^+\ BF_4^-$ (black) in acetonitrile.

Optimization of the phosphine leaving group. We achieved a further increase of the cation quantum yield by the use of tris(para-chlorophenyl)phosphine $P(p\text{-}Cl\text{-}C_6H_4)_3$ as leaving group. While for the cation Ph_2CH^+ the increase is rather small (18% vs. 20%) it becomes more pronounced for the more electrophilic cations: For dfp_2CH^+ in acetonitrile the quantum yield is more than doubled (~2% vs. 5%-8%[11]). The increase can be rationalized by the higher thermodynamic preference of the heterolytic pathway compared to the homolytic one. Furthermore, $P(p\text{-}Cl\text{-}C_6H_4)_3$ is less nucleophilic than PPh_3 (nucleophilicity parameter N: 12.58 vs. 14.33 [76]) leading to a smaller geminate recombination yield.

---

[11] There are no published value of the molar absorption coefficient of this cation. It was estimated to be in the range of similar benzhydryl cations.

### 3.6 Relative orientation of the photofragments

The transient absorption spectra shown within this work are almost all measured with a well defined angle between the polarization axes of pump and probe beam. This angle of ~54.7° is commonly called 'magic angle' since at this configuration the signal is not influenced by statistical rotational motions of the observed chromophores [77]. Transient data containing such signal changes do not allow for an easy determination of the quantum yields, since the proportionality between the concentration of a molecule and the absorbance is not valid anymore.

However, additional information can be gained when measuring with a parallel or perpendicular polarization configuration. From these measurements one easily obtains the time-dependent anisotropy [78]:

$$r(\lambda, t) = \frac{A_{\parallel}(\lambda, t) - A_{\perp}(\lambda, t)}{A_{\parallel}(\lambda, t) + 2A_{\perp}(\lambda, t)} \tag{3.10}$$

with the measured absorbance at parallel polarization $A_{\parallel}$ or perpendicular polarization $A_{\perp}$ at time t and wavelength λ. The anisotropy is therefore positive, when the measured absorbance at parallel polarization is greater than for perpendicular orientation. It becomes zero if the two signals are equal. The temporal decay of the anisotropy is typically exponential and yields the rotational relaxation time, i.e. the time after which the orientation of a chromophore is not correlated to the initial orientation anymore [77]. In temporal or spectral regions in which no transient absorption signal is observed (e.g., for negative delay times and in the shown case for the spectral region above 500 nm) the anisotropy is undetermined.

Anisotropy after photo-induced bond cleavage. The anisotropy r (λ,t) observed after UV excitation of Ph_2CHCl in acetonitrile is shown in Figure 3.13. Red colors indicate high anisotropy, while small (or negative) anisotropy is shown in blue. After the excitation, two spectral regions of high anisotropy are visible which coincide with the absorption bands of benzhydryl radical and cation. The anisotropy decays within the first tens of picoseconds. In order to obtain the rotational relaxation times, the anisotropy at the maxima of the benzhydryl cation and radical absorption bands was fitted monoexponentially. We found rotational relaxation times of 10.7 ps for the benzhydryl cation and 8.6 ps for the radical. A comparative fit on the integral over the absorption bands did not lead to any significant changes in the decay time. The slightly longer rotational relaxation time of the cation can be explained by the stronger interactions between the cation and the solvent compared to the radical. The polar acetonitrile molecules are attracted to the positive charge of the cation and slow down reorientational motions.
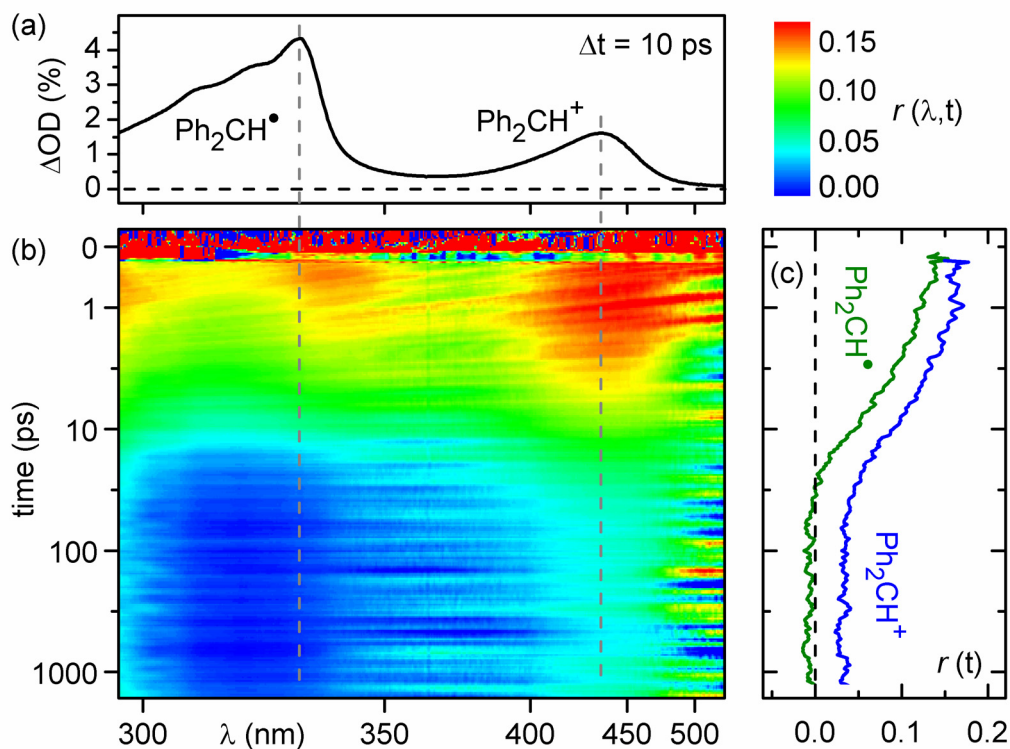
Figure 3.13: (a) Transient spectrum recorded after 10 ps and (b) time-dependent anisotropy r (λ,t) of Ph_2CHCl in acetonitrile after UV excitation. The position of the photoproduct absorption band maxima is given by the grey dashed lines. (c) Anisotropy r(t) at the indicated absorption maximum of benzhydryl cation (blue line) and radical (green).

The rotational relaxation times of about 10 ps are rather fast. For the resorufin anion in acetonitrile a rotational reorientation time of 34 ps is reported [79] although it is similar in shape and only slightly larger than the benzhydryl cation. The origin of the fast rotational relaxation is still not answered definitely. An explanation could be found in the bond cleavage process. Upon elongation of the C-Cl bond, the momentum is equally partitioned between the two nascent fragments and it is probable that the fragments acquire some angular momentum as frequently observed in the gas phase [80]. The rotational motion of the cation originating from the bond cleavage would lead to a decrease of the rotational relaxation time.

Persistent anisotropy. The anisotropy at the absorption maximum of the benzhydryl radical decays entirely with the time constant of 8.6 ps. In contrast, the anisotropy at the maximum of the cation band levels after the initial decay in the first tens of picoseconds (see Figure 3.13c). Between 50 ps up to the end of the measurement at about 2 ns, the cation absorption band exhibits a constant anisotropy of about 0.035.

The origin of the persistent anisotropy of the benzhydryl cation absorption band is not clear. A degradation of the sample solution or a change in the pump energy can be ruled out by a further reference measurement conducted shortly after the anisotropy measurements. As

the cation is a small chromophore, a full rotational relaxation in the low viscosity solvent acetonitrile should occur in the detection window of ~2 ns. However, the benzhydryl is not a single solute in an otherwise fully isotropic solvent environment but the Cl⁻ anion creates a preferred orientation. It is conceivable that the cation exhibits differing lifetimes depending on its orientation towards the anion: it might be more easy for the cation to undergo geminate recombination when the central methyl carbon atom is oriented towards the anion compared to an orientation where a phenyl group is next to the anion (for a discussion of diffusion terminated geminate recombination see Sections 3.4 and 3.5). This would lead to a preferential survival of the latter orientation and a resulting anisotropy. However, the question arises why no back rotation to the reactive orientation is observed and why the diffusional separation of the two photofragments with a rate of $(456 \text{ ps})^{-1}$ does not lead to a decay of the anisotropy.

New dedicated experimental efforts are needed to answer this question. First, any systematic error inherent to the anisotropy measurement has to be ruled out. Most important is a well defined polarization of the probe light over the whole spectral detection window. With the aid of a reference measurement of a dye with known anisotropy the setup can be calibrated. A prime candidate is nile blue which shows transient signals from 300 nm up to at least 650 nm. It exhibits a rotational relaxation time in methanol of 129 ps [81] which leads to an entire decay of the anisotropy after ~2 ns.

The measurement of the anisotropy in dichloromethane as solvent would clarify the role of the diffusional separation as it is negligibly compared to acetonitrile. The anisotropy of the benzhydryl cations, when they are generated by photolysis of phosphonium salts, would give further insight into this issue since the photo-leaving group is uncharged and the mutual attraction of the fragments is largely decreased.

Direction of transition dipole moments. The initial value of the anisotropy $r(\lambda_B, t = 0)$ at the spectral position λ_B of an absorption band is linked to the angle Θ between the transition dipole of the excitation towards the dipole of the detected transition [78]:

$$r\left(\lambda_B, t = 0\right) = \frac{1}{5}\left(3\cos^2\Theta - 1\right) \tag{3.11}$$

From the initial anisotropy of the cation ($r = 0.170$) and that of the radical ($r = 0.139$) one can calculate the angle Θ to be 38.3° and 41.3°. The result is in close agreement with the theoretical values obtained from coupled cluster theory calculations (CC2, basis set: def-SV(P)) for the detected $D_5 \leftarrow D_0$ transition of the radical and the $S_1 \leftarrow S_0$ transition of the cation of 47° [62]. The relative orientation of the dipoles is shown in Figure 3.14.
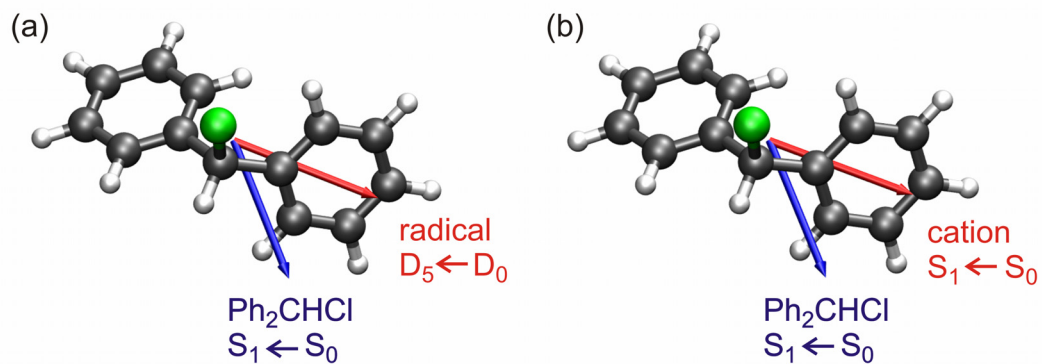
**Figure 3.14:** Orientation of the transition dipole of the excitation (blue arrows) towards the detected transition dipole of a) the benzhydryl radical and b) the benzhydryl cation (red arrows). The orientation is shown within the optimized geometry of the precursor Ph_2CHCl. The arrows lie all within the plotting plane, i.e., the angles between the dipoles are not biased by the perspective.

3.7 The fate of the photofragments

Even in solvents of rather low nucleophilicity (e.g., dichloromethane), the dynamics of the generated free benzhydryl radicals and free cations is not finished after the diffusional separation from the leaving group. Since both, radicals and cations, are highly reactive they can react on the nano- to microsecond on numerous ways. The possibilities include reactions with a chlorine radical / chloride anion after diffusional reencounter, reactions with the solvent, reactions with other precursor molecules, reactions with traces of water present in the sample or dimerization between two benzhydryl radicals which encounter by diffusion [11].
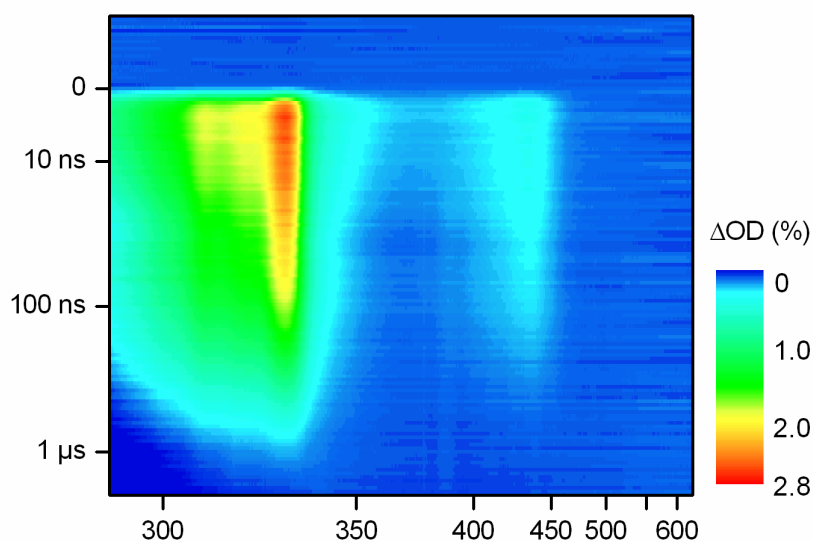
Figure 3.15: Transient spectrum observed after 270 nm excitation of Ph_2CHCl in acetonitrile measured with the nano- to microsecond setup described in Section 2.1.

The photo-induced dynamics of Ph_2CHCl in acetonitrile on the nano- to microsecond scale is shown in Figure 3.15 (see Section 2.1 for the experimental setup). Both, benzhydryl radical and cation, are present at the same spectral position as in the femto- to nanosecond measurement. They decay completely within the first microsecond and no residual signal is found throughout the spectrum at the end of the measurement. The absorption signal evolution of both photofragments have to be fitted with the sum of two exponential functions. A small part (12%) of the benzhydryl radical population decays with a time constant of 13 ns while the major part decays with a longer time constant of 330 ns. Similarly, a smaller fraction (26%) of the benzhydryl cations decays with a fast time constant of 15 ns, while the larger part decays significantly slower with a time constant of 280 ns.

3.8 Switching-off the effects of diffusion by encapsulation

The generated benzhydryl cations (and radicals) are highly reactive species which can react with rate constants as high as $(1 \text{ ps})^{-1}$ with an appropriate reaction partner (see for example Section 3.7). The leaving groups used within this work are highly reactive nucleophiles. Typical intrinsic rate constants for the geminate recombination after photolysis are on the order of $(200 \text{ ps})^{-1}$. If no further mechanism would be present, this would imply that after 200 ps more than 60% of the generated ion pairs had already recombined and after 1 ns hardly any cations would be detectable anymore. However, a significant population stable for (at least) nanoseconds is observed since the diffusion separates the two photofragments on a comparable time scale and impedes the recombination reaction effectively.
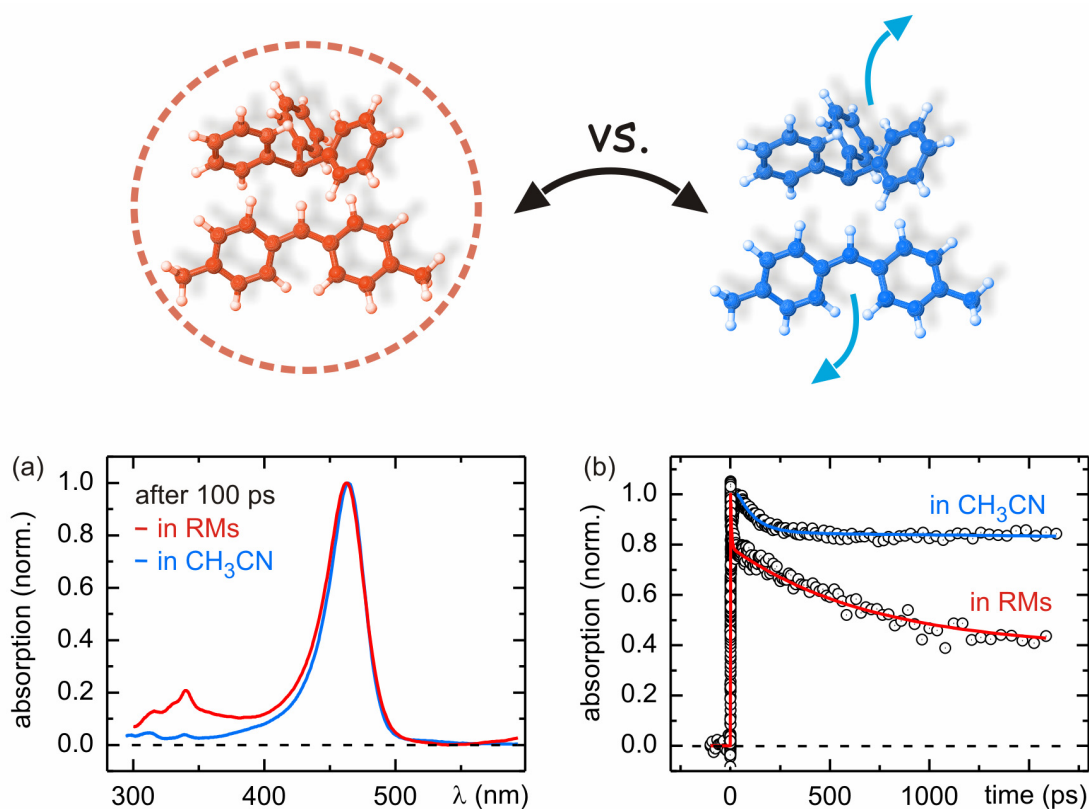
Figure 3.16: Geminate recombination dynamics of benzhydryl cations and PPh$_3$ encapsulated in a reverse micelle (in red) compared with the dynamics in bulk acetonitrile (in blue): (a) Normalized transient spectra after 100 ps. (b) Normalized transient absorption at the wavelength of the benzhydryl cation absorption band maximum. Both graphs are normalized independently.

This underlines the importance of proximity of two reaction partners for a fast, successful reaction with a high yield. In order to get a deeper inside in a bimolecular reaction when the diffusional separation is turned-off artificially we investigated the geminate recombination of a benzhydryl cation with the leaving group PPh$_3$ encapsulated within a reverse micelle:

"Encapsulation of diphenylmethyl phosphonium salts in reverse micelles: Enhanced bimolecular reaction of the photofragments"

C. F. Sailer, R. S. Singh, J. Ammer, E. Riedle, I. Pugliesi

Chemical Physics Letters **512**, 60-65 (2011).

We encapsulated $(tol)_2CH\text{-}PPh_3^+$ BF_4^- in reverse micelles (RM) filled with acetonitrile [82,83]. The solvent outside the RMs was cyclopentane which ensured that due to the ionic character of the precursor all precursors are located within the RMs.[12] The size of the RMs was hereby set to accommodate only one precursor.

The dynamics in the first picoseconds upon UV excitation of the precursor is very similar to the one observed in bulk acetonitrile (as shown in Section 3.5): The characteristic absorption band of the benzhydryl cation is fully formed indicating that the heterolytic bond cleavage and the subsequent geometric relaxation of the cation (as described in Section 3.3) are not disturbed decisively by the encapsulation (see Figure 3.16a). The subsequent geminate recombination dynamics differs, however, significantly. While in bulk acetonitrile the cation population is only decreased during the first ~200 ps, in RMs the decay lasts considerably longer and is not finished after 1.5 ns (see Figure 3.16b). Furthermore, a considerably larger part of the benzhydryl cations undergoes geminate recombination when encapsulated: 55% of the cations in RMs compared to 20% in bulk acetonitrile.

The longer lasting and more efficient geminate recombination of the encapsulated photofragments can be explained by the forced presence of the reaction partners in a reactive conformation. The rates for escape out of this conformation (e.g., by diffusion or rotation) and geminate recombination can be determined from the yields and dynamics (as shown in Section 2.3) and give insight into the process. While in bulk acetonitrile the two photofragments leave the reactive conformation with a rate of $(110\,\text{ps})^{-1}$, in the RMs the rate of $(1460\,\text{ps})^{-1}$ is more than one order of magnitude larger. The intrinsic rate for geminate recombination is also decreased from $(450\,\text{ps})^{-1}$ to $(1350\,\text{ps})^{-1}$ when the reaction partners are enclosed in a reverse micelle. This can be rationalized by the lowered solvent polarity in RMs [84] and the resulting lowered stabilization of the product (i.e., the precursor) compared to the benzhydryl cation.

A part of the cations generated in RMs survive the geminate recombination and lives for at least several nanoseconds. A possible explanation is that the photofragments rotate apart from each other, into a meta-stable conformation in which the geminate recombination is not likely.

---

[12] The solubility of the phosphonium salt in neat cyclopentane is negligibly small as shown in reference steady-state absorption measurements.

4. Bimolecular reactions faster than diffusion

Bimolecular chemical reactions in solution typically take place between two reactants which have to encounter by diffusion for a reaction to happen. For reactions that need many encounters of the reactants to overcome a barrier, the time for diffusional encounter is negligible compared to the time needed for the reaction itself. For very fast reactions on the other hand, diffusion is the factor which determines the speed of a reaction. The second-order rate constant is therefore limited to a value of about $k_2 \leq 10^{10}\,\mathrm{M}^{-1}\mathrm{s}^{-1}$ [67,85] which translate to several nanoseconds for the concentrations usually employed. The measured reaction rate is thus only the time needed for the diffusional encounter of the two reactants and no insight into the mechanism of the ultrafast bimolecular reaction itself is gained. Ultrafast spectroscopy has therefore not been considered to any degree for the study of bimolecular reactions.

Ultrafast spectroscopy can, however, be used to measure the bimolecular reaction process between the reactants A and B, provided that the reactants satisfy two conditions:

- The photo-generation of reactant A has to be as fast as possible. It is impossible to observe a reaction taking place in a few picoseconds, if one of the reactants is only formed within 100 ps. The carbocation precursors presented in Section 3 – benzhydryl chlorides and phosphonium salts – are therefore prime candidates for the study of ultrafast bimolecular reactions.

- Reactant B has to be readily available for a reaction. This implies that B is located in the immediate vicinity of the generated reactant A and no translational diffusion is needed for an encounter. There are several ways in which this requirement can be fulfilled, such as the encapsulation of the two compounds in a restricted environment (similar to the system described in Section 3.8) or the favorable association of the two reactants in solution[13] (as the ion pairs found in dichloromethane, see Sections 3.4 and 3.5).

The approach used in the following for the study of ultrafast bimolecular reactions is to photo-generate one reactant in a reactive solvent [86,87]. It constitutes a versatile approach as reactant A – in contrast to many association experiments – is always encompassed by reaction partners and the system cannot be influenced by the auxiliary environment as in encapsulation experiments. Through the absence of diffusional effects, the observed decay rate of the reactant is therefore directly linked to the solvent attack (see Figure 4.1a).

---

[13] This can also be regarded as an unimolar reaction of a complex.
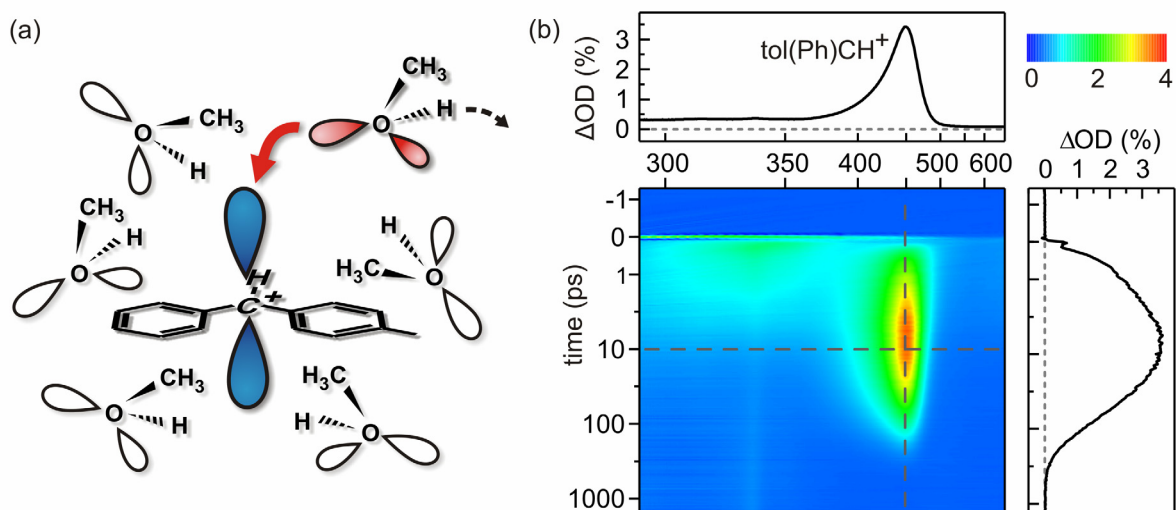
Figure 4.1: (a) Scheme of the attack of a solvent molecule (methanol) on a benzhydryl cation. The lone pairs of the attacking methanol are highlighted in red, the empty orbital of the cation in blue. (b) Transient absorption observed after UV excitation of tol(Ph)CH-PPh$_3$$^+BF_4$$^-$ in methanol. The transient absorption spectrum after 10 ps is shown in the top panel. In the right panel, the transient absorption at the maximum of the cations absorption band is shown.

Benzhydryl cations (Ar$_2$CH$^+$, Ar: Aryl) can react very fast with alcohols (e.g., methanol CH$_3$OH) [88-90] according to:

$$Ar_2CH^+ + CH_3OH \rightarrow Ar_2CH\text{-}OCH_3 + H^+$$
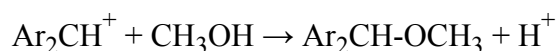
thus forming a benzhydryl ether and a proton which is transferred to neighboring solvent molecules. It opens up the possibility for photogenerating benzhydryl cations in alcohols and study the ultrafast bimolecular reaction with an alcohol molecule. Since the ether does only absorb in the deep UV (below 280 nm) the bimolecular reaction can be tracked by recording the decrease of the absorption band assigned to the benzhydryl cation. Figure 4.1b shows the measured transient absorption after UV excitation of tol(Ph)CH-PPh$_3$$^+BF_4$$^-$ in methanol. The benzhydryl cation band appears within the first picoseconds and reaches its maximum at about 10 ps in analogy to the photolysis of tol(Ph)CH-PPh$_3$$^+BF_4$$^-$ in acetonitrile (see Section 3.5). Subsequently, in strong contrast to the much less reactive acetonitrile, in methanol the cation absorption band decays completely within about 200 ps. The decay of the cation absorption band can be fitted exponentially with a rate constant of (62 ps)$^{-1}$. Since the cation is encompassed by reaction partners, the rate of (62 ps)$^{-1}$ is the intrinsic rate constant for the bimolecular reaction of a benzhydryl cation with a methanol molecule without the influence of diffusion.

4.1 Benzhydryl chlorides and phosphonium salts as precursors

The two leaving groups differ in two important aspects from each other: PPh_3 is twice as large as Cl^- (Onsager radius: 5.26 Å vs. 2.17 Å) and it is uncharged. As the leaving group is in the vicinity of the benzhydryl cations in the first hundreds of picoseconds, this provides the possibility to assess the influence of the leaving group on the ultrafast bimolecular reaction of a benzhydryl cation with an alcohol molecule.

For most of the studied benzhydryl cation / alcohol combinations, the cations were generated from the phosphonium salt. In contrast to the benzhydryl chlorides they do not undergo solvolysis which makes them a suitable class of precursor. They furthermore exhibit a higher cation quantum yield and no benzhydryl radical is formed as byproduct. However, the generation of benzhydryl cations by photolysis of the phosphonium salt is rather slow and the maximum of the cation population in inert solvents is reached only after 10 to 25 ps. This impedes the study of reactions with smaller time constants since the assignment of observed rate constants to the processes of generation and reaction is not trivial anymore. Furthermore, a reaction of the cations which is faster than their generation leads to small observable transient cation populations.

The reactions of the four most electrophilic cations in methanol have therefore been measured with the benzhydryl chlorides as precursors. Due to the substitution with fluorine on the aryl rings these derivatives undergo only a very slow solvolysis in methanol – from more than 9 hours for mfp(Ph)CHCl [91] to almost 100 years for $(dfp)_2CHCl$ [92]. This leaves enough time to measure the dynamics in methanol after UV excitation. Hereby, the first hundreds of femtoseconds are very similar to the behavior in inert, polar solvents such as acetonitrile: By ultrafast bond cleavage mainly benzhydryl radicals are formed but a small portion of cations appears as well. Interestingly, the electron transfer channel between the benzhydryl radical and the chlorine radical leading to an ion pair on the tens of picoseconds scale (as described in Section 3.4) seems to be not operational. After the initial signal increase due to planarization the radical signal remains virtually unchanged over the next hundreds of picoseconds. The slow characteristic solvation time of methanol and a connected inferior stabilization of the cation could be a reason for the absence of the electron transfer in the polar methanol: while the mean solvation time $\langle \tau \rangle$ in acetonitrile is 0.26 ps, it is almost 20 times longer in methanol ($\langle \tau \rangle$ = 5.0 ps) [54].

The benzhydryl cation $mfp(Ph)CH^+$ has been generated from the benzhydryl chloride mfp(Ph)CHCl as well as from the phosphonium salt $mfp(Ph)CH\text{-}PPh_3^+BF_4^-$. The rate constant of the subsequent reaction with methanol was hereby unaffected from the choice of the precursor: for the cations generated from mfp(Ph)CHCl a rate constant of $(21.2\,ps)^{-1}$ was found whereas the rate constant was $(21.6\,ps)^{-1}$ when the cation was generated from

mfp(Ph)CH-PPh$_3^+$BF$_4^-$. A significant influence of the photo-leaving group on the rate constant of the reaction can therefore be ruled out.

4.2 Variation of the alcohol

The bimolecular reaction of photogenerated benzhydryl cations with a series of different alcohols was investigated: methanol, ethanol, 1-propanol and 2-propanol. As the solubility of the benzhydryl cation precursor strongly decreases with the length of the alcohol it was not possible to measure reactions with longer alcohols (e.g., 1-butanol). Figure 4.2 shows the transient absorption of the photogenerated benzhydryl cation mfp(Ph)CH$^+$ in different alcohols. A significant, systematic increase of the reaction rate is observed with decreasing length of the alcohol (see Table 4.1): from $(62\,\text{ps})^{-1}$ for the reaction with 1-propanol to $(22\,\text{ps})^{-1}$ in methanol. This trend is observed for all studied cations. Furthermore, for all studied benzhydryl cations the reaction with the secondary alcohol 2-propanol is slower than with the corresponding primary alcohol 1-propanol.
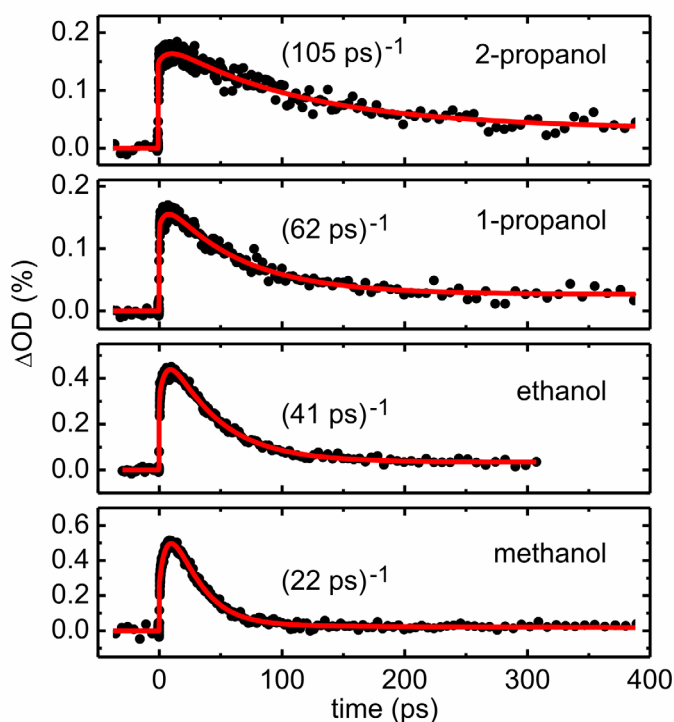
Figure 4.2: Transient absorption of the photogenerated benzhydryl cation mfp(Ph)CH$^+$ in different alcohols. The complete decay on the tens to hundreds picosecond scale is assigned to the bimolecular reaction of the cation with the alcohol. The first-order rate constant is indicated. The coherent signal contribution (see Section 2.5) around time zero has been subtracted.

4.3 Increasing the electrophilicity of the carbocation
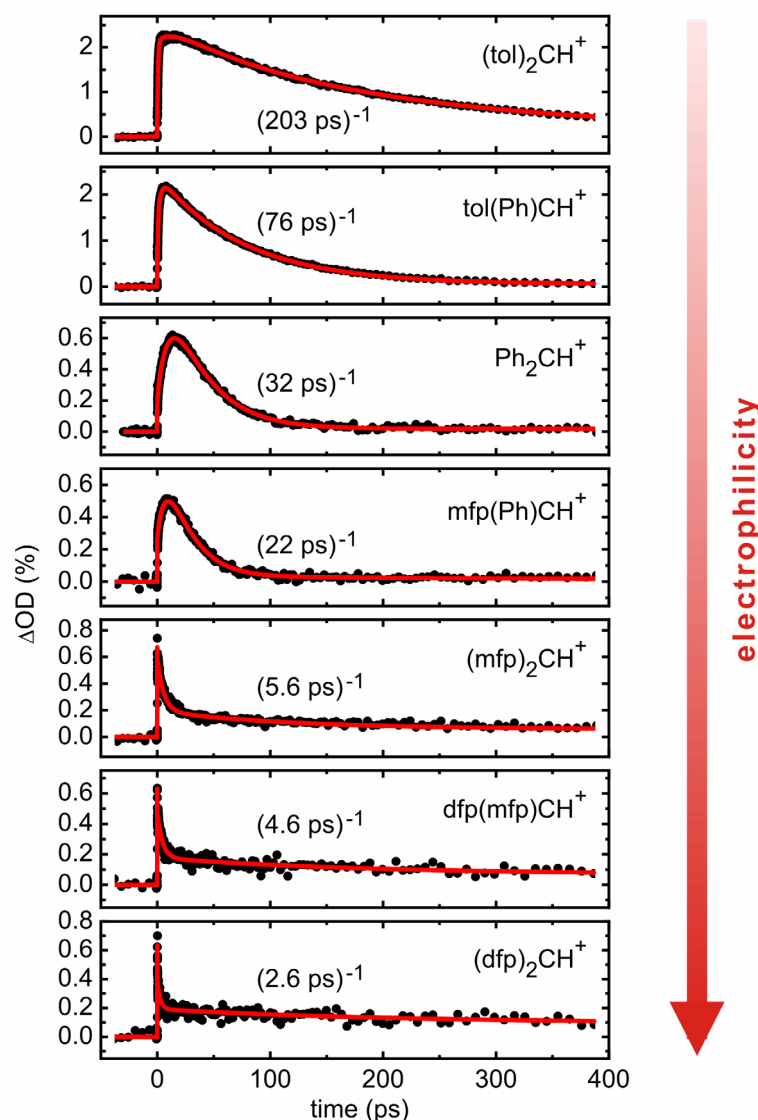
The electrophilicity, and therefore the reactivity, of the benzhydryl cation was varied over a large range: from the rather stable $(tol)_2CH^+$ up to the more than 10,000 times more electrophilic $(dfp)_2CH^+$ (see Table 3.1 for a list of the generated benzhydryl cations). Figure 4.3 shows the reaction of four different benzhydryl cations with methanol. The rate of the bimolecular reaction increases systematically with the electrophilicity (see Table 4.1). While a relatively slow reaction with a rate of $(203\ ps)^{-1}$ is observed for the reaction of $(tol)_2CH^+$ with methanol, the reaction of $(dfp)_2CH^+$ in methanol takes place with a rate of $(2.6\ ps)^{-1}$! The increasing rate constant with increasing electrophilicity is observed for all four alcohols.

Figure 4.3: Transient absorption of photogenerated benzhydryl cations in methanol. The first-order rate constant for the reaction is indicated. The electrophilicity of the cations increase from top to bottom. The coherent signal contribution (see Section 2.5) around time zero has been subtracted. The remaining, long-lived signal for the three fastest reactions is not due to absorption of the cation (see text for details).

77

Table 4.1: First-order time constants τ_1 (= $1/k_1$) in ps of the bimolecular reaction of photogenerated benzhydryl cations (with electrophilicity parameter E) with alcohols.

cation	E	methanol	ethanol	1-propanol	2-propanol
$(tol)_2CH^+$	3.63	203	239	271	388
$tol(Ph)CH^+$	4.43	76	103	146	282
Ph_2CH^+	5.47	32	56	89	182
$mfp(Ph)CH^+$	6.23	22	41	62	105
mfp_2CH^+	6.87	5.6			
$dfp(mfp)CH^+$	7.52	4.6			
dfp_2CH^+	8.02	2.6			

The absorption signals of the benzhydryl cations $(mfp)_2CH^+$, $dfp(mfp)CH^+$ and $(dfp)_2CH^+$ in methanol do not decay completely with the rate constant of the ultrafast bimolecular reaction. A long-lived signal is rather observed which only decays very slowly on the nanosecond time scale. These cations were, in contrast to the less electrophilic cations (see above), generated by photolysis of the corresponding benzhydryl chloride. A thorough inspection of the absorption spectra shows that the long-lived signal is not associated with an absorption from the cation but can be assigned to the benzhydryl radical which still absorbs slightly in the range of 400 nm to 500 nm.

4.4 Comparison with reaction rates predicted from slower measurements

In the last years, much effort has been invested in the quantification of electrophilicities and nucleophilicities of organic and inorganic compounds. Mayr and coworkers studied the reaction of benzhydryl cations with hundreds of nucleophiles on timescales up to a few nanoseconds and were thus able to construct the most wide-spanning linear free energy relationship (see Ref. [59] and literature therein). The relationship

$$\log k_2 = s \cdot (N + E) \tag{4.1}$$

connects the second-order rate constant of a reaction k_2 (in units of $M^{-1} s^{-1}$) with the nucleophilicity N and electrophilicity E of the reagents (see Appendix A for a discussion) [19,90]. The slope parameter s is furthermore needed for the characterization of a nucleophile and is usually close to unity. This linear dependency (Eq. 4.1) of the logarithm of the rate constant on the nucleophilicity as well as the electrophilicity holds over a large range of timescales. However, for rate constants $k_2 > 10^8 M^{-1} s^{-1}$ deviations from the linear relationship are observed due to the increasing influence of the time needed for diffusional encounter and for $k_2 > 10^{10} M^{-1} s^{-1}$ the reaction is diffusion-controlled [59,85].

With a small modification the relationship Eq. 4.1 still holds when the reaction takes place with a nucleophilic solvent (e.g., an alcohol) [90]:

$$\log k_1 = s \cdot (N_1 + E) \tag{4.2}$$

The equation now gives the first-order rate constant k_1 (in units of s^{-1}). While the electrophilicity parameter E is the same as for Eq. 4.2, the nucleophilicity parameter N_1 deviates from the definition given above. However, the two parameters can be easily interconverted (see Appendix A).

For a given nucleophilic solvent (i.e., an alcohol), the logarithm of the determined rate constants $\log k_1$ for the reaction with an electrophilic benzhydryl cation should, therefore, all be on a straight line. In Figure 4.4 the rate constants for the reaction of four alcohols with differing benzhydryl cations are shown. The experimentally determined rate constants with $\log k_1 < 8$ are taken from Refs. [90,93,94] and unpublished work by Johannes Ammer. The electrophilicity – and therefore the reactivity – of the benzhydryl cations is varied here over more than 18 orders of magnitude and the rate constant spans a range from $(5 \text{ min})^{-1}$ up to $(2.6 \text{ ps})^{-1}$! Four different methods have been used to determine these rates: steady-state UV/Vis spectrometry ($\tau_{1/2} > 10$ s), stopped-flow techniques (10 s $> \tau_{1/2} > 10^{-3}$ s), nanosecond laser flash photolysis (10^{-3} s $> \tau_{1/2} > 10^{-7}$ s) and femtosecond transient absorption spectroscopy ($\tau_{1/2} < 10^{-7}$ s).
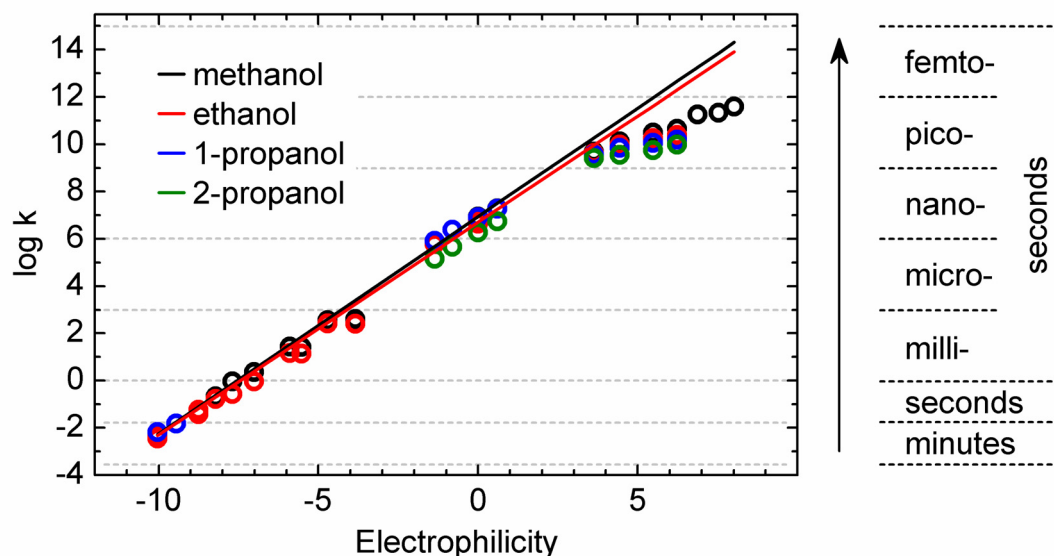
Figure 4.4: Measured (circles) and predicted (Eq. 4.2, solid lines) rate constant for the bimolecular reaction between a series of benzhydryl cations with varying electrophilicity and four alcohols. The time scale in which the reaction takes place is indicated on the right. The experimentally determined rate constants with $\log k_1 < 8$ are taken from Refs. [90,93,94] and unpublished work by Johannes Ammer.

Between the rates for bimolecular reactions of benzhydryl cations with alcohols published by Mayr and coworkers and the ultrafast rate presented within this work a gap exists between $k_1 \approx 3.5 \cdot 10^7 \text{ s}^{-1}$ and $k_1 \approx 2.5 \cdot 10^9 \text{ s}^{-1}$. This corresponds to a time regime between single nanoseconds to tens of nanoseconds. Bimolecular reactions with rates lying in this range have not been investigated in this work as the interpretation of the observed dynamics is hampered by the simultaneous occurrence of the bimolecular reaction, the geminate recombination and the diffusional separation. A possible solution could be to tackle the issue by the Smoluchowski framework developed in Section 3.4. This could allow to assess the influence of diffusion-terminated geminate recombination on the observed decay dynamics.

## 4.5 Deviation from the relationship log k₁ = s (N+E)

The expected linear dependence of $\log k_1$ from the electrophilicity is found for rate constants up to $k_1 \approx 10^8 \, \text{s}^{-1}$. Although the rate constant still rises with increasing electrophilicity, the fastest reactions with $k_1 > 10^9 \, \text{s}^{-1}$ deviate significantly from the linear slope (see Figures 4.4 and 4.5). Furthermore, a splitting of the rates for the reactions of a given cation with different alcohols is visible. The reaction with methanol is always the fastest, followed by ethanol, 1-propanol and 2-propanol. At a first glance, the splitting is rather surprising since no significant differences between the rate constants for reactions with these alcohols were found for the slower reactions ($k_1 < 10^8 \, \text{s}^{-1}$). Figure 4.5 compares two models to describe the deviation of the measured reaction rates from the linear relationship.

Limiting rate model. The rate constant of a bimolecular reaction cannot rise infinitely to increasingly higher rate constants. The ultimate limit of the rate constant is given by the time needed for the inertial motion of the reacting molecules towards each other. This time is on the same scale as the period of a large amplitude vibrational mode, i.e. a few hundreds of femtoseconds. Such motions can be expected to be part of every reaction, even of the fastest ones. The time needed for one reaction τ_{reaction} (= $1/k_{\text{reaction}}$) can therefore be written as:

$$\tau_{\text{reaction}} = \tau_{\text{calculated}} + \tau_{\text{limit}} \tag{4.3}$$

with $\tau_{\text{calculated}}$ (= $1/k_{\text{calculated}}$) the time constant of the reaction as calculated with the aid of Eq. 4.2. The time constant τ_{limit} represents the process which limits the time constant of the reaction, e.g., the inertial motion of the reactants towards each other. If the limiting process is fast compared to the calculated time constant, then Eq. 4.2 is valid and $\tau_{\text{reaction}} \approx \tau_{\text{calculated}}$. Only if the calculated time is comparable or even faster than the temporal limit, the observed reaction time constant τ_{reaction} deviates from the calculated time constant $\tau_{\text{calculated}}$ obtained from Eq. 4.2.

Alcohol molecules build a strong hydrogen bond network which slows down their translational and rotational motion significantly [95,96]. The motion of alcohol molecules towards the benzhydryl cations at the reaction process is therefore hampered. The progression of the rate constant k_{reaction} according to Eq. 4.3 is depicted in Figure 4.5a as solid lines for the case of methanol, ethanol and 1-propanol as nucleophilic solvent. The temporal limit was assumed to be the rotational relaxation time of the solvent as found from NMR studies [97]: 3.6 ps for methanol, 10.0 ps for ethanol and 22 ps for 1-propanol. While the three fastest rate constants for methanol are well reproduced, the model overestimates significantly the other rates. The same is true for the predicted progression of the rate constants in ethanol and 1-propanol.
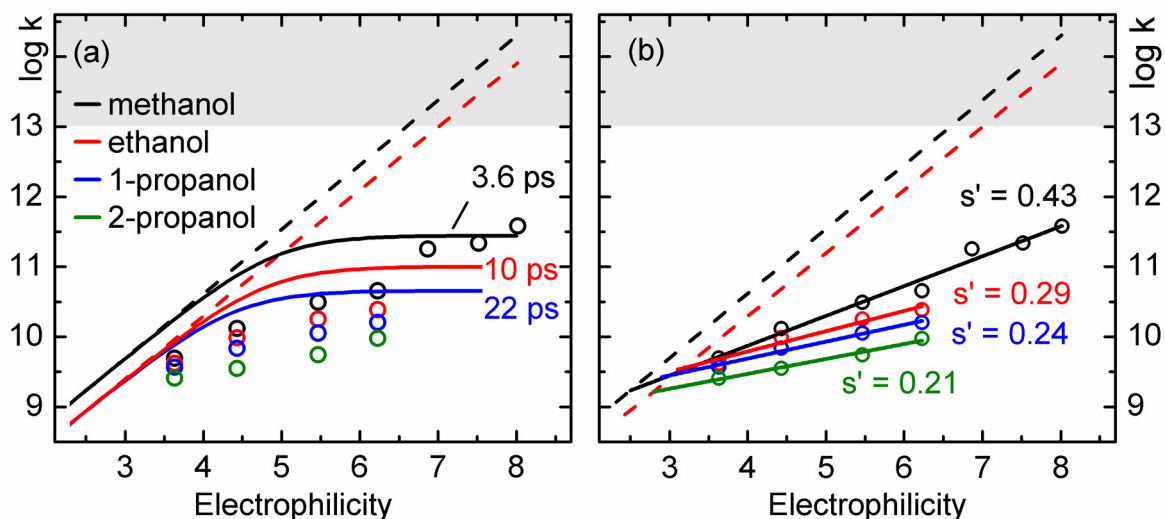
Figure 4.5: Magnified region of Figure 4.4 showing the fastest reactions with $k_1 > 10^9$ s^{-1} and the deviation of the measured rate constants (circles) from the linear relationship Eq. 4.2 (dashed lines). (a) The assumption of limiting rate constants depending on the size of the alcohol (solid lines, see text for details) can not fully reproduce the experiment. (b) Fit of the rate constants by new, less steep straights with slope s' (solid lines). The range of rate constants too fast for a bimolecular reaction to occur ($k_1 > 10^{13}$ s^{-1}, see text) is grey-colored.

Linear dependency. The increase of the rate constants for the fastest reactions with $k_1 > 10^9$ s^{-1} can again all be well approximated by a linear dependency as shown in Figure 4.5b (k_1 in units of s^{-1}):

$$\log k_1 = s' \cdot E + \text{const.} \tag{4.4}$$

with new slope parameters s' and solvent specific constants. The slopes s' are significantly smaller than the ones obtained for the slower reactions. Furthermore, the slopes s' depend on the solvent: from s' = 0.43 for methanol, s' = 0.29 for ethanol, s' = 0.24 for 1-propanol to s' = 0.21 for 2-propanol.

It should be noted that Eq. 4.4 must also be limited to an interval of reaction rates. For even higher electrophilicities, it does not describe the leveling of the rate constant due to a limiting process, like for example the inertial motion of the reactants towards each other.

Origin of the slow-down. Although the mechanism for the slow down of the fastest bimolecular reactions is not yet fully understood it can be rationalized by the following consideration. With rate constants as fast as $(2.6 \text{ ps})^{-1}$ a time regime is reached close to the timescale in which molecular motions take place. The fastest reactions with methanol are hereby in the range or even faster than the published value of 3.6 ps for the rotational relaxation of methanol [97]. Since it is likely that some degree of rotation of the alcohol is needed for a successful reaction to take place, the observed ultrafast reaction are already close to the fundamental limit. The dependency of the rate constants on the length of the alcohol further reflects the

importance of rotations for the reaction. The rate constant for the reaction with a given benzhydryl cation significantly decreases from methanol and ethanol to 1-propanol and 2-propanol. This is in line with the increase of the rotational relaxation times of these solvents: 3.6 ps for methanol, 10.0 ps for ethanol and 22 ps for 1-propanol [97].

Pre-association with alcohols. A possible explanation for reactions faster than the rotational relaxation of the alcohol could be a pre-association of the precursor and the methanol before the excitation and the resulting bond cleavage. Due to the pre-association, the generated benzhydryl cation and the methanol might be in a favorable configuration after the bond cleavage which allows for their ultrafast bimolecular reaction without large rotational motions, leave alone translational motion.

First experimental efforts have been made in order to clarify whether pre-association is present under the conditions of the measurements. The reaction of benzhydryl cations in mixtures of methanol with acetonitrile with varying ratio were studied and compared to the result in neat methanol. The cation was hereby generated by photolysis of the phosphonium salt. For a statistical distribution of the methanol and acetonitrile molecules one would expect that the rate constant for the reaction of the cation with methanol increases linearly with the concentration of the alcohol. The measured rates deviate, however, slightly from this linear relationship. The reactions are too fast for the actual methanol concentration. This is an indication that the methanol molecules tend to be in the vicinity of the precursor and that pre-association could be present.

5. Conclusion and outlook

In this thesis, the photo-generation and subsequent processes and reactions of highly reactive carbocations and carbon radicals were investigated. For the first time, a complete photo-induced S_N1 reaction was observed: from the photo-induced bond cleavage and relaxation of the nascent fragment to interconversion through electron transfer and recombination back to the precursor until the reaction with a nucleophile. The majority of the experimental results were gained by femto- to microsecond transient absorption spectroscopy. Novel techniques and data evaluation approaches were developed which helped to understand the reactions and processes on a microscopic level. It furthermore turned out that the determination of yields and quantum yields is a versatile method for deciphering photo-induced mechanisms as it provides more information about a process than the mere indication of time constants.

Experimental and analytical techniques

The quantitative analysis of transient absorption data has been established within the framework of this thesis. It provides an all-optical access to the determination of yields and quantum yields of the observed processes. The evaluation requires the thorough characterization of the pump and probe pulses as well as the knowledge of the molar absorption coefficients of the ground state and the photo-generated species involved. It is thus especially suited for the study of photo-induced processes in which stable or meta-stable species take part.

Many product absorption bands measured after photolysis of the presented precursors exhibit a small shift of the maximum wavelength. A novel algorithm was therefore developed which fits a parabola to a small spectral interval around the maximum. By iteratively reducing the interval and performing a new parabola fit, the position of the maximum can be found precisely, regardless of the exact form of the absorption band. Provided that the signal-to-noise ratio of the measurement is high, the position of the band and therefore the temporal peak shift can be determined with a precision better than 0.1 nm for band-widths in the order of tens of nanometers. This high accuracy does not only allow for the evaluation of photo-induced solvation by the solvent. It even permits to study more subtle effects arising after the photolysis of molecules. All these processes lead to peak shifts of just a few nm.

The spectroscopy of reactive species imposes several requirements not needed for the study of photostable compounds. The high yield with which the precursor molecules are chemically transformed after photo-excitation and the fact that some of the studied solutions are only stable on the order of minutes to hours demands for fast, low noise measurements and the reliable recognition of sample degradations. A series of – active and passive – techniques has therefore been established which keep the measurement time short or allow for checks of the sample condition during the measurement. The subdivision of the delay time

range into multiple interleaving scans hereby leads to a significant speedup and furthermore allows for an on-line inspection of the sample integrity. The implementation of an external steady-state UV-Vis spectrophotometer is a further step to monitor photo-induced changes of the sample. Due to its small dimensions and high flexibility it can be incorporated into the transient absorption setup without significant changes. The high sensitivity comparable to commercial systems allows for the detection of even smallest changes of the sample.

The photo-induced bond cleavage in benzhydryl chlorides occurs within about 100 fs. It therefore demands for a high temporal resolution and the precise knowledge of the absolute time-zero of the transient absorption experiment. A dedicated setup was thus designed which provides ultrafast temporal resolution by two-color absorption measurements and the possibility to precisely determine the time-zero with the aid of a second detection branch. Both, the pump and the probe pulses, are generated by nonlinear optical parametric amplification yielding a sub-40 fs time resolution. For these experiments the flow cell concept was abandoned as the windows of the flow cell lead to spurious non-linear signal contributions and introduce dispersion which deteriorate the high time resolution needed. A wire-guided liquid-jet was built instead in which the sample was measured. It also allows for a continuous sample exchange and provides films of the solution in optical quality with thicknesses adjustable between 20 μm and 200 μm. Simultaneously to the transient absorption measurement in the liquid jet, a reference transient absorption signal is detected in a crystal in a further, separate detection branch. The setup thus allows for the measurement of photo-induced dynamics with sub-40 fs temporal resolution and a calibration accuracy of the absolute time-zero far better than 5 fs.

The use of the liquid jet setup comes with the drawback of solvent evaporation and a resulting increase of the sample concentration. As this would lead to a change of the excitation conditions in the jet, the concentration has to be kept constant. A flow cell was therefore introduced in the liquid jet circuit through which the optical density and thus the concentration of the sample was measured. This optical density was used as input parameter for a closed-loop control which regulates the rate with which the solvent is replenished.

Tracking the life of carbocations and carbon radicals after their generation

Within the framework of this thesis the photolysis and subsequent processes of a series of carbocation precursors was investigated. After UV excitation benzhydryl chloride undergoes ultrafast bond cleavage giving rise to the ion pair benzhydryl cations / chlorine anion and the radical pair benzhydryl radical / chlorine radical. Contrary to the classical description, the process cannot be described by two competing rates which depopulate the excited state and lead to radicals and cations simultaneously. Rather, a dynamical picture incorporating the potential energy surfaces of the excited states has to be considered. The ultrafast excitation of the molecule generates a wavepacket in the Franck-Condon region of the S_1 state. The

wavepacket is accelerated from the Franck-Condon point towards longer C-Cl distance but it remains in the shallow minimum for some tens of femtoseconds. At about 80 fs the weak potential barrier is crossed and the major part of the wavepacket moves through a conical intersection to the potential energy surface leading to the radical pair. The remaining part of the wavepacket in the excited stated proceeds to a further, distinct conical intersection which finally leads to ion pairs within about 125 fs.

About 40% of the excited benzhydryl chloride molecules undergo homolytic bond cleavage and ~2% undergo heterolysis. The fate of the remaining ~60% is still an open question. Due to the short lifetime of the excited state (~100 fs) fluorescence can be ruled out. There is also no direct pathway for internal conversion from the excited state without the passing of the two conical intersections leading to bond cleavage. It is, however, conceivable that part of the generated chlorine atoms are reflected by the surrounding solvent molecules and directly go back to the ground state of the starting material. An experimental observation of this process is complicated due to the ultrafast time scale and the necessary spectral detection range. With the recently developed whitelight ranging down to about 230 nm [98] it could be possible, however, to detect the vibrationally hot ground state of benzhydryl chloride after the bounce of the chlorine at the solvent.

Since the bond cleavage and the solvation occur on a similar time scale, it is likely that the potential energy surfaces are influenced dynamically during the evolution of the wavepacket. As the calculations available so far were performed mainly in the gas phase, further theoretical efforts are needed to gain a deeper understanding of the solvent influence. A possible experimental approach to directly investigate the role of the solvent on the bond cleavage process was recently described by Kubarych and coworkers [99] within the framework of vibrational Stark-effect spectroscopy. Since it allows to observe the ultrafast response of the solvent shell to changes in the charge distribution of the solute, it could allow to track the course of the bond cleavage process.

The bond cleavage of benzhydryl chlorides within about 100 fs is an extremely fast process and does not allow for a full relaxation of the emerging fragments and the surrounding solvent molecules. Immediately after the cleavage, the nascent benzhydryl cations and radicals and the surrounding solvent molecules are therefore still in a similar configuration as before the photoexcitation. Only within the next hundreds of femtoseconds the benzhydryl moieties relax, planarize and become solvated by the solvent molecules. These processes cause a simultaneous change of the absorption signatures of benzhydryl cations and radicals. A strong increase of the oscillatory strength and a significant peak shift of the band is observed.

It is highly likely that a similar initial behavior can be found in a wide range of systems which undergo ultrafast bond cleavage. The breaking of a chemical bond usually causes geometrical rearrangements of the molecular structure and influences on the absorption sig-

natures can be safely expected. In earlier studies of the photolysis of benzhydryl chlorides with inferior time resolution the absorption signal increase due to planarization of the nascent photofragments was interpreted as the bond cleavage. This demonstrates the high potential for the misinterpretation of rearrangement processes after the bond cleavage as the cleavage itself. In case of doubt, the assignment of optical signal changes to the bond cleavage process should therefore always be corroborated with additional experimental or theoretical evidences, e.g., quantum chemical calculations of the involved electronic states. Even for systems in which no bond is cleaved, a similar effect can occur. The change of absorption or emission bands after photo-excitation in the first few picoseconds are often assigned to a generic solvation process or vibrational cooling of the solute. At least for some of the systems this could also be due to a molecular rearrangement when the ground state configuration deviates from the one in the excited state.

The electron transfer from the benzhydryl radical to the chlorine radical leads to the major part of the benzhydryl cation population observable in polar solvents on the pico- to nanosecond time scale. It is terminated as soon as the average separation between the radicals making up a pair is too large. A large part of the temporarily generated cations, however, cannot be observed on timescales longer than one nanosecond since they undergo an efficient geminate recombination with the anionic leaving group. Again, this reaction is terminated if the distance between the ions becomes too large. It turned out that a proper description of the found dynamics and yields can only be achieved by a microscopic description of distance distributions of radical pairs and ion pairs which are subject to distance dependent electron transfer and recombination rates. The possibility of processes occurring from a wide range of configurations means a turn away from the classical modeling of such processes. An unified description of the population dynamics emerges, with smooth transitions between the distinct species considered in traditional descriptions.

The extremely precise peak shift determination hereby opens up a new direct experimental observable giving access to the microscopic realm of (photo-)chemical reactions. It allows to track the evolution of the distance distribution of the radical pairs and ion pairs which otherwise – if at all – would only be detectable by dedicated experiments, e.g., ultrafast chemical exchange spectroscopy [100]. Further applications of the peak shift evaluation comprise a wide field, ranging from the observation of ultrafast intermolecular rearrangements [101] to solvation and vibrational cooling.

The geminate ion pair recombination was found to be the main loss channel for photo-generated benzhydryl cations in the first hundreds of picoseconds. Only in the highly polar acetonitrile a significant fraction of the carbocations escapes from the anion and becomes a free ion stable at least on the nanosecond timescale. In solvents of moderate polarity nearly all generated cations undergo recombination with the anion. This can be rationalized by the insufficient shielding of the Coulomb attraction between the oppositely charged ions which

does not allow for the separation of the pair needed for the formation of free ions. A substantial improvement of the carbocation yield is therefore obtained when uncharged photo-leaving groups are used instead. The photolysis of benzhydryl triarylphosphonium salts leads to high yields on the nanosecond scale even in solvents of lower polarity.

Further insight into the geminate recombination was gained by the photolysis of benzhydryl triphenylphosphonium salts encapsulated in reverse micelles. The generated photofragments are strongly restrained by the micellar environment which hinders any significant rotational or translational motion. The diffusional separation is thus prevented efficiently and a significantly higher fraction of the photofragments undergoes geminate recombination. It furthermore allows for a more direct investigation of the reaction process without interfering influences of the diffusion. It was shown, however, that the reaction of two encapsulated species is not fully comparable with the same reaction occurring in solution. The encapsulation can have an influence on many parameters, e.g., on the rotational relaxation times or the dielectric constants of the solvent.

Bimolecular reactions without diffusion

The disadvantages of the encapsulation can be avoided by the photolytic generation of a reactant in a reactive solvent. That implies that no translational diffusion is needed for the two reactants to encounter. The typical diffusion limit for bimolecular reaction rates of $\sim 10^{10}\,\mathrm{M^{-1}s^{-1}}$ is therefore not valid anymore. In this way it can be expected that the intrinsic reaction rate can be measured even for highly reactive pairs. The next possible limit for the reaction rate could be on the level of relative motions of the two partners towards each other, namely rotations, mutual approach motions or the breakage of hydrogen bonds. Depending on the size of the studied molecules, reaction rates even above $10^{12}\,\mathrm{s^{-1}}$, corresponding to hundreds of femtoseconds, seem to be feasible.

Within this work, the ultrafast bimolecular reaction between a series photo-generated benzhydryl cations and several alcohols was studied. The fastest observed rate constant of $(2.6\,\mathrm{ps})^{-1} = 3.8 \cdot 10^{11}\,\mathrm{s^{-1}}$ was found for the reaction of $\mathrm{dfp_2CH^+}$ with methanol. It is thus already faster than the reported rotational relaxation time of methanol which is expected to take place in 3.6 ps. Such fast reactions could be due to a suitable pre-association of the precursor and the methanol before the photo-induced bond cleavage so that no full rotational motion is necessary for a successful bond formation anymore. The existence of a steering force between the two reactive sites of the cation and methanol molecule could also be the reason for reaction times faster then the rotational diffusion.

Depending on the substituents on the phenyl rings of the cation – determining their electrophilicity – and the choice of the alcohol, the bimolecular reaction took place between 2.6 ps and several hundreds of picoseconds (corresponding to rate constants between $k_1 = 3.8 \cdot 10^{11}\,\mathrm{s^{-1}}$ and $2.6 \cdot 10^{9}\,\mathrm{s^{-1}}$). This series of ultrafast rate constants can be compared to

the comprehensive work of Mayr and coworkers [90,93,94] in which they studied the reaction of a large series of less electrophilic benzhydryl cations with alcohols. Due to the lower electrophilicity all reactions took place on a time scale ranging from minutes to tens of nanoseconds and were thus significantly slower than the rates measured within this work. The rates k_1 of the slower reactions obey the linear free energy relationship $\log k_1 = s \cdot (N_1 + E)$ which connects k_1 with the empirically determined nucleophilicity of the solvent N_1 and the electrophilicity of the cation E. The relationship does not hold anymore exactly for the rates of the ultrafast reactions. All measured rates are significantly slower than predicted by the linear free energy relationship. It was found, however, that higher electrophilic cations undergo a faster bimolecular reaction with alcohols. The order of the electrophilicity parameters E determined from bimolecular reactions on much slower time scales therefore still apply in the single picosecond regime.

In contrast, the ultrafast reaction rates are now significantly influenced by the identity of the alcohol. While for the slower reactions the rate is almost independent on the choice of the alcohol, deviating rates are found for the ultrafast regime: The longer the alcohol the slower the measured reaction rate. The dependency on the alcohol length indicates the rising influence of molecular motions on the dynamics of the reaction process.

With the data presented in this work, there is no indication yet of a fundamental barrier which limits the reaction rate. Up to now, the reaction rates were only limited by the electrophilicity of the cations and the rather moderate nucleophilicity of alcohols. Solvents containing amine groups (e.g., primary amines $R–NH_2$) are a prime candidate for the observation of even faster reactions, since their nucleophilicity – determined from slower reactions – is significantly higher than for alcohols [102,103]. However, it is likely that not all nucleophilic amines are equally suited for ultrafast bimolecular reactions. As already shown for the reactions with alcohols the size of the reactant plays a crucial role. Furthermore, attention should be paid, that the possibly pronounced hydrogen networks are well accounted for, as these intermolecular forces are known to slow down the rearrangements necessary for a successful reaction [53,104].

The observed reactions of the photo-generated benzhydryl cations with alcohols still can all be described in the framework of (photo-)$S_N 1$-type reactions: An intermediary carbocation is generated by photoexcitation and can be detected spectroscopically. It then lives for at least a few picoseconds until it reacts with an alcohol. For even faster reactions, the formation of the cation will be on the same time scale as the reaction with the nucleophile. Then the question arises whether the formation of the cation and the reaction should be described as two consecutive steps or rather as one concerted process, i.e. a (photo-)$S_N 2$ process. This transition between (photo-)$S_N 1$ and (photo-)$S_N 2$ is of general interest to physical chemistry [7,105] and might be observed directly for the first time with the newly available methods and concepts.

References

[1]   S. R. Forrest, *Nature* **2004**, *428*, 911-918.

[2]   B. O'Regan, M. Grätzel, *Nature*, **1991**, *353*, 737-740.

[3]   J. H. Burroughes, D. D. C. Bradley, A. R. Brown, R. N. Marks, K. Mackay, R. H. Friend, P. L. Burns, A. B. Holmes, *Nature* **1990**, *347*, 539-514.

[4]   J. D. McDonald, P. R. LeBreton, Y. T. Lee, D. R. Herschbach, *J. Chem. Phys.* **1972**, *56*, 769-788.

[5]   Y. T. Lee, *Science* **1987**, *236*, 793-798.

[6]   N. F. Scherer, L. R. Khundkar, R. B. Bernstein, A. H. Zewail, *J. Chem. Phys.* **1987**, *87*, 1451-1453.

[7]   M. B. Smith, J. March, *March's Advanced Organic Chemistry,* Wiley-Interscience, Hoboken, NJ, **2007**.

[8]   R. A. Moss, M. S. Platz, M. Jones Jr. (Eds.), *Reactive Intermediate Chemistry*, Wiley-Interscience, Hoboken, NJ, 2004.

[9]   G. A. Olah, *J. Org. Chem.* **2001**, *66*, 5943-5957.

[10]   P. J. Kropp, *Acc. Chem. Res.* **1984**, *17*, 131-137.

[11]   J. Bartl, S. Steenken, H. Mayr, R. A. McClelland, *J. Am. Chem. Soc.* **1990**, *112,* 6918-6928.

[12]   P. K. Das, *Chem. Rev.* **1993**, *93*, 119-144.

[13]   R. A. McClelland, *Tetrahedron*, **1996**, *52*, 6823-6858.

[14]   B. P. Fingerhut, D. Geppert, R. de Vivie-Riedle, *Chem. Phys.* **2008,** *343*, 329-339.

[15]   M. Lipson, A. A. Deniz, K. S. Peters, *Chem. Phys. Lett.* **1998**, *288*, 781-784.

[16]   H. Mayr, M. Patz, *Angew. Chem. Int. Ed.* **1994**, *33*, 938-957.

[17]   H. Mayr, T. Bug, M. F. Gotta, N. Hering, B. Irrgang, B. Janker, B. Kempf, R. Loos, A. R. Ofial, G. Remennikov, H. Schimmel, *J. Am. Chem. Soc.* **2001**, *123*, 9500-9512.

[18]   R. Lucius, R. Loos, H. Mayr, *Angew. Chem. Int. Ed.* **2002**, *41*, 91-95.

[19]   H. Mayr, B. Kempf, A. R. Ofial, *Acc. Chem. Res.* **2003**, *36*, 66-77.

[20]   A. H. Zewail, *J. Phys. Chem. A* **2000**, *104*, 5660-5694.

[21]   T. Wilhelm, J. Piel, E. Riedle, *Opt. Lett.* **1997**, *22*, 1494-1496.

[22] E. Riedle, M. Beutter, S. Lochbrunner, J. Piel, S. Schenkl, S. Spörlein, W. Zinth, *Appl. Phys. B* **2000**, *71*, 457-465.

[23] A. Baltuška, T. Kobayashi, *Appl. Phys. B* **2006**, *75*, 427-443.

[24] G. Cerullo, S. De Silvestri, *Rev. Sci. Instrum.* **2003**, *74*, 1-18.

[25] P. Baum, S. Lochbrunner, E. Riedle, *Appl. Phys. B* **2004**, *79*, 1027-1032.

[26] N.P. Ernsting, S.A. Kovalenko, T. Senyushkina, J. Saam, V. Farztdinov, *J. Phys. Chem. A* **2001**, *105*, 3443-3453.

[27] R. Huber, H. Satzger, W. Zinth, J. Wachtveitl, *Opt. Commun.* **2001**, *194*, 443-448.

[28] M. Bradler, P. Baum, E. Riedle, *Appl. Phys. B* **2009**, *97*, 561-574.

[29] M. Lorenc, M. Ziolek, R. Naskrecki, J. Karolczak, J. Kubicki, A. Maciejewski, Appl. *Phys. B* **2002**, *74*, 19-27.

[30] J.-Y. Bigot, M. T. Portella, R. W. Schoenlein, C. J. Bardeen, A. Migus, C. V. Shank, *Phys. Rev. Lett.* **1991**, *66*, 1138-1141.

[31] E. T. J. Nibbering, D. A. Wiersma, K. Duppen, *Phys. Rev. Lett.* **1991**, *66*, 2464-2467.

[32] A. Peralta Conde, R. Montero, A. Longarte, F. Castaño, *Phys. Chem. Chem. Phys.* **2010**, *12*, 15501-15504.

[33] R. Heyer, *Aufbau und Charakterisierung einer Messapparatur für transiente Spektroskopie im Nano- bis Mikrosekundenbereich*, Bachelorarbeit, Ludwig-Maximilians-Universität (München), **2011.**

[34] U. Megerle, I. Pugliesi, C. Schriever, C. F. Sailer, E. Riedle, *Appl. Phys. B* **2009**, *96*, 215-231.

[35] I. Z. Kozma, P. Krok, E. Riedle, *J. Opt. Soc. Am. B* **2005**, *22*, 1479-1485.

[36] U. Megerle, *Photoinduced molecular dynamics in increasingly complex systems: From ultrafast transient absorption spectroscopy to nanoscopic models*, Doktorarbeit, Ludwig-Maximilians-Universität (München), **2011.**

[37] M. N. Berberan-Santos, E. N. Bodunov, B. Valeur, *Chem. Phys.* **2005**, *315*, 171-182.

[38] K. C. Benny Lee, J. Siegel, S. E. D. Webb, S. Lévêque-Fort, M. J. Cole, R. Jones, K. Dowling, M. J. Lever, P. M. W. French, *Biophys. J.* **2001**, *81*, 1265-1274.

[39] Y.-T. Kao, X. Guo, Y. Yang, Z. Liu, A. Hassanali, Q.-H. Song, L. Wang, D. Zhong, *J. Phys. Chem. B* **2012**, *116*, 9130-9140.

[40] H. J. Kuhn, S. E. Braslavsky, R. Schmidt, *Pure. Appl. Chem.* **2004**, *76*, 2105-2146.

[41]   U. Megerle, R. Lechner, B. König, E. Riedle, *Photochem. Photobiol. Sci.* **2010**, *9*, 1400-1406.

[42]   M. Klessinger, J. Michl, *Excited States and Photochemistry of Organic Molecules*, VCH Publishers, New York, **1995**.

[43]   R. Schneider, H. Mayr, P. H. Plesch, *Ber. Bunsenges. Phys. Chem.* **1987**, *91*, 1369-1374.

[44]   B. Denegri, A. Streiter, S. Jurić, A. R. Ofial, O. Kronja, H. Mayr, *Chem. Eur. J.* **2006***, 12*, 1648-1656.

[45]   M. J. Tauber, R. A. Mathies, X. Chen, S. E. Bradforth, *Rev. Sci. Instrum.* **2003**, *74*, 4958-4960.

[46]   S. Laimgruber, H. Schachenmayr, B. Schmidt, W. Zinth, P. Gilch, *Appl. Phys. B* **2006**, *85*, 557-564.

[47]   F. Milota, J. Sperling, A. Nemeth, H.F. Kauffmann, *Chem. Phys.* **2009**, *357*, 45-53.

[48]   A. Nemeth, J. Sperling, J. Hauer, H. F. Kauffmann, F. Milota, *Opt. Lett.* **2009**, *34*, 3301-3303.

[49]   L. Maisenbacher, *Ultraschnelle Initialdynamik des photoinduzierten Bindungsbruchs im Diphenylmethylchlorid*, Bachelorarbeit, Ludwig-Maximilians-Universität (München), **2010**.

[50]   F. H. J. Hinzpeter, *Online-Breitbandmessung und Konzentrationsregelung in einem Flüssigkeitsstrahl mit Hilfe eines modularen Absorptionsspektrometers*, Bachelorarbeit, Ludwig-Maximilians-Universität (München), **2010.**

[51]   C. Reichardt, *Chem. Rev.* **1994**, *94*, 2319-2358.

[52]   M. Maroncelli, J. MacInnis, G. R. Fleming, *Science* **1989**, *243*, 1674-1680.

[53]   R. Jimenez, G. R. Fleming, P. V. Kumar, M. Maroncelli, *Nature*, **1994**, 369, 471-473.

[54]   M. L. Horng, J. A. Gardecki, A. Papazyan, M. Maroncelli, *J. Phys. Chem.* **1995**, *99*, 17311-17337.

[55]   I. Eom, T. Joo, *J. Chem. Phys.* **2009**, *131*, 244507.

[56]   T. Bultmann, N. P. Ernsting, *J. Phys. Chem.* **1996**, *100*, 19417-19424.

[57]   U. Megerle, F. Selmaier, C. Lambert, E. Riedle, S. Lochbrunner, *Phys. Chem. Chem. Phys.* **2008**, *10*, 6245-6251.

[58]   T. Elsaesser, W. Kaiser, *Annu. Rev. Phys. Chem.* **1991**, *42*, 83-107.

[59]   J. Ammer, C. Nolte, H. Mayr, *J. Am. Chem. Soc.* **2012**, *134*, 13902-13911.

[60]   C. Schriever, S. Lochbrunner, E. Riedle, D. J. Nesbitt, *Rev. Sci. Instrum.* **2008**, *79,* 013107.

[61]   K. S. Peters, *Chem. Rev.* **2007**, *107*, 859-873.

[62]   S. Thallmair, *Ultraschnelle photochemische Dissoziation von Diarylmethan-Derivaten: Theorie und Experiment*, Masterarbeit, Ludwig-Maximilians-Universität (München), **2010**.

[63]   A. R Ofial, K. Ohkubo, S. Fukuzumi, R. Lucius, H. Mayr, *J. Am. Chem. Soc.* **2003**, *125*, 10906-10912.

[64]   P. F. Barbara, T. J. Meyer, M. A. Ratner, *J. Phys. Chem.* **1996**, *100,* 13148-13168.

[65]   K. Weidemaier, H. L. Tavernier, S. F. Swallen, M. D. Fayer, *J. Phys. Chem. A* **1997**, *101*, 1887-1902.

[66]   A. Rosspeintner, D. R. Kattnig, G. Angulo, S. Landgraf, G. Grampp, *Chem. Eur. J.* **2008**, *14*, 6213-6221.

[67]   S. A. Rice, *Diffusion-limited reactions, Vol. 25*, Elsevier Science Publishers B.V., Amsterdam, **1985**.

[68]   V. O. Saik, A. A. Goun, J. Nanda, K. Shirota, H. L. Tavernier, M. D. Fayer, *J. Phys. Chem. A* **2004**, *108*, 6696-6703.

[69]   M. Wojcik, M. Tachiya, *Radiat. Phys. Chem.* **2005,** *74*, 132-138.

[70]   H. L. Tavernier, M. M. Kalashnikov, M. D. Fayer, *J. Chem. Phys* **2000**, *113*, 10191.

[71]   P. G. Wolynes, J. M. Deutch, *J. Chem. Phys.*, **1976**, *65*, 450-454.

[72]   J. A. Kloepfer, V. H. Vilchiz, V. A. Lenchenkov, A. C. Germaine, S. E. Bradforth, *J. Chem. Phys.* **2000**, *113*, 6288-6307.

[73]   C. Imrie, T. A. Modro, E. R. Rohwer, C. C. P. Wagener, *J. Org. Chem.* **1993**, *58*, 5643-5649.

[74]   C. M. R. Grill, *Ultraschnelle Photo-Dissoziation von Diphenylmethylverbindungen mit Triphenylphosphan als Abgangsgruppe*, Bachelorarbeit, Ludwig-Maximilians-Universität (München), **2009.**

[75]   S. Thallmair, M. Kowalewski, B. P. Fingerhut, C. F. Sailer, R. de Vivie-Riedle, *Ultrafast Phenomena XVIII*, accepted for publication.

[76]   B. Kempf, H. Mayr, *Chem. Eur. J.* **2005**, *11*, 917-927.

[77] J. R. Lakowicz, *Principles of Fluorescence Spectroscopy*, 3rd edition, Springer, New York, **2006**.

[78] T. Takaya, H. Hamaguchi, K. Iwata, *J. Chem. Phys* **2009**, *130*, 014501.

[79] E. F. Gudgin Templeton, E. L. Quitevis, G. A. Kenney-Wallace, *J. Phys. Chem.* **1985**, *89*, 3238-3243.

[80] H. Sato, *Chem. Rev.* **2001**, *101*, 2687-2725.

[81] M. Kubinyi, A. Grofcsik, I. Pápai, W. J. Jones, *Chem. Phys.* **2003**, *286*, 81-96.

[82] N. E. Levinger, L. A. Swafford, *Annu. Rev. Phys. Chem.* **2009**, *60*, 385-406.

[83] D. E. Moilanen, E. E. Fenn, D. Wong, and M. D. Fayer, *J. Chem. Phys.* **2009**, *131*, 014704.

[84] H. Shirota, K. Horie, *J. Phys. Chem. B* **1999**, *103*, 1437-1443.

[85] H. Schaller, U. Schmidhammer, E. Riedle, H. Mayr, *Chem. Eur. J.* **2008**, *14*, 3866-3868.

[86] K. Iwata, S. Takeuchi, T. Tahara, *Chem. Phys. Lett.* **2001**, *347*, 331-336.

[87] K. Iwata, *J. Raman. Spectrosc.* **2008**, *39*, 1512-1517.

[88] J. E. Chateauneuf, *J. Chem. Soc. Commun.* **1991**, 1437.

[89] J. Peon, D. Polshakov, B. Kohler, *J. Am. Chem. Soc.* **2002**, *124*, 6428-6438.

[90] S. Minegishi, S. Kobayashi, H. Mayr, *J. Am. Chem. Soc.* **2004**, *126*, 5174-5181.

[91] S. Nishida, *J. Org. Chem.* **1967**, *32*, 2692-2695.

[92] C. Nolte, H. Mayr, *Eur. J. Org. Chem.* **2010**, 1435-1439.

[93] B. T. Phan, H. Mayr, *Can. J. Chem.* **2005**, *83*, 1554-1560.

[94] C. Nolte, J. Ammer, H. Mayr, *J. Org. Chem.* **2012**, *77*, 3325-3335.

[95] B. M. Ladanyi, M. S. Skaf, *Annu. Rev. Phys. Chem.* **1993**, *44*, 335-368.

[96] H. Shirota, K. Yoshihara, N. A. Smith, S. Lin, S. R. Meech, *Chem. Phys. Lett.* **1997**, *281*, 27-34.

[97] B. M. Fung, T. W. McGaughy, *J. Chem. Phys.* **1976**, *65*, 2970-2976.

[98] M. Bradler, Doktorarbeit, Ludwig-Maximilians-Universität (München), **2012**.

[99] Baiz, C. R.; Kubarych, K. J. *J. Am. Chem. Soc.* **2010**, *132*, 12784-12785.

[100] J. Zheng, K. Kwak, J. Asbury, X. Chen, I. R. Piletic, M. D. Fayer, *Science* **2005**, *309*, 1338-1343.

[101] H. Schurkus, *Ultrakurzzeitdynamik der photochemischen Dissoziation von Benzhy-drylderivaten mit zwitterionischer Abgangsgruppe*, Bachelorarbeit, Ludwig-Maximilians-Universität (München), **2012**.

[102] F. Brotzel, Y. C. Chu, H. Mayr, *J. Org. Chem.* **2007**, *72*, 3679-3688.

[103] T. Kanzian, T. A. Nigst, A. Maier, S. Pichl, H. Mayr, *Eur. J. Org. Chem.* **2009**, 6379-6385.

[104] I. Ohmine, S. Saito, *Acc. Chem. Res.* **1999**, *32*, 741-749.

[105] T. B. Phan, C. Nolte, S. Kobayashi, A. R. Ofial, H. Mayr, *J. Am. Chem. Soc.* **2009**, *131*, 11392-11401.

Appendix A: Reactivity scales

In the last two decades, Mayr and coworkers developed comprehensive reactivity scales which allow to predict the rate constant of a reaction between an electrophile (e.g., a benzhydryl cation) and a nucleophile (e.g., a chloride anion):

$$\text{electrophile} + \text{nucleophile} \rightarrow \text{product}$$
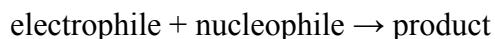
Typically, second order kinetics are observed for the evolution of the concentrations

$$\frac{d[\text{product}]}{dt} = k_2 [\text{electrophile}][\text{nucleophile}] \qquad (A.1)$$

For a large series of electrophiles and nucleophiles this second-order-rate constant k_2 (in units of $M^{-1} s^{-1}$) can be calculated according to [16-19]:

$$\log k_2 = s(N + E) \qquad (A.2)$$

in which electrophiles are described by electrophilicity parameters E and nucleophiles are described by nucleophilicity parameters N and the nucleophile-specific sensitivity parameter s.[14] For example, the logarithm of the rate constant of the reaction between the benzhydryl cation tol_2CH^+ (E = 3.63 [17]) and cyclopentadiene in dichloromethane (N = 2.30, s = 1.06 [19]) is $\log k_2 = 1.06 \cdot (2.30 + 3.63) \approx 6.29$ and the rate is $k_2 = 10^{6.29} M^{-1} s^{-1} \approx 2 \cdot 10^6 M^{-1} s^{-1}$.

Often the nucleophile is employed in great excess in the solution and therefore does not change significantly during the reaction. Then the reaction is of pseudo-first order and the rate constant is given by

$$k_1 = k_2 [\text{nucleophile}] \qquad (A.3)$$

and the concentration of the electrophile decays exponentially

$$[\text{electrophile}](t) = [\text{electrophile}]_0 \exp(-k_1 t) \qquad (A.4)$$

Especially, when studying reactions with the solvent (as in Section 3.7) the framework of pseudo-first order kinetics is helpful. Since the solvent is in great excess one will always observe a purely exponential decay with the first-order rate constant k_1. Therefore, the nucleophilicity parameter N_1 of solvents is given in literature [90] in such a way that first-order rate constants are obtained from Eq. A.2. The ordinary N parameter (used for the determination of k_2) can be obtained by subtracting the logarithm of the concentration log[nucleophile] from N_1 [90]. For neat methanol ([methanol] = 24.7 M), the ordinary N value is given by N_1 − 1.39.

---

[14] For a comprehensive database of nucleophilicity and electrophilicity parameters, see: http://www.cup.lmu.de/oc/mayr/DBintro.html.

Appendix B: Intrinsic rates for the geminate recombination

The photolysis of precursors leads to pairs of benzhydryl cations and the leaving group which are in close vicinity. The distance between the two fragments increases with time by diffusion. They can, however, undergo recombination as long as they are not separated diffusionally. Assuming that the escape of the fragments can be described by a rate constant k_{esc} the reaction scheme depicted in Figure B.1 can be used.
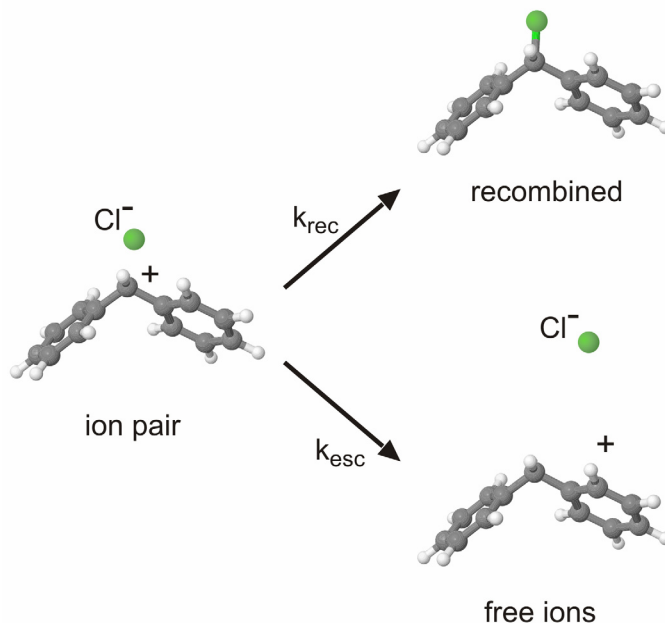
Figure B.1: Scheme of the processes after photolysis of Ph_2CHCl yielding an ion pair. The ions can either undergo recombination with a rate constant k_{rec} or escape to give rise to free ions with a rate k_{esc}.

The rate equations for the initially generated ion pairs, the free ions and the pairs which recombine can be written as:

$$-\frac{d[\text{ion pairs}]}{dt} = (k_{esc} + k_{rec}) \cdot [\text{ion pairs}] \tag{B.1}$$

$$\frac{d[\text{free ions}]}{dt} = k_{esc} \cdot [\text{ion pairs}] \tag{B.2}$$

$$\frac{d[\text{recombined pairs}]}{dt} = k_{rec} \cdot [\text{ion pairs}] \tag{B.3}$$

Integration of Eq. B.1 yields the solution for the ion pair concentration:

$$[\text{ion pairs}] = [\text{ion pairs}]_0 \cdot \exp(-(k_{esc} + k_{rec}) \cdot t) = [\text{ion pairs}]_0 \cdot \exp(-k_{tot}t) \tag{B.4}$$

with the initial concentration of ion pairs $[\text{ion pairs}]_0$ and the observable rate constant k_{tot}. The further concentrations are then given by:

Appendix B: Intrinsic rates for the geminate recombination terminated by diffusion

$$[\text{recombined pairs}] = [\text{ion pairs}]_0 \cdot \frac{k_{rec}}{k_{tot}} \cdot \left[1 - \exp\left(-k_{tot}\, t \right) \right] \qquad (B.5)$$

$$[\text{free ions}] = [\text{ion pairs}]_0 \cdot \frac{k_{esc}}{k_{tot}} \cdot \left[1 - \exp\left(-k_{tot}\, t \right) \right] \qquad (B.6)$$

For $t \rightarrow \infty$, Eq. B.5 becomes

$$[\text{recombined pairs}] = [\text{ion pairs}]_0 \cdot \frac{k_{rec}}{k_{tot}} \qquad (B.7)$$

Since the yield for geminate recombination Y_{GR} is given by

$$Y_{GR} = \frac{[\text{recombined pairs}]}{[\text{ion pairs}]_0} \qquad (B.8)$$

the recombination rate can be easily determined by the following relationship:

$$k_{rec} = k_{tot}\, Y_{GR} \qquad (B.9)$$

An analogous calculus leads to the escape rate

$$k_{esc} = k_{tot} \left(1 - Y_{GR} \right). \qquad (B.10)$$

Appendix C: Simulation of the observed photoinduced dynamics

In this section, the distance dependent rates needed for the simulation of the observed photoinduced dynamics for benzhydryl chlorides are discussed and compiled. Only the absolutely necessary formulas are given explicitly. A detailed description and the full mathematical framework can be found in

"A Comprehensive Microscopic Picture of the Benzhydryl Radical and Cation Photo-Generation and Interconversion through Electron Transfer"
C. F. Sailer, B. P. Fingerhut, S. Thallmair, C. Nolte, J. Ammer, H. Mayr, R. de Vivie-Riedle, I. Pugliesi, E. Riedle
ChemPhysChem., to be submitted.

and the corresponding Supporting Information.

In brief, the benzhydryl radical / cation and the chlorine radical / chloride anion are assumed to be spheres with radii $R_{benzhydryl}$ and R_{Cl}. R denotes the distance between the centers of the two spheres and $R_C = R_{benzhydryl} + R_{Cl}$ is the contact distance. The simulations were performed with the auxiliary quantities $S_{RP}(R,t)$ for the radical pairs and $S_{IP}(R,t)$ for the ion pairs. The time dependent population distributions $P_{RP}(R,t)$ for the radical pairs and $P_{IP}(R,t)$ for the ion pairs can be obtained by:

$$P_{RP}\left(R,t \right) = 4\pi R^2 S_{RP}\left(R,t \right) \exp\left[-V_{RP}\left(R \right)/k_B T \right] \tag{C.1}$$

$$\text{and } P_{IP}\left(R,t \right) = 4\pi R^2 S_{IP}\left(R,t \right) \exp\left[-V_{IP}\left(R \right)/k_B T \right] \tag{C.2}$$

V_{RP} and V_{IP} are the intrapair potentials (see Figure C.1):

$$V_{RP}\left(R \right) = -\ln\left[g\left(R \right) \right] \cdot k_B T \tag{C.3}$$

$$V_{IP}\left(R \right) = -\ln\left[g\left(R \right) \right] \cdot k_B T - \frac{e^2}{4\pi\varepsilon_0\varepsilon_{st}} \frac{1}{R} \tag{C.4}$$

V_{RP} arises from the solvent molecules around the radical pairs which are partly ordered. This can be described by the radial distribution function g(R) of the solvent. For the two fragments it is more favorable to be in a distance which corresponds to zero, one or two solvent diameters. The intrapair potential for the ion pairs V_{IP} exhibits additionally the Coulomb potential term. The involved relative static permittivity ε_{st} describes the shielding of the charges by the solvent and leads to a decreasing influence of the Coulomb attraction with increasing solvent polarity.

The evolution of the species is described with the following two coupled partial differential equations:

$$\frac{\partial}{\partial t} S_{RP}(R,t) = L^+ S_{RP}(R,t) - k_{ET}(R) S_{RP}(R,t)$$
$$- k_{rec}^{RP}(R) S_{RP}(R,t) - k_{esc}^{RP}(R) S_{RP}(R,t) \quad \text{(D.3)}$$

$$\frac{\partial}{\partial t} S_{IP}(R,t) = L^+ S_{IP}(R,t) + k_{ET}(R) S_{RP}(R,t) \exp\left[-\frac{e^2}{4\pi\varepsilon_0\varepsilon_{st}k_BT}\frac{1}{R}\right]$$
$$- k_{rec}^{IP}(R) S_{IP}(R,t) - k_{esc}^{IP}(R) S_{IP}(R,t) \quad \text{(D.4)}$$

L^+ is the adjoint Smoluchowski operator in spherical coordinates

$$L^+ = \frac{1}{R^2} \exp[V(R)] \frac{\partial}{\partial R}\left(D(R)R^2 \exp[-V(R)]\frac{\partial}{\partial R}\right) \quad \text{(D.5)}$$

$D(R)$ describes the mutual diffusion coefficient of the particles and is given by:

$$D(R) = D_F\left[1 - \frac{1}{2}\exp\left(-\frac{R-R_c}{d_{solv}}\right)\right] \quad \text{(D.6)}$$

It corresponds to the bulk value of the diffusion coefficient D_F for larger distances. At contact distance it is reduced to the half which accounts for the hydrodynamic effect. The particles have to force the solvent out of the path which is harder when the particles are in close to each other [71].

The electron transfer rate is described by Marcus theory:

$$k_{ET}(R) = \frac{2\pi}{\hbar} \cdot \frac{V_{eff}^2}{\sqrt{4\pi\lambda(R)k_BT}} \cdot \exp\left(-\frac{(\lambda(R)+\Delta G_{ET})^2}{4\lambda(R)k_BT}\right) \cdot \exp(-\beta(R-R_c)) \quad \text{(D.7)}$$

with V_{eff} the effective electronic coupling and ΔG_{ET} the change in Gibbs free energy. The last term describes the exponential decrease of the electron transfer rate with distance due to the exponential radial character of the electronic wave function of electron donor and acceptor [64]. The value of β was set to 0.7 Å^{-1}. The reorganization energy is also distance dependent and is given by:

$$\lambda(R) = \lambda_{in} + \frac{e^2}{8\pi\varepsilon_0}\left(\frac{1}{\varepsilon_{op}} - \frac{1}{\varepsilon_{st}}\right)\cdot\left(\frac{1}{r_{benzhydryl}} + \frac{1}{r_{Cl}} - \frac{2}{R}\right) \quad \text{(D.8)}$$

with λ_{in} the internal reorganization energy and ε_{op} the relative optical permittivity.
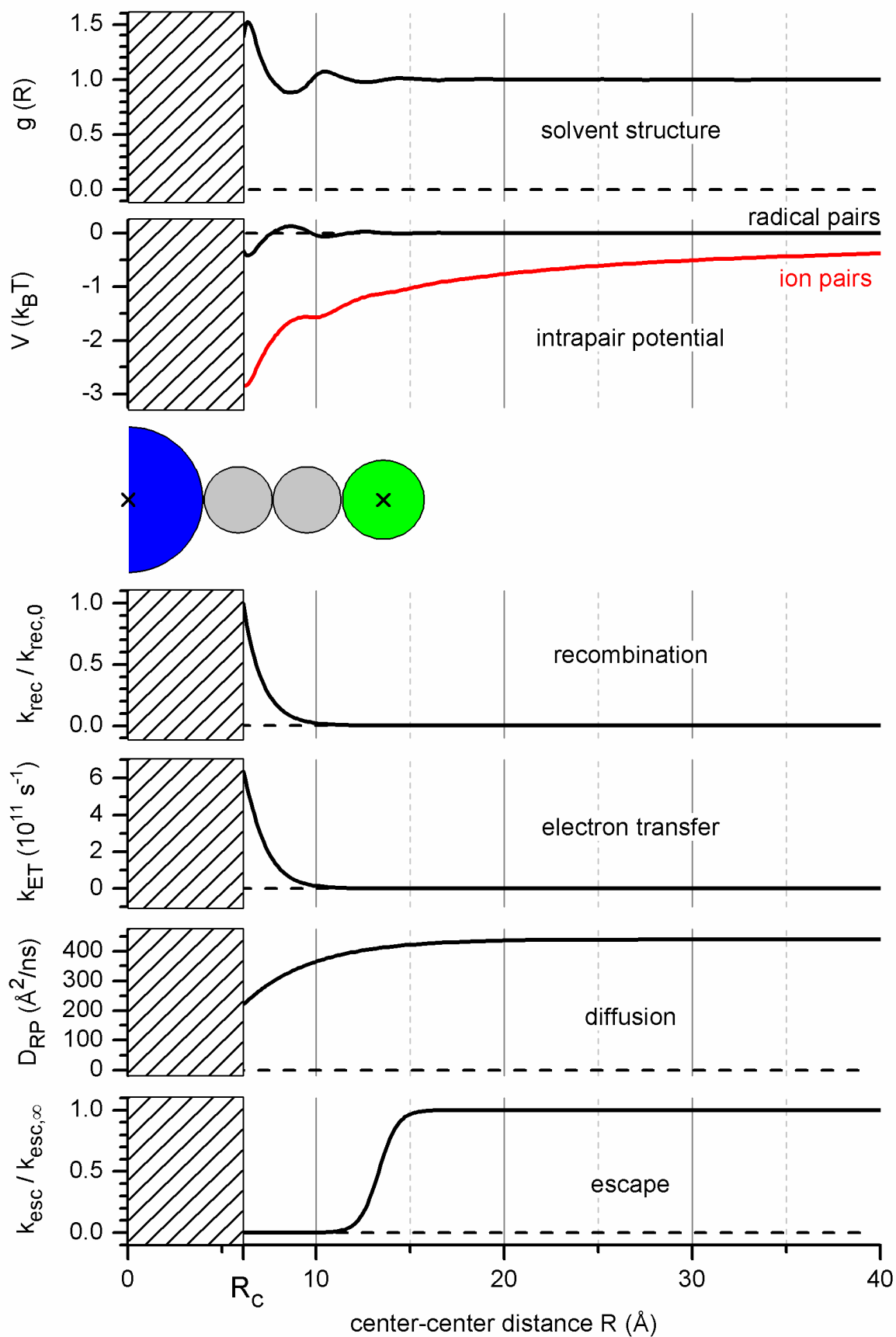
Figure C.1: Distance dependent rates and parameters used in the simulations.

The rate for recombination of both, radical pairs and ion pairs, is assumed to fall off exponentially in agreement with Ref. [69]. It is given by:

$$k_{rec}(R) = k_{rec}^0 \cdot \exp\left[-\alpha(R - R_c)\right] \tag{D.9}$$

The value of $\alpha = 1$ Å^{-1} was taken from Ref. [69]. The range of the recombination is therefore somewhat smaller than the range for the electron transfer.

The distance dependency of the escape rates of radical and ion pairs is modeled by a sigmoid function with the 50% turning point at two solvent diameters behind contact distance:

$$k_{esc}(R) = k_{esc}^\infty \cdot \frac{1}{1 + \exp\left[-2\left(R - (R_c + 2d_{solv})\right)\right]} \tag{D.10}$$

Radical or ion pairs in close contact therefore do not escape, while species at larger separations escape and become unreactive with the rate k_{esc}^∞.

Appendix D1

Sub-50 fs broadband absorption spectroscopy with tunable excitation: putting the analysis of ultrafast molecular dynamics on solid ground

U. Megerle, I. Pugliesi, C. Schriever, C. F. Sailer, E. Riedle

INVITED PAPER

Sub-50 fs broadband absorption spectroscopy with tunable excitation: putting the analysis of ultrafast molecular dynamics on solid ground

U. Megerle · I. Pugliesi · C. Schriever · C.F. Sailer · E. Riedle

Abstract We give a full description of a state-of-the-art femtosecond transient spectrometer. The setup has been put together under full consideration of all technical and conceptual developments that became available in the last few years. Particular care was taken to avoid any unneeded components and modules.

The spectrometer is operated at 1 kHz and based on a commercial Ti:sapphire amplifier. A noncollinear parametric amplifier and frequency doubling are used to provide pump tuning from the UV to the NIR. A CaF_2 based single filament white light allows for 290 to 720 nm probing. The multichannel detection is operated at the full 1 kHz rate and chopping of the pump light avoids the use of a reference channel. The resulting high detection sensitivity of better than $\Delta OD = 10^{-4}$ allows for the simultaneous recording of the spectral features of electronic states and species with differing transition strengths.

A prism-based polychromator is employed to avoid the order sorting problem with the more than octave wide probe spectrum and to enhance the throughput. Flow cells with 200 μm windows and down to 120 μm sample thickness reduce the coherent artifact and the group velocity mismatch. This results in an overall sub-50 fs temporal resolution.

U. Megerle · I. Pugliesi · C. Schriever · C.F. Sailer · E. Riedle (✉)
Lehrstuhl für BioMolekulare Optik,
Ludwig-Maximilians-Universität (LMU), Oettingenstr. 67,
80538 München, Germany
e-mail: riedle@physik.lmu.de
Fax: +49-89-21809202

1 Introduction

The study of photophysical and photochemical processes crosses the interest of many fields of research in physics, chemistry and biology. Among the experimental approaches developed for this purpose, transient absorption spectroscopy has become a powerful and widely used technique. The process investigated is triggered by exciting the molecules with a short laser pulse. The dynamics of the electronically excited states is then probed by a second light pulse that monitors the photo-induced transmission changes. This concept is not easily transferred to bimolecular reactions, since the observed rate is usually limited by diffusion. Unimolecular processes, however, can easily proceed in the pico- or femtosecond range.

In their early stages, ultrafast studies had to rely on the accidental coincidence of given laser lines—mostly from sub-ps dye lasers—with molecular absorptions, both in the spectrum of the educt and the transient spectrum of the intermediates or products. In prominent cases, this was already sufficient for a crucial breakthrough in understanding the underlying mechanisms [1]. In other situations however, a fair amount of "chemical intuition" had to be added to resolve any ambiguities. Ideally, however, the excitation should not be chosen by technical constraints but according to the sample of interest. To put the analysis on solid ground, all relevant transient signatures should be monitored.

The last two decades have witnessed the upgrowth of low noise and sufficient intensity ultrafast light sources freely tunable from the deep UV into the mid-IR. These sources are typically pumped by amplified Ti:sapphire lasers and are based on optical parametric amplification (OPA). A collinear OPA together with difference frequency mixing gives access to the spectral range from near-IR to mid-IR [2–5] while a noncollinear geometry (NOPA) with the

help of frequency doubling and sum frequency mixing allows for shortest pulses from the UV to the near-IR [6–9]. This development allowed for a selective triggering of photochemical processes, thereby dramatically enlarging the range of molecules that can be properly studied by transient spectroscopy. The spectral width of pulses generated in a NOPA routinely supports pulse lengths below 30 fs ensuring a time resolution on the scale of molecular vibrations.

The available tunability can also be used to probe the transient species developing from the photo-initiation by optical transitions occurring at various wavelengths [10–12]. However, employing probe pulses that cover an ultrabroad spectral range at once greatly simplifies the experiment. The wider the probe spectrum, the more spectral signatures of the transient species involved in a photoprocess can be monitored simultaneously, which significantly facilitates the assignment of the underlying reaction mechanism.

Towards this goal, one approach is to use ultrabroadband NOPA pulses that have a Fourier limit of only a few femtoseconds [13–15]. Combining such a probe pulse with a narrowband NOPA excitation allows one to achieve a time resolution in the sub-10 fs regime [16, 17] which is tailored to the investigation of the fastest photochemical processes.

However, even ultrabroad NOPA pulses can at best extend over 200 THz corresponding to most of the visible but not reaching down to the UV. The alternative approach to cover a much wider range is to use supercontinua. These are generated by focusing an ultrashort laser pulse under proper conditions into optically nonlinear transparent media like gases, liquids, photonic crystal fibers and solids [18]. The properties of the continua and their applicability to transient spectroscopy depend very much on the way they are generated. Even though time-resolved studies have been performed using white light from liquids [19–22] or microstructured fibers [23], the great majority of reported spectrometers relies on supercontinua obtained from bulk materials. The latter have been shown to yield continua with a very broad and smooth spectrum, high temporal and spatial coherence and a very high pulse-to-pulse energy stability. In contrast to broadband NOPA pulses, supercontinua cannot readily be compressed to the Fourier limit. Therefore, extra care has to be taken to reach a temporal resolution significantly better than 100 fs in spectrometers with chirped supercontinuum probing. For many studies this disadvantage is, however, heavily outweighed by the broad probing range [24–31].

The full potential of the broad supercontinua can best be exploited with a multichannel detection system in contrast to approaches where a stepwise scanning of the probe light is employed. In the past, multichannel detection faced some significant technical difficulties by posing high demands on electronics and data acquisition. Commercially available detectors were limited to read-out frequencies well below

the typical repetition rate of the pump system of 1 kHz. This required acquisition times of several minutes to reach sufficient signal-to-noise ratios. Only home-built systems were capable of real single pulse analysis at kHz repetition rates [32–34], however often with a rather small number of channels. Recent advancements in detector electronics have increased the read-out frequencies of arrays containing up to 1024 elements reliably to over 1 kHz. This development has already found its way into first spectroscopic setups [35–38].

Besides the progress in light sources and detectors, many additional advances have allowed transient spectrometers to mature to highly productive scientific instruments. Over the years, a considerable number of publications has been dedicated to the description and characterization of the large variety of pump-probe spectrometers. However, to the reader of spectroscopic journals it is often unclear whether the described setup is historically motivated or specifically built for a certain application. Furthermore, since the spectrometers are constantly improved, many of the contributions tend to focus on the newest developments and therefore concentrate on selected experimental aspects. Thus, a complete description of the setup and the link between the individual features comprising the spectrometer is often lacking.

In this paper we present a summary of all relevant concepts and components that we used to build and run a state-of-the-art femtosecond broadband pump-probe spectrometer, further details can be requested from the authors. From our experience gained over many years of activity in the field, the essential tools are optical parametric amplifiers, low dispersion optics and sample cells, a stable supercontinuum generation combined with a high transmission polychromator and a kHz multichannel detector, and last but not least the proper software for data recording and processing. We believe that a design based on these elements comes closest to the realization of the following principles: tunability of the excitation source, broad spectral coverage, sub-50 fs time resolution, high sensitivity, efficient data acquisition and evaluation, and finally flexibility of the whole setup. The implementation of these principles is crucial for reliable high quality time resolved measurements and essential for a sound analysis of the observed ultrafast molecular dynamics.

2 Experimental setup

2.1 Design of the pump-probe spectrometer

In this section we give an overview of our femtosecond pump-probe spectrometer before describing the most relevant components in more detail in the following sections. The complete schematic of our setup is shown in Fig. 1. It is directly linked to the actual layout on the optical table since
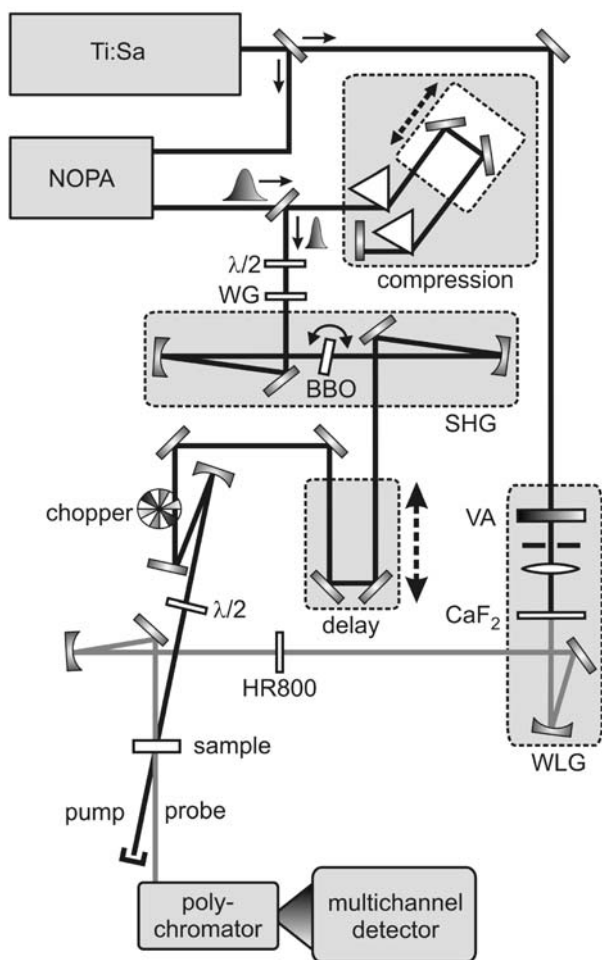
Fig. 1 Layout of the pump-probe spectrometer. WG: wire-grid polarizer; SHG: second harmonic generation; VA: variable attenuator; WLG: white light generation; HR800: custom-made dielectric mirror to block the CPA fundamental

it depicts essentially all of the employed components. The idea behind the design is on the one hand simplicity reached by omitting redundant optics. On the other hand, we deliberately keep an open layout on the optical table to facilitate the day-to-day operation and optimization. The aim of our setup is not to perform heroic measurements after many days of adjustment but rather to ensure a reliable performance when sensitive chemical samples become available.

As a light source we use a regenerative Ti:Sa amplifier system (CPA 2001; Clark MXR) that delivers 1 mJ-pulses at 775 nm with 150 fs duration and a repetition rate of 1 kHz. The comparatively long pulse duration ensures a stable operation and still is sufficient to perform measurements with highest temporal resolution due to the pulse shortening in the NOPA. For the pump, a fraction of 200–250 µJ is used to operate a two-stage noncollinearly phase-matched optical parametric amplifier (NOPA). The chirped visible output pulses with energies of several µJ are compressed with a sequence of two Brewster prisms. Subsequently, a thin achro-

matic half-wave plate and a wire-grid polarizer (ProFlux™; MOXTEK, Inc.) are used to adjust the pulse energy according to the needs of the spectroscopic experiment. The polarizer is set parallel to the pump polarization and the transmission is controlled by rotating the half-wave plate. If desired, the visible pulses can be frequency doubled in a type-I BBO crystal. Contrary to the simple model of pump-probe spectroscopy, we do not change the delay of the probe pulses but rather the pump pulses are delayed with a retro reflector mounted on a computer controlled linear stage and then focused to the sample. This ensures the most stable operation of the probe continuum and introduces only negligible changes in the pump focus. The polarization of the pump beam can be set with another achromatic half-wave plate which is placed directly before the sample. A reflection on mirrors at a polarization deviating from horizontal or vertical would turn linearly into elliptically polarized light.

As probe pulse we use the white light generated by focusing roughly 1 µJ of the fundamental Ti:Sa beam into a CaF_2 crystal. After passing through the sample at an external angle of $\sim 6°$ with respect to the pump, the probe is dispersed in a polychromator and focused onto a multichannel detector. A chopper wheel in the pump beam blocks every second excitation pulse such that changes in the optical density (OD) of the sample can be measured according to:

$$\Delta OD(\lambda, \Delta t) = -\log\left(\frac{I^*(\lambda, \Delta t)}{I_0(\lambda)}\right). \tag{1}$$

Here, I^* and I_0 are the transmitted probe light through the excited and the unpumped sample. With the knowledge of all relevant parameters like beam diameters and sample concentration, the ΔOD-signal allows for the determination of absolute values for the photoprocesses, e.g., extinction coefficients or concentrations of the transient species. Thus, the time resolved absorption spectroscopy can not only identify, but also quantify the processes occurring during a photoreaction.

The induced absorption changes can be followed up to times given by the length of the delay line, in our case from $\Delta t = -0.1$ ns to about 1.7 ns. For longer delays, the alignment of the pump beam becomes more and more difficult, e.g., due to the divergence and the associated change of the pump diameter and also the changing overlap with the probe inside the sample. To record dynamics from ultrafast charge transfer or wavepackets (<100 fs) up to slow population redistributions (>100 ps) within the same experiment we use a quasi-exponential time scale for sampling. The step size is chosen constant between -1 and 1 ps and is then linearly increased with the delay time according to

$$\Delta t(i) = \begin{cases} -1 + \frac{2i}{N} & \text{for } i = 0 \ldots N-1, \\ 10^{-1+i/N} & \text{for } i = N \ldots M. \end{cases} \tag{2}$$

Here, N denotes the number of points between -1 and 1 ps and M is given by the maximum delay time Δt_{max} by $M = N(1 + \log \Delta t_{max})$. This time scale generates the same number of delay points from -1 to 1 ps as between 1 and 10 ps, 10 and 100 ps, etc., respectively. If a fit routine is applied to such a data set, the dynamics on every time scale will have equal weighting. The initially linear scan ensures proper correction for the continuum chirp and the exponential sampling in addition minimizes the measurement time. For an appropriate data presentation we usually add some sparsely spaced points at negative delay times and typically start at $\Delta t = -100$ ps. This also allows for better statistics when analyzing the baseline in terms of sensitivity (see Sect. 4.2).

An important consideration is the choice of the optics in the setup. For the white light probe we only use metal coated planar mirrors for steering and spherical mirrors rather than lenses to avoid additional chirp. For highest throughput UV enhanced aluminium mirrors (RAL UVE; Linos Photonics GmbH & Co. KG[1]) are employed. For the focusing we have turned away from off-axis parabolic mirrors due to the unfavorable surface quality of available samples. We found that much better beam profiles and tenfold lower M^2 values can be achieved with spherical mirrors. To limit the influence of the astigmatism we keep the reflection angles low on all spherical mirrors by placing them in a folded geometry as seen in Fig. 1. We have also tested the use of spherical mirrors off-axis in alternating planes to minimize the astigmatism [39]. However, for most purposes we find no need for this implementation and believe that a slight deterioration for example of the pump and probe foci inside the sample is acceptable (see Sect. 2.4).

For the visible pump pulses an enhanced silver coating (Silflex™MK II; Optics Balzers GmbH (see footnote 1)) is a good choice since it has a very high reflectivity for the whole range from 450 nm into the IR. For the UV pump the enhanced aluminium mirrors provide the advantage of broad spectral coverage. For near unity efficiency and separation of the UV from the fundamental we use a few dielectric mirrors.

In contrast to the standard approach, our spectrometer does not include the detection of a reference beam to account for the shot to shot fluctuations of the white light. Instead, we exploit the high correlation between successive pulses (see Sect. 2.3) for the normalization of the probe intensity. This greatly simplifies the setup, since only one multichannel detector needs to be implemented. As shown in Sect. 4.2, the sensitivity still reaches excellent values beyond the 10^{-4}

level which is among the best reported sensitivities for femtosecond spectrometers.

All software based operations connected with the spectrometer and the evaluation of the measurements are performed with codes developed in our group utilizing the LabView 8.5 (National Instruments, Inc.) platform. The modules allow the experimenter to have full visual control of all relevant data and highly interactive handling. We find this most important to collect reliable and reproducible molecular dynamics information and to properly interpret the raw signals. The software is routinely adapted to the changing needs and insights.

2.2 Ultrashort tunable excitation pulses

As mentioned in the introduction, the need to excite a large variety of molecules at their specific electronic transitions requires a broad tunability of the pump pulses. For true versatility, a continuous tunability is favored over the detached excitation wavelengths reached when higher harmonic generation of the fundamental Ti:Sa output is applied [20, 25, 40–42]. Additionally, the pump pulses should be in the sub-100 fs regime to ensure a sufficient time resolution for the study of ultrafast photophysical and photochemical processes. Last but not least, sufficient energy has to be available to excite a few percent of the illuminated molecules under conditions of weak focusing.

All these requirements can be met by the use of a NOPA which has been described in detail in previous papers [6, 7, 9]. Briefly, less than a μJ of the Ti:Sa fundamental is used for the generation of a visible seed continuum by focusing it into a 3 mm sapphire plate. So far, in most applications a focal length of 30 mm was used, which goes back to early work [43]. However, recently the importance of the numerical aperture on the quality of the continuum has been shown [44]. We observed that the use of lenses with a longer focal length ($f = 50$–80 mm) yields broader continua, both in the visible and in the IR [45] and therefore widens the tunability of the NOPA.

For excitation pulses in the UV/Vis range, a selected portion of the white light is amplified in a 1 mm thick BBO crystal pumped by tens of μJs of the second harmonic of the Ti:Sa beam. For better beam profiles and higher pulse energies a second amplification stage with a 2 mm BBO and more pump energy can be employed. As shown on the right hand side of Fig. 2, pulses ranging from 450–760 nm with Fourier limits below 30 fs and energies of several μJs can easily be obtained by a suitable choice of the angle of noncollinearity between pump and seed and the phase matching angle of the BBO [7].

The spectral width of the NOPA pulses can be tailored depending on the specific needs of the spectroscopic experiment. For instance, spectrally narrow pulses can be obtained

---

[1]Mention of vendor names and model numbers is for technical communication purposes only and does not necessarily imply recommendation of these units, nor does it imply that comparable units from another vendor would be any less suitable for this application.

by adding chirp to the white light seed without sacrificing output power [46]. If the pump is chirped the output spectra can be broadened to reach shorter Fourier limits down to a few fs [13, 47, 48]. Therefore, the spectra shown in Fig. 2 are to be considered as examples for a typical pump-probe experiment without the particular need for extremely short or spectrally narrow pulses.

At the output of the NOPA the pulses are chirped to roughly 130 fs [49]. However, due to the large spectral width much shorter pulse lengths can be obtained, most easily by the use of a fused silica prism compressor. Above 550 nm the length of the compressor can be substantially shortened with SF10 instead of the fused silica prisms. A very helpful feature shown in Fig. 1 is the use of two mirrors acting as a retro reflector inside the prism compressor. This folding allows for a quick and easy adaptation of the length of the compressor to a change of the NOPA center wavelength. In this way the tunability of the NOPA can really be exploited on a day-to-day-basis requiring only minute changes in the alignment of the whole setup. After the compression, pulse durations below 30 fs are routinely achieved throughout the visible. To characterize these pulses we use a compact dispersion-free autocorrelator [50].

In order to extend the tunability of the NOPA into the UV, the visible pulses are focused into a thin BBO crystal. In contrast to the common approach we have not implemented a second prism compressor for the UV pulses. We found that a compression in the visible is sufficient to reach even sub 20-fs pulses in the UV [47]. The prism compressor for the visible is set to precompensate for the additional chirp introduced by the SHG and the further propagation of the pulse through the setup. For the spectra shown on the left hand side of Fig. 2 we used a 150 μm thick BBO crystal in the SHG. This leads to an increase of the pulse length but has the benefit of a higher conversion efficiency. Again, the specific needs of the spectroscopic experiment can be met by the right choice and alignment of the components in the doubling stage. Together with the SHG, the NOPA allows for a nearly continuous tunability of the excitation pulses from the region of the fundamental at 750 nm down to about 240 nm.
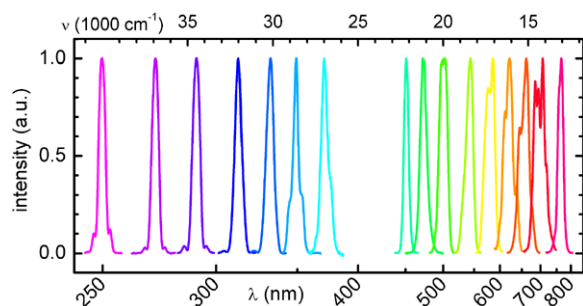
2.3 Octave spanning low noise supercontinuum probe

A commonly used material for white light generation is a sapphire crystal which is often used not only inside the NOPA but also to generate the probe pulse [26, 51–54]. Figure 3a shows the anti-Stokes side of a sapphire continuum obtained with the Ti:Sa fundamental at 775 nm. The spectroscopically useful range spans from about 420 to 720 nm. As strong spectral modulations and temporal fluctuations are present near the fundamental, this range is usually filtered out (e.g. Calflex™X; Optics Balzers GmbH (see footnote 1)).

As many organic molecules have their lowest transitions in the UV it is helpful to extend the probe to higher photon energies. This allows, e.g., for the direct observation of the ground state bleach. However, even for molecules with transitions in the visible it is often useful to be able to monitor the ground state recovery of higher absorption bands since they do not overlap with the stimulated emission or are distorted by stray light from the excitation pulse.

Recently, calcium fluoride crystals were successfully employed [25, 30, 39, 55–58] to generate an ultrabroad continuum that reaches much further into the UV than the one obtained from sapphire. As can be seen in Fig. 3a, the spectrum of a white light generated in a 5 mm CaF_2 plate extends from 290 to 720 nm showing an almost flat plateau. The dip at 400 nm is not a feature of the continuum but is due to the dielectric mirror used to block the fundamental (HR800 in Fig. 1). This custom-made mirror is specified to a high reflectivity at 800 nm and a high transmittance ($>90\%$) from 300 to 700 nm.
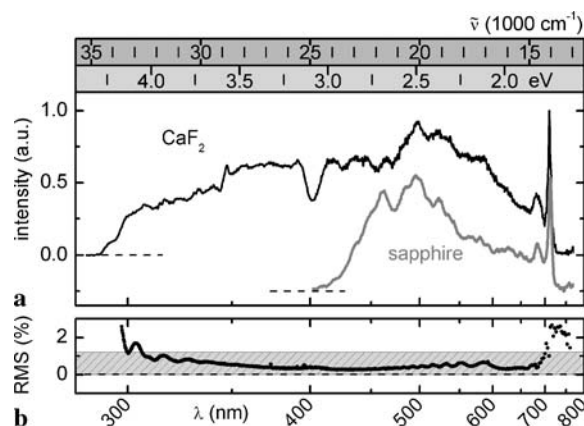
Fig. 3 (**a**) White light continua generated in CaF_2 and in sapphire. The fundamental was suppressed by the HR800 mirror (CaF_2) and a Calflex X filter (sapphire). The spectra were measured with a commercial fiber optic spectrometer and not corrected for its efficiency since a similar efficiency is relevant for the broadband detector. (**b**) RMS noise of the CaF_2 continuum evaluated for 2000 consecutive pulses with the multichannel detector. The low frequency contributions have been subtracted prior to the calculation of the RMS values. The *shaded area* contains 90% of the points

Fig. 2 Typical output spectra of the NOPA. The spectra below 400 nm were obtained by second harmonic generation in a BBO crystal

The spectrum of the CaF_2 white light corresponds to an energy window of over 20,000 cm^{-1}, which is more than twice the range of the sapphire continuum. Within this window, the modulation of the absolute spectral energy density is less than a factor of ten. In the range from 300–700 nm, the energy density is ~10 pJ/nm and the intensity modulation even decreases to a factor of three. This is considerably better than the modulation found when the white light is generated in other materials like microstructured fibers [23, 59] or gas cells [60–62]. The even distribution of the intensity allows for measurements with a high dynamic range and makes the CaF_2 continuum an ideal probe.

The quality of the CaF_2 white light strongly depends on several experimental parameters. These include the energy of the fundamental, the numerical aperture of the setup, the angle of incidence on the CaF_2 disk, its positioning relative to the focus along the beam and the orientation of the crystal axes with respect to the polarization of the laser.

To adjust the energy of the Ti:Sa fundamental we use a variable attenuator in combination with an iris whose aperture is set to about 5 mm. The latter also controls the diameter of the focus inside the CaF_2 disk. For the focusing we use a 10 cm lens which leads to a numerical aperture of 0.025. As described by Laimgruber et al. [37], the optimization of the focus position starts by placing the focus behind the CaF_2 plate. Then the plate is moved towards the focus until a stable single filament white light is obtained. For a good performance in the UV, the intensity of the fundamental has to be increased till a red ring surrounding the white light is seen on a white card. A further increase in pump energy leads to multifilamentation with even higher UV yield [63], however at the cost of a strongly structured beam profile. This causes significant problems in the beam guidance and therefore we restrict ourselves to the use of a single filament CaF_2 continuum with its near Gaussian profile (see Sect. 2.4).

As even CaF_2 plates of carefully selected quality have an insufficient damage threshold, the crystal has to be continuously moved in order to increase its lifetime. Contrary to our early impressions the possible damage does not occur at the surface but rather inside the bulk material. Several motion techniques are conceivable, e.g., translation, rotation or any combination of both. However, to maintain a linear polarization of the white light across the spectrum and over time, the orientation of the crystal axes relative to the polarization of the fundamental has to be kept constant [64–66]. This can be easily achieved by an eccentric motion of the plate, i.e. a circular translation rather than a classical rotation around the center [37]. For an arbitrary orientation of the CaF_2 crystal the white light is elliptically polarized. The complete extinction behind a polarizer is a good measure to adjust the crystal orientation, which will then remain perfectly linear (parallel to the horizontal pump polarization) and unchanged during the eccentric motion.

As a measure of the stability of the continuum we monitor online the root-mean-square (RMS) of the noise at all wavelength components of the white light using the multichannel detector described in Sect. 2.7. The RMS noise is given by the standard deviation of the intensity distribution of the measured pulse sequence divided by its RMS value. During the adjustment of the white light, one needs a quick feedback for practical reasons. We therefore typically evaluate 200 consecutive pulses corresponding to an update rate of 5 Hz. The obtained RMS spectra are sufficient for a daily optimization routine but this simple calculation generally overestimates the shot to shot noise.

As shown previously [45, 46], the intensity fluctuations of kilohertz laser systems are not purely statistical but are typically dominated by low frequency contributions. This holds not only for the fundamental, but also for the supercontinuum or the NOPA output. The implication that consecutive laser pulses are strongly correlated is exploited by the shot to shot referencing method described in Sect. 2.1. Therefore, a reasonable measure of the relevant white light stability is obtained when the long-term fluctuations are subtracted before calculating the RMS noise. A typical result for a CaF_2 continuum is shown in Fig. 3b. The RMS values lie well below 1.2% for 90% of the channels as marked by the shaded area and only rise slightly at the edges of the spectrum.

One should note that varying the parameters for the continuum generation leads to a changed wavelength dependence of the RMS values. Different settings, e.g., of the numerical aperture or the intensity of the fundamental, can be used to optimize the stability of selected parts of the spectrum. For most purposes an even distribution of the RMS values over the whole range is a good compromise.

2.4 Choice and check of the focusing geometry

For the optical excitation of the molecules only a fraction of the NOPA output energy is used to avoid multi-photon pump processes or saturation of the transition. In most cases an excitation probability below 10% assures a near linear dependence between the pump energy and the observed signal. In its simplest form the excitation probability P_{exc} is the product of the photon density n_{ph} in the focus and the absorption cross section σ of the sample molecules:
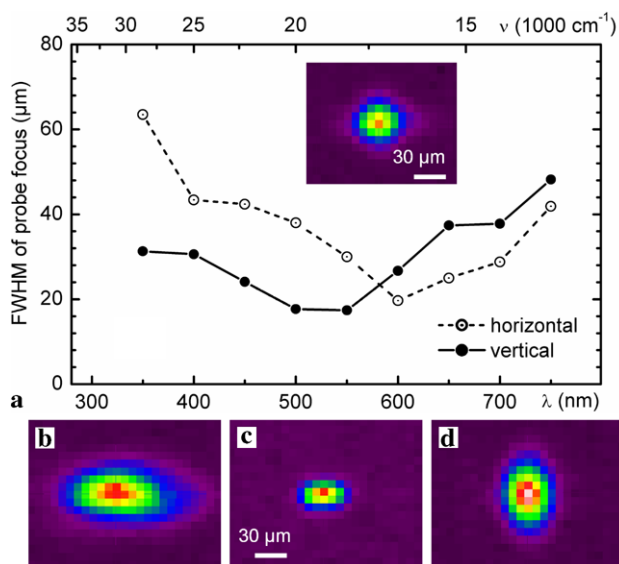
$$P_{exc} = n_{ph} \cdot \sigma = \frac{E_{pump}}{(hc/\lambda) \cdot \pi (D/2)^2} \cdot \varepsilon \frac{\ln 10}{N_A}. \tag{3}$$

For a given sample with an extinction coefficient ε at the excitation wavelength λ, P_{exc} can be tuned by changing the focal diameter D and/or the pump energy E_{pump}. While the latter is adjusted by the half-wave plate/wire-grid dyad after the prism compressor, the former can be controlled by a set of irises in the collimated part of the pump beam.

Decreasing their apertures increases the focal diameter and thereby lowers P_{exc}. Typical values used in our setup are $E_{pump} = 80$–150 nJ and $D = 100$–150 μm with a spherical mirror of $R = -1000$ mm ($f = 500$ mm) employed for focusing. The almost symmetric and near Gaussian beam profile of the NOPA output is well preserved at the focal plane inside the sample despite the slight astigmatism introduced by the spherical mirrors.

For an optimal pump-probe signal the excitation density in the sample should be constant over the probe beam. This is approximately achieved by keeping the waist of the probe beam significantly smaller than that of the pump beam. In our setup, the divergent probe beam after the white light generation is recollimated by a spherical mirror with $R = -150$ mm. This leads to a beam diameter of 2 mm FWHM. The probe is then focused into the sample by a $R = -300$ mm mirror resulting in a focal diameter of about 30 μm FWHM. For good pump-probe signals, other combinations of spherical mirrors are also feasible as long as the ratio between pump and probe beam diameters is not too large.

A more detailed analysis of the beam profiles at the position of the sample reveals that the spot sizes vary for different spectral components of the white light (see Fig. 4). To obtain this information we placed nine different bandpass filters with transmissions centered between 350 and 750 nm and a FWHM of 10 nm into the white light beam. While the beam profile of the complete white light is almost circular at the position of the sample (inset in Fig. 4a), the profiles of the spectral components show a moderate elliptic defor-

mation. As mentioned previously, this is a consequence of the astigmatism caused by the off-axis use of spherical mirrors. Since we deflect the beam in the plane parallel to the optical table the focus in this plane lies behind the one for the vertical plane. In the propagation direction of the beam the profile turns from a vertical ellipse into a circle and then into a horizontal ellipse. The data shown in Fig. 4 therefore indicate that the circular focal profile of the blue wavelength components lies in front of the sample and that of the red components behind the sample. We believe that the wavelength dependence of the position of the focus is related to the processes involved in the white light generation which include different beam geometries for different wavelengths [43, 67, 68].

2.5 Flow cell with thin windows and low sample thickness

Femtosecond pump-transient absorption probe spectroscopy has been applied to a large variety of samples in all three phases: solid [69–71], liquid [72, 73] and gaseous [46, 74]. However, most studies are performed in solution since this is where the majority of the chemically and biologically relevant processes take place. In order to avoid photodegradation or accumulation of photoproducts in the probed volume it is often necessary to exchange the solution continuously, i.e. to use flow cells instead of conventional cuvettes.

In our setup we use a custom-made flow cell which is shown in Fig. 5. The design has been optimized to keep the optical path length through the windows and the sample solution at a minimum. This improves significantly the time resolution due to the decreased contribution from the group velocity mismatch as will be discussed in more detail in Sect. 4.1. In addition, the coherent artifacts produced by nonlinear interaction of the pump and probe pulse in the cell windows are minimized. It is no trivial task to produce thin windows on the order of a few hundred microns that are stable enough for everyday performance in a flow cell.

Fig. 4 White light beam profile at the position of the sample: (**a**) diameters of the probe focus in vertical (*closed circles*) and horizontal (*open circles*) direction for different spectral components. The *inset* shows the profile of the complete white light continuum. Selected profiles at 350 nm (**b**), 550 nm (**c**) and 700 nm (**d**)
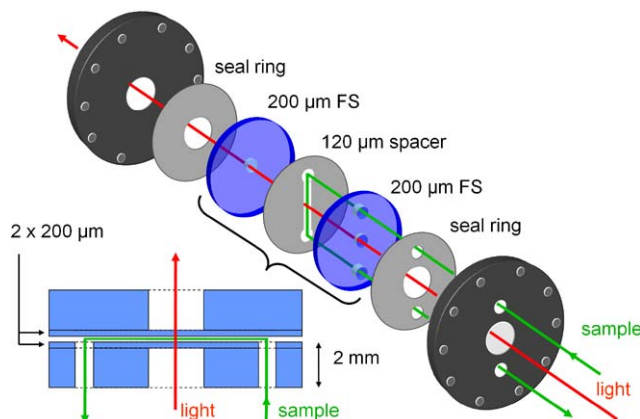
Fig. 5 Scheme of the custom-made flow cell designed for low dispersion and a small optical path length

To overcome this difficulty, special windows have been designed in cooperation with Hellma GmbH.

Each window consists of two fused silica disks with optically polished surfaces, one of 1.8 mm thickness and the other of only 200 μm. The two disks are fused together under clean-room conditions. The thicker disk has a drilled hole of 2 mm diameter in the middle such that the laser pulses propagate only through 200 μm of glass for each window. The front window has two additional holes in both disks, which allow the sample solution to enter the space between the front and back window. The path length can be adjusted by a Teflon spacer of typically 120 μm thickness which has a channel of $\sim 2 \times 20$ mm cut out for the sample solution. The flow cell is held together by two stainless steel flanges shown in black in Fig. 5. In comparison to standard absorption cells with an optical path of 1 mm and a window thickness of 1.25 mm our setup represents a considerable reduction of material in the light path without sacrifice of stability. The whole flow cell is mounted on a holder movable in three dimensions. This facilitates the fine adjustment of the cell position with respect to the spatial overlap of pump and probe.

Many spectroscopically interesting chemical and biological samples are the product of a complex synthetic route or purification and are therefore only available in small amounts. In order to reach suitable optical densities in the rather small sample thickness of 120 μm high concentrations are required. This calls for small volumina, which we assure by using a micro annular gear pump (mzr-2921-M2; HNP Mikrosysteme GmbH (see footnote 1)). This device allows for flow rates up to 18 ml/min and an overall sample volume as low as 1 ml.

2.6 High transmission prism polychromator

To exploit the full potential of the ultrabroad supercontinuum generated in CaF$_2$ we use a multichannel detection scheme with a home-built prism-based polychromator as shown in Fig. 6a. We find that this system best meets the key requirements of an ultrafast spectrometer, namely an effective data acquisition, a simple layout providing a straightforward alignment and a high transmission throughout the whole spectral range, especially in the UV.

The first two aims can be met equally well with a grating based spectrometer like the one we used previously in our lab (Fig. 6b). It can also be utilized as a polychromator and the implementation does not require a significantly larger number of optical components. A prism, however, poses significant advantages over a grating as dispersive element.

The most important one is the high transmission throughout the whole spectral range of the white light, especially when used in a Brewster angle configuration. This fixes the polarization of the probe beam and we choose to set
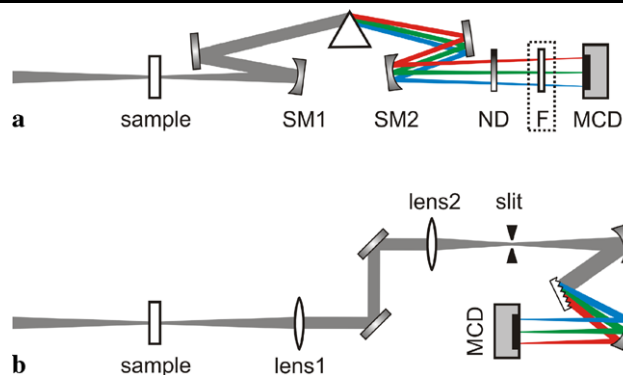
Fig. 6 Design of a polychromator: (**a**) prism-based polychromator used in our setups, (**b**) standard grating based polychromator for comparison. SM: spherical mirror; ND: neutral density wedge; F: optional filters; MCD: multichannel detector

the relative polarization of pump and probe by a half-wave plate in the pump beam (see Sect. 2.1). The high probe transmission increases the detection sensitivity in the region around and below 300 nm where the continuum has a low intensity. Even for highest quality gratings at their specific blaze wavelength, 10% of the incident light intensity is lost into the zeroth and higher orders of diffraction [75]. Moreover, commercially available gratings will not cover the complete range of the CaF$_2$ continuum with high efficiency but will fade strongly towards the edges of the spectrum. Hence, when we replaced the grating (600 lines/mm, $\lambda_{\text{Blaze}} = 400$ nm) with the prism-based polychromator, we could immediately extend our detection window by ~ 15 nm in the UV.

The second advantage is that prisms avoid the order sorting problem, i.e. the fact that higher orders of a short wavelength component are diffracted in the same direction as the first order of light at twice the respective wavelength. This is of particular importance when the continuum spans more than one octave like the CaF$_2$ white light. Then, order sorting filters have to be used to avoid the distorting coincidence of different spectral components on the same pixel of the multichannel detector. However, we found it virtually impossible to purchase a commercial or custom-made filter suitable for our application.

The third advantage of prisms over gratings is the wavelength dependence of the dispersion. For a grating, the dispersion is approximately linear in wavelength leading to a constant wavelength resolution $\Delta\lambda$. The consequence, however, is an energy or wavenumber resolution $\Delta\tilde{\nu}$ that decreases quadratically towards the UV. A typical value of $\Delta\lambda = 4$ nm for a grating spectrometer corresponds to a resolution of $\Delta\tilde{\nu} = 80$ cm^{-1} at 700 nm sufficient for solution phase spectroscopy but to a rather modest resolution of 440 cm^{-1} at 300 nm. In contrast, the dispersion of a prism is a complex function of the wavelength dependent refractive index $n(\lambda)$ of the prism material (see Sect. 3.1). The steeper

slope of $n(\lambda)$ towards the UV results in a high energy resolution for the blue side of the spectrum which does not drop dramatically towards the near IR (see Sect. 4.3). Overall, this leads to a more balanced spectral resolution which on average compares very well to standard grating spectrometers.

We use a metal neutral density wedge deposited on a fused silica substrate in front of the detector to balance the intensities of the channels by suppressing the stronger red components near the fundamental relative to the weaker UV components. Simultaneously, the attenuator adjusts the intensity of the white light to the full-well capacity or saturation charge of the detector. For optimal spectral resolution, the multichannel detector has to be placed in the focal plane of the dispersed white light. In the routine alignment of the detector we use a set of small bandwidth interference filters that are inserted into the white light beam path at the position of the sample. The camera is mounted on a linear translation stage in z-direction and positioned such that the widths of the transmitted profiles are minimized. The curvature of the focal plane arising from spherical aberration is much smaller than the Rayleigh range and therefore does not cause any problems.

The choice of the optics depends on the prism material and on the geometry of the multichannel detector. The prism dispersion together with the total length of the detector area fixes the focal length of the spherical mirror SM2 in Fig. 6a. The focal length of SM2 together with the size of the individual pixels then determines the necessary beam diameter of the collimated white light before the prism. This can be adjusted by the choice of the spherical mirror SM1 once the focusing geometry of the probe light into the sample is fixed. Overall the continuum is imaged once from the output face of the CaF_2 plate into the sample and a second time onto the detector. The ratios of focal lengths determine the magnification and only due to the single filament character of the continuum does the presented simple solution become possible.

In one of our laboratories we use a fused silica prism ($\alpha = 68.7°$, side length $1''$) and a CCD camera with a sensor area of $\sim 12.5 \times 1.5$ mm and a pixel size of 24×24 μm. There, the white light is recollimated after the sample with a $R = -500$ mm spherical mirror (SM 1 in Fig. 6a) to a diameter of ~ 3 mm. The dispersed spectral components are then focused onto the multichannel detector with a second spherical mirror (SM2, $R = -400$ mm). Interestingly, the astigmatism is a desirable side effect. By placing the CCD in the sagittal plane one ensures that the white light is spread in vertical direction over all lines of the CCD array without losing spectral resolution. The choice of reflective optics avoids chromatic aberrations that would result from lenses.

2.7 kHz multichannel detection with high dynamic range

For the measurement of the photo-induced transmission change alternating measurements of the transmission of the probe continuum through the sample with and without excitation are performed. The high correlation between successive probe pulses [46] can be exploited by chopping the pump pulse at half the laser repetition rate. For a typical amplified femtosecond laser system this requires a kHz read-out frequency of the multichannel detector. Dependent on the employed hardware adapted triggering schemes are needed. The cleanest solution is to trigger the detector at the laser repetition rate. If this is not possible, an asynchronous operation is also conceivable. This requires that the integration time of the detector is set to match the period between the laser pulses as closely as possible, or vice versa. In practice, the detector has to be resynchronized after the read-out of a burst as large as possible. Due to the limited long-term stability of the laser system it is important to keep the total measurement time at a minimum. Typically, the duration of one experiment should not exceed 2–3 hours. By maximizing the duty cycle of the data acquisition more laser pulses can be acquired within the measurement time. Thus, a better signal-to-noise ratio can be achieved. With the advent of fast multicore processors and large memories it is nowadays possible to use high level data acquisition languages such as LabView for a fast data recording and real-time processing and visualization.

Over the past decade, multichannel detectors with ever faster read-out electronics have become commercially available at affordable prices. In our lab we use two types of multichannel detection systems: a photodiode array (PDA) based camera (tec5 AG) which is operated in burst mode and a back-thinned full frame transfer (FFT) CCD camera (2000 series; Ingineurbüro Stresing) which is triggered synchronously to the laser.

The PDA sensor (NMOS; S3902-512Q; Hamamatsu) consists of 512 pixels, 50×500 μm each. Due to the large pixel size, the saturation output charge is $\sim 6 \times 10^7$ electrons. With a quantum efficiency of 50% at 600 nm, this corresponds to the absorption of 12×10^7 photons or an energy density of ~ 40 pJ per pixel at 600 nm. This is about a factor of 5 larger than the actual energy density of our supercontinuum (see Sect. 2.3). Thus, the dynamic range of the PDA cannot be exploited properly. In the UV the situation is even worse since the quantum efficiency of the PDA drops to below 30% and the energy density of the white light decreases. To operate the analog-to-digital converter of the PDA camera in the optimal regime we employ an analog pre-amplifier to scale the PDA output. This, however, increases both signal and noise and probably adds extra electronic noise. In total, we determined from the experiment an effective dynamic range of 1000:1 for the PDA.

The FFT sensor (S7030-0906; Hamamatsu) is a two-dimensional CCD array of 524×58 pixels, 24×24 μm each. After illumination, the 58 pixels in the vertical direction are rapidly binned into a reading register. The full-well-capacity of the register is 6×10^5 electrons. With a quantum efficiency of 85% at 600 nm, this corresponds to the absorption of 7×10^5 photons or an energy density of ~0.3 pJ per pixel at 600 nm. Furthermore, the quantum efficiency in the UV is well above 45% for the back-thinned detector. Now the energy in the white light continuum is sufficient throughout the whole spectral range to saturate the detector. Experimentally we measure a dynamic range of 4000:1, i.e. a fourfold increase compared to the PDA. This allows one to extend the detection window towards the UV where the intensity of the white light decreases. We therefore employ the CCD camera preferentially for samples with decisive transient absorption bands in the low wavelength region (see Sect. 5.2).

An often claimed disadvantage of the CCD as compared to a PDA sensor is its lower saturation threshold [76]. This can lead to the unwanted effect that the shot noise becomes higher than the technical laser noise and thereby the detection sensitivity deteriorates. An essential improvement is reached by the vertical binning described above. In our case, the resulting shot noise limit corresponding to the full-well capacity of the CCD reading register is 1.3×10^{-3}. Although quite large, this value is still well below the technical noise of the white light continuum (see Fig. 3b) and therefore does not determine the overall noise of the measurement. For the PDA sensor, the maximum number of generated electrons is about five times smaller than the saturation output charge. This still leads to a shot noise limit of 2.9×10^{-4} which is one order of magnitude better than for the CCD and much below the laser excess noise.

The quality of the spectroscopic data we obtain with these two detection systems is very similar (see Sects. 4 and 5). The differences arise mostly from the fact that the two setups are operated with different laser sources whose performance is never quite the same. Also the two supercontinua generated in CaF_2 will always have slightly different properties. From our experience, these contributions are larger than the actual differences between the CCD and the PDA based camera and therefore we find both systems equally suitable for the application in ultrafast transient absorption experiments.

3 Calibration and data post-processing

3.1 Wavelength calibration

For the wavelength calibration of our home-built prism polychromator we use a filter wheel with five color filters that can be rotated into the probe beam successively. It is important to position the filters for normal incidence of the beam
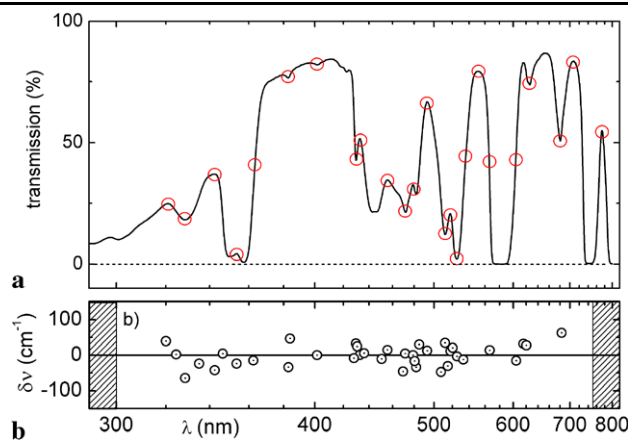
Fig. 7 (**a**) Transmission spectrum of the filter BG 36, the *red circles* exemplarily indicate features that can be used to calibrate the spectrometer. (**b**) Accuracy of the wavelength calibration as identified by the position of the same features in the recorded spectrum. For details see text

propagation to avoid a parallel shift of the continuum on the detector. To minimize the influence of a small wedge on the filter, the wheel is placed right in front of the camera. The set consists of the three longpass filters WG 320, GG 475 and RG 695 and the two multiband filters BG 20 and BG 36 from Schott. While the strongly modulated spectra of the latter allow for a calibration over the whole near-UV/Vis range (see Fig. 7a), the former serve as additional checks at specific points.

At the beginning of each transient measurement we record the transmission of all filters as a function of the pixel number. The known spectra of the filters can then be used to assign the proper wavelengths to selected pixels. The various maxima, minima and steep slopes of the curves render about 30 wavelength/pixel couples that are used as input data for a fit that correlates each of the 512 pixels to a wavelength λ_i.

The horizontal deflection of a wavelength λ_i with respect to a reference wavelength λ_0 corresponds to the pixel number $N(\lambda_i)$ according to the exit angle $\theta_{out}(\lambda)$ from the prism:

$$N(\lambda_i) = M - f \cdot \sin\big(\theta_{out}(\lambda_i) - \theta_{out}(\lambda_0)\big) + \text{const.} \qquad (4)$$

M is the total number of pixels on the detector and f the focal length of the spherical mirror SM2 in Fig. 6a. The exit angle depends on the index of refraction $n(\lambda)$ of the prism material which can be calculated from the Sellmeier equation:

$$\theta_{out}(\lambda) = \arcsin\left(n(\lambda) \cdot \sin\left(\alpha - \arcsin\frac{\sin\theta_{in}}{n(\lambda)}\right)\right). \qquad (5)$$

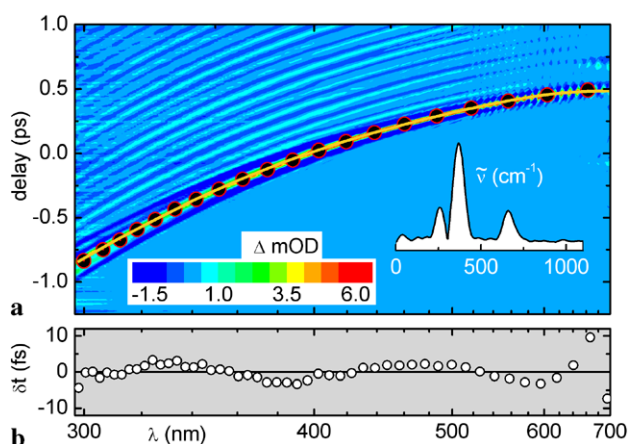Here, θ_{in} is the angle of incidence of the white light into the prism and α is its apex angle.

Only two of the parameters in (4) are fitted with a Levenberg–Marquardt algorithm: the constant offset and the

focal length f. Although the latter quantity is in principle determined by the radius of curvature of SM2, we also fit this parameter to account for imperfect collimation of the white light and the astigmatism inherent to the setup. After fitting (4) the sought-after function $\lambda(N_i)$ is obtained by numerically inverting the monotonic function $N(\lambda_i)$.

The quality of the calibration procedure is estimated by comparing the spectral position of the most prominent features of the BG 36 spectrum after the calibration with their actual position known from the reference measurement in a standard spectrometer. The results are shown in Fig. 7b. Over the whole range of the white light continuum we find the deviations to be mostly within a ± 50 cm^{-1} window, which translates to a precision of ± 0.5 nm at 300 nm and ± 2.5 nm at 700 nm. This is in the range of the spectral spacing of the pixels.

3.2 Chirp correction procedure

Due to the chirp of the white light, the temporal overlap between pump and probe—or time zero—is wavelength dependent. This can be seen in Fig. 8a which shows the raw transient absorption of chloroform excited at 600 nm. The nominal delay of 0 fs is arbitrarily set at 400 nm. The temporal overlap of a certain component of the continuum with the pump pulse results in a coherent artifact (see Sect. 4.1). Its position is marked with filled circles in Fig. 8a and reveals that there is a ~ 1.5 ps temporal dispersion between 300 and 750 nm, in good agreement with the calculated group velocity dispersion due to the optical components in the probe beam. To obtain the transient spectrum at a chosen delay time the raw data have to be corrected for the chirp. In a single-channel detection scheme this can be done online

during the measurement by adjusting the delay of the pump synchronously with the wavelength [72, 77]. For multichannel data acquisition the correction is best carried out after the measurement.

The proper chirp correction requires an accurate determination of the time zero. In degenerate pump-probe experiments, i.e. when the probe is a temporally shifted replica of the pump, one can use spectral interference on the detector to determine the time zero with an accuracy of 1 fs [38]. For nondegenerate broadband probing, the most commonly used methods are based on the coherent artifact [35, 36, 77, 78], even though the evaluation of the oscillatory signals arising from stimulated impulsive Raman scattering [79] has also been proposed [80]. The latter method has two requirements: The phase of the oscillation has to be known and the instrument response function has to be shorter than the vibrational period of the Raman active modes of the solvent molecules. It is therefore most useful for experiments with a time resolution better than ~ 50 fs. With time resolutions between 50 and ~ 100 fs impulsive Raman signals can still be observed for solvents like chloroform or dichloromethane which have low frequency vibrational modes. This case is shown in Fig. 8a where the oscillatory signals of chloroform are seen as stripes above the coherent artifact. The Fourier spectrum reveals three major contributions at 259, 367 and 662 cm^{-1} which closely match the known Raman active modes of chloroform.

When using other common solvents such as ethanol, acetonitrile or DMSO, the Raman active oscillations are more difficult to resolve and the determination of the time zero point is most easily done using the coherent artifact. Therefore, in most cases our chirp correction procedure relies on this method. To sufficient accuracy, the coherent artifact in a thin sample cuvette can be modeled by a Gaussian and/or its first and second time derivative [80]. About 20 time zero points are determined by fitting these functions to the raw data at selected wavelengths. We then fit a low order polynomial to these points to interpolate the time zero for the whole data set. This fit typically introduces an error δt of less then ± 5 fs into the chirp correction as shown in Fig. 8b. As discussed in Sect. 4.1, this is well below the time resolution of our setup. With the help of the chirp correction function the true transient spectra can be reconstructed by linear interpolation of the raw data along the time axis. Only after this chirp correction the molecular dynamics signatures are accessible to proper modeling in global fitting and target analysis [81].

Fig. 8 (**a**) Absorption changes of the white light continuum in pure chloroform ($\lambda_{exc} = 600$ nm, $\tau_{exc} = 25$ fs). *Orange curve*: polynomial fit to the center of the coherent artifact (*filled circles*). *Inset*: Fourier transform spectrum of the kinetic trace at 340 nm not including the coherent artifact. (**b**) Residuum of the polynomial fit to the time zero positions
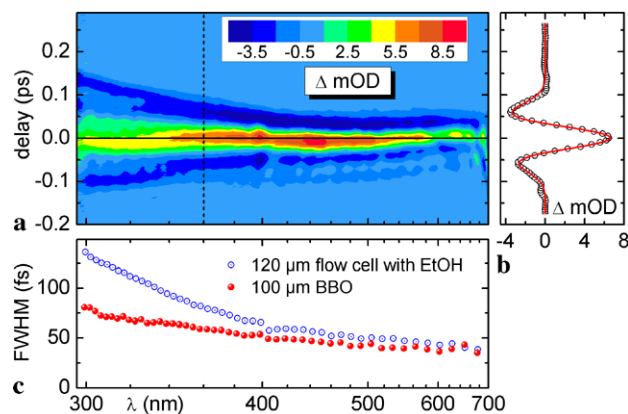
4 Performance of the setup

So far we have presented the concept and implementation of our transient spectrometer and discussed the tuning range

for the molecular excitation as well the observation range for the probe light. Now we want to present the achieved performance parameters that are most relevant to the use in molecular and chemical dynamics. As with any other kind of spectroscopy the prime concerns are the spectral and temporal resolution and the sensitivity of the detection.

4.1 Time resolution

A first estimate of the temporal resolution in a broadband experiment can be obtained from the width of the frequently observed coherent artifact [82]. By fitting a Gaussian and possibly its derivatives to the transients this can be done quantitatively. The FWHM of the Gaussian is taken as the time resolution and assumed to be very similar to the result of a crosscorrelation measurement performed in a thin nonlinear crystal. A measurement of the coherent artifact in the pure solvent is routinely obtainable with our setup for the whole spectral range of the white light (see Fig. 9a for ethanol). The single profile at 360 nm shown in Fig. 9b demonstrates the importance of the derivatives. Due to the varying group velocity mismatch [83] between the pump and the spectral components of the probe the width of the artifact varies with the probe wavelength, e.g., from 40 to 130 fs when a 120 μm flow cell is used (see Fig. 9c).

In general, it is complicated to accurately resolve an ultrafast process whose signature coincides with the coherent artifact. It is therefore very helpful to minimize the amplitude and the temporal width of the artifact. Experiments and theoretical considerations have shown that both the cuvette windows and the sample solution contribute to the artifact. For commercial cuvettes the group velocity mismatch can elongate the artifact up to some hundred femtoseconds [84]. Then, in most cases the modeling with standard functions like Gaussians is not possible any more [85, 86]. This makes

the separation of the artifact and the very fastest molecular signatures very challenging and renders the resolution of few femtoseconds dynamics almost impossible for spectral regions far from the pump wavelength. For this very reason our flow cell is designed such that not only the thickness of the sample is kept as low as possible but also the windows are very thin (see Sect. 2.5). The artifact then only extends to several ten femtoseconds before and after time zero and ultrafast processes down to well below the 100 fs level can be observed.

It is interesting to note that the effective time resolution lies below the width of the artifact measured in the presence of windows. A good estimate is obtained by measuring the artifact in a crystal or glass plate whose thickness is comparable to the thickness of the sample solution alone. As shown in Fig. 9c the FWHM of the artifact measured in a 100 μm BBO lies below 80 fs for the whole spectral range. A striking evidence of this discrepancy is the Fourier transform spectrum of the chloroform transients in Fig. 8 where the 669 cm^{-1} mode is clearly resolved even in regions where the coherent artifact is much longer than the vibrational period of 50 fs. We can therefore estimate the actual time resolution that can routinely be achieved with our setup to be below 50 fs.

4.2 Sensitivity, signal-to-noise ratio and quantitative measurement

To establish the sensitivity of the broadband spectrometer under realistic conditions and to determine the minimal detectable absorption change, we analyzed the noise of typical pump-probe traces like the ones shown in Figs. 8, 9, 12 and 13. For a purely statistical noise distribution the signal-to-noise ratio should increase with the square root of the averaging time. As mentioned in Sect. 2.7, we want to keep the total measurement time below 3 hours. With a laser repetition rate of 1 kHz, this corresponds to a maximum of 5.4×10^6 recordable pairs of probe pulses with and without excitation of the sample. Using the quasi-exponential timescale described in Sect. 2.1, 400 sampled points are typically enough to cover the range up to 1 ns. With a duty cycle of the data acquisition of ∼80% this allows for a maximum of ∼10^4 averages per measured spectrum, usually split into several faster scans to account for any drift of the laser power and to allow for consistency checks. Under these conditions a statistical analysis of the signal before time zero returns a standard deviation, i.e. a detection sensitivity of the instrument of 1×10^{-4} OD over the whole spectral range. With 10 scans and 2000 averages for each we can even reach an average sensitivity of 4.6×10^{-5} OD, some spectral regions being even a factor of 4 better as shown in Fig. 10.

These values hold for both detection systems used in our lab, the PDA based and the CCD camera. This indicates that the dominant contribution to the noise observed in

Fig. 9 Time resolution as a function of wavelength: (**a**) coherent artifact obtained from a flow cell filled with ethanol ($\lambda_{\text{exc}} = 510$ nm, $\tau_{\text{exc}} = 28$ fs); (**b**) kinetic trace at 360 nm (*circles*) and Gaussian fit (*solid line*); (**c**) FWHM of the coherent artifact of (**a**) (*open circles*) and of a 100 μm BBO crystal (*filled circles*)

our pump-probe spectrometer is the laser excess noise and nonstatistical fluctuations, whereas shot noise and electronic noise play only a minor role. In contrast to the standard approach, our setup presently does not include the detection of a reference beam, even though this might push the sensitivity to the 10^{-6} OD level [46]. However, in this regime it would be likely that stimulated impulsive Raman signals are observed even in solvents with low intensity Raman bands. These oscillatory signals can mask the sought-after dynamics of the solute. Thus, at least for studies in liquid phase, a sensitivity of several ten μOD seems to be a practical limit and this is already reached in our comparatively simple setup.

The signal after time zero suffers from two sources of noise: the fundamental noise of the setup determined above and in addition the noise of the pump pulse. The latter does not contribute to the noise of the data in linear fashion, but has to be weighted with the induced transmission change ((9) in Ref. [46]). With maximum absorption changes of a few percent, this results in a contribution of the pump noise that is somewhat smaller than the fundamental noise. Thus, the noise in the data, both before and after time zero, is mainly determined by the uncorrelated fluctuations in the white light continuum. This renders a correction for the fluctuations of the pump light unnecessary. With the high signal-to-noise ratio of presently more than 500:1 we can observe for instance a pure exponential decay over the whole spectral range for over six decay time constants.

The high sensitivity together with the smooth profiles of the pump and probe pulses (see Sect. 2.4) allows us to report quantitative values for the time dependent absorption changes. In many spectroscopic reports only data scaled in arbitrary units are given. This neglects the important information that is contained in the strength of the transient absorptions, e.g., the concentration of the intermediates or their extinction coefficient. The latter is a most powerful tool for the identification of the intermediates.
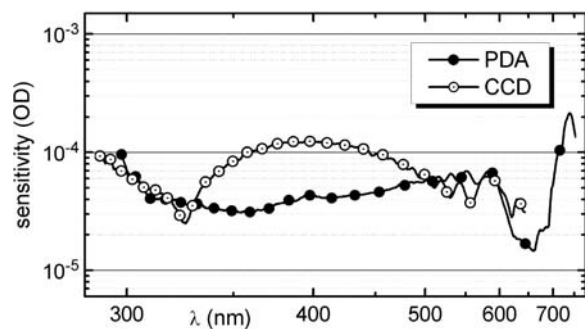
4.3 Spectral resolution

To determine the spectral resolution of our home-built prism polychromator we measured the line widths of a mercury-neon calibration lamp (Pen-Ray; L.O.T.-Oriel GmbH (see footnote 1)). The obtained line spectrum is shown in Fig. 11a. To ensure that the optical imaging matches that of the white light continuum we placed the lamp in front of a 50 μm pinhole. The latter was positioned at the focus of the continuum in the sample. Since the intensity of the cw-calibration lamp is much lower than that of the white light, we had to increase the integration time of the camera by a factor of 50. Therefore we replaced the kHz trigger from the laser with a 20 Hz TTL signal. After some averaging we obtained sharp lines over the whole spectral region. These lines can be associated to mercury transitions whereas the neon lines only show up shortly after the lamp is turned on and the temperature is still low. In principle the characteristic atomic lines could also be used for the wavelength calibration of the polychromator. However, the implementation in an everyday routine is somewhat more complicated and prone to errors than the use of the calibration filters described in Sect. 3.1.

The mercury lines can be fitted with Gaussian functions whose widths are plotted in Fig. 11b. At some wavelengths like 365 nm the spectrum consists of closely lying transitions. Their separation is close to the resolution of our setup and fitting them with a single Gaussian results in a FWHM value that is much larger than that of neighboring single lines. We therefore use as many Gaussians as the number of known transitions and fix the maxima according to the values given in the datasheet. The resulting FWHM values lie between 50 cm^{-1} in the UV and 100 cm^{-1} in the visible. This corresponds to a wavelength resolution as low as 0.5 nm. This is more than sufficient for UV/Vis spectroscopy


Fig. 10 Typical detection sensitivities determined from the baseline of 10 accumulated scans with 2×10^3 averages per point each. *Filled circles*: PDA based camera; *open circles*: CCD camera. The average sensitivities are 4.6×10^{-5} for the PDA and 7.6×10^{-5} OD for the CCD
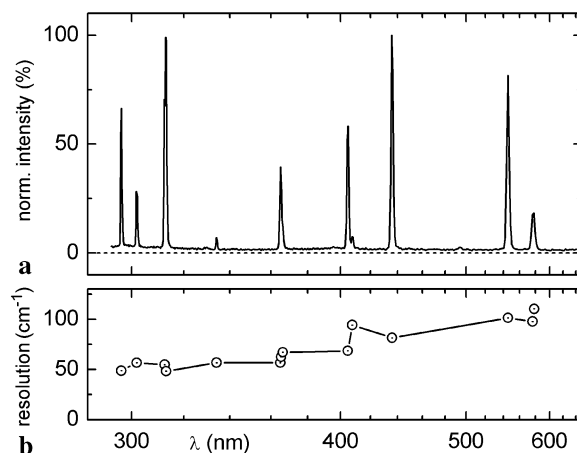
Fig. 11 (**a**) Line spectrum of a mercury-neon lamp after the prism-based polychromator measured with the CCD camera. (**b**) Determined line widths (FWHM) from Gaussian fits to the atomic transitions. For closely lying transitions the centers of the Gaussian fits were fixed to the established values

in solution were typical bands have widths on the order of 2000 cm^{-1}.

5 Representative data and modeling of the experimental recordings

5.1 Transient spectroscopy of naphthalene bisimide upon visible excitation

To illustrate the use of the new broadband pump-probe spectrometer for molecular dynamics we show data on a core-substituted naphthalene bisimide (NBI) after visible excitation in Fig. 12. The transient spectra were recorded with the PDA-based camera at 370 delay line positions between −15 and 300 ps and are an average of three scans. Each spectrum in these scans is computed from 2500 pairs of white light pulses with and without excitation. The optical density of the sample solution at the excitation wavelength was set to ∼0.2 at a thickness of 120 μm. This corresponds to a concentration of 0.8 mmol/l. The energy of the pump light centered at 620 nm was limited to 80 nJ and focused to a
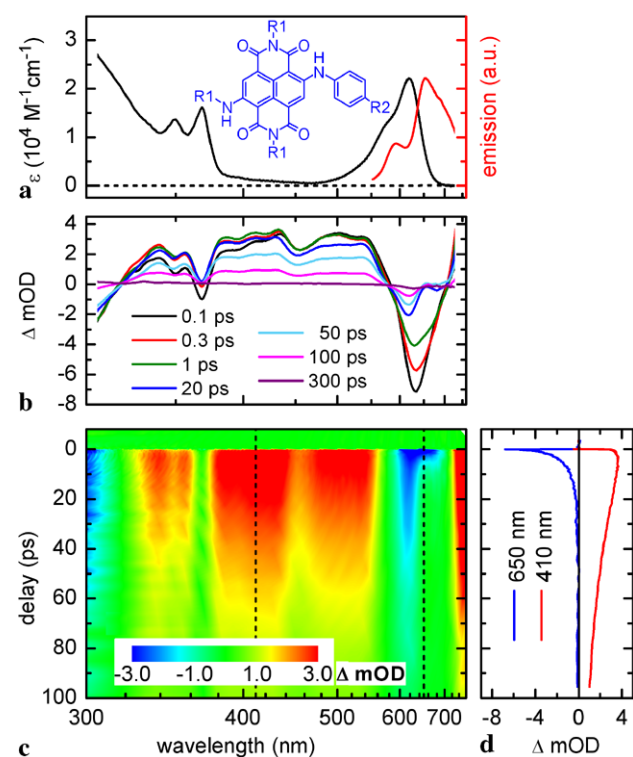
Fig. 12 (**a**) Steady state absorption (*black*) and emission (*red*) of a core-substituted NBI dissolved in chloroform: R1=C$_8$H$_{17}$, R2=C$_4$H$_9$. (**b**) Transient spectra at selected delay times detected with the PDA-based camera after excitation with 20 fs pulses centered at 620 nm. The spectra represent horizontal slices out of the 2D data shown in (**c**). Two kinetic traces in the excited state absorption band at 410 nm and the stimulated emission band at 650 nm (*dashed lines*) are shown in (**d**)

diameter of 150 μm. The stray light of the pump amounted to about 30% of the full molecular signal and was subtracted from the transient data using its signature at negative delay times.

Under these conditions, less than 10% of the molecules inside the pump volume are excited resulting in absorption changes between −7 and +3 mOD. Although these changes are quite small, the high sensitivity of the setup still allows for a very good signal-to-noise ratio of, e.g., 75:1 at 400 nm.

Due to the ultrabroad range of the CaF$_2$ white light we not only observe the ground state bleach of the first excited state around 620 nm, but also the signature of the second electronic transition at 368 nm and the onset of higher transitions below 320 nm. In these spectral regions the ground state bleach does not overlap with the stimulated emission and is not distorted by stray light from the pump. By comparison to the excited state absorption (ESA) signal in spectral regions without ground state absorption, an unambiguous determination of the dynamics of the ground state recovery is therefore possible. This is especially helpful in two important situations. If an optically dark photoproduct is irreversibly generated, a residual bleach signal can allow for an accurate calculation of its quantum yield. A differing decay of the ground state bleach and the ESA indicates long lived intermediates.

The inspection of the data in Fig. 12 reveals that the kinetics indeed differs significantly for well separated spectral regions. Between 380 and 550 nm the signal is dominated by a fairly structureless ESA. As seen in the red curve of Fig. 12d, the major contribution to the ESA signal appears instantaneously with the optical excitation and rises only slightly to its maximum within a few picoseconds. The most prominent dynamics is given by a large amplitude decay on the time scale of tens of picoseconds. In contrast, the decay in the region of the stimulated emission around 650 nm occurs predominantly on the few picosecond time scale. This finding explains the unusual steady state fluorescence spectrum shown in Fig. 12a which features a contribution from higher vibrational levels of the S$_1$ state at 590 nm: The electronic excitation decays before the vibrational cooling is completed and therefore resonance emission is comparable to the vibrationally relaxed one. Situations of this kind clearly show the importance of multichannel detection for the gain of a complete picture of the excited state dynamics of the molecular system under investigation.

5.2 Ultrafast photochemistry of diphenylmethyl chloride upon UV excitation

In a second showcase example we performed measurements on diphenylmethyl chloride (DPMC) in acetonitrile solution. These data were recorded with the CCD camera in three scans between −100 and +1900 ps each with 2000
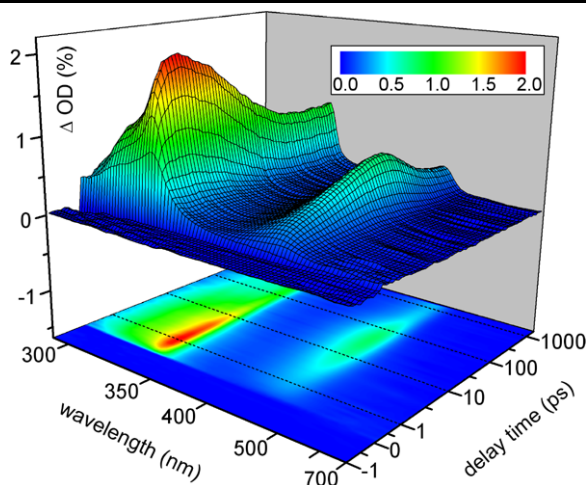
Fig. 13 Transient absorption spectra of diphenylmethyl chloride in acetonitrile after 270 nm excitation detected with the CCD camera. The delay time axis is linear between -1 and $+1$ ps and logarithmic between 1 and 1900 ps. The coherent artifact around time zero has been omitted from the graph. The absorption band at 330 nm is assigned to the radical pair and the one at 435 nm to the formation of an ion pair

averages per spectrum. The pump wavelength was tuned to the first absorption band at 270 nm. Since this transition is much weaker than the one pumped in NBI—the extinction coefficient at 270 nm is only $400 \, \mathrm{l \, mol^{-1} \, cm^{-1}}$—the pump photon density has to be increased. We therefore focused 140 nJ of the UV light down to a beam diameter of 80 μm in the sample leading to an excitation probability of roughly 0.5%. The concentration $c_{\mathrm{DPMC}} = 40$ mmol/l also had to be chosen much higher to reach an optical density of 0.2 in the 120 μm flow cell.

The transient spectra are depicted in Fig. 13 as a pseudo-3D plot which shows two induced absorption bands with maxima at 330 and 435 nm, well outside the absorption spectrum of DPMC. They correspond to the diphenylmethyl radical and the benzhydrilium cation that are formed by the photo-induced dissociation of DPMC. The rise of the bands in the first few hundred femtoseconds monitors the cleavage of the C–Cl bond, the first step of the photochemical reaction. The native ratio of ion pair to radical pair is subsequently increased by an intermolecular electron transfer from the diphenylmethyl radical to the chlorine radical. This is seen in the concerted decay (radical) and rise (cation) of the two bands on the time scale of 20 ps. At larger delay times above 100 ps, the decay of the cation band reflects the geminate recombination with the chloride anion. A more detailed analysis of the dynamics will be given in a future publication.

This example shows again the importance of a spectrally broad probe window as this allows one to fully resolve the signatures of all relevant photoproducts. Since the reaction dynamics has contributions from the femtosecond to the nanosecond regime, the implementation of the non-linear

sampling time scale is a key point for a direct understanding of the underlying processes. In addition, the multichannel detection in combination with the high spectral resolution enables us to observe and quantitatively treat shifts and spectral narrowing of bands that occur, e.g., due to solvation or vibrational cooling. A thorough analysis of the cation band indeed reveals such a shift by about 5 nm. Since transient absorption spectroscopy is a method that provides absolute values, knowing the relevant experimental parameters allows for a precise quantitative analysis and in this case is capable of supplying absolute quantum yields of the ultrafast photodissociation.

5.3 Post-processing of multichannel data: analysis of the ultrafast molecular dynamics

The availability of a 2D data set from the multichannel detection permits and requires a different post-processing than in the case of single-channel spectra or kinetic curves. The analysis we perform does not just aim at the full parameterization of the data obtained but rather follows a spectroscopy oriented approach. That means we use the available knowledge, e.g., from own steady state measurements or the literature to stepwise gain full insight into the mechanisms of the ultrafast processes on the molecular level.

To achieve this goal, at first we study the dynamics at distinguished positions throughout the whole spectrum like the maxima of the radical and ion bands in Fig. 13, but also in between for the determination of the ESA contribution. We have therefore developed a LabView routine that allows us to perform fits of kinetic traces which we obtain by averaging the data from a freely selectable number of neighboring pixels. Thus, step by step we can gather first hints of the relevant time scales for the different processes we observe. The fit function $F(t)$ we employ can thereby change according to the model we assume. In case of a simple rate model it can be written as:

$$F(t) = \mathrm{IRF} \otimes \left\{ \theta(t) \cdot \left[\sum_i A_i \exp\left(\frac{-t}{\tau_i} \right) + \mathrm{const} \right] \right\}$$

$$+ \text{artifact.} \qquad (6)$$

It consists of the instrumental response function IRF convoluted with the product of the step function θ and a sum of exponentials. If necessary, the fit function in our program can be augmented with damped oscillations or stretched exponentials [87].

Our LabView code also includes the calculation of the correlation matrix of all possible pairs of fit parameters. If one of the off-diagonal elements in this matrix approaches ± 1, the correlation of the two parameters is very high leading to compensation effects. This is an indication that more free parameters are used than are supported by the data. We

therefore use the correlation matrix to avoid too many exponential functions to characterize the observed dynamics. This approach is comparable to other proposed methods like singular value decomposition [39, 88], however less affected by noise in the data.

The fits of kinetic traces at single spectral positions often result in a systematic variation of the locally determined time constants. This can have technical reasons like varying contributions of the noise in the data, but it can more importantly be a consequence of an incomplete model. For example, the overwhelmingly used rate models do not include solvation, internal vibrational redistribution or vibrational cooling. These processes lead to spectral shifts as well as narrowing and broadening of bands. If these contributions are small compared to the absorption changes due to the population dynamics, a global fit can be used to find a unique set of decay time constants for the whole system. Our global analysis is based on the formalism developed by Fita et al. [89] which extracts decay associated difference spectra [90] from the transient data. The consistency of the obtained results can be checked with the help of qualitative data visualization methods like the logarithmic differentiation of the absorption changes [88].

If however the spectral shifts become dominant, then the evaluation of band integrals helps to disentangle electronic dynamics from solvation and vibrational relaxation. This method is best suited for isolated bands in the transient absorption spectra like the cation and the radical band in Fig. 13. Then, the integral $\int d\lambda \frac{OD}{\lambda}$ is proportional to the transition dipole moment squared [91, 92] and to the population of the absorbing electronic state. Therefore, the temporal evolution of the integral allows one to directly evaluate the population transfer between electronic states or chemical species. In some cases, the spectral shift itself is the quantity of interest, as it can for instance yield information on solvation dynamics [63, 93, 94]. Then, a spectral decomposition into the different contributing signals such as excited state absorption and stimulated emission can be used to quantify the shift of the individual bands [73].

These examples demonstrate that the multichannel data in the broad detection range between 290 and 720 nm lend themselves to a wealth of post-processing strategies that put the interpretation and modeling on solid ground. The quality of the final picture is closely related to the understanding and correct implementation of the technical and spectroscopic concepts presented in this paper. Almost all of these issues have been previously assessed by other groups. However, only the appropriate combination of all of them renders the described state-of-the-art spectrometer.

Changes in different directions are always possible, e.g., shifting the probe supercontinuum further towards the mid IR [45], using more advanced compression techniques to obtain even shorter excitation pulses [47] or replacing the

flow cell with a liquid jet [95]. The exact implementation depends on the particular requirements of the investigated sample. By combining tunable excitation with highly sensitive broadband detection and a simple but thoroughly conceived optical design the spectrometer as presented here allows for the investigation of a large variety of spectroscopic problems whilst keeping the technical flexibility necessary to address even more challenging systems.

References

1. A.H. Zewail, J. Phys. Chem. A **104**, 5660 (2000)
2. R. Danielius, A. Piskarskas, A. Stabinis, G.P. Banfi, P. Di Trapani, R. Righini, J. Opt. Soc. Am. B **10**, 2222 (1993)
3. P. Hamm, C. Lauterwasser, W. Zinth, Opt. Lett. **18**, 1943 (1993)
4. F. Seifert, V. Petrov, M. Woerner, Opt. Lett. **19**, 2009 (1994)
5. V. Petrov, F. Rotermund, F. Noack, J. Opt. A **3**, R1 (2001)
6. T. Wilhelm, J. Piel, E. Riedle, Opt. Lett. **22**, 1494 (1997)
7. E. Riedle, M. Beutter, S. Lochbrunner, J. Piel, S. Schenkl, S. Spörlein, W. Zinth, Appl. Phys. B **71**, 457 (2000)
8. J. Piel, M. Beutter, E. Riedle, Opt. Lett. **25**, 180 (2000)
9. G. Cerullo, S. De Silvestri, Rev. Sci. Instrum. **74**, 1 (2003)
10. A.J. Wurzer, T. Wilhelm, J. Piel, E. Riedle, Chem. Phys. Lett. **299**, 296 (1999)
11. K. Stock, T. Bizjak, S. Lochbrunner, Chem. Phys. Lett. **354**, 409 (2002)
12. V. de Waele, M. Beutter, U. Schmidhammer, E. Riedle, J. Daub, Chem. Phys. Lett. **390**, 328 (2004)
13. A. Baltuska, T. Kobayashi, Appl. Phys. B **75**, 427 (2002)
14. M. Zavelani-Rossi, D. Polli, G. Cerullo, S. de Silvestri, L. Gallmann, G. Steinmeyer, U. Keller, Appl. Phys. B **74**, S245 (2002)
15. P. Baum, S. Lochbrunner, E. Riedle, Opt. Lett. **29**, 1686 (2004)
16. G. Cerullo, C. Manzoni, L. Lüer, D. Polli, Photochem. Photobiol. Sci. **6**, 135 (2007)
17. D. Polli, M.R. Antognazza, D. Brida, G. Lanzani, G. Cerullo, S. De Silvestri, Chem. Phys. **350**, 45 (2008)
18. R.R. Alfano, *The Supercontinuum Laser Source* (Springer, Berlin, 2005)
19. A. Lochschmidt, N. Eilers-Knig, N. Heineking, N.P. Ernsting, J. Phys. Chem. A **103**, 1776 (1999)
20. A. Sugita, T. Furuhi, M. Yamashita, T. Kobayashi, J. Phys. Chem. A **106**, 581 (2002)
21. G. Duvanel, N. Banerji, E. Vauthey, J. Phys. Chem. A **111**, 5361 (2007)
22. D.B. Spry, A. Goun, M.D. Fayer, J. Phys. Chem. A **111**, 230 (2007)
23. V. Nagarajan, E. Johnson, P. Schellenberg, W. Parson, R. Windeler, Rev. Sci. Instrum. **73**, 4145 (2002)

24. R. Huber, T. Köhler, M.O. Lenz, E. Bamberg, R. Kalmbach, M. Engelhard, J. Wachtveitl, Biochemistry **44**, 1800 (2005)
25. A.N. Tarnovsky, W. Gawelda, M. Johnson, C. Bressler, M. Chergui, J. Phys. Chem. B **110**, 26497 (2006)
26. A.V. Zamyatin, A.V. Soldatova, M.A.J. Rodgers, Inorg. Chim. Acta **360**, 857 (2007)
27. J.L. Pérez Lustres, A.L. Dobryakov, A. Holzwarth, M. Veiga, Angew. Chem. Int. Ed. **46**, 3758 (2007)
28. T.A. Zeidan, Q. Wang, T. Fiebig, F.D. Lewis, J. Am. Chem. Soc. **129**, 9848 (2007)
29. V. Karunakaran, K. Kleinermanns, R. Improta, S.A. Kovalenko, J. Am. Chem. Soc. **131**, 5839 (2009)
30. C. Ley, J. Brazard, F. Lacombat, P. Plaza, M.M. Martin, G.A. Kraus, J.W. Petrich, Chem. Phys. Lett. **457**, 82 (2008)
31. P.Z. El-Khoury, A.N. Tarnovsky, Chem. Phys. Lett. **453**, 160 (2008)
32. M. Seel, E. Wildermuth, W. Zinth, Meas. Sci. Technol. **8**, 449 (1997)
33. T. Hirsch, H. Port, H.C. Wolf, B. Miehlich, F. Effenberger, J. Phys. Chem. B **101**, 4525 (1997)
34. R. Croce, M.G. Müller, R. Bassi, A.R. Holzwarth, Biophys. J. **80**, 901 (2001)
35. A. Maciejewski, R. Naskrecki, M. Lorenc, M. Ziolek, J. Karolczak, J. Kubicki, M. Matysiak, M. Szymanski, J. Mol. Struct. **555**, 1 (2000)
36. M. Raytchev, E. Pandurski, I. Buchvarov, C. Modrakowski, T. Fiebig, J. Phys. Chem. A **107**, 4592 (2003)
37. S. Laimgruber, H. Schachenmayr, B. Schmidt, W. Zinth, P. Gilch, Appl. Phys. B **85**, 557 (2006)
38. D. Polli, L. Lüer, G. Cerullo, Rev. Sci. Instrum. **78**, 103108 (2007)
39. N.P. Ernsting, S.A. Kovalenko, T. Senyushkina, J. Saam, V. Farztdinov, J. Phys. Chem. A **105**, 3443 (2001)
40. L. Boilet, G. Buntinx, C. Lefumeux, O. Poizat, J. Photochem. Photobiol. A **163**, 529 (2004)
41. A.C. Moskun, S.E. Bradforth, J. Thøgersen, S. Keiding, J. Phys. Chem. A **110**, 10947 (2006)
42. H.C. Wang, Y.C. Lu, C.Y. Chen, C.C. Yang, Opt. Express **15**, 3417 (2007)
43. M.K. Reed, M.K. Steiner-Shepard, M.S. Armas, D.K. Negus, J. Opt. Soc. Am. B **12**, 2229 (1995)
44. J.B. Ashcom, R.R. Gattass, C.B. Schaffer, E. Mazur, J. Opt. Soc. Am. B **23**, 2317 (2006)
45. M. Bradler, P. Baum, E. Riedle, Appl. Phys. B (2009, submitted)
46. C. Schriever, S. Lochbrunner, E. Riedle, D.J. Nesbitt, Rev. Sci. Instrum. **79**, 13107 (2008)
47. P. Baum, S. Lochbrunner, E. Riedle, Appl. Phys. B **79**, 1027 (2004)
48. P. Baum, M. Breuer, E. Riedle, Opt. Lett. **31**, 2220 (2006)
49. I.Z. Kozma, P. Baum, S. Lochbrunner, E. Riedle, G. Steinmeyer, Opt. Express **11**, 3110 (2003)
50. I.Z. Kozma, P. Baum, U. Schmidhammer, S. Lochbrunner, E. Riedle, Rev. Sci. Instrum. **75**, 2323 (2004)
51. T. Bizjak, J. Karpiuk, S. Lochbrunner, E. Riedle, J. Phys. Chem. A **108**, 10763 (2004)
52. B. Schmidt, C. Sobotta, S. Malkmus, S. Laimgruber, M. Braun, W. Zinth, P. Gilch, J. Phys. Chem. A **108**, 4399 (2004)
53. J. Savolainen, D. van der Linden, N. Dijkhuizen, J.L. Herek, J. Photochem. Photobiol. A **196**, 99 (2008)
54. J.M. Klopf, P. Norris, Appl. Surf. Sci. **253**, 6305 (2007)
55. G. Buntinx, R. Naskrecki, O. Poizat, J. Phys. Chem. **100**, 19380 (1996)
56. R. Huber, H. Satzger, W. Zinth, J. Wachtveitl, Opt. Commun. **194**, 443 (2001)
57. P. Tzankov, I. Buchvarov, T. Fiebig, Opt. Commun. **203**, 107 (2002)
58. C. Nagura, A. Suda, H. Kawano, M. Obara, K. Midorikawa, Appl. Opt. **41**, 3735 (2002)
59. J.M. Dudley, G. Genty, S. Coen, Rev. Mod. Phys. **78**, 1135 (2006)
60. P.B. Corkum, C. Rolland, T. Srinivasan-Rao, Phys. Rev. Lett. **57**, 2268 (1986)
61. S.A. Trushin, S. Panja, K. Kosma, W.E. Schmid, W. Fuß, Appl. Phys. B **80**, 399 (2005)
62. E. Goulielmakis, S. Koehler, B. Reiter, M. Schultze, A.J. Verhoef, E.E. Serebryannikov, A.M. Zheltikov, F. Krausz, Opt. Lett. **33**, 1407 (2008)
63. V. Karunakaran, M. Pfaffe, I. Ioffe, T. Senyushkina, S.A. Kovalenko, R. Mahrwald, V. Fartzdinov, H. Sklenar, N.P. Ernsting, J. Phys. Chem. A **112**, 4294 (2008)
64. I. Buchvarov, A. Trifonov, T. Fiebig, Opt. Lett. **32**, 1539 (2007)
65. V. Kartazaev, R.R. Alfano, Opt. Commun. **281**, 463 (2008)
66. R.S.S. Kumar, K.L.N. Deepak, D.N. Rao, Phys. Rev. A **78**, 43818 (2008)
67. A. Brodeur, S.L. Chin, J. Opt. Soc. Am. B **16**, 637 (1999)
68. V.P. Kandidov, O.G. Kosareva, I.S. Golubtsov, W. Liu, A. Becker, N. Akozbek, C.M. Bowden, S.L. Chin, Appl. Phys. B **77**, 149 (2003)
69. V.M. Farztdinov, A.L. Dobryakov, V.S. Letokhov, Y.E. Lozovik, Y.A. Matveets, S.A. Kovalenko, N.P. Ernsting, Phys. Rev. B **56**, 4176 (1997)
70. M. Kandyla, T. Shih, E. Mazur, Phys. Rev. B **75**, 214107 (2007)
71. H. Marciniak, M. Fiebig, M. Huth, S. Schiefer, B. Nickel, F. Selmaier, S. Lochbrunner, Phys. Rev. Lett. **99**, 176402 (2007)
72. U. Schmidhammer, U. Megerle, S. Lochbrunner, E. Riedle, J. Karpiuk, J. Phys. Chem. A **112**, 8487 (2008)
73. U. Megerle, F. Selmaier, C. Lambert, E. Riedle, S. Lochbrunner, Phys. Chem. Chem. Phys. **10**, 6245 (2008)
74. M. Barbatti, A.J.A. Aquino, H. Lischka, C. Schriever, S. Lochbrunner, E. Riedle, Phys. Chem. Chem. Phys. **11**, 1406 (2009)
75. W. Zinth, U. Zinth, *Optik* (Oldenbourg, München, 2009)
76. E.A. Juban, J.K. McCusker, J. Am. Chem. Soc. **127**, 6857 (2005)
77. V.I. Klimov, D.W. McBranch, Opt. Lett. **23**, 277 (1998)
78. S.A. Kovalenko, N.P. Ernsting, J. Ruthmann, Chem. Phys. Lett. **258**, 445 (1996)
79. S. Ruhman, A.G. Joly, K.A. Nelson, J. Chem. Phys. **86**, 6563 (1987)
80. S.A. Kovalenko, A.L. Dobryakov, J. Ruthmann, N.P. Ernsting, Phys. Rev. A **59**, 2369 (1999)
81. W. Wohlleben, T. Buckup, J.L. Herek, R.J. Cogdell, M. Motzkus, Biophys. J. **85**, 442 (2003)
82. M. Rasmusson, A.N. Tarnovsky, E. Akesson, V. Sundström, Chem. Phys. Lett. **335**, 201 (2001)
83. I.Z. Kozma, P. Krok, E. Riedle, J. Opt. Soc. Am. B **22**, 1479 (2005)
84. M. Ziolek, M. Lorenc, R. Naskrecki, Appl. Phys. B **72**, 843 (2001)
85. K. Ekvall, P. van der Meulen, C. Dhollande, L.-E. Berg, S. Pommeret, R. Naskrecki, J.-C. Mialocq, J. Appl. Phys. **87**, 2340 (2000)
86. M. Lorenc, M. Ziolek, R. Naskrecki, J. Karolczak, J. Kubicki, A. Maciejewski, Appl. Phys. B **74**, 19 (2002)
87. G. Williams, D.C. Watts, Trans. Farad. Soc. **66**, 80 (1970)
88. H. Satzger, W. Zinth, Chem. Phys. **295**, 287 (2003)
89. P. Fita, E. Luzina, T. Dziembowska, C. Radzewicz, A. Grabowska, J. Chem. Phys. **125**, 184508 (2006)
90. I.H.M. van Stokkum, D.S. Larsen, R. van Grondelle, Biochim. Biophys. Acta **1657**, 82 (2004)
91. S.J. Strickler, R.A. Berg, J. Chem. Phys. **37**, 814 (1962)
92. A.P. Thorne, *Spectrophysics* (Chapman and Hall, London, 1974)
93. M.L. Horng, J.A. Gardecki, A. Papazyan, M. Maroncelli, J. Phys. Chem. **99**, 17311 (1995)
94. J.L. Pérez Lustres, S.A. Kovalenko, M. Mosquera, T. Senyushkina, W. Flasche, N.P. Ernsting, Angew. Chem. Int. Ed. **44**, 5635 (2005)
95. M.J. Tauber, R.A. Mathies, X. Chen, S.E. Bradforth, Rev. Sci. Instrum. **74**, 4958 (2003)

Appendix D2

Encapsulation of Diphenylmethyl Phosphonium Salts in Reverse Micelles: Enhanced Bimolecular Reaction of the Photofragments

C. F. Sailer, R. B. Singh, J. Ammer, E. Riedle, I. Pugliesi

Encapsulation of diphenylmethyl phosphonium salts in reverse micelles: Enhanced bimolecular reaction of the photofragments

Christian F. Sailer [a], Rupashree Balia Singh [a], Johannes Ammer [b], Eberhard Riedle [a], Igor Pugliesi [a,*]

[a] *Lehrstuhl für BioMolekulare Optik, Ludwig-Maximilians-Universität München, Oettingenstr. 67, 80538 München, Germany*
[b] *Department Chemie, Ludwig-Maximilians-Universität, Butenandtstr. 5–13 (Haus F), 81377 München, Germany*

A R T I C L E   I N F O

A B S T R A C T

We investigate the effects of encapsulation on the dynamics after photoinduced bond cleavage of a diphenylmethyl phosphonium salt in acetonitrile reverse micellar nanopools by femtosecond UV/Vis transient absorption. The small volume of the nanopool is just large enough to accommodate one precursor molecule and therefore eliminates the effects of diffusion present in bulk solution. The tight environment keeps the fragments together and prolongs the time for geminate recombination to occur. We therefore observe an enhanced yield of this bimolecular reaction of the ground state photofragments.

© 2011 Elsevier B.V. All rights reserved.

1. Introduction

Chemistry in a confined environment differs in a number of ways from that in bulk solution [1,2]. The 100–1000 times slower solvation times of polar solvents [3–5] and the hindrance to large amplitude motions of molecules in confined environments have been found to have a dramatic effect on various chemical and biological reactions [1]. Elementary processes such as proton and electron transfer have been widely investigated under a variety of confinements such as micelles, reverse micelles, cyclodextrins, zeolites and even proteins [6–15]. Due to the ability of reverse micelles to form nanometer sized enclosed solvent pools, these systems can serve as 'nanoreactors', and are therefore of special interest to researchers as simple biomimetic models for catalytic reactions [11–13,16]. The size of the pools can be controlled at the nanometer level through the molar ratio between polar solvent and surfactant [12]. The surfactant AOT (Aerosol-OT, sodium bis (2-ethylhexyl)sulfosuccinate) is one of the most widely investigated RM systems for its thermal and mechanical stability and a preferential choice for the confinement of molecules that undergo photoinduced reactions [17]. The local polarity, viscosity and pH changes induced by these confined environments play a significant role in modifying the photoprocesses and influence the rates and directions of photochemical reactions [18].

Up to now not many successful reports of bimolecular reactions involving bond formation under confined solvent environments have been published. Benzhydryl derivatives are interesting candidates for such studies. For example, benzhydryl halides undergo homolysis and heterolysis upon UV irradiation [19–23]. The gener-

ated benzhydryl radicals and cations are highly reactive species which have strong and distinct absorption bands in the UV/Vis range [19].

In this work we have carried out a femtosecond UV/Vis transient absorption study on the photoinduced dynamics after bond cleavage of a diphenylmethyl phosphonium salt encapsulated in a reverse micelle. Unlike the transient study of 2-(2-hydroxyphenyl)benzothiazole (HBT) molecules encapsulated in zeolite where severe scattering in the UV prevented the observation of the dynamics below 350 nm [10], in reverse micelles detection of the complete probe window down to 290 nm is shown to be feasible. Our primary aim was to eliminate the effect of diffusion prevalent in bulk solvent by using acetonitrile nanopools as nanosize 'reaction flasks'. To investigate the effects of encapsulation, we compare the photoinduced dynamics of 4,4′-dimethylbenzhydryl triphenylphosphonium tetrafluoroborate ($BMe_2PPh_3^+BF_4^-$) dissolved in bulk acetonitrile (ACN) and in ACN/AOT/cyclopentane reverse micelles (RM). Due to its intrinsic positive charge, $BMe_2PPh_3^+$ undergoes heterolysis upon UV excitation to generate benzhydryl cations BMe_2^+ very efficiently [24]. The structure of the molecule is shown in Figure 1.

2. Experimental

We encapsulate $BMe_2PPh_3^+BF_4^-$ in a RM by preparing a concentrated stock solution of the molecule in ACN. A calculated volume of this concentrated stock solution is added to 0.2 M AOT in cyclopentane (see Supplementary material for preparation details and characterization). Our intention was to prepare RMs of a size just large enough to accommodate a single $BMe_2PPh_3^+BF_4^-$ molecule. It is known from studies on aqueous RMs that the solvent pool diameter can be controlled by the polar solvent-to-surfactant concentration ratio w = [polar solvent]/[surfactant] [12]. We determined

* Corresponding author. Fax: +49 89 2180 9202.
E-mail address: igor.pugliesi@physik.uni-muenchen.de (I. Pugliesi).
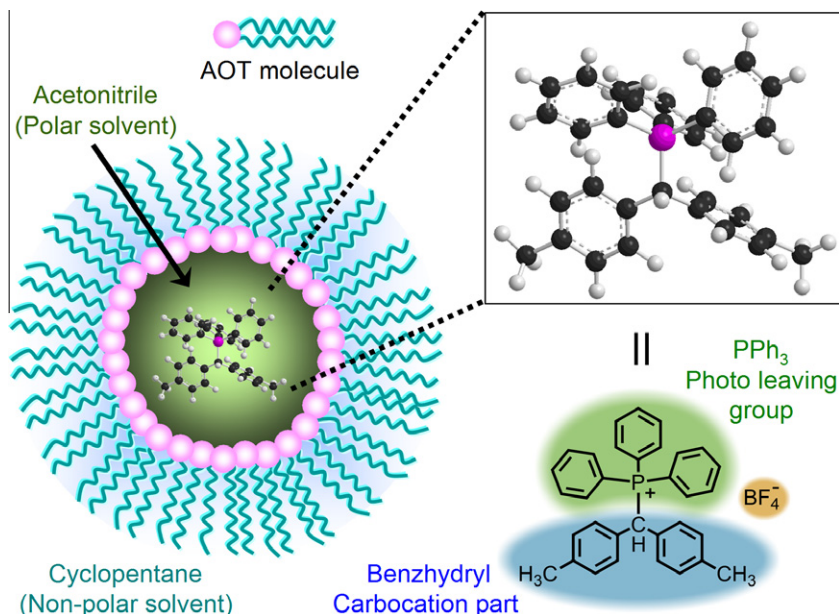
Figure 1. Structure of $BMe_2PPh_3^+$. The counterion BF_4^- is always assumed to be present in the vicinity though not shown in the 3D structure for simplicity. Upon UV irradiation the C–P bond is cleaved giving rise to the benzhydryl cation BMe_2^+ and the PPh_3 as the leaving group.

the diameters of the ACN/AOT/cyclopentane RMs loaded with $BMe_2PPh_3^+BF_4^-$ by dynamic light scattering. These measurements show that micelles with a solvent-to-AOT concentration ratio $w = 4$ have an external radius in the range of 16.8 ± 4 Å (see Supplementary Figure S1). The obtained values are very similar to those reported in Refs. [5,25]. Assuming a length of 8 Å for an AOT molecule [26] leads to an internal RM radius of ~8.8 Å. This is only slightly larger than the Onsager radius of 6.1 Å [27] for $BMe_2PPh_3^+$. Thus, in RMs with $w = 4$ there is not enough space for accommodating more than one benzhydryl molecule (Figure 1). Furthermore, RMs with $w < 4$ failed to keep the $BMe_2PPh_3^+BF_4^-$ encapsulated leading to a turbid suspension. The experimental observations and the size estimations conclusively show that the possibility of more than one $BMe_2PPh_3^+BF_4^-$ being encapsulated in a RM with $w = 4$ is negligible. Therefore the investigated RM consists of approximately 60 AOT molecules [26], 60 Na^+ ions, about 40 ACN molecules and a single $BMe_2PPh_3^+BF_4^-$. This tight confinement makes the RMs comparable to the spatial conditions present in reactive pockets of common enzymes.

Prior to performing the transient studies, the encapsulation of $BMe_2PPh_3^+BF_4^-$ in the ACN nanopools was verified by steady state absorption. We measured spectra of $BMe_2PPh_3^+BF_4^-$ in ACN, cyclopentane and the binary cyclopentane–ACN solvent mixture with the same concentration ratio as used for the generation of the RMs (see Figure 2). While in ACN the precursor molecule was found to be completely soluble, a negligible (~30 times smaller than in bulk ACN) optical density at 270 nm was found in cyclopentane as well as in the binary cyclopentane–ACN solvent mixture. This clearly indicates that the precursor molecules are almost insoluble in cyclopentane and the binary mixture. On the other hand, the precursor molecules were found to be completely soluble in the ACN/AOT/cyclopentane RMs. The comparable OD values in both bulk ACN and ACN RMs confirm dissolution of the ionic precursor molecules in the ACN nanopools inside the RMs (as depicted in Figure 1). The similarity in the absorption spectra of $BMe_2PPh_3^+BF_4^-$ in ACN and the RMs (see Figure 2) is a strong indication for the absence of specific interactions of the molecule with the interfacial surfactant layer. There appears to be neither aging of the sample nor leaking out of the molecules from the pools, as the
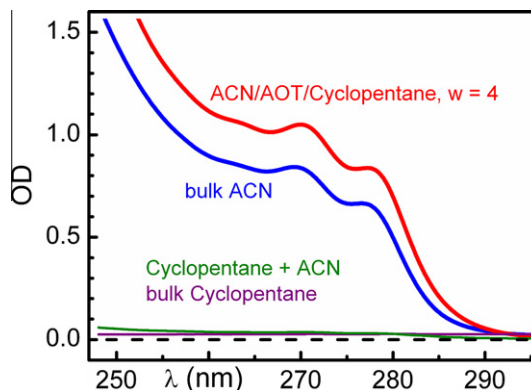
Figure 2. Steady state absorption spectra of $BMe_2PPh_3^+BF_4^-$ in (i) ACN/AOT/cyclopentane reverse micelles ($w = 4$), (ii) bulk ACN, (iii) cyclopentane–ACN solvent mixture and (iv) bulk cyclopentane. (For interpretation of the references in color in this figure legend, the reader is referred to the web version of this article.)

absorption profile remains unchanged even 72 h after sample preparation and after prolonged pumping through the flow cell.

For the femtosecond UV/Vis transient absorption experiments, the precursor molecules $BMe_2PPh_3^+BF_4^-$ in bulk ACN and in ACN/AOT/cyclopentane reverse micelles ($w = 4$) were excited at 270 nm with a pulse energy of 160 nJ. Under the experimental conditions (pump beam diameter 95 μm at the sample position, molar extinction coefficient of precursor 5250 L mol^{-1}cm^{-1}, OD = 0.13 at 270 nm), only $\sim4\%$ of the molecules were excited. A CaF_2 continuum spanning from below 290 to 750 nm and polarized at the magic angle with respect to the pump polarization was used as probe light. The temporal resolution was better than 100 fs, well below all relevant decay rates. For a gentle exchange of the excited sample volume, the RM solution was pumped through a flow cell of 120 μm thickness by a peristaltic pump. Details of the experimental set-up and data processing procedure are discussed in Ref. [28].

3. Results and discussion

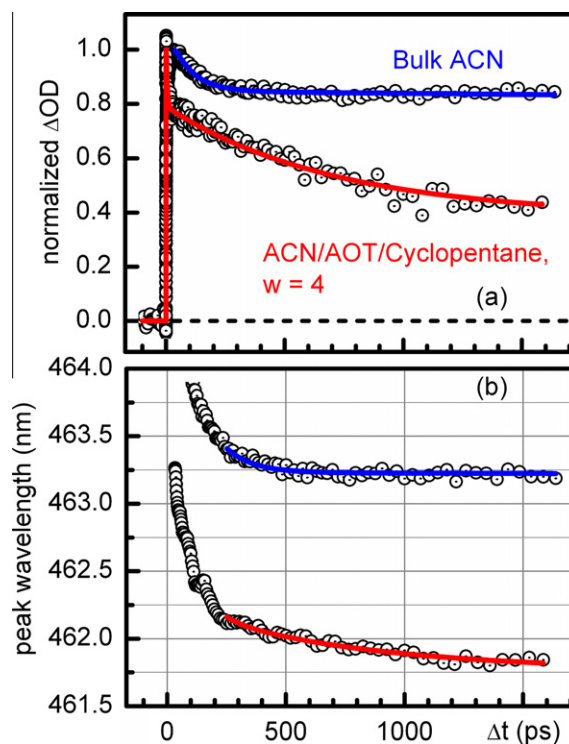Figure 3 shows the evolution of the transient absorption spectrum of $BMe_2PPh_3^+BF_4^-$ in ACN/AOT/cyclopentane reverse micelles.
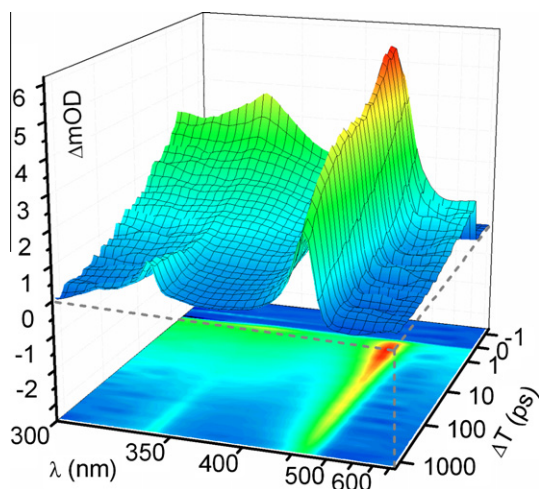
Figure 3. Transient absorption spectra of $BMe_2PPh_3^+BF_4^-$ in ACN/AOT/cyclopentane reverse micelles. For clarity the intense solvent artifact is not displayed (see Supplementary Figure S5 for details). The delay time axis is linear between −1 and 1 ps and logarithmic beyond 1 ps.

Figure 4. (a) Temporal evolution of the absorbance changes and (b) peak shift of the benzhydryl cation band in bulk ACN (blue line) and in ACN/AOT/cyclopentane reverse micelles ($w = 4$) (red line). The fits are shown as solid lines. In (b) only the component relevant to the geminate recombination (the slow component) is shown. The fast component is due to relaxation and cooling. (For interpretation of the references in color in this figure legend, the reader is referred to the web version of this article.)

After UV excitation, we observe the appearance of a long-lived product band around 465 nm, which can be ascribed to the benzhydryl cation (see Supplementary Figure S2) [19]. We additionally observe a weak band at 338 nm analogous to the band position of the benzhydryl radical [19]. Furthermore there is a broad and featureless absorption band located in the UV, which decays within the first 50 ps. The similarity of this spectral feature to the broad and long-lived excited state absorption (ESA) of bare PPh_3 (see Supplementary Figure S3) suggests that this feature arises from the optically excited PPh_3 moiety in $BMe_2PPh_3^+BF_4^-$. Signal contributions from empty ACN/AOT/cyclopentane RMs and the constituting AOT molecules can be ruled out as they are optically transparent down to 250 nm and show no transient absorption in the probe wavelength range (see Supplementary Figure S4).

For comparison to the above experiment transient spectra of $BMe_2PPh_3^+BF_4^-$ in bulk ACN have also been recorded and are shown in Supplementary Figure S6. $BMe_2PPh_3^+BF_4^-$ in bulk ACN shows the same spectral signatures as $BMe_2PPh_3^+BF_4^-$ in ACN/AOT/cyclopentane reverse micelles. However, the temporal behavior and the amplitude of the benzhydryl radical and cation band are different. As can be seen in Figure 3 and Supplementary Figure S6, upon UV excitation strong signals appear throughout the near UV and blue spectral range. These can be understood by the fact, that the precursor molecules in the ACN reverse micellar nanopools as well as in bulk ACN undergo dissociation along the C–P bond generating transient benzhydryl cations. After the initial cation generation, the cation signal in bulk ACN undergoes an initial decay which is terminated after ~200 ps leading to a constant cation population. In contrast, the benzhydryl cations in the reverse micellar nanopools show a much more pronounced and longer lasting decay. As in the bulk, a small fraction of the cations survives this prolonged decay (see Figure 4a).

To gain further insight into the dynamics of the cations we quantify the temporal evolution of the absorbance changes with a global fit procedure [29] based on a rate model. The decay associated difference spectra (DADS) can be found in Supplementary Figure S5 for $BMe_2PPh_3^+BF_4^-$ in ACN/AOT/cyclopentane reverse micelles and Supplementary Figure S6 for $BMe_2PPh_3^+BF_4^-$ in bulk ACN. Both systems display a gradual rise of the cation population in the low picosecond timescale. There are two possible pathways for the initial carbocation generation: (1) homolytic cleavage of the C–P bond leading to a benzhydryl radical/PPh_3 radical cation con-

tact pair, followed by electron transfer within this pair to generate the benzhydryl cation, (2) direct heterolytic cleavage of the C–P bond generating transient carbocations and neutral PPh_3 molecules. The mechanism behind the photolytic cleavage of the precursors leading to the benzhydryl cation generation is still an open debate [22,30]. Alonso et al. [31] in their nanosecond laser flash photolysis studies preferred a electron transfer mechanism to direct heterolysis for the carbocation generation. However, according to Bartl et al. [19] homolysis followed by electron transfer within the geminate cage is possible only if the solvation of the generated carbocation is concerted with the electron transfer process. As the complex dynamics of the initial carbocation generation requires a dedicated explanation, it goes far beyond the scope of this Letter: the effects of encapsulation on the geminate recombination of carbocations.

In bulk ACN, a small fraction of the generated benzhydryl cations decays with a time constant of 88 ps. The main part of the cation population remains unchanged for several nanoseconds. This behavior can be explained with the following mechanism: After the photoinduced C–P bond cleavage, a geminate pair consisting of the benzhydryl cation and the PPh_3 leaving group is generated. This pair can either separate to give rise to long lived cations or recombine to the precursor molecule. The recombination can only occur as long as the fragments are in close vicinity and is terminated by diffusional separation. This mechanism has already been reported for related benzhydryl derivatives [21,22]. Furthermore, the assignment of the 88 ps decay to diffusion-terminated geminate recombination is supported by the peak shift dynamics of the cation band (see Figure 4b), which displays a temporal blue shift with a comparable time constant of 112 ps. Com-

pared to the cation in the geminate pair, the free cation experiences a better solvation as it is surrounded by a full ACN solvent shell. The diffusional separation therefore leads to the observed temporal blue shift of the cation band. Analogously to the constant cation population after 200 ps (88 ps time constant), the peak wavelength shows no further changes.

In ACN nanopools, the encapsulated cations exhibit a very different decay dynamics (Figure 4a) to that in bulk ACN. The cation population decays in two sequential steps, a fast step with a 4.6 ps time constant and a slow step of 700 ps. The short time constant of 4.6 ps is too fast to involve any species present in the reverse micelle other than the photofragments themselves. We suggest that it might be due to a recoil of the photofragments from the walls of the micelle to regenerate the precursor. The subsequent 700 ps time constant is associated with the major loss of the cation population. Assigning this time constant to geminate recombination is again supported by the peak shift of the cation band. In analogy to the system in bulk, the shift occurs with a time constant of 740 ps that is comparable to the slow time constants of the cation population dynamics. The blue shift suggests, that also in the reverse micelle the cation becomes better solvated with the 700 ps time constant. This can be due to the insertion of a solvent shell of ACN molecules between the photofragments or due to the interaction of the cation with the polar SO_3^- headgroups of the AOT molecules. The much longer lasting geminate recombination of the cations with the PPh$_3$ leaving group in the micelle is a strong indication for the impact of the spatial restrictions to the process.

Although the decay of cation population in the bulk (88 ps) is much faster than in RMs (700 ps), the total efficiency of the loss process is much lower in bulk (20%) compared to that in RMs (55%). To understand this issue better, the rates for geminate recombination and the rate associated with its termination have to be determined. Since the formed cations can either undergo geminate recombination, or diffusional separation and/or rotational reorientation into a non-reactive conformation (Figure 5), the observed rate k_{tot} of (88 ps)$^{-1}$ in bulk and (700 ps)$^{-1}$ in RMs is the sum of two rates: the rate for geminate recombination k_{GR} and the rate for the transition into a non-reactive conformation (e.g. via diffusion or rotation) $k_{D/R}$. The intrinsic rate $k_{D/R}$ turns out to be (110 ps)$^{-1}$ in bulk and (1460 ps)$^{-1}$ in RMs (see Supplementary material for details). This indicates that the spatial restrictions in the RMs keeps the cation and leaving group in a close and reactive conformation for a longer period of time explaining the difference in cation loss efficiency. Although the micellar environment slows down the geminate recombination from (450 ps)$^{-1}$ in bulk to (1350 ps)$^{-1}$ in RMs, the overall efficiency is dominated by the much longer time the fragments spend in the reactive conformation. However, a small part goes into a non-reactive conformation. In this state the cations survive at least for several nanoseconds as seen in the global fit.

The evaluation of the cation dynamics via global fits, peak shifts and intrinsic rate determination shows, that the geminate recombination in the enclosed environment of a reverse micelle is significantly prolonged and also more efficient compared to the bulk solvent as the components of the geminate pair are prevented from diffusing apart. However, the intrinsic rate of geminate recombination is slower in the reverse micelle than in solution. The origin of this slowing down can be rationalized by the influence of the reverse micelle on the properties of the encapsulated solvent pool. Several studies have shown that the solvent polarity is lower in the micellar environment compared to the bulk [5,18]. A polar solvent stabilizes both the benzhydryl cation as well as the product of the geminate recombination (BMe$_2$PPh$_3^+$), as they are both charged. While in the product BMe$_2$PPh$_3^+$, the charge is localized on the phosphorus atom, in the cation the positive charge is delocalized
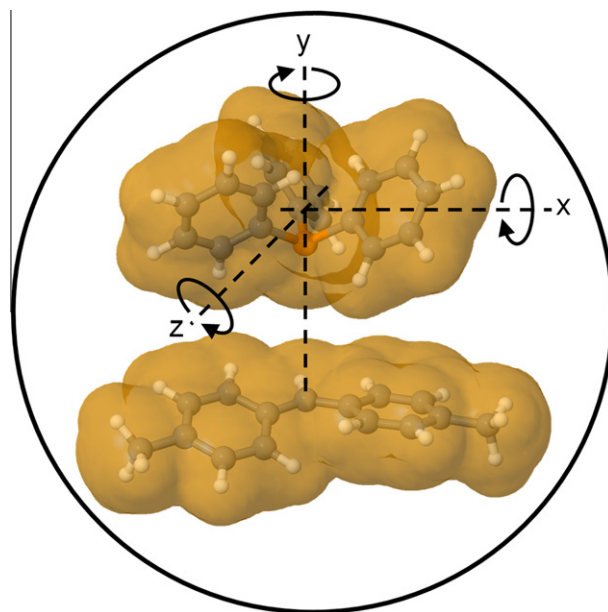

Figure 5. The shape of the Van der Waals radii of the photofragments drawn to scale with the reverse micelle inner diameter. The diffusion of the fragments is severely hindered by spatial restrictions. Additionally, the rotations about the x and z axes which cause the unfavorable orientation of PPh$_3$ with respect to the benzhydryl cation are hindered and therefore the geminate recombination yield is enhanced compared to the bulk.

over the entire molecule. As the solvation energy is lowered by an increased charge distribution [32], the positive charge is better stabilized in the product than in the cation. Therefore lowering the solvent polarity slows down the geminate recombination. To test the influence of solvent polarity on the rate of geminate recombination, we have carried out transient absorption measurements on the unsubstituted benzhydryl derivative BPPh$_3^+$BF$_4^-$ in different solvents. We observe that the intrinsic geminate recombination rate slows down from (370 ps)$^{-1}$ to (890 ps)$^{-1}$ when going from acetonitrile (ε = 35.9) to dichloromethane (ε = 8.9).

The time constant of 700 ps observed in the ACN/AOT/cyclopentane system is also associated with a small rise of the radical signature at 338 nm (Figure 6a and Supplementary Figure S5). However, the formation of benzhydryl radicals is only a minor process. From the radical and cation amplitudes of the 700 ps DADS and the extinction coefficients of the benzhydryl radical and cation published by Bartl et al. [19] (52 500 L mol^{-1} cm^{-1} for the radical and 74 100 L mol^{-1} cm^{-1} for the cation), we can derive that the final radical population is only 12% of the initial cation population. The exact mechanism behind this concerted rise and fall of radical and cation population is still not clear. We suggest that the benzhydryl radicals are generated by an electron transfer reaction involving the SO_3^- head groups of the surfactant molecules at the micellar interface. Other electron sources can be ruled out, since the counterion BF$_4^-$ is known to be hardly oxidizable [33] and electron transfer from PPh$_3$ to the benzhydryl cation is highly endothermic (ΔG_{ET} = 92 kJ/mol) [34]. To test if the sulfonate groups at the micellar interface can act as electron donors, we performed transient experiments of BMe$_2$PPh$_3^+$BF$_4^-$ dissolved in bulk ACN with excess tetraethylammonium methanesulfonate. As in the reverse micelle, we observe a delayed rise of radical signal (see Figure 6b). The amplitudes of the radical band obtained after a pump–probe delay of 1500 ps increase with increasing concentration of the methanesulfonate. Thus, it is probably the SO_3^- head groups of the AOT molecules which play a role as electron donors in the formation of benzhydryl radicals in the RMs.
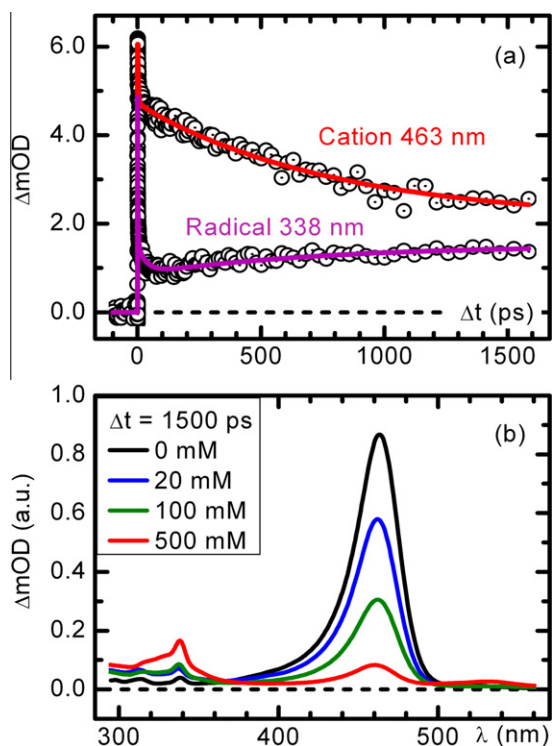
Figure 6. (a) Comparison of the temporal evolution of the cation and radical absorbance changes in ACN/AOT/cyclopentane reverse micelles ($w = 4$). (b) Transient spectra of $BMe_2PPh_3^+BF_4^-$ in bulk ACN with excess tetraethylammonium methanesulfonate after a delay of 1500 ps.

4. Conclusion

In summary, we have successfully performed femtosecond pump–probe spectroscopy on the photodynamics after bond cleavage of the triphenyl phosphonium salt $BMe_2PPh_3^+BF_4^-$ encapsulated in ACN reverse micellar nanopools. The reaction scheme arising from the data is shown in Figure 7. The reported results expand the range of processes investigated in RMs to a true ground state bimolecular reaction. The bond formation in the confined environment of a reverse micelle is slowed down, but in total largely enhanced. The present work highlights the feasibility of transient studies in the UV using reverse micelles, thus, opening up a whole new arena for investigation of the dynamics of photochemical processes under encapsulation. The small volumes available in RMs allow for the spectroscopic investigation of a single molecule in an isolated environment. Due to the bulkiness of the photofragments, material exchange during diffusional encounters of RMs as observed in Ref. [35] can be ruled out. Compared to the bulk we observe an enhanced geminate recombination of the photofragments, as the tight conditions in the RM (see Figure 5) keep cation and leaving group in close proximity for a much longer period of time. The size estimations of the photofragments with respect to the RM pool (see Supplementary Table S1) suggest that also the rotation of the fragments are hindered. Therefore the transition to a mutual orientation of PPh$_3$ and the benzhydryl cation unfavorable for bond formation seems generally inhibited. However, a small fraction of the cations does not undergo geminate recombination and lives for at least several nanoseconds. We suspect, that some of the generated photofragments, can rotate into an orientation preventing geminate recombination, in spite of the spatial restrictions. We envision that broad band time-resolved and anisotropy measurements reaching into the high nanosecond to microsecond regime can shed light on the nature of this unreactive species.
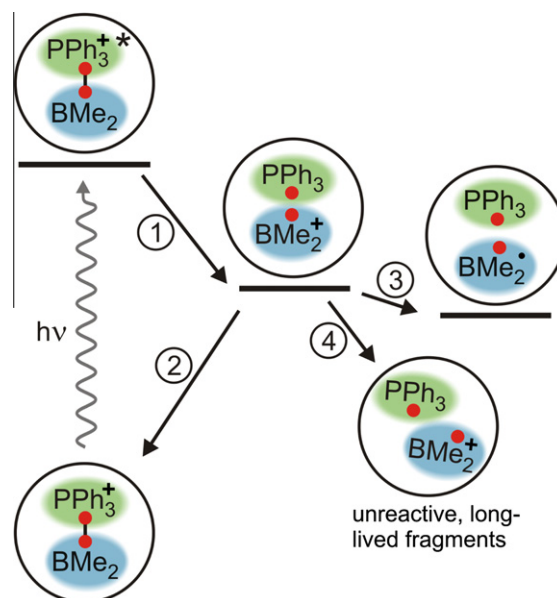
Figure 7. Reaction scheme of $BMe_2PPh_3^+BF_4^-$ in ACN/AOT/cyclopentane reverse micelles. The red dots represent the position of the benzhydryl C and PPh$_3$ P centers forming the C–P bond. The reaction steps are as follows: (1) Photoinduced C–P bond cleavage, (2) geminate recombination of the photofragments, (3) electron transfer from the SO_3^- head groups of the AOT molecules to the benzhydryl cation BMe_2^+ and (4) formation of long lived fragments.

The promotion of a reaction via restriction of substrate mobility is one of the concepts on which enzyme catalysis is based. Thus, RMs represent a first step towards the development of biomimetic nanoreactors. There is much more to enzymatic catalysis than keeping reactants together. Specific active groups in the enzyme pocket can lower the activation energy for product formation. Future investigations will therefore be directed towards the functionalization of the inner wall of the reverse micelles for further promotion of the desired chemical reaction.

Appendix A. Supplementary data

Supplementary data associated with this article can be found, in the online version, at doi:10.1016/j.cplett.2011.06.087.

References

[1] A. Douhal, M. Sanz, L. Tormo, Proc. Natl. Acad. Sci. USA 102 (2005) 18807.
[2] S. Polarz, A. Kuschel, Chem. Eur. J. 14 (2008) 9816.
[3] S.K. Pal, J. Peon, B. Bagchi, A.H. Zewail, J. Phys. Chem. B 106 (2002) 12376.
[4] D.E. Moilanen, E.E. Fenn, D. Wong, M.D. Fayer, J. Chem. Phys. 131 (2009) 014704.
[5] H. Shirota, K. Horie, J. Phys. Chem. B 103 (1999) 1437.
[6] A. Douhal, Acc. Chem. Res. 37 (2004) 349.
[7] M. Chachisvilis, I. Garcia-Ochoa, A. Douhal, A.H. Zewail, Chem. Phys. Lett. 293 (1998) 153.

[8] M. Gil, S. Wang, J.A. Organero, L. Teruel, H. Garcia, A. Douhal, J. Phys. Chem. C 113 (2009) 11614.
[9] A. Thomas, S. Polarz, M. Antonietti, J. Phys. Chem. B 107 (2003) 5081.
[10] U. Schmidhammer, V. De Waele, S. Mintova, E. Riedle, T. Bein, Adv. Funct. Mater. 15 (2005) 1973.
[11] A. Mallick, B. Haldar, S. Maiti, S.C. Bera, N. Chattopadhyay, J. Phys. Chem. B 109 (2005) 14675.
[12] B. Cohen, D. Huppert, K.M. Solntsev, Y. Tsfadia, E. Nachliel, M. Gutman, J. Am. Chem. Soc. 124 (2002) 7539.
[13] O.-H. Kwon, T.G. Kim, Y.-S. Lee, D.-J. Jang, J. Phys. Chem. B 110 (2006) 11997.
[14] S. Mahanta, R.B. Singh, N. Guchhait, J. Fluoresc. 19 (2009) 291.
[15] M.K. Sarangi, S. Basu, Chem. Phys. Lett. 506 (2011) 205.
[16] N.E. Levinger, L.A. Swafford, Annu. Rev. Phys. Chem. 60 (2009) 385.
[17] S. Nave, J. Eastoe, R.K. Heenan, D. Steytler, I. Grillo, Langmuir 16 (2000) 8741.
[18] A. Mallick, P. Purkayastha, N. Chattopadhyay, J. Photochem. Photobiol. C: Photochem. Rev. 8 (2007) 109.
[19] J. Bartl, S. Steenken, H. Mayr, R.A. McClelland, J. Am. Chem. Soc. 112 (1990) 6918.
[20] M. Lipson, A.A. Deniz, K.S. Peters, J. Am. Chem. Soc. 118 (1996) 2992.
[21] M. Lipson, A.A. Deniz, K.S. Peters, Chem. Phys. Lett. 288 (1998) 781.
[22] K.S. Peters, Chem. Rev. 107 (2007) 859.
[23] B.P. Fingerhut, D. Geppert, R. de Vivie-Riedle, Chem. Phys. 343 (2008) 329.
[24] J. Ammer, M. Baidya, S. Kobayashi, H. Mayr, J. Phys. Org. Chem. 23 (2010) 1029.

[25] R.E. Riter, J.R. Kimmel, E.P. Undiks, N.E. Levinger, J. Phys. Chem. B 101 (1997) 8292.
[26] C. Izquierdo, M.L. Moyá, J.L. Usero, J. Casado, Monatshefte für Chemie 123 (1992) 383.
[27] The Onsager radii were determined by ab initio calculations on the B3LYP/6-31G** optimized ground state geometry of $BMe_2PPh_3^+$ and the respective benzhydryl cation, the PPh_3 leaving group and the ACN solvent molecule. For these calculations the ab initio suite GAUSSIAN 09 was used., M.J. Frisch, et al., GAUSSIAN 09, Revision B01, Gaussian Inc., Wallingford, CT, 2009.
[28] U. Megerle, I. Pugliesi, C. Schriever, C.F. Sailer, E. Riedle, Appl. Phys. B 96 (2009) 215.
[29] P. Fita, E. Luzina, T. Dziembowska, Cz. Radzewicz, A. Grabowska, J. Chem. Phys. 125 (2006) 184508.
[30] R.A. McClelland, Tetrahedron 52 (1996) 6823.
[31] E.O. Alonso, L.J. Johnston, J.C. Scaiano, V.G. Toscano, Can. J. Chem. 70 (1992) 1784.
[32] C. Reichardt, Solvents and Solvent Effects in Organic Chemistry, Wiley–VCH, Weinheim, 2002.
[33] C. Imrie, T.A. Modro, E.R. Rohwer, C.C.P. Wagener, J. Org. Chem. 58 (1993) 5643.
[34] A.R. Ofial, K. Ohkubo, S. Fukuzumi, R. Lucius, H. Mayr, J. Am. Chem. Soc. 125 (2003) 10906.
[35] C.D. Borsarelli, J.J. Cosa, C.M. Previtali, Photochem. Photobiol. 68 (1998) 438.

Supplementary data

Encapsulation of Diphenylmethyl Phosphonium

Salts in Reverse Micelles: Enhanced Bimolecular

Reaction of the Photofragments

Christian F. Sailer[1], Rupashree Balia Singh[1], Johannes Ammer[2], Eberhard Riedle[1], and

Igor Pugliesi[1,*]

[1] Lehrstuhl für BioMolekulare Optik, Ludwig–Maximilians–Universität München, Oettingenstr. 67, 80538 München, Germany

[2] Department Chemie, Ludwig–Maximilians–Universität, Butenandtstr. 5–13 (Haus F), 81377 München, Germany

* Corresponding author:

e-mail: igor.pugliesi@physik.uni-muenchen.de,
Tel.: +49 89 2180 9255,
Fax.: +49 89 2180 9202

Sample preparation

For the reverse micelles preparation, we first prepared a 0.2 M solution of AOT (purchased from Sigma-Aldrich, used without further purification) in cyclopentane by direct weighing. For the preparation of ACN nanodroplets of size w = 4 (w = [polar solvent]/[AOT]), in the micellar solution we estimated the volume of ACN to be added. Now, to create these droplets of definite size and to have a concentration of ~ 2 x 10^{-3} M precursor molecules in the final solution we prepared a stock solution of ~ 48 x 10^{-3} M of the precursor molecules in ACN by direct weighing. Then the already estimated volume to reach the specific w = 4 value was added from this concentrated stock solution to the 0.2 M AOT solution in cyclopentane using a micropipette. This ensured preparation of reverse micelles of definite pore size with the precursor molecules already encapsulated in the nanopools. The mixture was shaken and left standing for ~1 hr for homogenization and stabilization of the loaded reverse micelles.

Estimation of the ratio of the number of precursor molecule to reverse micellar entities

To get an estimate of the number of precursor molecules per reverse micelle, we first estimated the number of AOT molecules in 1 ml of 0.2 M AOT solution which was ~ 1.2 x 10^{20} surfactant molecules. Assuming an aggregation number of 60 based on literature, [Izq92] the number of reverse micellar entities possible in 1 ml of the sample solution was estimated to be ~ 2 x 10^{18} . Similarly, the number of precursor molecules BMe$_2$PPh$_3$$^+BF_4$$^-$ in the 1ml of the reverse micellar solution was estimated to be ~ 1.2 x 10^{18} based on the concentration obtained using the Lambert-Beers Law (OD = 1.05 at 270 nm, ε = 52501 mol^{-1} cm^{-1}). Thus, the ratio of the precursor molecule to the reverse micelles came out to be 0.6. According to these calculations, less than one precursor molecule per micelle was observed in the experiments.

Dynamic light scattering experiment

The hydrodynamic diameters of the empty and loaded reverse micelles were estimated using dynamic light scattering measurements (Malvern Zetasizer Nano equipped with a 4 mW He-Ne laser (633 nm) and an avalanche photodiode detector, 10 runs were averaged). The average diameters lie in the range 3.35 ± 0.8 nm, at least 90% of the reverse micelles lie in this size distribution zone. A few are obviously above and below this size range. This matches very well with the values reported in literature. The empty reverse micelles were of slightly smaller size as expected.
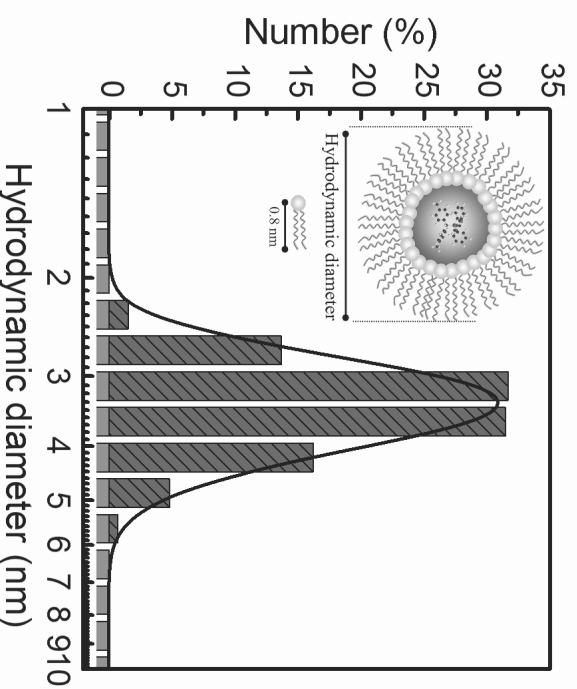
Fig. S1   Size distribution histogram of the ACN/AOT/cyclopentane reverse micelles at w = 4 loaded with $BMe_2PPh_3^+ BF_4^-$.

Transient absorption spectra

In both investigated systems, $BMe_2PPh_3^+BF_4^-$ in bulk ACN and in ACN/AOT/cyclopentane reverse micelles, the appearance of a long-lived product band around 465 nm is observed after UV excitation which can be ascribed to the benzhydryl cation. In the ACN/AOT/cyclopentane RM system we additionally observe a weak band at 338 nm analogous to the band position of the benzhydryl radical at later time delays.
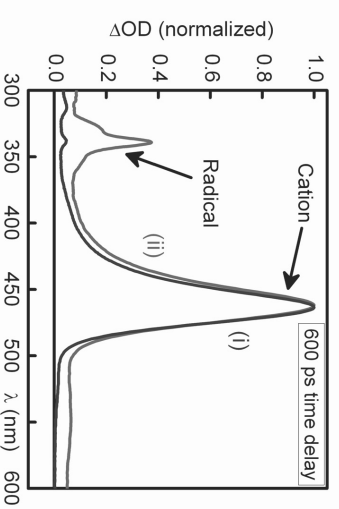
Fig. S2   Transient absorption spectra of $BMe_2PPh_3^+BF_4^-$ after 600 ps time delay in (i) bulk ACN and (ii) ACN/AOT/cyclopentane reverse micelles, w = 4 (normalized at the cation band position).

The broad and featureless absorption band located in the UV, which decays within the first 50 ps is ascribed to the excited state absorption (ESA) of the optically excited PPh_3 moiety in $BMe_2PPh_3^+BF_4^-$ due to its resemblance to the broad and long-lived ESA of neutral PPh_3 in ACN.

Reference measurements have been conducted to rule out any signal contributions from empty ACN/AOT/cyclopentane RMs and the constituting AOT molecules. They are optically transparent down to 250 nm and show no transient absorption in the probe wavelength range.
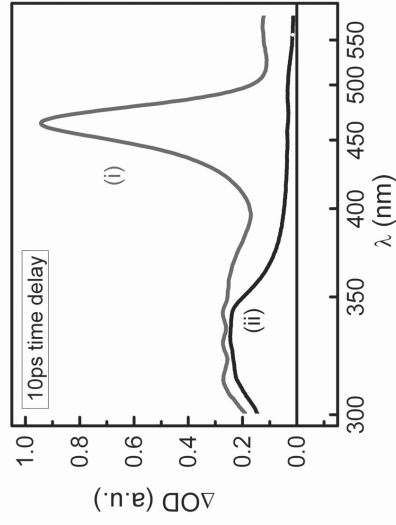
Fig. S3 Transient absorption spectra of (i) $BMe_2PPh_3^+BF_4^-$ in ACN/AOT/cyclopentane reverse micelles, w = 4 and (ii) neutral PPh_3 in bulk ACN solvent. The UV band of $BMe_2PPh_3^+BF_4^-$ in RMs decays in 36 ps.
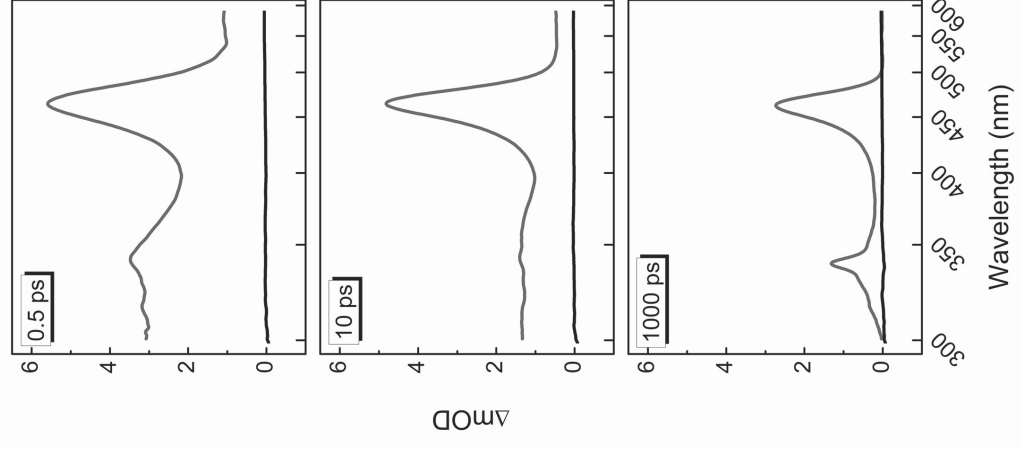
Fig. S4 Transient absorption spectra at selected delays displaying a comparison for the loaded (with $BMe_2PPh_3^+BF_4^-$; red curves) and empty ACN/AOT/cyclopentane (w = 4) reverse micelles (black curves) under similar experimental conditions.

Transient absorption measurement and global fit data for $BMe_2PPh_3^+BF_4^-$ in RMs
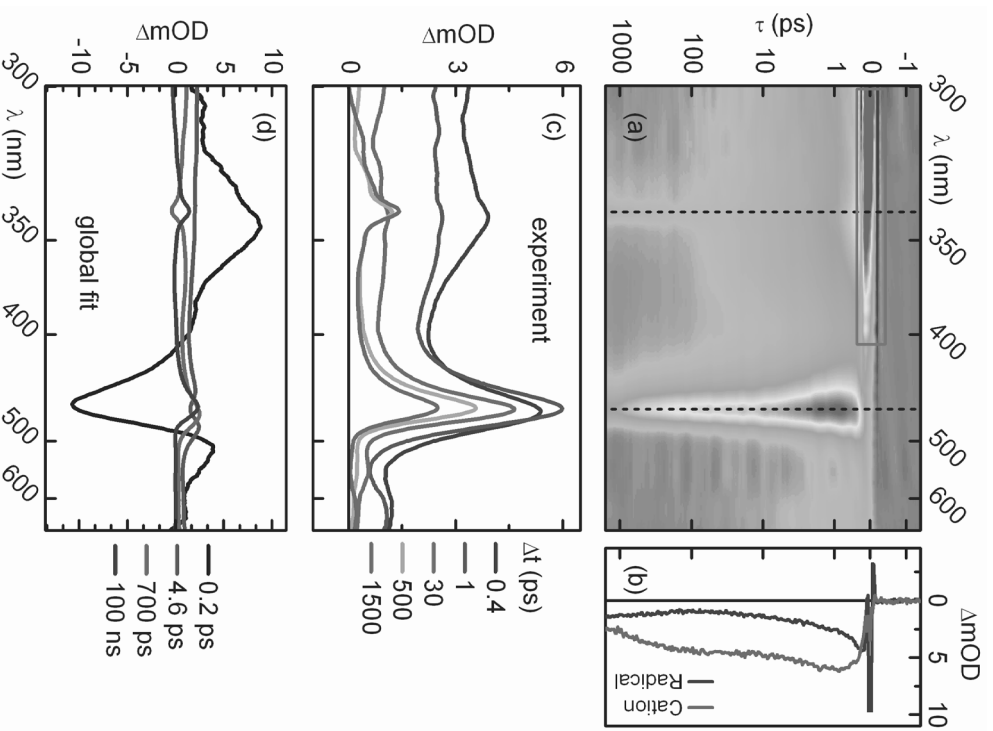
Fig. S5 (a) Color map of the transient absorption of $BMe_2PPh_3^+BF_4^-$ in ACN/AOT/cyclopentane reverse micelles, w = 4; warm colors represent positive and cold colors represent negative absorption changes. The time axis is linear up to 1 ps and logarithmic for longer delays. The pink box highlights the intense solvent artifact not displayed in Figure 3. (b) Time traces at the radical (338 nm) and cation (463 nm) spectral positions (dotted lines in (a)). (c) Spectral cuts at selected delay times. (d) Decay associated difference spectra from the global fit.

S7

Transient absorption measurement and global fit data for $BMe_2PPh_3^+BF_4^-$ in bulk ACN
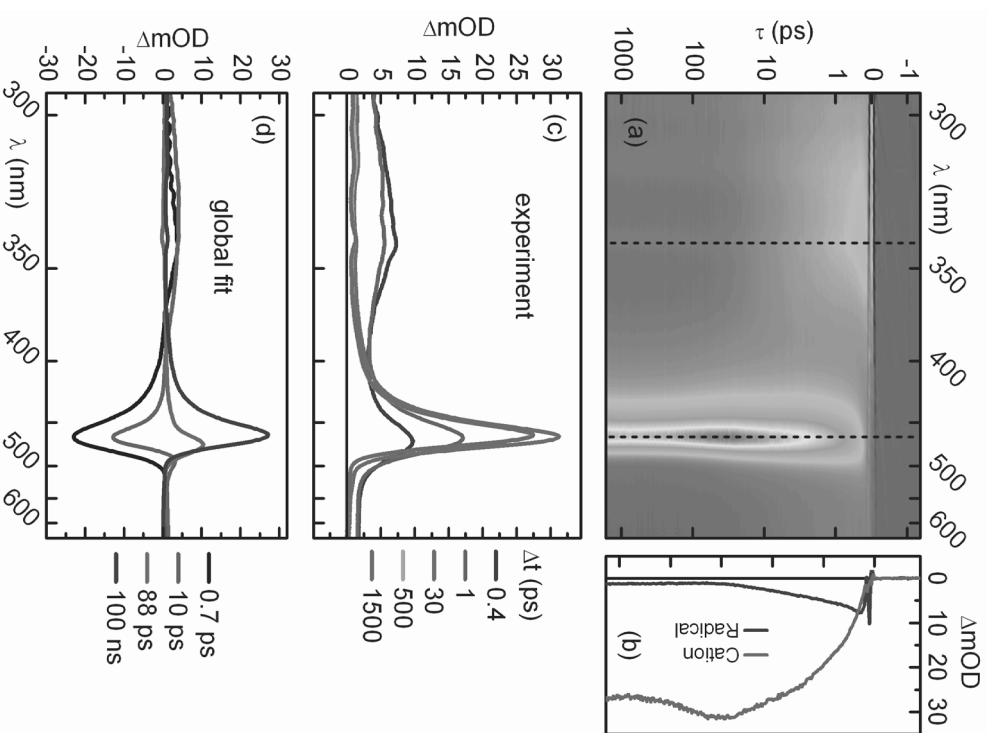
Fig. S6 (a) Color map of the transient absorption of $BMe_2PPh_3^+BF_4^-$ in bulk CAN; warm colors represent positive and cold colors represent negative absorption changes. The time axis is linear up to 1 ps and logarithmic for longer delays. (b) Time traces at the radical (338 nm) and cation (463 nm) spectral positions (dotted lines in (a)). (c) Spectral cuts at selected delay times. (d) Decay associated difference spectra from the global fit.

S8

Geminate recombination rates and quantum yields

Immediately after C-P bond cleavage the two photofragments are in close vicinity (contact pair). They can either undergo geminate recombination with the rate k_{GR} or the fragments diffuse apart or rotate away with the rate $k_{D/R}$ so that a bond formation is not feasible anymore. The observed decay rate in which the generated cations disappear is therefore the sum of the two channels:

$$k_{tot} = k_{GR} + k_{D/R}$$

It should be noted that although the observed cation absorption signal stems from the paired as well as from the free cations the observed rate is still k_{tot}. Assuming that the extinction coefficients for the paired and free cations are the same, one can calculate the quantum yield of the geminate recombination, QY_{GR} using the relation:

$$QY_{GR} = \frac{[GR]}{[Cat]_0} = \frac{\Delta OD_{GR}}{\Delta OD_{GR} + \Delta OD_\infty}$$

[GR] is the concentration of recombined photofragments, $[Cat]_0$ is the cation concentration before the geminate recombination or diffusion and rotation. The absorbance changes ΔOD_{GR} and ΔOD_∞ are obtained from the amplitude of the DADS at the cation maximum. Solving the differential equations for the rate model yields the concentration $[GR(t)]$ of recombined photofragments:

$$[GR(t)] = [Cat]_0 \frac{k_{GR}}{k_{tot}}(1-\exp(-k_{tot}t))$$

For $t \to \infty$ this simplifies to $[GR] = [Cat]_0 \dfrac{k_{GR}}{k_{tot}}$. Using the relation, $QY_{GR} = \dfrac{[GR]}{[Cat]_0}$, we obtain

$$k_{GR} = k_{tot} QY_{GR}$$

A similar calculation for the rotated or diffused apart fragments leads to

$$k_{D/R} = k_{tot}(1-QY_{GR})$$

a) in bulk ACN

The formed cations can either undergo geminate recombination with PPh3 or the fragments diffuse apart or rotate away so that a bond formation is not feasible anymore. We observe a decay rate of $k_{tot} = (88\text{ ps})^{-1}$ in which $QY_{GR} = 20\%$ of the generated cations disappear. This leads to the intrinsic rates for the respective processes in bulk ACN:

$$k_{GR} = k_{tot}QY_{GR} = (450\,ps)^{-1}$$
$$k_{diffusion} = k_{tot}(1-QY_{GR}) = (110\,ps)^{-1}$$

b) in Reverse Micelles

In reverse micelles, the encapsulated photofragments cannot diffuse apart but can undergo slow rotational reorientation or possibly translation out of the favourable conformation thus, hindering geminate recombination. We observe a decay rate $k_{tot} = (700\text{ ps})^{-1}$ in which 52% of the cation population (after initial loss via the ~ 4.6 ps time constant) disappears.

$$k_{GR} = k_{tot}QY_{GR} = (1350\,ps)^{-1}$$
$$k_{rotation} = k_{tot}(1-QY_{GR}) = (1460\,ps)^{-1}$$

The minor cation loss channel via electron transfer in principle contributes to k_{GR}. Since the radical generation only occurs to a small extent, the contribution is rather small and by neglecting it we therefore only slightly underestimate the pure geminate recombination rate. A rough estimation of $(1800\text{ ps})^{-1}$ for the pure geminate recombination rate can be made from the DADS.

Component sizes

To gain an overview of the spatial conditions inside the investigated reverse micelles, size estimations of the various components were done. Since the radius of the RM is only slightly larger than one $BMe_2PPh_3^+$ molecule it can be inferred that encapsulation of more than one of these precursors can be ruled out. The investigated RM therefore consists of approximately 60 AOT molecules, 60 Na^+, a single $BMe_2PPh_3^+BF_4^-$ and about 40 ACN molecules.

Table S1: Onsager radii and volumes calculated on optimised geometries of the components contained in the RM at the B3LYP/6-31G** level of theory. For the RM the radius is obtained from DLS (dynamic light scattering) measurements.

	$BMe_2PPh_3^+$	BMe_2^+	PPh_3	ACN	RM pool
Radius (Å)	6.09	4.77	5.26	3.10	8.75
Volume (cm^3)	0.55×10^{-21}	0.24×10^{-21}	0.34×10^{-21}	0.056×10^{-21}	2.85×10^{-21}
Molar volume (cm^3/mol)	330.593	147.128	204.153	33.432	–
Number				51 (w/o precursor) 42 (w/ precursor)	

Appendix D3

Build-up and Decay of the Optical Absorption in the Ultrafast Photo-Generation and Reaction of Benzhydryl Cations in Solution

B. P. Fingerhut, C. F. Sailer, J. Ammer, E. Riedle, R. de Vivie-Riedle

Buildup and Decay of the Optical Absorption in the Ultrafast Photo-Generation and Reaction of Benzhydryl Cations in Solution

Benjamin P. Fingerhut,[†,§] Christian F. Sailer,[‡] Johannes Ammer,[†] Eberhard Riedle,*[,‡] and Regina de Vivie-Riedle*[,†]

[†]Department Chemie, Ludwig-Maximilians-Universität (LMU), Butenandt-Strasse 11, 81377 München, Germany
[‡]Lehrstuhl für BioMolekulare Optik, Ludwig-Maximilians-Universität (LMU), Oettingenstrasse 67, 80538 München, Germany

S *Supporting Information*

ABSTRACT: The identification of the transition state or a short-lived intermediate of a chemical reaction is essential for the understanding of the mechanism. For a direct identification typically transient optical spectroscopy is used, preferentially with high temporal resolution. We combine broad-band femtosecond transient absorption measurements and on-the-fly molecular dynamics calculations to decipher the microscopic evolution of the geometry and solvation of photogenerated benzhydryl cations (Ar_2CH^+, Ar = phenyl, *p*-tolyl, *m*-fluorophenyl, or *m*,*m′*-difluorophenyl) in bulk solution. From the high level quantum chemical calculations on the microsolvated cation we can deduce a narrowing and blue shift of the cation absorption that is nearly quantitatively equal to the experimental finding. The roughly 300 fs initial increase in the absorption signal found for all investigated combinations of benzhydryl chlorides or phosphonium salts as benzhydryl cation precursors and solvents is therefore assigned to the planarization and solvation of the nascent fragment of the bond cleavage. The actual cleavage time cannot directly be deduced from the rise of the spectroscopic signal. For alcohols as solvent, the cation combines on the picosecond time scale either with one of the solvent molecules to the ether or to a lesser degree geminately with the leaving group. The study shows that the absorption signal attributable to a species like the benzhydryl cation does not mirror the concentration during the first instances of the process. Rather, the signal is determined by the geometrical relaxation of the photoproduct and the response of the solvent.
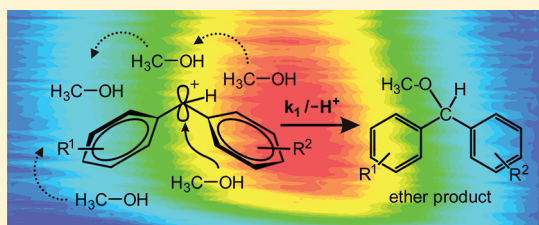
I. INTRODUCTION

Nucleophilic substitution reactions are at the very heart of chemistry and reactivity. The attack of a nucleophile can be preceded by the formation of a well-defined intermediate, typically a carbocation, through heterolytic bond cleavage. This stepwise S_N1 reaction seems easily distinguished from the concerted S_N2 reaction where no stabilized intermediate is formed but rather a transition complex develops from the two reactants for a very short time. In the borderline case between S_N1 and S_N2 it may be difficult to distinguish between a very short-lived carbocation and a true transition state. The situation becomes even more puzzling as the search for a signature of the intermediate becomes not only technically challenging, but also conceptually.

As has been pointed out, the study of the transition state is highly challenging due to the short duration of its existence.[1−4] Only a time of 100 fs or less is considered. In this study we describe the generation of very short-lived carbocations and how their absorption signal evolves after their generation. The most direct detection scheme for reactions on such a fast time scale is ultrafast transient absorption spectroscopy. It can nowadays readily render a temporal resolution well below 100 fs-at least in the visible and UV.[5] The mere observation of femtosecond absorbance changes does, however, not imply the desired information about the existence and concentration

evolution of the short-lived species. On the time scale of tens to hundreds of femtoseconds, the nuclear motion that is at the very heart of chemical transformations, will not only change the geometry of the observed moiety but also its electronic structure and energetics. A similar situation has recently been discussed for femtosecond resolved photoelectron spectroscopy.[6] The macroscopic experiment only monitors the optical transitions between the evolving states, a complex convolution of the microscopic properties. In addition, solvation by a polar solvent will proceed on the same time scale[7] and shift the energy levels of the reactants, intermediates and products in a complicated fashion. So far, solvation has mainly been discussed for nonreactive dye molecules and studies combining chemical reactivity and solvation only slowly emerge.[8,9]

A theoretical study on small gas phase molecules might come quickly to a decision how the reaction proceeds in detail, as the potential hypersurface can be scanned with the needed precision. Associated spectroscopic investigations of such isolated systems have been quite successful.[1,10] For most

bimolecular reactions in solution, the diffusional encounter of the reactants limits the temporal resolution of the experimental observation to the nanosecond regime and therefore can only provide indirect evidence.

We now report a combined experimental and theoretical study that is designed to address many of the mentioned issues. By irradiation of benzhydryl chlorides or benzhydryl triphenylphosphonium salts with femtosecond UV pulses, we generate benzhydryl cations in times well below one picosecond.[11,12] The evolving absorption signatures are then monitored over a very broad range spanning from 285 to 700 nm which encompasses the absorbance band of the benzhydryl cation in the visible. We show that formation of the signals is practically independent of the cation reactivity and the solvent. Because the use of alcohols as solvent offers the unique opportunity to observe a subsequent combination reaction to the ether without the need for diffusion, we choose methanol as specific model.

A microsolvation model is developed to interpret the experimental findings (Figure 1). After photolytic cleavage of
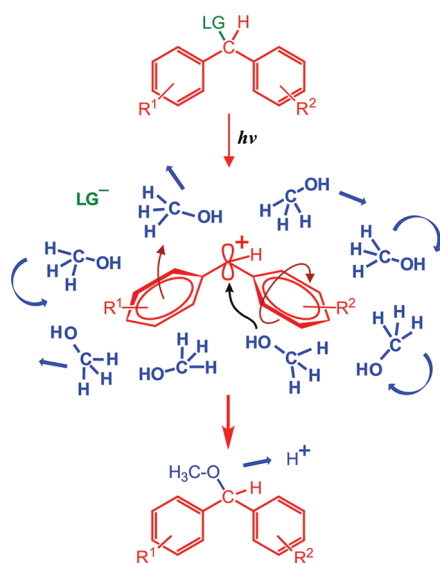
Figure 1. Reaction scheme for the photo-S_N1 reaction of benzhydryl derivatives. The benzhydryl cation initially has the same geometry and solvent shell (indicated by the blue CH_3OH molecules) as the benzhydryl moiety in the precursor. The arrows symbolize the planarization of the benzhydryl cations (red) and the adaption of the solvent molecules to the evolving charge distribution (blue).

the precursor Ar_2CH-LG, the photoleaving group LG^- (green) is separated from the benzhydryl cation Ar_2CH^+ (red), which initially has the same geometry and solvent shell as the benzhydryl moiety in the precursor (indicated by the blue CH_3OH molecules). Ar here stands for an aryl group, an aromatic hydrocarbon with one of the hydrogen atoms removed from a ring carbon atom. Subsequently, the benzhydryl cation relaxes and planarizes (red arrows), while the solvent shell simultaneously adapts to the new charge distribution (blue arrows). Nucleophilic attack of one of the CH_3OH molecules on the benzhydryl cation (black arrow) and subsequent deprotonation yield the benzhydryl methyl ether as the final reaction product. For this combination of solute and a limited number of small solvent molecules on-the-fly molecular dynamics simulations[13] are just possible. Both the solute and the solvent molecules are treated quantum chemically. From

the manifold of trajectories microscopic insights as well as the macroscopic observables can be deduced and compared with the measurements. The aim of the study is the identification and deep qualitative understanding of the complex series of mechanism and reactions steps.

We do not aim at a complete quantitative reproduction of all details of the experiment. What is much more important is the realization that the absorption signal attributable to the benzhydryl cation does not mirror the concentration in the first few hundreds of femtoseconds. Instead, the signal is determined by the planarization of the cation and the response of the solvent. Strictly speaking the phototriggering of the reaction does not exactly study a S_N type reaction, it is, however, the closest we can get at present to the real time observation of the elementary reaction process.

II. EXPERIMENTAL METHODS

Femtosecond Transient Absorption Measurements. The details of the femtosecond transient absorption setup have been described in ref 5. For the measurements presented here, solutions of the precursors were pumped through a flow cell of 120 μm optical path length and excited at 270 or 280 nm corresponding to the maximum of the first absorption band of the benzhydryl chlorides or benzhydryl phosphonium salts. The pulses with an energy of about 200 nJ and a pulse length of ~35 fs were focused down to a diameter of ~100 μm. A CaF_2 continuum spanning from 290 to 700 nm and polarized at the magic angle was used as probe light. The temporal resolution was ~100 fs. The concentration of the benzhydryl chloride solutions was ~3×10^{-2} M, and that of the phosphonium salt solutions, ~5×10^{-3} M, leading to an absorbance at the excitation wavelength of 0.1−0.3. The fraction of excited precursor molecules in the pumped volume was ≤2%.

Peak Shift Determination. The benzhydryl cation band observed after photolysis of benzhydryl chlorides undergoes small, time-dependent peak shifts already identifiable to the bare eye at close inspection. For a quantitative determination of the peak shift, one needs a consistent measure for the position at many delay times. We therefore employed an iterative fitting algorithm on the complete transient absorption data allowing for the determination of the cation band position for every time delay measured. The algorithm first fits a parabola to the band within a given, sufficiently large interval. The fitted maxima for every time delay are then taken as the middle of a new, smaller interval on which the parabola is fitted again. We do not have an a priori knowledge of the band shape and the reliable calculation of the center of gravity of the band is precluded both by a possible sloping background due to the time dependent excited state absorption and by the overlap between the radical and cation band. The maximum can, however, be well approximated by a parabola and this leads to a measure of the band position of the photoproducts with an uncertainty smaller than 0.1 nm. Any deviation of this choice of band position from another reasonable definition will at most lead to a systematic additive value that is constant for all delay times.

Multiexponential Fit. The majority of the transient absorption curves shown in Figure 2 can be fitted with a single exponential for the initial rise within the first picoseconds. An additional exponential decay with a time constant of about 150 ps is found for the cations and can be assigned to geminate recombination.[12] Similarly, a stretched exponential with an average time of 20 ps is found for the radicals. However, some of the initial cation signal rises have to be

B

dx.doi.org/10.1021/jp300986t | J. Phys. Chem. A XXXX, XXX, XXX−XXX

modeled by a biexponential model function. The additional time constant of about 10 ps can be assigned to the generation of extra cations by electron transfer within the radical pair.[11] Numerically, the 300 fs and the 10 ps time constants can be well separated and therefore the determination of the 300 fs constant is not impeded.

III. EXPERIMENTAL OBSERVATIONS

Photolysis of $Ar_2CH{-}Cl$[14] or $Ar_2CH{-}PR_3^+$[15] yields benzhydryl cations Ar_2CH^+ and/or benzhydryl radicals $Ar_2CH^\bullet$ as the primary photoproducts. The photoinduced bond cleavage of benzhydryl chloride ($Ph_2CH{-}Cl$) has been shown to proceed on the subpicosecond time scale[16] due to easily accessible conical intersections[17] and can be best observed by ultrafast transient absorption spectroscopy. The photocleavage of other precursors $Ar_2CH{-}Cl$ and $Ar_2CH{-}PR_3^+$ proceeds on a similar time scale. The first absorption band of all precursors is located around 270 nm irrespective of the substituents on the aryl rings, the photoleaving group, and the solvent. The first strong absorptions of the generated photoproducts are the $D_5 \leftarrow D_0$ transition around 330 nm for the radical $Ar_2CH^\bullet$ and the $S_1 \leftarrow S_0$ transition around 435 nm for the cation Ar_2CH^+.[14] The cation band can be determined from measurements of the persistent carbocations in concentrated sulfuric acid.[14] Because the UV/vis absorption bands of both photoproducts and the precursor absorption are all well separated, the bond cleavage dynamics and possible subsequent processes can be distinguished well.

We carried out measurements with a femtosecond spectrometer as described above. The absorption spectrum of benzhydryl chloride Ph_2CHCl is shown in Figure 2a together with the transient spectrum at 5 ps (see Chart 1 for details on the compounds and Table 1 for the compound–solvent numbering). The pronounced band around 435 nm is the signature of the benzhydryl cation Ph_2CH^+ and the band at 330 nm the signature for the benzhydryl radical $Ph_2CH^\bullet$. According to standard procedures the integral strength of these bands should be proportional to the respective product concentration.

Figure 2b displays the time-dependent absorbances of various benzhydryl cations Ar_2CH^+ determined at their respective λ_{cation}, which we obtained after irradiation of different diphenylmethyl derivatives (Chart 1) in various solvents. The combinations were chosen to sample a large range of molecular and solvation properties. In Figure 2c, the dynamics of the radical absorption band at the respective $\lambda_{radical}$ is shown. The curves are displayed with small scaling factors and an incremental offset for easier comparison. Signal contributions around zero delay time that can be attributed to the solvent response were determined by reference measurements and subtracted from the raw data according to standard procedure. In all cases we find a signal rise with an effective time constant of around 300 fs (see Table 1 for the time constants fitted to the initial signal rise). In some solutions there is an additional slower rise of the cation signal and an associated decrease of the radical signal due to electron transfer in the geminate $Ar_2CH^\bullet/Cl^\bullet$ radical pair.[18,19]

The very high similarity of the dynamics despite the largely differing reactivities of the cations[20,21] and the range of solvents used is surprising. Attempts to correlate the small variation in times with the solvent polarity and viscosity, or the electrophilicity of the cation, produced no significant result. Even though the cation reactivity is a property of the electronic ground state, one would still expect a rather large variation of
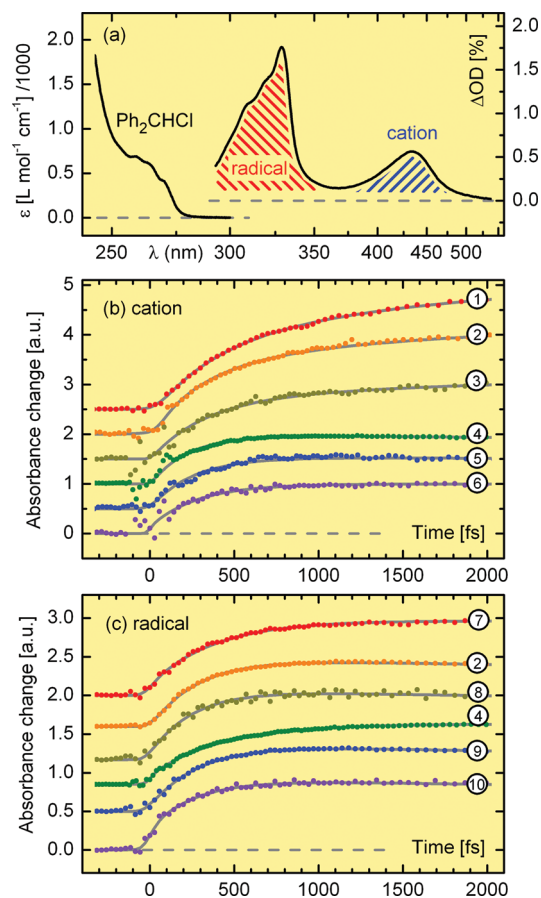
Figure 2. (a) Steady state absorption spectrum (black line) of Ph_2CHCl in CH_3CN and the benzhydryl radical and cation band observed 5 ps after UV excitation. (b) Initial increase of the absorbance signal within the first picosecond at the wavelength of the cation band and (c) of the radical band. The displayed compound–solvent combinations are as numbered in Table 1. The time constants fitted to this initial increase are given in Table 1, the solid lines in (b) and (c) are the fitted model. The partially observed increase of the cation signal beyond 1 ps is assigned to the inter-radical electron transfer (see text).

the bond cleavage dynamics with the electron withdrawing or donating substituents. These can be expected to alter the conical intersections that are known to cause the ultrafast dynamics.[17,22] Furthermore, the negligible influence of the solvent on the time constant implies that the early dynamics cannot be explained solely by solvation.

On closer inspection, the peak positions in the transient absorption spectra are found to shift with the temporal delay. This could be due to the solvation dynamics and geometric relaxation in the molecules. To determine the peak shift from the transient spectra, we use the protocol explained above. The resulting cation peak shift is depicted in Figure 3a for $mfp(Ph)CHCl$ in methanol. We find a pronounced shift of 16 nm within the first picosecond. A Gaussian fit (see eq 3 below) shows that 50% of the shift is reached at $t_{fast} = 500$ fs. A Gaussian fit and not the more common exponential is used to reflect the inertial aspect of the ultrafast process underlying the temporal evolution.[23]

The value of 500 fs is reasonably close to the 300 fs time constant found for the increase of the cation respectively radical signal in all investigated systems. Such a coincidence is not very likely fortuitous, and it has to be investigated in detail whether
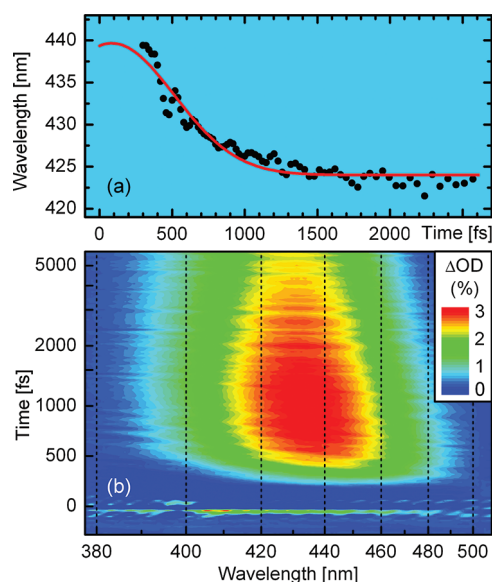
Chart 1. Benzhydryl Chlorides and Phosphonium Salts Studied in This Work

compound	abbreviation
(structure)	(tol)$_2$CH-Cl
(structure)	Ph$_2$CH-Cl
(structure)	mfp(Ph)CH-Cl
(structure)	dfp(mfp)CH-Cl
(structure)	tol(Ph)CH-PPh$_3^+$ BF$_4^-$
(structure)	(mfp)$_2$CH-PPh$_3^+$ BF$_4^-$
(structure)	(dfp)$_2$CH-P(CH$_3$)$_3^+$

Figure 3. (a) Peak shift of mfp(Ph)CH$^+$ in methanol. The band maximum (black dots) shifts to shorter wavelengths. The temporal behavior can be fitted with a Gaussian function (red line) according to eq 3. (b) Transient spectra of the mfp(Ph)CH$^+$ cation in methanol after 270 nm excitation showing a pronounced blue shift. The overall decrease of the band can be assigned to the reaction of the cation with the alcohol. Note that the time scale in (b) switches from linear to logarithmic at 1000 fs.

the simple interpretation of the signal rise as population dynamics is justified. Because purely experimental observables for the product population are not available on the subpicosecond time scale, we will resort to a close comparison with the results of a theoretical investigation.

Before we proceed to the theoretical modeling, we briefly comment the decrease in absorption signal seen in Figure 3b. We find the mfp(Ph)CH$^+$ cation and other highly electrophilic carbocations to react extremely fast with methanol[24] and thus the observable cation absorption is short-lived. Within the first picosecond, a rise of the cation band is observed, which is followed by a decrease in about 20 ps. By changing the substituents on the aryl rings of the precursor, we generate differing cations with largely varying reactivity. In this way we can vary the speed of combination with the alcohol and thereby separate the combination process from the early generation steps experimentally, just as the theory can dissect the complex dynamics by a detailed analysis.

IV. MODELING OF THE MICROSOLVATION, GEOMETRIC RELAXATION, AND REACTION WITH METHANOL

The experimental results on the initial 300 fs absorbance signal formation in the ultrafast bond cleavage of benzhydryl derivatives point at a close interplay between geometric relaxation of the fragments, solvation, and eventual reaction with an alcohol as solvent. For the theoretical modeling of all three steps the solute has to be treated quantum chemically and this is possible with high level methods for the size of benzhydryl derivatives considered. In particular, the relevant relaxation of the fragments already proceeds on the electronic ground state and this further facilitates the calculations. The surrounding bulk solvent cannot yet be treated fully quantum chemically and we therefore choose a microsolvation approach. The two approaches are combined in on-the-fly molecular dynamics (MD) simulations.[13] Within the on-the-fly dynamics we explicitly consider the solvation dynamics, the intramolecular relaxation and the electrophile—nucleophile bond formation. With appropriate correlation functions we analyze the relaxation process and quantify the accuracy of the

Table 1. Exponential Time Constant τ Fitted to the Initial Signal Increase of the Photogenerated Benzhydryl Cations and Radicals for the Compound—Solvent Combinations Shown in Figure 2

	cation				radical		
no.	precursor	solvent	τ (fs)	no.	precursor	solvent	τ (fs)
1	tol(Ph)CH-PPh$_3^+$BF$_4^-$	CH$_3$OH	379	7	Ph$_2$CHCl	butyronitrile	384
2	mfp(Ph)CHCl	CH$_3$CN	321	2	mfp(Ph)CHCl	CH$_3$CN	283
3	(mfp)$_2$CH-PPh$_3^+$BF$_4^-$	CH$_3$OH	322	8	Ph$_2$CHCl	CHCl$_3$	258
4	mfp(Ph)CHCl	CH$_3$OH	225	4	mfp(Ph)CHCl	CH$_3$OH	420
5	dfp(mfp)CHCl	CH$_3$CN	255	0	Ph$_2$CHCl	CH$_3$CN	295
6	Ph$_2$CHCl	CH$_3$OH	278	10	(tol)$_2$CHCl	CH$_2$Cl$_2$	274

microsolvation approach. The calculations are limited to the case of the cation, because it is the one that can react with the alcohols. The relaxation of the radical can safely be expected to proceed in analogy.

To describe the microsolvation, we determine in a first step how many methanol (CH_3OH) molecules are needed for a complete first solvation shell. Nine certainly turns out to be sufficient whereas eight seems to be marginal. Therefore, two precursor systems $(dfp)_2CH-P(CH_3)_3{}^+ \cdot 8CH_3OH$ and $(dfp)_2CH-P(CH_3)_3{}^+ \cdot 9CH_3OH$ are used to determine the equilibrium geometry and investigate the main characteristics of the microsolvated precursor. The choice of two different precursor clusters accounts for the fact that a first solvation shell is not uniquely defined and can take up more than one configuration. The quantum chemical methods used were tested with smaller benzhydryl cation/methanol clusters (Supporting Information). Between themselves the solvent molecules form a pronounced intersolvent hydrogen bond network; the coordination toward the F-atoms is only weakly developed. In a next step the bond between the central methyl carbon and the phosphorus atom in the phosphine leaving group is broken with the geometries of the benzhydryl moiety and of the methanol molecules kept constant. The resulting model system with eight/nine methanol molecules is denoted by MS. Finally, an ensemble $MS_{start} = \{MS_i(0)\}$ of $i = 1, 2, ...,$ 45 nonequilibrium start geometries for the on-the-fly MD simulations is chosen to mimic the nascent microsolvated benzhydryl cation, half with eight and half with nine methanols. For a discussion of bond lengths, strength of H-bonds and the importance of dispersion corrected functionals see Supporting Information.

On-the-Fly MD. The dynamics of the nascent micro-solvated benzhydryl cation is simulated by on-the-fly MD. The method requires an energy and a gradient calculation at every time-step ($\Delta t = 1$ fs) but avoids the construction of global potential energy surfaces. The energies and gradients are calculated on the RI-BLYP-D level of theory,[25−31] using a split valence double-ζ basis set (def-SV(P)). The accuracy of the RI-BLYP-D method is tested against different functionals and MP2 (for details see Supporting Information). The resulting equations of motion of the nuclei are calculated with the *Newton-X* package.[13] This yields the temporal development of both the intermolecular and intramolecular nuclear positions and velocities.

To initiate the dynamics of MS_{start}, the leaving group $P(CH_3)_3$ is placed at a distance of 5.0 Å from the central C-atom (Figure 1). The position and orientation of the methanol molecules is left unaltered. We thereby assume that the ultrafast bond cleavage proceeds faster than the intramolecular relaxation.[11,17,32] The initial velocities are generated by depositing the excitation energy $E_{h\nu} = 4.8$ eV ($\lambda = 258$ nm) as kinetic energy equally in all degrees of freedom[33] (for details see Supporting Information). Due to the dissociative character of the excited state potential energy surface, we assume that most of the excitation energy is directly converted into kinetic energy of the dissociating fragments within 200 fs.[17] The error due to the neglect of the ground state dissociation enthalpy is estimated to be only 10%. In the liquid phase, the fragments are confined in the first solvation shell and the kinetic energy is transferred by elastic scattering from the solute to the solvent molecules. The subsequent redistribution within the solute and solvent vibrational modes is obtained from the MD trajectories. All 45 trajectories lead to bond formation by attack of CH_3OH

or $P(CH_3)_3$ within 4 ps. The temporal evolution is compared in section IV to the experimental observables like transient spectra and population relaxation.

The bond formation in all trajectories within the 4 ps window is due to the extremely high reactivity of the tetrafluoro-substituted cation $(dfp)_2CH^+$. This cation was chosen intentionally to avoid even higher computational costs and inaccuracy for longer propagations. Still we are quite confident that more general conclusions can be drawn from this one example. This is due to the fact that the quantum chemical topology does not change much with the substituents.

The electronically excited $\pi-\pi^*$ states of the microsolvated $(dfp)_2CH^+$ cation are needed along the on-the-fly MD trajectories to evaluate the time-resolved UV−vis spectra $S_{UV-vis}(t;\lambda)$. The excitation energies and transition moments are determined by TD-DFT calculations[34−36] at the evolving geometry, the used B-LYP functional has been shown previously to yield reasonable results for excitation energies[37] owing to fortuitous cancellation of errors[38] (for details see Supporting Information).

Solvent Response to the Photolytic Bond Cleavage and Combination Reaction. For the analysis of the geometric changes along the MD trajectories we define appropriate correlation functions. The intersolvent radial correlation function $C_{ISR}(t)$ monitors the microscopic dynamics of the individual trajectory. This information is not directly accessible in an experiment. Therefore, we use the system-bath correlation function $C_{E/SB}(t)$, which establishes the link to experimental observables in the solvation process and validates the microsolvation approach by a comparison with the characteristic librational solvation time.

Intersolvent Radial Correlation Function $C_{ISR}^{ijk}(t)$. The nonequilibrium geometry of MS_{start} induces structural reorganization processes in the solvent. A qualitative picture of these processes is provided by movies of the trajectories (for an example see Supporting Information). A quantitative description is given by the intersolvent radial correlation function $C_{ISR}(t)$

$$C_{ISR}^{ijk}(t) = \frac{\vec{r}_{ij}(t) \cdot \vec{r}_{ik}(t)}{\vec{r}_{ij}(0) \cdot \vec{r}_{ik}(0)} \quad \text{for} \quad i \neq j \neq k \tag{1}$$

where $\vec{r}_{ij}(t)$ and $\vec{r}_{ik}(t)$ are the distances between the solvent molecule i and solvent molecules j and k measured at the oxygen atoms at time t. $\vec{r}_{ij}(0)$ is the equilibrium distance in the MS. The oxygen−oxygen distances, rather than carbon−carbon distances are chosen as the solvent interaction is mainly determined by dipolar hydrogen bond interactions. The value of the correlation function is changed by a change both in the distance between the solvent molecules and also in the relative orientation. It thus describes the spatial motion of the solvent molecules relative to each other. The first solvation shell of the MSs spans a hydrogen bond network without branching; thus three indices are sufficient to characterize the correlation. A decrease in $C_{ISR}^{ijk}(t)$ reflects the reorganization within the hydrogen-bond network.

Solvation Correlation Function $C_{Solv}(t)$. From the MD simulations, the system-bath correlation function $C_{E/SB}(t)$ can be calculated according to

$$C_{E/SB}(t) = \frac{\langle E(t) - E(\infty) \rangle}{\langle E(0) - E(\infty) \rangle} \tag{2}$$

E

dx.doi.org/10.1021/jp300986t | J. Phys. Chem. A XXXX, XXX, XXX−XXX

where $E(t)$ is the potential energy at a given time t, $E(\infty)$ is the potential energy at the end of the simulation ($t = 4$ ps), and $\langle \Delta E \rangle$ means averaging over the set of trajectories. The Fourier transform of $C_{E/SB}(t)$ gives the total spectral density $C_{E/SB}(\omega)$. To extract the experimentally accessible solvation correlation function $C_{Solv}(t)$, the intramolecular high frequency components of the solute and the solvent have to be eliminated. Therefore, we apply a low pass filter to $C_{E/SB}(\omega)$ (i.e., a Heaviside step function with a cutoff frequency of 500 cm^{-1}) and obtain the solvation spectral density $C_{Solv}(\omega)$. Inverse Fourier transformation of $C_{Solv}(\omega)$ yields the solvation correlation function $C_{Solv}(t)$ describing the macroscopic solute solvent reorganization.

$C_{Solv}(t)$ can be monitored in the spectral response function of experiments like the time-resolved Stokes shift demonstrated for complex systems[39,40] and biomolecules.[41] Electronic photon echo experiments[42,43] provide even more detailed information on the spectral response function, measured as the electronic transition frequency fluctuation. Hereby the solvent dynamics can be discriminated from internal system dynamics. More refined time-gated photon echo experiments[44] even allow us to extract the system-bath correlation function $C_{E/SB}(t)$ with the help of analytical models.[45] The solvation dynamics and subsequent chemical changes of the sample can also be determined by transient optical spectroscopy and in particular peak shifts.

The solvation correlation function $C_{Solv}(t)$ is often dominated by an ultrafast subpicosecond component, which resembles a Gaussian shape reflecting the inertial contribution, and a slower component in the pico- to nanosecond regime.[23,42] We focus on the ultrafast component, which is mediated by the first solvation shell.[23,46] The following function $C_{fit}(t)$ is fitted to $C_{Solv}(t)$:

$$C_{fit}(t) = A \cdot \frac{1}{\sigma\sqrt{2\pi}} \exp\left(-\frac{1}{2}\left(\frac{t - t_0}{\sigma}\right)^2\right) + B \tag{3}$$

characterizing the ultrafast component of the solvation process by the time $t_{fast} = \sigma (2 \ln 2)^{1/2}$. The parameter t_{fast} can be directly compared to experimental data and classical MD simulations and in this way we can test the accuracy of our microsolvation approach. The parameter B accounts for the offset in $C_{Solv}(t)$ due to the examined chemical reaction, t_0 accounts for a temporal shift modeling the initial intramolecular processes preceding the solvation.

## V. RESULTS OF THE CALCULATIONS AND COMPARISON TO THE EXPERIMENT

Temporal Evolution of the Model System. The 45 calculated trajectories all show typical patterns that provide a clear atomistic picture of the ultrafast dynamics following the heterolytic bond cleavage in the microsolvated phosphonium salt $(dfp)_2CH-P(CH_3)_3^+$. An example of a trajectory is depicted in Figure 4, where snapshots of the evolving MS geometry at characteristic times are shown. The entire trajectory is available as a movie in the Supporting Information. Different periods can be identified: initially, intramolecular relaxation starts within the benzhydryl cation $(dfp)_2CH^+$. The main relaxation coordinates are the sp^2-hybridization of the central C-atom and the low frequency torsion of the substituted phenyl rings toward a planar benzhydryl geometry (compare snapshot 1 and 2). The sp^2-hybridization is reached after 200 fs, strong oscillations in the rehybridization mode are preserved
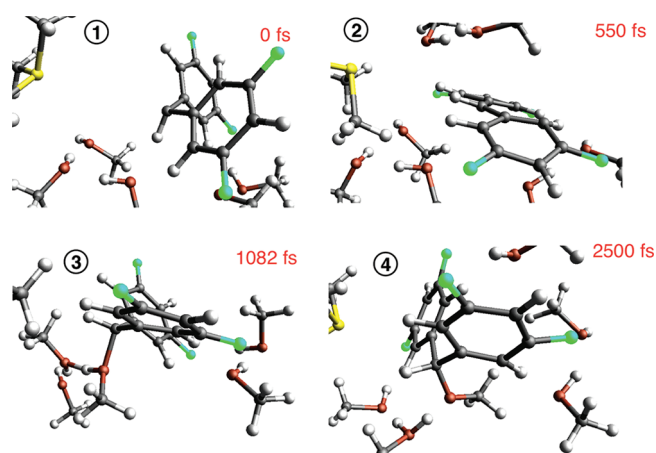
Figure 4. Snapshots at characteristic times of a selected trajectory MS$_i$. The $P(CH_3)_3$ leaving group can be identified by the yellow color of the phosphorus atom. The fluorine atoms at the benzhydryl cation $(dfp)_2CH^+$ are labeled in green. The entire trajectory is available as a movie in the Supporting Information. Every frame corresponds to a time-step $\Delta t = 1$ fs, the bond formation is clearly seen at $t = 1082$ fs (see lower left corner).

due to the remaining excess energy. The low-frequency torsion of the substituted phenyl rings requires about 500 fs to reach planarity. Also in the torsion coordinate the oscillatory motion is preserved.

In parallel to the intramolecular solute relaxation, solvent reorganization starts, which can be quantified by the correlation function $C_{ISR}^{ijk}(t)$ (see eq 1) depicted in Figure 5, which
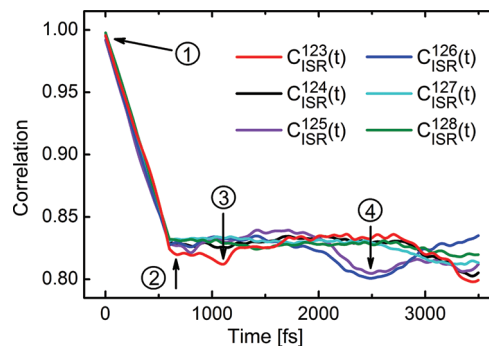
Figure 5. Intersolvent radial correlation function $C_{ISR}^{ijk}(t)$ of the oxygen–oxygen intersolvent vectorial distances of the trajectory shown in Figure 4. The indices ijk indicate the respective molecule in the first solvation shell (see eq 1). Characteristic features of the reaction are highlighted with arrows.

describes the spatial motion of the solvent molecules relative to each other; the indices i,j,k refer to different CH_3OH molecules. From time $t = 0$ fs (snapshot 1) to $t = 550$ fs (snapshot 2) the solvent molecules respond to the new charge distribution after the bond cleavage. The resulting hindered rotation (=librational motion) leads to a reordering within the hydrogen-bond network and reduces the correlation between the solvent molecules (see the steep decrease in $C_{ISR}^{ijk}(t)$ until $t = 550$ fs in Figure 5). After about 1 ps the lone pair of a solvent oxygen atom acts as a nucleophile and forms a new bond with the central C-atom of the benzhydryl cation. The bond formation is indirectly visible in the solvent as decrease of $C_{ISR}^{ijk}(t)$ of the respective solvent molecule (see $C_{ISR}^{123}(t)$ at $t = 1082$ fs, red line). Here the increased interaction between the attacking solvent

and the solute molecule reduces the intersolvent interaction. Subsequent to the nucleophile−electrophile bond formation, a proton transfer is induced to neighboring solvent molecules (see snapshot 4, $t = 2000-2500$ fs and full movie). The proton transfer in turn induces reorganization in the hydrogen-bond network and thus a decrease of the correlation functions $C_{ISR}^{ijk}(t)$ of the two participating solvent molecules (here $C_{ISR}^{125}(t)$ and $C_{ISR}^{126}(t)$). Finally, the solvent molecules adjust to the new charge distribution of the formed benzhydryl methyl ether molecule.

At $t = 0$ fs the total excess energy $E = 4.8$ eV is statistically distributed over the internal degrees of freedom in the MS_{start}. Due to the different initial conditions similarities and differences between the individual trajectories occur. All trajectories show an electrophile−nucleophile bond formation reaction within $t = 4$ ps. The majority of the trajectories involves nucleophilic attack of a methanol molecule, whereas by recombination with the leaving group $P(CH_3)_3$ (geminate recombination) the starting material is also regenerated as minor byproduct. Due to the fact that no kinetic energy is allotted to translational motion of the fragments, an analysis of the recombination reaction with the leaving group is beyond the present model. For a quantitative study of the geminate recombination, diffusion in a larger solvent volume would have to be considered.

In this work we focus on the initial ultrafast relaxation and solvation process within the first solvent shell together with the bond formation reaction of the highly reactive benzhydryl cation $(dfp)_2CH^+$ on a time scale much faster than bulk diffusion. From the analysis of the trajectories we can deduce that intramolecular relaxation of the solute, librational relaxation and hydrogen-bond reorganization occur within the first 4 ps. Which particular solvent molecule attacks the benzhydryl cation, however, varies in the individual trajectories, and so does the time when the bond is formed (700 fs to 2.2 ps). Interestingly, in all cases the conjugated benzhydryl cation is fully developed before the reaction with CH_3OH takes place. Even the ultrafast reaction considered here, which proceeds far below the diffusion limit, can therefore still be described as S_N1 type photosolvolysis.

Ensemble Behavior: Librational Relaxation. From the individual trajectories we can extract information about reactive modes, which are helpful for the mechanistic understanding but not observable in a macroscopic experiment. Instead, the ensemble dynamics has to be considered by averaging over all trajectories and can be used to validate the microsolvation approach. Directly accessible from the on-the-fly MD simulations is the system-bath correlation function $C_{E/SB}(t)$. The results averaged over 30 trajectories that show formation of the methyl ether are shown in Figure 6 as gray line. The decay of the correlation is superimposed by high frequency components arising solely from intramolecular vibrations. The weekly modulated solvation correlation function $C_{Solv}(t)$ (Figure 6, red line) is obtained by applying a low pass filter to $C_{E/SB}(t)$.

As reported for polar solvents,[7,42−44,46] we find that the shape of $C_{Solv}(t)$ resembles a Gaussian decay. Superimposed are low frequency oscillations on the order of 30 cm^{-1} from the torsions of the phenyl rings in the benzhydryl cation. Similar values for the torsional motion of phenyl rings have been reported.[47] The ultrafast initial rise (up to $t = 100$ fs) is an intramolecular artifact still contained in $C_{Solv}(t)$ and reflects the relaxation of the MS_{start} geometry. Part of the kinetic energy deposited in the vibrational modes is converted to potential
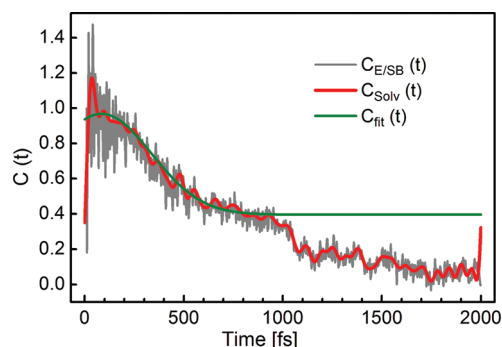
Figure 6. Initial solvent response showing the system-bath correlation $C_{E/SB}(t)$ (gray line), the solvation correlation $C_{Solv}(t)$ (red line), and a Gaussian fit $C_{fit}(t)$ of $C_{Solv}(t)$ according to eq 3 (green line). $C_{fit}(t)$ models the librational solvation process exclusively. The stepwise decay in $C_{Solv}(t)$ and $C_{E/SB}(t)$ is caused by the chemical reaction with the solvent molecules.

energy. In this sense the on-the-fly MD simulations mirror a situation opposite to time-gated stimulated photon echo experiments,[45] which are capable of monitoring the initial components of $C_{Solv}(t)$. Here free induction decay-like relaxation is observed in the solvation correlation function after excitation by a spectrally broad pulse and the excess potential energy is converted into kinetic energy.

The fit-function $C_{fit}(t)$ (eq 3) models the initial librational solvent response (Figure 6, green line) and provides the characteristic librational solvation time t_{fast}. The obtained value $t_{fast} = 296 \pm 5$ fs compares well with the reported experimental data $t_{fast,Exp} = 330$ and 271 fs for two different dye-molecules in CH_3OH.[7,45]

The solvation dynamics $C_{solv}(t)$ extracted from the ensemble of trajectories can now be compared to the experimental observations reported in section III. The solvation is seen as peak shift in the transient spectra. As the $(dfp)_2CH^+$ cation reacts extremely fast with methanol and thus the observable absorption is small and short-lived, we experimentally analyzed the related, somewhat less reactive monofluoro-substituted benzhydryl cation $mfp(Ph)CH^+$. The precursor $mfp(Ph)CHCl$ was dissolved in methanol and excited to the first $\pi-\pi^*$ state ($\lambda_{max} = 270$ nm). Within the first picosecond, the cation absorption band fully develops (Figure 2b, no. 4, and Figure 3). The cation signal disappears again in about 20 ps due to the reaction with methanol.

The experimentally observed shifts of λ_{cation} for the $mfp(Ph)CH^+$ cation during the first 2000 fs are depicted in Figure 3a. We find a pronounced blue shift of 16 nm; a fit according to eq 3 gives a solvation time of $t_{fast} = 507$ fs ($\sigma = 430$ fs). The origin shift t_0 of the Gaussian function $C_{fit}(t)$ is fixed to the theoretically obtained value of 84 fs, which reflects the fact that the geometric relaxation precedes the librational response. The close agreement between the value for t_{fast} derived from the experimental $C_{fit}(t)$ and the one from the Gaussian type decay of $C_{Solv}(t)$ in the theory quantitatively corroborates the proper modeling of the first solvation shell[23] with eight and nine CH_3OH in our model system.

At $t \approx 1100$ fs a significant step in $C_{E/SB}(t)$ and $C_{Solv}(t)$ can be recognized (Figure 6). Around this time a sizable fraction of the trajectories shows the beginning of bond formation between a solvent molecule and the solute. The ensemble data parallel the behavior of the individual trajectory shown in Figures 4 and 5. After $t = 1100$ fs the modulations in $C_{Solv}(t)$

increase again due to the low frequency torsion of the aryl rings reinforced within the generated protonated methyl ether. The reaction leads to a stabilization of 0.43 eV. The initial solvation stabilization within the first picosecond is about 0.84 eV.

Calculation of Time-Resolved UV−Vis Absorption Spectra. The solvation correlation function $C_{Solv}(t)$ discussed so far reflects the librational solvation time t_{fast} and the time of the nucleophile attack. In the following section we extract the spectroscopic UV−vis absorption signal of the benzhydryl cation during its formation and decay from the on-the-fly MD simulations. This signal is an often used probe for the existence of an intermediate structure in S_N type reactions. The prominent observable of the electrophile−nucleophile bond formation reaction is the decrease of absorption of the intermediate benzhydryl cation.[5,11,48,49] In the typical quasi-equilibrium situation the signal properly monitors the concentration of the intermediate cation. However, for the fastest time scales it has to be kept in mind that the optical absorbance is determined not only by the concentration but also by the product of the concentration and the momentary extinction coefficient. The latter can change on the femto-second time scale as we will show below. This is particularly important if the absorption signal is to be used to differentiate between S_N1 and S_N2 type mechanisms—a subject of ongoing discussion.[50] Broad-band UV−vis pump−probe experiments like the one reported above help to resolve the issue by directly monitoring not only the transient absorption at a fixed maximum but also the temporal evolution of the spectral shape and the position of the band maximum.

The time-resolved UV−vis spectrum $S_{UV-VIS}(t,\lambda)$ can be readily derived from the on-the-fly MD results and allows a direct comparison to the experiment. Every individual trajectory MS_i out of the total ensemble is sampled at time-steps Δt_{sample} to extract the actual geometry at time t (a sampling interval of $\Delta t_{sample} = 100$ fs is applied in the present situation). These geometries are used to calculate the excitation energy $\lambda_0(i,t)$ and the corresponding transition moment $I(\lambda_0,i,t)$ to the excited singlet states in a TD-DFT[34−36] calculation. Every electronic transition is subsequently modeled with a Gaussian line width $\Delta\tilde\nu = 800$ cm^{-1} (corresponding to $\Delta\lambda \approx 15$ nm) to account for inhomogeneous broadening due to intermolecular collisions. We want to emphasize that the line width $\Delta\tilde\nu$ is the only empirical parameter entering the simulation protocol. All other quantities are derived from density functional theory. The obtained absorption spectra at time t are averaged over all n trajectories. The final time-resolved spectrum $S_{UV-VIS}(t,\lambda)$ is expressed by

$$S_{UV-vis}(t,\lambda) = \frac{1}{n}\sum_{i=1}^{n}\left[\int I^2(\lambda_0,i,t)\cdot G(\lambda',\lambda_0(i,t))\,d\lambda'\right]$$

with

$$G(\lambda',\lambda_0(i,t)) = \frac{1}{\sqrt{2\pi}\,\Delta\lambda}\exp\left(-\frac{1}{2}\left(\frac{\lambda'-\lambda_0(i,t)}{\Delta\lambda}\right)^2\right)$$

(4)

With eq 4 we can follow the temporal evolution of the benzhydryl cations' electronic absorption spectra in a non-equilibrium ensemble subsequent to the photolytic bond cleavage.

The predicted time-resolved electronic absorption spectrum of the microsolvated $(dfp)_2CH^+$ is presented in Figure 7a and selected time slices of the signal in Figure 7b. At early times a
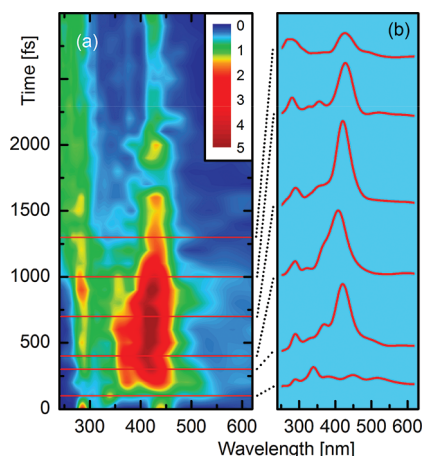
Figure 7. Calculated transient absorption signal (oscillator strength) of the microsolvated $(dfp)_2CH^+$ cation. (a) Calculated time-resolved UV−vis spectrum $S_{UV-VIS}(t,\lambda)$. (b) Time slices of the signal taken at times marked by the red lines in the left plot. The oscillator strength is given in atomic units $\times 10^{-1}$.

broad, but weak, band is already present ($t = 100$ fs, 370−460 nm; Figure 7). Within 600 fs this band narrows and increases in intensity. At $t = 700$ fs the cation band reaches the maximal intensity (see time slice 4 in Figure 7). The increase in the signal intensity correlates with the intra- and intermolecular relaxation processes, which lead to the formation of a planar, stabilized benzhydryl cation (see previous sections). Thus the rise of the observed transient cation signal is controlled by solvent reorganization and solute relaxation stabilizing the initially hot cation generated by the bond cleavage. It should be kept in mind that the MD calculations start after bond cleavage. This means that the increase in optical signal is not at all due to an increase in cation concentration.

We find that the complete stabilization takes 700 fs, which is significantly longer than the phototriggered bond cleavage, calculated to be completed within 220 fs in the case of benzhydryl chloride Ph_2CH-Cl.[17] Additionally, a blue shift of 20 nm of the absorption band from $\lambda_{edge} = 460-440$ nm is observed within the first picosecond. This shift is caused by the solvent stabilization and the intramolecular relaxation. The magnitude of the shift, but not the temporal evolution, is also accessible from electrostatic continuum model calculations[51,52] on the isolated $(dfp)_2CH^+$ cation. It should be noted that the values for solvation times and shifts of chemically stable chromophores that also do not undergo any significant geometric relaxation[7] are only one contribution to the complete relaxation observations on the system discussed here.

In Table 2 the experimental and calculated absorption spectra of the microsolvated $(dfp)_2CH^+$ cation are compared. Already the gas phase calculations for $(dfp)_2CH^+$ are in good agreement with the experimental excitation energy. The

Table 2. Calculated Excitation Energies (TDDFT-BLYP) at $t = 700$ fs for a Single $(dfp)_2CH^+$ and Microsolvated in Methanol in Comparison to the Measured Band Position

	λ_{max} (nm)	osc strength (au)
$(dfp)_2CH^+$ (gas phase)	433.3	0.53
$(dfp)_2CH^+ + P(CH_3)_3 + 8CH_3OH$	426	0.19
$(dfp)_2CH^+ + P(CH_3)_3 + 9CH_3OH$	424	0.23
experiment	433	

H

dx.doi.org/10.1021/jp300986t | J. Phys. Chem. A XXXX, XXX, XXX−XXX

excitations are characterized as a $\pi-\pi^*$ transition. The calculated spectrum for the microsolvated MS (Table 2, lines 3 and 4) is extracted at a simulation time $t = 700$ fs when the maximum of the signal has formed. The absorption wavelength shows excellent agreement with the experiment ($\lambda_{\mathrm{max,exp}} = 433$ nm vs $\lambda_{\mathrm{max,theo}} = 426$ nm).

After 700 fs the cation signal decreases due to the bond formation reaction with solvent molecules. The appearance of a new absorption band in the region of $\lambda \approx 270$ nm is attributed to the formation of the methyl ether. The mean calculated lifetime of the $(\mathrm{dfp})_2\mathrm{CH}^+$ cation is on the order of 1.2 ps, evaluated when the simulated signal drops beyond $1/e$ of its maximum value. For the less reactive $\mathrm{mfp}(\mathrm{Ph})\mathrm{CH}^+$ used in the experiment a time of 22 ps is found experimentally.

VI. SUMMARY, GENERAL DISCUSSION, AND CONCLUSIONS

Highly reactive cations can be generated by photolysis.[11,14,17,32] They undergo an electrophile−nucleophile bond formation reaction with nucleophilic solvents like $\mathrm{CH}_3\mathrm{OH}$ that can be much faster than typical diffusion-limited reactions.[48] With ultrafast photoinitiation of the bond cleavage, the transient absorption at the known electronic absorption band of the benzhydryl cation serves as a measure for the evolving cation concentration. Therefore, the appearance of a transient signal should allow us to decide whether the reaction proceeds as photo-S_N1 or photo-S_N2 type. This approach does, however, assume that the association between the benzhydryl cations' spectroscopic signal and the concentration holds even at the very fastest times.

In this work we provide a link between the atomistic reaction dynamics and the observable UV−vis absorption in the solvolysis of benzhydryl cations. We have calculated the time-resolved UV−vis spectrum $S_{\mathrm{UV-VIS}}(t,\lambda)$ from the reactive on-the-fly MD simulations covering the processes of intramolecular relaxation, librational solvation, bond formation, and subsequent proton transfer reactions. The solvent is simulated by a microsolvation approach, which is validated by the solute−solvent correlation function $C_{\mathrm{Solv}}(t)$ being in good agreement with initial libration solvation processes reported in literature.[7,45] The calculated solvation time closely matches the dynamic peak shift of the cation band found in the experiment and even the magnitudes of the spectral shifts match well. The dynamics of the transient absorption thus provides not only information about the concentration of the reactive intermediates. An elaborate evaluation of the experimental recordings reveals the additional information of the absorbance peak shift which provides extra insight into the evolution at the atomic level.

We show that the bimolecular reaction of the cation is completed within 4 ps, much before diffusional processes are relevant. Selected individual trajectories allow the microscopic interpretation of the photosolvolysis and show a 300 fs time scale for the intramolecular solute relaxation. The ensemble dynamics and the complete reaction time are captured by the solvation correlation function $C_{\mathrm{Solv}}(t)$ and the time-resolved UV−vis signal $S_{\mathrm{UV-VIS}}(t,\lambda)$. Both of them reveal a two step reaction mechanism.

In the first hundreds of femtoseconds the highly reactive $(\mathrm{dfp})_2\mathrm{CH}^+$ relaxes internally and is further stabilized by solvation, to form the equilibrated benzhydryl cation with its known spectroscopic signature. Subsequently, the electrophile−nucleophile bond formation, which leads to the generation of

the methyl ether after subsequent deprotonation restricts the cation lifetime to about 1 ps. The derived macroscopic observable $S_{\mathrm{UV-VIS}}(t,\lambda)$ can be directly compared to the experimentally observed transient cation signal. For this purpose we summarize the results presented above (Figures 2 and 7) in Figure 8.
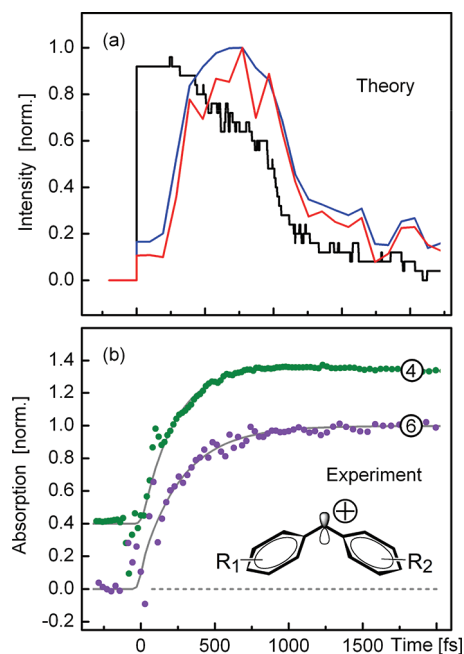
Figure 8. (a) Calculated decrease of the $(\mathrm{dfp})_2\mathrm{CH}^+$ cation population (black line) and evolution of the transient absorption signal $S_{\mathrm{UV-VIS}}(t)$ evaluated at the cation band maximum (426 nm, red line) and by integration over the band (blue line). (b) Normalized transient absorption signal of the benzhydryl cation for the compound−solvent combinations 4 and 6 in Figure 2b.

The transient absorption measurements (selected curves in Figure 8b, taken from Figure 2b) show an increase over the whole cation band with an effective 300 fs time constant. In the calculation the bond cleavage is assumed to be complete at $t = 0$ fs, but the nascent microsolvated benzhydryl cation is still in the equilibrium geometry of the precursor system. The cation population starts to decrease with just an inertial delay due to the statistical reaction with a neighboring methanol (see black line in Figure 8a). At the same time the predicted optical signals (red line in Figure 8a) for the maximum and blue line for the integral) only increase "slowly" due to the planarization and solvation investigated in detail by the on-the-fly MD calculations. It might be fortuitous, but the apparent rise of the signals match quite well between theory and experiment. We therefore postulate that the 300 fs time constant observed for the initial increase of the benzhydryl cations' absorbance in all investigated combinations of diphenylmethyl derivatives and solvents (Figure 2) do not provide a determination of the bond cleavage time but only an upper limit. The initial relaxation mechanisms investigated in detail seem to mask the even faster bond cleavage. As a consequence, there is no positive evidence for any kind of barrier that might be deduced from a 300 fs reaction time.

We believe that this retardation of the optical signal relative to the population is a general feature of practically barrierless chemical transformations. The change in electronic config-

uration, i.e., the bond cleavage, is faster than the geometric relaxation of the bulky molecular constituents and the solvent relaxation. The intensities and the absorption maxima of the UV/vis absorption bands that are used to identify the products are, however, strongly affected by the geometry. Because the spectroscopic signatures of the transient species are typically reported for largely relaxed structures they cannot directly be used for the interpretation of the experimental observations at very early times. As a consequence, the apparent time constant of cation generation (see above) might not yet monitor the actual generation of the species. Dedicated experimental investigations with largely improved temporal resolution are in progress to decipher the bond cleavage itself. A similar observation of signal retardation has been recently reported for the photodissociation of the methyl iodide dimer.[53]

A complete analysis of the fastest chemical events will only be possible by the combination of experimental observations with tens of femtosecond resolution and broad spectral coverage, state of the art quantum dynamical calculations, and the choice and synthesis of the proper molecules. The envisioned understanding is beyond the present possibility of each of these techniques by themselves, only the combination can succeed. The picture of a chromophore in a passive dielectricum will certainly not suffice for the theoretical description. Interestingly, UV−vis spectroscopy can render information on a wide range of aspects like the initial solvation following the ultrafast excitation, the intramolecular relaxation and the subsequent chemical reaction. Additional evidence could come from transient IR measurements that could help to identify the reactive modes and the role of the hydrogen bond network. To unravel the existing complexity, the methods for evaluation have to mature to the same level that both the calculations and experiments have already reached.

■ ASSOCIATED CONTENT

⑤ Supporting Information
Information on chemicals used. Detailed description for the On-the-fly MD calculations, the initial conditions of the cluster, the quantum chemical methods, and model compounds for microsolvation. A table of bond distances. A movie showing a calculated trajectory. This material is available free of charge via the Internet at http://pubs.acs.org.

■ AUTHOR INFORMATION

Corresponding Author
*E-mail: E.R., Riedle@physik.uni-muenchen.de; R.d.V.: Regina. de_Vivie@cup.uni-muenchen.de.

Present Address
§Department of Chemistry, University of California, Irvine, CA 92697-2025, USA. E-mail: bfingerh@uci.edu

Notes
The authors declare no competing financial interest.

■ ACKNOWLEDGMENTS

■ REFERENCES

(1) Neumark, D. M. *Acc. Chem. Res.* **1993**, *26*, 33−39.
(2) Polanyi, J. C.; Zewail, A. H. *Acc. Chem. Res.* **1995**, *28*, 119−132.
(3) Zewail, A. H. *J. Phys. Chem. A* **2000**, *104*, 5660−5694.
(4) Cahoon, J. F.; Sawyer, K. R.; Schlegel, J. P.; Harris, C. B. *Science* **2008**, *319*, 1820−1823.
(5) Megerle, U.; Pugliesi, I.; Schriever, C.; Sailer, C. F.; Riedle, E. *Appl. Phys. B: Laser Opt.* **2009**, *96*, 215−231.
(6) Schalk, O.; Boguslavskiy, A. E.; Stolow, A.; Schuurman, M. S. *J. Am. Chem. Soc.* **2011**, *133*, 16451−16458.
(7) Horng, M. L.; Gardecki, J. A.; Papazyan, A.; Maroncelli, M. *J. Phys. Chem.* **1995**, *99*, 17311−17337.
(8) Baiz, C. R.; Kubarych, K. J. *J. Am. Chem. Soc.* **2010**, *132*, 12784−12785.
(9) Glowacki, D. R.; Rose, R. R.; Greaves, S. J.; Orr-Ewing, A. J.; Harvey, J. N. *Nature Chem.* **2011**, *3*, 850−855.
(10) Mikosch, J.; Trippel, S.; Eichhorn, C.; Otto, R.; Lourderaj, U.; Zhang, J. X.; Hase, W. L.; Weidemüller, M.; Wester, R. *Science* **2008**, *319*, 183−186.
(11) Peters, K. S. *Chem. Rev.* **2007**, *107*, 859−873.
(12) Sailer, C. F.; Singh, R. B.; Ammer, J.; Riedle, E.; Pugliesi, I. *Chem. Phys. Lett.* **2011**, *512*, 60−65.
(13) Barbatti, M.; Granucci, G.; Persico, M.; Ruckenbauer, M.; Vazdar, M.; Eckert-Maksić, M.; Lischka, H. *J. Photochem. Photobiol. A* **2007**, *190*, 228−240.
(14) Bartl, J.; Steenken, S.; Mayr, H.; McClelland, R. A. *J. Am. Chem. Soc.* **1990**, *112*, 6918−6928.
(15) Alonso, E. O.; Johnston, L. J.; Scaiano, J. C.; Toscano, V. G. *Can. J. Chem.* **1992**, *70*, 1784−1794.
(16) Lipson, M.; Deniz, A. A.; Peters, K. S. *Chem. Phys. Lett.* **1998**, *288*, 781−784.
(17) Fingerhut, B. P.; Geppert, D.; de Vivie-Riedle, R. *Chem. Phys.* **2008**, *343*, 329−339.
(18) Miranda, M. A.; Pérez-Prieto, J.; Font-Sanchis, E.; Scaiano, J. C. *Acc. Chem. Res.* **2001**, *34*, 717−726.
(19) McClelland, R. A. *Tetrahedron* **1996**, *52*, 6823−6858.
(20) Mayr, H.; Kempf, B.; Ofial, A. R. *Acc. Chem. Res.* **2003**, *36*, 66−77.
(21) Nolte, C.; Mayr, H. *Eur. J. Org. Chem.* **2010**, 1435−1439.
(22) Nenov, A.; Cordes, T.; Herzog, T. T.; Zinth, W.; de Vivie-Riedle, R. *J. Phys. Chem. A* **2010**, *114*, 13016−13030.
(23) Ladanyi, B. M.; Stratt, R. M. *J. Phys. Chem.* **1995**, *99*, 2502−2511.
(24) Minegishi, S.; Kobayashi, S.; Mayr, H. *J. Am. Chem. Soc.* **2004**, *126*, 5174−5181.
(25) Treutler, O.; Ahlrichs, R. *J. Chem. Phys.* **1995**, *102*, 346−354.
(26) von Arnim, M.; Ahlrichs, R. *J. Comput. Chem.* **1998**, *19*, 1746−1746.
(27) Eichkorn, K.; Weigend, F.; Treutler, O.; Ahlrichs, R. *Theo. Chem. Acc.* **1997**, *97*, 119−124.
(28) Grimme, S. *J. Comput. Chem.* **2004**, *25*, 1463−1473.
(29) Grimme, S. *J. Comput. Chem.* **2006**, *27*, 1787−1799.
(30) Becke, A. D. *Phys. Rev. A* **1988**, *38*, 3098−3100.
(31) Lee, C.; Yang, W.; Parr, R..G. *Phys. Rev. B* **1988**, *37*, 785−789.
(32) Lipson, M.; Deniz, A. A.; Peters, K. S. *J. Am. Chem. Soc.* **1996**, *118*, 2992−2997.
(33) Sellner, B.; Barbatti, M.; Lischka, H. *J. Chem. Phys.* **2009**, *131*, 024312.
(34) Furche, F.; Rappoport, D. *Theo. Comput. Chem.* **2005**, *16*, 93−128.
(35) Bauernschmitt, R.; Häser, M.; Treutler, O.; Ahlrichs, R. *Chem. Phys. Lett.* **1997**, *264*, 573−578.
(36) Bauernschmitt, R.; Ahlrichs, R. *Chem. Phys. Lett.* **1996**, *256*, 454−464.
(37) Dreuw, A.; Weisman, J. L.; Head-Gordon, M. *J. Chem. Phys.*. **2003**, *119*, 2943.
(38) Dreuw, A.; Harbach, P. H. P.; Mewes, J. M.; Wormit, M. *Theor. Chem. Acc.* **2010**, *125*, 419−426.

(39) Pérez Lustres, J. L.; Kovalenko, S. A.; Mosquera, M.; Senyushkina, T.; Flasche, W.; Ernsting, N. P. *Angew. Chem.* **2005**, *117*, 5779−5783.

(40) Bose, S.; Adhikary, R.; Mukherjee, P.; Song, X.; Petrich, J. W. *J. Phys. Chem. B* **2009**, *113*, 11061−11068.

(41) Pal, S. K.; Peon, J.; Bagchi, B.; Zewail, A. H. *J. Phys. Chem. B* **2002**, *106*, 12376−12395.

(42) Cho, M.; Yu, J.-Y.; Joo, T.; Nagasawa, Y.; Passino, S. A.; Fleming, G. R. *J. Phys. Chem.* **1996**, *100*, 11944−11953.

(43) Nibbering, E. T. J.; Fidder, H.; Pines, E. *Annu. Rev. Phys. Chem.* **2005**, *56*, 337−67.

(44) de Boeij, W. P.; Pshenichnikov, M. S.; Wiersma, D. A. *Annu. Rev. Phys. Chem.* **1998**, *49*, 99−123.

(45) de Boeij, W. P.; Pshenichnikov, M. S.; Wiersma, D. A. *J. Phys. Chem.* **1996**, *100*, 11806−11823.

(46) Ladanyi, B. M.; Stratt, R. M. *J. Phys. Chem.* **1996**, *100*, 1266−1282.

(47) Glasbeek, M.; Zhang, H. *Chem. Rev.* **2004**, *104*, 1929−1954.

(48) Peon, J.; Polshakov, D.; Kohler, B. *J. Am. Chem. Soc..* **2002**, *124*, 6428−6438.

(49) Schaller, H. F.; Schmidhammer, U.; Riedle, E.; Mayr, H. *Chem. Eur. J.* **2008**, *14*, 3866−3868.

(50) Phan, T. B.; Nolte, C.; Kobayashi, S.; Ofial, A. R.; Mayr, H. *J. Am. Chem. Soc.* **2009**, *131*, 11392−11401.

(51) Cammi, R.; Mennucci, B.; Tomasi, J. *J. Phys. Chem. A* **2000**, *104*, 5631−5637.

(52) Scalmani, G.; Frisch, M. J.; Mennucci, B.; Tomasi, J.; Cammi, R.; Barone, V. *J. Chem. Phys.* **2006**, *124*, 094107.

(53) de Nalda, R.; Durá, J.; González-Vázquez, J.; Loriot, V.; Banares, L. *Phys. Chem. Chem. Phys.* **2011**, *13*, 13295−13304.

Supplementary Information

Build-up and Decay of the Optical Absorption in the Ultrafast Generation and Reaction of Benzhydryl Cations in Solution

Benjamin P. Fingerhut,[a,§] Christian F. Sailer,[b] Johannes Ammer,[a] Eberhard Riedle,*[b] and Regina de Vivie-Riedle*[a]

[a] Department Chemie, Ludwig-Maximilians-Universität (LMU), Butenandt-Str. 11, 81377 München, Germany.

[b] Lehrstuhl für BioMolekulare Optik, Ludwig-Maximilians-Universität (LMU), Oettingenstr. 67, 80538 München, Germany.

* Corresponding author: E-mail: Riedle@physik.uni-muenchen.de

Regina.de_Vivie@cup.uni-muenchen.de

§ Current address:

Department of Chemistry, University of California, Irvine, California 92697-2025, USA

E-mail: bfingerh@uci.edu

1   Materials

The solvents used were of the highest spectroscopic grade available. Benzhydryl chloride (Ph_2CHCl) was purchased from Sigma-Aldrich and used without further purification. The derivatives $(tol)_2CHCl$ and $mfp(Ph)CHCl$ were prepared as described in references [2, 3]. The synthesis of $tol(Ph)CH-PPh_3^+ BF_4^-$ and $(mfp)_2CH-PPh_3^+ BF_4^-$ will be reported elsewhere.

3,3',5-Trifluorobenzhydryl chloride dfp(mfp)CHCl was obtained from thionyl chloride (1.3 mL, 18 mmol) and 3,3',5-trifluorobenzhydrol (dfp(mfp)CHOH) [3] (3.00 g, 12.6 mmol) in dichloromethane (10 mL). The crude product was distilled in the vacuum (196–198 °C / 1.1×10^{-2} mbar) to give a colorless oil (2.3 g, 72 %).

1H NMR (300 MHz, $CDCl_3$): $\delta = 5.98$ (s, 1 H, CHCl), 6.74 (tt, $^3J_{HF} = 8.7$ Hz, $^4J_{HH} = 2.3$ Hz, 1 H, 4-ArH), 6.89-7.04 (m, 3 H, ArH), 7.08-7.16 (m, 2 H, ArH), 7.28-7.35 ppm. (m, 1 H, ArH);

13C NMR {1H}(75.5 MHz, $CDCl_3$): $\delta = 61.8$ (td, $^4J_{CF} = 2.3$ Hz, $^4J_{CF} = 2.1$ Hz, CHCl), 103.8 (t, $^2J_{CF} = 25.3$ Hz, 4-Ar), 110.7-111.1 (m, AXX'-system, 2,6-Ar), 114.9 (d, $^2J_{CF} = 23.0$ Hz, 2'-Ar or 4'-Ar), 115.7 (d, $^2J_{CF} = 21.2$ Hz, 2'-Ar or 4'-Ar), 123.3 (d, $^4J_{CF} = 3.0$ Hz, 6'-Ar), 130.4 (d, $^3J_{CF} = 8.3$ Hz, 5'-Ar), 142.3 (d, $^3J_{CF} = 7.2$ Hz, 1'-Ar), 144.2 (t, $^3J_{CF} = 9.0$ Hz, 1-Ar), 162.8 (d, $^1J_{CF} = 247.5$ Hz, 3'-Ar), 163.0 ppm. (dd, $^1J_{CF} = 249.4$ Hz, $^3J_{CF} = 12.1$ Hz, 3,5'-Ar);

19F-NMR (282 MHz, $CDCl_3$): −108.4 - −108.5 ppm. (m, 3,5-F); −111.6 (m, 3'-F);

MS (+EI): m/z (%) = 256.1 (3) [M+], 237.2 (4) 222.2 (36), 221.1 (100) [M−Cl], 219.1 (34), 201.1 (35);

Anal. calcd. for $C_{13}H_8ClF_3$: C, 60.84; H, 3.14. Found: C, 60.61; H, 3.16.
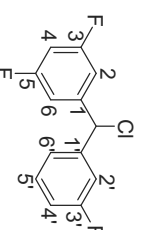
2 Theoretical concepts

We summarize the theoretical methods for the microsolvation approach. Different quantum chemical methods are used to obtain accurate ground state geometries, which are needed to generate the initial conditions for the on-the-fly MD simulations. We consider the solvation dynamics, the intramolecular relaxation and the electrophile-nucleophile bond formation. With appropriate correlation functions we analyze the relaxation process and quantify the accuracy of the microsolvation approach.

On-the-fly Molecular Dynamics (MD)

The dynamics of the nascent microsolvated benzhydryl cation (designated as model system MS_{start}) is simulated by on-the-fly MD. The method requires an energy and a gradient calculation of the MS_{start} on the respective level of theory at every time-step ($\Delta t = 1$ fs), but avoids the construction of global potential energy surfaces. In all dynamics simulations energies and gradients are calculated on the RI-BLYP-D level of theory [4-10] with the parallel version of the Turbomole program package [11]. The accuracy of the RI-BLYP-D method is tested against different functionals and MP2 as a wave function based method which inherently includes the dispersion interaction (for details see below). The resulting equations of motion of the nuclei are calculated with the Newton-X package [12]. Time integration is performed with the velocity-verlet algorithm [13].

Initial conditions. The non-equilibrium start geometries MS_{start} for the on-the-fly MD simulations that mimic the nascent microsolvated benzhydryl cation are generated by breaking the bond between the central methyl carbon and the phosphor atom in the phosphine leaving group (C^1-P bond) in $(dfp)_2CH-P^+(CH_3)_3$ with all other degrees of freedom frozen in the precursor cluster (PC: $(dfp)_2CH-P^+(CH_3)_3 \cdot XCH_3OH$) equilibrium geometry. The leaving group $P(CH_3)_3$ is placed at a distance of 5.0 Å from the central C^1-Atom (see Fig. 1). According to the best available knowledge [14-16] we assume that the ultrafast bond cleavage (fs-ps) proceeds faster than the intramolecular relaxation. The initial velocities are generated by depositing the excitation energy of an assumed pump pulse $E_{h\nu} = 4.8$ eV ($\lambda = 258$ nm) as kinetic energy equally in all degrees of freedom [17] in the MS_{start}. The error due to the neglect of the ground state dissociation enthalpy is estimated to be only 10 % [18]. A Gaussian distributed random number is assigned as initial velocity v_i to every atom i. After

removing the center of mass translation and rotation, the kinetic energy of atom i can be rescaled according to

$$v_i^{ini} = \sqrt{\frac{2E_{Kin}}{\sum_k M_k v_k^2}}\, v_i, \quad for \quad k \neq i \qquad (1)$$

where M_k is the mass of all other atoms k. The Gaussian distributed initial velocities v_i^{ini} describe the non-equilibrium ensemble subsequent to photolysis and not a canonical ensemble under equilibrium conditions.

This velocity distribution (vs. Wigner) is motivated by the ultrafast bond cleavage. Due to the dissociative character of the excited state potential energy surface most of the excitation energy is directly converted into kinetic energy of the dissociating fragments within 200 fs [16]. In the liquid phase the fragments are confined in the first solvation shell and kinetic energy is transferred by elastic scattering from the solute to solvent molecules. In this work the subsequent redistribution within the solute and solvent vibrational modes is investigated. The total simulation time of the individual trajectories is 4 ps (time step $\Delta t = 1$fs). For the given initial conditions a total of 45 independent trajectories $\{MS_i(0)\}$ (i = 1, 2, … 45) are generated. The considered bond formation reaction of the benzhydryl cation obeys a single reaction channel which makes the statistical discrimination and assignment of branching ratios, typically requiring many trajectories [19, 20], unnecessary. All 45 trajectories lead to a bond formation within 4 ps. The statistical acceptability for the temporal evolution is tested against experimental observable correlation functions and spectra (see Results and Discussion).

Quantum chemical methods. The electronic Schrödinger equation, required to be evaluated in in every time step, is solved on the DFT level of theory [4, 5] within the resolution of the identity approximation [6], including empirical dispersive energy correction (RI-DFT-D) [7, 8]. All calculations are done with the Turbomole program package [11] using a split valence double zeta basis set (def-SV(P)). The Coulomb 2-el integrals are evaluated within the resolution of the identity approximation [6], where an auxiliary def-TZVP basis is used. Regarding the choice of the basis set, one could argue that the limited def-SV(P) is inadequate to properly describe excited states; however, the main interest here is the simulation of geometrical changes in the ground state and the analysis of excited states is limited to valence

states π - π* (see below), for which the use of larger basis sets including diffuse functions should not be necessary [21, 22].

The B-LYP functional [9, 10] is used to obtain reliable equilibrium geometries, gradients and potential energy curvatures (i.e. harmonic frequencies) [23] probably due to systematic error compensation [24-27]. We optimized a reference cluster (RC) consisting of the precursor molecule $Ph_2CH-P^+(CH_3)_3$ and four methanol molecules (RC: $DPM-P^+(CH_3)_3 \cdot 4CH_3OH$, 57 atoms). The moderate size of the cluster allows to test the accuracy of the quantum chemical method against other functionals (RI-BLYP-D [4-10] vs. RI-BLYP [4-6, 9, 10] vs. tpss [28, 29] vs. M06-HF [30, 31]) and to estimate the importance of the dispersion correction. Further reference calculations with wave function based methods (RI-MP2) [32-34], which inherently include the intermolecular interactions, were also performed.

Based on this comparison, RI-BLYP-D is selected to determine how many methanol (CH_3OH) molecules are needed to complete the first solvation shell. In order to reduce the MD simulation time, the more reactive tetra-fluoro derivate $(dfp)_2CH-P^+(CH_3)_3$ rather than $Ph_2CH-P^+(CH_3)_3$ was chosen as precursor molecule. Two different precursor clusters (PC), one surrounded by eight methanol molecules (PC1: $(dfp)_2CH-P^+(CH_3)_3 \cdot 8CH_3OH$, 85 atoms) and one surrounded by nine methanol molecules (PC2: $(dfp)_2CH-P^+(CH_3)_3 \cdot 9CH_3OH$, 90 atoms) are optimized as reference geometry for the molecular dynamics simulations. The choice of two different precursor clusters accounts for the fact that a first solvation shell is not uniquely defined and can take up more than one configuration. The CPU-requirement for a combined energy and gradient calculation of the PC's at each time-step is on the order of two minutes on eight processors of a modern linux cluster. This allows for a dynamic description of the electrophile-nucleophile bond formation reaction in on-the-fly MD simulations up to a ps timescale.

The electronically excited π− π* states of the micro-solvated $(dfp)_2CH^+$ cation are needed along the on-the-fly MD trajectories to evaluate the time resolved UV-VIS spectra $S_{UV-VIS}(t, \lambda)$. The excitation energies and transition moments are calculated by TD-DFT calculations [35-37] at the evaluated geometries. Though the B-LYP functional neglects non-local exchange the used methodology has been shown previously to yield reasonable results for excitation energies [38] owing to fortuitous cancelation of errors [24]. Abundant excited charge transfer (CT) states suffer from electron transfer self-interaction in TD-DFT, resulting in too low excitation energies of the spurious CT states [39, 40]. Here they are discarded in

the discussion of the locally excited π - π* valence state of $(dfp)_2CH^+$ (characterized by the HOMO-LUMO single excitation).

Model compounds for microsolvation.

A reference cluster (RC) consisting of the precursor molecule $Ph_2CH-P^+(CH_3)_3$ surrounded by four methanol molecules is used as a benchmark for the ab initio method appropriate for the larger precursor clusters (PC1 and PC2). The moderate cluster size allows the optimization of the equilibrium geometry of the RC with different functionals (tpss, RI-BLYP, RI-BLYP-D, M06-HF) and at a wave function based level of theory (RI-MP2). RI-MP2 serves as reference method for the intermolecular interactions as they are inherently included. All equilibrium geometries are confirmed by normal mode analysis and are summarized in Table 1.

The hydrogen bond network (upper block in Table 1) is of similar strength in all DFT based methods, but the bonds are slightly shorter than in the RI-MP2 optimized minimum. The inter-solvent C-C distances ($C_{CH_3OH} - C_{CH_3OH}$, middle block in Table 1) obtained from traditional DFT methods differ substantially from the RI-MP2 results, which show much shorter $C_{CH_3OH} - C_{CH_3OH}$ - distances ($\Delta r = 0.2$ Å for the minimal distances). This error can be eliminated by the dispersion corrected functional RI-BLYP-D indicating that traditional DFT methods underestimate the non-polar C-C interaction of the hydrogen bonded solvent. $C_{CH_3OH} - C_{CH_3OH}$ - distances calculated with the hybrid meta-GGA functional M06-HF are similar to the RI-BLYP-D values. The binding interaction between solute and solvent are described well by the RI-MP2 and the RI-BLYP-D calculations as visible in similar mean values for $C^1 - O_{CH_3OH}$ distances (lower block in Table 1). Again traditional DFT underestimates this solute-solvent interaction. As a consequence we selected the RI-BLYP-D method as best compromise between accuracy and computational efficiency to optimize the PC's.

The PC is designed as a precursor molecule $(dfp)_2CH-P^+(CH_3)_3$ surrounded by a first solvation shell. We find that eight to nine CH_3OH molecules are required to close the first shell. The large variances of the $C^1 - O_{CH_3OH}$ solute-solvent distances in the PC equilibrium geometries (see lower block in Table 1), compared to the RC geometries are a result of surface crowding effects. Due to steric hindrance not all solvent molecules can cover the solute simultaneously. Between themselves the solvent molecules form a pronounced inter-solvent hydrogen bond network, the coordination towards the F-atoms is only weakly

developed. Furthermore our calculations show that already the solvation of a charged solute in the polar solvent CH_3OH ($\varepsilon = 32.63$, dipole-moment = 1.77 debye) requires the dispersion interaction to be considered besides the dipolar interaction. Otherwise over-binding within the hydrogen-bond network is observed, at the cost of the solute-solvent interaction.

3 References

[1] Megerle, U.; Pugliesi, I.; Schriever, C.; Sailer, C. F.; Riedle, E. *Appl. Phys. B* **2009**, *96*, 215-231.

[2] Denegri, B.; Streiter, A.; Jurić, S.; Ofial, A. R.; Kronja, O.; Mayr, H. *Chem. Eur. J.* **2006**, *12*, 1648-1656.

[3] Nolte, C.; Mayr, H. *Eur. J. Org. Chem.* **2010**, 1435-1439.

[4] Treutler, O.; Ahlrichs, R. *J. Chem. Phys.* **1995**, *102*, 346-354.

[5] von Arnim, M.; Ahlrichs, R. *J. Comput. Chem.* **1998**, *19*, 1746-1746.

[6] Eichkorn, K.; Weigend, F.; Treutler, O.; Ahlrichs, R. *Theo. Chem. Acc.* **1997**, *97*, 119-124.

[7] Grimme, S. *J. Comput. Chem.* **2004**, *25*, 1463-1473.

[8] Grimme, S. *J. Comput. Chem.* **2006**, *27*, 1787-1799.

[9] Becke, A. D. *Phys. Rev. A* **1988**, *38*, 3098-3100.

[10] Lee, C.; Yang, W.; Parr, R.G. *Phys. Rev. B* **1988**, *37*, 785-789.

[11] Ahlrichs, R.; Bär, M.; Häser, M.; Horn, H.; Kölmel, C. *Chem. Phys. Lett.* **1989**, *162*, 165-169.

[12] Barbatti, M.; Granucci, G.; Persico, M.; Ruckenbauer, M.; Vazdar, M.; Eckert-Maksić, M.; Lischka, H. *J. Photochem. Photobiol. A* **2007**, *190*, 228-240.

[13] Swope, W. C.; Andersen, H. C.; Berens, P. H.; Wilson, K. R. *J. Chem. Phys.* **1982**, *76*, 637.

[14] Peters, K. S. *Chem. Rev.* **2007**, *107*, 859-873.

[15] Lipson, M.; Deniz, A. A.; Peters, K. S. *J. Am. Chem. Soc.* **1996**, *118*, 2992-2997.

[16] Fingerhut, B. P.; Geppert, D.; de Vivie-Riedle, R. *Chem. Phys.* **2008**, *343*, 329-339.

[17] Sellner, B.; Barbatti, M.; Lischka, H. *J. Chem. Phys.* **2009**, *131*, 024312.

[18] Bartl, J.; Steenken, S.; Mayr, H.; McClelland, R. A. *J. Am. Chem. Soc.* **1990**, *112*, 6918-6928.

[19] Tachikawa, H.; Igarashi, M.; Ishibashi, T. *Chem. Phys. Lett.* **2002**, *363*, 355-361.

[20] Rudić, S.; Murray, C.; Harvey, J. N.; Orr-Ewing, A. J. *J. Chem. Phys.* **2004**, *120*, 186-198.

[21] Scalmani, G.; Frisch, M. J.; Mennucci, B.; Tomasi, J.; Cammi, R.; Barone, V. *J. Chem. Phys.* **2006**, *124*, 94107.

[22] Cammi, R.; Mennucci, B.; Tomasi, J. *J. Phys. Chem. A* **2000**, *104*, 5631-5637.

[23] Zhao, Y.; Truhlar, D. G. *Theo. Chem. Account* **2008**, *120*, 215-241.

[24] Dreuw, A.; Harbach, P. H. P.; Mewes, J. M.; Wormit, M. *Theor. Chem. Acc.* **2010**, *125*, 419–426.

[25] Zhou, Z.; Du, D.; Fu, A.; Yu, Q. *THEOCHEM* **2000**, *530*, 149-154.

[26] Prall, M.; Wittkopp, A.; Fokin, A. A.; Schreiner, P. R. *J. Comput. Chem.* **2001**, *22*, 1605-1614.

[27] Kraka, E.; Cremer, D. *J. Am. Chem. Soc.* **2000**, *122*, 8245-8264.

[28] Perdew, J. P.; Wang, J. *Phys. Rev. B* **1992**, *45*, 13244-13249.

[29] Tao, J.; Perdew, J. P.; Staroverov, V. N.; Scuseria, G. E. *Phys. Rev. Lett.* **2003**, *91*, 146401-146404.

[30] Zhao, Y.; Truhlar, D. G. *J. Phys. Chem. A* **2006**, *110*, 13126-30.

[31] Gaussian 09, R. A., M. J. Frisch, G. W. Trucks, H. B. Schlegel, G. E. Scuseria, M. A. Robb, J. R. Cheeseman, G. Scalmani, V. Barone, B. Mennucci, G. A. Petersson, H. Nakatsuji, M. Caricato, X. Li, H. P. Hratchian, A. F. Izmaylov, J. Bloino, G. Zheng, J. L. Sonnenberg, M. Hada, M. Ehara, K. Toyota, R. Fukuda, J. Hasegawa, M. Ishida, T. Nakajima, Y. Honda, O. Kitao, H. Nakai, T. Vreven, J. A. Montgomery, Jr., J. E. Peralta, F. Ogliaro, M. Bearpark, J. J. Heyd, E. Brothers, K. N. Kudin, V. N. Staroverov, R. Kobayashi, J. Normand, K. Raghavachari, A. Rendell, J. C. Burant, S. S. Iyengar, J. Tomasi, M. Cossi, N. Rega, J. M. Millam, M. Klene, J. E. Knox, J. B. Cross, V. Bakken, C. Adamo, J. Jaramillo, R. Gomperts, R. E. Stratmann, O. Yazyev, A. J. Austin, R. Cammi, C. Pomelli, J. W. Ochterski, R. L. Martin, K. Morokuma, V. G. Zakrzewski, G. A. Voth, P. Salvador, J. J. Dannenberg, S. Dapprich, A. D. Daniels, Ö. Farkas, J. B. Foresman, J. V. Ortiz, J. Cioslowski, and D. J. Fox, Gaussian, Inc. Wallingford CT: 2009.

[32] Hättig, C.; Weigend, F. *J. Chem. Phys.* **2000**, *113*, 5154.

[33] Hättig, C. *J. Chem. Phys.* **2003**, *118*, 7751.

[34] Hättig, C.; Hellweg, A.; Köhn, A. *Phys. Chem. Chem. Phys.* **2006**, *8*, 1159-1169.

[35] Furche, F.; Rappoport, D. *Theo. Comput. Chem.* **2005**, *16*, 93-128.

[36] Bauernschmitt, R.; Häser, M.; Treutler, O.; Ahlrichs, R. *Chem. Phys. Lett.* **1997**, *264*, 573-578.

[37] Bauernschmitt, R.; Ahlrichs, R. *Chem. Phys. Lett.* **1996**, *256*, 454-464.

[38] Dreuw, A.; Weisman, J. L.; Head-Gordon, M. *J. Chem. Phys.* **2003**, *119*, 2943.

[39] Starcke, J. H.; Wormit, M.; Schirmer, J.; Dreuw, A. *Chem. Phys.* **2006**, *329*, 39-49.

[40] Dreuw, A. *Chem.Phys.Chem.* **2006**, *7*, 2259-2274.

Table 1: (next page)

Calculated hydrogen bonds (r(O···H)), inter-solvent C-C distances ($C_{CH_3OH} - C_{CH_3OH}$) and solute C^1 - solvent O_{CH_3OH} distances ($C^1 - O_{CH_3OH}$) in the optimized reference cluster (RC) geometries $Ph_2CH-P^+(CH_3)_3 \cdot 4\ CH_3OH$ and in the optimized precursor cluster (PC) geometries $Ph_2CH-P^+(CH_3)_3 \cdot 8\ CH_3OH$, $PC2 = (dfp)_2CH-P^+(CH_3)_3 \cdot 9\ CH_3OH$). Basis: def-SV(P), aug:def-TZVP, for the M06-HF functional the comparable basis 6-31G* was used; the optimized precursor cluster (PC) geometries PC1 and PC2 are starting clusters for the on-the-fly MD trajectories. All bond lengths are given in [Å].

method	r(O$\cdots$H)max	r(O$\cdots$H)min	mean
RC:			
tpss	1.677	1.628	1.654
BLYP	1.702	1.647	1.675
RI-BLYP-D	1.688	1.617	1.650
RI-MP2	1.743	1.654	1.705
M06-HF	1.807	1.762	1.777
PC:			
RI-BLYP-D (PC1)	1.745	1.699	1.717
RI-BLYP-D (PC2)	1.736	1.601	1.660

method	r(C$_{CH_3OH}$ $-$ C$_{CH_3OH}$)max	r(C$_{CH_3OH}$ $-$ C$_{CH_3OH}$)min	mean
RC:			
tpss	4.247	4.141	4.210
BLYP	4.277	4.237	4.254
RI-BLYP-D	4.286	3.810	4.029
RI-MP2	4.184	3.970	4.100
M06-HF	4.690	3.881	4.229
PC:			
RI-BLYP-D (PC1)	4.264	3.442	3.955
RI-BLYP-D (PC2)	4.337	3.563	4.101

method	r(C^1 $-$ O$_{CH_3OH}$)max	r(C^1 $-$ O$_{CH_3OH}$)min	mean
RC:			
tpss	4.251	3.566	3.988
BLYP	4.351	3.383	4.026
RI-BLYP-D	4.035	3.188	3.549
RI-MP2	4.010	3.312	3.555
M06-HF	3.941	3.183	3.584
PC:			
RI-BLYP-D (PC1)	5.458	3.090	4.607
RI-BLYP-D (PC2)	5.327	3.096	4.450

Appendix D4

**Photolytic Generation of Benzhydryl Cations and Radicals
from Quaternary Phosphonium Salts:
How Highly Reactive Carbocations Survive Their First Nanoseconds**

J. Ammer, C. F. Sailer, E. Riedle, H. Mayr

Journal of the American Chemical Society 134, 11481-11494 (2012).

Photolytic Generation of Benzhydryl Cations and Radicals from Quaternary Phosphonium Salts: How Highly Reactive Carbocations Survive Their First Nanoseconds

Johannes Ammer,[†] Christian F. Sailer,[‡] Eberhard Riedle,[‡] and Herbert Mayr*,[†]

[†]Department Chemie, Ludwig-Maximilians-Universität München, Butenandtstrasse 5-13 (Haus F), 81377 München, Germany
[‡]Lehrstuhl für BioMolekulare Optik, Ludwig-Maximilians-Universität München, Oettingenstrasse 67, 80538 München, Germany

S *Supporting Information*

ABSTRACT: UV irradiation (266 or 280 nm) of benzhydryl triarylphosphonium salts $Ar_2CH\text{-}PAr_3^+X^-$ yields benzhydryl cations Ar_2CH^+ and/or benzhydryl radicals $Ar_2CH^\bullet$. The efficiency and mechanism of the photo-cleavage were studied by nanosecond laser flash photolysis and by ultrafast spectroscopy with a state-of-the-art femtosecond transient spectrometer. The influences of the photo-electrofuge (Ar_2CH^+), the photo-nucleofuge (PPh_3 or $P(p\text{-}Cl\text{-}C_6H_4)_3$), the counterion ($X^- = BF_4^-$, SbF_6^-, Cl^-, or Br^-), and the solvent (CH_2Cl_2 or CH_3CN) were investigated. Photogeneration of carbocations from $Ar_2CH\text{-}PAr_3^+BF_4^-$ or $\text{-}SbF_6^-$ is considerably more efficient than from typical neutral precursors (e.g., benzhydryl chlorides or bromides). The photochemistry of phosphonium salts is controlled by the degree of ion pairing, which depends on the solvent and the concentration of the phosphonium salts. High yields of carbocations are obtained by photolyses of phosphonium salts with complex counterions ($X^- = BF_4^-$ or SbF_6^-), while photolyses of phosphonium halides $Ar_2CH\text{-}PPh_3^+X^-$ ($X^- = Cl^-$ or Br^-) in CH_2Cl_2 yield benzhydryl radicals $Ar_2CH^\bullet$ due to photo-electron transfer in the excited phosphonium halide ion pair. At low concentrations in CH_3CN, the precursor salts are mostly unpaired, and the photo-cleavage mechanism is independent of the nature of the counter-anions. Dichloromethane is better suited for generating the more reactive benzhydryl cations than the more polar and more nucleophilic solvents CH_3CN or CF_3CH_2OH. Efficient photo-generation of the most reactive benzhydryl cations $(3,5\text{-}F_2-C_6H_3)_2CH^+$ and $(4\text{-}(CF_3)\text{-}C_6H_4)_2CH^+$ was only achieved using the photo-leaving group $P(p\text{-}Cl\text{-}C_6H_4)_3$ and the counter-anion SbF_6^- in CH_2Cl_2. The lifetimes of the photogenerated benzhydryl cations depend greatly on the decay mechanisms, which can be reactions with the solvent, with the photo-leaving group PAr_3, or with the counter-anion X^- of the precursor salt. However, the nature of the photo-leaving group and the counterion of the precursor phosphonium salt do not affect the rates of the reactions of the obtained benzhydryl cations toward added nucleophiles. The method presented in this work allows us to generate a wide range of donor- and acceptor-substituted benzhydryl cations Ar_2CH^+ for the purpose of studying their electrophilic reactivities.
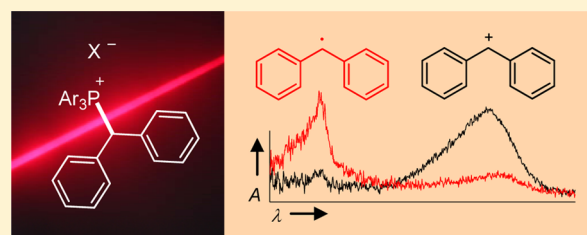
1. INTRODUCTION

The photolytic generation of carbocations by heterolytic cleavage of neutral (R-X) and charged (R-X$^+$) precursors has been employed not only for studying the rates of fast reactions of carbocations with nucleophiles[1−19] but also for the photo-initiation of carbocationic polymerizations.[20] Furthermore, photogenerated carbenium ions are the initial cleavage products of the photolysis of certain photoacid and photobase generators.[21−26] Common precursors for such applications are halides R-Hal,[2−5,21a,27] acetates R-OAc,[6−10,28] aryl ethers,[6−9] and onium salts such as halonium,[25,29] sulfonium,[21b,25,30] ammonium,[2,11,14,22,31] and phosphonium salts.[14−20,23,32−34] Heterolytic bond cleavages are often accompanied by formation of radicals via homolytic processes, particularly when the resulting carbocations are not highly stabilized and less polar solvents are employed.[35]

Among the many photo-leaving groups, phosphines turned out to be particularly advantageous, because they combine high stability,[36] even in alcoholic and aqueous solution, with a high preference for heterolytic cleavage and low tendency to produce radicals.[14−20,32−34,38] While we have recently reported several examples for the photolytic generation of carbocations from quaternary phosphonium salts,[14−19] there was no systematic investigation about the relationship between the structure of the precursor salt and the yields of the generated carbocations. The lack of information became obvious when we failed to generate benzhydrylium ions with empirical electrophilicity parameters $E > 7$ by laser flash photolysis of phosphonium salts $Ar_2CH\text{-}PPh_3^+BF_4^-$. As the photolytic generation of highly electrophilic carbocations is of general importance, we have now examined how the efficiency of carbocation formation can be influenced by the reactivity of the photo-electrofuge (carbocation-to-be), the photo-nucleofuge (photo-leaving group), and the counterion of

the phosphonium salt. To gain insight into the ultrafast dynamics of these processes, the nanosecond laser flash photolysis experiments are supplemented by experiments on a state-of-the-art femtosecond transient spectrometer.[39]

The use of benzhydryl derivatives is advantageous for these investigations because of the clearly assignable distinct spectra of the resulting cations and radicals.[40] Benzhydryl cations furthermore do not have β-protons and therefore cannot eliminate H$^+$, which reduces the number of subsequent processes.[15] Moreover, a systematic variation of the reactivity of the generated carbocations is achieved by using substituted benzhydryl cations Ar$_2$CH$^+$ (E$^+$) whose electrophilic reactivities are quantified accurately by the empirical electrophilicity parameters E.[41]

In the following, we will first investigate how the yields and dynamics of the photoproducts change with variations of the benzhydryl (section 3.2) and phosphine moieties (section 3.3) of the precursor molecules, of the solvent (section 3.4), and of the counter-anions of the phosphonium salts (section 3.5). We will then show how this information can be employed to generate highly reactive carbocations such as E(18−20)$^+$ (section 3.6). After discussing how the reaction conditions affect the lifetimes of the carbocations on the >10 ns time scale (section 3.7), we will finally demonstrate that the method presented in this work is well suitable for the study of bimolecular reactions of the generated benzhydryl cations (section 3.8).

2. EXPERIMENTAL SECTION

2.1. Materials. *Solvents.* For the nanosecond laser flash photolysis experiments, p.a. grade dichloromethane (Merck) was subsequently treated with concentrated sulfuric acid, water, 10% NaHCO$_3$ solution, and again water. After predrying with anhydrous CaCl$_2$, it was freshly distilled over CaH$_2$. Commercially available CH$_2$Cl$_2$ (Merck, spectrophotometric grade) was used for the ultrafast measurements because reactions with impurities are too slow to be observed on the picosecond time scale. Acetonitrile (HPLC grade, VWR or spectrophotometric grade, Sigma-Aldrich) and 2,2,2-trifluoroethanol (99%, Apollo) were used as received.

Phosphonium Salts. The phosphonium salts E-PAr$_3$$^+X^-$ were prepared by heating Ar$_2$CH-OH with Ph$_3$PH$^+$X$^-$ or by treating Ar$_2$CH-Br with PAr$_3$ and subsequent anion metathesis.[42]

2.2. Laser Flash Photolysis. *Nanosecond Laser Flash Photolysis.* Solutions of E-PAr$_3$$^+X^-$ ($A_{266\,nm} \approx 0.1–1.0$, ca. 5×10^{-5} to 10^{-4} M) were irradiated with a 7-ns laser pulse from the fourth harmonic of a Nd/YAG laser (λ_{exc} = 266 nm, 30−60 mJ/pulse, diameter ∼1 cm). A xenon lamp was used as probe light for UV/vis detection (d = 1 cm). Transient spectra were obtained as difference spectra from subsequent determinations with and without laser pulse using an ICCD camera with 10 ns gate width; i.e., the ns time scale spectra published in this work show the average of the transient signals during the first 10 ns after the laser pulse. To reduce noise, 4−16 such spectra were averaged, whereby the solutions of the substrates were replaced completely between subsequent laser pulses by using a flow cuvette.

Decay kinetics of the benzhydryl cations E$^+$ were measured by following the absorbances A at λ_{max}; typically ≥64 individual decay curves were averaged. The decay rate constants k_{obs} (s^{-1}) were obtained from the averaged curve by least-squares fitting to the single-exponential function $A(t) = A_0 e^{-k_{obs}t} + C$. The non-exponential decays were evaluated with the software Gepasi.[43]

Femtosecond UV/Vis Transient Absorption Measurements. The employed broadband transient absorption spectrometer is described in detail in ref 39. Solutions of E-PAr$_3$$^+X^-$ ($A_{280\,nm} \approx 0.1–0.3$, ca. 4×10^{-4} to 6×10^{-3} M) were pumped through a flow cell of 120 μm or 1 mm thickness and irradiated with 35-fs pulses (λ_{exc} = 280 nm, 200 nJ/pulse) from the frequency-doubled output of a noncollinear optical parametric amplifier (NOPA). The pulses were focused down to a diameter of about 100 μm inside the sample. A CaF$_2$ white light continuum spanning

from 290 to 700 nm and polarized at the magic angle was used as probe light.

The time-dependent transient spectra were recorded with temporal resolutions between 100 and 400 fs, depending on the thickness of the sample layer, but always well below all observed decay rates. The decay kinetics were followed at λ_{max} of the benzhydryl cations or radicals. The absorbances were converted to quantum yields using the absorption coefficients of the benzhydryl cations[40] and the accurately determined excitation probability.[39] A least-squares fit of the time-dependent absorbances $A(t)$ to the sum of exponential curves and a constant provided the decay rate constants and amplitudes from which the quantum yields and rate constants for the different processes were derived (see Supporting Information for details).

3. RESULTS AND DISCUSSION

3.1. General. Scheme 1 shows a mechanism for the photo-generation of benzhydryl cations E$^+$ and benzhydryl radicals E$^\bullet$

Scheme 1. Generation of Benzhydryl Cations E$^+$ and Benzhydryl Radicals E$^\bullet$ by Photolysis of Phosphonium Ions E-PPh$_3$$^+$
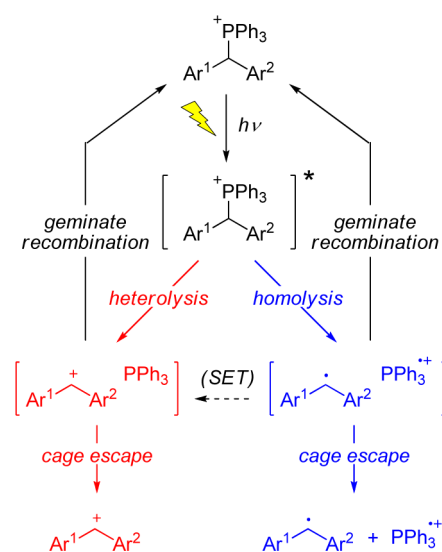
from benzhydryl phosphonium ions E-PPh$_3$$^+$ in line with previously proposed mechanisms for similar systems.[35] The excited precursor molecules can either undergo heterolytic bond cleavage to the carbocation/triphenylphosphine pair [E$^+$ PPh$_3$] (red pathway) or homolytic bond cleavage to the radical pair [E$^\bullet$PPh$_3$$^{\bullet+}$] (blue pathway). Both pairs can then either undergo geminate recombination to the starting material or diffusional separation, which results in the free benzhydryl cations E$^+$ or radicals E$^\bullet$. Only the UV/vis-absorbing species which escape the geminate solvent cage (E$^+$, E$^\bullet$, and PR$_3$$^{\bullet+}$; bottom line of Scheme 1) have sufficient lifetimes (>10 ns) to be observed spectroscopically with a nanosecond laser flash setup.

3.2. Effect of the Photo-electrofuge (i.e., Structure of the Benzhydrylium Ion). *Nanosecond Spectroscopy in CH$_2$Cl$_2$.* The transient spectra which we obtained by irradiation of $10^{-5}–10^{-4}$ M solutions of E(1−20)-PPh$_3$$^+BF_4$$^-$ in CH$_2$Cl$_2$ with a 7-ns laser pulse (266 nm, 30−60 mJ/pulse) are compiled in section S3 of the Supporting Information; four characteristic examples are shown in Figure 1. The transient spectra feature three types of absorption bands: (i) broad bands with λ_{max} = 426−535 nm, which can be assigned to the cations E$^+$ by comparison with the previously reported spectra of benzhydrylium ions,[40] and the cation-like reactivities (see below); (ii)
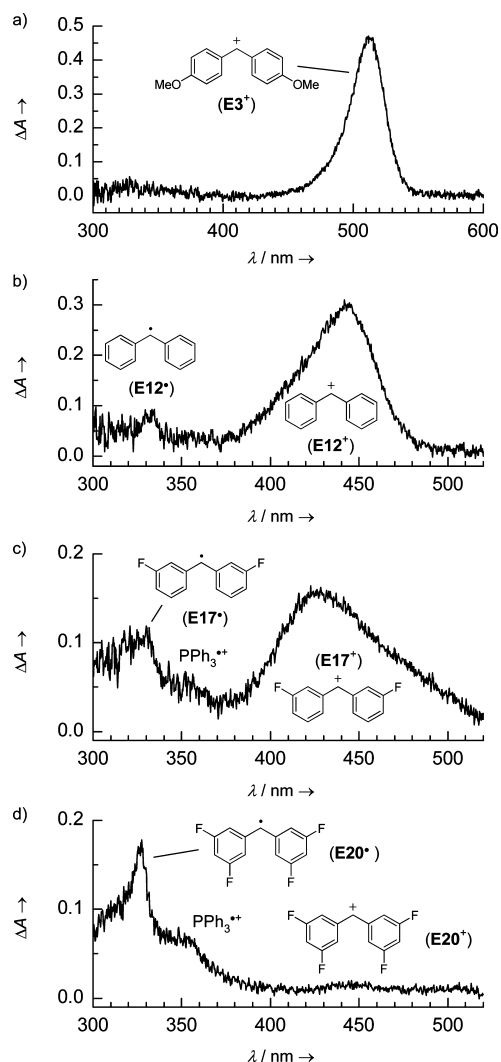
Figure 1. Transient spectra obtained after irradiation (7-ns pulse, λ_{exc} = 266 nm, gate width = 10 ns) of CH$_2$Cl$_2$ solutions of benzhydryl triphenylphosphonium tetrafluoroborates: (a) **E3**-PPh$_3^+$BF$_4^-$ ($A_{266\,nm}$ = 0.16), (b) **E12**-PPh$_3^+$BF$_4^-$ ($A_{266\,nm}$ = 0.49), (c) **E17**-PPh$_3^+$BF$_4^-$ ($A_{266\,nm}$ = 0.90), (d) **E20**-PPh$_3^+$BF$_4^-$ ($A_{266\,nm}$ = 0.64).

Table 1. Electrophilicity Parameters E of the Benzhydryl Cations E(1-20)$^+$ and Absorption Maxima λ_{max} (nm) of Benzhydryl Radicals E$^\bullet$ and Benzhydryl Cations E$^+$ in CH$_2$Cl$_2$

no.	X	Y	E (E$^+$)^a	λ_{max} / nm E$^\bullet$	λ_{max} / nm E$^+$	absorbance ratio^b
E1$^+$			−1.36	^{c}	535	^{c}
E2$^+$			−0.81^d	^{c}	524	^{c}
E3$^+$	4-MeO	4-MeO	0.00	^{c}	513	^{c}
E4$^+$	4-MeO	4-PhO	0.61	^{c}	517	^{c}
E5$^+$	4-MeO	4-Me	1.48	^{c}	484	^{c}
E6$^+$	4-MeO	H	2.11	^{c}	466	^{c}
E7$^+$	4-PhO	H	2.90	^{c}	473	^{c}
E8$^+$	4-Me	4-Me	3.63	^{c}	473	^{c}
E9$^+$	4-Me	H	4.43^d	^{c}	456	^{c}
E10$^+$	4-F	4-F	5.01^d	~327	447	≥ 7
E11$^+$	4-F	H	5.20^d	~333	451	≥ 5
E12$^+$	H	H	5.47^d	~332	443	~4
E13$^+$	4-Cl	4-Cl	5.48^d	~344	480	~4
E14$^+$	3-F	H	6.23^d	~337	438	~3
E15$^+$	4-(CF$_3$)	H	6.70^d	~338	430	~2
E16$^+$	3,5-F$_2$	H	6.74^d	~332	434	~1.7
E17$^+$	3-F	3-F	6.87^d	~331	426	~1.5
E18$^+$	3,5-F$_2$	3-F	7.52^d	~328	435	~0.25
E19$^+$	4-(CF$_3$)	4-(CF$_3$)	(7.96)^{d,e}	~337	439	<0.1
E20$^+$	3,5-F$_2$	3,5-F$_2$	(8.02)^{d,e}	~328	445	<0.1

^{a}Electrophilicity parameters E of the benzhydryl cations E$^+$; from ref 41a unless noted otherwise. ^{b}Ratio of absorbances at λ_{max} (E$^+$) and at λ_{max} (E$^\bullet$) obtained by laser flash photolysis (7-ns pulse, λ_{exc} = 266 nm) of E(1−20)-PPh$_3^+$BF$_4^-$ in CH$_2$Cl$_2$. Due to the overlap with the PPh$_3^{\bullet+}$ band, absorbances at λ_{max} (E$^\bullet$) overestimate the amount of radicals present. ^{c}No radicals detected. ^{d}New or revised E parameters from unpublished work. ^{e}Approximate values.

sharp bands with λ_{max} = 328−344 nm, which closely resemble the published spectra of benzhydryl radicals E$^\bullet$ in CH$_3$CN;[40] and (iii) a shoulder at ca. 350−360 nm, which we assign to the triphenylphosphine radical cation PPh$_3^{\bullet+}$, in agreement with its reported spectrum in CH$_2$Cl$_2$ solution (with $\lambda_{max} \approx$ 330 nm).[44]

The photo-cleavage of the phosphonium ions E(1−9)-PPh$_3^+$ in CH$_2$Cl$_2$ yields the stabilized benzhydrylium ions E(1−9)$^+$ exclusively. When we irradiated solutions of E(10−20)-PPh$_3^+$BF$_4^-$ in CH$_2$Cl$_2$, the ratios of the absorbances of the benzhydryl cations E$^+$ and benzhydryl radicals E$^\bullet$ decreased with increasing electrophilicity E of the carbocations (Table 1). The least stable carbocations in the series, E(18−20)$^+$ are hardly detectable after photolysis of E(18−20)-PPh$_3^+$BF$_4^-$, and the radicals E(18−20)$^\bullet$ are obtained almost exclusively (Figure 1d and Figure S3 in the Supporting Information).

Picosecond Dynamics in CH$_2$Cl$_2$. The processes which lead to the formation of E$^+$ and E$^\bullet$ are too fast to be followed with the nanosecond laser flash photolysis instrument. A closer look at these processes is provided by transient absorption measurements with sub-100-fs time resolution which we performed for selected benzhydryl triarylphosphonium salts. Figure 2 shows a

false color representation of the ps transient absorption data obtained by irradiating E12-PPh$_3^+$BF$_4^-$ in CH$_2$Cl$_2$ with a ~35-fs pulse (280 nm, 200 nJ/pulse): The wavelength is plotted on the horizontal axis and the time after the laser pulse on the vertical axis. Blue color indicates low absorbance and red color high absorbance.

The plot features three types of bands: (i) a broad absorption band below 400 nm, which disappears in the first 30 ps, is assigned to the excited state absorption (ESA) of the phosphonium salt precursor; (ii) the band of the benzhydryl cation E12$^+$ ($\lambda_{max} \approx$ 443 nm), which reaches a maximum within the first 25 ps; and (iii) a small band of the benzhydryl radical E12$^\bullet$ ($\lambda_{max} \approx$ 332 nm), which becomes visible after the decay of the excited state of the phosphonium ion. The graph to the right of the color plot shows the dynamics of the absorbance at λ_{max} of the carbocation E12$^+$ (red) and at 332 nm (blue), λ_{max} of the radical E12$^\bullet$ overlapping with the excited-state absorption in the first tens of picoseconds.

The intense short-lived (<0.1 ps) signal directly after the laser pulse is a coherent artifact that is also observed in the pure
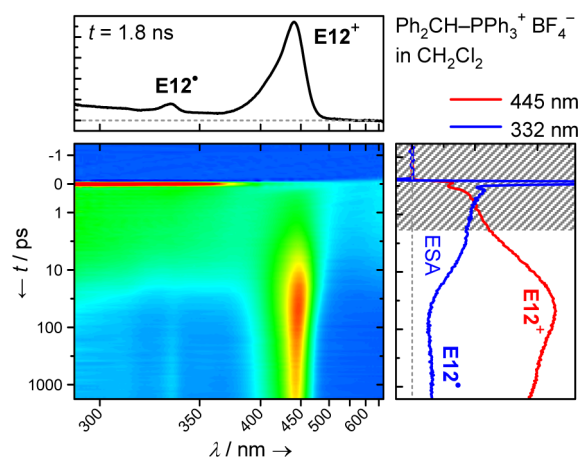
Figure 2. Transient absorptions observed after irradiating a 5.2×10^{-3} M solution of $E12$-$PPh_3^+BF_4^-$ in CH_2Cl_2 by a 35-fs pulse ($\lambda_{exc} = 280$ nm, $A_{280\,nm} = 0.2$, $d = 120$ μm). The graph above the color plot shows the spectrum after 1.8 ns (black). The graph on the right shows the dynamics of the absorbances at selected wavelengths: Absorbance of benzhydryl cation $E12^+$ (445 nm, red); and absorbance of the excited state (ESA) of the phosphonium ion and the benzhydryl radical $E12^\bullet$ (332 nm, blue). The time scale is linear between -1 and $+1$ ps and logarithmic above 1 ps.

solvent and will be ignored in the following.[39] A discussion of the absorption changes during the first 2 ps (shaded area) which include relaxation, planarization, and solvation effects is beyond the scope of this paper and is treated in detail elsewhere.[45]

The ESA disappears during the first 30 ps, accompanied by a simultaneous increase of the absorbance of $E12^+$ which suggests that $E12^+$ is formed by direct heterolysis of the excited precursor salt. It does not, however, exclude the generation of the benzhydryl cations $E12^+$ by homolytic bond cleavage and subsequent considerably faster single electron transfer (SET) in the geminate radical pair (Scheme 1, dashed arrow).

After the ESA has disappeared and the absorbance of $E12^+$ has reached its maximum, the population of $E12^+$ decreases as a result of the geminate recombination of $E12^+$ with the photo-leaving group PPh_3; in part, the photo-fragments diffuse away from each other and these $E12^+$ persist on this time scale. Once the band of the radical $E12^\bullet$ is clearly developed, it does not show noticeable dynamics. After 1.8 ns, we observe the spectrum shown in the graph above the color plot (Figure 2), which is essentially the same as the spectrum obtained by the 7-ns laser pulse (Figure 1b).

The corresponding plot for the photolysis of the tetrafluoro-substituted benzhydryl phosphonium ion $E20$-$PPh_3^+BF_4^-$ in CH_2Cl_2 is shown in Figure S4.1 in the Supporting Information. The heterolysis of this precursor is much less effective and the radical $E20^\bullet$ is formed predominantly. In addition, the small initial concentration of carbocations $E20^+$ decays rapidly so that only a very low concentration can be observed on the nanosecond time scale (Figure 1d; also see Table 2).[46]

Picosecond Dynamics in CH_3CN. Figure S4.2 in the Supporting Information illustrates that in CH_3CN essentially the same kind of photo-processes occur after irradiation of $E12$-$PPh_3^+BF_4^-$ as in CH_2Cl_2 (Figure 2). Figure 3 shows the time-dependent quantum yields of the substituted benzhydryl cations E^+ during the first 1.6 ns after the excitation pulse; the numeric values are listed in Table 2. It is evident that the quantum yields of the initial heterolytic photo-cleavage, Φ_{het}, decrease with increasing electrophilicity of the generated benzhydryl cations. At the same time, homolytic bond cleavage becomes more favorable although the overall efficiency of bond cleavage decreases (not shown). Due to the overlap of the bands of $E^\bullet$ with the ESA and the $PAr_3^{\bullet+}$ band we could not evaluate the radical yields on the early picosecond time scale.

As illustrated by Figure 3, the concentrations of the benzhydryl cations E^+ decrease considerably during the first 300 ps after their formation which is rationalized by the geminate recombination with the photo-leaving group PPh_3. Immediately after C−P bond cleavage, the two photofragments are in close vicinity (ion pairs).

Table 2. Yields and Rate Constants Associated with the Dynamics of E^+ after Irradiation of E-$PAr_3^+BF_4^-$ with Ar = Ph or p-Cl-C_6H_4 (Bold) in CH_3CN or CH_2Cl_2 with a 35-fs Laser Pulse ($\lambda_{exc} = 280$ nm)[a]

E^+	$E(E^+)$[b]	PAr_3	solvent	Φ_{het}[c] (%)	Y_{recomb}[d] (%)	Φ_{free}[e] (%)	k_{recomb}[f] (s^{-1})	k_{esc}[g] (s^{-1})
$E8^+$	3.63	PPh_3	CH_3CN	34	21	27	1.9×10^9	7.2×10^9
$E9^+$	4.43	PPh_3	CH_3CN	30	25	23	2.5×10^9	7.5×10^9
$E12^+$	5.47	PPh_3	CH_3CN	24	25	18	2.7×10^9	8.3×10^9
			CH_2Cl_2	11	19	9	1.1×10^9	4.9×10^9
		$P(p\text{-Cl-}C_6H_4)_3$	CH_3CN	25	21	20	7.9×10^8	3.0×10^9
			CH_2Cl_2	(~16)[h]	(~10)[h]	14	(6×10^8)[h]	(5×10^9)[h]
$E14^+$	6.23	PPh_3	CH_3CN	6−10[i]	29	4−7[i]	3.6×10^9	8.5×10^9
$E17^+$	6.87	PPh_3	CH_3CN	5−8[i]	32	3−5[i]	3.6×10^9	7.5×10^9
$E18^+$	7.52	PPh_3	CH_3CN	4−7[i]	35	3−4[i]	3.8×10^9	6.9×10^9
		$P(p\text{-Cl-}C_6H_4)_3$	CH_3CN	8−12[i]	36	5−7[i]	8.9×10^9	1.6×10^{10}
$E20^+$	(8.02)	PPh_3	CH_3CN	3−4[i]	42	~2[i]	6.6×10^9	9.3×10^9
			CH_2Cl_2	(~1)[i,j]	(29)[j]	(≤1)[i,j]	(2×10^9)[j]	(5×10^9)[j]
		$P(p\text{-Cl-}C_6H_4)_3$	CH_3CN	8−12[i]	36	5−8[i]	8.8×10^9	1.6×10^{10}

[a]See section S5 in the Supporting Information for details. [b]Electrophilicity parameters E of the benzhydryl cations E^+; see Table 1 for references. [c]Quantum yield of heterolytic bond cleavage (including the possibility of initial homolytic bond cleavage and subsequent fast electron transfer). [d]Yield of geminate recombination of E^+ with the phosphine PAr_3. [e]Overall quantum yield of free E^+ (at ~2 ns) after diffusional separation of the photo-leaving group. [f]First-order rate constant for the geminate recombination of E^+ with PAr_3. [g]First-order rate constant for the diffusional separation of E^+ and PAr_3. [h]The different behavior of this photo-leaving group in the early photo-dissociation process in CH_2Cl_2 reduces the accuracy of our fit and we give only approximate values for this system. [i]To calculate the quantum yields, absorbance coefficients of $(5.0-7.5) \times 10^4$ M^{-1} cm^{-1} were assumed for the benzhydryl cations $E(14,17,18,20)^+$ in analogy to reported values for similar benzhydrylium ions.[40] [j]The values have to be considered approximate because of the low absorbance of $E20^+$.
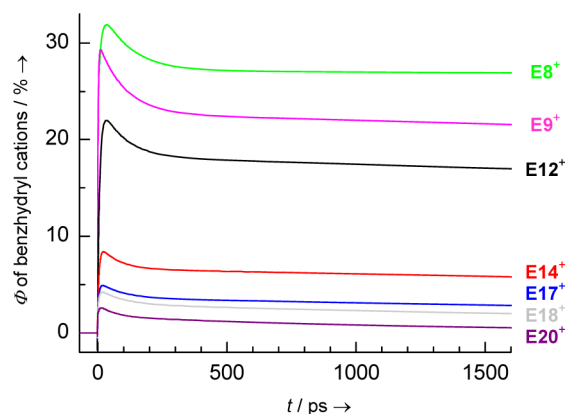
Figure 3. Time-dependent quantum yields Φ of E^+ observed after irradiation of E-$PPh_3^+BF_4^-$ solutions in CH_3CN with a 35-fs laser pulse (λ_{exc} = 280 nm).

Figure 4. Transient spectra obtained after irradiation (7-ns pulse, λ_{exc} = 266 nm, gate width: 10 ns) of CH_2Cl_2 solutions of benzhydryl triarylphosphonium tetrafluoroborates $E18$-$PAr_3^+BF_4^-$ with different photoleaving groups $PAr_3 = PPh_3$ (black, $A_{266\,nm}$ = 1.0) and $PAr_3 = P(p\text{-}Cl\text{-}C_6H_4)_3$ (orange, $A_{266\,nm}$ = 1.0).

They can either undergo geminate recombination or the fragments diffuse apart. After complete diffusional separation of E^+ from the photo-leaving group, bond formation is no longer possible (more precisely: is too slow to be observable on this time scale) and the absorbances of E^+ reach a plateau (Figure 3). The yields for the geminate recombination of the benzhydryl cations E^+ with the phosphine PPh_3, Y_{recomb}, increase with the electrophilicity E of the carbocations E^+, and diminish the final quantum yields of the diffusionally separated (free) benzhydryl cations, Φ_{free} (Table 2).

The rate constants listed in Table 2 for the geminate recombination of E^+ with PPh_3, k_{recomb} (s^{-1}), and for the diffusional separation of E^+ from PPh_3, k_{esc} (s^{-1}), can be derived from $Y_{recomb} = k_{recomb}/(k_{recomb}+k_{esc})$ and the observed rate constants for the decrease of the benzhydrylium ions (see section S5 in the Supporting Information for details). With increasing electrophilicity E of the benzhydryl cations E^+, the recombination rate constant k_{recomb} increases steadily while k_{esc} remains almost constant at $(7-9) \times 10^9\ s^{-1}$.

3.3. Effect of the Photo-nucleofuge (i.e., Triarylphosphine). It was already observed by Modro and co-workers that the use of a more nucleophilic phosphine as photo-leaving group decreased the amount of cation-derived photo-products in photolyses of phosphonium salts.[32] When we employed tris(4-chlorophenyl)phosphine $P(p\text{-}Cl\text{-}C_6H_4)_3$ as a photo-leaving group instead of PPh_3, the formation of benzhydryl cations E^+ was considerably more efficient and even allowed us to generate highly electrophilic benzhydrylium ions.

Figure 4 shows the transient spectra obtained after irradiation of the benzhydryl triarylphosphonium tetrafluoroborates $E18$-$PAr_3^+BF_4^-$ with $PAr_3 = PPh_3$ (black curves) and $PAr_3 = P(p\text{-}Cl\text{-}C_6H_4)_3$ (orange curves). Considerably higher concentrations of the carbocations $E18^+$ and lower amounts of the radicals $E18^\bullet$ were obtained when $P(p\text{-}Cl\text{-}C_6H_4)_3$ was employed as photo-leaving group. Similarly, irradiation of $E20$-$P(p\text{-}Cl\text{-}C_6H_4)_3^+BF_4^-$ gave higher yields of $E20^+$ and lower yields of $E20^\bullet$ than irradiation of $E20$-$PPh_3^+BF_4^-$, but the absorbance of $E20^+$ was still too low ($A < 0.04$) to study its reaction rates on the nanosecond time scale. The shoulders of the radical bands ($PAr_3^{\bullet+}$) are weaker and red-shifted to 350−380 nm when $P(p\text{-}Cl\text{-}C_6H_4)_3$ is used as photo-leaving group (Figure 4), in agreement with the fact that the absorbance maxima of the tris(4-chlorophenyl)phosphine radical cation $P(p\text{-}Cl\text{-}C_6H_4)_3^{\bullet+}$ are slightly red-shifted compared to $PPh_3^{\bullet+}$.[47]
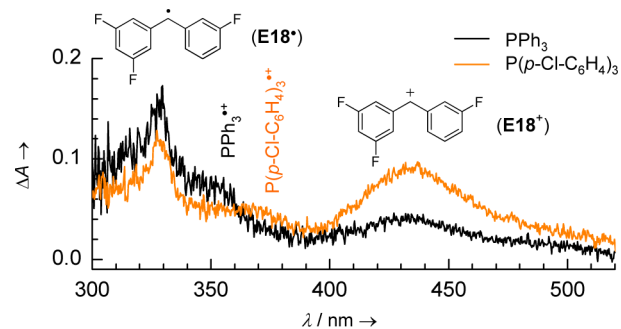
Two reasons might account for the increased carbocation yields with $P(p\text{-}Cl\text{-}C_6H_4)_3$ as photo-leaving group: First, the oxidation potentials of the two phosphines (E^0_{ox} = 1.06 V for PPh_3 and 1.28 V for $P(p\text{-}Cl\text{-}C_6H_4)_3$ in CH_3CN)[48] indicate a higher thermodynamic preference of E^+/PAr_3 pairs over $E^\bullet/PAr_3^{\bullet+}$ pairs in the case of $P(p\text{-}Cl\text{-}C_6H_4)_3$ than in the case of PPh_3. Thus, the preference for the heterolytic over the homolytic pathway should be larger for E-$P(p\text{-}Cl\text{-}C_6H_4)_3^+$ than for E-PPh_3^+. Furthermore, $P(p\text{-}Cl\text{-}C_6H_4)_3$ is less nucleophilic than PPh_3 (ΔN = 1.75)[37] and, therefore, allows more carbocations to undergo diffusional separation instead of geminate recombination.

The data from the ultrafast spectroscopic measurements illustrate that both effects contribute to the better overall quantum yields Φ_{free} when $P(p\text{-}Cl\text{-}C_6H_4)_3$ is used as photo-leaving group instead of PPh_3 (Table 2, bold entries): For this leaving group, the observed initial quantum yields of the heterolytic bond cleavage, Φ_{het}, are higher and the yields of the geminate recombination, Y_{recomb}, are lower. While the differences are small for the photolysis of $E12$-$PAr_3^+BF_4^-$ in CH_3CN, the effects are more important in CH_2Cl_2 and crucial for the generation of the most reactive benzhydryl cations (Table 2).

3.4. Effect of Solvent on the Picosecond Dynamics. The overall quantum yields of the free carbocations, Φ_{free}, are considerably lower in CH_2Cl_2 than in CH_3CN (Table 2), which is a consequence of the decreased quantum yields for the heterolytic bond cleavage, Φ_{het}. The lower solvent nucleophilicity of CH_2Cl_2 compared to CH_3CN only becomes relevant at longer time scales (see below).

The rate constants for the cage escape, k_{esc}, are of comparable magnitude in CH_2Cl_2 and CH_3CN for both photo-nucleofuges PAr_3 (Table 2). In contrast, the diffusional separation of E^+ from Cl^- is very slow after the photolysis of E-Cl in CH_2Cl_2 due to the Coulombic attraction between the charged photo-fragments,[4] which explains why photolyses of E-PAr_3^+ give much higher yields of carbocations in CH_2Cl_2 than photolyses of E-Cl.

3.5. Effect of the Counterion in the Precursor Phosphonium Salt. *Transient Spectra in CH_3CN and CH_2Cl_2.* At low phosphonium salt concentrations ($\sim 1 \times 10^{-4}$ M), the association equilibria of $E12$-$PPh_3^+X^-$ in acetonitrile are entirely on the side of the free (unpaired) ions.[42] Since the lifetime of the excited state is only a few ps, which is too short for the diffusive approach of external X^-, the photochemistry of $E12$-PPh_3^+ is not affected by the counter-anion X^- under these conditions.

11485

dx.doi.org/10.1021/ja3017522 | *J. Am. Chem. Soc.* 2012, 134, 11481−11494

Accordingly, ~1.2×10^{-4} M solutions of **E12**-PPh$_3^+$X$^-$ with different counter-anions X$^-$ in CH$_3$CN gave very similar transient spectra upon irradiation with a 7-ns laser pulse (Figure 5a): Irrespective of the counter-anion X$^-$, the predominant
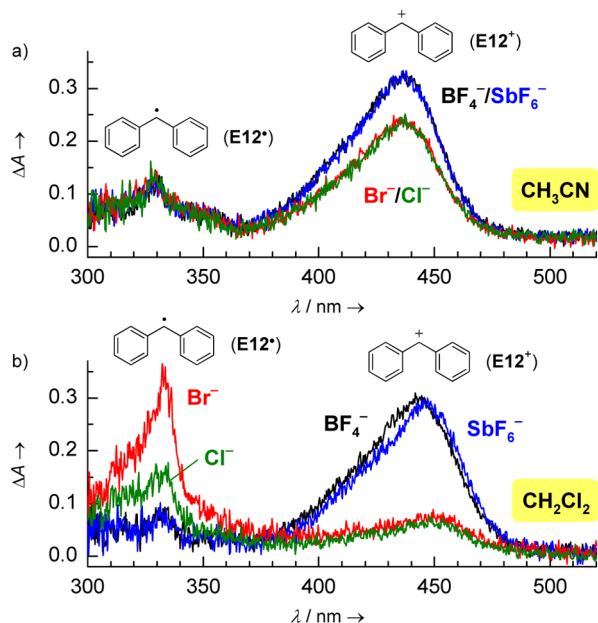
Figure 5. Transient spectra obtained by irradiation of **E12**-PPh$_3^+$X$^-$ ($A_{266\ nm} = 0.5$, $(1.0-1.2) \times 10^{-4}$ M) with different counterions X$^-$ = BF$_4^-$ (black), SbF$_6^-$ (blue), Br$^-$ (red) or Cl$^-$ (green) in CH$_3$CN (a) and CH$_2$Cl$_2$ (b) with a 7-ns laser pulse ($\lambda_{exc} = 266$ nm, gate width: 10 ns).

photoproduct was the benzhydrylium ion **E12$^+$** ($\lambda_{max} \approx 436$ nm) together with small amounts of the radical **E12$^\bullet$** ($\lambda_{max} \approx 329$ nm). Since the absorption coefficients of **E12$^+$** and **E12$^\bullet$** are similar,[40] the absorbance ratios in Figure 5 directly translate to concentration ratios. The slightly lower concentrations of **E12$^+$**

obtained from precursors with X$^-$ = Cl$^-$ or Br$^-$ (Figure 5a) result from the diffusion-controlled trapping of **E12$^+$** by the halide ions (see below),[7] which can already be noticed on this time scale (first 10 ns).

In CH$_2$Cl$_2$, the phosphonium salts **E12**-PPh$_3^+$X$^-$ have a considerably higher tendency to form ion pairs. At concentrations of 1×10^{-4} M, which we typically used in the nanosecond laser flash photolysis experiments, ~57% of the Cl$^-$, ~43% of the Br$^-$, ~40% of the BF$_4^-$, and roughly (10–30)% of the SbF$_6^-$ salts exist as ion pairs in CD$_2$Cl$_2$.[42] When we irradiated solutions of **E12**-PPh$_3^+$BF$_4^-$ in CH$_2$Cl$_2$, we obtained mostly the benzhydrylium ion **E12$^+$** ($\lambda_{max} \approx 443$ nm) together with small amounts of the radical **E12$^\bullet$** ($\lambda_{max} \approx 332$ nm) (Figure 5b, black curve). Irradiation of CH$_2$Cl$_2$ solutions of **E12**-PPh$_3^+$SbF$_6^-$ gave almost the same concentrations of **E12$^+$** and **E12$^\bullet$** as the tetrafluoroborate precursor (Figure 5b, blue curve). In contrast, the concentration ratio of **E12$^+$** and **E12$^\bullet$** was reversed when we used the phosphonium bromide **E12**-PPh$_3^+$ Br$^-$ as precursor (Figure 5b, red curve). Irradiation of the phosphonium chloride **E12**-PPh$_3^+$ Cl$^-$ gave an intermediate amount of **E12$^\bullet$** while the concentration of **E12$^+$** was almost the same as with the phosphonium bromide precursor (Figure 5b, green curve). Transient spectra obtained by analogous experiments with **E12**-PPh$_3^+$ BPh$_4^-$ are difficult to interpret because of the overlap with the absorbances of photoproducts derived from BPh$_4^-$ and are discussed in section S6 in the Supporting Information.

Mechanism. The reduced yield of carbocations **E12$^+$** obtained from the phosphonium halides in CH$_2$Cl$_2$ (Figure 5b) can in part be explained by the immediate combination of **E12$^+$** with Br$^-$ or Cl$^-$ which are in close vicinity if they have been generated from the paired phosphonium halides. However, the increased yields of the radicals obtained from the phosphonium halides cannot be explained by the mechanism in Scheme 1 and subsequent reactions with the counterions, because Cl$^-$ and Br$^-$ do not reduce the benzhydrylium ions in the dark. Scheme 1, therefore, has to be extended as depicted in Scheme 2.

Scheme 2. Generation of Benzhydryl Cations E$^+$ and Benzhydryl Radicals E$^\bullet$ by Photolysis of Phosphonium Salts E-PR$_3^+$X$^-$ (R = Ph or p-Cl-C$_6$H$_4$): (a) Reactions of Unpaired Phosphonium Ions (Predominant Mechanism in CH$_3$CN) and (b) Reactions of Paired Phosphonium Ions (Predominant Mechanism in CH$_2$Cl$_2$)^a
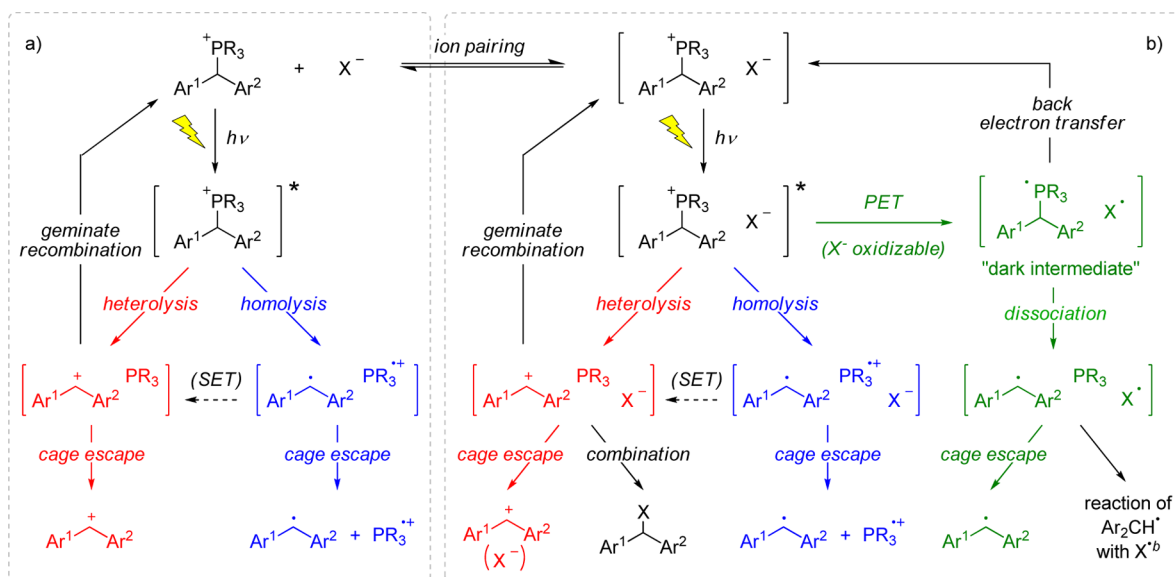
^{a}For the sake of simplicity, the geminate recombination reactions for the radical pairs are not shown. ^{b}Radical combination or electron transfer.[4]
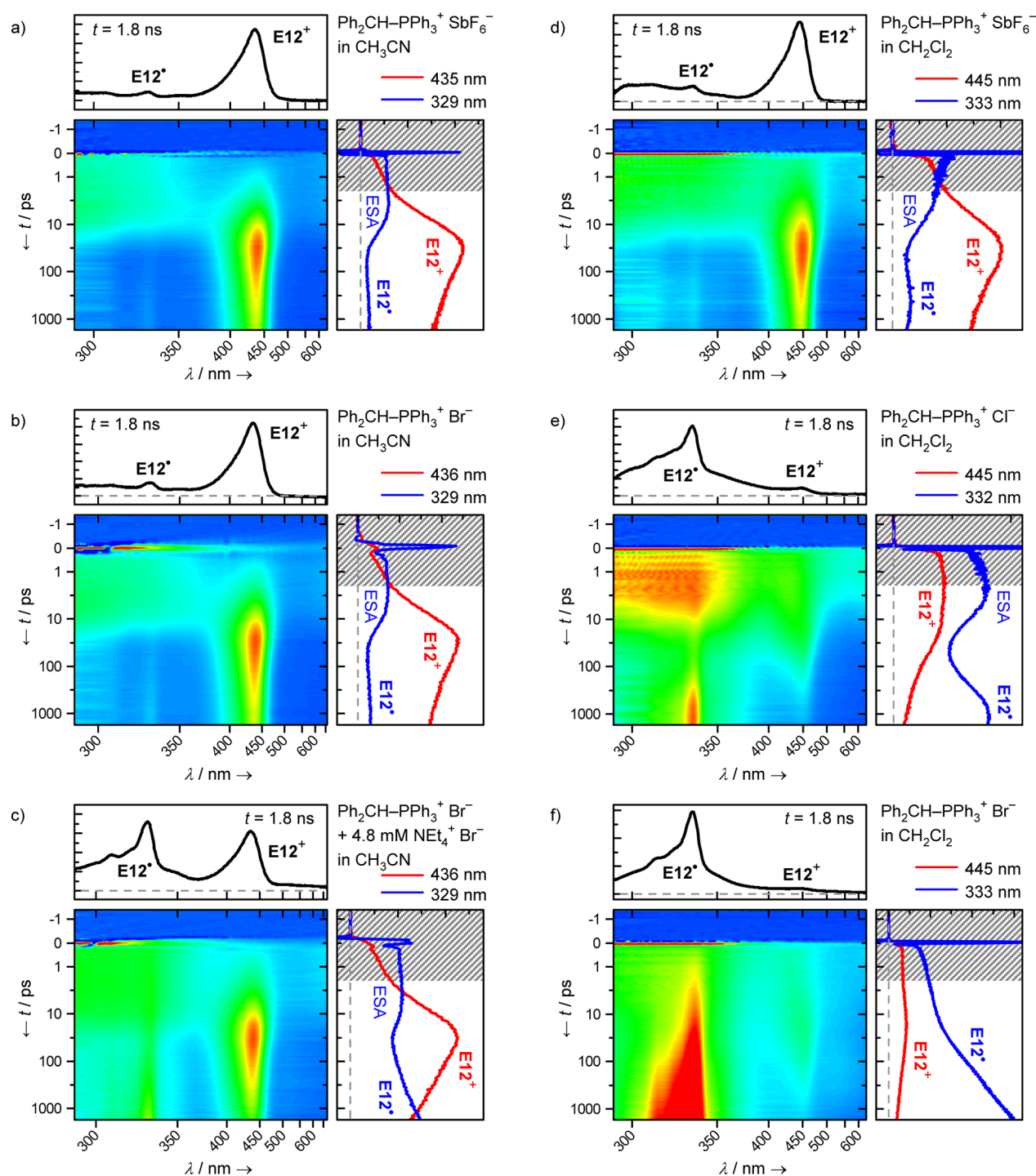
Figure 6. Transient absorptions obtained after irradiating solutions of **E12**-PPh$_3^+$X$^-$ with different counterions X$^-$ in CH$_3$CN (a−c) and CH$_2$Cl$_2$ (d−f) by a 35-fs laser pulse (λ_{exc} = 280 nm). The graphs above the color plots show the spectra after 1.8 ns (black). The graphs on the right show the dynamics of the absorbances at certain wavelengths: absorbance of benzhydryl cation **E12**$^+$ (436 or 445 nm, red) and absorbance of the excited state (ESA) and the benzhydryl radical **E12**$^\bullet$ (329 or 333 nm, blue). (a) X$^-$ = SbF$_6^-$ in CH$_3$CN; (b) X$^-$ = Br$^-$ in CH$_3$CN; (c) X$^-$ = Br$^-$ in CH$_3$CN with 4.8 × 10^{-3} M added NEt$_4^+$ Br$^-$; (d) X$^-$ = SbF$_6^-$ in CH$_2$Cl$_2$; (e) X$^-$ = Cl$^-$ in CH$_2$Cl$_2$; (f) X$^-$ = Br$^-$ in CH$_2$Cl$_2$. The color scales in the false color plots are comparable in Figures (a-f), but the absorbances in the small graphs (spectra and dynamics) were scaled to the available space and cannot be compared directly. The time scale is linear between −1 and +1 ps and logarithmic above 1 ps. For the reasons discussed in context of Figure 2, the absorption changes during the first 2 ps (shaded area) are discussed elsewhere.[45] Experimental conditions: (a,d−f) (5−7) × 10^{-3} M precursor ($A_{280 nm}$ = 0.2), d = 120 μm; (b,c) 4 × 10^{-4} M precursor ($A_{280 nm}$ = 0.1), d = 1 mm.

The phosphonium precursors can exist as free phosphonium ions or paired with the counter-anions. Like the unpaired phosphonium ions (Scheme 2a), the ion pairs can undergo heterolytic bond cleavage to the benzhydryl cations **E**$^+$ (Scheme 2b, red pathway) or homolytic bond cleavage to the benzhydryl radicals **E**$^\bullet$ (Scheme 2b, blue pathway). If the counter-anion is oxidizable, there is the additional possibility of a photo-electron transfer (PET) in the excited phosphonium ion pair (Scheme 2b,

green pathway). Such a PET was already proposed by Griffin et al.[49] and further substantiated by Modro and co-workers who suggested a mechanism similar to Scheme 2 for the photolysis of arylmethyl phosphonium salts with oxidizable counterions.[32,50] As expected for an electron transfer mechanism, the yields of the radicals $E12^{\bullet}$ obtained from $E12\text{-}PPh_3{}^+X^-$ increase with decreasing oxidation potentials of the counterions X^- ($Br^- < Cl^- \ll BF_4^-$ and SbF_6^-). Related to the degree of ion pairing of the precursor salts in these solvents,[42] Scheme 2a is the predominant pathway in CH_3CN and Scheme 2b predominates in CH_2Cl_2.

Our results agree with those of Johnston, Scaiano, and co-workers, who studied the photolyses of arylmethyl triphenyl-phosphonium *chlorides* in CH_3CN and other solvents under conditions where ion-pairing is not negligible.[33] They had already noticed that the concentrations of transient arylmethyl cations increased and the concentrations of radicals decreased when inorganic salts of non-nucleophilic anions (e.g., $LiClO_4$, $NaBF_4$) were added to the phosphonium chloride solutions, because these anions replace the Cl^- in the initial phosphonium salt ion pairs. As expected, this effect is larger in less polar solvents.[33]

Picosecond Dynamics in CH_3CN and CH_2Cl_2. The data from the ultrafast measurements corroborate this interpretation. Figure 6 shows the false color representations of the ps transient absorptions obtained after irradiation of $E12\text{-}PPh_3{}^+X^-$ with different counter-anions ($X^- = SbF_6^-$, Cl^-, and Br^-) in CH_3CN or CH_2Cl_2. The plots for $E12\text{-}PPh_3{}^+SbF_6^-$ in CH_3CN (Figure 6a) and CH_2Cl_2 (Figure 6d) are very similar to that of the tetrafluoroborate precursor (Figure 2) and can be interpreted analogously (see above). Likewise, the color plot obtained with 4×10^{-4} M $E12\text{-}PPh_3{}^+$ Br^- in CH_3CN (Figure 6b) closely resembles that of $E12\text{-}PPh_3{}^+SbF_6^-$ (Figure 6a), because ion pairing is negligible at these concentrations[42] and the PET mechanism depicted in Scheme 2b (green pathway) cannot occur. In all these cases, $E12^+$ is the predominant photo-product, and only very small amounts of $E12^{\bullet}$ are obtained.

At larger precursor concentrations or in the presence of added bromide, however, the association equilibrium of the precursor phosphonium salt is shifted toward the ion pairs, and the PET pathway becomes available also in CH_3CN. Figure 6c shows the false color plot obtained after irradiation of $E12\text{-}PPh_3{}^+$ Br^- in the presence of 4.8×10^{-3} M added $NEt_4{}^+$ Br^-. We now observed a significant amount of benzhydryl radicals $E12^{\bullet}$ while the yield of the benzhydryl cations $E12^+$ decreased.

The false color representations of the transient absorption data recorded after irradiation of $E12\text{-}PPh_3{}^+X^-$ with different counter-anions ($X^- = SbF_6^-$, Cl^-, and Br^-) in CH_2Cl_2 are shown in Figure 6d–f. As already discussed, the plot for $E12\text{-}PPh_3{}^+SbF_6^-$ (Figure 6d) is similar to that observed in CH_3CN. Irradiation of $E12\text{-}PPh_3{}^+Cl^-$ gave the color plot shown in Figure 6e, which is an intermediate case between the SbF_6^- and the Br^- salts. At any time, only a small amount of carbocations $E12^+$ is present. In addition, most of the initially generated $E12^+$ decay during the first 1.8 ns due to the combination reaction of $E12^+$ with Cl^-. The decay of the ESA is not associated with an increase of the carbocation absorbance, indicating that the excited state disappears predominantly by the PET mechanism and not by heterolytic bond cleavage. The dynamics at 332 nm is most interesting (Figure 6e, blue curve), because the ESA decreases within ~30 ps, while the benzhydryl radicals $E12^{\bullet}$ appear with a marked delay ($k_{obs} = 3.8 \times 10^9$ s^{-1}). The dent between the decrease of the ESA and the formation of $E12^{\bullet}$ implies the

accumulation of a "dark" intermediate with a relatively low absorption coefficient which cannot be detected within the large probe range from 290 to 700 nm. This intermediate might be the phosphoranyl/chlorine radical pair $[E12\text{-}PPh_3{}^{\bullet}Cl^{\bullet}]$ (Scheme 2b, green pathway), which can either dissociate to $E12^{\bullet}$ and PPh_3 or undergo a back electron transfer to regenerate the phosphonium chloride $E12\text{-}PPh_3{}^+Cl^-$. After ~800 ps, the "dark" intermediate is completely consumed and the formation of $E12^{\bullet}$ ceases.

Due to the lower oxidation potential of bromide, electron transfer reactions from Br^-, which generate $Br^{\bullet}$, are more favorable than the corresponding reactions of Cl^-. Thus, the PET pathway yielding the radical $E12^{\bullet}$ from the excited state is extremely effective when $X^- = Br^-$. As a result, the ESA disappears almost instantaneously and the band of $E12^{\bullet}$ appears within a few ps (Figure 6f). Accordingly, only a very small amount of carbocation $E12^+$ is generated from $E12\text{-}PPh_3{}^+Br^-$ in CH_2Cl_2; again the decay of $E12^+$ is very effective due to combination with Br^-. In contrast to the observations with the chloride precursor, the radical band keeps rising with an observed rate constant of $k_{obs} = 6.3 \times 10^8$ s^{-1} throughout the whole time scale (Figure 6f, blue curve), i.e., the radical formation is slower but more effective in the case of $X^- = Br^-$. This effect is also explained by the lower oxidation potential of Br^-: After formation of the not observable phosphoranyl radical, homolytic cleavage of $E12\text{-}PPh_3{}^{\bullet}$ yields $Ph_2CH^{\bullet}$ (green pathway in Scheme 2b). On the other hand, the concurrent back electron transfer depends greatly on the reduction potential of $X^{\bullet}$ and is much less important with $Br^{\bullet}$ than with $Cl^{\bullet}$. As the back electron transfer decay pathway for the "dark" state is suppressed, this state becomes longer-lived and benzhydryl radicals $E12^{\bullet}$ keep forming over the whole time scale (Figure 6f) in a more effective and longer-ongoing[51] process. Furthermore, many benzhydryl radicals $E12^{\bullet}$ survive due to the less important electron transfer and radical combination reactions between $E12^{\bullet}$ and $Br^{\bullet}$.

Ion-Pairing and UV/Vis Spectra of the Photo-generated Benzhydryl Cations. It should be noted that the carbocations E^+ which are obtained by the heterolytic cleavage from the paired precursor salts $[E\text{-}PR_3{}^+X^-]$ (Scheme 2b, red pathway) may remain paired with the negatively charged counterions during escape of PR_3 from the solvent cage $[E^+PR_3X^-]$. Thus, if the association equilibrium of the benzhydrylium salt E^+X^- is favorable enough and X^- is a weakly nucleophilic counter-ion (e.g., SbF_6^-), photolysis of $[E\text{-}PR_3{}^+X^-]$ yields long-lived ion pairs $[E^+X^-]$.

Figure 5b shows that the absorption maxima of the carbocations in CH_2Cl_2 vary slightly with the counter-anions. The absorption maxima λ_{max} of the benzhydryl cations $E12^+$ which were generated from the phosphonium halide precursors are at slightly higher wavelengths ($\lambda_{max} \approx 450$ nm, Figure 5b, red and green curves) than those of the benzhydrylium ions generated from the phosphonium tetrafluoroborate or hexa-fluoroantimonate precursors ($\lambda_{max} \approx 443$ and 445 nm, Figure 5b, black and blue curves). It has previously been reported that the absorption maxima of the paired benzhydrylium tetrachlorobo-rates $[E(3-8)^+BCl_4^-]$ are at ~2 nm shorter wavelengths than those of the free ions.[52] Thus, the lower λ_{max} of the benzhydrylium ions $E12^+$ which were generated from BF_4^- or SbF_6^- salts are in agreement with the presence of benzhydrylium ion pairs. The same λ_{max} as shown in Figure 5b (determined with 10 ns gate width) are also observed by the ultrafast measure-ments after ~1 ns and then remain constant during the whole lifetime (μs time scale) of $E12^+$ (see Figure S7 in the Supporting Information). As the diffusional approach of external anions is

comparably slow, the paired benzhydrylium ions observed after ~1 ns must originate from paired phosphonium salts.

The higher λ_{max} for the benzhydryl cations $E12^+$ obtained from the halide precursors (Figure 5b, red and green curves) can be explained by the fact that carbocations which originate from the paired fraction of the phosphonium halide precursors are immediately trapped by the halide anions. Thus, the carbocations which we can observe spectrophotometrically on the >10 ns time scale[53] are only the free (unpaired) benzhydrylium ions $E12^+$ which are obtained from the unpaired fraction of the phosphonium halides. External halide ions subsequently consume the unpaired benzhydrylium ions in a diffusion-controlled reaction (see below) which does not affect λ_{max} of the remaining unpaired benzhydrylium ions but only reduces the signal intensity.

In CH_3CN, the precursor salts as well as the benzhydryl cations are mostly unpaired in the concentration range employed in our experiments, and we observe the unpaired carbocations $E12^+$ predominantly. Thus, the absorption bands of $E12^+$ feature identical absorption maxima ($\lambda_{max} \approx 436$ nm) irrespective of the counterions in this solvent (Figure 5a).

Counterion Effects in the Photochemistry of Other Onium Salts. The counterion effects discussed in the preceding paragraphs should also be relevant for the photochemistry of other onium salts. For example, we have previously shown that one can generate $E12^+$ in CH_2Cl_2 by laser flash photolysis of the quaternary ammonium tetrafluoroborate $E12$-$DABCO^+BF_4^-$ (DABCO = 1,4-diazabicyclo[2.2.2]octane) but not from the corresponding quaternary ammonium bromide.[14] Benzhydryl trimethylammonium iodide has also been used as photo-base-generator because irradiation of $E12$-$NMe_3^+I^-$ yields trimethyl-amine but not the benzhydryl cation $E12^+$ which would trap the amine.[22] To account for the formation of NMe_3 and the absence of $E12^+$, Jensen and Hanson discarded the PET mechanism and favored a photo-S_N1 reaction in CH_3CN and CH_3OH which involves photoheterolysis of the precursor with subsequent trapping of the benzhydryl cations $E12^+$ by the I^- anions or the nucleophilic solvent.[22b] Our results with the phosphonium analogues suggest that the PET mechanism may well be a relevant pathway for the generation of tertiary amines in less polar solvents.

3.6. Laser Flash Photolytic Generation of Highly Electrophilic Benzhydrylium Ions. The information on the influence of photo-nucleofuges (PAr_3) and counter-ions X^- on carbocation yields derived in the previous sections have subsequently been used to generate highly reactive carbocations in order to study their reactivities in bimolecular reactions on the >10 ns time scale. For these investigations, we were restricted to the solvent CH_2Cl_2, because CH_3CN reacts fast with highly electrophilic benzhydrylium ions such as $E(14-20)^+$ (see below). In section 3.3 we have already demonstrated that the use of $P(p$-Cl-$C_6H_4)_3$ as photo-nucleofuge gives higher yields of carbocations than when PPh_3 is employed. Figure 7a shows the transient spectra obtained by irradiating solutions of the phosphonium salts $E18$-$P(p$-Cl-$C_6H_4)_3^+X^-$ with different counter-anions X^- in CH_2Cl_2 with a 7-ns laser pulse (λ_{exc} = 266 nm). As discussed in section 3.3, the phosphonium tetrafluoroborate $E18$-$P(p$-Cl-$C_6H_4)_3^+BF_4^-$ gave a moderate yield of $E18^+$ along with significant amounts of $E18^\bullet$ (Figure 7a, black curve). In view of the results presented in section 3.5 it is no surprise that we could not observe any carbocation $E18^+$ but only the radical $E18^\bullet$ when we irradiated the phosphonium bromide $E18$-$P(p$-Cl-$C_6H_4)_3^+Br^-$ (Figure 7a, red curve).
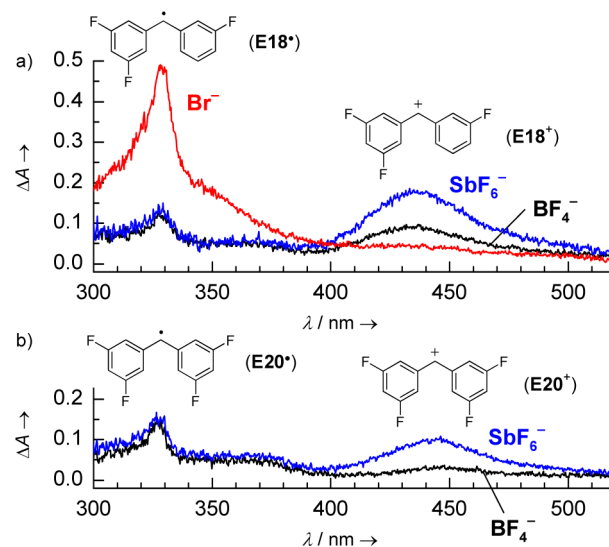
Figure 7. Transient spectra obtained after irradiation of CH_2Cl_2 solutions of benzhydryl tris(p-chlorophenyl)phosphonium salts with different counter-anions with a 7-ns laser pulse (λ_{exc} = 266 nm, gate width: 10 ns): (a) $E18$-$P(p$-Cl-$C_6H_4)_3^+X^-$ with X^- = BF_4^- (black, $A_{266\,nm}$ = 1.0), X^- = SbF_6^- (blue, $A_{266\,nm}$ = 1.0) and X^- = Br^- (red, $A_{266\,nm}$ = 1.0); (b) $E20$-$P(p$-Cl-$C_6H_4)_3^+X^-$ with X^- = BF_4^- (black, $A_{266\,nm}$ = 1.0) and X^- = SbF_6^- (blue, $A_{266\,nm}$ = 0.9).

When we irradiated CH_2Cl_2 solutions of the phosphonium hexafluoroantimonate $E18$-$P(p$-Cl-$C_6H_4)_3^+SbF_6^-$, however, the intensity of the cation band was doubled compared with that obtained from the corresponding BF_4^- salt, while that of the radical band remained virtually unchanged (Figure 7a, blue line).

Similarly, the absorbance of $E20^+$ more than tripled when we used the hexafluoroantimonate $E20$-$P(p$-Cl-$C_6H_4)_3^+SbF_6^-$ (Figure 7b, blue curve) instead of the corresponding tetrafluoroborate (Figure 7b, black curve), while the yield of the benzhydryl radical $E20^\bullet$ was unaffected. The combination of the $P(p$-Cl-$C_6H_4)_3$ photo-leaving group and the SbF_6^- counter-ion hence finally allowed us to generate $E20^+$ in sufficient concentrations to study its kinetics with nucleophiles in CH_2Cl_2. Similarly, we could also obtain the highly electrophilic 4,4'-bis(trifluoromethyl)benzhydrylium ion $E19^+$ from $E19$-$P(p$-Cl-$C_6H_4)_3^+SbF_6^-$ (Figure S8 in the Supporting Information).

Apparently, the BF_4^- anions trap a significant portion of the carbocations $E(18-20)^+$ within the $[E^+BF_4^-]$ ion pairs that are generated by the laser pulse. This is not the case for the parent benzhydryl cation $E12^+$ which was obtained in similar concentrations from the hexafluoroantimonate and the tetra-fluoroborate precursor (Figure 5b, black and blue curves); on the microsecond time scale we also see a faster decay with the BF_4^- counterion than with SbF_6^- (see below). The trapping of the carbocation by BF_4^- within the ion pair becomes less efficient as the electrophilicity of the carbocations is reduced. The higher reactivity of BF_4^- compared to SbF_6^- is in agreement with the calculated enthalpies of fluoride abstractions in the gas phase, which are 151 kJ mol^{-1} more exothermic for BF_4^- than for SbF_6^-.[54] Furthermore, the photoinitiation efficiencies of onium salts in cationic polymerizations generally depend on the nature of the anions and decrease in the order $SbF_6^- > AsF_6^- > PF_6^- > BF_4^-$.[26] This is usually explained by the different nucleophilicities of the anions which are considered to be relevant for the stability of the active center in the propagation step of cationic polymerizations.[26]

3.7. Lifetimes of Benzhydrylium Ions in CH_2Cl_2, CH_3CN, and CF_3CH_2OH. Not only the yields of the carbocations E^+ on the ≤ 10 ns time scale but also their lifetimes on the μs time scale depend greatly on the experimental conditions. Figure 8 shows
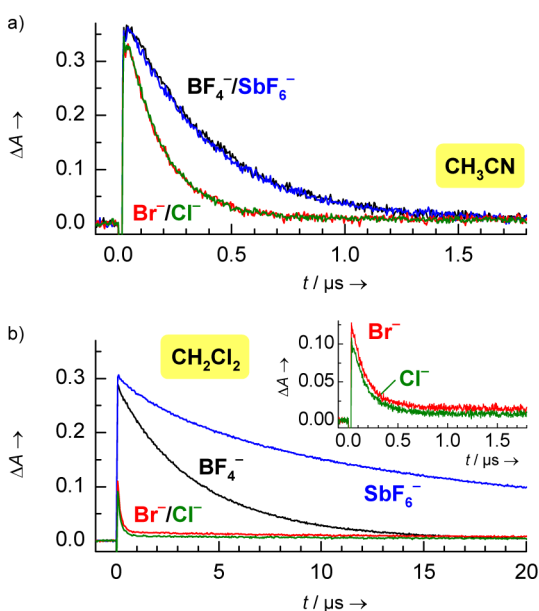

Figure 8. Time-dependent absorbances of $E12^+$ obtained after 7-ns irradiation of $E12$-$PPh_3^+X^-$ ($A_{266\,nm} = 0.5$, $(1.0-1.2) \times 10^{-4}$ M) with different counter-anions $X^- = BF_4^-$ (black), SbF_6^- (blue), Br^- (red) or Cl^- (green) with a 7-ns laser pulse: (a) in CH_3CN and (b) in CH_2Cl_2 (inset: enlarged decay curves for $E12^+$ from precursors with halide counterions).

the time-dependent absorbances of the parent benzhydrylium ion $E12^+$, which we observed when we generated this carbocation from precursors $E12$-$PPh_3^+X^-$ with different counter-anions ($X^- = BF_4^-$, SbF_6^-, Br^-, or Cl^-) in CH_3CN or CH_2Cl_2. The lifetime of $E12^+$ depends on the decay mechanism of the carbocation, which can be (i) recombination with the photo-leaving group PPh_3, (ii) reaction with the counter-anions X^- of the phosphonium salt precursor, or (iii) reaction with the solvent.

Recombination with the Photo-nucleofuge. A general limitation of the laser flash photolysis technique is entailed by the recombination reactions of the carbocations with the free (diffusionally separated) photo-nucleofuges. Photo-nucleofuges (e.g., Hal^-, NR_3, PR_3, RCO_2^-) typically undergo diffusion-controlled recombination reactions with highly electrophilic carbocations ($E > 0$) in solvents of low nucleophilicity.[55] Exceptions to this rule are anionic photo-leaving groups in fluorinated alcohols which stabilize anions very well (e.g., acetate or *p*-cyanophenolate in CF_3CH_2OH).[8] In our case, the triarylphosphines ($N \geq 12.58$, $s_N = 0.65$)[37] undergo diffusion-controlled or almost diffusion-controlled reactions with the benzhydrylium ions $E(1-20)^+$.

The blue curve in Figure 8b shows that the recombination reaction with PPh_3 can be observed when $E12^+$ is generated by irradiation of $E12$-$PPh_3^+SbF_6^-$ in CH_2Cl_2. Since $E12^+$ and PPh_3 are generated in equimolar amounts by the laser pulse, the observed decay of the absorbance is not mono-exponential. Using the software Gepasi,[43] we could fit the observed decay to a kinetic model which takes into account the second-order recombination reaction with PPh_3 and a general first-order

reaction which summarizes all (pseudo-)first-order reactions which may occur (Figure 9). Details and more examples of such
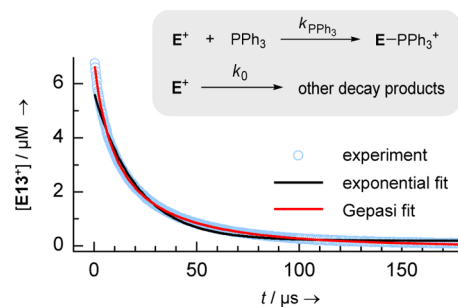
Figure 9. Decay of the concentration of $E12^+$ observed after irradiation of $E12$-$PPh_3^+SbF_6^-$ ($A_{266\,nm} = 0.53$, 1.03×10^{-4} M) in CH_2Cl_2 with a 7-ns laser pulse: Superposition of experimental data ($\bigcirc$), an exponential fit (black), and a fit calculated by Gepasi (red) according to the kinetic model with variable $[PPh_3]$ shown in this Figure ($k_{PPh_3} = (1.31 \pm 0.003) \times 10^{10}$ M^{-1} s^{-1} and $k_0 = (6.49 \pm 0.02) \times 10^3$ s^{-1}).

fits can be found in section S9 of the Supporting Information. As expected, second-order rate constants $k_{PPh_3} \approx 1 \times 10^{10}$ M^{-1} s^{-1} are found for the combinations of $E8^+$, $E9^+$, and $E12^+$ with PPh_3, indicating diffusion-controlled reactions. The obtained rate constants k_0 (s^{-1}) for the first-order background decay reactions agree with the trends discussed below.

At typical concentrations of the photofragments E^+ and PAr_3 in our experiments ($\sim 10^{-6} - 10^{-5}$ M), we find such non-exponential decay kinetics for all systems in which the benzhydryl cations E^+ have lifetimes >10 μs. The recombination reaction with the photo-leaving group thus sets a lower limit for measuring pseudo-first-order kinetics of the benzhydryl cations E^+ with external nucleophiles: Only pseudo-first-order rate constants larger than $(1-5) \times 10^5$ s^{-1} can be determined reliably by fitting the data to an exponential decay curve; otherwise the decay kinetics will be dominated by the second-order reaction with the photo-leaving group.

Reaction with the Counter-anion of the Precursor Phosphonium Salt. When precursors E-$PPh_3^+X^-$ with halide counter-anions were used for the generation of benzhydryl cations E^+, we observed exponential decays of the carbocations which were significantly faster than the decays of carbocations generated from phosphonium salts with $X^- = BF_4^-$ or SbF_6^- (Figure 8). Halide ions undergo diffusion-controlled reactions with reactive carbocations ($E > -2$) in aprotic solvents[7] and the reactions follow pseudo-first-order kinetics since $[E^+] \ll [X^-]$ (only a small fraction of Ar_2CH-$PPh_3^+X^-$ is cleaved to the carbocations). For example, irradiation of 1.2×10^{-4} M solutions of $E12$-$PPh_3^+X^-$ with $X^- = Br^-$ or Cl^- in CH_3CN (Figure 8a, red and green curves) gave pseudo-first-order rate constants $k_{obs} \approx 6 \times 10^6$ s^{-1} for the decay of $E12^+$. Irradiation of 1.0×10^{-4} M solutions of the same precursors in CH_2Cl_2 (Figure 8b, red and green curves) yielded similar rate constants ($k_{obs} \approx 7 \times 10^6$ s^{-1}). These values correspond to second-order rate constants of $k_2 \approx 5 \times 10^{10}$ M^{-1} s^{-1} (CH_3CN) and $k_2 \approx 7 \times 10^{10}$ M^{-1} s^{-1} (CH_2Cl_2) for the diffusion-controlled reactions of $E12^+$ with Br^- and Cl^-.

An almost mono-exponential decay of $E12^+$ was also observed in CH_2Cl_2 when we irradiated $E12$-$PPh_3^+X^-$ with $X^- = BF_4^-$ (Figure 8b, black curve, $k_{obs} \approx 2.6 \times 10^5$ s^{-1}). This decay is much slower than the decays for $X^- = Cl^-$ or Br^- but significantly faster than the non-exponential decay observed for $X^- = SbF_6^-$ (Figure 8b, blue curve) indicating that $E12^+$ reacts with BF_4^-. Similar

mono-exponential decays were found for the benzhydrylium ions $E(10-17)^+$ which were generated from the phosphonium tetrafluoroborates $E(10-17)$-$PAr_3^+BF_4^-$; the decay rate constants increase with the electrophilicities E of the carbocations (see section S10 in the Supporting Information for details). As the yields of the more reactive benzhydryl cations $E(18-20)^+$ obtained from the BF_4^- salt precursors were lower than those from the SbF_6^- salt precursors (see above), one can conclude that the reactions of $E(18-20)^+$ with BF_4^- already occur on time scales <10 ns. For the highly reactive carbocations $E(18-20)^+$ we also observed mono-exponential decays when they were generated from the corresponding hexafluoroantimonate salts $E(18-20)$-$P(p$-Cl-$C_6H_4)_3^+SbF_6^-$. As the background decay rates k_0 of the carbocations $E(18-20)^+$ observed on the >10 ns time scale after irradiation of $E(18-20)$-$P(p$-Cl-$C_6H_4)_3^+X^-$ with $X^- = BF_4^-$ and SbF_6^- also become similar (Figure S10.2 in the Supporting Information), we assume that now the reactions of E^+ with solvent impurities such as residual water in CH_2Cl_2 are dominating.
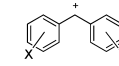
We have already discussed in section 3.5 that the benzhydrylium tetrafluoroborates $E^+BF_4^-$ predominantly exist as ion pairs in CH_2Cl_2 solutions (in the presence of $\sim 1 \times 10^{-4}$ M phosphonium tetrafluoroborate). Accordingly, a further increase of the concentration of BF_4^- has little effect on the kinetics. Thus, the decay rate constant of $E18^+$ increased only slightly (factor 1.5) when we irradiated CH_2Cl_2 solutions of $E18$-$P(p$-Cl-$C_6H_4)_3^+BF_4^-$ in the presence of 1.4×10^{-2} M KBF_4/18-crown-6. The high concentration of BF_4^- ions reduced the initial absorbance of $E18^+$ by less than 30%, i.e., the effect is much smaller than when exchanging 5.7×10^{-5} M SbF_6^- for the same concentration of BF_4^- (Figure 7a).

Reactions with the Solvent. In CH_3CN or 2,2,2-trifluoroethanol (TFE), which are typical solvents for the laser-flash-photolytic generation of carbocations,[1] the characterization of highly electrophilic carbocations is hampered by the nucleophilicity of these solvents. In CH_3CN, for example, the parent benzhydryl cation $E12^+$ decays mono-exponentially with a first-order rate constant of $k_1 = 2.52 \times 10^6$ s^{-1} when it is generated from $E12$-$PPh_3^+BF_4^-$ or SbF_6^- (Figure 8a), that is, it decays at least 1 order of magnitude faster than in CH_2Cl_2. A slightly larger value ($k_1 = 3.21 \times 10^6$ s^{-1}) was observed for the decay of $E12^+$ in trifluoroethanol (TFE). These rate constants are independent of the choice of the photo-leaving groups (Table 3). As solvation effects have a relatively small influence on the reactivities of carbocations,[56] the ~440-fold increase of the decay rate of $E12^+$ in CH_3CN and TFE compared with CH_2Cl_2 ($k_0 \approx 6.5 \times 10^3$ s^{-1}, Figure 9) must result from reactions of $E12^+$ with these solvents.[8,9,40]

The most reactive benzhydryl cations of this series, $E18^+$, $E19^+$, and $E20^+$, decay too fast in CH_3CN or TFE ($\tau < 10$ ns) to be observed with the nanosecond laser flash photolysis setup. It is possible, however, to generate the acceptor-substituted benzhydrylium ions $E(14-17)^+$ in these solvents and to follow the exponential decays of their UV/vis absorbances. Since the first-order rate constants for their reactions with CH_3CN and TFE are $\geq 1 \times 10^7$ s^{-1} (Table 3), it is difficult to characterize the electrophilic reactivities of these benzhydrylium ions toward other nucleophiles in these solvents, because only nucleophiles that react with rate constants close to the diffusion limit can efficiently compete with these solvents.

Dichloromethane is considerably less nucleophilic than CH_3CN or TFE. First-order decay rate constants of $\sim 2 \times 10^6$ s^{-1} ($E18^+$) and $\sim 3 \times 10^6$ s^{-1} ($E20^+$) were measured when these

Table 3. First-Order Rate Constants k_1 (s^{-1}) for the Decay of Benzhydryl Cations E^+ in CH_3CN and 2,2,2-Trifluoroethanol (TFE) at 20 °C

E^+	X	Y	E^a	k_1 (CH$_3$CN) / s^{-1}	k_1 (TFE) / s^{-1}
$E10^+$	4-F	4-F	5.01	1.1×10^6 [b]	5.82×10^5 [c]
$E11^+$	4-F	H	5.20	1.8×10^6 [b]	[d]
$E12^+$	H	H	5.47	2.52×10^6 [c,e]	3.21×10^6 [c,f]
$E13^+$	4-Cl	4-Cl	5.48	2.8×10^6 [b]	1.47×10^6 [c]
$E14^+$	3-F	H	6.23	1.00×10^7 [c]	1.29×10^7 [c]
$E15^+$	4-(CF$_3$)	H	6.70	3.8×10^7 [b]	[d]
$E17^+$	3-F	3-F	6.87	3.49×10^7 [c]	4.6×10^7 [c]

[a]Electrophilicity parameters E of the benzhydryl cations E^+; see Table 1 for references. [b]Photolysis of E-Cl in CH_3CN.[40] [c]Photolysis of E-$PPh_3^+BF_4^-$, this work. [d]Not determined. [e]Photolysis of $E12$-Cl in CH_3CN gave a value of 2.5×10^6 s^{-1}.[40] [f]Photolysis of benzhydryl p-cyanophenyl ether in TFE gave a value of 3.2×10^6 s^{-1}.[8]

carbocations were generated from $E(18,20)$-$P(p$-Cl-$C_6H_4)_3^+SbF_6^-$ (Figure S10.2 in the Supporting Information). However, these values are probably due to impurities and do not reflect the reactivity of CH_2Cl_2 (see above). They just represent an upper limit for the nucleophilic reactivity of CH_2Cl_2. Anyway, the lifetimes of the benzhydrylium ions in highly purified CH_2Cl_2 (see Experimental Section) are much longer than in anhydrous CH_3CN and TFE and allow us to study the electrophilic reactivities of $E(14-20)^+$ toward a variety of nucleophiles.

3.8. Counter-ion Effects on Bimolecular Reactions. As discussed in section 3.5, the usual assumption that only free ions are observed in nanosecond laser flash photolysis experiments[1a,b] does not hold when the carbocations are generated by photolysis of certain onium salts with low-nucleophilicity counter-ions (e.g., BF_4^-, SbF_6^-). Consequently, the question arises whether bimolecular reactions of the photolytically generated carbocations are affected by the nature of the counter-anion in the precursor salt. Previous results already showed that the rate constants for the reactions of moderately stabilized benzhydrylium ions such as methoxy- or methyl substituted benzhydrylium ions $E(3-9)^+$ with neutral nucleophiles like π-nucleophiles[3d,56,57] or hydride donors[58] in CH_2Cl_2 are independent of the nature of the counter-anion and the degree of ion pairing. We now investigated the influence of the counter-anion on the reactions of the considerably more electrophilic benzhydrylium ions $E12^+$ and $E18^+$ with π-nucleophiles (Table 4).

When we generated the benzhydrylium ions E^+ from different precursors E-$PAr_3^+X^-$ with different counter-anions X^- in the presence of a large excess of π-nucleophiles, we observed exponential decays of the UV/vis absorbances of the benzhydryl cations E^+ from which we obtained the pseudo-first-order rate constants k_{obs} (s^{-1}). Plots of k_{obs} versus the nucleophile concentrations were linear in all cases, as exemplified in Figure 10 for the reaction of $E12^+$ with allyltrimethylsilane.

The intercepts of these plots vary with the counter-anion X^- of the phosphonium salts and correspond to the rate constants k_0 for the background decay reactions discussed in section 3.7. For $X^- = Br^-$ and Cl^-, we find quite large intercepts of $k_0 \approx 7 \times 10^6$ s^{-1} due to the diffusion-controlled reactions of E^+ with the halide anions. For $X^- = BF_4^-$ and SbF_6^-, the intercepts are substantially

Table 4. Second-Order Rate Constants k_2 (M^{-1} s^{-1}) for the Reactions of π-Nucleophiles with Benzhydryl Cations E^+ Obtained from Different Precursors E-$PAr_3^+X^-$ in CH_2Cl_2 at 20 °C

E^+	precursor E-$PAr_3^+X^-$		
	PAr_3	X^-	$k_2/M^{-1}\,s^{-1}$
$E12^+$	Reaction with allyltrimethylsilane		
	PPh_3	BF_4^-	1.60×10^7
	PPh_3	SbF_6^-	1.43×10^7
	PPh_3	Br^-	1.42×10^7
	PPh_3	Cl^-	1.53×10^7
$E18^+$	Reaction with 2,3-dimethyl-1-butene		
	PPh_3	BF_4^-	8.22×10^7
	$P(p\text{-}Cl\text{-}C_6H_4)_3$	BF_4^-	8.24×10^7
	$P(p\text{-}Cl\text{-}C_6H_4)_3$	SbF_6^-	8.27×10^7
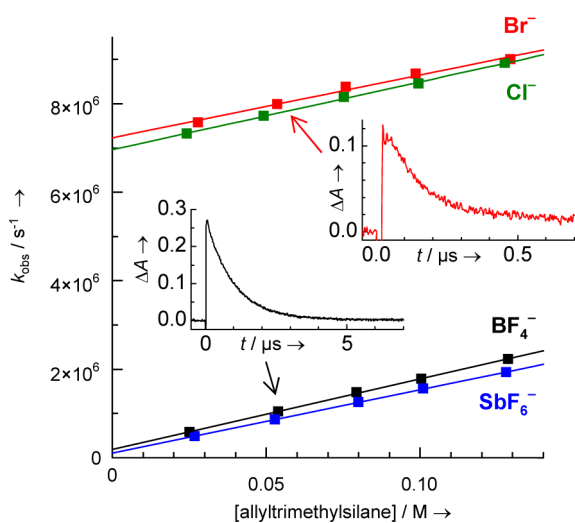
Figure 10. Plots of the pseudo-first-order rate constants k_{obs} (s^{-1}) for the reactions of $E12^+$ with allyltrimethylsilane in CH_2Cl_2 when $E12^+$ was generated by irradiation of 1.0×10^{-4} M solutions of the precursors $E12$-PPh_3X^- with different counter-anions $X^- = BF_4^-$ (black squares), SbF_6^- (blue squares), Br^- (red squares), or Cl^- (green squares) against the concentration of allyltrimethylsilane. The small graphs show the absorbance decays of $E12^+$ in presence of 5.4×10^{-2} M allyltrimethylsilane (black curve, $X^- = BF_4^-$; red curve, $X^- = Br^-$).

lower and their origin has been discussed above. The slopes of the four plots are independent of the counter-anion and provide the second-order rate constants k_2 (M^{-1} s^{-1}) for the reaction of $E12^+$ with allyltrimethylsilane listed in Table 4. We thus measured the same rate constants within experimental error for the reactions of $E12^+$ with allyltrimethylsilane when $E12^+$ was generated from different precursors $E12$-$PPh_3^+X^-$ with $X^- = BF_4^-$, SbF_6^-, Br^-, or Cl^- (Table 4). As discussed in section 3.5, the benzhydryl cations obtained from precursors with halide ions are the free (unpaired) cations because $[E12^+\ Hal^-]$ pairs collapse to covalent $E12$-Hal in less than 10 ns. Since $E12^+BF_4^-$ and $E12^+SbF_6^-$ are significantly paired, on the other hand, we can conclude that paired and unpaired benzhydrylium ions $E12^+$ react with the same rate constants in bimolecular reactions and can be characterized by an anion-independent electrophilicity parameter ($E = 5.47$).

The same situation has been observed for the reactions of 2,3-dimethyl-1-butene with $E18^+$, which is the most electrophilic

carbocation ($E = 7.52$) in our series that could be obtained from precursors with different counterions. When we generated $E18^+$ from either $E18$-$P(p\text{-}Cl\text{-}C_6H_4)_3^+BF_4^-$ or $E18$-$P(p\text{-}Cl\text{-}C_6H_4)_3^+SbF_6^-$, we again measured the same rate constants within experimental error (Table 4). Moreover, we also obtained the same rate constant when we used $E18$-$PPh_3^+BF_4^-$ as precursor, which shows that the photo-leaving group does not have any effect on the carbocations' reactivities either. As discussed in section 3.6, we could not generate $E18^+$ from the phosphonium bromide precursor in CH_2Cl_2 (radical formation), and therefore we cannot compare the reactivities of free and paired carbocations in this case. The counterion independence of the experimental rate constants for carbocation alkene combination reactions implies that ion pairing stabilizes the transition states to about the same extent as the reactant carbocations.

4. CONCLUSION

The efficiencies of the photo-generation of benzhydrylium ions and benzhydryl radicals from phosphonium salts E-$PAr_3^+X^-$ depend not only on the photo-electrofuge (E^+) and the photo-leaving group PAr_3, but also on the counter-ion X^-, the solvent, and the concentration of the precursor molecules. Depending on the reaction conditions, benzhydryl radicals $E^\bullet$ or benzhydryl cations E^+ may be obtained almost exclusively. The results presented in this work should also be relevant for the photochemistry of other onium salts. Spectroscopic investigations on the fs to ps time scale like those performed in this and related work[4,5,16,45] provide a complete microscopic understanding of the photo-generation and the dynamics of reactive intermediates in the geminate solvent cage. With the knowledge of phosphonium salt photochemistry acquired from the present study, we can now select the proper precursor salts for the efficient generation of highly reactive carbocations which are not easily accessible by conventional methods. The method described in this work will subsequently be used to characterize the electrophilic reactivities of the acceptor-substituted benzhydrylium ions $E(14-20)^+$ in CH_2Cl_2 at 20 °C, which provides a further extension of our long-ranging electrophilicity scale.[41]

■ ASSOCIATED CONTENT

ⓢ Supporting Information

Additional transient spectra, details of the experimental procedures and data evaluation, details of the kinetic measurements. This material is available free of charge via the Internet at http://pubs.acs.org.

■ AUTHOR INFORMATION

Corresponding Author

Herbert.Mayr@cup.uni-muenchen.de

Notes

The authors declare no competing financial interest.

■ REFERENCES

(1) Reviews: (a) McClelland, R. A. In *Reactive Intermediate Chemistry*; Moss, R. A., Platz, M. S., Jones, M. J., Eds.; Wiley: Hoboken, NJ, 2004, p 3–40. (b) McClelland, R. A. *Tetrahedron* **1996**, *52*, 6823–6858. (c) Fleming, S. A.; Pincock, J. A. *Mol. Supramol. Photochem.* **1999**, *3*, 211–281. (d) Das, P. K. *Chem. Rev.* **1993**, *93*, 119–144.

(2) McClelland, R. A.; Chan, C.; Cozens, F. L.; Modro, A.; Steenken, S. *Angew. Chem.* **1991**, *103*, 1389–1391; *Angew. Chem., Int. Ed.* **1991**, *30*, 1337–1339.

(3) (a) Bartl, J.; Steenken, S.; Mayr, H. *J. Am. Chem. Soc.* **1991**, *113*, 7710–7716. (b) Johnston, L. J.; Kwong, P.; Shelemay, A.; Lee-Ruff, E. *J. Am. Chem. Soc.* **1993**, *115*, 1664–1669. (c) Kobayashi, S.; Hori, Y.; Hasako, T.; Koga, K.-i.; Yamataka, H. *J. Org. Chem.* **1996**, *61*, 5274–5279. (d) Mayr, H.; Schimmel, H.; Kobayashi, S.; Kotani, M.; Prabakaran, T. R.; Sipos, L.; Faust, R. *Macromolecules* **2002**, *35*, 4611–4615. (e) Phan, B. T.; Nolte, C.; Kobayashi, S.; Ofial, A. R.; Mayr, H. *J. Am. Chem. Soc.* **2009**, *131*, 11392–11401.

(4) Sailer, C. F.; Fingerhut, B. P.; Thallmair, S.; Nolte, C.; Ammer, J.; Mayr, H.; de Vivie-Riedle, R.; Pugliesi, I.; Riedle, E. *J. Am. Chem. Soc.* **2012**, submitted.

(5) Sailer, C. F.; Fingerhut, B. P.; Ammer, J.; Nolte, C.; Pugliesi, I.; Mayr, H.; de Vivie-Riedle, R.; Riedle, E. In *Ultrafast Phenomena XVII*; Chergui, M., Jonas, D., Riedle, E., Schoenlein, R. W., Taylor, A., Eds.; Oxford University Press: New York, 2011; pp 427–429.

(6) (a) McClelland, R. A.; Banait, N.; Steenken, S. *J. Am. Chem. Soc.* **1986**, *108*, 7023–7027. (b) McClelland, R. A.; Kanagasabapathy, V. M.; Banait, N. S.; Steenken, S. *J. Am. Chem. Soc.* **1989**, *111*, 3966–3972. (c) McClelland, R. A.; Kanagasabapathy, V. M.; Banait, N. S.; Steenken, S. *J. Am. Chem. Soc.* **1991**, *113*, 1009–1014. (d) McClelland, R. A.; Kanagasabapathy, V. M.; Banait, N.; Steenken, S. *J. Am. Chem. Soc.* **1992**, *114*, 1816–1823. (e) Van Pham, T.; McClelland, R. A. *Can. J. Chem.* **2001**, *79*, 1887–1897.

(7) Minegishi, S.; Loos, R.; Kobayashi, S.; Mayr, H. *J. Am. Chem. Soc.* **2005**, *127*, 2641–2649.

(8) McClelland, R. A.; Kanagasabapathy, V. M.; Steenken, S. *J. Am. Chem. Soc.* **1988**, *110*, 6913–6914.

(9) Minegishi, S.; Kobayashi, S.; Mayr, H. *J. Am. Chem. Soc.* **2004**, *126*, 5174–5181.

(10) (a) Hallett-Tapley, G.; Cozens, F. L.; Schepp, N. P. *J. Phys. Org. Chem.* **2009**, *22*, 343–348. (b) Horn, M.; Mayr, H. *Chem.—Eur. J.* **2010**, *16*, 7478–7487. (c) Horn, M.; Mayr, H. *Eur. J. Org. Chem.* **2011**, 6470–6475.

(11) Baidya, M.; Kobayashi, S.; Brotzel, F.; Schmidhammer, U.; Riedle, E.; Mayr, H. *Angew. Chem.* **2007**, *119*, 6288–6292; *Angew. Chem., Int. Ed.* **2007**, *46*, 6176–6179.

(12) (a) Cozens, F.; Li, J.; McClelland, R. A.; Steenken, S. *Angew. Chem.* **1992**, *104*, 753–755; *Angew. Chem., Int. Ed.* **1992**, *31*, 743–745. (b) Mladenova, G.; Chen, L.; Rodriquez, C. F.; Siu, K. W. M.; Johnston, L. J.; Hopkinson, A. C.; Lee-Ruff, E. *J. Org. Chem.* **2001**, *66*, 1109–1114. (c) Loos, R.; Kobayashi, S.; Mayr, H. *J. Am. Chem. Soc.* **2003**, *125*, 14126–14132. (d) Schaller, H. F.; Schmidhammer, U.; Riedle, E.; Mayr, H. *Chem.—Eur. J.* **2008**, *14*, 3866–3868.

(13) See refs 14–18 for kinetic studies using quaternary triarylphosphonium salts and refs 18 and 19 for kinetic studies with other quaternary phosphonium salts as precursors.

(14) Ammer, J.; Baidya, M.; Kobayashi, S.; Mayr, H. *J. Phys. Org. Chem.* **2010**, *23*, 1029–1035.

(15) Ammer, J.; Mayr, H. *Macromolecules* **2010**, *43*, 1719–1723.

(16) Sailer, C. F.; Singh, R. B.; Ammer, J.; Riedle, E.; Pugliesi, I. *Chem. Phys. Lett.* **2011**, *512*, 60–65.

(17) (a) Shi, L.; Horn, M.; Kobayashi, S.; Mayr, H. *Chem.—Eur. J.* **2009**, *15*, 8533–8541. (b) Troshin, K.; Schindele, C.; Mayr, H. *J. Org. Chem.* **2011**, *76*, 9391–9408.

(18) (a) Baidya, M.; Kobayashi, S.; Mayr, H. *J. Am. Chem. Soc.* **2010**, *132*, 4796–4805. (b) Duan, X.-H.; Maji, B.; Mayr, H. *Org. Biomol. Chem.* **2011**, *9*, 8046–8050. (c) Nigst, T. A.; Ammer, J.; Mayr, H. *Angew. Chem.* **2011**, *124*, 1381–1385; *Angew. Chem., Int. Ed.* **2011**, *51*, 1353–1356. (d) Nolte, C.; Ammer, J.; Mayr, H. *J. Org. Chem.* **2012**, *77*, 3325–3335.

(19) (a) Kanzian, T.; Lakhdar, S.; Mayr, H. *Angew. Chem.* **2010**, *121*, 9717–9720; *Angew. Chem., Int. Ed.* **2010**, *49*, 9526–9529. (b) Streidl, N.; Branzan, R.; Mayr, H. *Eur. J. Org. Chem.* **2010**, 4205–4210. (c) Lakhdar, S.; Ammer, J.; Mayr, H. *Angew. Chem.* **2011**, *123*, 10127–10130; *Angew. Chem., Int. Ed.* **2011**, *50*, 9953–9956.

(20) For examples of carbocations generated by photolysis of phosphonium precursors acting as initiating species in carbocationic polymerizations, see: (a) Takata, T.; Takuma, K.; Endo, T. *Makromol. Chem., Rapid Commun.* **1993**, *14*, 203–206. (b) Takuma, K.; Takata, T.; Endo, T. *J. Photopolym. Sci. Technol.* **1993**, *6*, 67–74.

(21) Examples of photoacid generation mechanisms with heterolytic cleavage of carbon–heteroatom bonds: (a) Pohlers, G.; Scaiano, J. C.; Step, E.; Sinta, R. *J. Am. Chem. Soc.* **1999**, *121*, 6167–6175. (b) Sanrame, C. N.; Brandao, M. S. B.; Coenjarts, C.; Scaiano, J. C.; Pohlers, G.; Suzuki, Y.; Cameron, J. F. *Photochem. Photobiol. Sci.* **2004**, *3*, 1052–1057.

(22) Examples for the photogeneration of tertiary amines from benzhydryl derivatives: (a) Hanson, J. E.; Jensen, K. H.; Gargiuolo, N.; Motta, D.; Pingor, D. A.; Novembre, A. E.; Mixon, D. A.; Kometani, J. M.; Knurek, C. In *Microelectronics Technology. Polymers for Advanced Imaging and Packaging*; Reichmanis, E., Ober, C. K., MacDonald, S. A., Iwayanagi, T., Nishikubo, T., Eds.; ACS Symposium Series *614*; American Chemical Society: Washington, DC, 1995. (b) Jensen, K. H.; Hanson, J. E. *Chem. Mater.* **2002**, *14*, 918–923.

(23) Examples for the photogeneration of PPh$_3$ from quaternary phosphonium salts: (a) Önen, A.; Arsu, N.; Yagci, Y. *Angew. Makromol. Chem.* **1999**, *264*, 56–59. (b) Kasapoglu, F.; Aydin, M.; Arsu, N.; Yagci, Y. *J. Photochem. Photobiol., A* **2003**, *159*, 151–159.

(24) For reviews about photoinitiators, see refs 25 and 26 and the following: (a) Yagci, Y.; Reetz, I. *Prog. Polym. Sci.* **1998**, *23*, 1485–1538. (b) Yagci, Y.; Durmaz, Y. Y.; Aydogan, B. *Chem. Rec.* **2007**, *7*, 78–90. (c) Allonas, X.; Croutxé-Barghorn, C.; Fouassier, J.-P.; Lalevée, J.; Malval, J.-P.; Morlet-Savary, F. In *Lasers in Chemistry*; Lackner, M., Ed.; Wiley-VCH: Weinheim, 2008; Vol. 2, pp 1001–1027. (d) Suyama, K.; Shirai, M. *Prog. Polym. Sci.* **2009**, *34*, 194–209. (e) Yagci, Y.; Jockusch, S.; Turro, N., J. *Macromolecules* **2010**, *43*, 6245–6260.

(25) (a) Toba, Y. *J. Photopolym. Sci. Technol.* **2003**, *16*, 115–118. (b) Crivello, J. V. *J. Photopolym. Sci. Technol.* **2008**, *21*, 493–497.

(26) (a) Fouassier, J.-P. In *Photoinitiation, Photopolymerization, and Photocuring: Fundamentals and Applications*; Hanser: Munich, 1995; pp 102–144. (b) Lazauskaite, R.; Grazulevicius, J. V. In *Handbook of Photochemistry and Photobiology*; Nalwa, H. S., Ed.; American Scientific Publishers: Stevenson Ranch, CA, 2003; Vol. 2, pp 335–392.

(27) (a) Miranda, M. A.; Pérez-Prieto, J.; Font-Sanchis, E.; Scaiano, J. C. *Acc. Chem. Res.* **2001**, *34*, 717–726. (b) Kropp, P. J. In *CRC Handbook of Organic Photochemistry and Photobiology*, 2nd ed.; Horspool, W., Lenci, F., Eds.; CRC Press: Boca Raton, 2004; pp 1-1–1-32. (c) Kitamura, T. In *CRC Handbook of Organic Photochemistry and Photobiology*, 2nd ed.; Horspool, W., Lenci, F., Eds.; CRC Press: Boca Raton, 2004; pp 11-1–11-10. (d) Peters, K. S. *Chem. Rev.* **2007**, *107*, 859–873.

(28) Pincock, J. A. *Acc. Chem. Res.* **1997**, *30*, 43–49.

(29) Dektar, J. L.; Hacker, N. P. *J. Org. Chem.* **1991**, *56*, 1838–1844.

(30) Dektar, J. L.; Hacker, N. P. *J. Am. Chem. Soc.* **1990**, *112*, 6004–6015.

(31) Appleton, D. C.; Bull, D. C.; Givens, R. S.; Lillis, V.; McKenna, J.; McKenna, J. M.; Thackeray, S.; Walley, A. R. *J. Chem. Soc., Perkin Trans. 2* **1980**, 77–82.

(32) Imrie, C.; Modro, T. A.; Rohwer, E. R.; Wagener, C. C. P. *J. Org. Chem.* **1993**, *58*, 5643–5649.

(33) Alonso, E. O.; Johnston, L. J.; Scaiano, J. C.; Toscano, V. G. *Can. J. Chem.* **1992**, *70*, 1784–1794.

(34) (a) Alonso, E. O.; Johnston, L. J.; Scaiano, J. C.; Toscano, V. G. *J. Am. Chem. Soc.* **1990**, *112*, 1270–1271. (b) Imrie, C.; Modro, T. A.; Wagener, C. C. P. *J. Chem. Soc., Perkin Trans. 2* **1994**, 1379–1382.

(35) For general reviews, see refs 1 and 26. Similar photocleavage mechanisms were previously discussed for halides (refs 4 and 27), carboxylates (ref 28), halonium salts (ref 29), sulfonium salts (ref 30), ammonium salts (ref 31), and phosphonium salts (refs 32 and 33).

(36) For equilibrium constants of stabilized benzhydryl cations with triarylphosphines, see ref 37. In cases where highly stabilized carbocations do not give stable triarylphosphonium salts, one may use a more Lewis-basic phosphine such as $P(n\text{-Bu})_3$ as the photo-leaving group (refs 18 and 19).

(37) Kempf, B.; Mayr, H. *Chem.—Eur. J.* **2005**, *11*, 917−927.

(38) For a review of the literature up to 1994, see: Dankowski, M. In *The chemistry of organophosphorus compounds*; Hartley, F. R., Ed.; Wiley: Chichester, 1994; Vol. 3, pp 325−343.

(39) Megerle, U.; Pugliesi, I.; Schriever, C.; Sailer, C. F.; Riedle, E. *Appl. Phys. B: Laser Opt.* **2009**, *96*, 215−231.

(40) Bartl, J.; Steenken, S.; Mayr, H.; McClelland, R. A. *J. Am. Chem. Soc.* **1990**, *112*, 6918−6928.

(41) (a) Mayr, H.; Bug, T.; Gotta, M. F.; Hering, N.; Irrgang, B.; Janker, B.; Kempf, B.; Loos, R.; Ofial, A. R.; Remennikov, G.; Schimmel, H. *J. Am. Chem. Soc.* **2001**, *123*, 9500−9512. (b) Mayr, H.; Kempf, B.; Ofial, A. R. *Acc. Chem. Res.* **2003**, *36*, 66−77. (c) For a comprehensive database of nucleophilicity and electrophilicity parameters, see: http://www.cup.lmu.de/oc/mayr/DBintro.html.

(42) Syntheses, structural investigations, and ion-pairing phenomena of benzhydryltriarylphosphonium salts will be reported in a subsequent publication.

(43) (a) Mendes, P. *Comput. Appl. Biosci.* **1993**, *9*, 563−571. (b) Mendes, P. *Trends Biochem. Sci.* **1997**, *22*, 361−363. (c) Mendes, P.; Kell, D. B. *Bioinformatics* **1998**, *14*, 669−883. (d) Further information about Gepasi: www.gepasi.org.

(44) Alfassi, Z. B.; Neta, P.; Beaver, B. *J. Phys. Chem. A* **1997**, *101*, 2153−2158.

(45) Fingerhut, B. P.; Sailer, C. F.; Ammer, J.; Riedle, E.; de Vivie-Riedle, R. *J. Phys. Chem. A* **2012**, DOI: 10.1021/jp300986t.

(46) Exclusive formation of $\mathbf{E8}^+$ is observed after irradiation of $\mathbf{E8}$-$PPh_3{}^+BF_4{}^-$ in CH_3CN; the plot for this system is shown in Figure S6 in the Supporting Information of ref 16.

(47) (a) Nakamura, M.; Miki, M.; Majima, T. *J. Chem. Soc., Perkin Trans. 2* **2000**, 1447−1452. (b) Tojo, S.; Yasui, S.; Fujitsuka, M.; Majima, T. *J. Org. Chem.* **2006**, *71*, 8227−8232.

(48) Fukuzumi, S.; Shimoosako, K.; Suenobu, T.; Watanabe, Y. *J. Am. Chem. Soc.* **2003**, *125*, 9074−9082.

(49) Griffin, C. E.; Kaufman, M. L. *Tetrahedron Lett.* **1965**, *12*, 773−775.

(50) Both groups have derived their conclusions from product studies after extended irradiation of benzyl triphenylphosphonium salts. It should be noted that product studies do not necessarily give the same results as transient measurements. Multiple irradiation of the same starting material molecules in preparative photolyses will distort the product ratios if the geminate recombination of one or both types of photofragment pair is a relevant process. Further complications arise if the photoproducts (e.g., arylmethyl halides) can undergo subsequent photolysis reactions.

(51) The observed rate constant k_{obs} for formation of $\mathbf{E12}^\bullet$ is the sum of the rate constants for phosphoranyl radical dissociation and back electron transfer. The derivation of this relationship is analogous to the case of the carbocation dynamics in the geminate solvent cage, cf. section S5 in the Supporting Information.

(52) Schneider, R.; Mayr, H.; Plesch, P. H. *Ber. Bunsen-Ges.* **1987**, *91*, 1369−1374.

(53) The absorbance maximum of the short-lived (<300 ps) $\left[\mathbf{E}^+\,Cl^-\right]$ ion pairs is also blue-shifted compared to the free $\mathbf{E}^+$. The dependence of λ_{max} on the distance between $\mathbf{E}^+$ and Cl^- is investigated in detail in ref 4.

(54) Krossing, I.; Raabe, I. *Chem.—Eur. J.* **2004**, *10*, 5017−5030.

(55) For nucleophilicity parameters of common photo-nucleofuges such as halides, carboxylates, tertiary amines, pyridines, tertiary phosphines, and others, see ref 41c.

(56) Mayr, H.; Schneider, R.; Schade, C.; Bartl, J.; Bederke, R. *J. Am. Chem. Soc.* **1990**, *112*, 4446−4454.

(57) (a) Mayr, H.; Schneider, R.; Irrgang, B.; Schade, C. *J. Am. Chem. Soc.* **1990**, *112*, 4454−4459. (b) Hagen, G.; Mayr, H. *J. Am. Chem. Soc.* **1991**, *113*, 4954−4961. (c) Mayr, H.; Patz, M. *Macromol. Symp.* **1996**,

107, 99−110. (d) Burfeindt, J.; Patz, M.; Müller, M.; Mayr, H. *J. Am. Chem. Soc.* **1998**, *120*, 3629−3634.

(58) (a) Mayr, H.; Basso, N.; Hagen, G. *J. Am. Chem. Soc.* **1992**, *114*, 3060−3066. (b) Mayr, H.; Lang, G.; Ofial, A. R. *J. Am. Chem. Soc.* **2002**, *124*, 4076−4083.

– Supporting Information –

Photolytic Generation of Benzhydryl Cations and Radicals from Quaternary Phosphonium Salts:

How Highly Reactive Carbocations Survive Their First Nanoseconds

Johannes Ammer,[a] Christian F. Sailer,[b] Eberhard Riedle,[b] and Herbert Mayr[a]*

[a] Department Chemie, Ludwig-Maximilians-Universität München, Butenandtstr. 5-13 (Haus F), 81377 München, Germany.
[b] Lehrstuhl für BioMolekulare Optik, Ludwig-Maximilians-Universität München, Oettingenstr. 67, 80538 München, Germany.

Table of Contents

S1 Materials

Phosphonium Salts and Reagents. The syntheses of the phosphonium salts **E–PAr₃⁺ X⁻** will be described elsewhere.[42] Tetraethylammonium bromide (Aldrich, 98%), allyltrimethylsilane (ABCR, 98%) and 2,3-dimethyl-1-butene (Aldrich, 97%) were used as received.

Solvents. For the nanosecond LFP experiments, p.a. grade CH₂Cl₂ (Merck) was subsequently treated with concentrated sulfuric acid, water, 10% NaHCO₃ solution, and again water. After predrying with anhydrous CaCl₂, it was freshly distilled over CaH₂. Acetonitrile (VWR or Sigma-Aldrich, HPLC grade) and 2,2,2-trifluoroethanol (TFE) (Apollo, 99%) were used as received. For the femtosecond UV/Vis transient absorption measurements, acetonitrile (Sigma-Aldrich, spectrophotometric grade) and dichloromethane (Merck, spectrophotometric grade) were used as received.

S2 Experimental procedures for laser flash photolysis measurements

S2.1 Nanosecond laser flash photolysis

Instrumentation. The laser pulses (7-ns pulse length, λ = 266 nm, 30-60 mJ/pulse) from a Nd:YAG laser system (Innolas SpitLight 600, 1064 nm) with second (532 nm) and fourth (266 nm) harmonic generators were directed into a fluorescence flow cell (Starna 73.2-F/MCTC/Q/10/Z15, UV-quartz glass Spectrosil Q, 2 mm wide and 10 mm pathlength) containing the sample solution. Perpendicular to the laser pulse, we used the probe light from a xenon short-arc lamp (Osram XBO 150W/CR OFR in a Hamamatsu E7536 housing with Hamamatsu C8849 power supply) to record transient UV/vis spectra with an ICCD camera (PI Acton PI-MAX:1024) or follow the absorbance change at a specified wavelength with a photomultiplier (Hamamatsu H-7732-10 with Hamamatsu C7169 power supply and Standford Research Systems SR445A amplifier). A 350 MHz oscilloscope (Tektronix DPO 4032) was used for data acquisition of the photomultiplier output. A shutter was used to prevent long exposure of the sample to the light from the xenon lamp, and the sample solution in the fluorescence flow cell was replaced completely between subsequent laser pulses by a membrane dosage pump (KNF Stepdos 03RC).

For the precise timing of the laser pulses and measurements we used a pulse/delay generator (Berkeley Nucleonics BNC 565). The wavelengths of the CCD output were calibrated using the emission lines of a Pen-Ray Hg(Ne) lamp (LOT-Oriel).

Transient spectra. Solutions of the precursor phosphonium salts with $A_{266\,nm} \approx 0.2$ to 0.9 (ca. 10^{-5} to 10^{-4} M) were irradiated with a 7-ns laser pulse ($\lambda_{exc} = 266$ nm, 30-60 mJ/pulse) and transient spectra were obtained as difference spectra from subsequent determinations without and with laser irradiation using the ICCD camera with a gate width of 10 ns. Typically, four to eight such spectra were averaged to obtain the spectra published in this work.

Decay kinetics. Kinetics were measured by following the decay of the absorbance of the benzhydryl cations (see below for wavelengths). Typically, ≥64 individual runs were averaged for each measurement, and the (pseudo-)first-order rate constants k_{obs} (s^{-1}) were obtained by least-squares fitting to the single exponential curve $A(t) = A_0\,e^{-k_{obs}t} + C$. The second-order rate constants k_2 (M^{-1} s^{-1}) for the combination reactions with nucleophiles were obtained from the slopes of plots of k_{obs} versus the concentrations of the nucleophiles. The non-exponential decays were evaluated with the software Gepasi.[43]

S2.2 Ultrafast spectroscopic measurements with sub-100 fs time resolution

Instrumentation. The employed broadband transient absorption spectrometer is described in detail in ref.[39]

Transient absorption measurements. Solutions of E–PAr$_3$$^+$ X$^-$ ($A_{480\,nm} \approx 0.1$ to 0.3, ca. 4×10^{-4} to 6×10^{-3} M) were pumped through a flow cell of 120 μm or 1 mm thickness and irradiated with 35-fs pulses (280 nm, 200 nJ/pulse) from the frequency doubled output of a noncollinear optical parametric amplifier (NOPA). The pulses were focused down to a diameter of about 100 μm inside the sample. A CaF$_2$ white light continuum spanning from 290 nm to 700 nm and polarized at the magic angle was used as probe light. The temporal resolution was between 100 fs and 300 fs depending on the sample layer thickness but always well below all observed decay rates.

Quantum yields, yields and rate constants. See section S5.

S3 Transient spectra obtained by irradiation of E–PPh$_3$$^+$ BF$_4$$^-$ in CH$_2$Cl$_2$

Figure S3. Transient spectra of E$^+$ and E$^\bullet$ obtained after irradiation of CH$_2$Cl$_2$ solutions of E–PPh$_3$$^+$ BF$_4$$^-$ with a 7-ns laser pulse ($\lambda_{exc} = 266$ nm, gate width: 10 ns).

[E13–PPh$_3$$^+$ BF$_4$$^-$] = 1.05 × 10^{-4} M
$A_{266\,nm}$ = 0.50
A_{480nm}/A_{344nm}^{a} ≈ 4

pcp$_2$CH$^\bullet$ (**E13$^\bullet$**)
λ_{max} = 344 nm

pcp$_2$CH$^+$ (**E13$^+$**)
λ_{max} = 480 nm

[E14–PPh$_3$$^+$ BF$_4$$^-$] = 1.01 × 10^{-4} M
$A_{266\,nm}$ = 0.54
A_{438nm}/A_{337nm}^{a} ≈ 3

mfp(Ph)CH$^\bullet$ (**E14$^\bullet$**)
λ_{max} ≈ 337 nm

mfp(Ph)CH$^+$ (**E14$^+$**)
λ_{max} = 438 nm

[E15–PPh$_3$$^+$ BF$_4$$^-$] = 1.77 × 10^{-4} M
$A_{266\,nm}$ = 0.90
A_{430nm}/A_{338nm}^{a} ≈ 2

p-CF$_3$-C$_6$H$_4$(Ph)CH$^\bullet$ (**E15$^\bullet$**)
λ_{max} ≈ 338 nm

p-CF$_3$-C$_6$H$_4$(Ph)CH$^+$ (**E15$^+$**)
λ_{max} = 430 nm

[E16–PPh$_3$$^+$ BF$_4$$^-$] = 1.67 × 10^{-4} M
$A_{266\,nm}$ = 0.87
A_{434nm}/A_{332nm}^{a} ≈ 1.7

dfp(Ph)CH$^\bullet$ (**E16$^\bullet$**)
λ_{max} ≈ 332 nm

dfp(Ph)CH$^+$ (**E16$^+$**)
λ_{max} = 434 nm

[E17–PPh$_3$$^+$ BF$_4$$^-$] = 1.38 × 10^{-4} M
$A_{266\,nm}$ = 0.90
A_{420nm}/A_{331nm}^{a} ≈ 1.5

mfp$_2$CH$^\bullet$ (**E17$^\bullet$**)
λ_{max} = 331 nm

mfp$_2$CH$^+$ (**E17$^+$**)
λ_{max} = 426 nm

Figure S3 (continued). Transient spectra of **E$^+$** and **E$^\bullet$** obtained after irradiation of CH$_2$Cl$_2$ solutions of **E**–PPh$_3$$^+$ BF$_4$$^-$ with a 7-ns laser pulse (λ_{exc} = 266 nm, gate width: 10 ns).

^{a}) The absorbance maxima at the lower wavelengths can be assigned to the radicals **E**,$^\bullet$^{40} but only approximate numeric values can be obtained from the spectra due to the overlap of the PPh$_3$$^{\bullet+}$ absorption band and the relatively large noise in this range of the spectrum.
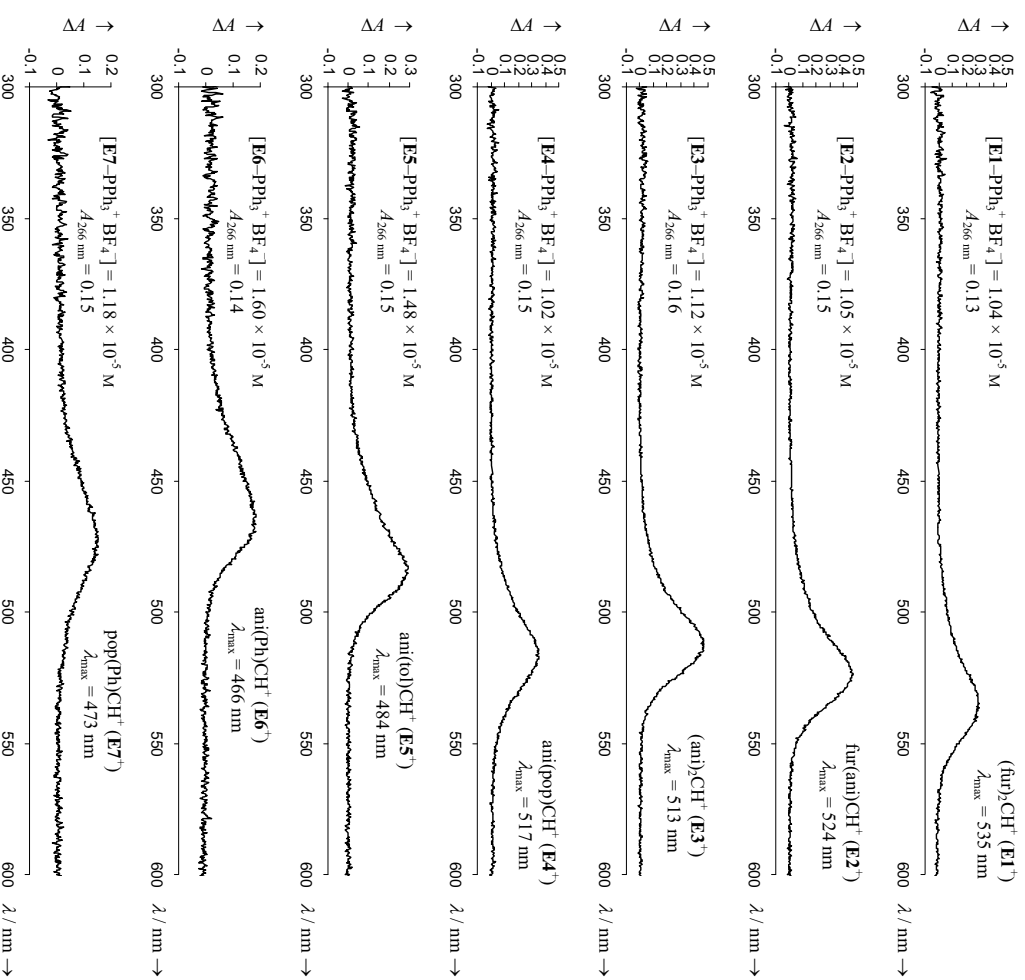
[E8–PPh$_3$$^+$ BF$_4$$^-$] = 6.72 × 10^{-5} M
$A_{266\,nm}$ = 0.50

tol$_2$CH$^+$ (**E8$^+$**)
λ_{max} = 473 nm

[E9–PPh$_3$$^+$ BF$_4$$^-$] = 8.23 × 10^{-5} M
$A_{266\,nm}$ = 0.44

tol(Ph)CH$^+$ (**E9$^+$**)
λ_{max} = 456 nm

[E10–PPh$_3$$^+$ BF$_4$$^-$] = 9.99 × 10^{-5} M
$A_{266\,nm}$ = 0.54
A_{447nm}/A_{327nm}^{a} ≥ 7

pfp$_2$CH$^\bullet$ (**E10$^\bullet$**)
λ_{max} ≈ 327 nm

pfp$_2$CH$^+$ (**E10$^+$**)
λ_{max} = 447 nm

[E11–PPh$_3$$^+$ BF$_4$$^-$] = 8.76 × 10^{-5} M
$A_{266\,nm}$ = 0.49
A_{451nm}/A_{333nm}^{a} ≥ 5

pfp(Ph)CH$^\bullet$ (**E11$^\bullet$**)
λ_{max} ≈ 333 nm

pfp(Ph)CH$^+$ (**E11$^+$**)
λ_{max} = 451 nm

[E12–PPh$_3$$^+$ BF$_4$$^-$] = 1.03 × 10^{-4} M
$A_{266\,nm}$ = 0.49
A_{443nm}/A_{332nm}^{a} ≈ 4

Ph$_2$CH$^\bullet$ (**E12$^\bullet$**)
λ_{max} = 332 nm

Ph$_2$CH$^+$ (**E12$^+$**)
λ_{max} = 443 nm

Figure S3 (continued). Transient spectra of **E$^+$** and **E$^\bullet$** obtained after irradiation of CH$_2$Cl$_2$ solutions of **E**–PPh$_3$$^+$ BF$_4$$^-$ with a 7-ns laser pulse (λ_{exc} = 266 nm, gate width: 10 ns).

^{a}) The absorbance maxima at the lower wavelengths can be assigned to the radicals **E**,$^\bullet$^{40} but only approximate numeric values can be obtained from the spectra due to the overlap of the PPh$_3$$^{\bullet+}$ absorption band and the relatively large noise in this range of the spectrum.

dfp(mfp)CH• (E18•)
λmax = 328 nm

(PPh3•+)

dfp(mfp)CH+ (E18+)
λmax = 435 nm

[E18–PPh3+ BF4–] = 1.55 × 10–4 M
A266 nm = 0.99
A435nm/A328nm a ≈ 0.25

(p-CF3-C6H4)2CH• (E19•)
λmax ≈ 337 nm

(PPh3•+)

[E19–PPh3+ BF4–] = 1.78 × 10–4 M
A266 nm = 0.89
A439nm/A337nm a < 0.1

dfp2CH• (E20•)
λmax = 328 nm

(PPh3•+)

dfp2CH+ (E20+)
λmax ≈ 445 nm

[E20–PPh3+ BF4–] = 1.11 × 10–4 M
A266 nm = 0.64
A445nm/A328nm a < 0.1

Figure S3 (continued). Transient spectra of E+ and E• obtained after irradiation of CH2Cl2 solutions of E–PPh3+ BF4– with a 7-ns laser pulse (λexc = 266 nm, gate width: 10 ns).

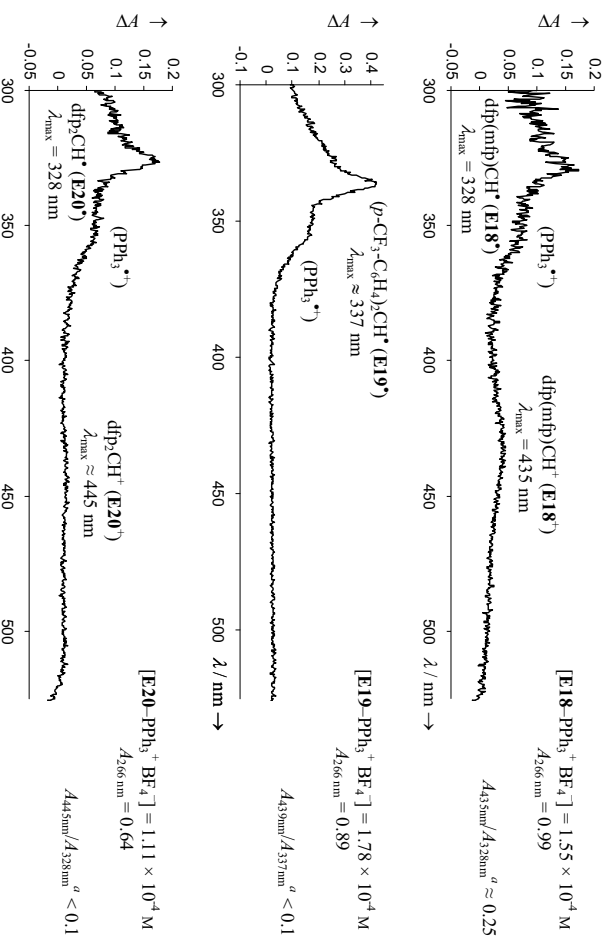a) The absorbance maxima at the lower wavelengths can be assigned to the radicals E•, but only approximate numeric values can be obtained from the spectra due to the overlap of the PPh3•+ absorption band and the relatively large noise in this range of the spectrum.
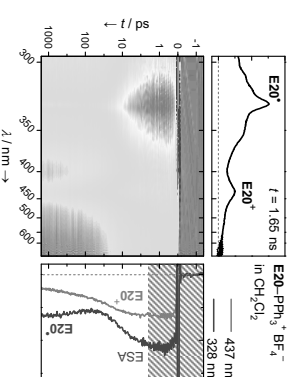
S4 Additional transient absorption plots from ultrafast measurements

S4.1 E20–PPh3+ BF4– in CH2Cl2

Figure S4.1. Transient absorptions observed after irradiating a 6 × 10–3 M solution of E20–PPh3+ BF4– in CH2Cl2 by a 35-fs laser pulse (λexc = 280 nm, A280 nm = 0.1, d = 120 µm). The graph above the color plot shows the spectrum after 1.65 ns. The graph on the right shows the dynamics of the absorbances at certain wavelengths: Red curve: absorbance of benzhydryl cation E20+ (437 nm); blue curve: absorbance of the excited state (ESA) and the benzhydryl radical E20• (328 nm). The time scale is linear between –1 and +1 ps and logarithmic beyond 1 ps.

S4.2 E12–PPh3+ BF4– in CH3CN

Figure S4.2. Transient absorptions observed after irradiating a 4 × 10–3 M solution of E12–PPh3+ BF4– in CH3CN by a 35-fs laser pulse (λexc = 280 nm, A280 nm = 0.2, d = 120 µm). The graph above the color plot shows the spectrum after 1.8 ns. The graph on the right shows the dynamics of the absorbances at certain wavelengths: Red curve: absorbance of benzhydryl cation E12+ (436 nm); blue curve: absorbance of the excited state (ESA) and the benzhydryl radical E12• (329 nm). The time scale is linear between –1 and +1 ps and logarithmic beyond 1 ps.

S5 Determination of quantum yields, yields and rate constants for processes in the geminate solvent cage

S5.1 Time-dependent quantum yields

The time-dependent quantum yield $\Phi(t)$ of the benzhydryl cations is defined by eq. S5.1.

$$\Phi(t) = \frac{[\text{benzhydryl cations}](t)}{[\text{precursor*}]} \qquad (S5.1)$$

The concentration of benzhydryl cations, [benzhydryl cations], at a certain time t is obtained from the time-dependent absorbances $A(t)$ of the benzhydryl cations at their absorption maxima λ_{max}, the absorption coefficients $\varepsilon_{\text{carbocation}}$ and the layer thickness d (eq. S5.2)

$$[\text{benzhydryl cations}](t) = \frac{A(t)}{\varepsilon_{\text{carbocation}} \cdot d} \qquad (S5.2)$$

The exact absorption coefficients for the *meta*-fluorinated benzhydryl cations **E(14,17,18,20)**$^+$ are not known. The quantum yields listed in Table 3 for these systems were calculated using estimated absorbance coefficients ε of $(5.0–7.5) \times 10^4$ M^{-1} cm^{-1}, which are typical values for analogous benzhydryl cations.[40] For the traces of the time-dependent quantum yields in Fig. 3, the following absorption coefficients were assumed: **E14**$^+$: lg ε = 4.72; **E(17,18,20)**$^+$: lg ε = 4.865, which correspond to the averaged lg ε for the *p*-fluoro-substituted systems.[40]
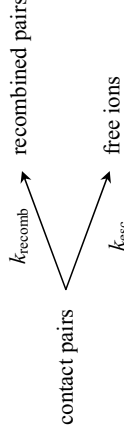
The concentration of precursor molecules wich are excited by the laser pulse, [precursor*], is obtained by multiplication of the total precursor concentration, [precursor], with the probability of excitation, P_{exc} (eq. S5.3):[39]

$$[\text{precursor*}] = [\text{precursor}] \cdot P_{\text{exc}} = [\text{precursor}] \cdot \frac{E_{\text{pump}} \cdot \ln 2}{(hc/\lambda_{\text{exc}}) \cdot \pi (D/2)^2} \cdot \varepsilon_{\text{precursor}} \cdot \frac{\ln 10}{N_A} \qquad (S5.3)$$

The calculation requires the precise determination of the pump pulse energy E_{pump}, the pump focal diameter D at the sample, the pump wavelength λ_{exc} and the absorption coefficient $\varepsilon_{\text{precursor}}$ of the precursor at the pump wavelength as described in ref.[39] (h = Planck's constant, c = velocity of light, N_A = Avogadro's number).

S5.2 Rate laws associated with the carbocation dynamics

After heterolytic bond cleavage, the two photofragments (carbocation and the photo-nucleofuge PAr$_3$) are in close vicinity (contact pair). They can either undergo geminate recombination with the rate constant k_{recomb}, or the fragments diffuse apart with the rate constant k_{esc} so that a bond formation is not feasible anymore (Scheme S5).

Scheme S5. Initially generated contact pairs can either undergo geminate recombination with the rate constant k_{recomb} or separate diffusionally to the free ions with the rate constant k_{esc}.

The time-dependent changes of the concentrations of the contact pairs, of the diffusionally separated ions, and of the carbocations lost by geminate recombination are described by the differential equations S5.4-6.

$$-\frac{d[\text{contact pairs}]}{dt} = (k_{\text{esc}} + k_{\text{recomb}}) \cdot [\text{contact pairs}] \qquad (S5.4)$$

$$\frac{d[\text{free ions}]}{dt} = k_{\text{esc}} \cdot [\text{contact pairs}] \qquad (S5.5)$$

$$\frac{d[\text{recombined pairs}]}{dt} = k_{\text{recomb}} \cdot [\text{contact pairs}] \qquad (S5.6)$$

Integration of eq. S5.4 provides the time-dependent concentration of the contact pairs (eq. S5.7),

$$[\text{contact pairs}] = [\text{contact pairs}]_0 \cdot e^{-(k_{\text{esc}} + k_{\text{recomb}}) \cdot t} \qquad (S5.7)$$

in which [contact pairs]$_0$ is the initial concentration of contact pairs generated by the laser pulse. Substitution of eq. S5.7 into eqs. S5.5 and S5.6 and assuming the initial concentrations [free ions]$_0$ = [recombined pairs]$_0$ = 0 allows to calculate the time-dependent concentrations of the diffusionally separated carbocations (eq. S5.8) and of the carbocations lost by geminate recombination (eq. S5.9).

$$[\text{free ions}] = [\text{contact pairs}]_0 \cdot \frac{k_{\text{esc}}}{(k_{\text{esc}} + k_{\text{recomb}})} \cdot \left[1 - e^{-(k_{\text{esc}} + k_{\text{recomb}}) \cdot t} \right] \qquad (S5.8)$$

$$[\text{recombined pairs}] = [\text{contact pairs}]_0 \cdot \frac{k_{\text{recomb}}}{(k_{\text{esc}} + k_{\text{recomb}})} \cdot \left[1 - e^{-(k_{\text{esc}} + k_{\text{recomb}})t}\right] \qquad (S5.9)$$

Both paired and free carbocations are observed spectroscopically in our experiments; the small differences between the spectra of paired and unpaired benzhydrylium ions are negligible.[52] Thus, addition of the equations S5.7 and S5.8 yields the time-dependent concentration of the spectroscopically observed species (eq. S5.10). Alternatively, the same expression is obtained by substracting eq. S5.9 from the initial concentration of carbocations, [contact pairs]$_0$.

$$[\text{contact pairs}] + [\text{free ions}] = [\text{contact pairs}]_0 - [\text{recombined pairs}] =$$
$$= [\text{contact pairs}]_0 \cdot \frac{k_{\text{recomb}}}{(k_{\text{esc}} + k_{\text{recomb}})} \cdot e^{-(k_{\text{esc}} + k_{\text{recomb}})t} + [\text{contact pairs}]_0 \cdot \frac{k_{\text{esc}}}{(k_{\text{esc}} + k_{\text{recomb}})} \qquad (S5.10)$$

Comparing eq. S5.10 with the single exponential decay function $A(t) = A_0 \cdot e^{-k_{\text{obs}}t} + C$ shows that the experimentally observed rate constant for the decay of the carbocations, k_{obs}, is the sum of the two rate constants k_{recomb} and k_{esc} (eq. S5.11).

$$k_{\text{obs}} = k_{\text{esc}} + k_{\text{recomb}} \qquad (S5.11)$$

S5.3 Fitting of the time-dependent absorbance curves

The absorbance of the benzhydryl cations initially increases due to heterolytic bond cleavage of the excited precursor, subsequently decreases due to geminate recombination, and finally reaches a plateau when all benzhydryl cations are diffusionally separated from PAr$_3$ (Fig. 3). To model the the experimentally observed dynamics of the benzhydryl cations, the time-dependent absorbances $A(t)$ were fitted to a sum of two exponential functions and a constant (eq. S5.12):

$$A(t) = -A_{\text{het}} \cdot e^{-k_{\text{het}}t} + A_{\text{recomb}} \cdot e^{-k_{\text{obs}}t} + A_{\text{free}} \qquad (S5.12)$$
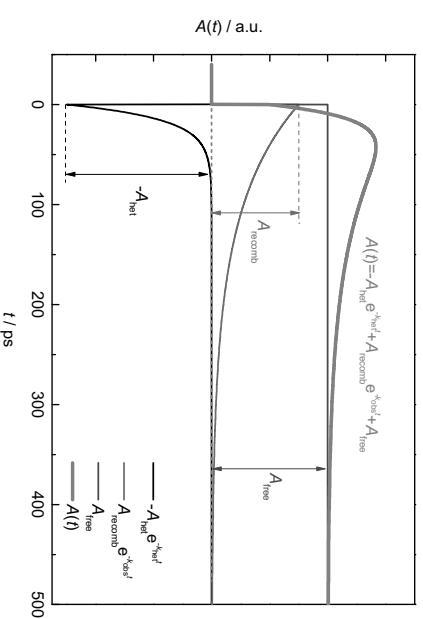
which was corrected for the instrumental response function (for details see refs. 4 and 39).

The fit parameters correspond to the following physical quantities:

A_{het}, absorbance corresponding to the total of all carbocations generated by heterolytic bond cleavage ($A_{\text{het}} = A_{\text{recomb}} + A_{\text{free}}$);

k_{het}, rate constant for heterolytic bond cleavage;

A_{recomb}, total absorbance decrease resulting from geminate recombination;

k_{obs}, experimentally observed decay rate constant for paired and free carbocations (eq. S5.11) as derived in section S5.2; and

A_{free}, remaining absorbance of free carbocations after diffusional separation.

The fit function and the meanings of the different terms are illustrated in Fig. S5 (red curve).

Figure S5. Graphical representation of the different terms in the fit function (eq. S5.12): $-A_{\text{het}} \cdot e^{-k_{\text{het}}t}$ (black curve); $A_{\text{recomb}} \cdot e^{-k_{\text{obs}}t}$ (green curve); and A_{free} (blue curve). The sum of these terms (red curve) is a good fit function for the experimentally observed dynamics.

The employed fit equation (eq. S5.12) closely relates to the equation for the time-dependent concentration of paired and free carbocations (eq. S5.10). Comparing eq. S5.12 with eq. S5.10 reveals that k_{obs} corresponds to ($k_{\text{esc}} + k_{\text{recomb}}$) and the terms for A_{recomb} and A_{free} in eq. S5.12 correspond to the following expressions

$$A_{\text{recomb}} = A_0 \cdot \frac{k_{\text{recomb}}}{(k_{\text{esc}} + k_{\text{recomb}})} \qquad (S5.13)$$

$$A_{\text{free}} = A_0 \cdot \frac{k_{\text{esc}}}{(k_{\text{esc}} + k_{\text{recomb}})} \qquad (S5.14)$$

in which A_0 is the absorbance of the carbocations at the initial concentration of [contact pairs]$_0$ ($A_0 = A_{\text{recomb}} + A_{\text{free}}$).

S5.3 Yields and rate constants associated with the carbocation dynamics

The yields and rate constants associated with the dynamics of E^+ after irradiation of the precursor molecules with the 35-fs laser pulse (Table 3) were determined as follows:

The quantum yield of the benzhydryl cations initially generated by heterolytic bond cleavage, Φ_{het}, is given by eq. S5.15.

$$\Phi_{het} = \frac{A_{het}}{[\text{precursor*}] \cdot \varepsilon_{carbocation} \cdot d} \qquad (S5.15)$$

The quantum yield of the free carbocations after diffusional separation from the photo-leaving group, Φ_{free}, is defined by eq. S5.16.

$$\Phi_{free} = \frac{A_{free}}{[\text{precursor*}] \cdot \varepsilon_{carbocation} \cdot d} \qquad (S5.16)$$

The yield for the geminate recombination, Y_{recomb}, is obtained from eq. S5.17.

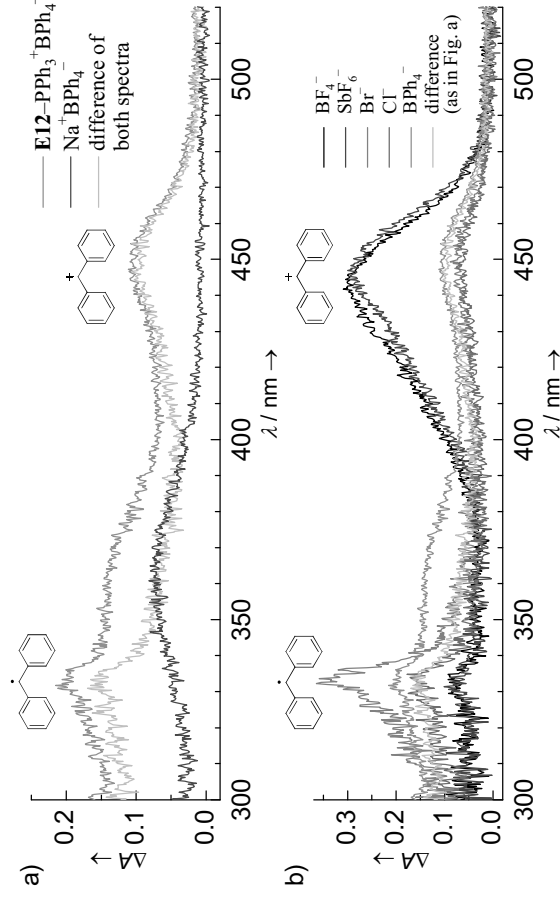$$Y_{recomb} = \frac{A_{recomb}}{A_{recomb} + A_{free}} \qquad (S5.17)$$

Rearranging eqs. S5.13 and S5.14 using eq. S5.17 gives the expressions for the rate constant k_{recomb} (eq. S5.18) and the rate constant k_{esc} (eq. S5.19):[16]

$$k_{recomb} = k_{obs} \, Y_{recomb} \qquad (S5.18)$$

$$k_{esc} = k_{obs} (1 - Y_{recomb}) \qquad (S5.19)$$

S6 Laser flash photolysis of E12–PPh₃⁺ BPh₄⁻ in CH₂Cl₂

We also tested the photobehavior of the tetraphenylborate salt $E12$–PPh$_3^+$ BPh$_4^-$ in CH$_2$Cl$_2$. With this precursor, the phosphonium ion and the tetraphenylborate anion can both be excited by the laser pulse. When a solution of $E12$–PPh$_3^+$ BPh$_4^-$ ($A_{266\ nm}$ = 0.5, 5.7 × 10^{-5} M) in CH$_2$Cl$_2$ was irradiated with a 7-ns laser pulse (λ_{exc} = 266 nm), we obtained the transient spectrum shown in Fig. S6.1 (pink curve). The spectrum features the absorption bands of $E12^+$ and $E12^{\bullet}$ together with a broad absorbance at $\lambda < 400$ nm. A similar band with $\lambda_{max} \approx 363$ nm was observed when we irradiated a CH$_2$Cl$_2$ solution of NaBPh$_4$/15-crown-5 with the same BPh$_4^-$ concentration (Fig. S6.1a, purple curve). The difference spectrum (Fig. S6.1, grey curve) obtained from the two measurements resembles the transient spectrum obtained from the $E12$–PPh$_3^+$ Cl$^-$ precursor (Fig. S6.1b).

a)

legend:
— $E12$–PPh$_3^+$BPh$_4^-$
— Na$^+$BPh$_4^-$
— difference of both spectra

$\Delta A \rightarrow$ 0.2   0.1   0.0   300   350   400   450   500 λ / nm $\rightarrow$

b)

legend:
— BF$_4^-$
— SbF$_6^-$
— Br$^-$
— Cl$^-$
— BPh$_4^-$
— difference (as in Fig. a)

$\Delta A \rightarrow$ 0.3   0.2   0.1   0.0   300   350   400   450   500 λ / nm $\rightarrow$

Figure S6.1. (a) Transient spectra obtained after irradiation of $E12$–PPh$_3^+$ BPh$_4^-$ ($A_{266\ nm}$ = 0.5, 5.7 × 10^{-5} M) in CH$_2$Cl$_2$ (pink) and after irradiation of a solution of NaBPh$_4$ (5.7 × 10^{-5} M) and 15-crown-5 (1.7 × 10^{-3} M) in CH$_2$Cl$_2$ (purple) with a 7-ns laser pulse (λ_{exc} = 266 nm, gate width: 10 ns). The difference between the two spectra is also shown (grey). (b) Comparison with the transient spectra obtained from $E12$–PPh$_3^+$ X$^-$ ($A_{266\ nm}$ = 0.5, (1.0-1.2) × 10^{-4} M) with different counterions X$^-$ = BF$_4^-$ (black), SbF$_6^-$ (blue), Br$^-$ (red), or Cl$^-$ (green) (see Fig. 5b in the article).

The data presented in Figure S6.1 are not in conflict with the general photocleavage mechanism outlined in the main article. However, we refrain from discussing the mechanism because the situation is complicated by the fact that the anion BPh_4^- also absorbs at the excitation wavelength.

Irradiation of a 9.2×10^{-5} M solution of $E12$–PPh_3^+ BPh_4^- gave a pseudo-first-order rate constant of $k_{obs} = 7.93 \times 10^6$ s^{-1} for the decay of $E12^+$ (Fig. S6.2). This value corresponds to a second-order rate constant of $k_2 \approx 9 \times 10^{10}$ M^{-1} s^{-1}, indicating a diffusion-controlled reaction of $E12^+$ with BPh_4^-.

Figure S6.2. Absorbance decay of $E12^+$ obtained after irradiation of $E12$–PPh_3^+ BPh_4^- ($A_{266\ nm}$ = 0.9, 9.2×10^{-5} M) in CH_2Cl_2 with a 7-ns laser pulse (λ_{exc} = 266 nm).

S7 Ion pairing of E12–PPh$_3^+$ BF$_4^-$ in CH$_2$Cl$_2$

As discussed in the main article, we assume that E^+ exist as ion pairs with the BF_4^- counter-anions when they are obtained by laser flash photolysis of E–PAr_3^+ BF_4^-. The nanosecond laser flash photolysis transient spectra of E^+ published in this work were recorded immediately after the laser pulse (0 ns gate delay, 10 ns gate width). To confirm that the association equilibrium of E^+ BF_4^- is already established in our measurements, we measured additional spectra of $E12^+$ at varying gate delays up to 15 μs after irradiation of $E12$–PPh_3^+ BF_4^- in CH_2Cl_2 (Fig. S7). The constant λ_{max} of $E12^+$ in these spectra indicate that the degree of ion pairing does not change substantially during the lifetime of $E12^+$, that is, the association equilibrium is already established in the first spectrum.

Figure S7. Transient spectra of $E12^+$ recorded with varying ICCD gate delays after irradiation of a 1.01×10^{-4} M solution of $E12$–PPh_3^+ BF_4^- in CH_2Cl_2 ($A_{266\ nm}$ = 0.5) with a 7-ns laser pulse (λ_{exc} = 266 nm, gate width: 10 ns).

S8 Transient spectra obtained by irradiation of E19–PAr$_3^+$ X$^-$ in CH$_2$Cl$_2$

Figure S8. Transient spectra of **E19**$^+$ and **E19**$^\bullet$ obtained after irradiation of CH$_2$Cl$_2$ solutions of **E19**–PPh$_3^+$ BF$_4^-$ (black, 1.8×10^{-4} M, $A_{266\,nm}$ = 0.89) and **E19**–P(p-Cl-C$_6$H$_4$)$_3^+$ SbF$_6^-$ (orange, 5.9×10^{-5} M, $A_{266\,nm}$ = 0.90) by a 7-ns laser pulse (λ_{exc} = 266 nm, gate width: 10 ns).

Legend: **E19**–PPh$_3^+$ BF$_4^-$ / **E19**–P(p-Cl-C$_6$H$_4$)$_3^+$ SbF$_6^-$

S9 Evaluation of non-exponential decays of E$^+$ in CH$_2$Cl$_2$

For benzhydryl cations **E**$^+$ with lifetimes $> \sim 10$ μs, we observed non-exponential UV/vis absorption decays of the carbocations which we examined more closely in a few cases (Fig. 9 and Fig. S9).

Plot a): k_{PPh_3} = $(1.19 \pm 0.004) \times 10^{10}$ M^{-1} s^{-1}; k_0 = $(2.33 \pm 0.03) \times 10^3$ s^{-1}

Plot b): k_{PPh_3} = $(1.06 \pm 0.003) \times 10^{10}$ M^{-1} s^{-1}; k_0 = $(5.78 \pm 0.02) \times 10^3$ s^{-1}

Legend: experimental data / Gepasi fit

Figure S9. Decays of **E8**$^+$ (a) and **E9**$^+$ (b) observed after irradiation of $(4.2\text{-}4.7) \times 10^{-5}$ M solutions of **E(8-9)**–PPh$_3^+$ BF$_4^-$ in CH$_2$Cl$_2$ with a 7-ns laser pulse of λ_{exc} = 266 nm. Experimental data (black) and fit according to the kinetic model discussed in the text (red).

The non-exponential decay kinetics result from a combination of second- and first-order processes. The second-order component is the combination reaction of the benzhydryl cations **E**$^+$ with the photo-leaving group PAr$_3$ (eq. S9.1) which is generated by the laser pulse in the same initial concentration as the benzhydrylium ions.

$$\mathbf{E}^+ + PAr_3 \xrightarrow{\ k_{PAr}\ } \mathbf{E}\text{–}PAr_3^+ \qquad (S9.1)$$

However, second-order kinetics according to eq. S9.1 alone do not describe our experimental data satisfactorily. For that reason, we included a general first-order reaction (eq. S9.2) which summarizes all first-order reactions which may occur and which are discussed in section 3.7 of the main article.

$$\mathbf{E}^+ \xrightarrow{k_0} \text{other decay products} \qquad (S9.2)$$

The absorbances of **E**$^+$ were converted to concentrations [**E**$^+$] by means of the published log ε (CH$_3$CN).[40] Using the software Gepasi,[43] the concentration data was then fitted according to the kinetic scheme indicated by equations S9.1 and S9.2, which yielded diffusion-controlled rate constants for the combination reaction with PAr$_3$, $k_{PAr_3} \approx 1 \times 10^{10}$ M^{-1} s^{-1}, and rate constants k_0 for the first-order background decay reaction. Direct determination of the second-order rate constants for the diffusion-controlled reactions of benzhydrylium ions **E**$^+$ with PPh$_3$ was not attempted because PPh$_3$ absorbs at the excitation wavelength of the laser. Johnston, Scaiano and coworkers reported a rate constant of 5 × 10^9 M^{-1} s^{-1} for the reaction of PPh$_3$ with the 2-naphthyl-(phenyl)methyl cation in CH$_3$CN.[33]

The Gepasi fits for the decays of **E(8-9)**$^+$ obtained by irradiation of **E(8-9)**–PPh$_3^+$ BF$_4^-$ in CH$_2$Cl$_2$ (Fig. S9) yielded k_0 values which probably reflect the reactions **E(8-9)**$^+$ wi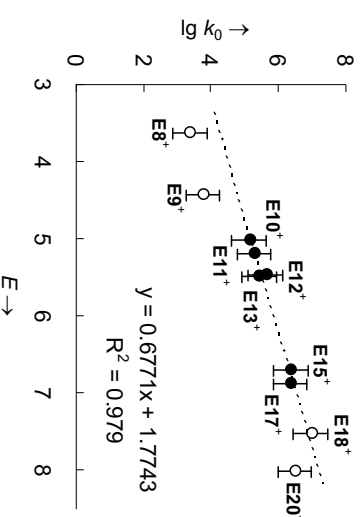th BF$_4^-$. The obtained values are in good agreement with the directly measured background decay rate constants k_0 of the more electrophilic carbocations **E(10-17)**$^+$ when these were generated from **E(10-17)**–PPh$_3^+$ BF$_4^-$ precursors (see section S10). For the example of **E12**$^+$ obtained by irradiation of **E12**–PPh$_3^+$ SbF$_6^-$ in CH$_2$Cl$_2$ (Fig. 9 in the article), the exact nature of the background decay reaction is not clear; as expected the determined k_0 value is considerably smaller than that for the tetrafluoroborate salt.

S10 Reactions of E$^+$ with BF$_4^-$ in CH$_2$Cl$_2$

Generally, the background decay rate constants k_0 (s^{-1}) measured for **E**$^+$ which were obtained by irradiation of **E**–PAr$_3^+$ BF$_4^-$ in CH$_2$Cl$_2$ correlate roughly with the electrophilicity parameters E of the benzhydryl cations **E**$^+$ (Fig. S10.1). However, the observed k_0 values vary considerably between different experiments which may be a result of varying precursor concentrations and/or varying concentrations of solvent impurities in the experiments. Since a large fraction of the carbocations are paired and the k_0 values partly reflect first-order reactions within the **E**$^+$ BF$_4^-$ ion pairs, we do not derive nucleophilicity parameters for BF$_4^-$ in CH$_2$Cl$_2$ from these decay rate constants.

Figure S10.1. Typical background decay rate constants k_0 (s^{-1}) of **E**$^+$ observed after irradiation of **E**–PAr$_3^+$ BF$_4^-$ in CH$_2$Cl$_2$ with a 7-ns laser pulse (λ_{exc} = 266 nm) versus the electrophilicity parameters E of the benzhydryl cations **E**$^+$. Arbitrary error bars (one logarithmic unit) symbolize the large uncertainties associated with the individual measurements. Open symbols: Data for **E(8-9)**$^+$ (obtained by Gepasi fits) and **E(28-29)**$^+$ (which show a lower dependence on the counter-anions) were not included in the fit.

Fig S10.2 clearly shows the lower initial absorbances of **E(18,20)**$^+$ when the benzhydryl cations were obtained by irradiation of **E(18,20)**–P(p-Cl-C$_6$H$_4$)$_3^+$ X$^-$ with X$^-$ = BF$_4^-$ instead of precursors

S11 Decay kinetics of benzhydryl cations in CH_3CN and TFE

S11.1 First-order decay rate constants of benzhydryl cations in acetonitrile

benzhydryl cation		$[E–PPh_3^+ BF_4^-]$ / M	λ / nm	k_1 / s^{-1}
E12[+]	Ph_2CH^+	1.22×10^{-4}	435	$2.52 \times 10^{6\ a}$
E14[+]	$mfp(Ph)CH^+$	1.09×10^{-4}	432	1.00×10^{7}
E17[+]	$(mfp)_2CH^+$	1.39×10^{-4}	435	$3.49 \times 10^{7\ b}$

[a] A value of 2.5×10^6 was reported in ref.[40 b] This rate constant is slightly above the limit which can be measured accurately with our instrument. To minimize the statistical error, 352 individual runs were averaged to obtain this k_{obs} value.

S11.2 First-order decay rate constants of benzhydryl cations in 2,2,2-trifluoroethanol (TFE)

benzhydryl cation		$[E–PPh_3^+ BF_4^-]$ / M	λ / nm	k_1 / s^{-1}
E10[+]	$(pfp)_2CH^+$	6.15×10^{-5}	447	5.82×10^{5}
E12[+]	$(Ph)_2CH^+$	1.13×10^{-4}	440	$3.21 \times 10^{6\ a}$
E13[+]	$(pcp)_2CH^+$	1.12×10^{-5}	481	1.47×10^{6}
E14[+]	$mfp(Ph)CH^+$	1.10×10^{-4}	440	1.29×10^{7}
E17[+]	$(mfp)_2CH^+$	$(1.4 - 1.5) \times 10^{-4}$	428	$4.6 \times 10^{7\ b}$

[a] A value of 3.2×10^6 was reported in ref.[8 b] Such high rate constants cannot be measured accurately with our instrument. To minimize the statistical error, 384 individual runs were averaged to obtain this k_{obs} value.

---

with X^- = SbF_6^- (also see Fig. 7 in the main article). Again, this suggests that BF_4^- very quickly traps a significant fraction of E(18,20)[+] in the ion pairs generated by the laser pulse.

Figure S10.2. Absorbance decays of E(18,20)[+] obtained after irradiation of (a) 5.7×10^{-5} M solutions of E18–P(p-Cl-C_6H_4)$_3$ X^- or (b) 6.5×10^{-5} M solutions of E20–P(p-Cl-C_6H_4)$_3$ X^- with different counter-anions X^- = BF_4^- (black) and SbF_6^- (blue) in CH_2Cl_2 with a 7-ns laser pulse.

We observed exponential decays of the carbocations E(18,20)[+] with similar rate constants k_0 when they were generated from precursors with X^- = BF_4^- or SbF_6^- in CH_2Cl_2 (Fig S10.2). This suggests that the benzhydryl cations E[+] also undergo some additional decay reaction which is independent of the counter-ions and becomes more dominant with higher electrophilicity E of the carbocations. This additional decay pathway probably results from the reactions of E[+] with solvent impurities such as residual water in our CH_2Cl_2, which also explains why we find slightly varying k_0 values in different experiments (different batches of CH_2Cl_2). Even small amounts of water may have a significant effect on carbocation lifetimes: 1 ppm water in CH_2Cl_2 corresponds to a 7.3×10^{-5} M solution of water in CH_2Cl_2. From the N_1 and s parameters for pure water (ref.[9]) one can estimate that the rate constants for reactions of water with benzhydrylium ions E(10-20)[+] will only be a few orders of magnitude below the diffusion limit and the observed rate constants will be quite high in spite of the low water content.

S12 Counter-ion effects on the kinetics of bimolecular reactions of E$^+$ with nucleophiles in CH$_2$Cl$_2$

S12.1 Reactions of E12$^+$ with allyltrimethylsilane in dichloromethane at 20 °C.

[E12-PPh$_3$$^+$ X$^-$] / M	[Nu] / M	k_{obs} / s^{-1}
1.02 × 10^{-4} (X$^-$ = BF$_4$$^-$)	2.52 × 10^{-2}	5.78 × 10^5
	5.39 × 10^{-2}	1.05 × 10^6
	7.94 × 10^{-2}	1.48 × 10^6
	1.00 × 10^{-1}	1.79 × 10^6
	1.29 × 10^{-1}	2.23 × 10^6

λ = 449 nm

k_{obs} = 1.60 × 10^7 [Nu] + 1.88 × 10^5
R^2 = 0.9994

k_2 / M^{-1} s^{-1} = 1.60 × 10^7

[E12-PPh$_3$$^+$ X$^-$] / M	[Nu] / M	k_{obs} / s^{-1}
1.02 × 10^{-4} (X$^-$ = SbF$_6$$^-$)	2.69 × 10^{-2}	4.89 × 10^5
	5.29 × 10^{-2}	8.66 × 10^5
	8.00 × 10^{-2}	1.25 × 10^6
	1.01 × 10^{-1}	1.56 × 10^6
	1.28 × 10^{-1}	1.93 × 10^6

k_{obs} = 1.43 × 10^7 [Nu] + 1.08 × 10^5
R^2 = 0.9999

1.43 × 10^7

[E12-PPh$_3$$^+$ X$^-$] / M	[Nu] / M	k_{obs} / s^{-1}
9.95 × 10^{-5} (X$^-$ = Br$^-$)	2.79 × 10^{-2}	7.57 × 10^6
	5.37 × 10^{-2}	7.99 × 10^6
	7.59 × 10^{-2}	8.38 × 10^6
	9.86 × 10^{-2}	8.67 × 10^6
	1.29 × 10^{-1}	9.00 × 10^6

k_{obs} = 1.42 × 10^7 [Nu] + 7.23 × 10^6
R^2 = 0.9881

1.42 × 10^7

[E12-PPh$_3$$^+$ X$^-$] / M	[Nu] / M	k_{obs} / s^{-1}
1.03 × 10^{-4} (X$^-$ = Cl$^-$)	2.42 × 10^{-2}	7.32 × 10^6
	4.93 × 10^{-2}	7.72 × 10^6
	7.53 × 10^{-2}	8.14 × 10^6
	9.94 × 10^{-2}	8.45 × 10^6
	1.27 × 10^{-1}	8.92 × 10^6

λ = 449 nm

k_{obs} = 1.53 × 10^7 [Nu] + 6.96 × 10^6
R^2 = 0.9987

k_2 / M^{-1} s^{-1} = 1.53 × 10^7

S12.2 Reactions of E18$^+$ with 2,3-dimethyl-1-butene in dichloromethane at 20 °C.

[E18-PAr$_3$$^+$ X$^-$] / M	[Nu] / M	k_{obs} / s^{-1}
5.62 × 10^{-5} (Ar = p-ClC$_6$H$_4$, X$^-$ = BF$_4$)	3.51 × 10^{-2}	1.09 × 10^7
	6.66 × 10^{-2}	1.42 × 10^7
	9.63 × 10^{-2}	1.72 × 10^7
	1.30 × 10^{-1}	1.92 × 10^7
	1.58 × 10^{-1}	2.17 × 10^7
	1.93 × 10^{-1}	2.41 × 10^7

λ = 440 nm

k_{obs} = 8.24 × 10^7 [Nu] + 8.57 × 10^6
R^2 = 0.9924

k_2 / M^{-1} s^{-1} = 8.24 × 10^7

[E18-PAr$_3$$^+$ X$^-$] / M	[Nu] / M	k_{obs} / s^{-1}
5.68 × 10^{-5} (Ar = p-ClC$_6$H$_4$, X$^-$ = SbF$_6$)	2.83 × 10^{-2}	5.29 × 10^6
	6.35 × 10^{-2}	9.16 × 10^6
	9.65 × 10^{-2}	1.16 × 10^7
	1.23 × 10^{-1}	1.34 × 10^7
	1.67 × 10^{-1}	1.71 × 10^7

k_{obs} = 8.27 × 10^7 [Nu] + 3.39 × 10^6
R^2 = 0.9932

8.27 × 10^7

$[\text{E18-PAr}_3^{+}\,\text{X}^{-}]$ / M	$[\text{Nu}]$ / M	k_{obs} / s^{-1}	$\lambda = 440$ nm	k_2 / M^{-1} s^{-1}
1.11×10^{-4}	3.67×10^{-2}	1.86×10^{7}		8.22×10^{7}
(Ar = Ph,	5.03×10^{-2}	2.00×10^{7}		
$\text{X}^{-} = \text{BF}_4^{-}$)	6.49×10^{-2}	2.15×10^{7}		
	7.89×10^{-2}	2.33×10^{7}		
	9.99×10^{-2}	2.34×10^{7}		
	1.14×10^{-1}	2.62×10^{7}		

$k_{\text{obs}} = 8.22 \times 10^{7}\,[\text{Nu}] + 1.59 \times 10^{7}$

$R^2 = 0.9278$

Appendix D5

A Comprehensive Microscopic Picture of the Benzhydryl Radical and Cation Photo-Generation and Interconversion through Electron Transfer

C. F. Sailer, S. Thallmair, B. P. Fingerhut, C. Nolte, J. Ammer, H. Mayr, R. de Vivie-Riedle, I. Pugliesi, E. Riedle

A Comprehensive Microscopic Picture of the Benzhydryl Radical and Cation Photo-Generation and Interconversion through Electron Transfer

Christian F. Sailer[a], Sebastian Thallmair[a,b], Benjamin P. Fingerhut[b], Christoph Nolte[b], Johannes Ammer[b], Herbert Mayr[b], Regina de Vivie-Riedle[b], Igor Pugliesi[a], Eberhard Riedle*[a]

[a] Lehrstuhl für BioMolekulare Optik, Ludwig-Maximilians-Universität München, Oettingenstr. 67, 80538 München, Germany

[b] Department Chemie, Ludwig-Maximilians-Universität München, Butenandtstr. 5–13, 81377 München, Germany

Email: Riedle@physik.uni-muenchen.de

RECEIVED DATE

*Author to whom correspondence should be addressed.

Eberhard Riedle:

Tel: +49 (0)89 2180 9210

Fax: +49 (0)89 2180 9202

E-mail address: Riedle@physik.uni-muenchen.de

ABSTRACT

The precise mechanism and dynamics of the photo-generation of carbocations and carbon radicals is a fundamental issue in organic chemistry. Especially the role and importance of electron transfer for the generation of carbocations from the radical pair is still unclear. We present a quantitative transient absorption study with femtosecond resolution and ultrabroad probing on selected donor- and acceptor-substituted benzhydryl chlorides irradiated with 270 nm (35 fs) pulses. The ultrafast bond cleavage of benzhydryl chloride within 300 fs is almost exclusively homolytic, leading to a benzhydryl/chlorine radical pair. The carbocations observable in the nanosecond regime are generated from these radicals by electron transfer from the benzhydryl to the chlorine radical within the first tens of picoseconds. Their concentration is subsequently reduced by geminate recombination within hundreds of picoseconds. In moderately polar solvents like dichloromethane this depletion almost extinguishes the cation population, in highly polar solvents like acetonitrile free ions are still observable on the nanosecond time scale. The explanation of our experimental findings beyond an empirical kinetic model requires that the microscopic realm of the intermediates, which comprehends their spatial and environmental distributions, is taken into account. We combine a distance dependent electron transfer model given by Marcus theory with the Smoluchowski diffusion model. The depletion of the radical pair distribution at small distances causes a temporal increase of the mean distance and leads to the observed stretched exponential electron transfer dynamics. A close accord with the experiment can only be reached if a broad distance distribution of the nascent radical pairs is assumed. The increase in the inter-radical and inter-ion pair distance is directly measured as a shift of the UV-Vis absorption maxima of the products. Our results demonstrate that traditional descriptions of reaction mechanisms based on the concept of contact and solvent-separated pairs have to be reassessed.
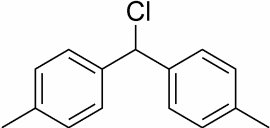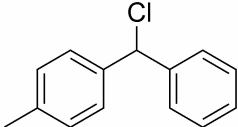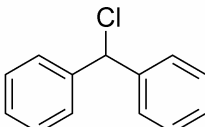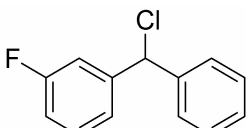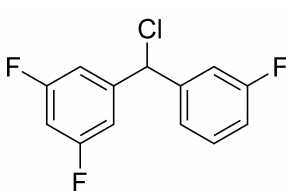
1. Introduction

Carbocations are key intermediates in many organic reactions.[1-5] They can be generated by photoinduced heterolysis of organic halides such as R-Cl[6-22] or other precursors.[6-8,23-26] The photolysis of these precursors can also lead to the generation of carbon-centered radicals.[9-11,26] Photoinduced heterolysis and homolysis are ideal processes for the time-resolved investigation of bond cleavage and subsequent reactions involving the photogenerated ionic and radical intermediates via ultrafast pump-probe spectroscopy. Such processes were previously investigated by nanosecond pump-probe experiments of McClelland[6] as well as Miranda, Scaiano and coworkers,[10] and by product studies of Hilborn et al..[27] Their data have led the researchers to propose that in addition to the direct generation of carbocations and carbon-centered radicals by photoinduced bond cleavage, there is a pathway by which initially generated radical pairs decay into ion pairs via electron transfer.[6,10,27] It was suggested that this pathway is the main source of carbocations.[27,28] However, the factors contributing to the electron transfer responsible for the interconversion of radicals to cations are not yet clear. Early work of Peters and coworkers on the photolysis of benzhydryl halides suggests that the interconversion occurs via electron transfer in the vicinity of the radical and cation potential energy surface crossing.[11,29,30] However, as was shown by several groups, intermolecular electron transfer can occur on much larger donor-acceptor distances and is strongly affected by diffusion.[31-34] It is therefore conceivable that carbocations are not only generated from radical pairs in contact distance but also from radical pairs separated by at least one solvent shell.

Furthermore, it is not clear how the carbocation yield is related to the electron transfer. It has been reported that the yield of the benzhydryl cations observable with nanosecond techniques is strongly solvent dependent and that in many solvents virtually no carbocations can be detected.[6-9] For example, moderately stabilized benzhydryl cations Ar_2CH^+ ($E \geq 0$, compare Chart 1) can be obtained by photolysis of the corresponding benzhydryl chlorides in CH_3CN but not in CH_2Cl_2[9] and the photo-generation of these benzhydryl cations in CH_2Cl_2 requires other photo-leaving groups such as PPh_3.[25,26] In view of the important role these reactive intermediates play in organic chemistry and as initiators of organic polymerizations,[21,35-37] it is desirable to find out whether an inhibition of the electron transfer or an efficient depletion of the ion pairs by geminate recombination is responsible for the negligible quantum yields in solvents of low polarity.

Here we present ultrafast broadband pump-probe experiments on the photolysis of a set of benzhydryl chlorides (shown in Chart 1). The sub-100 fs time resolution and the ultrabroad probe (290 nm – 700 nm) allow for the observation of the dynamics of all evolving product bands and make even subtle effects visible, such as shifts of the maxima of the UV-Vis product absorption band (peak shifts) and

possible non-exponential population dynamics. The wealth of data generated by the quantitative evaluation of the broadband measurements and the modifications in the substitution pattern lead to a detailed reaction scheme which is presented in Section 3. In Section 4 we develop a microscopic model to quantifiy and detail the proposed mechanism. Furthermore, we analyze the temporal shifts of the benzhydryl cation and radical absorption band to trace the microscopic changes in the solute environment. In Section 5 we study the influence of solvent and temperature variations on the dynamics and yields. A further dimension is gained by changing the nature of the substituents on the aryl groups.

Chart 1   Benzhydryl Chlorides Investigated in this Work and Empirical Electrophilicity Parameters E of the Corresponding Benzhydryl Cations[a].

compound	abbreviations	E [b]
	(tol)$_2$CHCl	3.63
	tol(Ph)CHCl	4.43
	Ph$_2$CHCl	5.47
	mfp(Ph)CHCl	6.23
	dfp(mfp)CHCl	7.52

[a]) $\Delta E \approx 4$ on the logarithmic E scale indicates that dfp(mfp)CH$^+$ is approximately 10,000 times more electrophilic than (tol)$_2$CH$^+$.
[b]) From Ref. 38

3

2. Quantitative femtosecond pump-probe spectroscopy

Materials. Benzhydryl chloride (Ph$_2$CHCl) was purchased from Sigma-Aldrich and used without further purification. The derivatives (tol)$_2$CHCl, tol(Ph)CHCl and mfp(Ph)CHCl were prepared as described in references 39 and 40. The details for the synthesis of 3,3',5-trifluorobenzhydryl chloride dfp(mfp)CHCl are given in Section S6 of the Supporting Information. The solvents used were of the highest spectroscopic grade available.

Femtosecond transient absorption measurements. The details of the femtosecond transient absorption setup have been described in reference 41. For the measurements presented here, solutions of the precursors were pumped through a flow cell of 120 μm optical path length and excited at 270 nm, close to the maximum of the first absorption band. The pulses had an energy of about 200 nJ and a pulse duration of ~35 fs. They were focused down to a diameter of ~ 100 μm leading to a fraction of excited precursor molecules in the pumped volume of ≤ 1% (see SI, Section S1.2). A CaF$_2$ continuum spanning from 290 nm to 700 nm and polarized at the magic angle was used as probe light. The temporal resolution was ~ 100 fs, well below all observed decay rates.

Temperature dependent measurements have been carried out with a slightly modified flow cell system. The temperature of the sample, the pump and the flow cell itself were kept at a constant temperature between 5 °C and 60 °C by a thermostat. The temperature of the sample solution was additionally monitored by a digital thermometer.

Conversion of absorption changes into absolute quantum yields. Absolute quantum yields are an essential measure to gain detailed insight in the mechanism and dynamics of photochemical processes. While rates give information on the speed of a reaction, quantum yields give access to the efficiency of the product formation on the sub-pico to microsecond timescale. They often allow for the determination of competing rates that can otherwise not be measured. The concentration of excited precursors can be derived from the pump pulse wavelength, energy and FWHM diameter as well as the molar absorption coefficient of the precursor. Since the molar absorption coefficients of the benzhydryl radicals and cations are well documented in the literature,[9] we are able to calculate the time-dependent concentrations of photogenerated benzhydryl radicals and cations. By comparing the concentration of the photofragments to the concentration of excited precursors, one obtains the time-dependent quantum yields of benzhydryl cations and radicals. Final yields of specific sub-processes (e.g., electron transfer) are the limit to "infinite" time and technically determined from the preexponential factors in the fit. The details of the calculations of the yields are given in the Supporting Information, Section S1 and S2. The resulting values are summarized in Table 2.

3. Photoinduced dynamics of benzhydryl chloride and its photoproducts

Figure 1b shows the evolution of the transient absorption spectrum after UV-irradiation of benzhydryl chloride (Ph_2CHCl) in acetonitrile (CH_3CN): The probe wavelength is plotted on the horizontal axis and the pump-probe delay on the vertical axis. Blue color indicates low absorbance and red color high absorbance. The delay on the vertical axis is shown in a linear scale for the first ps and in a logarithmic scale afterwards. After UV irradiation, we observe the appearance of two bands at 329 nm and 435 nm (see Figure 1a for the spectrum observed after 40 ps). The two spectral signatures coincide with the product bands observed in nanosecond laser flash photolysis experiments on benzhydryl halides[9] and on benzhydryl phosphonium ions.[26] In line with refs. 9 and 26, and other reports we assign the band at 329 nm to the benzhydryl radical and the 435 nm band to the benzhydryl cation. After a fast initial rise, the radical band reaches its maximum at ~ 1 ps and subsequently decays within 100 ps to about half of its initial intensity and then remains constant on the nanosecond time scale. In contrast, the cation band reaches its maximum within 40 ps and subsequently decays within a few hundred picoseconds. The residue of the cation signal is stable on the nanosecond time scale (compare Figures 1b and 2).

The temporal evolution of the signal attributed to the cation and radical population along the vertical lines in Figure 1b is shown in Figure 2 (grey circles). To quantify the product dynamics we employed fits on the band maxima of cation and radical (red lines): Both products show a fast initial rise which can be fitted with a 300 fs (radical) / 260 fs (cation) exponential time constant. While the fast rise of the radical signal is associated with a large increase of its population, the rise of the cation signal amplitude is 20 times weaker. For the subsequent picosecond decay of the radical and rise of the cation a satisfactory fit can not be obtained with a single or double exponential. However, we obtained an excellent fit by employing a stretched-exponential function like $A(t) = A_{SE} \exp\left(-\left(t/\tau_{SE}\right)^{\beta_{SE}}\right)$. A comparative mono-exponential fit for the $Ph_2CH^{\bullet}$ radical is shown in Figure S2. It turned out that the dynamics of the large number of measurements with differing substituents, solvents and temperatures can all be well fitted with $\beta_{SE} = 0.5$. In order to confine the number of free fit parameters β_{SE} was therefore set to 0.5. For the decay of the radical and the rise of the cation we obtain the same time constant of $\tau_{SE} = 11.1$ ps. With this time constant the cation signal increases largely and the cation population reaches its maximum. The radical population decreases with the same time constant and then remains unchanged for several nanoseconds. The magnitude of the population changes matches closely. At later times the cation absorption shows a further decay with a time constant of 140 ps before it reaches a constant level after 1 ns. The need to include standard and stretched exponentials into a stable fit of the complete experimental data set is in distinct contradiction to earlier analyses.[29,30] The

conclusions drawn from the earlier multi-exponential fits of single wavelength measurements, therefore, have to be viewed with care.
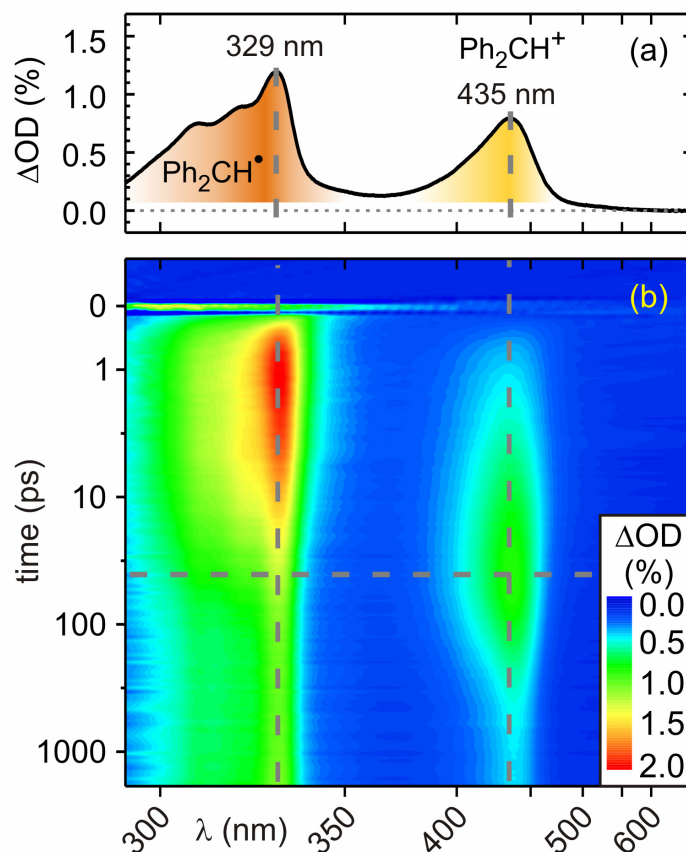
Figure 1 (a) Transient spectrum at a pump-probe delay of 40 ps and (b) false color representation of the 2D transient absorption data matrix of Ph_2CHCl in CH_3CN after 270 nm UV excitation. The delay time axis is linear between -1 and 1 ps and logarithmic beyond 1 ps.

Based on the experimental data and fits presented so far, we develop a kinetic reaction scheme for the population dynamics of the photoproducts which is shown in Scheme 1. We assign the 300 / 260 fs time constants to simultaneous photoinduced homolytic and heterolytic C–Cl bond cleavages and subsequent solvent and geometric relaxation of the benzhydryl radical and cation. Details of this complex evolution of the earliest signals, that can also explain the slightly different times, are discussed elsewhere.[42] While the homolysis leads to the radical pair $Ph_2CH^\bullet$ / $Cl^\bullet$ (path ① in Scheme 1) with a quantum yield of $\Phi_{Hom} = 40\%$, the heterolysis generates the ion pair Ph_2CH^+ / Cl^- (pathway ②) with $\Phi_{Het} = 2\%$ (see Figure 2 and Table 2). The mechanism of the ultrafast bond cleavage of Ph_2CHCl has recently been investigated by high level ab inito calculations[28] which suggest that in solution homolysis is favored over heterolysis.

The stretched exponential time constant $\tau_{SE} = 11.1$ ps is associated with a dramatic rise of the cation signal and a substantial decrease of the radical signal. This coordinated rise and fall indicates that the

6

cations are formed from the radicals via an electron transfer from the benzhydryl radical to the $Cl^{\bullet}$ radical in close vicinity (pathway ③ in Scheme 1). As has been shown,[43,44] the fact that the electron transfer has to be fitted with a non-exponential function indicates that the observed kinetics is coupled to a process which occurs on a slower time scale. It will be shown that this process is diffusion which is too slow to overcome the depletion of close $Ph_2CH^{\bullet}$ and $Cl^{\bullet}$ radicals by electron transfer (see Section 4). Consequently, the distance dependent electron transfer rate translates to the time-dependent electron transfer rate seen in the experiment. The mean electron transfer time is given by twice τ_{SE}[45], i.e. $\tau_{ET} = 2\,\tau_{SE} = 22.2$ ps.
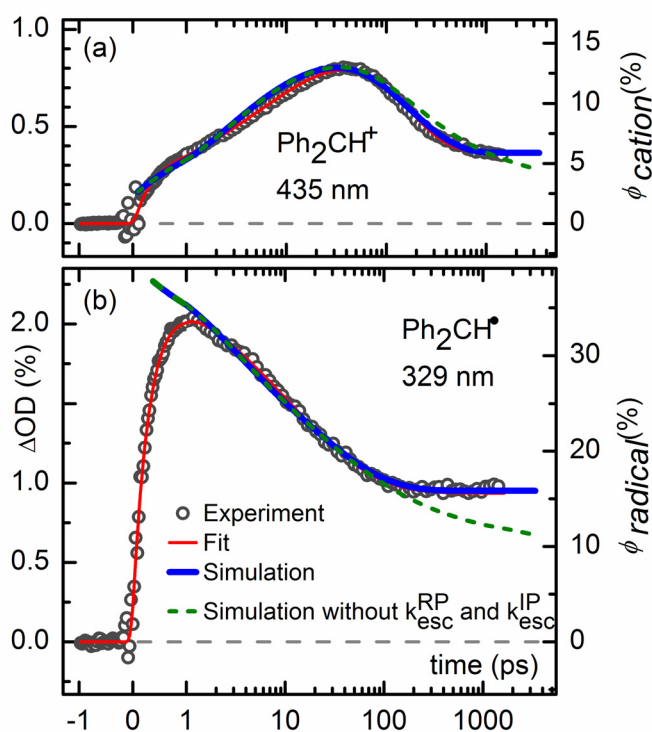
Figure 2   Temporal evolution of the signal of (a) the benzhydryl cation and (b) the benzhydryl radical in CH_3CN. The corresponding cation and radical quantum yields Φ_{cation} and $\Phi_{radical}$ are indicated on the right vertical axes. Fits are shown in red. Results from the simulations which combine Marcus type electron transfer and Smoluchowski type diffusion with and without the fragment escape rates k_{esc}^{RP} and k_{esc}^{IP} (see Section 4.1) are shown in blue and green. The calculated signals have been normalized with respect to the radical population after the homolytic bond cleavage.

The electron transfer is the main process depleting the radical population. Still, a sizable part of the radical pairs can avoid electron transfer and also geminate recombination (pathway ⑤) and separate by diffusion leading to free radicals (pathway ④). A major part of the formed cations decays with an additional time constant of 138 ps while a smaller fraction remains unchanged for hundreds of nanoseconds or even longer. This behavior can be explained by a competition between the geminate

recombination of the ion pair and diffusional separation of the ions: After the photoinduced C–Cl bond cleavage, the ion pairs generated by heterolysis or electron transfer can either separate to give rise to long lived free ions (pathway ⑥) or recombine to Ph_2CHCl (pathway ⑦). The geminate recombination can only occur as long as the fragments are in close vicinity and is terminated by diffusional separation. The observed cation decay time of 138 ps therefore is determined jointly by the geminate recombination and the cation escape. The individual rates can be extracted from the data and turn out to be $k_{rec}^{IP} = 5.05 \times 10^9\,s^{-1}$ and $k_{esc}^{IP} = 2.19 \times 10^9\,s^{-1}$ (see Supporting Information for details).
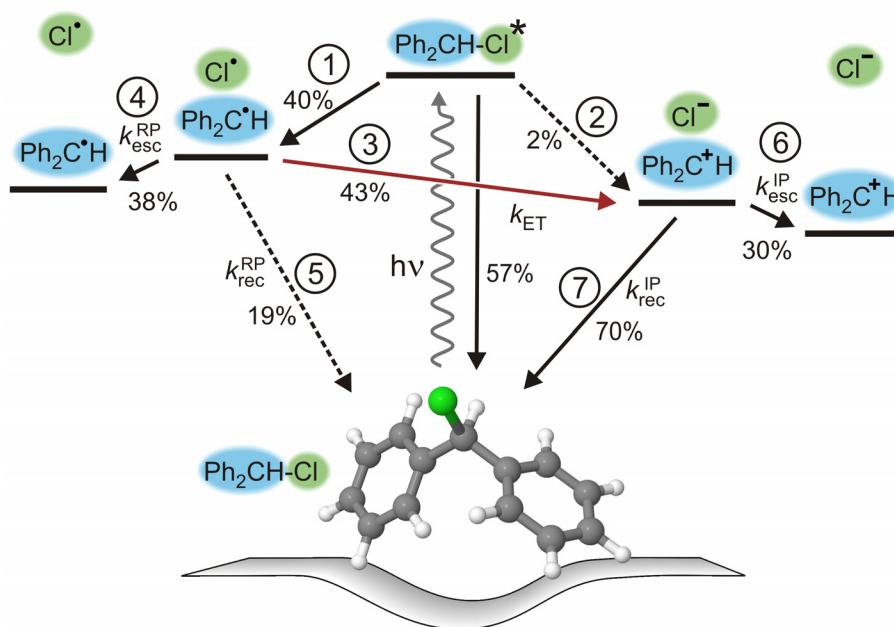
Scheme 1 Reaction mechanism (not to scale) with reaction yields observed in CH_3CN. After UV excitation of Ph_2CHCl the excited molecules undergo predominantly homolytic bond cleavage ①. The heterolytic pathway ② is only of minor importance. An electron can be transferred within the radical pair ③ leading to the major part of the observed cation population. The simultaneously occurring diffusional separation of the radical pair ④ slows down the electron transfer and eventually leads to free radicals. A minor fraction of the radical pairs recombines to reform Ph_2CHCl ⑤. The ion pairs in close vicinity either undergo geminate recombination to the starting material ⑦ or escape and diffuse apart ⑥ to form free ions.

4. Microscopic picture of the photo-induced reactions in time and space

The temporal evolution and the final quantum yield of the photogenerated radicals and cations are the result of a subtle interplay between the time-dependent electron transfer, the geminate recombination

and the diffusion. However, the mechanism in Scheme 1 is only a simplification to illustrate the fundamentals of the photo-process. The non-exponential kinetics observed for the depletion of the radical population and the generation of cations cannot be modeled by reaction mechanisms solely based on a simple picture of transitions between intermediates with well-defined spatial and environmental conditions, such as contact pairs and solvent-separated pairs.[11,46] The generated radical and ion pairs actually span a range of distances, configurations and environments leading to a varying behavior. Therefore, we replace the kinetic model used so far by a microscopic description that explicitly takes into account the distribution of intermediates involved in the processes. In the microscopic model inter-radical and inter-ion distance dependent rates for the electron transfer, the geminate recombination and the escape are used. The spatial average of these rates over the time dependent spatial distribution then renders the experimentally observable rates that actually correspond to the ensemble average.

4.1 Theory: Combined Marcus - Smoluchowski model

The reaction mechanism proposed at the end of Section 3 incorporates electron transfer and geminate recombination subject to diffusion. Based on Scheme 1, these concepts are used to simulate the population dynamics and the associated signals. We embed the two processes in a joint theoretical model by combining diffusion with distance-dependent electron transfer and geminate recombination of the photofragments (these processes are associated with the steps ③ to ⑦ in Scheme 1). A similar approach has already been employed by Fayer and coworkers[47] for describing electron transfer processes in dyes and by Grampp and coworkers[33] for bimolecular fluorescence quenching. The bond cleavage and the initial solvation dynamics occur in the first hundreds of femtoseconds and are not topic of the present investigation. It suffices to start with the effective situation present after a few hundred femtoseconds. We begin the description by a first overview of all relevant aspects and detail them later in the Section together with the results of the simulation.

Time dependent population distributions. We consider the time dependent population distribution $P_{RP}(R,t)$ for the radical pairs and $P_{IP}(R,t)$ for the ion pairs. We assume spherical symmetry and R denotes the distance between the centers of the two species making up each pair. The two functions correspond to the probability that a radical or ion pair is separated by the distance R at time t. The diffusional evolution is described in the frame work of the Smoluchowski formalism,[48] the distance dependent electron transfer rate $k_{ET}(R)$ by Marcus theory,[49,50] and the geminate recombination rates $k_{rec}^{RP}(R)$ and $k_{rec}^{IP}(R)$ as well as the escape rates $k_{esc}^{RP}(R)$ and $k_{esc}^{IP}(R)$ by a distance dependent rate each. To obtain the overall population $P(t)$ which is proportional to the experimentally accessible

product absorption, integration over the distance coordinate starting from the contact distance $R_c = r_{benzhydryl} + r_{Cl} = 6.13$ Å is necessary

$$P(t) = \int_{R_c}^{\infty} P(R,t)\,dR \tag{1}$$

$r_{benzhydryl}$ and r_{Cl} are the radii of the fragment radicals deduced from the cavity volume found by a DFT calculation in a continuum solvation model.

$P_{RP}(R,t)$ and $P_{IP}(R,t)$ cannot be directly propagated, instead underlying distribution functions $S_{RP}(R,t)$ and $S_{IP}(R,t)$ have to be used.[33,51] These are related to $P_{RP}(R,t)$ and $P_{IP}(R,t)$ by[52-54]

$$P_{RP}(R,t) = 4\pi R^2\, S_{RP}(R,t)\exp\left[-V_{RP}(R)/k_BT\right] \tag{2}$$

$$P_{IP}(R,t) = 4\pi R^2\, S_{IP}(R,t)\exp\left[-V_{IP}(R)/k_BT\right] \tag{3}$$

with the intrapair potentials $V_{RP}(R)$ and $V_{IP}(R)$. The radial distribution function $g(R)$ modeling the partially ordered solvent shell is entering the description through the potentials. k_BT is the thermal energy. This step is needed to ensure that the Boltzmann distribution is an equilibrium solution of the model.

Differential equations with sink and source terms. The resulting set of coupled differential equations is

$$\begin{aligned}
\frac{\partial}{\partial t} S_{RP}(R,t) &= L^+ S_{RP}(R,t) - k_{ET}(R) S_{RP}(R,t) \\
&\quad - k_{rec}^{RP}(R) S_{RP}(R,t) - k_{esc}^{RP}(R) S_{RP}(R,t)
\end{aligned} \tag{4}$$

$$\begin{aligned}
\frac{\partial}{\partial t} S_{IP}(R,t) &= L^+ S_{IP}(R,t) + k_{ET}(R) S_{RP}(R,t)\exp\left[-\frac{e^2}{4\pi\varepsilon_0\varepsilon_{st}k_BT}\frac{1}{R}\right] \\
&\quad - k_{rec}^{IP}(R) S_{IP}(R,t) - k_{esc}^{IP}(R) S_{IP}(R,t)
\end{aligned} \tag{5}$$

The exponential factor accompanying the source term in eq. 5 ensures that the population transfer between $P_{RP}(R,t)$ and $P_{IP}(R,t)$ is properly described by $S_{RP}(R,t)$ and $S_{IP}(R,t)$ within the Smoluchowski formalism. L^+ is the adjoint Smoluchowski operator in spherical coordinates. The exact form of L^+ and all other necessary details are given in Section 4 of the supporting information. The system of partial differential equations is solved numerically for a given set of parameters. Various input parameters were taken from the literature and others were fitted by comparing the result of the simulation to the experiment. Particularly important values are discussed below, all values are summarized in Table S1.

The electron transfer is a sink term for the radical distribution and a source term for the ion pairs. The back electron transfer pathway is neglected in our simulations since it is highly endergonic in solvents such as CH_3CN or CH_2Cl_2 due to the ultrafast solvation of the cation. The driving force for the electron transfer is given by the change in Gibbs free energy ΔG_{ET}. Values for ΔG_{ET} are known in some cases from measurements and a complete set has been calculated (see Section S4.3). An explicit distance dependence of $k_{ET}(R)$ is taken as $\exp[-\beta(R-R_c)]$ with $\beta = 0.7$ Å^{-1}.[50] The distance dependence of relevant quantities for the simulation of the photo-triggered processes in Ph_2CHCl dissolved in CH_3CN is displayed in Figure S3a.

Geminate recombination is a sink term for both the radicals and the ions. Strictly speaking it should only happen at contact, but the quantum mechanical nature of the system allows for some spread. In accordance with Ref. 55 we model the recombination as $k_{rec}(R) = k_{rec}^0 \cdot \exp\left[-\alpha\left(R - R_c \right) \right]$ with $\alpha = 1.0$ Å^{-1}. Finally, eqs. (4) and (5) contain formal sink terms for an escape. These terms refine the description of the solvent. The Marcus-Smoluchowski equations (4) and (5) are based on a continuum solvation model where the dielectric constant of the solvent remains invariant for the photofragment separation distance. In other words, the continuum model assumes that the fragments are surrounded by a complete solvation shell for all fragment distances. In actual fact however, fully stabilizing solvation shells are only formed at distances large enough to accommodate two solvent molecules between the two ions. This leads to a sudden decrease of the energy of the system as the photofragments move apart and prevents them from reencounter. We use a sigmoidal function with a 50% value at R_c + $2\,d_{solv} = 13.3$ Å for $k_{esc}(R)$ to model the transfer from reactive (bound) radical/ion pairs to free ones. Here d_{solv} denotes the solvent diameter. For the evaluation of the time dependent populations (eqs. 1-3) we add the populations of the reactive species and the free ones to $P_R(R,t)$ and $P_I(R,t)$ since they contribute equally to the experimental signal.

Initial conditions. In our model, the initial distribution of radical pairs is described by a Gaussian for $S_{RP}(t=0)$ centered at a mean benzhydryl radical - Cl$^\bullet$ radical distance larger than the contact distance R_c by half a solvent diameter d_{solv} and with a half-width at half-maximum (HWHM) of 1.8 d_{solv}. These values were obtained as best fit to the experimental data from simulation runs with varied distributions. A similar distance distribution has been found for electrons that have been photo-detached from I$^-$ in aqueous solution.[56] The need for a nascent distribution which far exceeds direct contact of the radicals can be seen directly from the experimental data (compare Figure 2). The cation yield from electron transfer increases rapidly in the first 10 ps. This means that the electron transfer rate has to be quite significant, roughly $k_{ET}(R_c) = 10^{12}$ s^{-1}. If only pairs close to contact would be present, the same high rate would lead to a nearly complete depletion of the radical population. Only the rather wide nascent distribution used in our simulation can lead to the observed survival of roughly half the radicals. The stretched exponential behavior observed is a direct consequence of this evolution of the population

distribution and the ensuing slow down of the ensemble averaged electron transfer rate. It should be noted that we effectively start to consider the evolution of the benzhydryl cations and radicals after a few hundred femtoseconds when the planarization and solvation is complete, and the distance distribution has become quasi-stationary. For distances smaller than R_c the distribution is set to zero. This mirrors the fact that fragments which are not ejected far enough are nearly instantaneously recombining. This is also seen in the total yield of fragments that is far from quantitative.

Results of the simulation. The time dependent radical and ion distributions in CH_3CN for the best fit are shown in Figure 3 a) and b). The calculated population dynamics for the benzhydryl radical and cation are compared to the experiment in Figure 2 (blue lines). For delay times above 1 ps there is an excellent agreement between the experimental and the simulated signal. For times below 1 ps the effective increase of optical signal strength by planarization and solvation prevents the direct extraction of populations from the experiment.[42] A list of all the input parameters used in the model (taken from literature) and the values determined for the best fit is given in Table S1.
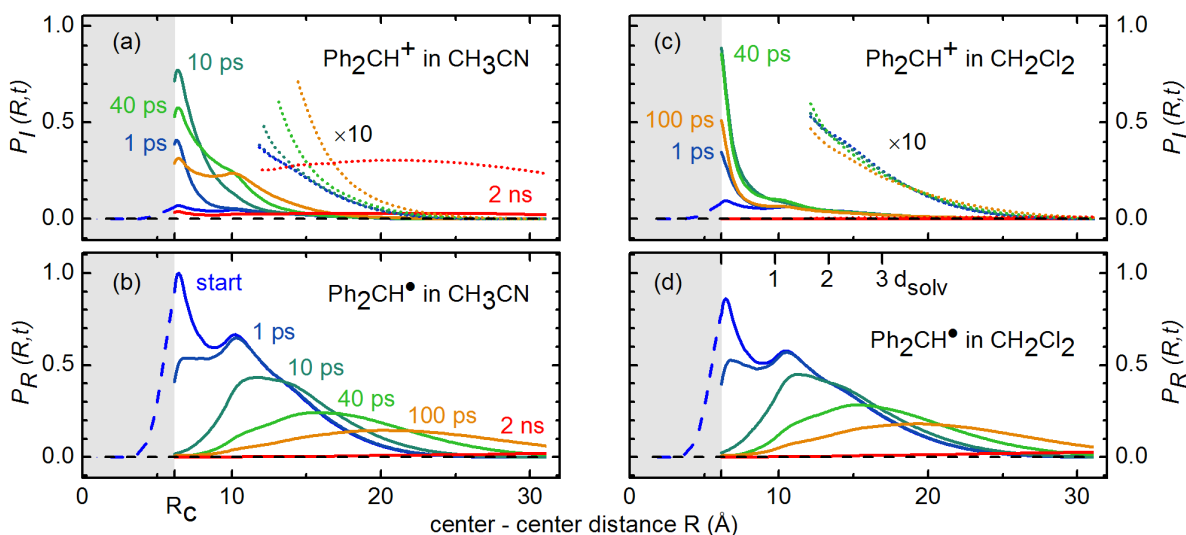
Figure 3   Simulated time-dependence of the population distribution with CH_3CN as solvent for (a) the sum of the bound and free ion pairs $P_I(R,t)$ and (b) the sum of the bound and free radical pairs $P_R(R,t)$. Population distribution with CH_2Cl_2 as solvent (c) for the ions and (d) for the radicals (see Section 5). The shaded area indicates distances smaller than the contact distance R_c. Nascent photofragments generated in this area (dashed lines) are assumed to recombine immediately.

The initial distribution $P_{RP}(R,t=0)$ shows some degree of structure due to the solvent shells. Within the first few ps the closest radical pairs are converted to ion pairs or recombine. At $t = 10$ ps the probability to find radical pairs in the range from R_c to $R_c + d_{solv}$ is already extremely small. Simultaneously the ion distribution $P_{IP}(R,t)$ rises from the small nascent values with a large distribution to sizable values close to R_c. At tens of ps the radical distribution broadens due to diffusion and

effectively shifts to larger average values, both due to diffusion and the still ongoing yet decreasingly important electron transfer and radical recombination at close distance. The ion pairs are held together by Coulomb attraction and therefore geminate recombination can compete with the diffusional separation. The value for the radical pair mutual diffusion coefficient D_F was taken from Ref. 47. The value for the ion pair was varied in the optimization of the model and the best value of $D_F(IP) = 60$ Å^2/ns is in the range of recently published values.[57,58] It is significantly smaller than the value for the radical pair since the mobility of the ions is decreased by the stronger solvent-solute interactions and the resulting larger hydrodynamic radius.[59]

The distance integrated radical population shows a pronounced decay and the cation population an increase with a stretched time constant of 10.8 ps (compare blue lines in Figure 2), nearly identical to the experimental value of 11.1 ps. The conversion of radicals to ions is slowed down from 20 ps on and ceases shortly after 100 ps due to the depletion of the radical distribution close to contact and the diffusional separation. The depletion is caused by both the electron transfer and the partial geminate recombination and in turn stops these processes eventually.

The cation population clearly decreases from the maximum achieved at 40 ps. This is due to the geminate recombination which we model with $k_{rec,0}^{IP} = 25 \times 10^9 s^{-1}$ at contact distance. The experimental value of $5.05 \times 10^9 s^{-1} = (198 ps)^{-1}$ is five times smaller. This directly reflects the fact that the value in the simulation is distance dependent and only a part of the ion pairs are in the range where geminate recombination becomes effective, while the experimental value is deduced for the whole ensemble. To obtain more comparable values, we calculated the recombination rate, i.e. the ensemble averaged probability, for selected times (see Table 1, second to last column). At 1 ps the calculated rate is nearly twice as fast as the experimental rate due to the large fraction ions pairs with a small separation. At 40 ps it is roughly equal and at 2 ns it starts to become unimportant.

For the radical recombination a much faster value of $k_{rec,0}^{RP} = 300 \times 10^9 s^{-1}$ is found. This might seem surprising at first sight. We calculated the driving forces ΔG_{RP} and ΔG_{IP} and find the change in Gibbs free energy by 1.61 eV more exergonic for the radical recombination (see Table S2). This can readily explain the observed situation.

Without the consideration of escape rates for both the radicals and the ions (see above), we cannot reproduce the leveling of the radical population in the sub-ns range, the recombination would keep going. This is shown in Figure 2 as green dashed lines. To reproduce the experimentally observed stable radical and cation population on the nanosecond timescale, equal escape rates $k_{esc,\infty}^{RP} = k_{esc,\infty}^{IP} = 6.67 \times 10^9 s^{-1}$ are used. Due to the sigmoidal function centered at two solvent diameters from contact distance, only pairs that have already been separated by diffusion are "stabilized" by the escape rate. The calculated escape rate (see Table 1, last column) at 1 ps shows little

likelihood for the ions to escape due to the tight distribution. At 40 ps it even decreases since the newly generated ions are close to R_c and only at 2 ns it becomes quite sizable. The escape rate only has effect in a distance range where the electron transfer and the geminate recombination are no longer active.

Ensemble averaged properties. The ability to calculate ensemble averaged properties and in this way to link the microscopic picture with the experimental observables has been used for a number of further analyses. The results are summarized in Tables 1 and 2 and compared to the experimental values.

The electron transfer rate is dominantly determined by ΔG_{ET} and the effective electronic coupling element V_{eff}. We calculated values for ΔG_{ET} (see Table S2) that compare favorably with the experimental values where available. For the simulations we allowed a variation within the known accuracy of the calculations of 0.1 eV. The value of $V_{eff} = 57$ cm^{-1} is within the range reported for these types of systems.[50,60] As a result an electron transfer rate of $667 \times 10^9 s^{-1}$ is found on contact. The ensemble averaged rate k_{ET} drops from $66.7 \times 10^9 s^{-1}$ at 1 ps to $3.77 \times 10^9 s^{-1}$ at 40 ps and finally practically vanishes at 2 ns when all remaining radical pairs have converted to free radicals. The theoretical model shows that the experimentally observed deviations from mono-exponential decays are caused by the starting distance distribution of the radical pairs and the distance-dependence of the electron transfer rates. This leads to the effectively time dependent electron transfer rate depicted in Figure S5.

The various yields clearly become time dependent as the constituting processes evolve. By $t = 2$ ns the accumulated yields obtained from the simulation are all very close to the experimental values. Since we mainly used the comparison with the optical signals, i.e. the radical and cation population for the adjustment of the model parameters, the close match of all individual yields nicely confirms the consistency of our model.

In summary, the simulation highlights the importance of diffusion for the persistent generation of free ions and free radicals. The electron transfer predominantly happens in a narrow part of the distribution of benzhydryl - Cl$^{\bullet}$ inter-radical distances, even though a fairly wide range of distances arises from the photo-induced bond cleavage. This is a consequence of the electron transfer rate which decays exponentially with increasing distance. The generated ion pairs still experience the Coulomb potential and cannot diffuse apart as easily as the uncharged radicals. This more than compensates the smaller driving force for recombination as compared to the radicals and leads to a higher overall recombination yield. The kinetic model invoking transitions between distinguishable species, i.e. contact ion pairs, solvent-separated ion pairs and free ions as well as geminate radical pairs and free radicals used in the extensive work on the photolysis of benzhydryl halides by Peters and coworkers[11,29,30] does not consider these microscopic details and renders at best a phenomenological description.

14

Table 1. Experimental and Theoretical (*italic*) Driving Forces ΔG and Rate Constants *k* of the Electron Transfer, Geminate Recombination and Escape for Different Benzhydryl Derivatives and Solvents (See Supporting Information, Section S1.4 and S4.2 for Definitions)

solvent	derivative	ΔG_{ET} [a] (eV)	ΔG_{ET} [b] (eV)	τ_{SE} [c] (ps)		k_{ET} $(10^9$/s) ③ [d]	k_{rec}^{IP} $(10^9$/s) ⑦ [e]	k_{esc}^{IP} $(10^9$/s) ⑥ [f]
	(tol)₂CHCl	-1.79	-1.82	17.6			3.57	1.98
	tol(Ph)CHCl	-1.69	-1.70	18.7			4.10	1.93
	Ph₂CHCl	-1.68	-1.61	11.1			5.05	2.19
CH₃CN					*1 ps*	*66.7*	*7.87*	*0.86*
	simulation		*-1.71*	*10.8*	*40 ps*	*3.77*	*5.81*	*0.46*
					2000 ps	*0.13*	*1.33*	*3.23*
	mfp(Ph)CHCl		-1.48	8.4			5.13	2.52
	dfp(mfp)CHCl		-1.19	-			14.5	5.59
	(tol)₂CHCl	-	-1.45	19.3			4.08	< 0.25
	tol(Ph)CHCl	-	-1.32	24.2			5.68	< 0.25
CH₂Cl₂	Ph₂CHCl	-	-1.23	11.2			7.46	< 0.25
					1 ps	*35.7*	*7.30*	*0*
	simulation		*-1.13*	*12.3*	*40 ps*	*2.31*	*10.0*	*0*
					2000 ps	*0.004*	*0.37*	*0*
butyronitrile	Ph₂CHCl	-	-	27.3			6.06	1.12
chloroform	Ph₂CHCl	-	-	13.0			8.00	< 0.25

[a]) Experimental and [b]) calculated Gibbs free reaction energy of the electron transfer within the radical pair. Experimental values from the one electron reduction potentials for benzhydryl cations (from Ref. 61) and the Cl• radical (from Ref. 62). For calculation see Section S4.3 [c]) Stretched exponential time constant assigned to the electron transfer ③. [d]) Microscopic model ensemble average of the electron transfer rate at selected times. [e]) Rate of the ion pair geminate recombination ⑦. [f]) Rate for the cation escape by diffusional separation ⑥.

Table 2. Experimental and Theoretical (*italic*) Yields *Y* and Quantum Yields Φ of the Electron Transfer, Geminate Recombination and Escape for Different Benzhydryl Derivatives and Solvents. See Supporting Information, Sections S1.3 and S4.2 for Definitions. All Values in %.

solvent	derivative	Φ_{Hom}	Φ_{Het}		Y_{ET}	Y_{rec}^{RP}	Y_{esc}^{RP}	Y_{rec}^{IP}	Y_{esc}^{IP}	Φ_{rad}	Φ_{cat}
		①[g]	②[h]		③[i]	⑤[j]	④[k]	⑦[l]	⑥[m]	n	o
CH₃CN	(tol)₂CHCl	46	2		75	0[p]	25[p]	64	36	19.3	11.4
	tol(Ph)CHCl	47	<1		73	0[p]	27[p]	68	32	17.7	11.0
	Ph₂CHCl	40	2		43	19	38	70	30	15.7	6.0
				1 ps	*7*	*3*	*0*	*0*	*0*	*35.0*	*5.4*
	simulation			*40 ps*	*36*	*14*	*9*	*20*	*1*	*19.5*	*13.2*
				2000 ps	*43*	*17*	*40*	*69*	*31*	*(15.7)*	*6.0*
	mfp(Ph)CHCl	29	2		16	35	49	67	33	14.2	2.2
	dfp(mfp)CHCl	20	1		0	49	51	72	28	10.3	<1
CH₂Cl₂	(tol)₂CHCl	27	2		60	0[p]	40[p]	>95	<5	12.3	1.3
	tol(Ph)CHCl	36	<1		56	2	42	>95	<5	15.4	<1
	Ph₂CHCl	32	<1		27	28	45	>95	<5	14.5	<1
				1 ps	*4*	*3*	*0*	*0*	*0*	*28.8*	*4.5*
	simulation			*40 ps*	*21*	*20*	*9*	*29*	*0*	*18.1*	*7.2*
				2000 ps	*27*	*26*	*47*	*99*	*0*	*(14.5)*	*0.3*
butyronitrile	Ph₂CHCl	25	<1		21	0[p]	79[p]	84	16	21.7	<1
chloroform	Ph₂CHCl	34	2		20	33	47	>95	<5	15.7	<1

[g]) Quantum yield for direct homolytic bond cleavage. [h]) Quantum yield for direct heterolytic bond cleavage. [i]) Yield of the electron transfer (pathway ③ in Scheme 1). [j]) Yield of recombination of the radical pair ⑤. [k]) Yield of escape by diffusional separation of the radical pair ④. [l]) Yield of the ion pair geminate recombination ⑦. [m]) Yield of escape by diffusional separation of the ion pair ⑥. [n]) Final (nanosecond) radical quantum yield for the experimental values, cumulative quantum yield up to the specific time for the simulation. [o]) Final (nanosecond) cation quantum yield for the experimental values, cumulative quantum yield up to the specific time for the simulation. [p]) Slightly more cations appear than radicals disappear. Therefore, Y_{rec}^{RP} has been set to 0% and Y_{esc}^{RP} has been set so that $Y_{ET} + Y_{rec}^{RP} = 100\%$.

4.2 Spectral shifts resolve spatial information

Due to the high signal to noise ratio and the sub 100 cm^{-1} (about 1 nm) resolution provided by our setup we were able to observe that the product bands shift in the sub-nanometer range. This observable has not been accessible previously as only two color pump-probe experiments have been carried out on comparable systems. Due to electronic interactions the absorption band position of a single solute molecule is a sensitive probe for its immediate environment. With the ensemble averaging in our measurements the overall band position is given by the convolution of the time dependent distance distribution and the distance dependent spectral position of the absorption band. Therefore, temporal shifts of the absorption maximum (peak shift) reveal changes of the distance distribution and thereby the immediate surrounding in solution, specifically the leaving group and the solvent molecules.
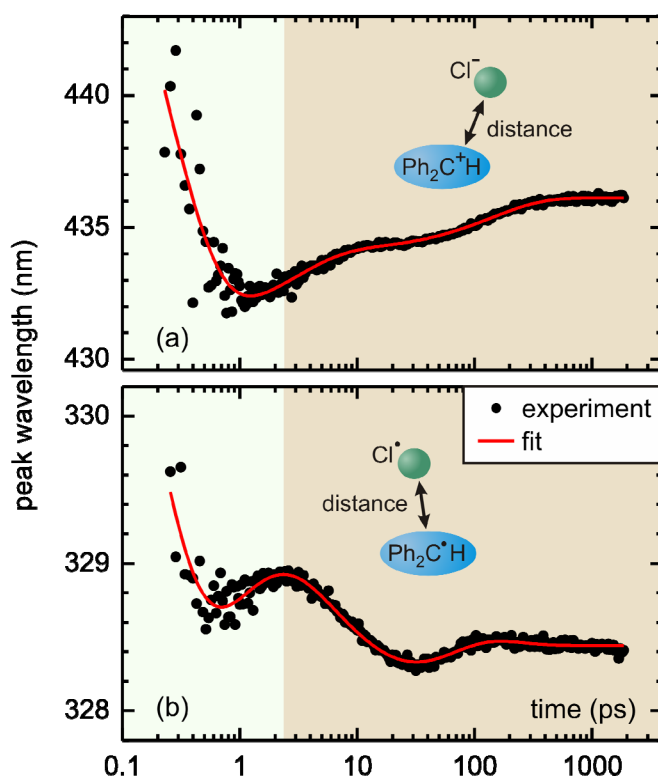
Figure 4   Measured (dots) and fitted (red line) temporal evolution of the benzhydryl (a) cation and (b) radical peak position after photolysis of Ph_2CHCl in CH_3CN. The temporal regime where the shift is dominated by the changes in the radical and ion pair distance distributions caused by electron transfer, geminate recombination and diffusion is highlighted in light brown.

Temporal shifts of the absorption band due to microscopic changes have already been observed in the infrared[32] as well as in the visible.[63,64] In the first hundreds of femtoseconds also the geometric relaxation of the nascent fragment can contribute to the peak shift.[42] In the following we will discuss the

peak shift determined from the transient spectra (compare Figure 1) by an iterative procedure described in Section S3 of the supporting information.

- The observed temporal evolution of the peak shifts (see Figure 4) shows a complex behavior that can only be fitted with a sum of exponential functions. After excitation, both the radical and the cation band experience a pronounced initial blue shift. These shifts can be fitted with time constants of 170 fs for the radical and 250 fs for the cation.

The values compare well with the published solvation times of 140 fs - 500 fs of CH_3CN[65-68] indicating that the blue shift is caused by the rearrangement of the solvation shell in the immediate vicinity of the photogenerated radical and ion pair.[42] The radical shows a further red shift within the first 2 ps. While the initial dynamics up to 2 ps is caused by solvent rearrangement and by relaxation and planarization of the photofragments, the subsequent peak shifts are caused by the interplay between the diffusional separation and the population dynamics of the cations and radicals.

- The cation shows a red shift which can be fitted with two exponential functions with time constants of 2.9 ps and 140 ps. At pump-probe delays larger than 500 ps the cation peak position reaches a wavelength of 436.1 nm and undergoes no further shift indicating that free and fully solvated cations have been formed.

From a quantum chemical point of view it is reasonable that the absorption shifts to the red. For increasing inter-ion distances the energy of the ground state of the benzhydryl cation can be expected to increase slightly more than the energy of the excited state. Our observation also reproduces the findings of Schneider et al.[69] who observed that the absorption maximum of free (unpaired) benzhydryl cations (e.g., $(tol)_2CH^+$) is red-shifted by ~ 2 nm compared to cations paired with BCl_4^- anions.

- The radical undergoes a blue shift from 2 to 30 ps - in contrast to the cation - which can be modeled with the 11.1 ps stretched exponential found in the kinetic analysis. After a further red shift from 30 to 100 ps with a time constant of 45 ps, the radical peak position reaches a stable wavelength of 328.4 nm.

Unlike for the cation, an increase in the inter-radical distance apparently leads to a blue shift. This can be rationalized by the fact that the exchange of the $Cl^\bullet$ radical by CH_3CN solvent molecules leads to a better stabilization of the radical ground state and thus a blue shift of the absorption band. By the observation of the peak shift we trace the change in the inter-radical distance distribution, which is caused predominantly by the electron transfer.

The 140 ps time constant of the cation peak shift is equal within experimental precision to the 138 ps total decay time found in the analysis of the cation population. Together with the equality of the 11.1 ps stretched exponential for the radical peak shift and population kinetics we find a reassuring match between the population and the peak shift evolution. We therefore arrive at the following microscopic picture for the reaction scheme: The individual photofragment pairs have a peak position dependent on

their mutual distance. After photolysis a relatively broad distribution of distances exists leading to an inhomogeneous peak broadening additional to that caused by solvent interactions. Peak shifts are now caused by two mechanisms: a) the tendency of the species to diffuse apart and hence to increase the mean distance and b) the efficient depletion of sub-ensembles with small distances by electron transfer and geminate recombination. It is the second mechanism that mainly leads to the peak shifts that can be reproduced with time constants also found in the population dynamics.

5. Effects of temperature, solvent polarity and substitution on the radical and cation yield

By a suitable variation of physical and chemical parameters we can influence the kinetics and the yields of the different pathways shown in Scheme 1. While changes in temperature and solvent viscosity mainly affect the diffusional contribution, solvent polarity and redox potentials of the benzhydryl radicals and cations affect the driving force of the electron transfer. Control of the redox potential is achieved by attaching electron donating or electron withdrawing substituents to the phenyl rings of the benzhydryl chloride precursors (see Chart 1).

Temperature dependence of the electron transfer and geminate recombination. In order to verify the important role of diffusion experimentally, we carried out transient absorption measurements in a temperature interval from 5 °C to 60 °C. Figure 5 shows the temporal evolution of the radical and cation absorption at different temperatures normalized to the maximum. The curves for 22 °C were already shown in Figure 2. The initial rise of the radical signal within the first 300 fs shows no significant variation with temperature and is therefore not shown in Figure 5b. Note that in Figure 5 the time axis is linear as compared to the combined linear/logarithmic scale in Figure 2. In contrast to the 300 fs increase, we observe a significant decrease of the stretched exponential time constant modeling the electron transfer from 11.5 ps at 5 °C to 9.4 ps at 60 °C. A consideration of the absolute amplitudes of the fit gives access to the efficiencies of the processes. While at 5 °C only 37% of the generated radicals do not undergo electron transfer and become free radicals, 44% of the radicals survive at 60 °C (see Table S3 in the Supporting Information). Electron transfer quantum efficiencies Y_{ET} can be determined from the stretched exponential amplitudes of the cation and radical associated with the electron transfer. We observe a distinct decrease of the efficiency from 46% at 5 °C to 38% at 60 °C (see Figure 5b).

The lower efficiency and the smaller time constant of the electron transfer can be explained by the lowered viscosity of acetonitrile with increasing temperature.[70] At low temperatures the high viscosity slows down the diffusional separation of the radical pairs. While the change in viscosity does not affect the electron transfer efficiency for radical pairs at small distances, it becomes important for radical pairs

at the shoulder of the Gaussian distance distribution. Here the electron transfer rate is substantially lower compared to the center of the distribution. Therefore, an increase in the effective radical escape rate k_{esc}^{RP} due to a decrease of the viscosity lowers the overall efficiency of the electron transfer.
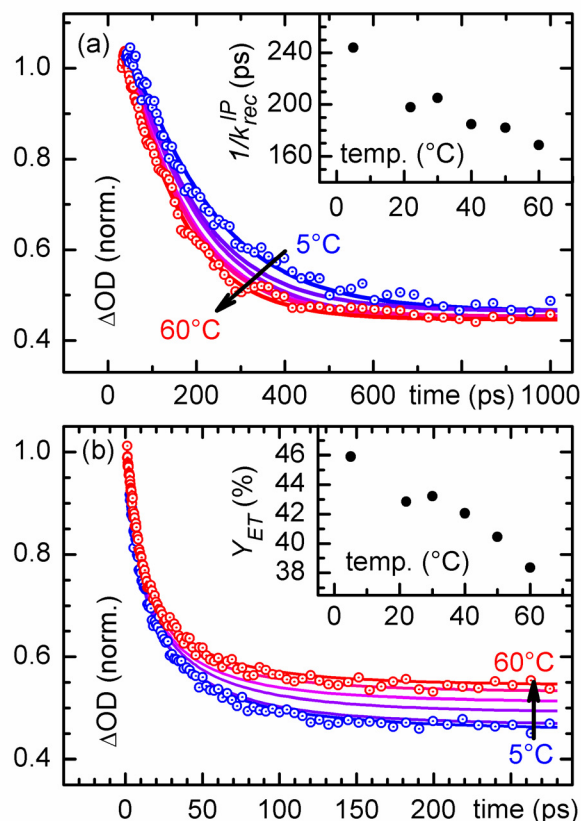
Figure 5 Temperature dependence of (a) the geminate recombination of the cation and (b) the radical absorption due to electron transfer after UV excitation of Ph$_2$CHCl in CH$_3$CN. Time traces are normalized to the maximum of the absorption. Fits are represented by solid lines. For clarity, only the data for the highest and lowest temperatures are shown. The initial rise of the radical signal within the first 300 fs as well as the rise of the cation signal within 40 ps are not shown.

The temperature has also an impact on the geminate recombination of the cations (see Figure 5a; data before the cation maximum not shown). Raising the temperature from 5 °C to 60 °C leads to a faster decay of the cation population. The determination of the intrinsic rates for geminate recombination k_{rec}^{IP} and diffusional separation of the ion pair k_{esc}^{IP} reveals that both are strongly affected by the temperature (see Table S3). In analogy to the case of the radicals the higher temperature leads to a faster diffusional separation and therefore the rate k_{esc}^{IP} rises from $1.78 \times 10^9\,s^{-1}$ at 5 °C to $2.40 \times 10^9\,s^{-1}$ at 60 °C. The higher temperature also facilitates the movement of the reactants towards each other and thus accelerates the geminate recombination reaction of the ion pair Ph$_2$CH$^+$ / Cl$^-$. The rate constant for geminate recombination k_{rec}^{IP} therefore rises from $4.10 \times 10^9\,s^{-1}$ at 5 °C to $5.92 \times 10^9\,s^{-1}$ at 60 °C

However, the yield of the geminate recombination is hardly affected by the temperature as the faster geminate recombination is compensated by the faster diffusional separation.
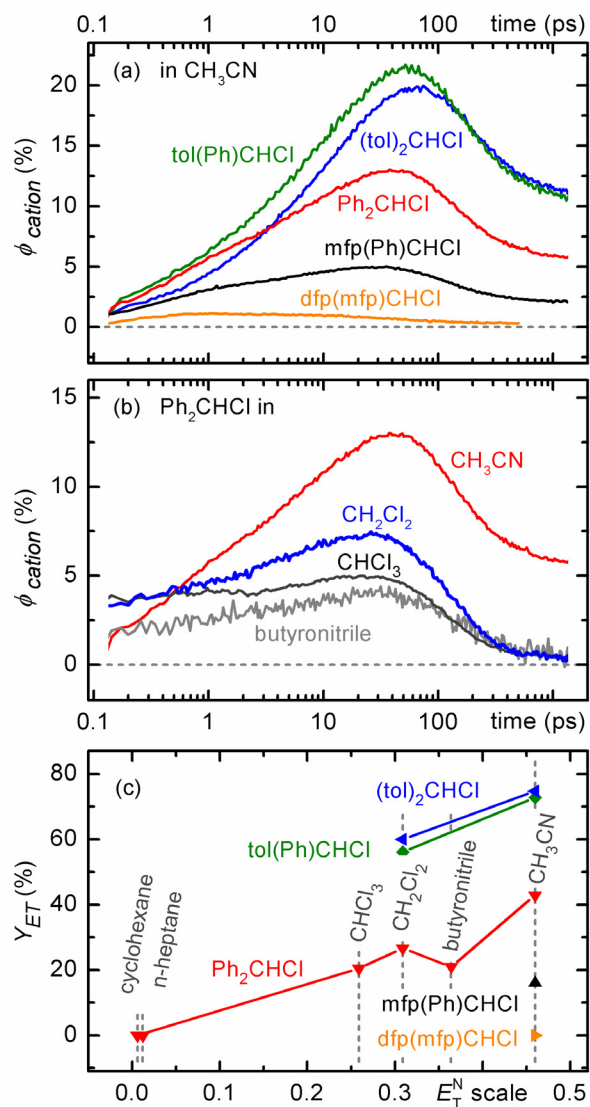
Figure 6 (a) Substitution dependence of the transient cation quantum yield Φ_{cation} in CH_3CN. (b) Solvent dependence of the transient cation quantum yield from Ph_2CHCl (c) Solvent dependence of the final electron transfer yield Y_{ET} for different benzhydryl chloride derivatives.

Influence of substitution and solvent polarity on the intermediate (ps) and final (ns) quantum yields of the cation generation. Figure 6a shows the experimental results obtained for Ar_2CHCl derivatives with different substituents attached to the phenyl rings in CH_3CN (Chart 1). For the cation with the most electron withdrawing substituents, $dfp(mfp)CH^+$, the observed carbocation population stems only from direct heterolysis. An increase of the population due to an electron transfer is not observed. For the less electrophilic cations, when the substituents at the aryl rings are varied, we observe an increase in both the intermediate cation quantum yield Φ_{cation} on the ps time scale and the

electron transfer yield Y_{ET} when going from electron withdrawing to electron donating substituents (see Figure 6a and 6c and Table 1).

Ofial et al.[61] have demonstrated that the oxidation potentials of benzhydryl radicals and hence the driving force ΔG_{ET} for electron transfer depend on the aryl substituents, but experimental data for the *m*-fluoro-compounds are not available. Ab initio calculations for the electron transfer reaction within the radical pair $Ar_2CH^\bullet$ / $Cl^\bullet$ yielding the ion pair Ar_2CH^+ / Cl^- at the M06-2X/6-311+G(d) level of theory with a PCM solvent continuum for CH_3CN show a change in ΔG_{ET} from -1.82 eV for the reaction $(tol)_2CH^\bullet$ $Cl^\bullet$ $\rightarrow$ $(tol)_2CH^+$ Cl^- to -1.19 eV for the reaction $dfp(mfp)_2CH^\bullet$ $Cl^\bullet$ $\rightarrow$ $dfp(mfp)CH^+$ Cl^- (see Tables 1 and S2). Thus, the electron transfer becomes thermodynamically less favorable as we go from electron donating to electron withdrawing substituents. However, the electron transfer times observed in our experiments (Fig. 6a and Table 1) increase with increasing driving force. This behavior indicates that the electron transfer already approaches the Marcus-inverted regime (see Table 1). As the reorganization energy $\lambda(R)$ changes with inter-radical distance, both the normal and the inverted regime can contribute to the effective electron transfer rate.

There is also a significant influence of the substituents on the geminate recombination of the ion pair. The rate of the geminate recombination k_{rec}^{IP} increases when going from the least electrophilic cation $(tol)_2CH^+$ to the cation with the highest electrophilicity $dfp(mfp)CH^+$. This behavior is reproduced by the ab initio free reaction energy for geminate recombination of the ion pair ΔG_{IP} shown in Table S2. An increase of the rate constants for activation-controlled reactions of benzhydryl ions with chloride anions was also reported for bimolecular reactions on the >10 ns time scale[71] and nicely matches the increasing rate k_{rec}^{IP} for increasing electrophilicity. Increasing electrophilicity of the benzhydryl cation leads to a distinct decrease of the nanosecond cation quantum yield $\Phi_{cat,\infty}$ as the yield of geminate recombination Y_{rec}^{IP} grows and the yield of the electron transfer Y_{ET} drops (see Figure 6a and Table 1).

As mentioned in the Introduction, the quantum yield of carbocations resulting from the photolysis of benzhydryl halides is negligibly small in many solvents on the nanosecond time-scale.[6-9] Our femtosecond pump-probe measurements show that for Ph_2CHCl no electron transfer occurs in apolar solvents like cyclohexane ($E_T^N = 0.006$[72]) and *n*-heptane ($E_T^N = 0.012$) (see Figure 6c). The ab initio Gibbs free reaction energy values ΔG_{ET} of the electron transfer indicate that in these solvents the electron transfer is an endergonic process (see Table S2 in the Supporting Information). In contrast, in the moderately polar solvents dichloromethane ($E_T^N = 0.309$) and chloroform ($E_T^N = 0.259$) electron transfer does occur, with an electron transfer yield Y_{ET} of about 20% (see Figure 6b, 6c and S8). As in CH_3CN ($Y_{ET} = 43\%$, $E_T^N = 0.460$) this leads to a significant intermediate cation quantum yield on the picosecond time scale. The large cation population is however quickly extinguished by an extremely

efficient geminate recombination ($Y_{rec}^{IP} > 95\%$) with a rate of $7.46 \times 10^9 s^{-1}$ in dichloromethane and $8.00 \times 10^9 s^{-1}$ in chloroform (see Figure 6b and Table 1).

Only in the highly polar acetonitrile a significant fraction of the ion pairs (~30-35%) can separate diffusionally to free ions which are observable on the nanosecond time scale. This can be explained by the large difference in the relative permittivities of the solvents. While in CH$_3$CN the large permittivity ($\varepsilon_r = 35.94$) promotes dissociation of ions, the moderate permittivities of dichloromethane ($\varepsilon_r = 8.93$) and chloroform ($\varepsilon_r = 4.89$) do not allow for a shielding of the Coulomb attraction that is sufficient for the generation of free ions.[72] This leads to the pronounced decrease observed for the rate of cation escape when going from acetonitrile ($k_{esc}^{IP} = 2.19 \times 10^9 s^{-1}$) to dichloromethane or chloroform ($k_{esc}^{IP} < 0.25 \times 10^9 s^{-1}$).

An analogous behavior has been found for the solvent dependence of the cation generation from (tol)$_2$CHCl and tol(Ph)CHCl. While a large intermediate cation quantum yield is observed in acetonitrile, as well as in dichloromethane and chloroform, only in acetonitrile a significant fraction of the ion pairs separate diffusionally and give rise to free ions. In the moderately polar solvents CH$_2$Cl$_2$ and CHCl$_3$, the initially generated ion pairs again undergo highly efficient geminate recombination.

Simulation for CH$_2$Cl$_2$ as solvent. To corroborate our microscopic model, we performed additional simulations for the photo-initiated processes of Ph$_2$CHCl in CH$_2$Cl$_2$. For the description of the reactions we had to use only slightly varied parameters as compared to CH$_3$CN. The mutual diffusion coefficient $D_F(RP)$ is lowered due to the larger cavity radius of both radical fragments in CH$_2$Cl$_2$. The optimum coefficient $D_F(IP)$ is roughly doubled in accord with the much lower polarity and the subsequent decrease in solute-solvent association. The escape rate for the radicals could be left unchanged and this is reasonable since the uncharged radicals should not be influenced too strongly by the solvent polarity. In contrast, the escape rate for the ions has to be set very low since the low polarity of CH$_2$Cl$_2$ does not stabilize the cation well. We therefore set the rate to zero. The electronic coupling for the electron transfer is only slightly changed. The main factor for the decreased yield is the decreased ΔG_{ET}. We also find the recombination rates to increase slightly. For the ion pairs this can be rationalized by the decreased stabilization of the ions in the less polar CH$_2$Cl$_2$. The resulting simulation of the distribution evolution (see Figure 3 c) and d)) nicely shows that the radicals evolve quite similarly in both solvents while the ions in CH$_2$Cl$_2$ never separate sufficiently to be eventually stabilized to free ions. The population kinetics are reproduced with high fidelity as seen in Figure S4 c) and d).

6.   Conclusion

The photolysis of benzhydryl chloride (Ph_2CHCl) shows that the photogeneration of radicals and cations and their quantum yields observed on different time-scales are the result of several complex and interconnected processes. In order to decipher these processes and understand their interplay, the population dynamics obtained from transient spectroscopy is complemented with a quantitative analysis of the species concentrations. This leads to absolute reaction quantum yields and is substantiated with a spectral peak shift analysis. Together with a theoretical model that faithfully reproduces the experimental findings on the Ph_2CHCl precursor and gives insight into decisive properties that are not accessible by experiment, we obtain a mechanism for the radical and cation generation which contains several unexpected aspects:

- After excitation at 270 nm, Ph_2CHCl undergoes predominantly homolytic C–Cl bond cleavage (41%) in CH_3CN and relaxation into a radical pair with a time constant of 300 fs. The photo-induced heterolytic C–Cl bond cleavage is a minor reaction channel (2%). Relaxation into the ion pair occurs with a somewhat shorter time constant of 260 fs. The remaining 57% of the excited molecules do not contribute to the photofragment population and probably relax directly back into the ground state.

- The radical pairs with small inter-radical distances undergo geminate recombination (19%), diffusional separation to free radicals (38%), or electron transfer to form benzhydryl cations and Cl^- anions (43%). The latter process generates the major part of the cation population.

- As the electron transfer occurs from a distribution of distances between the benzhydryl and $Cl^\bullet$ radical, the system exhibits a wide range of electron transfer rates leading to the observed stretched exponential with a mean electron transfer time of 22.2 ps.

- 70% of the generated ion pairs undergo geminate recombination in CH_3CN, while the competing diffusional separation leads to free ions for the remaining 30%. As shown by the combined Marcus-Smoluchowski model the ion pairs generated by electron transfer at larger distances have a higher survival probability.

Previously the photolysis of benzhydryl halides was described in a kinetic model invoking transitions between distinguishable species, i.e. contact ion pairs, solvent-separated ion pairs and free ions as well as geminate radical pairs and free radicals.[11] Our femtosecond broadband transient absorption experiments display a much richer set of information than the former transients recorded at a single wavelength. It turns out that it is essential to refine the classical treatment by including the coupling of the distance dependent electron transfer with diffusion. With this microscopic model that does not rely on exponential transfer rates between well defined species, we are able to obtain an excellent agreement between the experimental findings and the simulation. This leads to a unified description of the

population dynamics and shows that there is a smooth transition between the distinct species considered in traditional descriptions.[46] Electron transfer does not only happen in radical pairs at contact distance but up to distances incorporating at least one solvent molecule.

The observed populations dynamics can only be explained with a distance distribution of nascent radical pairs spanning out to as much as three solvent molecules in between the benzhydryl radical and the chlorine radical. Such a wide distribution allows efficient early generation of cations by electron transfer as well as sufficient survival of radicals at late times. The increase of the mean distance within the ion pairs in the first 100 ps is not dominated by the diffusional separation of the ions but results from the fact that the electron transfer at later times occurs in radical pairs which are located further apart. It is therefore not meaningful to discuss the generation of free ions in terms of a transition from a contact ion pair via a solvent separated ion pair to free ions. Only at later times diffusion becomes the main process increasing the mean distance and thus certainly generating free ions.

The dynamics and outcome of the interweaved processes can be steered by the variation of physical and chemical parameters. The investigation of the cation formation in a series of solvents with varying polarity unveiled the existence of three regimes. In apolar solvents such as cyclohexane and n-heptane the photogenerated radical pairs do not undergo electron transfer as the process is endergonic in these media. In moderately polar solvents, such as dichloromethane, electron transfer occurs but the carbocation population is almost totally extinguished by geminate recombination, as the low solvent permittivity does not allow for an efficient ion pair separation. The use of a neutral leaving group can avoid this problem and lead to a high benzhydryl cation yield.[26] Only in highly polar solvents (CH_3CN) a large fraction of the ion pair population is able to avoid geminate recombination and separates to free ions which are detectable on the nanosecond time scale.

Beyond the population kinetics, the benzhydryl chlorides allow for the observation of the temporal development of the distance distribution of the transient species via the analysis of the photoproduct quantum yields and their peak shifts. This constitutes the basis for more advanced multi-pulse non-linear experiments that have been developed in recent years. For example THz experiments[73] and 2D IR chemical exchange spectroscopy[74] allow for a more direct measurement of the Cl^- anion and $Cl^\bullet$ radical displacement from the benzhydryl rest. Furthermore, as recently shown by Baiz et al.[75] vibrational Stark-effect spectroscopy can be employed to measure the solvent response during the electron transfer between the radicals.

A major impetus of this study was the investigation of the reaction kinetics of photolytically generated benzhydryl cations with a variety of nucleophiles. As these bimolecular reactions occur on time scales longer than nanoseconds, the final quantum yields of the free carbocations are the aspect most important to the practical application of benzhydryl chlorides as precursors for benzhydryl cations. As many processes that increase or decrease the cation population occur on the femto to picosecond

time scale, their direct observation and understanding is crucial for the maximization of the final (nanosecond) cation quantum yield. The reported investigations show that this can be achieved when the radical pair sticks together as long as possible for an efficient electron transfer and the generated ions are efficiently separated with the aid of the solvent.

Acknowledgment

7. References

(1)   Moss, R. A.; Platz, M. S.; Jones, M. Jr. (Eds.) *Reactive Intermediate Chemistry*, Wiley-Interscience, Hoboken, N. J. **2004**.

(2)   Olah, G. A.; Schleyer, P. v. R. (Eds.) *Carbonium Ions, Vols. I-V*, Wiley, New York, **1968-1976**.

(3)   Olah, G. A. *Angew. Chem.* **1973**, *85*, 183-234.

(4)   Olah, G. A. *J. Org. Chem.* **2001**, *66*, 5943-5957.

(5)   Olah, G. A.; Prakash, G. K. S. (Eds.) *Carbocation Chemistry*; Wiley-Interscience, Hoboken, N. J. **2004**.

(6)   McClelland, R. A. *Tetrahedron* **1996**, *52*, 6823-6858.

(7)   McClelland, R. A., In *Reactive Intermediate Chemistry*; Moss, R. A.; Platz, M. S.; Jones, M. J., Eds.; Wiley: Hoboken (N. J.), 2004, pp 3-40.

(8)   Das, P. K. *Chem. Rev.* **1993**, *93*, 119-144.

(9)   Bartl, J.; Steenken, S.; Mayr, H.; McClelland, R. A. *J. Am. Chem. Soc.* **1990**, *112*, 6918-6928.

(10)   Miranda, M. A.; Pérez-Prieto, J.; Font-Sanchis, E.; Scaiano, J. C. *Acc. Chem. Res.* **2001**, *34*, 717-726.

(11)   Peters, K. S. *Chem. Rev.* **2007**, *107*, 859-873.

(12)   Kropp, P. J. in *CRC Handbook of Organic Photochemistry and Photobiology*; 2 ed.; Horspool, W., Lenci, F., Eds.; CRC Press: Boca Raton, 2004, p 1-1 - 1-32

(13) Kitamura, T. in *CRC Handbook of Organic Photochemistry and Photobiology*; 2 ed.; Horspool, W., Lenci, F., Eds.; CRC Press: Boca Raton, 2004, p 11-1 - 11-10

(14) Johnston, L. J.; Kwong, P.; Shelemay, A.; Lee-Ruff, E. *J. Am. Chem. Soc.* **1993**, *115*, 1664-1669.

(15) Sammes, J. P. In *Chemistry of the Carbon–Halogen Bond*; Patai, S., Ed.; Wiley: New York, 1973, chapter 11, 747-794.

(16) Pohlers, G.; Scaiano, J. C.; Step, E.; Sinta, R. *J. Am. Chem. Soc.* **1999**, *121*, 6167-6175.

(17) Kobayashi, S.; Hori, Y.; Hasako, T.; Koga, K.-i.; Yamataka, H. *J. Org. Chem.* **1996**, *61*, 5274-5279.

(18) Peon, J.; Polshakov, D.; Kohler, B. *J. Am. Chem. Soc.* **2002**, *124*, 6428-6438.

(19) Baidya, M.; Kobayashi, S.; Brotzel, F.; Schmidhammer, U.; Riedle, E.; Mayr, H. *Angew. Chem.* **2007**, *119*, 6288-6292.

(20) Phan, B. T.; Nolte, C.; Kobayashi, S.; Ofial, A. R.; Mayr, H. *J. Am. Chem. Soc.* **2009**, *131*, 11392-11401.

(21) Hallett-Tapley, G.; Cozens, F. L.; Schepp, N. P. *J. Phys. Org. Chem.* **2009**, *22,* 343-348.

(22) O'Ferrall, R. M. Stabilities and Reactivities of Carbocations In *Advances in Physical Organic Chemistry*; Richard, J. P., Ed.; Elsevier: Amsterdam, 2010; Vol 44, pp 19-122.

(23) Pincock, J. A. *Acc. Chem. Res.* **1997**, *30*, 43-49.

(24) Dankowski, M. In *The chemistry of organophosphorus compounds*; Hartley, F. R., Ed.; Wiley: Chichester, 1994; Vol. 3, pp 325-343.

(25) Ammer, J.; Baidya, M.; Kobayashi, S.; Mayr, H. *J. Phys. Org. Chem.* **2010**, *23*, 1029-1035.

(26) Ammer, J.; Sailer, C. F.; Riedle, E.; Mayr, H. *J. Am. Chem. Soc.* **2012**, *134*, 11481-11494.

(27) Hilborn, J. W.; MacKnight, E.; Pincock, J. A.; Wedge, P. J. *J. Am. Chem. Soc.* **1994**, *116*, 3337-3346.

(28) Fingerhut, B. P.; Geppert, D.; de Vivie-Riedle, R. *Chem. Phys.* **2008**, *343*, 329-339.

(29) Lipson, M.; Deniz, A. A.; Peters, K. S. *Chem. Phys. Lett.* **1998**, *288*, 781-784.

(30) Heeb, L. R.; Peters, K. S. *J. Am. Chem. Soc.* **2008**, *130*, 1711-1717.

(31) Vauthey, E. *J. Photochem. Photobiol., A* **2006**, *179*, 1-12.

(32) Mohammed, O. F.; Adamczyk, K.; Banerji, N.; Dreyer, J.; Lang, B.; Nibbering, E. T. J.; Vauthey, E. *Angew. Chem., Int. Ed.* **2008**, *47*, 9044-9048.

(33) Rosspeintner, A.; Kattnig, D. R.; Angulo, G.; Landgraf, S.; Grampp, G. *Chem. Eur. J.* **2008**, *14*, 6213-6221.

(34) Gladkikh, V. S.; Burshtein, A. I.; Tavernier, H. L.; Fayer, M. D. *J. Phys. Chem. A* **2002**, *106*, 6982-6990.

(35) Mayr, H.; Ofial, A. R. in *Carbocation Chemistry*; Olah, G. A., Prakash, G. K. S., Eds.; Wiley: Hoboken (N. J.), 2004, pp 331-358.

(36) Mayr, H.; Bug, T.; Gotta, M. F.; Hering, N.; Irrgang, B.; Janker, B.; Kempf, B.; Loos, R.; Ofial, A. R.; Remennikov, G.; Schimmel, H. *J. Am. Chem. Soc.* **2001**, *123*, 9500-9512.

(37) Mayr, H.; Kempf, B.; Ofial, A. R. *Acc. Chem. Res.* **2003**, *36,* 66-77.

(38) Ammer, J.; Nolte, C.; Mayr, H. *J. Am. Chem. Soc.* **2012**, *134*, 13902-13911.

(39) Denegri, B.; Streiter, A.; Jurić, S.; Ofial, A. R.; Kronja, O.; Mayr, H. *Chem. Eur. J.* **2006,** *12*, 1648-1656.

(40) Nolte, C.; Mayr, H. *Eur. J. Org. Chem.* **2010**, 1435-1439.

(41) Megerle, U.; Pugliesi, I.; Schriever, C.; Sailer, C. F.; Riedle, E. *Appl. Phys. B* **2009**, *96*, 215-231.

(42) Fingerhut, B. P.; Sailer, C. F.; Ammer, J.; Riedle, E.; de Vivie-Riedle, R. *J. Phys. Chem. A,* DOI: 10.1021/jp300986t

(43) Chernyak, V.; Schulz, M.; Mukamel, S. *J. Chem. Phys.* **1999**, *111*, 7416-7425.

(44) Kao, Y.-T.; Guo, X.; Yang, Y.; Liu, Z.; Hassanali, A.; Song, Q.-H.; Wang, L.; Zhong, D. *J. Phys. Chem. B* **2012**, *116*, 9130-9140.

(45) Berberan-Santos, M. N.; Bodunov, E. N.; Valeur, B. *Chem. Phys.* **2005**, *315*, 171-182.

(46) Raber, D. J.; Harris, J. M.; Schleyer, P. v. R. Ions and Ion Pairs in Solvolysis Reactions. In *Ions and Ion Pairs in Organic Chemistry*; Szwarc, M., Ed.; John Wiley & Sons: New York, 1974; pp 248-366.

(47) Goun, A.; Glusac, K.; Fayer, M. D. *J. Chem. Phys.* **2006**, *124*, 084504.

(48) Rice, S. A. *Diffusion-limited reactions*; Bamford, C. H., Tipper, C. F. H., Compton, R. G., Eds.; Elsevier Science Publishers B.V.: Amsterdam, 1985.

(49) Marcus, R. A.; Sutin, N. *Biochim. Biophys. Acta* **1985**, *811*, 265-322.

(50) Barbara, P. F.; Meyer, T. J.; Ratner, M. A. *J. Phys. Chem.* **1996**, *100*, 13148-13168.

(51) Schulten, K. private communication

(52) Tachiya, M. *Radiat. Phys. Chem.* **1983**, *21*, 167-175.

(53) Weidemaier, K.; Tavernier, H. L.; Swallen, S. F.; Fayer, M. D. *J. Phys. Chem. A* **1997**, *101*, 1887-1902.

(54) Saik, V. O.; Goun. A. A.; Nanda, J.; Shirota, K.; Tavernier, H. L.; Fayer, M. D. *J. Phys. Chem. A* **2004**, *108*, 6696-6703.

(55)   Wojcik, M.; Tachiya, M. *Radiat. Phys. Chem.* **2005**, *74*, 132-138.

(56)   Kloepfer, J. A.; Vilchiz, V. H.; Lenchenkov, V. A.; Germaine, A. C.; Bradforth, S. E. *J. Chem. Phys.* **2000**, *113*, 6288-6307.

(57)   Zugmann, S.; Fleischmann, M.; Amereller, M.; Gschwind, R. M.; Wiemhöfer, H. D.; Gores, H. J. *Electrochim. Acta*, **2011**, *56*, 3926-3933.

(58)   Zugmann, S.; Fleischmann, M.; Amereller, M.; Gschwind, R. M.; Winter, M.; Gores, H. J. *J. Chem. Eng. Data*, **2011**, *56*, 4786-4789.

(59)   Atkins, P.; de Paula, J. *Physical Chemistry*; 9th ed.; Oxford University Press: Oxford, 2009.

(60)   Saik, V. O.; Goun, A. A.; Fayer, M. D. *J. Chem. Phys.* **2004**, *120*, 9601-9611.

(61)   Ofial, A. R.; Ohkubo, K.; Fukuzumi, S.; Lucius, R.; Mayr, H. *J. Am. Chem. Soc.* **2003**, *125*, 10906-10912.

(62)   Isse, A. A.; Lin, C. Y.; Coote, M. L.; Gennaro, A. *J. Phys. Chem. B* **2011**, *115*, 678-684.

(63)   Bultmann, T.; Ernsting, N. P. *J. Phys. Chem.* **1996**, *100*, 19417-19424.

(64)   Sailer, C. F.; Singh, R. B.; Ammer, J.; Riedle, E.; Pugliesi, I. *Chem. Phys. Lett.* **2011**, *512*, 60-65.

(65)   Horng, M. L.; Gardecki, J. A.; Papazyan, A.; Maroncelli, M. *J. Phys. Chem.* **1995**, *99*, 17311-17337.

(66)   Ladanyi, B. M.; Stratt, R. M. *J. Phys. Chem.* **1995**, *99*, 2502-2511.

(67)   de Boeij, W. P.; Pshenichnikov, M. S.; Wiersma, D. A. *J. Phys. Chem.* **1996**, *100*, 11806-11823.

(68)   Eom, I.; Joo, T. *J. Chem. Phys.* **2009**, *131*, 244507.

(69)   Schneider, R.; Mayr, H.; Plesch, P. H. *Ber. Bunsenges. Phys. Chem.* **1987**, *91*, 1369-1374.

(70)   Dymond, J. H.; Awan, M. A.; Glen, N. F.; Isdale, J. D. *Int. J. Thermophysics* **1991**, *12*, 433-447.

(71)   Minegishi, S.; Loos, R.; Kobayashi, S.; Mayr, H. *J. Am. Chem. Soc.* **2005**, *127*, 2641-2649.

(72)   Reichardt, C. *Solvents and Solvent Effects in Organic Chemistry*; 4th ed.; Wiley-VCH: Weinheim, 2010.

(73)   Heugen, U.; Schwaab, G.; Bründermann, E.; Heyden, M.; Yu, X.; Leitner, D. M.; Havenith, M. *Proc. Natl. Acad. Sci. U.S.A.* **2006**, *103*, 12301-12306.

(74)   Zheng, J.; Kwak, K.; Asbury, J.; Chen, X.; Piletic, I. R.; Fayer, M. D. *Science* **2005**, *309*, 1338-1343.

(75)   Baiz, C. R.; Kubarych, K. J. *J. Am. Chem. Soc.* **2010**, *132*, 12784-12785.

A Comprehensive Microscopic Picture of the Benzhydryl Radical and Cation Photo-Generation and Interconversion through Electron Transfer

*Christian F. Sailer[a], Sebastian Thallmair[a,b], Benjamin P. Fingerhut[b], Christoph Nolte[b], Johannes Ammer[b], Herbert Mayr[b], Regina de Vivie-Riedle[b], Igor Pugliesi[*a], Eberhard Riedle[*a]*

a Lehrstuhl für BioMolekulare Optik, Ludwig-Maximilians-Universität München, Oettingenstr. 67, 80538 München, Germany

b Department Chemie, Ludwig-Maximilians-Universität München, Butenandtstr. 5–13, 81377 München, Germany

Supporting Information

List of Contents

*Author to whom correspondence should be addressed.

Eberhard Riedle:

Tel: +49 (0)89 2180 9210

Fax: +49 (0)89 2180 9202

E-mail address: Eberhard.Riedle@physik.uni-muenchen.de

S1. Determination of absolute quantum yields and intrinsic rates

The precise knowledge of the excitation conditions when recording transient absorption data allows for the determination of the quantum yields for the generation of benzhydryl radicals and cations after UV excitation. The quantum yield is hereby defined as the number of formed product molecules N_{prod} divided by the number of absorbed photons $N_{ph,abs}$.

S1.1 Concentration of benzhydryl radicals and cations

The molar absorption coefficients of benzhydryl radical and cation generated from $(tol)_2CHCl$, $tol(Ph)CHCl$ and Ph_2CHCl are well-documented in the literature.[1] By stabilizing the benzhydryl cation Ph_2CH^+ in concentrated H_2SO_4 we were able to reproduce the published value. From the molar absorption coefficients the time-dependent concentration $c_{radical}(t)$ of the photogenerated benzhydryl radical can be calculated by

$$c_{radical}(t) = \frac{OD(t)}{\varepsilon_{radical} \cdot L}$$ (S1.1)

and analogously for the concentration of benzhydryl cations $c_{cation}(t)$. Here, L is the sample thickness, $OD(t)$ is the measured transient absorption and $\varepsilon_{radical}$ and ε_{cation} are the molar absorption coefficients at the absorption maximum of the photoproducts. As it is shown in Section S1.3, the change of photoproduct concentration during a specific process can be determined analogously from the fitting amplitudes. It should be noted that due to the absorption of the pump pulse within the sample the concentration of the photofragments decreases with the distance in the cuvette. Therefore, our measurements detect the mean concentration of the photofragments within the cuvette, which is accounted for in Section S1.2.

Since, to the best of our knowledge, no molar absorption coefficients have been published for the radicals and cations generated from mfp(Ph)CHCl and dfp(mfp)CHCl we approximate them with the values for the para-substituted fluoro and di-fluoro benzhydryl chloride compounds given in Ref. 1. If more than one molar absorption coefficient was reported the mean value is used.

Molar absorption coefficients used for the calculation of product concentrations:

compound	$\varepsilon_{radical}$ (L mol⁻¹ cm⁻¹)	ε_{cation} (L mol⁻¹ cm⁻¹)
(tol)₂CHCl	52480	74130
tol(Ph)CHCl	44670	52480
Ph₂CHCl	43650	45010
mfp(Ph)CHCl	40740	52480
dfp(mfp)CHCl	44670	73280

S1.2 Concentration of excited precursors

The fraction of precursors which are excited by the pump pulse is given by:[2]

$$P_{exc} = \frac{E_{pump} \cdot \ln 2}{(hc/\lambda) \cdot \pi (D/2)^2} \cdot \varepsilon_{prec} \frac{\ln 10}{N_A}$$
(S1.2)

The calculation therefore requires the precise determination of the pump pulse energy E_{pump}, the pump focal FWHM (full width at half maximum) diameter D at the sample, the pump wavelength λ and the molar absorption coefficient ε_{prec} of the precursor at the pump wavelength. However, by the optical density of the sample, the pump pulse energy is attenuated within the sample according to

$$E_{pump}(x) = E_{pump}\,10^{-ODx/L}$$
(S1.3)

The average pump pulse energy with which the benzhydryl chlorides are excited is therefore given by

$$E_{pump,avg} = \frac{1}{L}\int_0^L E_{pump}(x)\,dx = -\frac{E_{pump}}{OD\ln 10}\left[10^{-ODx/L}\right]_0^L$$

$$= E_{pump}\,\frac{1-10^{-OD}}{OD\ln 10}$$
(S1.4)

This leads to a correction factor of 20% to 28% for the optical densities (0.2 to 0.3) used in the transient measurements. Multiplying P_{exc} (typically $\leq 1\%$) with the concentration of precursor in the solution leads to the concentration of excited precursors c_{exc}.

S1.3 Quantum yields and efficiencies

The time-dependent quantum yield of benzhydryl radical generation $\Phi_{radical}(t)$ is given by the ratio of the radical concentration to the concentration of excited molecules:

$$\Phi_{radical}(t) = \frac{c_{radical}(t)}{c_{exc}}$$
(S1.5)

and analogously for the time-dependent quantum yield of benzhydryl cation generation $\Phi_{cation}(t)$. With the aid of the amplitudes of the exponential fit functions, the final (nanosecond) radical and cation quantum yields $\Phi_{rad,\infty}$ and $\Phi_{cat,\infty}$ and the quantum yields for direct homolytic and heterolytic bond cleavage Φ_{Hom} and Φ_{Het} can be determined:

$$\Phi_{rad,\infty} = \frac{c_{rad,\infty}}{c_{exc}},$$
(S1.6)

$$\Phi_{cat,\infty} = \frac{c_{cat,\infty}}{c_{exc}},$$
(S1.7)

$$\Phi_{Hom} = \frac{c_{rad,ET} + c_{rad,\infty}}{c_{exc}},$$
(S1.8)

$$\Phi_{Het} = \frac{c_{cat,rec} + c_{cat,\infty} - c_{cat,ET}}{c_{exc}}$$
(S1.9)

The concentration c_i of a species involved in a specific process is proportional to the corresponding absorption contribution and and therefore the fitted preexponential amplitudes, e.g., for the ion pair geminate recombination $c_{cat,rec} = A_{cat,rec}/(L\,\varepsilon_{cation})$. For the definition of the preexponential amplitudes see Figure S1 and Section S2. The determination of the yield of a specific process, e.g., electron transfer or geminate recombination, therefore requires the fitted preexponential amplitude of this processes. This yield is time-independent and describes the absolute efficiency of the processes for $t \rightarrow \infty$. The following relationships between the concentrations have been used:

Fraction of the ion pairs benzhydryl cation $-$ Cl⁻ anion that undergoes geminate recombination:

$$y_{rec}^{IP} = \frac{c_{cat,rec}}{c_{cat,rec} + c_{cat,\infty}}$$
(S1.10)

Fraction of ion pairs which are separated by diffusion to give rise to free ions:

$$Y_{esc}^{IP} = 1 - Y_{rec}^{IP} \qquad (S1.11)$$

Fraction of radical pairs generated by homolysis that undergo electron transfer leading to ion pairs:

$$Y_{ET} = \frac{c_{cat,ET}}{c_{rad,ET} + c_{rad,\infty}} \qquad (S1.12)$$

Fraction of radical pairs which are separated by diffusion to give rise to free radicals:

$$Y_{esc}^{RP} = \frac{c_{rad,\infty}}{c_{rad,\infty} + c_{rad,ET}} \qquad (S1.13)$$

Fraction of radical pairs that undergo geminate recombination back to the precursor:

$$Y_{rec}^{RP} = 1 - Y_{esc}^{RP} - Y_{ET} \qquad (S1.14)$$

Figure S1 Definition of photoproduct concentrations derived from the fitting amplitudes. The actual concentrations can deviate from the ones plotted due to mutual compensations of the basis functions used in the fit.

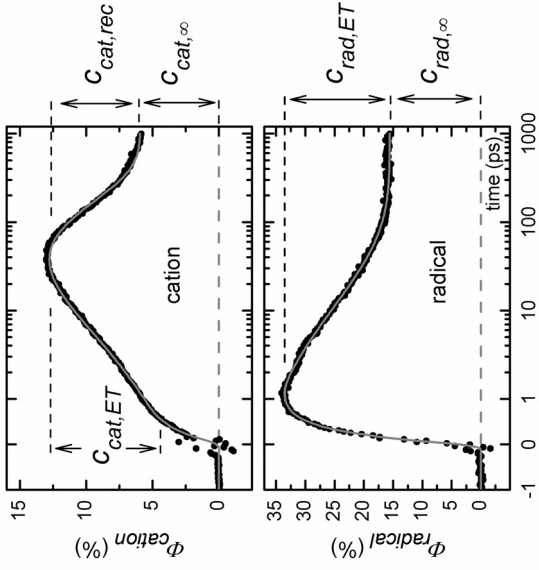## S1.4 Determination of intrinsic recombination and escape rates for the geminate ion pairs

Directly after their generation the benzhydryl cation and Cl⁻ anion are in close enough vicinity to potentially allow recombination. The distance distribution of the ion pairs evolves with time and we model the effective kinetics by considering geminate recombination with the rate k_{rec}^{IP} or diffusive separation with the rate for cation escape k_{esc}^{IP}. Therefore, the observed cation decay rate k_{tot} is the sum of these two rate constants:

$$k_{tot} = k_{rec}^{IP} + k_{esc}^{IP} \qquad (S1.15)$$

With the yield of the geminate recombination of the ion pairs Y_{rec}^{IP} one obtains the two intrinsic rates k_{rec}^{IP} and k_{esc}^{IP} from:[3]

$$k_{rec}^{IP} = k_{tot} Y_{rec}^{IP} \qquad (S1.16)$$

$$k_{esc}^{IP} = k_{tot} \left(1 - Y_{rec}^{IP}\right) \qquad (S1.17)$$

S2. Fitting the transient absorption data

The observed dynamics of the benzhydryl radical and cation after UV excitation of the studied benzhydryl chlorides has been fitted with a fit function which incorporates exponentials as well as one stretched exponential. It can be written as:

$$F(t) = IRF \otimes \left\{ \theta(t) \left[\sum_i A_i \exp\left(-\frac{t}{\tau_i}\right) + A_{SE} \exp\left(-\left(\frac{t}{\tau_{SE}}\right)^{\beta_{SE}}\right) + const \right] \right\} + artifact \qquad (S2.1)$$

The kernel of the fit function is the product of the step function $\theta(t)$ with the sum of (stretched) exponentials and a constant pedestal. The finite temporal resolution is reflected by the convolution with the instrumental response function *IRF*. The *IRF* is assumed to be Gaussian with the experimentally determined width. While the convolution with the exponential functions can be carried out analytically the convolution with the stretched exponential is calculated numerically. The coherent artifact due to non-linear pump-probe pulse interactions in the solvent and the flow cell windows around time zero[4] can be included into the fit. It is modeled by a Gaussian function and its first and second derivative and has the same width as the *IRF*.

The decay of the radical and the rise of the cation signal due to electron transfer cannot be fitted monoexponentially. These fits show pronounced deviations from the measured transient absorption data

between 1 ps and 100 ps and therefore do not reproduce the observed dynamics (see Figure S2). We find that for the radical the use of a fit function consisting of an exponential rise, a stretched exponential decay and a pedestal matches the dynamics faithfully. In the case of the cation one more exponential decay is necessary to reproduce the decay associated with the geminate recombination. It turns out that the dynamics of the large number of measurements with differing substituents, solvents and temperatures can all be well fitted with β_{SE} = 0.5. In order to confine the number of free fit parameters β_{SE} is therefore set to 0.5.
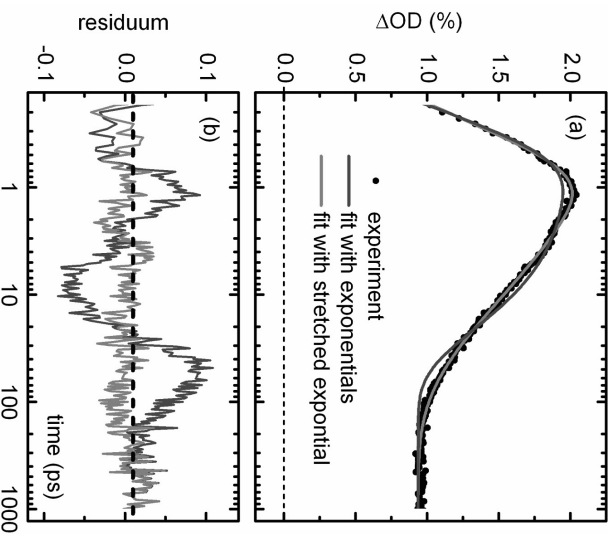
Figure S2 (a) Temporal evolution of the benzhydryl radical signal after UV excitation of Ph$_2$CHCl in CH$_3$CN with two different fits and (b) the residuum of the fits. The fit represented by the blue line with one exponential rise ($\tau = 0.20$ ps), an exponential decay ($\tau = 21$ ps) and a constant pedestal shows significant deviations from the measurement. The fit used throughout the manuscript for the radical dynamics (red line) with one exponential rise ($\tau = 0.30$ ps), a stretched exponential decay ($\tau_{SE} = 11.1$ ps) and a pedestal matches the radical signal faithfully.

S3. Peak shift determination

The benzhydryl radical and cation bands observed after photolysis of benzhydryl chloride undergo small, time-dependent peak shifts already identifiable to the bare eye at a close inspection. However, for a precise determination of the temporal behavior of the peak shifts, one needs the knowledge of the exact position for many delay times. We therefore employed an iterative fitting algorithm on the complete transient absorption data allowing for the determination of the radical and cation band position for every time delay measured (compare Figure S3). The algorithm first fits a parabola to the band within a given, sufficiently large interval. The fitted peak wavelength for every time delay is then taken as the middle of a new, smaller interval on which the parabola is fitted again. The maximum of the parabola is used as band position. The repetition of this procedure leads to the band position of the photoproducts with uncertainty smaller than 0.1 nm. Any deviation of this band position from the one obtained by another definition will only lead to a systematic additive value that is constant for all delay times.
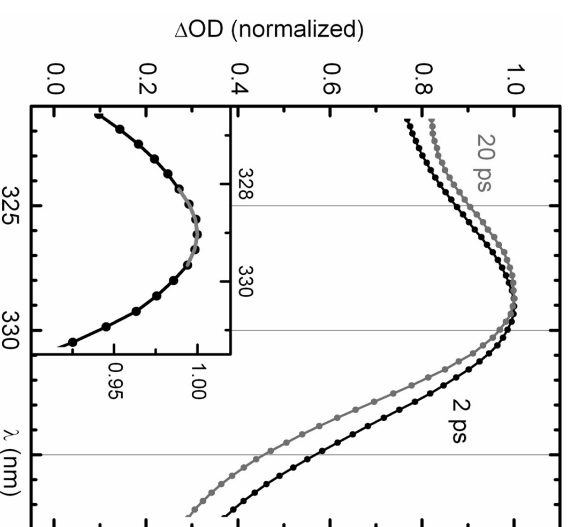
Figure S3 Normalized benzhydryl radical absorption band after UV photolysis of Ph$_2$CHCl in CH$_3$CN for two different delay times. A slight temporal blue shift of 0.6 nm is visible from 2 ps (black) to 20 ps (green). A magnified detail of the radical absorption band after 2 ps together with the fitted parabola (red line) is shown in the inset.

S4. Theory

S4.1 Evolution of the radical and ion pair distribution: coupled electron transfer and diffusion

The transient absorption experiment measures the optical absorbance at selected wavelengths that correspond to the known absorption features of the species involved in the dynamic process. In the usual description given by the Lambert-Beer law the optical density is proportional to both the molar extinction coefficient and the concentration of a selected species. In recent work we were able to show that the extinction coefficient of the benzhydryl radical and the cation increase with about a 300 fs time constant after their optical generation due to planarization and solvation.[5] Therefore the measured optical signal can indeed be taken as a faithful measure of the concentrations from 1 ps on.

To model the evolution of the concentrations after UV excitation of benzhydryl chloride one would classically start with a nascent ratio of generated radicals and cations and then add a rate model in accord with Scheme 1. This model then includes the electron transfer that converts radical population to the cation, the geminate recombination and possibly a stabilization of species that prevents recombination. In Sec. 3 of the paper it was found that time dependent rates are needed to fit the data. This is not satisfactory from a chemical standpoint. Rather a microscopic insight into the reaction mechanism is sought.

For a proper treatment we therefore consider the time dependent population distribution $P_{RP}(R,t)$ for the radical pairs and $P_{IP}(R,t)$ for the ion pairs. We assume spherical symmetry and R denotes the distance between the centers of the two species making up each pair. The diffusional evolution is described in the frame work of the Smoluchowski formalism, the electron transfer rate $k_{ET}(R)$ by Marcus theory, and the geminate recombination rates $k_{rec}^{RP}(R)$ and $k_{rec}^{IP}(R)$ as well as the escape rates $k_{esc}^{RP}(R)$ and $k_{esc}^{IP}(R)$ by a distance dependent rate each.

To obtain the overall population $P(t)$ which is proportional to the experimentally accessible product absorption, integration over the distance coordinate starting from the contact distance R_c is necessary

$$P(t) = \int_{R_c}^{\infty} P(R,t)\,dR \tag{S4.1}$$

It has been discussed that $P_{RP}(R,t)$ and $P_{IP}(R,t)$ cannot be directly propagated, instead underlying distribution functions $S_{RP}(R,t)$ and $S_{IP}(R,t)$ have to be used.[6,7] These are related to $P_{RP}(R,t)$ and $P_{IP}(R,t)$ by[8-10]

$$P_{RP}(R,t) = 4\pi R^2\, S_{RP}(R,t)\exp\left[-V_{RP}(R)/k_B T\right] \tag{S4.2}$$

$$P_{IP}(R,t) = 4\pi R^2\, S_{IP}(R,t)\exp\left[-V_{IP}(R)/k_B T\right] \tag{S4.3}$$

with the intrapair potentials $V_{RP}(R)$ and $V_{IP}(R)$. $k_B T$ is the thermal energy. This step is needed to ensure that the Boltzmann distribution is an equilibrium solution of the model.

The resulting set of coupled differential equations is

$$\frac{\partial}{\partial t} S_{RP}(R,t) = L^+ S_{RP}(R,t) - k_{ET}(R)S_{RP}(R,t)$$
$$- k_{rec}^{RP}(R)S_{RP}(R,t) - k_{esc}^{RP}(R)S_{RP}(R,t) \tag{S4.4}$$

$$\frac{\partial}{\partial t} S_{IP}(R,t) = L^+ S_{IP}(R,t) + k_{ET}(R)S_{RP}(R,t)\exp\left[-\frac{e^2}{4\pi\varepsilon_0\varepsilon_{st}k_B T}\frac{1}{R}\right]$$
$$- k_{rec}^{IP}(R)S_{IP}(R,t) - k_{esc}^{IP}(R)S_{IP}(R,t) \tag{S4.5}$$

L^+ is the adjoint Smoluchowski operator in spherical coordinates[8]

$$L^+ = \frac{1}{R^2}\exp[V(R)]\frac{\partial}{\partial R}\left(D(R)R^2\exp[-V(R)]\frac{\partial}{\partial R}\right). \tag{S4.6}$$

The electron transfer is a sink term for the radical distribution and a source term for the ion pairs. The back electron transfer pathway is neglected in our simulations since it is highly endergonic in polar solvents such as CH_3CN or CH_2Cl_2 due to the ultrafast solvation of the cation (see Section S4.3). The exponential factor accompanying the source term ensures that the population transfer between $P_{RP}(R,t)$ and $P_{IP}(R,t)$ is properly described by $S_{RP}(R,t)$ and $S_{IP}(R,t)$ within the Smoluchowski formalism. This can be understood as follows.

The intrapair potentials are given by

$$V_{RP}(R) = -\ln(g(R))\cdot k_B T \tag{S4.7}$$

$$V_{IP}(R) = -\ln(g(R))k_B T - \frac{e^2}{4\pi\varepsilon_0\varepsilon_{st}}\frac{1}{R} \tag{S4.8}$$

with e the elementary charge, ε_0 the vacuum permittivity, and ε_{st} the relative static permittivity (see Figure S3a). $g(R)$ is the radial distribution function that describes the arrangement around the

benzhydryl fragment in a solvent shell structure. For these potentials eqs (S4.2) and (S4.3) can be rewritten as

$$P_{RP}(R,t) = S_{RP}(R,t) \cdot g(R) \cdot 4\pi R^2 \qquad (S4.9)$$

$$P_{IP}(R,t) = S_{IP}(R,t) \cdot g(R) \cdot \exp\left[\frac{e^2}{4\pi\varepsilon_0 \varepsilon_{st} k_B T}\frac{1}{R}\right]\frac{1}{4\pi R^2} \qquad (S4.10)$$

and the factor accompanying the electron transfer source term in eq (S4.5) can be readily understood.

The radial distribution function $g(R)$ has been modeled by Monte-Carlo sampling[11] of the pure solvent. It resembles a partly ordered solvent structure with a maximum in probability at $R \approx d_{solv}$, 2 d_{solv} and 3 d_{solv}, i.e. multiples of the solvent diameter d_{solv}. The solvent structure is transferred to the radical (ion) pair distribution by shifting $g(R)$ by R_c - d_{solv}. By this procedure we assume that the solvent structure around the benzhydryl radical or cation is similar to the one found around a selected solvent molecule. The chlorine radical or anion is thought to replace one of the solvent molecules. In the actual simulations we used the geometric mean $\sqrt{g(R)}$ between a fully structured ($g(R)$) and a random surrounding ($g(R)=1$) to mimic the deviation from spherical symmetry.

The fragments (benzhydryl radicals and cations, chlorine radicals and anions) are assumed to be spherical with radii $r_{benzhydryl}$ and r_{Cl}. The radii were deduced from the cavity volume determined by a DFT calculation in a continuum solvation model. The contact distance

$$R_c = r_{benzhydryl} + r_{Cl} \qquad (S4.11)$$

is found to be practically identical for the radical pair and the ion pair.

In the Smoluchowski operator we use a distance dependent diffusion coefficient $D(R)$ which accounts for the hydrodynamic effects.[12] The diffusion is decelerated from the bulk value D_F when the two fragments are in close vicinity:

$$D(R) = D_F\left[1 - \frac{1}{2}\exp\left(-\frac{R-R_c}{d_{solv}}\right)\right] \qquad (S4.12)$$

The rate for the geminate recombination of the radical and ion pairs is assumed to fall off exponentially ($\alpha \approx 1$ Å^{-1}) with distance, starting with a rate constant $k_{rec,0}$ when the pair is in contact at $R = R_c$:[13]

$$k_{rec}(R) = k_{rec,0} \cdot \exp\left[-\alpha(R-R_c)\right] \qquad (S4.13)$$

S11

The electron transfer rate is described by Marcus theory[14,15]

$$k_{ET}(R) = \frac{2\pi}{\hbar} \cdot \frac{V_{eff}^2}{\sqrt{4\pi\lambda(R)k_B T}} \cdot \exp\left(-\frac{(\lambda(R)+\Delta G_{ET})^2}{4\lambda(R)k_B T}\right) \cdot \exp(-\beta(R-R_c)) \qquad (S4.14)$$

with V_{eff} the effective electronic coupling that incorporates the Franck-Condon factor and ΔG_{ET} the change in Gibbs free energy. The driving force ΔG_{ET} of the different benzhydryl systems ((tol)$_2$CH/Cl, tol(Ph)CH/Cl, Ph$_2$CH/Cl, mfp(Ph)CH/Cl, dfp(mfp)CH/Cl) are derived from quantum chemical calculations (see Section S4.4) and are given in Table S2.

The reorganization energy $\lambda(R)$ is given by

$$\lambda(R) = \lambda_{in} + \frac{e^2}{8\pi\varepsilon_0}\left(\frac{1}{\varepsilon_{op}} - \frac{1}{\varepsilon_{st}}\right) \cdot \left(\frac{1}{r_{benzhydryl}} + \frac{1}{r_{Cl}} - \frac{2}{R}\right) \qquad (S4.15)$$

with λ_{in} the internal reorganization energy and ε_{op} the relative optical permittivity. The last term in eq (S4.14) describes the fall-off of the ET rate with increasing distance from contact. β is around 1 Å^{-1}.[15] We do not use the density of states weighted Franck-Condon factor, since we find that it scales exponentially with R and cannot be distinguished at the constant temperature of our experiments from the $\exp(-\beta(R-R_c))$ factor. It just increases β by a small amount.

We model the distance-dependency of the escape rates with a sigmoid function (see Figure S3a) which is essentially zero at contact distance R_c, reaches half its amplitude at a distance R_{sig} around the second solvation shell and provides for an escape with the full escape rate $k_{esc,\infty}^{RP}$ or $k_{esc,\infty}^{IP}$ for larger distances

$$k_{esc}^{RP}(R) = k_{esc,\infty}^{RP} \cdot \frac{1}{1+\exp\left[-2(R-R_{sig})\right]} \qquad (S4.16)$$

$$k_{esc}^{IP}(R) = k_{esc,\infty}^{IP} \cdot \frac{1}{1+\exp\left[-2(R-R_{sig})\right]} \qquad (S4.17)$$

Escape rates are found to be necessary to reproduce the finite survival probability of radicals and cations found in the experiment. The introduction of k_{esc}^{RP} and k_{esc}^{IP} refine the description of the solvent. The Marcus-Smoluchowski equations (S4.4) and (S4.5) are based on a continuum solvation model where the dielectric constant of the solvent remains invariant for the photofragment separation distance. In other words, the continuum model assumes that the fragments are surrounded with a complete solvation shell for all fragment distances. In actual fact however, a fully stabilizing solvation shell is only formed at distances large enough to accommodate a solvent molecule between the two ions. This leads to a sudden

S12

decrease of the energy of the system as the photofragments move apart and prevents them from reencounter. We model this solvation induced barrier by the introduction of the escape rates.

The escape rates transfer part of the radical (ion) distribution to distributions of nonreactive free radicals (ions). For a consistent description, the "free" distributions are propagated with the Smoluchowski formalism and result in population distributions $P_{FR}(R,t)$ and $P_{FI}(R,t)$ in analogy to eqs (S4.2) and (S4.3). The signals due to bound and free pairs are not differentiated in the experiment and therefore eq. (S4.1) transfers to

$$P_R(t) = \int_{R_c}^{\infty} \left(P_{RP}(R,t) + P_{FR}(R,t) \right) dR \quad (S4.18)$$

$$P_I(t) = \int_{R_c}^{\infty} \left(P_{IP}(R,t) + P_{FI}(R,t) \right) dR \quad (S4.19)$$

These two quantities are directly proportional to the experimental concentrations $c_{radical}(t)$ and $c_{cation}(t)$ as seen in eq. (S1.1). The two coupled differential equations (S4.4) and (S4.5) are solved numerically by the "pdepe"-solver[16] which is part of the MatLab suite. The numerical solution is hereby calculated on a restricted distance interval starting from the contact distance R_c up to a maximum distance R_{max} = 80 Å. Special care was taken to ensure that the outer limit is chosen large enough to assure an unperturbed diffusional separation of the photofragments.

As initial conditions we assume a Gaussian distribution for the radical pairs with a maximum at R_{Gauss} and a HWHM R_{HWHM} of the distribution. The Gaussian distribution is set to 0 for distances smaller than the contact distance R_c

$$S_{RP}(R, t=0) = \begin{cases} A\exp\left[-\ln 2 \left(\dfrac{R - R_{Gauss}}{R_{HWHM}} \right)^2 \right] & , \text{for } R \geq R_c \\ 0 & , \text{for } R < R_c \end{cases} \quad (S4.20)$$

The latter assumption mirrors the experimental observation that not all optically excited molecules lead to radicals or ions. It effectively models the observed internal conversion that likely can be viewed as chlorine fragments bouncing off a solvent molecule to rapidly recombine.

The assumed initial distance distribution of the ion pair population $P_{IP}(R, t = 0)$ has the same shape as the radical pair population. The overall population ratio is set in agreement with the experimental findings.

We use reflecting boundary conditions for both species at contact distance R_c as well as at the maximum R_{max}. Since we treat the geminate recombination as explicit sink terms, the diffusion toward the inner boundary should not lead to an extra loss of population. This translates to[6,17]

$$\left. \frac{dS_{RP}(t,R)}{dR} \right|_{R=R_c} = 0, \quad \left. \frac{dS_{RP}(t,R)}{dR} \right|_{R=R_{max}} = 0$$

$$\left. \frac{dS_{IP}(t,R)}{dR} \right|_{R=R_c} = 0, \quad \left. \frac{dS_{IP}(t,R)}{dR} \right|_{R=R_{max}} = 0 \quad (S4.21)$$

Within the model we make several assumptions. First we assume a low radical pair concentration in order to neglect any crowding effects. This assumption is fully satisfied by the experimental conditions (concentration of excited precursors ≈ 100 µmol/L): together with the dissociation quantum yield ($\Phi_{Hom} \approx 40\%$) the radical pair concentration can be estimated as ~40 µmol/L. Second, our model starts just after the ultrafast bond cleavage process (300 fs).[18,19] As shown in Figure 1 and 2, radical pairs are the initially generated species in a ratio of 20 to 1. Finally, we assume that solvent stabilization occurs faster than the actually observed electron transfer rate $k_{ET}(R)$ ($\tau_{ET} = 1/k_{ET}(R) >> \tau_{solv}$), which is justified for the investigated solvents acetonitrile and dichloromethane with typical relatively fast solvation times τ_{solv} = 140 – 500 fs.[20-23] The focus of our model is on the limiting case of diffusion controlled electron transfer reactions. To investigate the opposite limit of the dielectric relaxation in solvents with slower solvation times (e.g., ethylene glycol or 1-4-dioxane), a straightforward approach within the Sumi-Marcus model would have to be applied.[24-26]
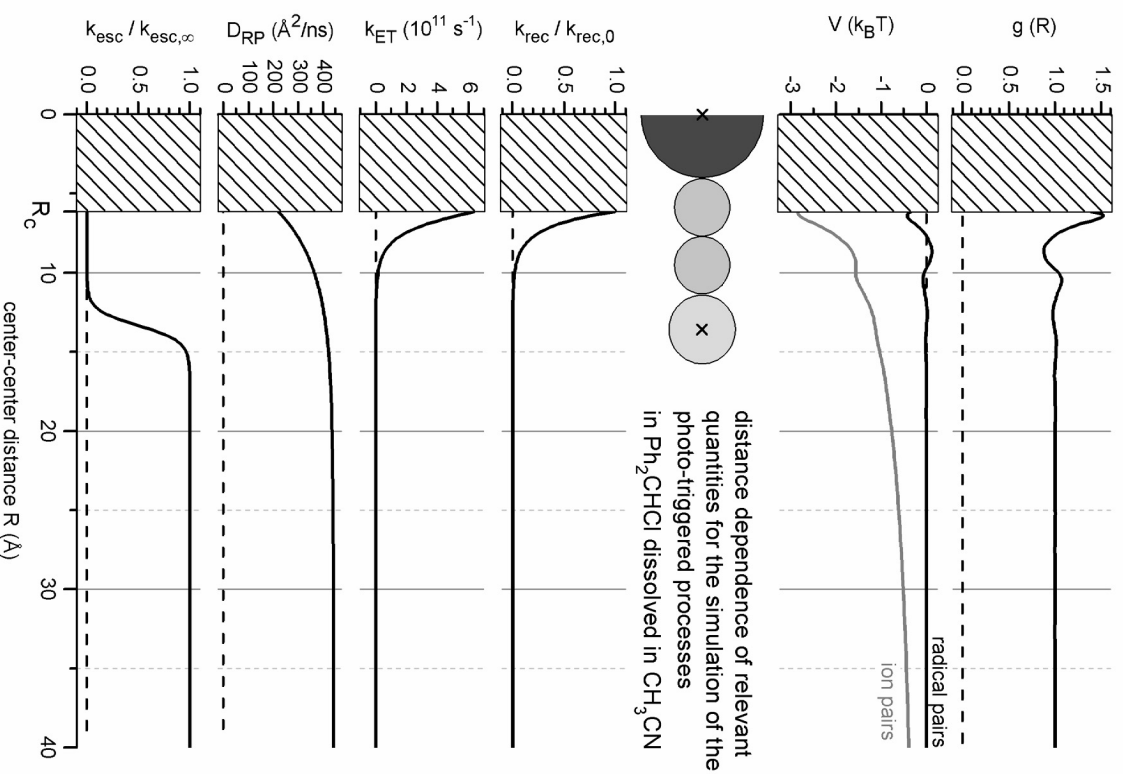
Figure S3a Distance dependence of relevant quantities for the simulation of the photo-triggered processes in Ph$_2$CHCl dissolved in CH$_3$CN.

distance dependence of relevant quantities for the simulation of the photo-triggered processes in Ph$_2$CHCl dissolved in CH$_3$CN

radical pairs
ion pairs

Table S1: Parameters used for the simulation of Scheme 1 according to the model described in S4.1.

parameter		CH$_3$CN	CH$_2$Cl$_2$	Ref.
solvent				
	D_F (RP) (Å^2/ns)	440	342 [a]	27
	D_F (IP) (Å^2/ns)	60	110	this work
	d_{solv} (Å)	3.60	3.79	27,28 / this work
	ε_{op}	1.80	2.02	
	ε_{st}	36.6	8.93	
	T (K)	298		
solute				
	$R_c = r_{benzhydryl} + r_{Cl}$ (Å)	3.96 + 2.17 = 6.13		this work
	$k_{esc,\infty}^{RP}$ (10^9/s)	6.67	6.67	this work
	$k_{esc,\infty}^{IP}$ (10^9/s)	6.67	0	this work
	R_{Sig}	$R_c + 2\,d_{solv}$		this work
electron transfer				
	ΔG_{ET} (eV) [b]	-1.71 (-1.61)	-1.13 (-1.23)	this work
	V_{eff} (cm^{-1}) [c]	57	47	this work
	β (Å^{-1})	0.7		29
	λ_{in} (eV)	0.2		28
recombination				
	$k_{rec,0}^{RP}$ (10^9/s)	300	370	this work
	$k_{rec,0}^{IP}$ (10^9/s)	25	32	this work
	α (Å^{-1})	1.0		13
starting distribution				
	R_{Gauss}	$R_c + 0.5\,d_{solv}$		this work
	R_{HWHM}	1.8 d_{solv}	2.0 d_{solv}	this work

a) Estimated values from comparison of CH$_3$CN with CH$_2$Cl$_2$. b) Driving forces were derived by quantum chemical calculation and are given in parentheses. For details see Section S3.4 and Table S2. c) V_{eff} has been adopted by a fit to the experimental dynamics.

strength due to planarization and solvation of the benzhydryl radicals and cations.[5] Clearly evident from Figure S4 is the non-exponential character of $P_R(t)$ and $P_I(t)$ caused by the diffusion controlled electron transfer from a non-equilibrium radical pair distribution. To illustrate the influence of the escape rates, we additionally ran the simulations without them. The result is shown as dashed green lines for comparison.

For a direct comparison between the simulation and the experimental dynamics we applied the same fit function (eq S2.1) to $P_R(t)$ and $P_I(t)$ as for the evaluation of the transient absorption data (see Section S2). The obtained electron transfer time constant for Ph$_2$CHCl in CH$_3$CN is $\langle \tau_{SE} \rangle = 21.6$ ps; the decay of the ion signal can be fitted with a single exponential time constant of $\tau_{tot} = 1/k_{tot} = 137$ ps reflecting the geminate recombination and diffusion (see Section 3). Both derived lifetimes are in excellent agreement with the experimental results.
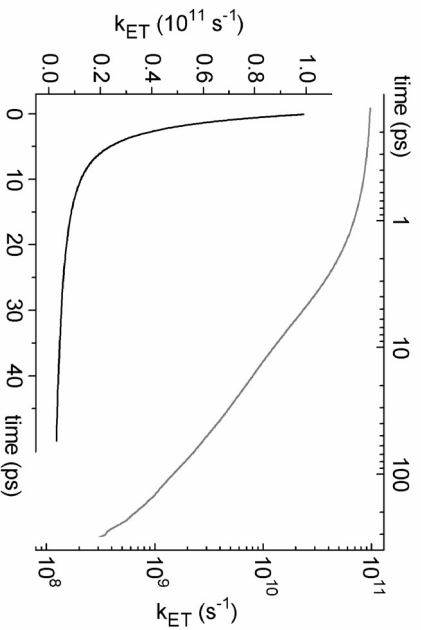
S4.2.2 Time dependent electron transfer rates $k_{ET}(t)$

The good agreement between simulations and experiment allows for a quantitative interpretation of the time and distance dependent populations $P_R(t,r)$ and $P_I(t,r)$ and thus to derive additional information which is not accessible from the experiment

The time dependent ensemble averaged electron transfer rate $k_{ET}(t)$, which is central to the complete reaction process, is determined from the microscopic model by

$$k_{ET}(t) = \frac{\int_{r_0}^{\infty} P_{RP}(t,r) \cdot k_{ET}(r)\, dr}{\int_{r_0}^{\infty} P_{RP}(t,r)\, dr} \qquad (S4.22)$$

$k_{ET}(t)$ is depicted in Figure S5. At very early times ($t < 1$ ps) $k_{ET}(t)$ is close to $(10\ \text{ps})^{-1}$. This results from the combination of the on-contact rate of $667 \times 10^9\ s^{-1}$ and the initial fraction of slightly below 10 % of radical pairs with a small enough distance for efficient ET. As close-to-contact pairs are quickly used up, $k_{ET}(t)$ drops to $10 \times 10^9\ s^{-1}$ at 10 ps. In the long time range diffusion cannot overcome the depletion of the radical distribution in the sub-10 Å range needed for further ET and the effective ET rate drops further to an insignificant level. Diffusion rather increases the average radical distance.

S4.2 Non-exponential processes: comparison between experiment and model calculations

S4.2.1 Transient absorption signal of benzhydryl radicals and cations

The model presented in Section S4.1 is used to investigate the electron transfer between benzhydryl radicals and chlorine radicals in CH$_3$CN and CH$_2$Cl$_2$ subsequent to ultrafast photolysis, the diffusional evolution and the partial recombinations. The input parameters used in the model (taken from literature) and the values determined for the best fit are given in Table S1. The model describes the experimentally observed evolution of the total radical and cation population very well despite the rather complex functional form. In addition, the microscopic model allows us to calculate experimental observables like the ensemble averaged (stretched exponential) electron transfer time τ_{SE} and the quantum yield of generated free radicals and ions.
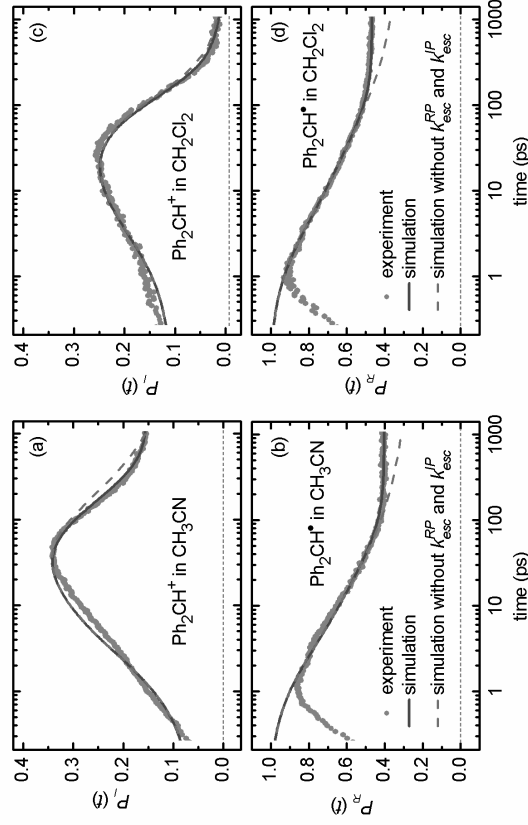
Fig S4: Normalized simulated signals (blue and green) for (a) $P_I(t)$ for Ph$_2$CH$^+$ in CH$_3$CN, (b) $P_R(t)$ for Ph$_2$CH$^\bullet$ in CH$_3$CN; (c) $P_I(t)$ for Ph$_2$CH$^+$ in CH$_2$Cl$_2$ and (d) $P_R(t)$ for Ph$_2$CH$^\bullet$ in CH$_2$Cl$_2$ together with the respective experimental signals (grey dots).

The simulated time evolution of $P_R(t)$ and $P_I(t)$ for Ph$_2$CHCl in CH$_3$CN and CH$_2$Cl$_2$ is depicted in Figure S4 (blue line) as a semi-logarithmic plot. The experimentally observed evolution of the signals (grey dots) are well reproduced from about 1 ps up to the maximum delay time in the experiment. The deviation at the very earliest times can be readily explained by the 300 fs exponential increase in signal

Fig S5: Time-dependent electron transfer rate $k_{ET}(t)$ calculated according to eq S4.15 and displayed once linearly (black curve) and once logarithmically (red curve).

S4.2.3 Evaluation of individual time-dependent rates and yields from the simulation

The ensemble averaged rates $k_{rec}^{IP}(t)$ and $k_{esc}^{IP}(t)$ are derived form the distance dependent rates given in eqs. S4.13 and S4.17 and the population distribution in analogy to the electron transfer rate (eq. S4.22).

The accumulative yield for various processes are determined in the following way. Each sink term in the differential equations S4.4 and S4.5 is added up during the numerical propagation and properly transformed into associated population distributions. To obtain the total yield Y_{ET} of electron transfer, Y_{esc}^{RP} of radical escape and Y_{rec}^{RP} of radical recombination, the distance dependent quantities are integrated over the full range.

The same procedure is used for the ion yields Y_{esc}^{IP} and Y_{rec}^{IP}. All the radical yields are reported in % of the originally generated radical pairs. The ion yields refer to the totally generated ion pairs up to a given time. This includes the small nascent contribution directly from the photoexcitation.

The quantum yields Φ_{rad} and Φ_{cat} are the ratio of the benzhydryl radicals / cations to the optically excited molecules at a given time. Since the model does not account for the finite probability of radical production, we had to fix the lasting radical yield in the model to the experimental values. The according values are shown in Table 2 in parentheses.

S4.3 Quantum chemical calculations: Driving force ΔG_{ET} of the electron transfer

The quantum chemical calculations are performed with the program package Gaussian09.[30] All calculations rely on density functional theory, the geometries of the different precursors, benzhydryl cations and radicals are optimized and confirmed by frequency analysis showing no imaginary frequency. We use the recently developed hybrid meta-GGA functional M06-2X (see Table S2), which has proven to give accurate results for the study of main group thermochemistry.[31] Additionally we tested the popular hybrid functional B3LYP. Implicit solvent effects of acetonitrile, dichloromethane and cyclohexane are included using the integral equation formalism variant of the polarizable continuum model (IEFPCM).[32-34] The thermodynamic data are calculated with two different basis sets, the double ζ basis 6-31G(d) and the triple ζ basis 6-311+G(d). Values obtained with the functional M06-2X and the triple ζ basis (see Table S2) are used slightly adapted in the model of distance dependent electron transfer reactions (see Section S4.2). A further enlargement of the basis set (6-311++G(d,p)) does not improve the calculated Gibbs free reaction energies. The coordinates of the optimized geometries (functional M06-2X and basis set 6-311+G(d)) are given in Section S7 together with the absolute electronic energies.

The Gibbs free reaction energy for the electron transfer (ΔG_{ET}) as well as the driving force of recombination of the radical and ion pairs are calculated at standard conditions (298.15 K and 1.0 bar). The solvation energies for the benzhydryl cations and radicals in CH$_3$CN, CH$_2$Cl$_2$ and cyclohexane are calculated as the difference $\langle \Psi | H + V/2 | \Psi \rangle - \langle \Psi | H | \Psi \rangle$, where H is the electronic Hamiltonian and $V/2$ the perturbation by the solvent reaction field.

Table S2. Gibbs free reaction energy of the electron transfer within the radical pair ΔG_{ET}, of the geminate recombination of the radical pair ΔG_{RP} and the ion pair ΔG_{IP}, as well as the solvation energy of the benzhydryl radical $\Delta G_{solv,rad}$ and cation $\Delta G_{solv,cat}$. The Gibbs free energy values are calculated for different derivatives and solvents (IEFPCM) with DFT (functional M06-2X, basis set 6-311+G(d)). For comparison and validation ΔG_{ET} has also been calculated I with the functional M06-2X, basis set 6-31G(d) and II with functional B3LYP, basis set 6-31G(d).

solvent	Derivative	ΔG_{RP} (eV)	ΔG_{IP} (eV)	$\Delta G_{solv,rad}$ (eV)	$\Delta G_{solv,cat}$ (eV)	$\Delta G_{ET,exp}$ (eV) [a]	ΔG_{ET} (eV)		
								I	II
aceto-nitrile	(tol)$_2$CHCl	-2.539	-0.715	-0.199	-1.681	-1.79	-1.823	-1.707	-1.905
	tol(Ph)CHCl	-2.504	-0.806	-0.196	-1.738	-1.69	-1.698	-1.619	-1.756
	Ph$_2$CHCl	-2.536	-0.924	-0.191	-1.798	-1.68	-1.612	-1.507	-1.658
	mfp(Ph)CHCl	-2.552	-1.075	-0.200	-1.910		-1.477	-1.382	-1.532
	dfp(mfp)CHCl	-2.492	-1.307	-0.206	-2.096		-1.185	-1.106	-1.284
dichloro-methane	(tol)$_2$CHCl	-2.538	-1.087	-0.164	-1.527		-1.451	-1.319	-1.484
	tol(Ph)CHCl	-2.534	-1.218	-0.162	-1.580		-1.316	-1.197	-1.371
	Ph$_2$CHCl	-2.503	-1.271	-0.158	-1.634		-1.232	-1.110	-1.257
	mfp(Ph)CHCl	-2.506	-1.427	-0.168	-1.729		-1.079	-0.974	-1.120
	dfp(mfp)CHCl	-2.485	-1.719	-0.167	-1.887		-0.766	-0.680	-0.860
cyclo-hexane	(tol)$_2$CHCl	-2.575	-2.874	-0.064	-0.853		0.299	0.487	0.350
	tol(Ph)CHCl	-2.519	-2.959	-0.064	-0.884		0.440	0.632	0.478
	Ph$_2$CHCl	-2.571	-3.143	-0.063	-0.914		0.572	0.746	0.601
	mfp(Ph)CHCl	-2.531	-3.288	-0.070	-0.954		0.757	0.908	0.764
	dfp(mfp)CHCl	-2.509	-3.651	-0.078	-1.021		1.142	1.258	1.069

a) experimental values calculated via one electron reduction potentials in acetonitrile for the benzhydryl cations (from Ref. 35) and the Cl• radical (from Ref. 36) vs. SCE.

S5. Effects of variation on the radical and cation yield

S5.1 Temperature variation

The photolysis of Ph₂CHCl in CH₃CN has been measured for a temperature interval from 5 °C to 60 °C.

Table S3. Temperature dependence of the yields and rates of the electron transfer and the geminate recombination after photolysis of Ph₂CHCl in CH₃CN.

T (°C)	Y_{ET} [a] (%)	Y_{esc}^{RP} [b] (%)	Y_{rec}^{RP} [c] (%)	Y_{rec}^{IP} [d] (%)	τ_{SE} (ps)	k_{tot} (10⁹/s)	k_{rec}^{IP} (10⁹/s)	k_{esc}^{IP} (10⁹/s)
5	45.9	37.3	16.8	69.7	11.5	5.88	4.10	1.78
22	42.8	37.8	19.4	69.7	11.1	7.25	5.05	2.19
30	43.2	39.8	17.0	71.1	10.7	6.85	4.88	1.98
40	42.1	41.2	16.8	70.3	9.7	7.69	5.41	2.28
50	40.5	42.7	16.8	69.2	9.2	7.94	5.49	2.44
60	38.4	43.8	17.9	71.1	9.4	8.33	5.92	2.40

[a]) Yield of the electron transfer [b]) Yield of escape by diffusional separation of the radical pair [c]) Yield of recombination of the radical pair [d]) Yield of geminate recombination of the ion pair.
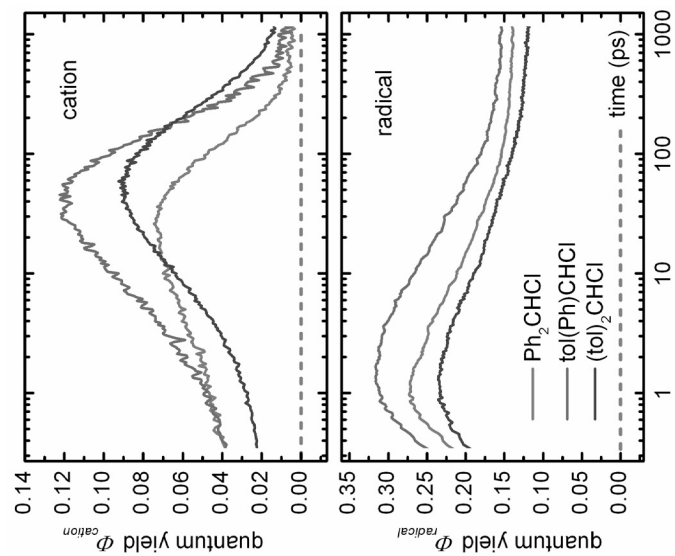
S5.2 Variation of substituents
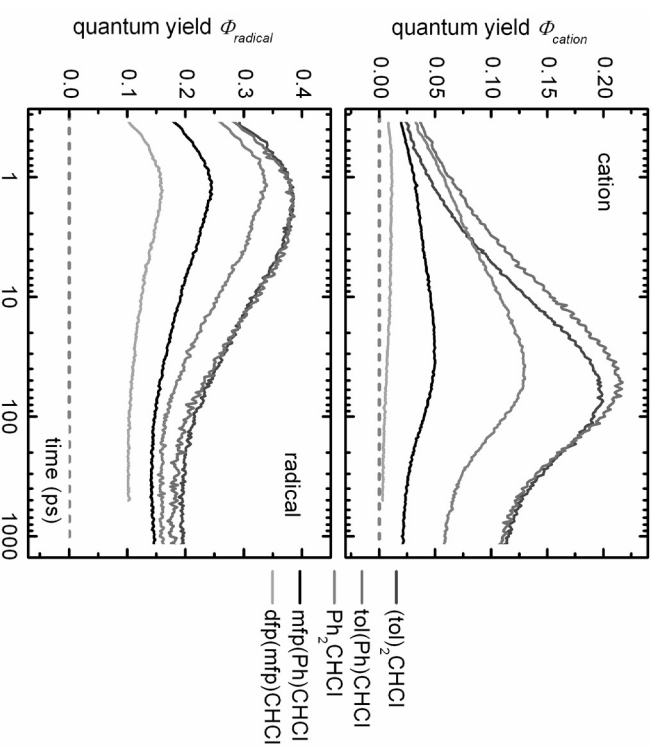
Figure S6 Influence of the substituents on the phenyl rings on the cation and radical quantum yield in acetonitrile.

S5.3 Variation of the solvent

Figure S7 Influence of the substituents on the phenyl rings on the cation and radical quantum yield in dichloromethane.
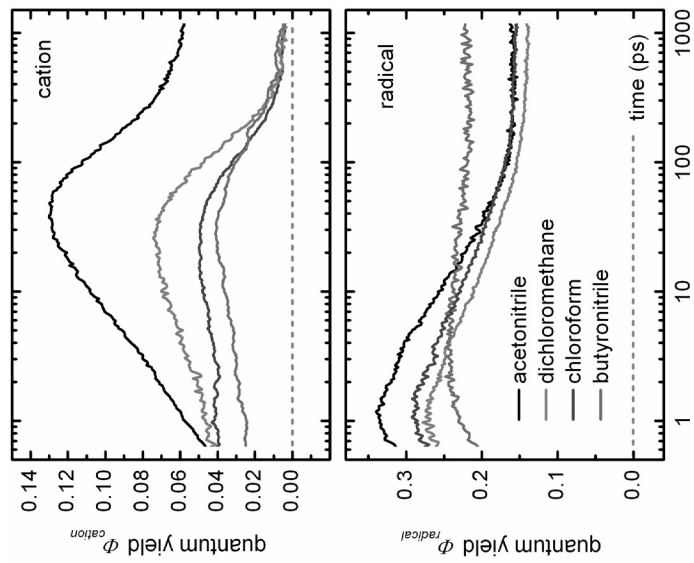
Figure S8 Solvent-dependence of cation and radical quantum yield after UV photoexcitation of Ph_2CHCl in different solvents.

S6. Synthesis of 3,3',5-trifluorobenzhydryl chloride

3,3',5-Trifluorobenzhydryl chloride dfp(mfp)CHCl was obtained from thionyl chloride (1.3 mL, 18 mmol) and 3,3',5-trifluorobenzhydrol[37] (3.00 g, 12.6 mmol) in dichloromethane (10 mL). The crude product was distilled in the vacuum (196–198 °C / 1.1×10^{-2} mbar) to give a colorless oil (2.3 g, 72%).


^{1}H NMR (300 MHz, CDCl$_3$): δ = 5.98 (s, 1 H, CHCl), 6.74 (tt, $^{3}J_{HF}$ = 8.7 Hz, $^{4}J_{HH}$ = 2.3 Hz, 1 H, 4'-ArH), 6.89-7.04 (m, 3 H, ArH), 7.08-7.16 (m, 2 H, ArH), 7.28-7.35 ppm. (m, 1 H, ArH);

^{13}C NMR (75.5 MHz, CDCl$_3$): δ = 61.8 (td, $^{4}J_{CF}$ = 2.3 Hz, $^{4}J_{CF}$ = 2.1 Hz, CHCl), 103.8 (t, $^{2}J_{CF}$ = 25.3 Hz, 4-Ar), 110.7-111.1 (m, AXX'-system, 2,6-Ar), 114.9 (d, $^{2}J_{CF}$ = 23.0 Hz, 2'-Ar or 4'-Ar), 115.7 (d, $^{2}J_{CF}$ = 21.2 Hz, 2'-Ar or 4'-Ar), 123.3 (d, $^{4}J_{CF}$ = 3.0 Hz, 6'-Ar), 130.4 (d, $^{3}J_{CF}$ = 8.3 Hz, 5'-Ar), 142.3 (d, $^{3}J_{CF}$ = 7.2 Hz, 1'-Ar), 144.2 (t, $^{3}J_{CF}$ = 9.0 Hz, 1-Ar), 162.8 (d, $^{1}J_{CF}$ = 247.5 Hz, 3'-Ar), 163.0 ppm. (dd, $^{1}J_{CF}$ = 249.4 Hz, $^{3}J_{CF}$ = 12.1 Hz, 3,5-Ar);

^{19}F NMR (282 MHz, CDCl$_3$): –108.4 – –108.5 ppm. (m, 3,5-F); –111.6 (m, 3'-F).

MS (+EI): m/z (%) = 256.1 (3) [M$^+$], 237.2 (4) 222.2 (36), 221.1 (100) [M–Cl], 219.1 (34), 201.1 (35);

Elemental analysis: Calcd. for C$_{13}$H$_8$ClF$_3$: C, 60.84; H, 3.14, Found: C, 60.61; H, 3.16.
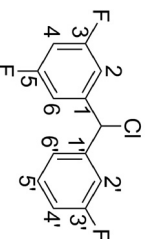
S7. References

(1) Bartl, J.; Steenken, S.; Mayr, H.; McClelland, R. A. *J. Am. Chem. Soc.* **1990**, *112*, 6918-6928.

(2) Megerle, U.; Pugliesi, I.; Schriever, C.; Sailer, C. F.; Riedle, E. *Appl. Phys. B* **2009**, *96*, 215-231.

(3) Sailer, C. F.; Singh, R. B.; Ammer, J.; Riedle, E.; Pugliesi, I. *Chem. Phys. Lett.* **2011**, *512*, 60-65.

(4) Lorenc, M.; Ziolek, M.; Naskrecki, R.; Karolczak, J.; Kubicki, J.; Maciejewski, A. *Appl. Phys. B* **2002**, *74*, 19-27.

(5) Fingerhut, B. P.; Sailer, C. F.; Ammer, J.; Riedle, E.; de Vivie-Riedle, R. *J. Phys. Chem. A*, DOI: 10.1021/jp300986t

(6) Rosspeintner, A.; Kattnig, D. R.; Angulo, G.; Landgraf, S.; Grampp, G. *Chem. Eur. J.* **2008**, *14*, 6213-6221.

(7) Schulten, K. private communication

(8) Saik, V. O.; Goun, A. A.; Nanda, J.; Shirota, K.; Tavernier, H. L.; Fayer, M. D. *J. Phys. Chem. A* **2004**, *108*, 6696-6703.

(9) Weidemaier, K.; Tavernier, H. L.; Swallen, S. F.; Fayer, M. D. *J. Phys. Chem. A* **1997**, *101*, 1887-1902.

(10) Tachiya, M. *Radiat. Phys. Chem.* **1983**, *21*, 167-175.

(11) Metropolis, N.; Rosenbluth, A. W.; Rosenbluth, M. N.; Teller, A. H.; Teller, E. *J. Chem. Phys.* **1953**, *21*, 1087-1092.

(12) Northrup, S. H.; Hynes, J. T. *J. Chem. Phys.* **1979**, *71*, 871-883.

(13) Wojcik, M.; Tachiya, M. *Radiat. Phys. Chem.* **2005**, *74*, 132-138.

(14) Marcus, R. A.; Sutin, N. *Biochim. Biophys. Acta* **1985**, *811*, 265-322.

(15) Barbara, P. F.; Meyer, T. J.; Ratner, M. A. *J. Phys. Chem.* **1996**, *100*, 13148-13168.

(16) Skeel, R. D.; Berzins, M. *SIAM J. Sci. Stat. Comp.* **1990**, *11*, 1-32.

(17) Saik, V. O.; Goun, A. A.; Fayer, M. D. *J. Chem. Phys.* **2004**, *120*, 9601-9611.

(18) Lipson, M.; Deniz, A. A.; Peters, K. S. *Chem. Phys. Lett.* **1998**, *288*, 781-784.

(19) Fingerhut, B. P.; Geppert, D.; de Vivie-Riedle, R. *Chem. Phys.* **2008**, *343*, 329-339.

(20) Horng, M. L.; Gardecki, J. A.; Papazyan, A.; Maroncelli, M. *J. Phys. Chem.* **1995**, *99*, 17311-17337.

(21) Ladanyi, B. M.; Stratt, R. M. *J. Phys. Chem.* **1995**, *99*, 2502-2511.

(22) de Boeij, W. P.; Pshenichnikov, M. S.; Wiersma, D. A. *J. Phys. Chem.* **1996**, *100*, 11806-11823.

(23) Eom, I.; Joo, T. *J. Chem. Phys.* **2009**, *131*, 244507.

(24) Sumi, H.; Marcus, R. A. *J. Chem. Phys.* **1986**, *84*, 4272-4276.

(25) Sumi, H.; Marcus, R. A. *J. Chem. Phys.* **1986**, *84*, 4894-4914.

(26) Wang, H.; Lin, S.; Allen, J. P.; Williams, J. C.; Blankert, S.; Laser, C.; Woodbury, N. W. *Science,* **2007**, *316*, 747-750.

(27) Goun, A.; Glusac, K.; Fayer, M. D. *J. Chem. Phys.* **2006**, *124*, 084504.

(28) Tavernier, H. L.; Kalashnikov, M. M.; Fayer, M. D. *J. Chem. Phys.* **2000**, *113*, 10191-10201.

(29) Page, C. C.; Moser, C. C.; Chen, X.; Dutton, P. L. *Nature* **1999**, *402*, 47.

(30) Gaussian 09, Revision A.02, M.J. Frisch, G. W. Trucks, H. B. Schlegel, G. E. Scuseria, M. A. Robb, J. R. Cheeseman, G. Scalmani, V. Barone, B. Mennucci, G. A. Petersson, H. Nakatsuji, M. Caricato, X. Li, H. P. Hratchian, A. F. Izmaylov, J. Bloino, G. Zheng, J. L. Sonnenberg, M. Hada, M. Ehara, K. Toyota, R. Fukuda, J. Hasegawa, M. Ishida, T. Nakajima, Y. Honda, O. Kitao, H. Nakai, T. Vreven, J. A. Montgomery, Jr., J. E. Peralta, F. Ogliaro, M. Bearpark, J. J. Heyd, E. Brothers, K. N. Kudin, V. N. Staroverov, R. Kobayashi, J. Normand, K. Raghavachari, A. Rendell, J. C. Burant, S. S. Iyengar, J. Tomasi, M. Cossi, N. Rega, J. M. Millam, M. Klene, J. E. Knox, J. B. Cross, V. Bakken, C. Adamo, J. Jaramillo, R. Gomperts, R. E. Stratmann, O. Yazyev, A. J. Austin, R. Cammi, C. Pomelli, J. W. Ochterski, R. L. Martin, K. Morokuma, V. G. Zakrzewski, G. A. Voth, P. Salvador, J. J. Dannenberg, S. Dapprich, A. D. Daniels, O. Farkas, J. B. Foresman, J. V. Ortiz, J. Cioslowski, and D. J. Fox, Gaussian, Inc., Wallingford CT, 2009.

(31) Zhao, Y.; Truhlar, D. G. *Theor. Chem. Account* **2008**, *120*, 215-241.

(32) Caricato, M.; Mennucci, B.; Tomasi, J.; Ingrosso, F.; Cammi, R.; Corni, S.; Scalmani, G. *J. Chem. Phys.* **2006**, *124*, 124520.

(33) Improta, R.; Barone, V.;Scalmani, G.; Frisch, M. J. *J. Chem. Phys.* **2006**, *125*, 054103.

(34) Scalmani, G.; Frisch, M. J. *J. Chem. Phys.* **2010**, *132*, 114110.

(35) Ofial, A. R.; Ohkubo, K.; Fukuzumi, S.; Lucius, R.; Mayr, H. *J. Am. Chem. Soc.* **2003**, *125*, 10906-10912.

(36) Isse, A. A.; Lin, C. Y.; Coote, M. L.; Gennaro, A. *J. Phys. Chem. B* **2011**, *115*, 678-684.

(37) Nolte, C.; Mayr, H. *Eur. J. Org. Chem.* **2010**, 1435-1439.

Appendix D6

Ultrafast photochemical reaction with two product channels: wavepacket motion through two distinct conical intersections

C. F. Sailer, N. Krebs, B. P. Fingerhut, R. de Vivie-Riedle, E. Riedle

Ultrafast photochemistry with two product channels:

wavepacket motion through two distinct conical intersections

Christian F. Sailer [a], Nils Krebs [a], Benjamin P. Fingerhut [b,c], Regina de Vivie-Riedle [b], and

Eberhard Riedle [a]*

[a]   Lehrstuhl für BioMolekulare Optik, Ludwig-Maximilians-Universität (LMU), Oettingenstr. 67, 80538 München, Germany.

[b]   Department Chemie, Ludwig-Maximilians-Universität (LMU), Butenandt-Str. 11, 81377 München, Germany.

[c]   Current address: Chemistry Department, University of California, Irvine, California 92697-2025, United States.

* corresponding author:

Phone: +49-89-2180-9210

Fax: +49-89-2180-9202

e-mail: riedle@physik.uni-muenchen.de

Abstract

Light induced bond-cleavage is an ubiquitous process in large molecules, yet its quantum nature is not fully understood. We present a comprehensive description of the ultrafast light induced C-Cl bond cleavage in diarylmethyl chlorides combining femtosecond transient absorption measurements with ab initio calculations. We observe a delayed appearance of radicals (80 fs) and cations (125 fs). The excited-state wavepacket moves inertially towards two conical intersections and the passing through these intersections determines the partitioning into the differing product channels.

The optical excitation of valence electrons in atoms leads to long lived excited states that can only relax by fluorescence. In polyatomic molecules the extra degrees of freedom provided by the nuclear motion allow for nonradiative decay where part or all of the excitation energy is converted to vibrations. Ultrafast internal conversion from an excited singlet state to a lower one has been found to proceed even on a sub-picosecond scale if the energetic difference between the electronic states is small. More precisely, the geometric distortion leads to points in the 3N-6 dimensional vibrational space (N atoms in the molecule) where states with differing electronic configuration cross and the energy gap vanishes. Strictly speaking, the non-crossing rule of diatomics is not valid for larger systems and the displacement along non-symmetric coupling modes leads to a conical intersection (CoIn) [1-3]. In the vicinity of the CoIn the Born-Oppenheimer separation breaks down completely and highly efficient and rapid photodissociation [4] or isomerization can take place [5,6].

Experimentally, the presence and effectiveness of a CoIn is detected as femtosecond decay of the optical signature attributed to the excited state or the equally fast recovery of the ground state absorption. For a photochemical process the newly appearing product signal serves as indication. The detection and interpretation gets more complex as more than one CoIn is involved. Theory has shown convincing examples for this situation and it now seems to be rather the rule than the exception [1,2,7]. Once the existence of CoIns is accepted, the next step is to move away from the description of the ultrafast process in terms of populations toward the motion of a vibronic wavepacket from the Franck-Condon point toward the CoIn and beyond. This has recently been demonstrated in a particularly comprehensible study of the isomerization of rhodopsin [8].

For many chemical processes not only the channels of return to the ground state and a single product like a ring opened structure [9,10] exist, but two or more product channels. In a classical kinetic description (rate model) one expects a decay of the excited state signal with $\tau = 1/(k_{IC} + k_1 + k_2)$ where k_1 and k_2 are the effective product formation rates and k_{IC} is the internal conversion rate. The products are expected to appear equally fast and the ratio of products is given by $r = k_1/k_2$. From the theoretical point of view the question arises whether one or two CoIns are responsible. To clarify this experimentally, the sole determination of the ultrafast rates is not sufficient. Additional and more specific signatures have to be found.

We investigate the bond cleavage of a benzhydryl chloride in solution that is known to either proceed homolytically (benzhydryl radical + chlorine radical) or heterolytically (benzhydryl cation + chlorine anion). Previously it was found that both processes occur in well under 1 ps and the benzhydryl moieties can be easily distinguished spectroscopically [11-13]. The earlier experiments were performed with a broadband transient absorption spectrometer with

2

high but still limited temporal resolution. We now report two-color measurements with 40 fs resolution. In this way we can uniquely and unambiguously decipher the complex dynamics and show that one of two distinct CoIns is responsible for each reaction channel.

As model system for the two-channel bond cleavage we choose diphenylmethyl chloride (DPMC). The molecule absorbs at 270 nm and below by excitation in the phenyl rings (see Fig. 1b). The bond between the central sp^3 hybridized carbon and the chlorine is eventually broken. If the bond electrons are shared between the fragments (homolysis), the benzhydryl radical with a strong absorption at 327 nm results. If both electrons go to the chlorine (heterolysis), the benzhydryl cation with an absorption centered at 435 nm emerges.
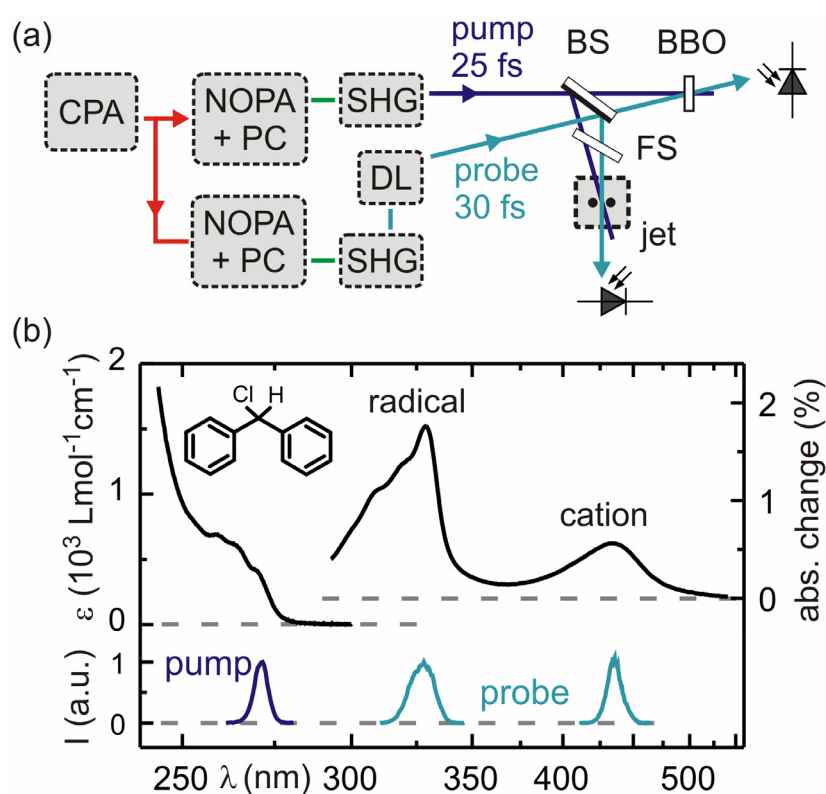

Fig. 1   a) Transient absorption setup. CPA: chirped pulse amplifier; NOPA: noncollinear optical parametric amplifier; PC: prism compressor; SHG: second harmonic generation; DL: delay line; BS: beam splitter; FS: fused silica plate for compensation of dispersion. b) Absorption spectrum of DPMC in acetonitrile (left) and its transient absorption spectrum (right) 5 ps after 270 nm excitation. The spectrum of the pump and the probe pulses are shown below.

For a full resolution of the temporal evolution we use two noncollinear optical parametric amplifiers (NOPA) and frequency doubling (see Fig. 1a). Optimal compression leads to pulses with about 25 fs duration [14]. A mechanical delay line affords the delay between the 270 nm pump pulse and the probe pulse at either 327 or 436 nm. To avoid spurious contribu-

tions from the cell windows, the recordings were performed in a 50 μm free-flowing jet [15]. The evaporating solvent was replenished to ensure a constant optical density. Special care was taken to determine the delay between pump and probe pulse to a single femtosecond accuracy. This was accomplished by splitting both pulses and a second "transfer experiment" (for details see SI). By referencing the transient signal with the shot-to-shot measured pump energy we increase the sensitivity [14].
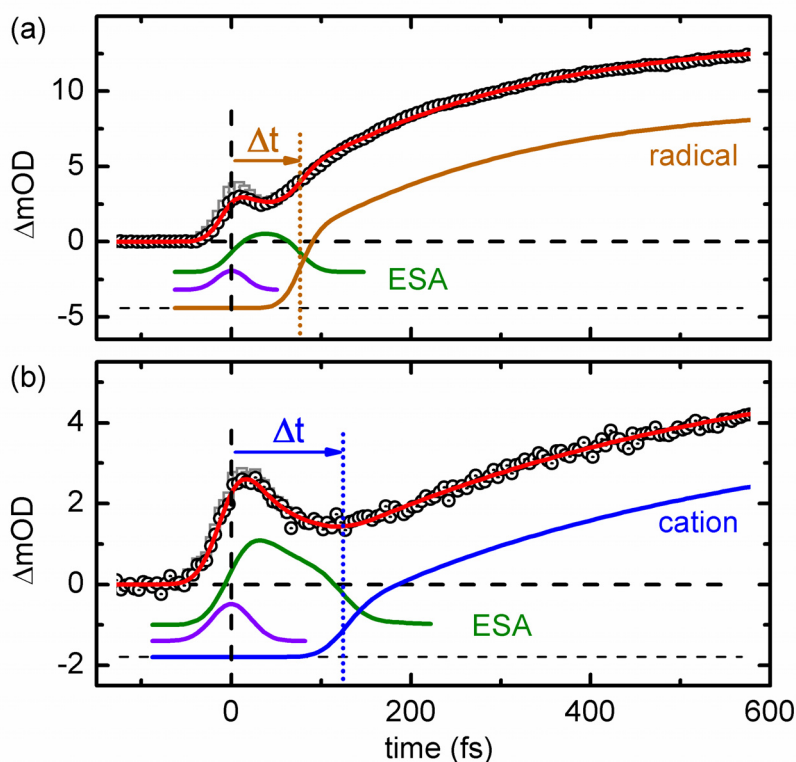

Fig. 2   Transient absorption (black circles) after UV excitation of DPMC in acetonitrile at a) 327 nm (benzhydryl radical) and b) 436 nm (benzhydryl cation). The coherent signal from the solvent is subtracted from the raw data (open grey squares) to yield the pure molecular signal. The fit is shown in red, the excited state absorption (ESA) in green, the coherent signal from the molecule in purple. The product absorption from the cation and radical are shown in blue and orange.

With 200 nJ pump energy focused to 76 μm FWHM we excite about 2 % of the DPMC molecules dissolved in acetonitrile. The large molar extinction coefficient of the fragments (about 50,000 L/mol*cm as compared to 500 L/mol*cm for DPMC) leads to a sizable absorption change at the respective wavelength of each benzhydryl fragment. The time dependence of the transient absorption (see Fig. 2) is the experimental observable that has to be evaluated and interpreted to recover the microscopic reaction dynamics. Through careful monitoring of the beam sizes, sample concentration and pulse energies we obtain not only a picture of the temporal behavior but even the quantitative yields [13].

Roughly 40 % of the excited DPMC dissociates homolytically. The transient signal rises with the cross correlation (CC) of the pump and probe pulse (38 fs FWHM) and falls off within the next tens of femtoseconds (see Fig. 2a). A comparison to the signal measured for pure acetonitrile shows that part of this early signal is due to two-photon absorption in the solvent that is proportional to the Gaussian shaped CC [16]. We correct the raw data (grey squares) by the properly scaled solvent contribution to obtain the pure molecular signal (black circles; compare SI). Even the pure molecular signal still contains a Gaussian shaped contribution centered exactly at delay zero and with a width equal to the optically measured CC. We assign this contribution to a coherent, nonresonant two-photon absorption. One of the pulses prepares a polarization in the molecule and the other pulse adds a second interaction leading to a higher electronic state. This interaction depletes the probe pulse as long as the pump-probe delay is within the CC convoluted with the electronic dephasing time of DPMC of likely a few tens of femtoseconds [17,18].

The remaining population part of the early molecular signal is proportional to the integral of the pump-probe CC as population in the S_1 state is accumulated from the initial polarization and the subsequent electronic dephasing. The signal strength is due to the excited state absorption (ESA) in the Franck-Condon (FC) region. Immediately after the pump pulse the wavepacket accelerates away from the FC point and the signal changes weakly. At a delay $\Delta t = 76$ fs the signal increases significantly within the time resolution. Finally it increases further with a quasi-exponential behavior and a time constant of 270 fs.

Only about 2 % of the excited DPMC dissociates heterolytically and leads to a weak but well detectable transient absorption signal at 435 nm. The temporal behavior is analogous to the radical signal with two exceptions: the delay is now 124 fs and the signal increases much more at later times. The increase from 76 to 124 fs for the delay in signal increase is the decisive difference between the homolytic and the heterolytic channel. Already the clearly non-exponential signal increase in the first 150 fs and even more the different times for the two distinct product channels deviate not only quantitatively but conceptually from the expectation of a rate model with two processes drawing from the same reservoir.

We used the described concepts of the signal evolution to model it quantitatively and to fit values to the data (see SI). The resulting fit is shown in Fig. 2 as red line and fits extremely well for both the radical and the cation. For demonstration of the various contributions we depict the time dependent ESA as green lines and the actual radical or cation contribution as orange and blue curve. For proper modeling the 20 ps electron transfer (ET) within the radical pairs that depletes the radical population and increases the cation population is included [13]. The effective 300 fs increase of both signals has been previously shown to originate from both planarization of the benzhydryls after the bond cleavage and from solvation [12].
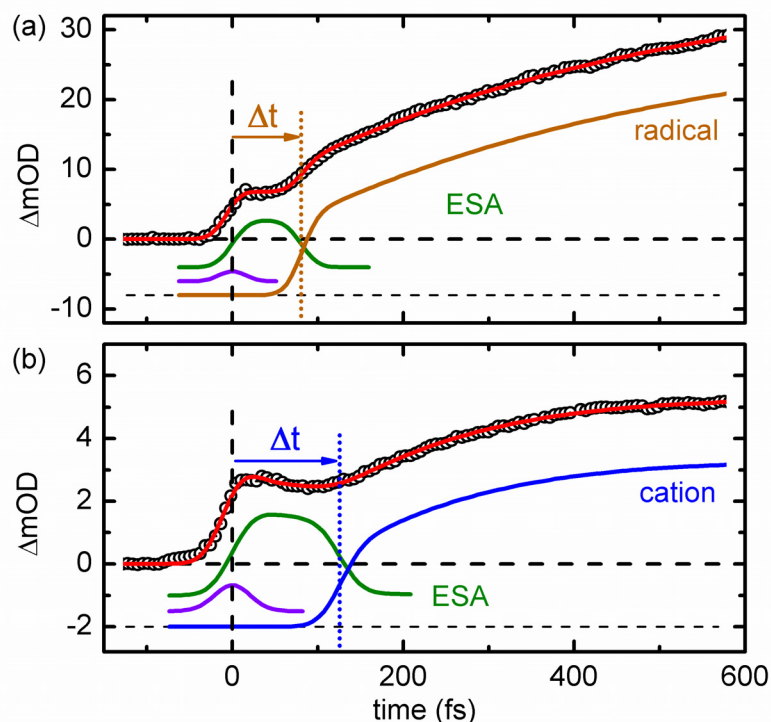
Fig. 3   Transient absorption (black circles) after UV excitation of FDPMC in methanol at a) 327 nm (benzhydryl radical) and b) 427 nm (benzhydryl cation). The coherent signal from the solvent is subtracted. The fit is shown in red, the excited state absorption (ESA) in green, the coherent signal from the molecule in purple. The product absorption from the cation and radical are shown in blue and orange.

The ET in the radical pair is only possible if the cation is better stabilized than the radical. We therefore performed preliminary experiments with the transient absorption setup [19] and found that in methanol the ET does not contribute effectively to the cation generation. DPMC itself is not stable in methanol, but properly substituted derivatives are [20]. We chose the monofluoro-substituted benzhydryl chloride (FDPMC) for additional measurements in methanol. The curves in Fig. 3 demonstrate that the general behavior is quite similar to DPMC and that the strong slow increase due to ET is indeed absent in the cation signal. FDPMC thus allows an even more unambiguous interpretation. As the same features are observed in DPMC and FDPMC, we can readily conclude that the bond cleavage is neither altered by the substitution nor the solvent. It is purely a property of the molecular core. Most importantly, we find times of 81 and 126 fs for the two delays, within experimental precision equal to the times found for DPMC.

From the experimental evidence the involvement of conical intersections (CoIn) in the bond cleavage dynamics can only be inferred indirectly due to the ultrafast reaction times. In a first quantum chemical investigation of DPMC the importance of CoIns for the cation channel was already demonstrated [11]. We now include more electronic states to differentiate be-

tween homolysis and heterolysis and to quantitatively interpret the experimental observations. Calculations were performed on the CASSCF level of theory for the ground and the first five excited singlet states along the bond cleavage coordinate R_{C-Cl}. They were followed by a multi-reference second order perturbation treatment (MRPT2) [21] to obtain accurate excitation energies (see SI). All other coordinates were relaxed at each position of R_{C-Cl}. The potential energy curves are shown in Fig. 4. The optical excitation is allowed in both phenyl rings and leads to the degenerate S_1 and S_1' states with $\pi\pi^*$ character (black and blue lines). Close to the FC-point both states are crossed by the repulsive S_2 and S_2' states, whose electronic structure corresponds to transitions from the Cl lone pair np_x or np_z to the π^* system of the phenyl ring (orange line representing both states). The leading configurations of the S_3 state are of $\pi\pi^*$ and $\pi\sigma^*$ character. Due to the σ^* contribution the S_3 state is also repulsive.
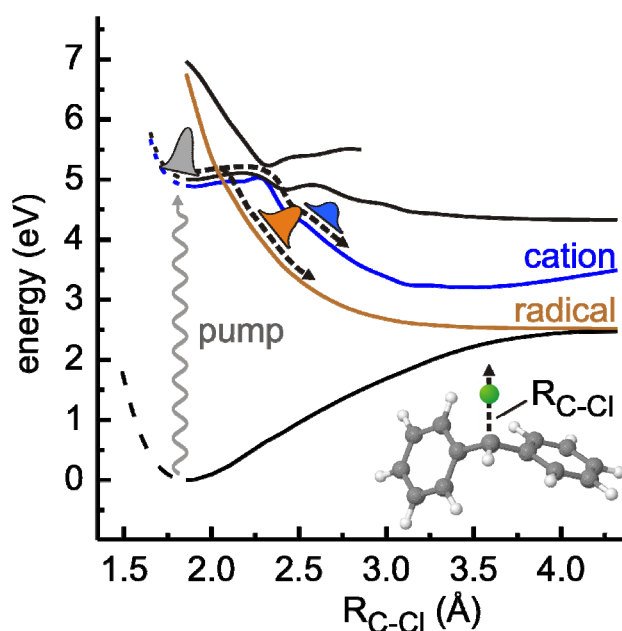

Fig. 4   Potential energy curves along the ground state minimum energy path vs. C–Cl-distance R_{C-Cl} calculated on the CASSCF level of theory. Shown are the ground state S_0, the excited states S_1 (blue turning orange), S_1' (black), S_2 and S_2' (orange turning blue) and S_3 (black).

To highlight the significance of the S_2 and S_2' states they are represented in the diabatic description, all others in the adiabatic description. Coupling among all states is needed to describe the dynamic situation properly. As a result two spatially separated CoIns are found. The first corresponds to bond cleavage into the radical pair and the second into the ion pair. The existence of CoIns does not yet warrant an effective and ultrafast process, but it provides the possibility. Only dynamical calculations can clarify this question [3,22].

For the CoIn leading to the radical pair we performed nonadiabatic on-the-fly molecular dynamics [23,24]. The transition from the originally excited states S_1 and S_1' to the repulsive

7

radical pair states is treated by surface hoping [25] where transitions are possible when two states approach closely in energy and the nonadiabatic coupling becomes large. Of the 52 trajectories roughly a quarter show bond cleavage subsequent to a nonadiabatic $\pi\pi^* \rightarrow np_z$-$\pi^*$ transition. This compares well to the 40 % found experimentally. The potential energies of the electronic states for a typical trajectory are shown as Fig. S6 in the SI and as movie including the atomistic motions. As the DPMC vibrates after the UV excitation, part of the available energy is transferred to kinetic energy of the atoms and the potential energy of the various states changes.

In the trajectory the first CoIn is reached after 45 fs (joining of blue and orange lines). The energies stay closely matched up to about 100 fs when the nonadibatically populated state acquires repulsive character and the curve crossing is finally accomplished. The molecular system follows the orange curve that slopes downward and separates from the blue curve. The evolving electronic character of the system correlates with the radical bond cleavage channel. The time scale of the calculated cleavage is in the same range as the 76 fs found experimentally.

In line with the small probability of 2 % for heterolysis already found experimentally, we do not find evidence for ionic bond cleavage from our set of trajectories. We therefore performed 2D quantum dynamical calculations with a reduced set of electronic states. The optical excitation was confined to one phenyl ring and the repulsive S_2/S_2' states leading to the radicals were omitted to allow propagation of the wavepacket towards the second CoIn. As in the previous investigation [11], the two reactive coordinates R_{CM} and ϕ are used. R_{CM} is the distance between the center of mass of the benzhydryl fragment and the Cl atom. The polar angle ϕ is defined relative to the center of mass of the whole molecule and describes the bending of the Cl atom towards one of the phenyl rings.

The wavepacket first moves to nominally smaller R_{CM} values due to the multidimensional character of the full motion (see Fig. S7 in the SI). At about 110 fs the main part of the wavepacket accelerates to larger values of R_{CM} and reaches a constant speed. The point of acceleration corresponds to the passing of the second CoIn. This CoIn is responsible for the ionic bond cleavage. Again, the experimental value of 124 fs is very close to the result of the 2D wavepacket propagation.

The two dynamical calculations show that both channels given by the two CoIns are indeed active on the ultrafast time scale. They lead to the two distinct products, the benzhydryl radical and the benzhydryl cation. It is most likely from the potential topology that the radical is produced at a slightly earlier time than the cation.

The following overall picture of the photoinitiated processes in DPMC evolves. The system (wavepacket) accelerates from the FC-point upon optical excitation, but it stays in the

shallow minimum for some tens of femtoseconds. The atomic motion is not describable by a single normal mode, but a truly multidimensional motion develops. At close to 100 fs the weak potential barrier is crossed and now the homolytic bond cleavage happens. The experiment suggests a time of 80 fs for the appearance of the radical pair in the electronic ground state. The remaining part of the wavepacket in the excited state proceeds to the second CoIn and at 125 fs ion pairs are generated. This cooperative picture of highest temporal resolution and sensitivity measurements, thorough analysis and high level quantum chemical and dynamical calculation clearly establishes that the ultrafast photochemistry with two product channels is due to wavepacket motion through two distinct conical intersections. The relative reaction yield depends on the detailed motion of the wavepacket and the position of the CoIns. A traditional rate model of two competing stochastic processes cannot explain the dynamics and branching ratio. For many other systems with two ultrafast appearing products, a similar behavior can be expected and a deviation from the traditional rate models will be needed for a correct description.

References

[1]   M. Olivucci, M. A. Robb, and F. Bernardi, *Conformational Analysis of Excited States* (Wiley-VCH, New York, 2000).

[2]   D. R. Yarkony, J. Phys. Chem. A **105**, 6277 (2001).

[3]   W. Domcke, D. R. Yarkony, and H. Köppel, *Conical Intersections: Electronic Structure, Dynamics and Spectroscopy* (World Scientific Publishing, Singapore, 2004).

[4]   S. A. Harich, X. Yang, X. Yang, R. N. Dixon, Phys. Rev. Lett. **87**, 253201 (2001).

[5]   Y. H. Jiang, A. Rudenko, O. Herrwerth, L. Foucar, M. Kurka, K. U. Kühnel, M. Lezius, M. F. Kling, J. van Tilborg, A. Belkacem, K. Ueda, S. Düsterer, R. Treusch, C. D. Schröter, R. Moshammer, and J. Ullrich, Phys. Rev. Lett. **105**, 263002 (2010).

[6]   M. E.-A. Madjet, O. Vendrell, and R. Santra, Phys. Rev. Lett. **107**, 263002 (2011).

[7]   A. Nenov, T. Cordes, T. T. Herzog, W. Zinth, and R. de Vivie-Riedle, J. Phys. Chem. A **114**, 13016 (2010).

[8]   D. Polli, P. Altoè, O. Weingart, K. M. Spillane, C. Manzoni, D. Brida, G. Tomasello, G. Orlandi, P. Kukura, R. A. Mathies, M. Garavelli, and G. Cerullo, Nature **467**, 440 (2010).

[9]   J. L. White, J. Kim, V. S. Petrović, and P. H. Bucksbaum, J. Chem. Phys. **136**, 054303 (2012).

[10]   K. Kosma, S. A. Trushin, W. Fuß, and W. E. Schmid, Phys. Chem. Chem. Phys. **11**, 172 (2009).

[11]   B. P. Fingerhut, D. Geppert, and R. de Vivie-Riedle, Chem. Phys. **343**, 329 (2008).

[12]   B. P. Fingerhut, C. F. Sailer, J. Ammer, E. Riedle, and R. de Vivie-Riedle, J. Phys. Chem. A, DOI: 10.1021/jp300986t

[13]   C. F. Sailer, S. Thallmair, B. P. Fingerhut, C. Nolte, J. Ammer, H. Mayr, R. de Vivie-Riedle, I. Pugliesi, and E. Riedle, submitted.

[14]   C. Schriever, S. Lochbrunner, E. Riedle, and D. J. Nesbitt, Rev. Sci. Instrum. **79**, 013107 (2008).

[15]   F. Milota, J. Sperling, A. Nemeth, and H. F. Kauffmann, Chem. Phys. **357**, 45 (2009).

[16]   M. Lorenc, M. Ziolek, R. Naskrecki, J. Karolczak, J. Kubicki, and A. Maciejewski, Appl. Phys. B **74**, 19 (2002).

[17]   J.-Y. Bigot, M. T. Portella, R. W. Schoenlein, C. J. Bardeen, A. Migus, and C. V. Shank, Phys. Rev. Lett. **66**, 1138 (1991).

[18]   E. T. J. Nibbering, D. A. Wiersma, K. Duppen, Phys. Rev. Lett. **66**, 2464 (1991).

[19]   U. Megerle, I. Pugliesi, C. Schriever, C. F. Sailer, and E. Riedle, Appl. Phys. B **96**, 215 (2009).

[20]   B. Denegri, A. Streiter, S. Jurić, A. R. Ofial, O. Kronja, and H. Mayr, Chem. Eur. J. **12**, 1648 (2006).

[21]   P. Celani, and H.-J. Werner, J. Chem. Phys. **112**, 5546 (2000).

[22]   T. K. Allison, H. Tao, W. J. Glover, T. W. Wright, A. M. Stooke, C. Khurmi, J. van Tilborg, Y. Liu, R. W. Falcone, T. J. Martínez, and A. Belkacem, J. Chem. Phys. **136**, 124317 (2012).

[23]   M. Barbatti, G. Granucci, M. Persico, M. Ruckenbauer, M. Vazdar, M. Eckert-Maksić, and H. Lischka, J. Photochem. Photobiol. A **190**, 228 (2007).

[24]   B. P. Fingerhut, S. Oesterling, K. Haiser, K. Heil, A. Glas, W. J. Schreier, W. Zinth, T. Carell, and R. de Vivie-Riedle, J. Chem. Phys. **136**, 204307 (2012).

[25]   J. C. Tully, J. Chem. Phys. **93**, 1061 (1990).

Ultrafast photochemical reaction with two product channels: wavepacket motion through two distinct conical intersections

Christian F. Sailer [a], Nils Krebs [a], Benjamin P. Fingerhut [b,c], Regina de Vivie-Riedle [b], and Eberhard Riedle [a*]

[a] Lehrstuhl für BioMolekulare Optik, Ludwig-Maximilians-Universität (LMU), Oettingenstr. 67, 80538 München, Germany.

[b] Department Chemie, Ludwig-Maximilians-Universität (LMU), Butenandt-Str. 11, 81377 München, Germany.

[c] Current address: Chemistry Department, University of California, Irvine, California 92697-2025, United States.

Supporting Information

* corresponding author:

Phone: +49-89-2180-9210

Fax: +49-89-2180-9202

e-mail: riedle@physik.uni-muenchen.de

1. Setup for 30 fs UV pump-probe measurements

The experimental setup is shown in Fig. S1. As primary light source we use a regenerative Ti:Sa amplifier system (CPA 2001; Clark MXR). For the pump and probe pulse generation we employ two noncollinear optical parametric amplifiers (NOPA). The NOPA which delivers the pump pulses operates at 540 nm. The pump wavelength of 270 nm is then generated by second harmonic generation in a 35 µm thin BBO crystal. Precompression of the pulses in a fused silica prism compressor in the visible beam ensures that the pulses have a temporal width of the FWHM of about 29 fs at the position of the sample after propagation through all dispersive materials. The pulse length is measured by two photon absorption [1]. Analogously, the probe pulses are generated by frequency doubling in a 62 µm thick BBO crystal and compression is again achieved by a prism compressor in the visible. The pulse length was measured to be about 30 fs and 45 fs for pulses centered at 327 nm and 430 nm, respectively. The spot sizes for the pump beam at the sample position was about 76 µm in size and had a FWHM with a pulse energy of about 200 nJ. The probe was about 45 µm in size and had a pulse energy up to a few nJ.
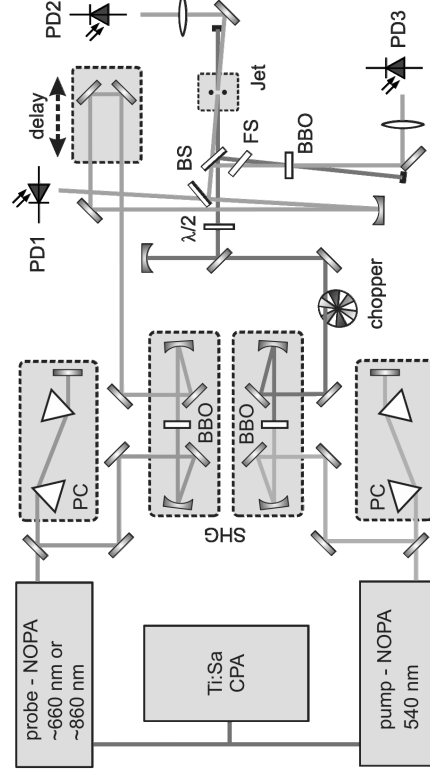

Fig. S1   Scheme of the transient absorption setup. NOPA: noncollinear optical parametric amplifier; PC: prism compressor; SHG: second harmonic generation; BS: beam splitter; FS: fused-silica plate; PD: photo-diode.

The probe intensity fluctuations were measured with a fraction of the probe before transmission through the sample. The change in transmission with and without pump, measured with the photodiode after the sample, was then divided by the probe reference diode signal as described in [2]. To minimize dispersion and coherent artifacts, the sample was a free flowing jet with a thickness of about 50 μm [3]. The increase of the molecular concentration due to evaporation of the solvent was continuously monitored by an absorption spectrometer of our own design that is incorporated into the jet's circuit. A computer controlled pump then refilled the necessary pure solvent to keep the concentration constant.

The absolute zero-time delay, i.e. the timing when the temporal peaks of the Gaussian shaped pump and probe pulses are incident in the sample at the same time, was determined as follows. We generated an additional reference pump-probe branch by splitting a fraction of the probe and the pump beam with a dielectrically coated fused silica UV beam splitter in front of the sample. As the beams are focused before impinging on the beam splitter this generates an identical pump-probe overlapping region as for the transmitted beams. A compensation plate identical to the beam splitter, but without coating, compensates for the difference in dispersion for the two branches.
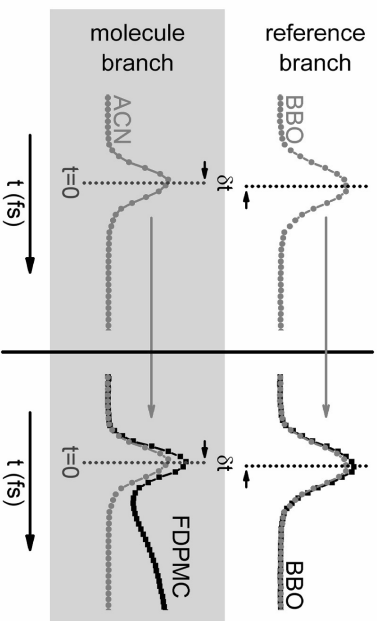

Fig. S2   Scheme for the determination of the absolute time-zero delay (t=0). The reference branch (top) is overlaid for the pure solvent (left) and molecule (right) measurement (lower right). This allows to compare the two measurements with absolute timing precision of better than 4 fs. The time-zero for the molecule measurement is then given by the peak of the pure solvent artifact which is shifted to the reference branch by a slight value of δt.

In the reference pump-probe branch the cross-correlation between the pump and probe pulse was measured via two-photon absorption in a 100 μm thick BBO. The sample branch and the reference branch measurements were recorded in parallel for all measurements. The reference branch cross-correlation can then be used to link the time delay between multiple measurements where only the sample in the jet is changed. The procedure to retrieve the absolute-time zero delay is shown in Fig. S2. Prior to each measurement of the molecular solution the pure solvent artifact was measured in the jet. To link the two successive measurements the two reference arm cross-correlations are then temporally shifted by at most a few femtoseconds to achieve optimal overlap. The pure solvent artifact signal is then correctly overlaid with the molecule measurement in time. This procedure allows us to determine the absolute zero-time delay with a precision of better than 4 fs. It also allows us to determine the amount and temporal profile of the solvent contribution for the molecule measurement.

2. Subtraction of the signal contribution due to the solvent

Part of the measured transient absorption signal after UV excitation of DPMC in acetonitrile or FDPMC in methanol is due to two-photon-absorption in the solvent [4]. Therefore the signal of the neat solvent was always measured before a measurement of the solution. However, in order to subtract the signal of the solvent from the data it has to be scaled properly, since the pump is depleted by the absorption from DPMC or FDPMC.

A transient two-photon absorption (TPA) signal in a pump-probe experiment arises when one pump photon and one probe photon are absorbed to excite a high-lying state. Therefore, for pump and probe pulses propagating along the z-axis with intensities $I_{pump}(z)$ and $I_{probe}(z)$ in a sample of thickness d, the absorption of the probe pulse due to TPA can be expressed as:

$$A_{TPA} = const. \cdot I_{probe} \int_0^d I_{pump}(z)\,dz,$$
(S1)

This assumes that the attenuation of the probe by one or two photon absorption is small. This is justified for our experimental conditions.

In neat solvent the one-photon absorption for the pump is very small and the intensity is approximately constant. Then the signal amplitude is given by:

$$A_{TPA,solvent} = const. \cdot I_{probe} \int_0^d I_{pump,0}\,dz = const. \cdot I_{probe}I_{pump,0}\,d$$
(S2)

For the solution containing the absorbing molecule (concentration c, molar absorption coefficient ε), the pump intensity decays exponentially within the sample layer:

$$I_{pump,solution}(z) = I_{pump,0} \cdot 10^{-\varepsilon c z} \qquad (S3)$$

The amplitude of the two-photon absorption signal can then be expressed as:

$$A_{TPA,solution} = const. \cdot I_{probe} \int_0^d I_{pump,0} \cdot 10^{-\varepsilon c z} dz$$

$$= \frac{const. \cdot I_{probe}\, I_{pump,0}}{\varepsilon c \ln 10}\left(1 - 10^{-\varepsilon c d}\right)$$

and the ration between the two amplitudes becomes:

$$\frac{A_{TPA,solution}}{A_{TPA,solvent}} = \frac{1}{\varepsilon c d \ln 10}\left(1 - 10^{-\varepsilon c d}\right) = \frac{1}{OD \ln 10}\left(1 - 10^{-OD}\right) \qquad (S4)$$

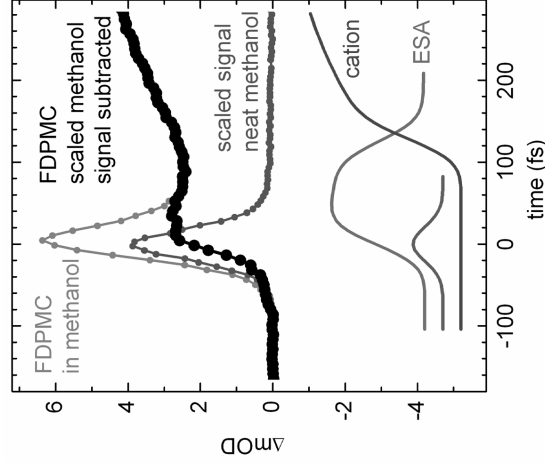with the optical density of the sample OD at the pump wavelength.

Fig. S3   Subtraction of the scaled transient signal in neat methanol (brown) from the raw data of FDPMC in methanol (grey) leads to the molecular transient signal of FDPMC (black). For ease of comparison the contributions from the ESA (green), the benzhydryl cation (blue) and the coherent signal from FDPMC (purple) are shown below.

The OD of the solution in the experiment was 0.11 for DPMC and 0.31 for FDPMC. This

leads to a scaling factor for the two-photon absorption signal in neat solvent of 0.88 in the case of DPMC and 0.71 for FDPMC. In Figure S3 the subtraction of the scaled solvent contribution is shown for FDPMC in methanol when the transient absorption is probed at 427 nm.

3. Decomposition of the signal contributions

Several processes and the resulting possible optical transitions contribute to the transient absorption signal measured after UV excitation of DPMC in acetonitrile or FDPMC in methanol:

- two-photon absorption in the solvent as discussed in Section 2

- coherent, non-resonant two-photon absorption from the solute

- a short-lived excited state absorption (ESA) directly after UV excitation

- the product absorption of benzhydryl cations or radicals which appears delayed with respect to the optical excitation

- the strong increase of the benzhydryl cation and radical absorption with a time constant of ~ 300 fs due to planarization and solvation [5].

The Jablonski diagram of DPMC and the benzhydryl radical as the main photoproduct is shown in Figure S4a. Figure S4b depicts the temporal evolution of the optical signal at the maximum wavelength of the radical band. The pump pulse generates a wavepacket in the S_1 state of DPMC. The probe pulse can now be depleted by the $S_n \leftarrow S_1$ transition (ESA, green arrow). The wavepacket evolves towards the first conical intersection (CoIn) and after a time delay of Δt the CoIn is reached. Here, the major part of the wavepacket couples to the potential energy surface which leads to radical pairs and the ESA vanishes. The newly formed benzhydryl radicals are in the electronic ground state and can be detected via the $D_5 \leftarrow D_0$ transition. The subsequent planarization of the radical and solvation leads to a strong signal increase [5] with a time constant of ~300 fs. An analogous discussion can be made for the cation channel with the exception of a longer time delay due to the later encounter of the second CoIn.
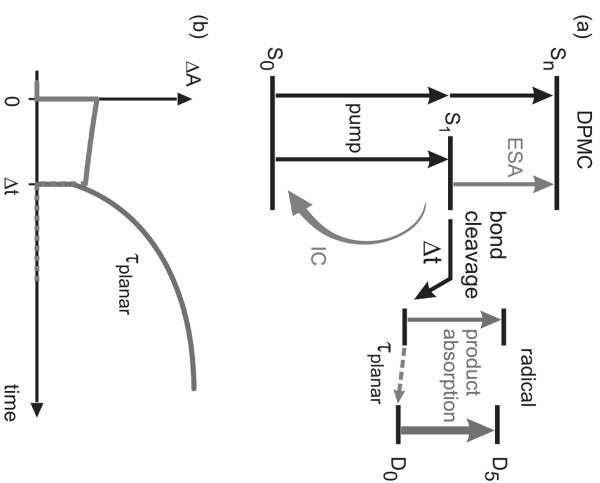
Fig. S4 (a) Jablonski diagram showing the involved transitions and processes after UV irradiation of DPMC in acetonitrile when the radical channel is probed. (b) Scheme of the corresponding transient absorption signal for the same transitions and processes.

The measured time-dependent transient absorption changes shown in Figure 2 and 3 in the manuscript are fitted with a LabView routine which is slightly modified compared to the one described in Ref. [6]. The fit function F(t) can account for signal contributions starting with time zero as well as for contributions starting with a temporal delay Δt with respect to time zero:

$$F(t) = \mathrm{IRF}(t) \otimes \Big\{ A_{\mathrm{coherent}}\, \delta(t) + \Theta(t) \cdot \Theta(\Delta t - t)\Big[A_{\mathrm{ESA},\infty} + A_{\mathrm{ESA}} \exp\Big(-\frac{t}{\tau_{\mathrm{ESA}}}\Big)\Big]$$
$$+ \Theta(t - \Delta t) \cdot \Big[A_{\mathrm{product,initial}} + A_{\mathrm{planar}} \Big(1 - \exp\Big(-\frac{t - \Delta t}{\tau_{\mathrm{planar}}}\Big)\Big)\Big]\Big\}$$

(S5)

The kernel of the fit function consists of

- A δ function centered at $t = 0$ with amplitude A_{coherent} which accounts for the coherent signal contribution of the molecule.

- A constant and a fast decaying absorption which is multiplied by two step functions $\Theta(t)$ and $\Theta(\Delta t- t)$. This reproduces the instantaneous ESA with a possible, small decay due to the wavepacket motion and the sudden disappearance of the ESA at $t = \Delta t$ when the CoIns are reached.

- A constant and a rising absorption which are multiplied by the step function $\Theta(t-\Delta t)$. This accounts for the delayed dynamics of the photoproducts (i.e., benzhydryl radical and cation). It reproduces the absorption of the unrelaxed photofragments after their generation at $t = \Delta t$ and the signal rise due to planarization and solvation.

- Further, delayed exponential dynamics can also be fitted (not shown in Eq. S5). It is needed to account for the evolution of the signal on the tens to hundreds of picosecond scale due to electron transfer and geminate recombination [7] and rotational relaxation.

The kernel is convoluted with the instrumental response function (IRF(t)) to account for the finite temporal evolution of the experiment. The IRF(t) is a Gaussian function with the temporal FWHM given by the width of the CC measured in pure solvent.

4. Calculation of the potential energy curves

To rationalize the bond-cleavage process investigated in the experiment, one dimensional potential energy curves are calculated along the C-Cl distance of DPMC from the FC-region to the dissociation limit. In the electronic ground state all remaining coordinates are relaxed during the C-Cl elongation. Along these minimum energy path coordinates the first five excited singlet states were evaluated. The calculations were performed on the CASSCF (14/12) level of theory with the 6-31G* split valence double zeta basis set, using the program package Molpro [8]. The 12 molecular orbitals forming the complete active space are two bonding and two anti-bonding π orbitals for each phenyl ring; the bonding and anti-bonding C–Cl σ orbital and the two lone pair n orbitals of the Cl-atom. Accurate excitation energies (253 nm (calc.)/ 270 nm (exp.)) are obtained by a subsequent multi-reference second order perturbation treatment (MRPT2) which takes into account the dynamic electron correlation [9,10]. The active space is designed to follow the electronic structure changes in the ground and the first five excited states of singlet symmetry along the bond-cleavage reaction coordinate. The resulting potential energy curves are shown in Fig. 4.

The optical excitation corresponds to a $\pi\pi^*$ excitation and populates the S_1 state. This excitation is possible from both phenyl rings and leads to the two nearly degenerate singlet states S_1 and S_1' in the FC-region. Both show a local minimum with a geometry very similar

(a) DPMC — Jablonski diagram with S_0, S_1, S_n, pump, ESA, IC, bond cleavage, Δt, radical, τ_{planar}, product absorption, D_0, D_5.
(b) ΔA vs time with τ_{planar}, Δt.

to the ground state. They are crossed close to their minimum structure (at 2.1 Å) by the two repulsive states S_2 and S_2'. S_2 and S_2' correspond to an excitation from the Cl lone pair n_{px} or n_{pz}, respectively, to the first π^* orbital of the phenyl ring. Due to admixtures form $n_p\sigma^*$ character in the electronic structure both states lead directly to the homolytic bond cleavage for increasing C-Cl distances with the benzhydryl radical and the Cl radical as products. At the curve crossing C-Cl distances $(S_1, S_1')/(S_2, S_2')$ electron/hole exchange between the n_p Cl orbitals and the π orbitals of the phenyl ring occurs leading to the repulsive S_1 $n_p\sigma^*$ configuration.

The leading configurations of the S_3 state are of $\pi\pi^*$ and $\pi\sigma^*$ character. Due to the σ^* contribution the S_3 state is also repulsive. However, this state correlates to the heterolytic bond cleavage channel, yielding the benzhydryl cation and the Cl anion as products. Due to geometrical reasons the S_3 state only interacts with the S_1 state. Crossing between both states with exchange of the electronic configuration ($\pi\pi^*$-$\sigma\sigma^*$) occurs at a C-Cl distance of 2.3 Å, which is slightly larger than for the S_2 and S_2' state crossing and is controlled by the overlap of the phenyl ring π- and the C-Cl σ-system. Due to the torsion between the phenyl rings (torsion angle between rings: 79.5°, see Fig. S5) only one phenyl ring is oriented favorable to allow the overlap between the π and σ system. The S_1' state is nearly unaffected and thus not involved in the energy transfer processes leading to bond cleavage.

In summary, after photo excitation the degenerate $\pi\pi^*$ states S_1 and S_1' are populated. Early curve crossings occur with the lone pair states $n_p\pi^*/n_p\sigma^*$ and a $\pi\sigma^*$ state in quick succession. The two crossing events correlate to the two different bond cleavage channels.
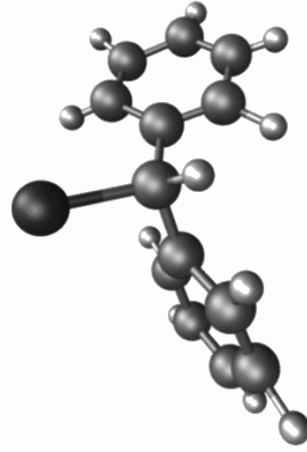

Fig. S5 S_0 equilibrium geometry of DPMC.

5. On-the-fly molecular dynamics calculations

To obtain a first insight into the dynamical behavior in full dimension, we performed on-the-fly calculations with a newly developed ONIOM approach for non-adiabatic on-the-fly molecular dynamics simulations (NA-O-MD) described in detail in Ref. [11]. In brief, we follow the idea of the hybrid partitioning approach ONIOM [12,13] where the complete system is separated in a high level quantum mechanical part and a low level quantum mechanical part. Steric effects and ground state polarization effects of the complete molecule are included on the QM/QM level of theory. The high level quantum mechanical (QM) part refers to one phenyl-ring and the central C-atom with the H- and Cl-atom attached to it. From the quantum chemical calculation of the potential energy curves it is clear that the excitation and bond cleavage process can be well described by considering the π system of one phenyl ring and its interaction with the C-Cl σ bond system and the n_p lone pair orbitals of the Cl atom, thus omitting the S_1' state from the start. This allows to reduce the CASSCF space now comprising three bonding and three anti bonding π orbitals, the bonding and anti bonding C-Cl σ orbitals and the n_p lone pair orbitals of the Cl atom (CASSCF (12,10)). The additional π orbitals ensure accurate excitation energies without the need of MRPT2, which is still out of reach for trajectory calculations. Within this high level QM part the electronic excitation, the subsequent bond rearrangement, the energy transfer processes and the bond cleavage can be described.

The ONIOM-NA-O-MD [11] treats the nuclei classically by Newton's equation of motion and the electronic states as QM degrees of freedom. The quantum mechanical nature of radiationless transitions in the vicinity of crossings between potential energy surfaces due to conical intersections is incorporated in the surface-hopping approach [14,15]. The performed ONIOM dynamics of the DPMC is based on the NewtonX program [16], which requires the evaluation of the electronic ONIOM wavefunction in every timestep. Our implementation [11] of the ONIOM method into the NewtonX framework allows for the evaluation of excited state and ground state gradients, as well as derivative coupling vectors within the CLS approximation [17]. It links the program packages Molpro [8] and Gaussian [18], and provides a balanced multi-state CASSCF(12/10) wavefunction on the high level QM part for the on-the-fly dynamics. For the initial conditions of the trajectories an uncorrelated Wigner distribution of the electronic ground state of the complete system was sampled and 52 trajectories were generated for the NA-O-MD simulations. Due to convergence problems of the electronic wavefunction 11 trajectories are discarded. From the remaining 41 trajectories 13 reach the curve crossing S_1/S_2 and S_1/S_2' between the $\pi\pi^*$ state and the $n_p\pi^*/n_p\sigma^*$ states.

An exemplary trajectory is shown in Fig. S6. and in a movie provided as electronic SI.

The actually populated state is marked by dots. Like in all trajectories, showing population transfer or bond cleavage, the energy gap between S_1/S_2 (bound $\pi\pi^*$ and repulsive $n_p\pi^*$) is significantly reduced for the first time at t ~ 45 fs but no instantaneous cleavage is observed. Population transfer between S_1 (blue turning orange) and S_2 (orange turning blue) occurs thereafter. It takes up to 100 fs for the curve crossing to be accomplished and the purely repulsive configuration to be reached. This leads to the radical formation, observable as degeneration of the S_0 state (black) and the actual S_1 state (orange).

From the ONIOM-NA-O-MD simulations on DPMC we can conclude that the observed retardation in the radical signal arises from the initial motion in the bound $\pi\pi^*$ potential. The CoIn with the repulsive $n_p\pi^*$ state is reached subsequent to an initial motion on the time scale of 80 to 100 fs.
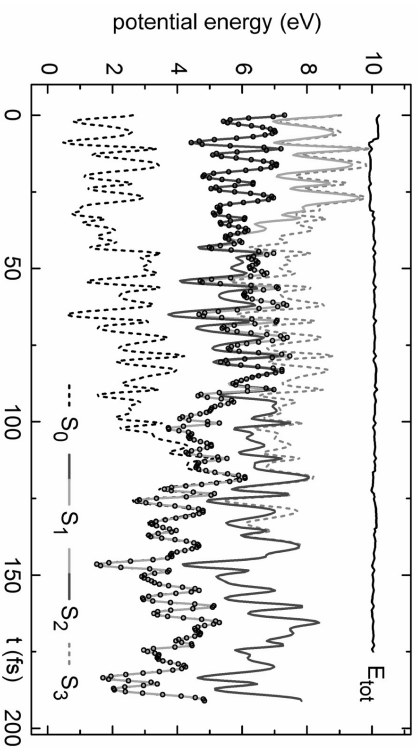

Fig. S6 Exemplary trajectory for the bond cleavage process in DPMC. Shown are the electronic energies of the ground state S_0 (black), the excited state S_1 (blue turning orange), S_2 (orange turning blue) and S_3 (gray-dashed). S_3 corresponds to S_2' in the FC region, i.e. during the first 35 fs. After the conical intersection S_1/S_2 is passed, the leading configuration of the S_1 state is a $n_p\sigma^*$ configuration directly correlated to the radical formation channel. S_2 and S_3 (S_2') change their character to $\pi\pi^*$ and $\pi\sigma^*$ configurations at the same time.

6. Wavepacket dynamics in a two-dimensional subspace

Two-dimensional quantum dynamical calculations were performed on a potential surface spanned by two reactive coordinates, R_{CM} and ϕ. They elucidate the wavepacket dynamics after photoexcitation. R_{CM} is the distance between the center of mass of the benzhydryl frag-

11

ment and the Cl atom. The polar angle ϕ is defined relative to the center of mass of the whole molecule and describes the bending of the Cl atom towards one of the phenyl ring [19]. Due to computational costs the complete active space of DPMC was reduced to one phenyl ring and the C–Cl σ bond system, thus focusing on the conical intersection (CoIn) between S_1 and S_3 describing the $\pi\pi^*$–σσ* electron/hole transfer and the heterolytic bond cleavage. The repulsive S_2 and S_2' states leading to the radicals were omitted to allow efficient propagation of the wavepacket towards the second CoIn. For details of the calculation see Ref. [19]. Fig. S7 shows the time evolution of the wavepacket in the adiabatic S_1 state after excitation with an ultrafast pulse. The 2D wavepacket is projected onto the bond cleavage coordinate R_{CM}. The time evolution is shown as false-color plot. For some time the wavepacket remains in the small valley close to the FC point, before it reaches the CoIn S_3/S_1. After a propagation time of 110 fs the main part of the wavepacket has passed the intersection region and has left the FC area towards the heterolytic bond cleavage channel which correlates to the ionic products. A small portion of the wavepacket follows with a further time delay of about 100 fs.
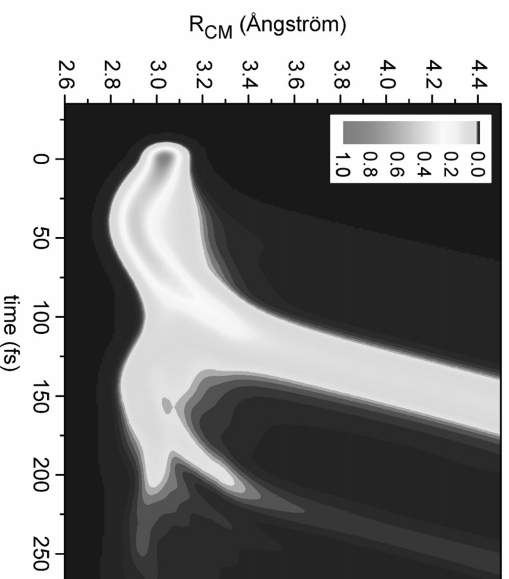

Fig. S7 Time evolution of the wavepacket in the adiabatic S_1 state after excitation with an ultrafast pulse. The time evolution of the wavepacket was followed on two dimensional potential energy curves spanned by two reactive coordinates R_{CM} and ϕ; for details see [19]. The two-dimensional wavepacket is projected onto the bond cleavage coordinate R_{CM} and the time evolution is shown as false-color plot with the wavepacket's amplitude encoded in the color code.

12

7. References

[1] C. Homann, N. Krebs, and E. Riedle, Appl. Phys. B **104**, 783 (2011).

[2] C. Schriever, S. Lochbrunner, E. Riedle, and D. J. Nesbitt, Rev. Sci. Instrum. **79**, 013107 (2008).

[3] S. Laimgruber, H. Schachenmayr, B. Schmidt, W. Zinth, and P. Gilch, Appl. Phys. B **85**, 557 (2006).

[4] M. Lorenc, M. Ziolek, R. Naskrecki, J. Karolczak, J. Kubicki, and A. Maciejewski, Appl. Phys. B **74**, 19 (2002).

[5] B. P. Fingerhut, C. F. Sailer, J. Ammer, E. Riedle, and R. de Vivie-Riedle, J. Phys. Chem. A, published online, DOI: 10.1021/jp300986t.

[6] U. Megerle, I. Pugliesi, C. Schriever, C. F. Sailer, and E. Riedle, Appl. Phys. B **96**, 215 (2009).

[7] C. F. Sailer, S. Thallmair, B. P. Fingerhut, C. Nolte, J. Ammer, H. Mayr, R. de Vivie-Riedle, I. Pugliesi, and E. Riedle, submitted.

[8] H.-J. Werner, P. J. Knowles, R. Lindh, F. R. Manby, M. Schätz et al., MOLPRO, version 2006.1, a package of ab initio programs 2006, see http://www.molpro.net.

[9] H. J. Werner, Mol. Phys. **89**, 645 (1996).

[10] P. Celani, and H. J. Werner, J. Chem. Phys. **112**, 5546 (2000).

[11] B. P. Fingerhut, S. Oesterling, K. Haiser, K. Heil, A. Glas, W. J. Schreier, W. Zinth, T. Carell, and R. de Vivie-Riedle, J. Chem. Phys. **136**, 204307 (2012).

[12] T. Vreven and K. Morokuma, J. Chem. Phys. **113**, 2969 (2000).

[13] M. J. Bearpark, F. Ogliaro, T. Vreven, M. Boggio-Pasqua, M. J. Frisch, S. M. Larkin, M. Morrison, and M. A. Robb, J. Photochem. Photobiol. A **190**, 207 (2007).

[14] J. C. Tully, J. Chem. Phys. **93**, 1061 (1990).

[15] S. Hammes-Schiffer, and J. C. Tully, J. Chem. Phys. **101**, 4657 (1994).

[16] M. Barbatti, G. Granucci, M. Persico, M. Ruckenbauer, M. Vazdar, M. Eckert-Maksić, and H. Lischka, J. Photochem. Photobiol. A **190**, 228 (2007).

[17] M. J. Bearpark, S. M. Larkin, and T. Vreven, J. Phys. Chem. A **112**, 7286 (2008).

[18] M. J. Frisch, G. W. Trucks, H. B. Schlegel et al., GAUSSIAN 03, Gaussian, Inc., Wallingford, CT, 2004.

[19] B. P. Fingerhut, D. Geppert, and R. de Vivie-Riedle, Chem. Phys. **343**, 329 (2008).

Danksagung

An dieser Stelle möchte ich mich bei all denjenigen herzlich bedanken, die mich im Laufe dieser Arbeit mit Rat und Tat unterstützt haben. Mein besonderer Dank gilt dabei:

Herrn **Prof. Eberhard Riedle** für die herausragende wissenschaftliche Betreuung sowie sein großes persönliches Engagement bei der Aufklärung spannender Fragestellungen. Sein Spürsinn für interessante Themen führten dabei zu vielen neuen Ideen und Erkenntnissen. Durch die mit ihm geführten Diskussionen gewann ich viele neuen Einsichten und Ideen – auch abseits des Physikeruniversums.

Herrn **Prof. Herbert Mayr** für viele interessante und fruchtbare Diskussionen rund um die untersuchte Chemie. Die von ihm eingebrachten Ideen und Ansätze sowie die Zurverfügungstellung der großen Anzahl an Ausgangssubstanzen bereicherten diese Arbeit sehr.

Frau **Prof. Regina de Vivie-Riedle** für die vielen Rechnungen und Diskussionen im Lauf der letzten Jahre. Die Vermittlung verschiedener Konzepte der theoretischen Chemie erwiesen sich dabei als besonders wertvoll.

Herrn **Prof. Wolfgang Zinth**, der die Fortschritte des Projektes und dieser Arbeit stets mit Interesse verfolgte.

Herrn **Dr. Igor Pugliesi** für viele interessante Gespräche über Spektroskopie, Auswertungsstrategien sowie über Fragen der Molekülphysik. Des Weiteren war seine Bereitschaft, kleine ab initio Rechnungen „anzuwerfen" um aktuelle Fragen beantworten zu können, sehr hilfreich.

Johannes Ammer und **Dr. Christoph Nolte** für die Synthese der meisten der in dieser Arbeit gemessenen Ausgangssubstanzen. Die mit Johannes geführten Diskussionen halfen darüber hinaus, die chemische Nomenklatur und Sichtweise zu verstehen.

Sebastian Thallmair und **Dr. Benjamin Fingerhut** für die inzwischen unzähligen theoretischen Rechnungen und Studien, die sie im Umfeld dieser Arbeit durchgeführt haben. Ohne die dadurch gewonnenen Ergebnisse wären viele Einblicke verwehrt geblieben

Nils Krebs, dessen experimentelles Geschick die direkte Messungen des Benzhydrylchlorid-Bindungsbruch in überragender Qualität ermöglichte.

„meinen" Bachelor-Studenten **Christoph Grill**, **Lothar Maisenbacher**, **Florian Hinzpeter**, **Robert Heyer** und **Henry Schurkus** für ihren unermüdlichen Einsatz im Labor und die dabei gewonnenen Erkenntnisse.

meinen aktuellen und ehemaligen Kollegen am BMO, die es schafften eine angenehme Atmosphäre am Lehrstuhl zu erzeugen. Stellvertretend für die große Anzahl an Leuten seien hier nur **Maximilian Bradler, Christian Homann**, **Dr. Uwe Megerle** und **Matthias Wen-**